frontiers | Research Topics

Insights in synaptic neuroscience 2022

Edited by
Karri P. Lamsa and Alfredo Kirkwood

Coordinated by
P. Jesper Sjöström

Published in
Frontiers in Synaptic Neuroscience
Frontiers in Neuroscience

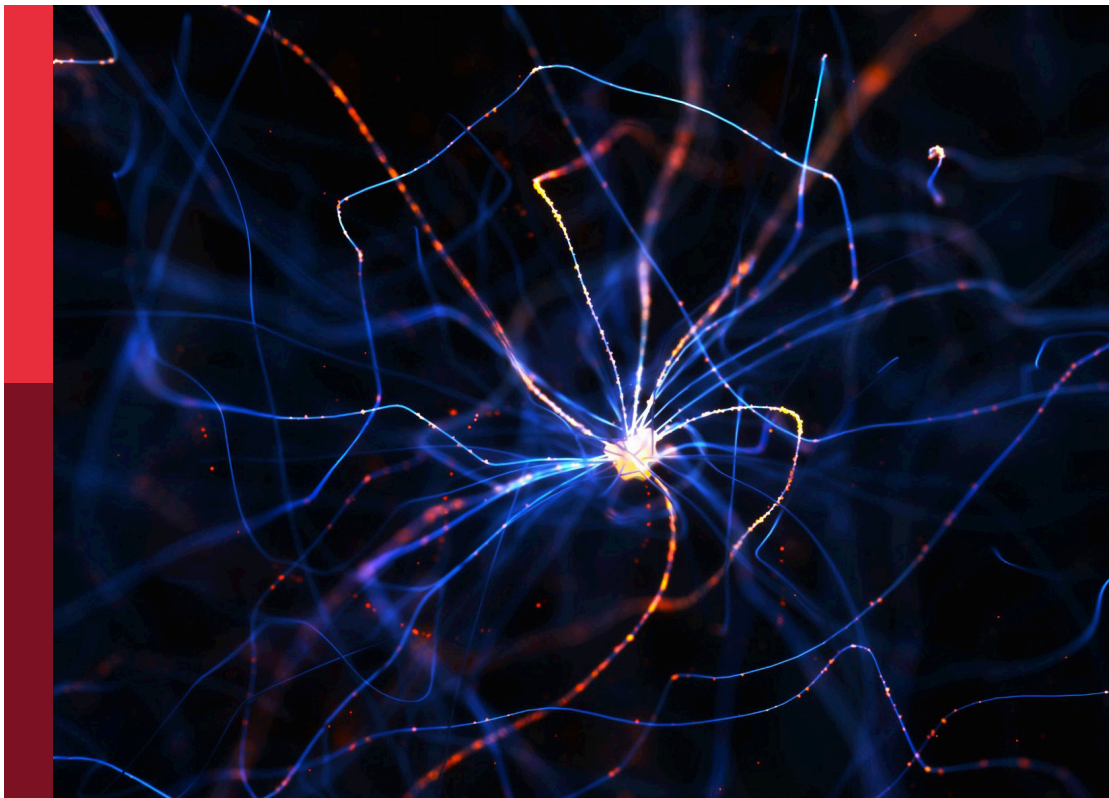

FRONTIERS EBOOK COPYRIGHT STATEMENT

The copyright in the text of individual articles in this ebook is the property of their respective authors or their respective institutions or funders. The copyright in graphics and images within each article may be subject to copyright of other parties. In both cases this is subject to a license granted to Frontiers.

The compilation of articles constituting this ebook is the property of Frontiers.

Each article within this ebook, and the ebook itself, are published under the most recent version of the Creative Commons CC-BY licence. The version current at the date of publication of this ebook is CC-BY 4.0. If the CC-BY licence is updated, the licence granted by Frontiers is automatically updated to the new version.

When exercising any right under the CC-BY licence, Frontiers must be attributed as the original publisher of the article or ebook, as applicable.

Authors have the responsibility of ensuring that any graphics or other materials which are the property of others may be included in the CC-BY licence, but this should be checked before relying on the CC-BY licence to reproduce those materials. Any copyright notices relating to those materials must be complied with.

Copyright and source acknowledgement notices may not be removed and must be displayed in any copy, derivative work or partial copy which includes the elements in question.

All copyright, and all rights therein, are protected by national and international copyright laws. The above represents a summary only. For further information please read Frontiers' Conditions for Website Use and Copyright Statement, and the applicable CC-BY licence.

ISSN 1664-8714
ISBN 978-2-8325-5050-2
DOI 10.3389/978-2-8325-5050-2

About Frontiers

Frontiers is more than just an open access publisher of scholarly articles: it is a pioneering approach to the world of academia, radically improving the way scholarly research is managed. The grand vision of Frontiers is a world where all people have an equal opportunity to seek, share and generate knowledge. Frontiers provides immediate and permanent online open access to all its publications, but this alone is not enough to realize our grand goals.

Frontiers journal series

The Frontiers journal series is a multi-tier and interdisciplinary set of open-access, online journals, promising a paradigm shift from the current review, selection and dissemination processes in academic publishing. All Frontiers journals are driven by researchers for researchers; therefore, they constitute a service to the scholarly community. At the same time, the *Frontiers journal series* operates on a revolutionary invention, the tiered publishing system, initially addressing specific communities of scholars, and gradually climbing up to broader public understanding, thus serving the interests of the lay society, too.

Dedication to quality

Each Frontiers article is a landmark of the highest quality, thanks to genuinely collaborative interactions between authors and review editors, who include some of the world's best academicians. Research must be certified by peers before entering a stream of knowledge that may eventually reach the public - and shape society; therefore, Frontiers only applies the most rigorous and unbiased reviews. Frontiers revolutionizes research publishing by freely delivering the most outstanding research, evaluated with no bias from both the academic and social point of view. By applying the most advanced information technologies, Frontiers is catapulting scholarly publishing into a new generation.

What are Frontiers Research Topics?

Frontiers Research Topics are very popular trademarks of the *Frontiers journals series*: they are collections of at least ten articles, all centered on a particular subject. With their unique mix of varied contributions from Original Research to Review Articles, Frontiers Research Topics unify the most influential researchers, the latest key findings and historical advances in a hot research area.

Find out more on how to host your own Frontiers Research Topic or contribute to one as an author by contacting the Frontiers editorial office: frontiersin.org/about/contact

Insights in synaptic neuroscience 2022

Topic editors
Karri P. Lamsa – University of Szeged, Hungary
Alfredo Kirkwood – Johns Hopkins University, United States

Topic coordinator
P. Jesper Sjöström – McGill University, Canada

Citation
Lamsa, K. P., Kirkwood, A., Sjöström, P. J., eds. (2024). *Insights in synaptic neuroscience 2022*. Lausanne: Frontiers Media SA.
doi: 10.3389/978-2-8325-5050-2

Table of contents

frontiers | Frontiers in Synaptic Neuroscience

TYPE Editorial
PUBLISHED 10 June 2024
DOI 10.3389/fnsyn.2024.1432259

Check for updates

OPEN ACCESS

EDITED AND REVIEWED BY
Dirk Feldmeyer,
Helmholtz Association of German Research Centres (HZ), Germany

*CORRESPONDENCE
P. Jesper Sjöström
jesper.sjostrom@mcgill.ca

RECEIVED 13 May 2024
ACCEPTED 24 May 2024
PUBLISHED 10 June 2024

CITATION
Lamsa KP, Kirkwood A and Sjöström PJ (2024) Editorial: Insights in synaptic neuroscience 2022. *Front. Synaptic Neurosci.* 16:1432259. doi: 10.3389/fnsyn.2024.1432259

COPYRIGHT
© 2024 Lamsa, Kirkwood and Sjöström. This is an open-access article distributed under the terms of the Creative Commons Attribution License (CC BY). The use, distribution or reproduction in other forums is permitted, provided the original author(s) and the copyright owner(s) are credited and that the original publication in this journal is cited, in accordance with accepted academic practice. No use, distribution or reproduction is permitted which does not comply with these terms.

Editorial: Insights in synaptic neuroscience 2022

Karri P. Lamsa[1,2], Alfredo Kirkwood[3] and P. Jesper Sjöström[4,5]*

[1]Hungarian Centre of Excellence for Molecular Medicine Research Group for Human Neuron Physiology and Therapy, Szeged, Hungary, [2]Department of Physiology, Anatomy and Neuroscience, University of Szeged, Szeged, Hungary, [3]Department of Neuroscience, Mind/Brain Institute, Johns Hopkins University, Baltimore, MD, United States, [4]Centre for Research in Neuroscience, Brain Repair and Integrative Neuroscience Program, Department of Neurology and Neurosurgery, The Research Institute of the McGill University Health Centre, Montreal General Hospital, Montreal, QC, Canada, [5]Department of Medicine, The Research Institute of the McGill University Health Centre, Montreal General Hospital, Montreal, QC, Canada

KEYWORDS

plasticity, synaptic release, neurotransmission, cortex, cell type

Editorial on the Research Topic
Insights in synaptic neuroscience 2022

Introduction

We are delighted to present the inaugural "*Insights in synaptic neuroscience 2022*" Research Topic. With this Research Topic, our goal was to shed light on the progress made in the past decade in the neuroscience field and on its future challenges to provide a thorough overview of the status of the art of the synaptic neuroscience field. We thus wished to showcase high-impact and authoritative articles on topical research at the frontiers of synaptic neuroscience, to highlight the diversity of research performed in the field of synaptic neuroscience. We originally aimed chiefly for review articles, but we are happy to report that the majority of works in this Research Topic ended up being original research. Below follows a brief editorial discourse of the papers in our Research Topic of articles.

Papers in this Research Topic

Long-term and structural forms of plasticity

In this Research Topic, Piette, Gervasi et al. reviews the recent development of synaptic plasticity investigation in intact brain in experimental animals. Fast development of methods and analyses of *in vivo* brain electrophysiology in unanesthetized animals, with molecular techniques to manipulate cellular plasticity mechanisms, enable neuronal plasticity studies under more and more naturalistic conditions in the brain. Piette, Gervasi et al. demonstrate with various examples how novel methodology allows us to study new research hypotheses closely linked to real-life brain functions and brain-body communication.

Chokshi et al. explored how the history of neural activity influences synaptic plasticity in the brain. Previous research showed that exposure to darkness followed by light re-exposure leads to a rapid weakening of excitatory synapses onto layer 2/3 pyramidal neurons in the primary visual cortex. The authors tested whether the period in the dark changed cortical plasticity such that the activity elicited by the re-exposure to light depressed the layer 2/3 synapses. To that end they first recorded *in vivo* in primary visual cortex the spike patterns evoked by re-exposure to light and subsequently they replayed theses spike patterns *ex-vivo* in slices from dark-exposed and in normal reared control mice. This stimulation, and also a Poisson pattern with the average rate both reduce the synaptic strength in the slices from dark-exposed missed, but not in the slices from control mice. These findings suggest that the history of visual experience alters how neurons in primary visual cortex respond to stimulation and that rapid synaptic depression can occur through various neural activity patterns.

Synaptic formation and establishment of long-term plasticity are orchestrated by protein complexes, and recent genomic and proteomic studies have uncovered new molecules possibly involved in these processes. In this Research Topic, León et al. provide an overview of the structure and molecular mechanisms by which glycoprotein M6a participates in synapse formation and maintenance. They summarize evidence collected from patients carrying mutations in the *GPM6A* gene, animal models, and *in vitro* studies that together suggest important role for M6a in normal function of synapses and in neurological conditions.

Tyro3 is a receptor tyrosine kinase that is expressed in neurons across several key brain areas such as striatum, neocortex, hypothalamus, and hippocampus. Despite this widespread expression, the role of Tyro3 has been unknown. Combining a battery of approaches—e.g., electron microscopy, patch-clamp electrophysiology, cell culturing, acute slices, and Tyro3 knockout mice—Miao et al. tightly link Tyro3 to the maturation of glutamatergic synapses. For instance, Tyro3 helps drive translocation of GluA2 AMPA receptor subunits to the plasma membrane. The authors propose that postsynaptic Tyro3 signals to coordinate activity that consolidates Hebbian synaptic plasticity. This study thus provides a hitherto unappreciated perspective on this receptor tyrosine kinase.

Another much more well-studied receptor is the ionotropic N-methyl-D-aspartate receptor (NMDAR), which is key mediator of glutamatergic neurotransmission and subcellular signaling. NMDARs famously signal via calcium to trigger synaptic plasticity, in particular long-term potentiation, but this capacity to flux calcium is to a large extent determined by NMDAR subunit composition. In their study, Beesley et al. reveal that NMDAR subunit composition can in fact be determined in acute brain slices using confocal microscopy and antibody labeling. This is an important achievement because elucidating NMDAR subunit composition is key to understanding NMDAR function, yet the subunit-specific pharmacology for NMDARs has long been less than adequate.

Endogenous release of nitric oxide plays a key role in the induction and establishment of synaptic long-term potentiation of excitatory synapses to hippocampal pyramidal cell apical dendrites, but not to their basal dendrites. Ivanova et al. compared synaptic inputs to apical and basal dendrites of these neurons and found a difference in their function indicating distinct contribution of GluA2-lacking AMPA receptors. Although the GluA2-lacking receptors are present both in apical and basal dendrites, their contribution to synaptic transmission in apical dendrites is higher than in basal dendrites, and the nitric oxide synthase blockade flattens this difference. The results show that inhibition of nitric oxide synthase selectively reduces signaling through GluA2-lacking AMPAR to the apical dendrites, a feature which may contribute to establishment long-term potentiation in these excitatory synapses.

Endocannabinoids are important signaling molecules during neuronal development in the brain and retina, and they regulate maturation of axons of projection neurons. Del Rio et al. analyzed axonal arbors of retinal ganglion cells following targeted downregulation of cannabinoid receptor type 1 (CB1R) in Xenopus tadpoles and exposing them to pharmacologic agents. They found that retinal ganglion cells modulated their axonal growth through CB1R signaling, and that the endogenous cannabinoid signaling also contributed to structural differentiation of postsynaptic neuron dendrites in optic tectum in the brain. Their study shows that alterations in endocannabinoid levels in a developing embryo regulated neuronal connectivity through pre- and postsynaptic sites in the intact brain. The study highlights sensitivity of developing brain to exposure to cannabinoids.

Synaptic release and neurotransmission

In neurotransmitter release, four modes of synaptic vesicle cycling have been identified, yet it has remained unclear which are most biologically relevant. To address this, Paksoy et al. explored the role of clathrin in synaptic vesicle recycling at the calyx of Held under physiological conditions. They relied on the clathrin inhibitor Pitstop-2 combined with serial sectioning scanning electron microscopy to reveal that, under biologically plausible conditions, clathrin plays a role in synaptic vesicle recycling from both large endosomes as well as the plasma membrane.

The balance between glutamatergic excitatory and GABAergic inhibitory synaptic transmission is crucial for information processing in the neocortex. Moreover, even transient disruptions in this balance during early development can contribute to neuropsychiatric disorders later in life. Notably, in the KI mouse line mice the haplodeficiency of the GABA synthetizing enzyme GAD67 does not result in epileptic activity and only in mild behavioral deficits. The examination by Ueberbach et al. confirmed the expected decrease in fast inhibitory synaptic activity in in this mouse line, yet network activity was seemingly balanced by a compensatory increased tonic activation of the slow $GABA_B$ receptors. In turn, the enhanced $GABA_B$ receptors were likely to result from increased GABA release via GABA transporter 3 (GAT-3) working in reverse mode.

Cell types of deep cortical layers

The frontal eye field in primates contains diverse neurons with different functions. While some neurons signal movement and fixation, others also respond to visual stimuli. However, identifying distinct cell types has been challenging. In this Research Topic, Piette, Vandecasteele et al. examined biophysical properties of deep layer pyramidal neurons in slices and identified two main subtypes: one with low resistance and low excitability, and another with high resistance and strong excitability. These findings suggest the presence of at least two distinct populations of deep-layer neurons in the frontal eye field, which has implications for understanding visual attention and saccade production.

The precuneus—which is part of the human posteromedial cortex—contributes to processing of multimodal information including emotion, social behavior, and spatial cognition. In an anatomical study of human brain tissue that relied on Nissl and Golgi stains, Fuentealba-Villarroel et al. reveal that the presence of elongated spindle-shaped neurons in cortical layer 5 that are suggestive of von Economo neurons. These neurons are of interest, because they can be found in humans and other primates, but not in all mammals. A tentative link between these neurons and neuropsychiatric disorders involving the precuneus highlights the need for a better and more detailed understanding of this intriguing cell type.

Concluding remarks

To summarize, this Research Topic has highlighted recent advances in synaptic neuroscience. We hope and expect that this Research Topic will inspire, inform, and provide direction and guidance to researchers in the emerging subfield of synaptic neuroscience. We would like to extend our gratitude to all the authors who contributed.

Author contributions

KL: Writing – original draft, Writing – review & editing. AK: Writing – original draft, Writing – review & editing. PJS: Writing – original draft, Writing – review & editing.

Funding

The author(s) declare financial support was received for the research, authorship, and/or publication of this article. KL was funded by the Ministry of Culture and Innovation of Hungary from the National Research, Development and Innovation Fund, TKP2021-EGA funding scheme, Project No. 2022-2.1.1-NL-2022-00005, financed under the 2022-2.1.1-NL funding scheme, and EU's Horizon 2020 No. 739593. AK acknowledges funding from NIH grants EY025922 and AG009973. PJS was supported by CIHR Project Grants: 191969 and 191997 as well as by NSERC Discovery Grant: RGPIN-2024-06712.

Acknowledgments

The authors would like to thank Alanna Watt for help and useful discussions.

Conflict of interest

The authors declare that the research was conducted in the absence of any commercial or financial relationships that could be construed as a potential conflict of interest.

The author(s) declared that they were an editorial board member of Frontiers, at the time of submission. This had no impact on the peer review process and the final decision.

Publisher's note

All claims expressed in this article are solely those of the authors and do not necessarily represent those of their affiliated organizations, or those of the publisher, the editors and the reviewers. Any product that may be evaluated in this article, or claim that may be made by its manufacturer, is not guaranteed or endorsed by the publisher.

frontiers in Synaptic Neuroscience

ORIGINAL RESEARCH
published: 15 April 2021
doi: 10.3389/fnsyn.2021.663282

Naturalistic Spike Trains Drive State-Dependent Homeostatic Plasticity in Superficial Layers of Visual Cortex

Varun Chokshi[1,2†], *Bryce D. Grier*[1,3†], *Andrew Dykman*[1], *Crystal L. Lantz*[4], *Ernst Niebur*[1,3], *Elizabeth M. Quinlan*[4,5] *and Hey-Kyoung Lee*[1,2,3,6*]

[1]*The Zanvyl-Krieger Mind/Brain Institute, Johns Hopkins University, Baltimore, MD, United States,* [2]*Cell Molecular Developmental Biology and Biophysics (CMDB) Graduate Program, Johns Hopkins University, Baltimore, MD, United States,* [3]*The Solomon H. Snyder Department of Neuroscience, Johns Hopkins School of Medicine, Baltimore, MD, United States,* [4]*Department of Biology, University of Maryland, College Park, MD, United States,* [5]*Neuroscience and Cognitive Science Program, Brain and Behavior Institute, University of Maryland, College Park, MD, United States,* [6]*The Kavli Neuroscience Discovery Institute, Johns Hopkins University, Baltimore, MD, United States*

The history of neural activity determines the synaptic plasticity mechanisms employed in the brain. Previous studies report a rapid reduction in the strength of excitatory synapses onto layer 2/3 (L2/3) pyramidal neurons of the primary visual cortex (V1) following two days of dark exposure and subsequent re-exposure to light. The abrupt increase in visually driven activity is predicted to drive homeostatic plasticity, however, the parameters of neural activity that trigger these changes are unknown. To determine this, we first recorded spike trains *in vivo* from V1 layer 4 (L4) of dark exposed (DE) mice of both sexes that were re-exposed to light through homogeneous or patterned visual stimulation. We found that delivering the spike patterns recorded *in vivo* to L4 of V1 slices was sufficient to reduce the amplitude of miniature excitatory postsynaptic currents (mEPSCs) of V1 L2/3 neurons in DE mice, but not in slices obtained from normal reared (NR) controls. Unexpectedly, the same stimulation pattern produced an up-regulation of mEPSC amplitudes in V1 L2/3 neurons from mice that received 2 h of light re-exposure (LE). A Poisson spike train exhibiting the same average frequency as the patterns recorded *in vivo* was equally effective at depressing mEPSC amplitudes in L2/3 neurons in V1 slices prepared from DE mice. Collectively, our results suggest that the history of visual experience modifies the responses of V1 neurons to stimulation and that rapid homeostatic depression of excitatory synapses can be driven by non-patterned input activity.

Keywords: metaplasticity, homeostatic plasticity, synaptic depression, visual experience, mEPSCs, miniature excitatory postsynaptic currents, Poisson stimulation

OPEN ACCESS

Edited by:
Lu Chen,
Stanford University, United States

Reviewed by:
Suk-Ho Lee,
Seoul National University, South Korea
Pete Wenner,
Emory University, United States

****Correspondence:***
Hey-Kyoung Lee
heykyounglee@jhu.edu

†These authors have contributed equally to this work and share first authorship

Received: *02 February 2021*
Accepted: *22 March 2021*
Published: *15 April 2021*

Citation:
Chokshi V, Grier BD, Dykman A, Lantz CL, Niebur E, Quinlan EM and Lee H-K (2021) Naturalistic Spike Trains Drive State-Dependent Homeostatic Plasticity in Superficial Layers of Visual Cortex. Front. Synaptic Neurosci. 13:663282. doi: 10.3389/fnsyn.2021.663282

INTRODUCTION

Drastic changes in visual experience can induce long-lasting effects on excitatory synapses (Espinosa and Stryker, 2012; Cooke and Bear, 2014). In addition to inducing Hebbian plasticity, alterations in visual experience produce homeostatic plasticity of excitatory synapses in primary visual cortex (V1) of rodents (Kirkwood and Bear, 1994; Kirkwood et al., 1996; Desai et al., 2002; Goel et al., 2006; Keck et al., 2013). Specifically, in L2/3 neurons, removal of visually-driven

activity by dark-exposure (DE) increases the amplitude of miniature excitatory postsynaptic currents (mEPSCs), while re-exposing DE mice to light for 2 h (LE) is sufficient to reduce mEPSC amplitudes to basal levels (Goel and Lee, 2007; Gao et al., 2010; Petrus et al., 2014; Chokshi et al., 2019). Mechanistically, the bidirectional homeostatic adaptation of excitatory synaptic strength in V1 is mediated by regulation of α-amino-3-hydroxy-5-methyl-4-isoxazolepropionic acid (AMPA) receptor function (Goel et al., 2011). Recent studies suggest that DE and LE-induced changes in excitatory synaptic transmission is input-specific to lateral intracortical inputs to L2/3 (Petrus et al., 2015; Chokshi et al., 2019), and is dependent on N-methyl-D-aspartate receptor (NMDAR) activation (Bridi et al., 2018; Chokshi et al., 2019; Rodriguez et al., 2019). These results support the idea that DE and LE-induced homeostatic plasticity of excitatory synapses are likely due to metaplasticity (Lee and Kirkwood, 2019) as proposed by the sliding threshold Bienenstock-Cooper-Monroe (BCM) model (Bienenstock et al., 1982; Bear et al., 1987; Cooper and Bear, 2012). According to the BCM model, DE would slide down the synaptic modification threshold to promote long-term potentiation (LTP), while LE would slide up the synaptic modification threshold to favor long-term depression (LTD). In this framework, DE-induced increase in mEPSCs would be a manifestation of LTP, while LE-induced reduction in mEPSCs would reflect LTD. Input-specificity and dependence on NMDAR activity of visual experience-dependent homeostatic synaptic plasticity support this interpretation (Chokshi et al., 2019; Rodriguez et al., 2019). Furthermore, consistent with the fact that sliding down of synaptic modification threshold is mediated by up-regulation of GluN2B-containing NMDARs (Quinlan et al., 1999; Philpot et al., 2001, 2003), DE-induced potentiation of mEPSCs is blocked by GluN2B specific antagonist and is dependent on spontaneous activity (Bridi et al., 2018). Although it is assumed that changes in input activity to L2/3 neurons are driving these synaptic changes, what aspect of neural activity drives homeostatic metaplasticity is currently unknown.

Hebbian plasticity is widely accepted to bring about long-term modifications to synapses as a function of the level of correlation between the activity of pre- and post-synaptic neurons (Hebb, 1949). Highly correlated neuronal activity induces LTP while low correlation drives LTD. From *ex vivo* slice experiments, the activity parameters required to induce LTP and LTD are well-characterized. Such studies have found that bursting activity or a tight temporal order of pre- then postsynaptic activity leads to synaptic strengthening, while low frequency or a post- then presynaptic order of activity leads to synaptic depression (Lisman, 1997). However, it is not known what synaptic activity profile can induce homeostatic plasticity. Based on studies of dissociated cultures where activity can be globally manipulated by pharmacological means, it was hypothesized that the average postsynaptic firing rate of a cell determines the polarity of homeostatic synaptic plasticity (Turrigiano et al., 1998; Turrigiano, 2008). However, studies in more intact circuitry have demonstrated that homeostatic plasticity can be induced in an input-specific manner (Kim and Tsien, 2008; Beique et al., 2011; Petrus et al., 2015; Chokshi et al., 2019), which suggests that postsynaptic firing rate may not be the factor that drives this form of plasticity, but rather, it may be driven by input activity. In support of this idea, maintaining the average firing rate of postsynaptic neurons by optogenetic stimulation during the blockade of synaptic activity still induces homeostatic up-regulation of excitatory synapses in cultured neurons (Fong et al., 2015). This suggests that input activity patterns may be a critical factor that triggers homeostatic changes.

In this study, we aimed to determine the temporal patterns of synaptic activity received by L2/3 neurons from feed-forward inputs that drive homeostatic plasticity. Based on the observation that a homeostatic reduction in synaptic strength is rapidly induced by re-exposing DE mice to light for 2 h, we determined that depression of synaptic strength from DE levels would be an ideal system to examine the relationship between activity patterns and homeostatic plasticity in an *ex vivo* V1 slice preparation. In order to use a more naturalistic activity pattern as occurs during LE, we first measured and analyzed single-unit spike trains recorded from V1 layer 4 (L4) of awake head-fixed DE mice re-exposed to light. When we used this *in vivo* spike train pattern to stimulate L4 in V1 slices obtained from DE mice, we observed a reduction in the amplitude of mEPSCs recorded in L2/3 neurons. Synaptic depression was also observed by a Poisson random stimulation pattern of the same average frequency. Unlike LE-induced synaptic changes, naturalistic spike pattern-driven plasticity was not dependent on GluN2B-containing NMDAR or mGluR5 activity. Interestingly, the polarity of the change was dependent on the prior visual experience of the animal.

MATERIALS AND METHODS

Mice

Male and female mice C57BL/6 (The Jackson Laboratory) were reared in a 12 h light/12 h dark cycle. Young animals were dark exposed (DE) for 2 days (DE) between postnatal day 21 (P21) and 35 (P35). DE animals were cared for in a dark room with infrared vision goggles using dim infrared light. Some mice were re-exposed to normal light conditions for 2 h (LE) to study the effects of light exposure. All experiments were done in accordance with protocols approved by the Institutional Animal Care and Use Committees of Johns Hopkins University and University of Maryland.

In vivo Single-Unit Recordings in Awake Head-Fixed Mice

Custom-made 16-channel laminar arrays were constructed and implanted as previously described (Murase et al., 2016). Briefly, a 1.2 mm 16-channel platinum-iridium electrode shank (15–20 kΩ) with a head post was implanted into the binocular region of primary visual cortex (3.00 mm lateral to the midline/0.01 mm rostral to lambda) to a depth of 1 mm, to center the electrode shank on the vertical center of cortex. For implantation, adult mice were anesthetized in 3% isoflurane in 100% O_2. The mice received post-surgical buprenorphine

(0.1 mg/kg) after return of the righting reflex and were allowed 3–4 days to recover from surgery. One day prior to recording, subjects were habituated to the head restraint for 45 min. Single unit activity was recorded in awake head restrained animals in response to square wave gratings (100% contrast, 0.05 cycles per degree, 135 orientation) presented on a CRT monitor (Clinton, 28 cm × 36 cm, 60-Hz) placed 18 cm from the eyes, subtending 75 degrees of visual space vertically and 90 degrees horizontally (+Pattern group) or a gray screen at equal luminance (27 cd/m^2) (+Gray group).

L4 was identified as the location of the short-latency (∼150 ms) visually-evoked current source in the current source density (CSD) analysis of laminar local field potential (LFP) profiles. For isolated single-unit activity, the acquired signal was filtered from 300-Hz (high pass) to 5-kHz (low pass) and sampled at 25-kHz. Unit activity was acquired for 200 trials (1 s each) using an RZ5 Bioamp Processor (TDT). Spike sorting was based on waveform shape and a Bayesian fixed variable principle component analysis using Open Sorter (TDT). Neuron classification was based on three parameters: slope of the wave for 0.5 ms after the trough, time elapsed between the trough and peak, and the ratio between the height of the trough and peak (Niell and Stryker, 2008). Only regular spiking units, defined by a low peak to trough ratio, a long duration, and a small end slope, were included for analysis.

Spike Train Analysis

Single unit spike data were analyzed following processing with a non-biased method to delineate single spikes from bursts (Chen et al., 2009). Inter-spike intervals (ISIs) were used to generate a 1-dimensional data array from which we calculated the mean ISI value. ISIs which were greater or equal to the mean value were removed, and the remaining ISI values were used to calculate a second mean ISI for this population which was used as the threshold for detecting bursts. A burst was defined as a group of ISIs in which two or more consecutive ISIs had values that fell below the threshold. Using this method of burst detection, we wrote an algorithm in MATLAB that allowed automatic analysis of bursts and non-burst spikes from each *in vivo* recorded spike train data set. The specific algorithm used for this burst detection program and the MATLAB code is available online[1].

The following parameters were analyzed for each spike train: average firing rate, average number of intraburst ISIs, average duration of bursts, average number of interburst ISIs, average duration of interburst intervals, mean burst frequency (inverse of mean intraburst ISI), mean non-burst frequency (inverse of mean interburst ISI), and fraction of spikes in bursts [(Number of ISIs in burst)/(Total number of ISIs per spike train)].

Generation of Synthetic Spike Train With Poisson Distribution

A synthetic spike train was generated in MATLAB using a Poisson process with the mean ISI set equal to the average ISI of the +Gray group (see **Tables 1**, **2**).

[1]https://github.com/heykyounglee/spike-train-analysis

Acute Slice Preparation for mEPSC Recording

The mice were anesthetized by isoflurane vapors and decapitated after verifying the absence of a toe-pinch response. Brain blocks containing visual cortex were coronally sliced into 300-μm sections using a vibratome (Leica VT1200S or Ted Pella Pelco easislicer^{TM}) in ice-cold dissection buffer containing 212.7 mM sucrose, 10 mM dextrose, 3 mM $MgCl_2$, 1 mM $CaCl_2$, 2.6 mM KCl, 1.23 mM $NaH_2PO_4 \bullet H_2O$, and 26 mM $NaHCO_3$, which was bubbled with a 95%-O_2/5%-CO_2 gas mixture. The slices were incubated at room temperature for 60 min in artificial cerebrospinal fluid (ACSF: solution containing 124 mM NaCl, 5 mM KCl, 1.25 mM $NaH_2PO_4 \bullet H_2O$, 26 mM $NaHCO_3$, 10 mM dextrose, 2.5 mM $CaCl_2$, and 1.5 mM $MgCl_2$, bubbled with 95% O_2/5% CO_2).

Whole-Cell Voltage-Clamp Recordings of mEPSCs

Visual cortical slices were transferred to a submersion-type recording chamber mounted on the fixed stage of an upright microscope with oblique illumination and were continually supplied with ACSF bubbled with 5% CO_2/95% O_2(30°C) with a flow rate of approximately 2 ml/min. AMPA receptor-mediated mEPSCs were isolated by adding 1 μM tetrodotoxin (TTX), 20 μM bicuculline (Bic), and 100 μM DL-2-amino-5-phosphonopentanoic acid (APV). Recording pipettes were filled with internal solution containing: 130 mM Cs-gluconate, 10 mM HEPES, 8 mM KCl, 1 mM EGTA, 4 mM disodium-ATP (Sigma–Aldrich, Cat #A6419), 10 mM disodium-phosphocreatine (Sigma–Aldrich, Cat #P7936), 0.5 mM Sodium-GTP (Sigma–Aldrich, Cat #G8877), 5 mM Lidocaine N-ethyl bromide (Sigma–Aldrich, Cat #L5783). Biocytin (1 mg/ml) was added to the internal solution to confirm morphology and location of the recorded cells *post hoc*. Pyramidal neurons in L2/3 of V1 were recorded in voltage-clamp at −80 mV and the recorded mEPSCs were digitized at 10-kHz by a National Instruments data acquisition board and acquired through an Igor based program (Wavemetrics). Two-hundred mEPSCs were analyzed from each cell with Mini Analysis (Synaptosoft).

Ex vivo Stimulations to Induce Plasticity

Visual cortical slices were transferred to a submersion-type recording chamber mounted on the fixed stage of an upright microscope with oblique infra-red illumination. Slices were continually supplied with ACSF bubbled with 5% CO_2/95% O_2 (30°C) with a flow rate of about 2 ml/min. Pyramidal neurons in L2/3 of V1 were recorded in the whole-cell configuration. To generate activity patterns, a bipolar stimulation electrode was placed in V1 L4. Prior to stimulation a V1 L2/3 pyramidal cell was recorded under voltage clamp at −80 mV to determine the intensity of stimulation from L4. The stimulus intensity was adjusted using a stimulation isolated unit (SIU91A, Cygnus Instruments) to produce EPSCs of approximately 200 pA in the V1 L2/3 cell. The recording was then switched to the current clamp configuration, and we confirmed that the L4 stimulus results in subthreshold EPSPs.

TABLE 1 | Spike train properties analyzed from *in vivo* primary visual cortex (V1) layer 4 (L4) cells.

Spike train property	DE	LE groups	
		+Gray stimulation	+Pattern stimulation
Average firing rate (Hz)	2.74 ± 0.32	5.52 ± 0.73**	5.82 ± 0.71**
Mean burst length (# of spikes/burst)	5.82 ± 0.34	11.61 ± 1.82**	10.12 ± 1.60*
Mean burst frequency (Hz)	33.17 ± 1.86	54.28 ± 10.56	51.30 ± 11.75
Mean non-burst frequency (Hz)	1.39 ± 0.16	2.34 ± 0.49*	2.56 ± 0.36*
Frequency of bursts (Hz)	0.30 ± 0.04	0.34 ± 0.05	0.40 ± 0.04
Fraction of spikes in bursts	0.61 ± 0.01	0.68 ± 0.04	0.66 ± 0.04

*Statistics: ANOVA with Newman–Keuls multiple comparison test; **$p < 0.01$, *$p < 0.05$.*

TABLE 2 | Spike train properties of the exemplar cells used for *ex vivo* stimulations.

Spike train property	+Gray stimulation	+Pattern stimulation	Poisson stimulation
Average firing rate (Hz)	4.77	4.05	5.52
Mean burst length (# of spikes/burst)	9.45	7.91	2.38
Mean burst frequency (Hz)	46.40	44.12	43.04
Mean non-burst frequency (Hz)	1.64	1.60	5.35
Frequency of bursts (Hz)	0.39	0.37	0.14
Fraction of spikes in bursts	0.76	0.71	0.06

A small holding current was injected to keep the membrane potential at −65 mV in current-clamp, and Igor NIDAQ Tools MX was used to generate the desired stimulation pattern for 2 h.

Statistics

All data is displayed as Mean ± S.E.M. Normality was confirmed with the D'Agostino and Pearson normality test. Unpaired *t*-tests and ANOVAs were performed to compare the averages of two or more normally distributed data sets, respectively. Data sets that were not normally distributed were compared using non-parametric statistical tests (e.g., Mann-Whitney or Kruskal–Wallis). Cumulative distribution of individual mEPSC amplitudes were compared using the Kolmogorov–Smirnov test. Statistical analyses were performed in Prism (Graphpad). $P < 0.05$ was taken as a statistically significant difference on all tests, except for Kolmogorov–Smirnov tests in which we used $P < 0.001$ as the cutoff.

RESULTS

Analysis of V1 L4 Neuronal Spiking Activity Recorded During LE

In the canonical feedforward pathway, visually driven activity is conveyed to L2/3 neurons by excitation from thalamo-recipient L4 neurons. Hence, we aimed to test whether activating L4 with naturalistic neural activity associated with LE would drive metaplasticity in V1 L2/3 principal neurons. To identify activity patterns (neuronal spiking activity) in V1 L4 neurons with LE, we recorded single-unit activity in awake mice during two hours of re-exposure to light following two days of DE. Single unit recordings from V1 L4 regular spiking neurons were acquired in awake head-fixed mice *via* a chronically implanted multielectrode array. Recordings were acquired from DE mice during presentation of a blank screen (no visual stimulation) and during LE in response to a homogenous gray screen (+Gray) or a patterned visual stimulus (equiluminant high contrast grating; +Pattern). The *in vivo* spike trains recorded from the three groups (DE, +Gray, and +Pattern) were analyzed to extract various metrics of spike patterns. We used an ISI-based spike train analysis method (Chen et al., 2009) to distinguish spike bursts from non-burst spike activity (**Table 1** and **Figure 1**). There was no statistically significant difference in the measured firing properties of V1 L4 neurons from when mice viewed the visual stimulus (+Pattern) or the gray screen (+Gray; **Figure 1**). The average firing rate (overall firing rate), mean burst length (mean number of spikes within bursts), and mean non-burst frequency (spike rate outside of bursts) were significantly higher in the +Gray and +Pattern LE groups (**Figure 1** and **Table 1**). The spike rate within identified burst periods trended towards an increase in the LE groups, but did not reach a statistical significance likely due to the increase in variance (**Figure 1D** and **Table 1**). There was no statistically significant increase in the overall frequency of bursts across the three groups (**Figure 1C** and **Table 1**). Furthermore, there were no statistical differences in the metrics of spike patterns of V1 L4 neurons between +Gray and +Pattern groups (**Figure 1** and **Table 1**). Our results demonstrate that the increase in visual evoked activity during LE is largely due to an increase in burst length and non-burst spike rates.

In vivo LE Spike Patterns Reduce mEPSC Amplitude in V1 L2/3 of DE Mice *Ex vivo*

We examined if naturalistic spike patterns obtained from V1 L4 neurons during LE could drive homeostatic reduction in the strength of excitatory synapses onto L2/3 neurons. To do this, we stimulated L4 of V1 slices obtained from DE mice with the *in vivo* spike patterns recorded from L4 of LE mice (+Gray and +Pattern conditions; **Figure 2**). For both +Gray and +Pattern, the cell with the average firing rate closest to the group mean was chosen as the exemplar to provide the stimulation pattern for that group (**Table 2**). For each experiment, we

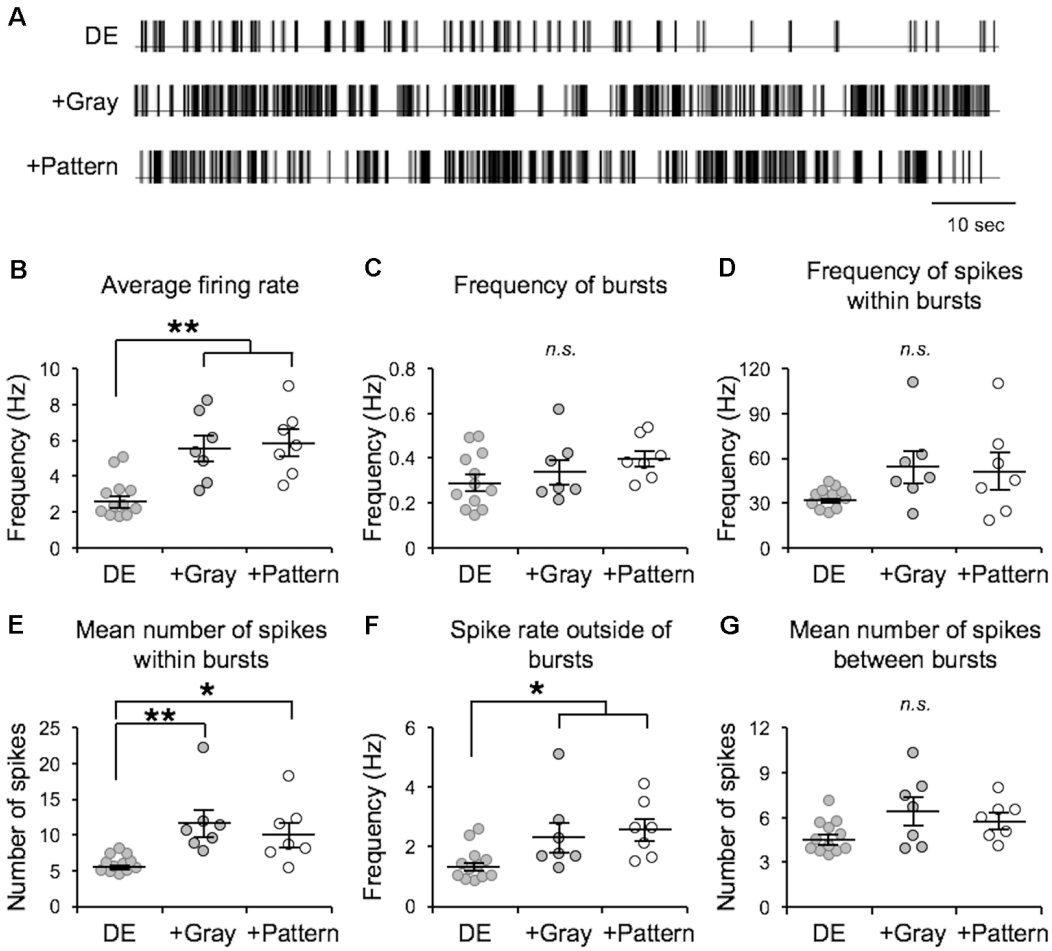

FIGURE 1 | Analysis of visual experience-dependent *in vivo* spike activity. Single unit recordings were acquired in primary visual cortex (V1) layer 4 (L4) of awake head-fixed dark exposed (DE) mice facing a blank screen in a dark room (DE), DE mice placed in a lighted room facing a gray screen (+Gray), and DE mice placed in a lighted room facing a screen with a grating (+Pattern). See "Materials and Methods" section for details. **(A)** Example inter-spike-interval trains recorded from DE (top), +Gray (middle), and +Pattern (bottom) conditions. Each vertical line represents an action potential. **(B)** Average overall firing rate was significantly elevated in the two groups receiving visual stimuli (DE = 2.74 ± 0.32 Hz; DE+Gray = 5.52 ± 0.73 Hz; DE+Pattern = 5.82 ± 0.70 Hz; ANOVA, $F = 1.341$, $p = 0.0004$; Newman–Keuls multiple comparison $^{**}p < 0.01$). **(C)** There was no significant difference in the frequency of bursts (see "Materials and Methods" section for quantification of bursts) across groups (DE = 0.295 ± 0.036 Hz; DE+Gray = 0.341 ± 0.054 Hz; DE+Pattern = 0.397 ± 0.037 Hz; ANOVA, $F = 1.511$, $p = 0.2417$). n.s.: not statistically significant. **(D)** There was an increase in the average frequency of spikes within a burst in the two groups receiving visual stimuli, which did not reach statistical significance (DE = 33.17 ± 1.86 Hz; DE+Gray = 54.28 ± 10.56 Hz; DE+Pattern = 51.30 ± 11.75 Hz; ANOVA, $F = 2.647$, $p = 0.0923$). This was due to a large increase in variance (Bartlett's test for standard deviations, Bartlett's *statistic* = 18.4, $p = 0.0001$). **(E)** The mean number of spikes within a burst was significantly increased in the visual stimuli groups (DE = 5.82 ± 0.34; DE+Gray = 11.61 ± 1.82; DE+Pattern = 10.12 ± 1.60; ANOVA, $F = 7.575$, $p = 0.0030$; Newman–Keuls multiple comparison $^{*}p < 0.05$, $^{**}p < 0.01$). **(F)** There was a significant increase in the frequency of spikes outside of bursts in the two visual stimuli groups (DE = 1.39 ± 0.16; DE+Gray = 2.35 ± 0.49; DE+Pattern = 2.56 ± 0.36; ANOVA, $F = 4.472$, $p = 0.0229$; Newman–Keuls multiple comparison $^{*}p < 0.05$). **(G)** There was no significant difference in the mean number of spikes between bursts across the three groups (DE = 4.63 ± 0.31; DE+Gray = 6.40 ± 0.90; DE+Pattern = 5.78 ± 0.49 ANOVA, $F = 3.043$, $p = 0.0672$).

first determined the stimulation intensity that was sufficient to evoke an approximately 200 pA EPSC in a L2/3 neuron (**Figure 2B**). We determined the stimulation intensity based on reports that visual stimulus presentation results in EPSCs of roughly 100–500 pA in V1 L2/3 pyramidal neurons recorded *in vivo* at similar holding potentials in the whole-cell voltage-clamp configuration (Sun and Dan, 2009; Haider et al., 2016). We found that the stimulation intensity, generated subthreshold EPSPs in current-clamp (**Figure 2B**). L4 was then stimulated at the determined intensity with the +Gray or +Pattern exemplar cell activity for 2 h to match the duration of LE shown to produce a reduction in mEPSC amplitudes in L2/3 neurons without changes in mEPSC frequency (**Figure 3A**). Following stimulation with either +Gray or +Pattern activity, mEPSCs were recorded from L2/3 neurons directly above the L4 stimulating electrode (**Figure 2C**).

Stimulation of DE slices with the spike pattern of the +Gray exemplar cell (see **Table 2** for parameters) significantly

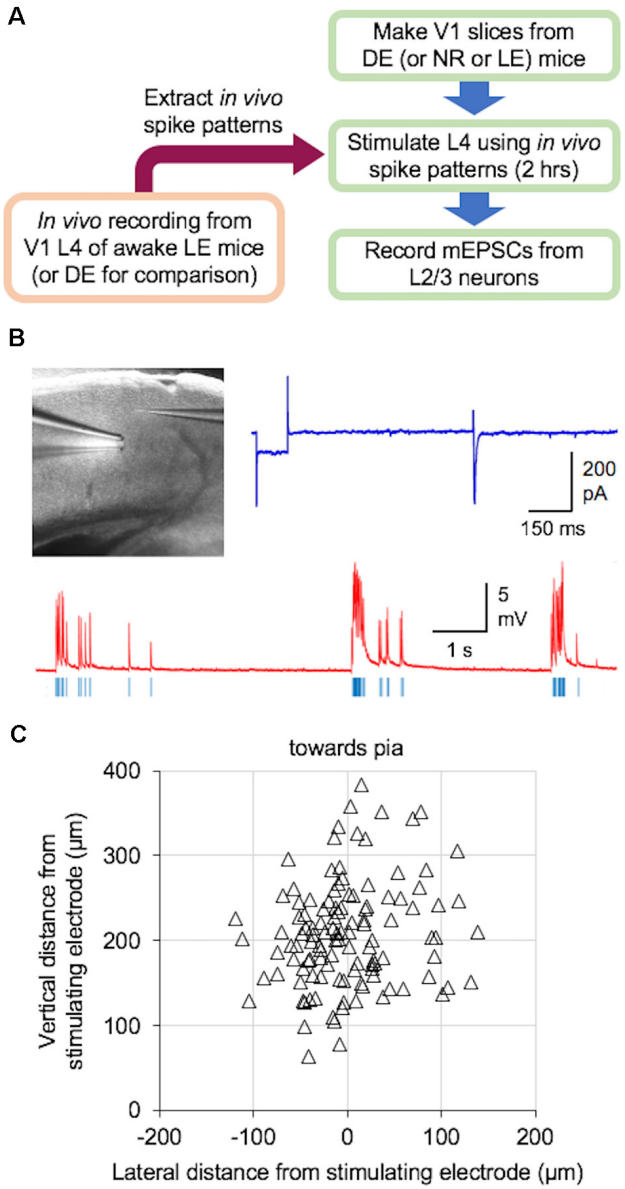

FIGURE 2 | *Ex vivo* paradigm to examine plasticity outcome following naturalistic spike pattern stimulation. **(A)** Schematic diagram of the experiments. *In vivo* spike trains were recorded from V1 L4 of awake head-fixed mice that were dark-exposed and brought out to light (LE) to view drifting gratings (+Pattern) or an equal luminance gray screen (+Gray). A group of DE mice was recorded in the dark (DE) for comparison. Recorded spike trains were analyzed to extract inter-spike-interval (ISI) information, which was then used to construct the stimulus train. V1 slices were obtained from DE [or normal reared (NR) or LE] mice. L4 of these slices were stimulated with the *in vivo* spike pattern for 2 h. Stimulus intensity was adjusted to produce subthreshold activation of L2/3 neurons (see **B**). After the 2-h stimulation, miniature excitatory postsynaptic currents (mEPSCs) were recorded from L2/3 pyramidal cells under whole-cell voltage clamp. **(B)** *Ex vivo* experimental setup in acute V1 slice preparation. Top left: image of a V1 slice with a stimulating electrode in L4 and a whole-cell recording electrode patched onto a L2/3 pyramidal cell. Top right: an example voltage-clamp trace recorded when determining the stimulation intensity, which was adjusted to induce approximately 200 pA evoked excitatory

(*Continued*)

FIGURE 2 | Continued
postsynaptic currents (EPSCs) in V1 L2/3 neurons. Bottom: an example current-clamp recording trace while delivering an *in vivo* pattern of activity (red, current-clamp trace from V1 L2/3 neuron; blue vertical lines, stimulation delivered to an electrode in L4). Stimulation was done for 2 h. **(C)** Distribution of recorded V1 L2/3 neuron location (open triangles) relative to the location of the stimulating electrode in L4 (0,0 coordinate).

decreased the average mEPSC amplitude in L2/3 neurons (**Figure 3B**). We saw no significant change in mEPSC frequency in the *ex vivo* stimulated slices. While the decrease in mEPSC amplitude on average looks similar to what we observed with LE (**Figure 3A**), the cumulative probability of mEPSC amplitudes from LE and +Gray conditions were statistically different from each other (**Figure 3C**). This suggests that plasticity induced by LE and +Gray is either not the same across synapses or that they are affecting a non-identical subset of synapses. Stimulating DE slices with the spike pattern of the +Pattern exemplar cell (see **Table 2** for parameters) also produced similar results as the +Gray group, except this was accompanied by a significant increase in mEPSC frequency. To control for possible confounding effects of prolonged exposure to the perfusion bath prior to recording mEPSCs, a subset of DE slices was placed in the recording chamber for 2 h with a stimulating electrode, but received no stimulation (+No Stim) before recording. We observed no difference in average mEPSC amplitude or frequency between the +No Stim and DE control (amplitude: DE = 13.08 ± 0.35 pA, n = 41; DE+No stim = 13.08 ± 0.54 pA, n = 22; Unpaired t-test, t = 0.0634, p = 0.5485; frequency: DE median = 4.021 Hz; DE+No stim median = 4.368 Hz; Mann–Whitney test, U = 391, p = 0.3939). These data demonstrate that stimulating V1 L4 of DE mice with naturalistic spiking patterns obtained from L4 neurons during LE is sufficient to reduce the amplitude of mEPSCs in L2/3 neurons. Given that our stimulation is subthreshold for postsynaptic spike generation, these data suggest that the average frequency of input activity onto a given cell, not the postsynaptic firing rate, is the key factor driving homeostatic weakening of excitatory synapses in V1 L2/3 neurons.

Stimulation With a Poisson Spike Train Mimics the Effect of Naturalistic LE Spike Patterns

The average firing rate *in vivo* of V1 L4 neurons was higher in DE +Gray and +Pattern groups compared to DE alone (**Figure 1B** and **Table 1**), thus we hypothesized that the average firing rate of presynaptic neurons was a key factor in engaging homeostatic downregulation of synaptic strength. To test this, we wanted to manipulate the average firing rate in the absence of other aspects of patterned neuronal activity, such as bursts. We therefore generated a Poisson distribution of ISI values with a mean equivalent to the average ISI of the +Gray group, and sampled a series of ISIs from this distribution to use as a stimulation pattern (**Figure 3C** and **Tables 1**, **2**). Because the average firing rate of +Gray and +Pattern group are similar (**Figure 1B** and **Table 2**), our

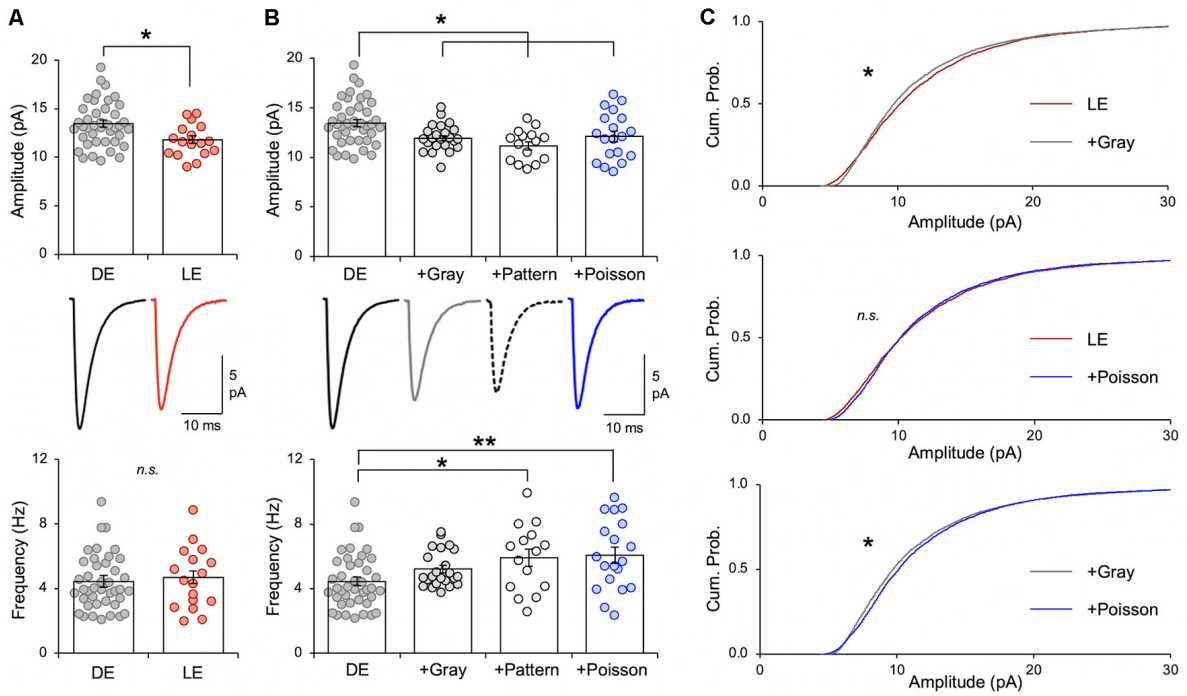

FIGURE 3 | Naturalistic spike patterns induce homeostatic synaptic depression. **(A)** LE decreases excitatory synaptic strength in mouse V1 L2/3 pyramidal neurons, as reported previously (Goel and Lee, 2007; Gao et al., 2010). Comparison of average mEPSC amplitude from V1 L2/3 pyramidal neurons following 2 days of DE and a subsequent 2 h of LE in P23–35 mice. Top: average mEPSC amplitude from individual cells are shown as circles and mean ± S.E.M. are shown as bars (DE = 13.46 ± 0.36 pA, n = 41, LE = 11.81 ± 0.40 pA, n = 17; unpaired t-test, t = 2.716, $^{**}p$ = 0.0088). Middle: average mEPSC traces. Bottom: there was no change in average mEPSC frequency (DE median = 4.021 Hz, LE median = 4.592 Hz; Mann–Whitney test, U = 330, p = 0.761). **(B)** Top: comparison of average mEPSC amplitudes from different stimulation regimes. mEPSCs were recorded from the following groups: V1 slices from DE mice (DE), V1 slices from DE mice stimulated with *in vivo* spike patterns from exemplar cells of LE (+Gray; +Pattern), and V1 slices from DE mice stimulated with a Poisson random train (+Poisson). Average mEPSC amplitudes of individual cells are plotted as circles and mean ± S.E.M are shown as bars (DE: the same data shown in panel **A** are replotted here for comparison; DE+Gray = 11.93 ± 0.28 pA, n = 23; DE+Pattern = 11.18 ± 0.41 pA, n = 15; DE+Poisson = 12.11 ± 0.55 pA, n = 19; ANOVA, F = 5.138, p = 0.0025; Newman–Keuls multiple comparison test, $^{*}p < 0.05$). Middle: average mEPSC traces. Bottom: comparison of average mEPSC frequency across groups (DE median = 4.021 Hz; DE+Gray = 4.753 Hz; DE+Pattern = 6.298 Hz; DE+Poisson = 5.695 Hz; Kruskal—Wallis statistic = 13.47, p = 0.0037; Dunn's multiple comparison test, $^{*}p < 0.05$, $^{**}p < 0.01$). **(C)** Top: cumulative probability of mEPSC amplitudes of LE (red line) and +Gray (gray line) group. There is a significant difference between the two groups (Kolmogorov–Smirnov test: $^{*}p < 0.0001$). Middle: cumulative probability of mEPSC amplitudes of LE (red line) and +Poisson (blue line) group. There was no statistical difference in the distribution (n. s.). Bottom: cumulative probability of mEPSC amplitudes of +Gray (gray line) and +Poisson (blue line) group. There is a significant difference between the two groups (Kolmogorov–Smirnov test: $^{*}p < 0.0001$).

Poisson spike train would reflect the average firing rate of both LE conditions. We confirmed that the distribution of ISI of the Poisson spike train is different from those of +Gray and +Pattern (**Figure 4**). Stimulating V1 L4 of DE slices with the Poisson spike train induced a significant reduction in mEPSC amplitude in L2/3 neurons similar to what we observed with naturalistic pattern stimulations (**Figure 3B**). However, the cumulative probability distribution of mEPSC amplitudes in the +Poisson group was significantly different from that seen in the naturalistic pattern stimulated groups (**Figure 3C**). This suggests that Poisson random activity is sufficient to produce homeostatic depression of mEPSC amplitudes, even though the changes across individual synapses are not identical to those produced by naturalistic patterned stimuli. There was also an increase in mEPSC frequency following Poisson stimulation, which mirrors what we observed with the +Pattern exemplar cell (**Figure 3B**).

Effect of GluN2B and mGluR5 Antagonists on the Expression of *In vivo* Spike Train-Induced Plasticity of mEPSCs

We recently reported that the LE-induced reduction of mEPSC amplitudes is dependent on NMDAR and metabotropic glutamate receptor 5 (mGluR5) activity (Chokshi et al., 2019; Rodriguez et al., 2019). Therefore, we examined whether the naturalistic spike train-induced depression of mEPSCs presented here is also dependent on similar signaling. We stimulated slices from DE mice with the +Gray exemplar cell activity pattern (**Table 2**) in the presence of either ifenprodil (3 μM) or 2-methyl-6-(phenylethynyl)pyridine (MPEP, 50 μM) to block GluN2B-containing NMDARs or mGluR5s, respectively. Neither of the pharmacological antagonist prevented the reduction in average mEPSC amplitude driven by +Gray stimulation delivered to L4 (**Figure 5**). Our results suggest that the molecular signaling required for synaptic depression induced with naturalistic spike

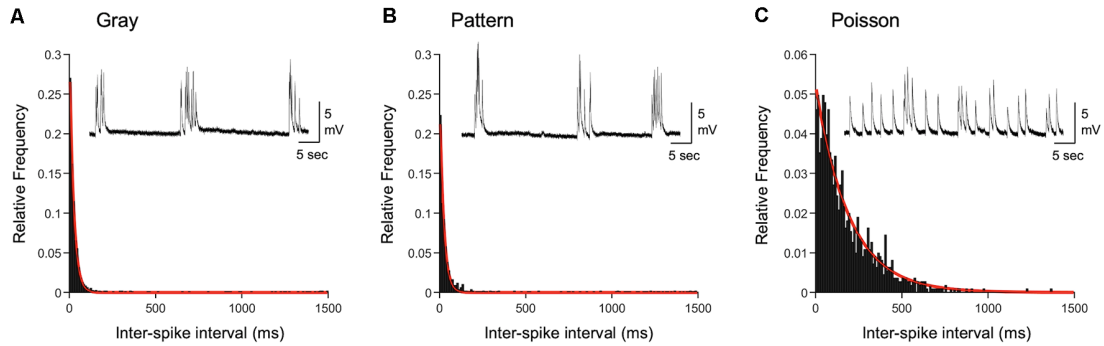

FIGURE 4 | Comparison of inter-spike intervals of naturalistic spike trains. **(A)** Histogram of inter-spike intervals (ISIs) recorded from L4 of a DE mouse exposed to light and viewing a gray screen (corresponding to +Gray exemplar cell in **Table 2**). The histogram is fitted with a single exponential decay function (red line). Inset: an example current-clamp recording trace from a V1 L2/3 neuron of a DE mouse. Stimulation train from the +Gray exemplar cell was delivered through an electrode placed in L4 of the slice. **(B)** Histogram of ISIs recorded from L4 of a DE mouse exposed to light and viewing a screen with patterned gratings (corresponding to +Pattern exemplar cell in **Table 2**). The histogram is fitted with a single exponential decay function (red line). Inset: an example current-clamp recording from a V1 L2/3 neuron of a DE mouse receiving a train of +Pattern stimulation through an electrode in L4. **(C)** Histogram of ISIs of a Poisson train with the same average firing frequency as the exemplar neuron of the Gray group. The histogram is fitted with a single exponential decay function (red line). Inset: an example current-clamp recording from a V1 L2/3 neuron of a DE mouse while delivering a train of +Poisson stimulation (see **Table 2** for details) to L4. Note that the stimulation intensity used generates subthreshold EPSPs. Distribution of ISIs between Gray and Pattern is not statistically significant (Kolmogorov–Smirnov test: $D = 0.0776$, $p = 0.009$), while that of Poisson is significantly different from those of Gray (Kolmogorov–Smirnov test: $D = 0.5530$, $p < 0.0001$) and Pattern (Kolmogorov–Smirnov test: $D = 0.4893$, $p < 0.0001$).

trains is different from those required for synaptic depression with LE. This finding together with our observation that +Gray results in a different shift in mEPSC amplitude distribution when compared to that of LE (**Figure 3C**) suggests that the plasticity induced by naturalistic spike pattern stimulation is not identical to that seen with LE.

The Outcome of Naturalistic Spike Pattern Stimulation Is Dependent on the History of Visual Experience

Next, we examined whether the naturalistic spike pattern stimulation-induced reduction of mEPSC amplitudes in L2/3 neurons is dependent on the initial state of V1 circuitry, as determined by prior visual experience. To test this, we stimulated V1 L4 of slices obtained from normal reared (NR) control animals (NR slices) with spike pattern of the +Gray exemplar cell (**Figure 6A**). In contrast to the decrease in mEPSC amplitudes observed with DE slices, 2 h of +Gray stimulation in NR slices did not induce significant changes in the average amplitude or frequency of mEPSCs in L2/3 neurons (**Figure 6B**). However, the same spike pattern (+Gray) delivered to V1 L4 of slices from LE mice (2 h of light re-exposure after 2 days of DE; **Figure 6A**) induced a significant increase in both the average mEPSC amplitude and frequency (**Figure 6C**). Thus, the history of prior visual experience impacts the response of V1 circuit following stimulation of feedforward inputs from L4 with the same naturalistic spike pattern.

DISCUSSION

We found that visual experience during LE elevated the overall firing rate of V1 L4 neurons, which was primarily driven by an increase in the non-burst firing rate and an increase in mean burst length (**Figure 1**). By using naturalistic spike trains recorded from V1 L4 of a LE mouse to stimulate L4 of *ex vivo* V1 slices obtained from DE mice, we were able to induce homeostatic depression of mEPSC amplitudes in L2/3 pyramidal neurons (**Figure 3**). Homeostatic synaptic depression was also obtained with a Poisson random spike train with an average firing rate matched to the naturalistic spike train (**Figure 3**). While *ex vivo* stimulation with naturalistic spike trains was effective at driving depression of excitatory synaptic transmission similar to that observed with LE, it did not share signaling pathways with LE-induced plasticity (**Figure 5**). Interestingly, homeostatic response to *ex vivo* stimulation was dependent on the nature of prior visual experience, as demonstrated by the observation that using the same naturalistic spike train to stimulate V1 slices obtained from NR and LE mice yielded no change or an increase in mEPSC amplitudes, respectively (**Figure 6**).

Average Input Activity as a Determinant for Homeostatic Metaplasticity

Bursting activity is believed to provide more robust and reliable synaptic transmission than single spikes (Lisman, 1997). It is especially important for inducing Hebbian plasticity where brief bursts of high frequency stimulation (50–100 Hz) induce robust LTP (Bliss and Gardner-Medwin, 1973; Bliss and Lomo, 1973). Conversely, prolonged stimulation at lower frequencies (1–3 Hz) induces LTD at excitatory synapses (Dudek and Bear, 1992). Here, we sought to elucidate which properties of neuronal activity drive the homeostatic metaplasticity observed in V1 following increases in visual experience. We found that V1 L4 neurons recorded *in vivo* from LE mice showed an

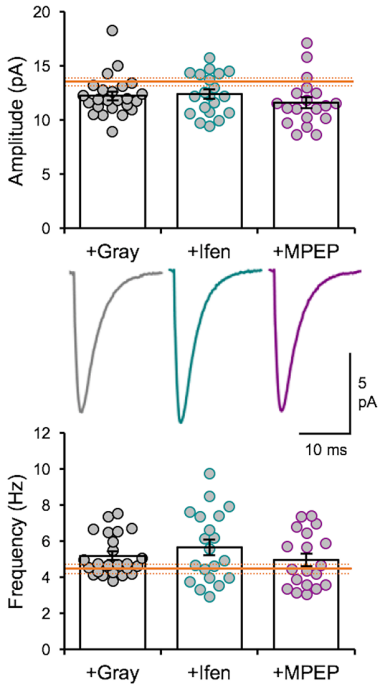

FIGURE 5 | Naturalistic pattern stimulation-induced synaptic depression is not dependent on GluN2B-containing NMDARs or mGluR5s. Stimulation with +Gray activity while blocking GluN2B-containing NMDARs with ifenprodil (+Ifen) or mGluR5s with MPEP (+MPEP) did not yield significantly different changes from stimulation with +Gray alone. Top: average mEPSC amplitudes of individual neurons are shown as circles and mean ± S.E.M are shown as bars (DE+Gray = 11.93 ± 0.28 pA; DE+Gray+Ifen = 12.36 ± 0.42 pA; DE+Gray+MPEP = 11.6 ± 0.51 pA; ANOVA, $F = 0.8522$, $p = 0.4317$). For reference, the mean mEPSC amplitude for DE is shown as the orange line with ± S.E.M. shown in dotted orange lines. Middle: average mEPSC traces for each group. Bottom: average mEPSC frequency comparison across groups (DE+Gray median = 4.753 Hz; DE+Gray+Ifen median = 5.258 Hz; DE+Gray+MPEP median = 4.454Hz; ANOVA, $F = 1.076$, $p = 0.3475$). For reference, the mean mEPSC frequency for DE is shown as the orange line with ± S.E.M. shown in dotted orange lines.

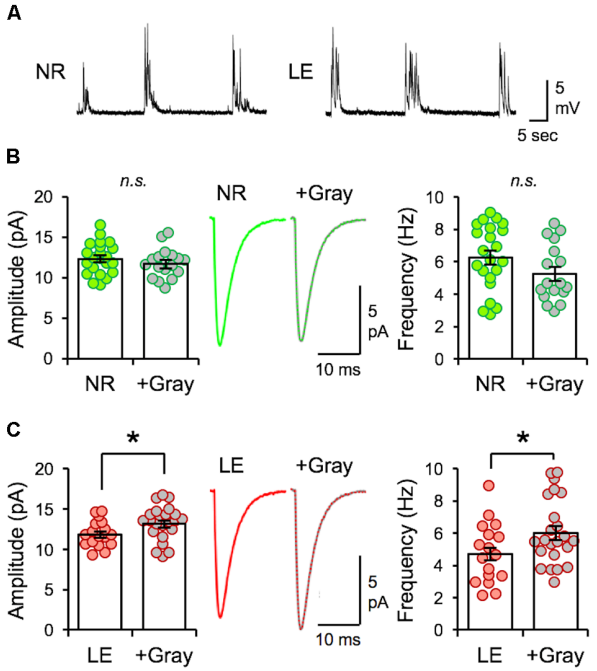

FIGURE 6 | The same naturalistic pattern stimulation yields distinct synaptic changes dependent on prior visual experience. **(A)** Example current-clamp recording traces recorded from V1 L2/3 neurons while stimulating L4 with +Gray spike train in slices obtained from NR (left) and LE (right) mice. Stimulation intensity used produced subthreshold EPSPs. **(B)** No difference in the average amplitude of mEPSCs recorded from NR slices stimulated with the +Gray activity when compared to unstimulated NR slices. Left: average mEPSC amplitudes of individual neurons are shown as circles and mean ± S.E.M are shown as bars (NR = 12.32 ± 0.42 pA, $n = 22$; NR+Gray = 11.7 ± 0.44 pA, $n = 17$; unpaired t-test: $t = 1.003$, $p = 0.3222$). n.s.: not statistically significant. Middle: average mEPSC traces. Right: average mEPSC frequency comparison (NR = 6.26 ± 0.43 Hz, NR+Gray stim = 5.24 ± 0.43 Hz, unpaired t-test, $t = 1.643$, $p = 0.1088$). n.s.: not statistically significant. **(C)** A significant increase in average amplitude of mEPSC recorded from LE slices stimulated with the +Gray activity when compared to unstimulated LE slices (LE). Left: average mEPSC amplitudes of individual neurons are shown as circles and mean ± S.E.M are shown as bars (LE = 11.81 ± 0.40 pA, $n = 17$; LE+Gray = 13.15 ± 0.44 pA, $n = 23$; unpaired t-test: $t = 2.716$, $p = 0.0088$). Middle: average mEPSC traces. Right: average mEPSC frequency comparison (LE = 4.70 ± 0.45 Hz, LE+Gray = 6.02 ± 0.43 Hz; unpaired t-test, $t = 2.084$ *$p = 0.0440$).

elevated average firing rate compared to that of DE mice. This difference was largely driven by an increase in the non-burst firing rate and the average length of bursts (**Figure 1**). *Ex vivo* stimulation of V1 L4 in slices obtained from DE mice using naturalistic spike patterns obtained from V1 L4 neurons in LE mice was sufficient to reduce mEPSC amplitudes in L2/3 neurons, but the details of the change are not identical to what is observed in LE mice. We used stimulation intensities that produced subthreshold postsynaptic responses (**Figures 2**, **3**), hence our results suggest that homeostatic synaptic depression can be induced by monitoring synaptic input activity rather than postsynaptic spiking activity.

While there were some differences in the plasticity of mEPSCs resulting from naturalistic pattern stimulation *ex vivo* and LE (**Figures 3**, **5**), our results suggest that feedforward activity from L4 is able to drive synaptic depression in L2/3 as predicted with homeostatic plasticity. The differences in mEPSC regulation between *ex vivo* stimulation and LE may stem from many factors. One possibility is that the electrical stimulation given here may produce synchronized activity in the slices, which is not likely to occur with visual experience *in vivo*. Another possibility is that stimulation of L4 may not activate all of the inputs onto L2/3 neurons that visual experience does. A third possibility is that inputs other than L4 may participate in homeostatic plasticity driven by LE. There is evidence that changes in mEPSCs reflect mainly the plasticity of lateral intracortical synapses onto L2/3 neurons in V1 (Petrus et al., 2015; Chokshi et al., 2019). It is likely that these intracortical synapses will be active *in vivo* with LE, but we are unable to mimic this with our feedforward stimulation paradigm. A fourth possibility is that neurons in *ex vivo* slices tend to be relatively hyperpolarized with minimum spontaneous firing, hence may not fully recapitulate the situation *in vivo* where neurons are often in an "up-state" closer to action potential thresholds.

We found that simply presenting a Poisson random stimulation train with the same average frequency as that of V1 L4 neurons recorded from LE mice was sufficient to drive homeostatic weakening of mEPSCs in L2/3 neurons (**Figure 3**). This suggests that L2/3 neurons are likely computing the average input frequency, rather than specific patterns of activity, to induce homeostatic plasticity. It is of interest to note that previous studies have used Poisson random stimulation in V1 L4, but with different outcomes than what we report here (Perrett et al., 2001; Guo et al., 2012). This likely reflects the fact that the plasticity is dependent on the metaplastic state of synapses. Here, we have clearly shown that the same *in vivo* spike train results in either depression, no change, or potentiation of mEPSC amplitudes depending on the prior visual experience of the mouse (**Figures 3**, **6**). One study that failed to induce plasticity with a Poisson random stimulation train was performed in V1 of NR guinea pig (Perrett et al., 2001). This is similar to our finding that delivering naturalistic pattern of stimulation to V1 slices from NR mice does not produce changes in mEPSCs (**Figure 5B**), which suggests that prior visual experience is an important variable to consider when assessing plasticity. Poisson random stimulation has previously been shown to be effective at inducing LTD in V1 of DE rats (Guo et al., 2012), but in contrast to what we have shown here, it was completely blocked by the GluN2B antagonist, ifenprodil. The difference may be due to the use of different frequency and duration of Poisson train: Guo et al. used a shorter duration (10 min) 0.5-Hz Poisson train, which is a lower frequency than what we used here (**Table 2**). It is possible that a short duration lower frequency Poisson train may act on GluN2B-containing NMDARs, which are up-regulated by DE (Quinlan et al., 1999; Philpot et al., 2001), to produce LTD. Our results would add to this finding by demonstrating that a more prolonged (2 h) Poisson train stimulation, which has the same average frequency as neural activity seen during LE, induces GluN2B-independent homeostatic plasticity.

The Polarity of Plasticity Induced by the Same Naturalistic Stimulation Pattern Is Dependent on the Prior Visual Experience

The threshold for inducing Hebbian plasticity is adjusted by changes in visual experience (Abraham, 2008; Cooper and Bear, 2012). An altered synaptic modification threshold can lead to opposite polarities of synaptic changes even with activity of the same input frequency. Our observation that the same naturalistic spike train produces distinct changes to mEPSC amplitudes depending on prior visual experience (**Figure 6**) is consistent with the idea that prior visual experience changes the metaplastic state of V1 circuitry. Further, it suggests that naturalistic spike patterns that induce homeostatic adaptation act on the existing metaplastic state to drive synaptic adaptation.

Metaplasticity is largely driven by changes in the function of NMDA receptors, which result from alterations in subunit composition (GluN2B and GluN2A ratio). Bidirectional regulation of NMDAR subunit composition with DE and LE is well established (Quinlan et al., 1999; Philpot et al., 2001, 2003; Guo et al., 2012). DE reduces the threshold for LTP such that previously weak inputs are able to be potentiated (Kirkwood et al., 1996; Guo et al., 2012). We recently reported that in V1 L2/3 the reduction of mEPSC amplitudes with LE is dependent on NMDARs (Chokshi et al., 2019; Rodriguez et al., 2019), and DE-induced potentiation of mEPSCs is dependent on GluN2B-containing NMDARs (Bridi et al., 2018). Therefore, alterations in NMDAR function with prior visual experience may be responsible for the differential outcome of plastic changes induced by *ex vivo* stimulation. We found that blocking NMDARs containing the GluN2B subunit, which is known to be up-regulated in V1 following DE (Quinlan et al., 1999), or mGluR5s, which we recently reported to play a role in LE-induced metaplasticity (Chokshi et al., 2019), was rather ineffective at preventing *in vivo* spike train-driven decreases in mEPSC amplitudes. The molecular signaling of the homeostatic plasticity observed here will require further investigation. Nonetheless, our study demonstrates that stimulating the feedforward inputs to L2/3 with naturalistic activity patterns is sufficient to produce homeostatic synaptic depression even if the resulting plasticity is not identical to that produced with LE. Furthermore, our findings suggest that homeostatic synaptic plasticity, similar to Hebbian plasticity, is dependent on the metaplastic state of the circuit set by prior visual experience.

DATA AVAILABILITY STATEMENT

The original contributions presented in the study are included in the article, further inquiries can be directed to the corresponding author.

ETHICS STATEMENT

The animal study was reviewed and approved by Johns Hopkins University Animal Care and Use Committee and University of Maryland Institutional Animal Care and Use Committee.

AUTHOR CONTRIBUTIONS

VC and BG performed *ex vivo* experiments and analyses. AD wrote the MATLAB code for spike pattern analysis. EN provided input on the spike pattern analysis program. AD and VC ran the spike pattern analysis program and statistics. CL and EQ performed *in vivo* single unit recordings and analyses. H-KL conceived the project. VC, BG, CL, EN, EQ, and H-KL wrote the manuscript. All authors contributed to the article and approved the submitted version.

FUNDING

This work was supported by National Institutes of Health (NIH) grant R01-EY014882 to H-KL, NIH grant R01-EY027544 to EN, and NIH grants R01-EY016431 and R01-EY025922 to EQ.

ACKNOWLEDGMENTS

We thank Dr. Alfredo Kirkwood for helpful discussions.

REFERENCES

Abraham, W. C. (2008). Metaplasticity: tuning synapses and networks for plasticity. *Nat. Rev. Neurosci.* 9:387. doi: 10.1038/nrn2356

Bear, M. F., Cooper, L. N., and Ebner, F. F. (1987). A physiological basis for a theory of synapse modification. *Science* 237, 42–48. doi: 10.1126/science.3037696

Beique, J. C., Na, Y., Kuhl, D., Worley, P. F., and Huganir, R. L. (2011). Arc-dependent synapse-specific homeostatic plasticity. *Proc. Natl. Acad. Sci. U S A* 108, 816–821. doi: 10.1073/pnas.1017914108

Bienenstock, E. L., Cooper, L. N., and Munro, P. W. (1982). Theory for the development of neuron selectivity: orientation specificity and binocular interaction in visual cortex. *J. Neurosci.* 2, 32–48. doi: 10.1523/JNEUROSCI.02-01-00032.1982

Bliss, T. V. P., and Gardner-Medwin, A. R. (1973). Long-lasting potentiation of synaptic transmission in the dentate area of the unanaesthetized rabbit following stimulation of the perforant path. *J. Physiol.* 232, 357–574. doi: 10.1113/jphysiol.1973.sp010274

Bliss, T. V. P., and Lomo, T. (1973). Long-lasting potentiation of synaptic transmission in the dentate area of the anaesthetized rabbit following stimulation of the perforant path. *J. Physiol.* 232, 331–356. doi: 10.1113/jphysiol.1973.sp010273

Bridi, M. C. D., De Pasquale, R., Lantz, C. L., Gu, Y., Borrell, A., Choi, S. Y., et al. (2018). Two distinct mechanisms for experience-dependent homeostasis. *Nat. Neurosci.* 21, 843–850. doi: 10.1038/s41593-018-0150-0

Chen, L., Deng, Y., Luo, W., Wang, Z., and Zeng, S. (2009). Detection of bursts in neuronal spike trains by the mean inter-spike interval method. *Prog. Nat. Sci.* 19, 229–235. doi: 10.1016/j.pnsc.2008.05.027

Chokshi, V., Gao, M., Grier, B. D., Owens, A., Wang, H., Worley, P. F., et al. (2019). Input-specific metaplasticity in the visual cortex requires homer1a-mediated mglur5 signaling. *Neuron* 104, 736.e736–748.e736.doi: 10.1016/j.neuron.2019.08.017

Cooke, S. F., and Bear, M. F. (2014). How the mechanisms of long-term synaptic potentiation and depression serve experience-dependent plasticity in primary visual cortex. *Philos. Trans. R. Soc. Lond. B Biol. Sci.* 369:20130284. doi: 10.1098/rstb.2013.0284

Cooper, L. N., and Bear, M. F. (2012). The BCM theory of synapse modification at 30: interaction of theory with experiment. *Nat. Rev. Neurosci.* 13, 798–810. doi: 10.1038/nrn3353

Desai, N. S., Cudmore, R. H., Nelson, S. B., and Turrigiano, G. G. (2002). Critical periods for experience-dependent synaptic scaling in visual cortex. *Nat. Neurosci.* 5, 783–789. doi: 10.1038/nn878

Dudek, S. M., and Bear, M. F. (1992). Homosynaptic long-term depression in area CA1 of hippocampus and effects of N-methyl-D-aspartate receptor blockade. *Proc. Natl. Acad. Sci. U S A* 89, 4363–4367. doi: 10.1073/pnas.89.10.4363

Espinosa, J. S., and Stryker, M. P. (2012). Development and plasticity of the primary visual cortex. *Neuron* 75, 230–249. doi: 10.1016/j.neuron.2012.06.009

Fong, M.-F. F., Newman, J. P., Potter, S. M., and Wenner, P. (2015). Upward synaptic scaling is dependent on neurotransmission rather than spiking. *Nat. Commun.* 6:6339. doi: 10.1038/ncomms7339

Gao, M., Sossa, K., Song, L., Errington, L., Cummings, L., Hwang, H., et al. (2010). A specific requirement of Arc/Arg3.1 for visual experience-induced homeostatic synaptic plasticity in mouse primary visual cortex. *J. Neurosci.* 30, 7168–7178. doi: 10.1523/JNEUROSCI.1067-10.2010

Goel, A., and Lee, H. K. (2007). Persistence of experience-induced homeostatic synaptic plasticity through adulthood in superficial layers of mouse visual cortex. *J. Neurosci.* 27, 6692–6700. doi: 10.1523/JNEUROSCI.5038-06.2007

Goel, A., Jiang, B., Xu, L. W., Song, L., Kirkwood, A., Lee, H. K., et al. (2006). Cross-modal regulation of synaptic AMPA receptors in primary sensory cortices by visual experience. *Nat. Neurosci.* 9, 1001–1003. doi: 10.1038/nn1725

Goel, A., Xu, L. W., Snyder, K. P., Song, L., Goenaga-Vazquez, Y., Megill, A., et al. (2011). Phosphorylation of ampa receptors is required for sensory deprivation-induced homeostatic synaptic plasticity. *PLoS One* 6:e18264. doi: 10.1371/journal.pone.0018264

Guo, Y., Huang, S., De Pasquale, R., Mcgehrin, K., Lee, H. K., Zhao, K., et al. (2012). Dark exposure extends the integration window for spike-timing-dependent plasticity. *J. Neurosci.* 32, 15027–15035. doi: 10.1523/JNEUROSCI.2545-12.2012

Haider, B., Schulz, D. P., Hausser, M., and Carandini, M. (2016). Millisecond coupling of local field potentials to synaptic currents in the awake visual cortex. *Neuron* 90, 35–42. doi: 10.1016/j.neuron.2016.02.034

Hebb, D. O. (1949). *The Organization of Behavior: Neuropsychological Theory*. New York, NY: Wiley & Sons Inc.

Keck, T., Keller, G. B., Jacobsen, R. I., Eysel, U. T., Bonhoeffer, T., Hubener, M., et al. (2013). Synaptic scaling and homeostatic plasticity in the mouse visual cortex *in vivo*. *Neuron* 80, 327–334. doi: 10.1016/j.neuron.2013.08.018

Kim, J., and Tsien, R. W. (2008). Synapse-specific adaptations to inactivity in hippocampal circuits achieve homeostatic gain control while dampening network reverberation. *Neuron* 58, 925–937. doi: 10.1016/j.neuron.2008.05.009

Kirkwood, A., and Bear, M. F. (1994). Hebbian synapses in visual cortex. *J. Neurosci.* 14, 1634–1645. doi: 10.1523/JNEUROSCI.14-03-01634.1994

Kirkwood, A., Rioult, M. C., and Bear, M. F. (1996). Experience-dependent modification of synaptic plasticity in visual cortex. *Nature* 381, 526–528. doi: 10.1038/381526a0

Lee, H. K., and Kirkwood, A. (2019). Mechanisms of homeostatic synaptic plasticity *in vivo*. *Front. Cell. Neurosci.* 13:520. doi: 10.3389/fncel.2019.00520

Lisman, J. E. (1997). Bursts as a unit of neural information: making unreliable synapses reliable. *Trends Neurosci.* 20, 38–43. doi: 10.1016/S0166-2236(96)10070-9

Murase, S., Lantz, C. L., Kim, E., Gupta, N., Higgins, R., Stopfer, M., et al. (2016). Matrix metalloproteinase-9 regulates neuronal circuit development and excitability. *Mol. Neurobiol.* 53, 3477–3493. doi: 10.1007/s12035-015-9295-y

Niell, C. M., and Stryker, M. P. (2008). Highly selective receptive fields in mouse visual cortex. *J. Neurosci.* 28, 7520–7536. doi: 10.1523/JNEUROSCI.0623-08.2008

Perrett, S. P., Dudek, S. M., Eagleman, D., Montague, P. R., and Friedlander, M. J. (2001). LTD induction in adult visual cortex: role of stimulus timing and inhibition. *J. Neurosci.* 21, 2308–2319. doi: 10.1523/JNEUROSCI.21-07-02308.2001

Petrus, E., Isaiah, A., Jones, A. P., Li, D., Wang, H., Lee, H. K., et al. (2014). Crossmodal induction of thalamocortical potentiation leads to enhanced information processing in the auditory cortex. *Neuron* 81, 664–673. doi: 10.1016/j.neuron.2013.11.023

Petrus, E., Rodriguez, G., Patterson, R., Connor, B., Kanold, P. O., Lee, H. K., et al. (2015). Vision loss shifts the balance of feedforward and intracortical circuits in opposite directions in mouse primary auditory and visual cortices. *J. Neurosci.* 35, 8790–8801. doi: 10.1523/JNEUROSCI.4975-14.2015

Philpot, B. D., Espinosa, J. S., and Bear, M. F. (2003). Evidence for altered NMDA receptor function as a basis for metaplasticity in visual cortex. *J. Neurosci.* 23, 5583–5588. doi: 10.1523/JNEUROSCI.23-13-05583.2003

Philpot, B. D., Sekhar, A. K., Shouval, H. Z., and Bear, M. F. (2001). Visual experience and deprivation bidirectionally modify the composition and function of NMDA receptors in visual cortex. *Neuron* 29, 157–169. doi: 10.1016/s0896-6273(01)00187-8

Quinlan, E. M., Olstein, D. H., and Bear, M. F. (1999). Bidirectional, experience-dependent regulation of N-methyl-D-aspartate receptor subunit composition in the rat visual cortex during postnatal development. *Proc. Natl. Acad. Sci. U S A* 96, 12876–12880. doi: 10.1073/pnas.96.22.12876

Rodriguez, G., Mesik, L., Gao, M., Parkins, S., Saha, R., Lee, H. K., et al. (2019). Disruption of NMDAR function prevents normal experience-dependent homeostatic synaptic plasticity in mouse primary visual cortex. *J. Neurosci.* 39, 7664–7673. doi: 10.1523/JNEUROSCI.2117-18.2019

Sun, W., and Dan, Y. (2009). Layer-specific network oscillation and spatiotemporal receptive field in the visual cortex. *Proc. Natl. Acad. Sci. U S A* 106, 17986–17991. doi: 10.1073/pnas.0903962106

Turrigiano, G. (2008). The self-tuning neuron: synaptic scaling of excitatory synapses. *Cell* 135, 422–435. doi: 10.1016/j.cell.2008.10.008

Turrigiano, G. G., Leslie, K. R., Desai, N. S., Rutherford, L. C., and Nelson, S. B. (1998). Activity-dependent scaling of quantal amplitude in neocortical neurons. *Nature* 391, 892–896. doi: 10.1038/36103

Conflict of Interest: The authors declare that the research was conducted in the absence of any commercial or financial relationships that could be construed as a potential conflict of interest.

Copyright © 2021 Chokshi, Grier, Dykman, Lantz, Niebur, Quinlan and Lee. This is an open-access article distributed under the terms of the Creative Commons Attribution License (CC BY). The use, distribution or reproduction in other forums is permitted, provided the original author(s) and the copyright owner(s) are credited and that the original publication in this journal is cited, in accordance with accepted academic practice. No use, distribution or reproduction is permitted which does not comply with these terms.

frontiers in Synaptic Neuroscience

MINI REVIEW
published: 04 May 2021
doi: 10.3389/fnsyn.2021.661681

Neuronal Glycoprotein M6a: An Emerging Molecule in Chemical Synapse Formation and Dysfunction

*Antonella León†, Gabriela I. Aparicio† and Camila Scorticati**

Instituto de Investigaciones Biotecnológicas "Rodolfo A. Ugalde", Universidad Nacional de San Martín and Consejo Nacional de Investigaciones Científicas y Técnicas (IIBio-UNSAM-CONICET), Buenos Aires, Argentina

The cellular and molecular mechanisms underlying neuropsychiatric and neurodevelopmental disorders show that most of them can be categorized as synaptopathies—or damage of synaptic function and plasticity. Synaptic formation and maintenance are orchestrated by protein complexes that are in turn regulated in space and time during neuronal development allowing synaptic plasticity. However, the exact mechanisms by which these processes are managed remain unknown. Large-scale genomic and proteomic projects led to the discovery of new molecules and their associated variants as disease risk factors. Neuronal glycoprotein M6a, encoded by the *GPM6A* gene is emerging as one of these molecules. M6a has been involved in neuron development and synapse formation and plasticity, and was also recently proposed as a gene-target in various neuropsychiatric disorders where it could also be used as a biomarker. In this review, we provide an overview of the structure and molecular mechanisms by which glycoprotein M6a participates in synapse formation and maintenance. We also review evidence collected from patients carrying mutations in the *GPM6A* gene; animal models, and *in vitro* studies that together emphasize the relevance of M6a, particularly in synapses and in neurological conditions.

Keywords: GPM6A, neuronal plasticity, synaptopathy, synaptic interactome, PLP family

OPEN ACCESS

Edited by:
Christian Gonzalez-Billault, University of Chile, Chile

Reviewed by:
Constanze I. Seidenbecher, Leibniz Institute for Neurobiology (LG), Germany
Vladimir Sytnyk, University of New South Wales, Australia

***Correspondence:**
Camila Scorticati
cscorticati@iib.unsam.edu.ar

† These authors have contributed equally to this work and share first authorship

Received: *31 January 2021*
Accepted: *07 April 2021*
Published: *04 May 2021*

Citation:
León A, Aparicio GI and Scorticati C (2021) Neuronal Glycoprotein M6a: An Emerging Molecule in Chemical Synapse Formation and Dysfunction. Front. Synaptic Neurosci. 13:661681. doi: 10.3389/fnsyn.2021.661681

INTRODUCTION

The excitatory synapses are specific neuron–neuron communications between axon and dendritic processes that orchestrate the information stream and storage in the brain (Tu et al., 2018). Synapse formation involves a complex series of events with at least three primary stages: axon elongation and guidance by which axons reach their target area; synaptic specificity governed by an appropriate association of synaptic molecules, and synaptogenesis which creates functional synapses (Shen and Cowan, 2010).

Functional synapses are supported by specialized protein complexes, whose function is regulated in time and space during neuronal development, allowing effective synaptic plasticity (Torres et al., 2017). The cellular and molecular mechanisms underlying neuropsychiatric and neurodegenerative disorders reveal that most of them can be classified as synaptopathies (Sengpiel, 2018), however, their full understanding so far remains unknown. Large scale genome-wide association studies (GWAS, reviewed in Claussnitzer et al., 2020) promote the study of additional candidates. Candidates arise either as genetic vulnerability or susceptibility loci allowing researchers to explore

how they might be involved in the molecular mechanisms governing neurological diseases with complex etiology and heterogeneous genetic predisposition.

Neuronal glycoprotein M6a, encoded by the *GPM6A* gene, is a member of the tetraspan proteolipid protein (PLP) family together with PLP/DM20 and M6b. Since its discovery in 1992 (Baumrind et al., 1992; Lagenaur et al., 1992), M6a has emerged as one of many proteins involved in neuron development, synapse plasticity, and as a key component in various neuropsychiatric disorders (Michibata et al., 2009; El-Kordi et al., 2013; Gregor et al., 2014; Fuchsova et al., 2015). This review provides a quick overview of the structure and molecular mechanisms by which M6a participates in synapse formation and maintenance. Moreover, we review evidence collected from patients carrying mutations within *GPM6A*; animal models, and *in vitro* studies that highlight the relevance of M6a, particularly in synapses and related neurological conditions.

GENE, PROTEIN, AND STRUCTURAL DOMAINS

The PLP family members are integral membrane proteins with a conserved topology: four transmembrane domains (TMDs), two extracellular loops (EC1 and EC2), one intracellular loop (IC), and the N- and C-termini both at the cytoplasmic face (**Figure 1A**). M6a exhibits low sequence identity with both PLP (38%) and M6b (52%), however, the TMDs are highly conserved (Greer and Lees, 2002; Fernandez et al., 2010).

Human glycoprotein M6a is encoded by a 369,731 kb gene organized into seven exons and located at chromosome 4q34.2. The full-length gene encodes a 278 amino acid membrane protein with a molecular mass of approximately 32 kDa (Olinsky et al., 1996). The amino acid sequence of M6a is highly conserved within mammals (more than 98% of identity). Post-translational modifications in M6a are summarized in **Figure 1A**. M6a has seven potential phosphorylation sites, and some of them are responsible for specific features described below. M6a has four cysteine residues within its EC2, critical for its folding and function, particularly C174 and C192 are linked by a disulfide bond, forming an intradomain important for protein-protein interactions (Fuchsova et al., 2009). The EC2 also contains two predicted N-glycosylation sites. Only glycosylation at N164 was experimentally corroborated, although there are no reported functions to date (Fang et al., 2016). Seven other cysteine residues close to the TMDs in the cytoplasmic side are potential palmitoylation sites, three of which (C17/18/21)—conserved within the PLP family—are necessary for M6a inclusion in lipid rafts (Honda et al., 2017; Ito et al., 2018).

GPM6A's RNA-expression rapidly increases during development in human and murine brains. M6a is a brain-specific gene with a very high level of expression, representing one of the most abundant palmitoylated proteins in the CNS (Huminiecki et al., 2003; Kang et al., 2008). By contrast, low expression was detected in the lung, spleen, ovary, and the thyroid gland (Fagerberg et al., 2014; Yu et al., 2014; Yue et al., 2014). M6a protein levels are enriched in the hippocampus, cerebellum, striatum, and prefrontal cortex among other brain areas[1]. Regarding specific cell expression at the CNS, M6a is mostly placed at the cell surface of neurons and epithelial cells of the choroid plexus, but not in glial cells. The neuronal expression of M6a gives it a distinctive feature within the PLP family members as PLP is expressed only in glial cells and M6b is expressed in both neurons and glia (Werner et al., 2013).

M6a AND SYNAPSE FORMATION

M6a's Role in the Presynaptic Formation

The coordination of neuronal differentiation, axonal growth, and guidance involves timely expression of cell surface proteins and extracellular adhesion molecules escorted by structural changes in the cellular cytoskeleton (Caceres et al., 2012). During neurite outgrowth, plasma membrane proteins are directed toward neurites first, and then they are concentrated in growth cones (GCs). There, proteins will be available to respond to orientation signals and to signal the path to a specific destination (Fuentes and Arregui, 2009; Ulloa et al., 2018). Indeed, M6a was identified as an "edge-membrane antigen" (EMA) because it was found concentrated at the edge of neuronal GCs and their lamellipodia in cultured neurons from the cerebellum, cortex, and hippocampus (Baumrind et al., 1992; Lagenaur et al., 1992). Later on, M6a was found to be critical for neurite growth in a wide variety of *in vitro* models, from brain tissue explants to neuronal cell lines and from human to Xenopus (Lagenaur et al., 1992; Mukobata et al., 2002; Alfonso et al., 2005; Zhao et al., 2008; Michibata et al., 2009; Formoso et al., 2015a). Noteworthy, Sato et al. (2011a) observed a reduction of the axon projections in the olfactory bulb from embryonic brains at E14.5 of Gpm6a knockout mice. Besides, double knockout mice for Gpm6a and Gpm6b show decreased axon elongation and a thinner corpus callosum which could be rescued by forced expression of M6 proteins (Mita et al., 2015).

To date, redundant signaling pathways of Src/MAPK/ERK, PKC, and PI3K/AKT kinases mediate M6a-induced neurite extension in hippocampal neurons and neuroblastoma cells (Mukobata et al., 2002; Scorticati et al., 2011; Formoso et al., 2015a). The phosphorylation of tyrosine 251 close to M6a's C-terminus is critical for neuritogenesis (Formoso et al., 2015a). By contrast, cells expressing a truncated form of M6a lacking the N-terminus did not show neurite outgrowth inhibition (Mita et al., 2015). The direct association of M6a's C-terminus with coronin1A—a cytoskeleton adaptor molecule—verify its essential role in the extension of projections (Alvarez Julia et al., 2016; Martorella et al., 2017). Furthermore, Honda et al. (2017) identified that M6a induces neuron polarity through the Rufy3-Rap2-STEF/Tiam2 pathway.

[1]www.proteinatlas.org

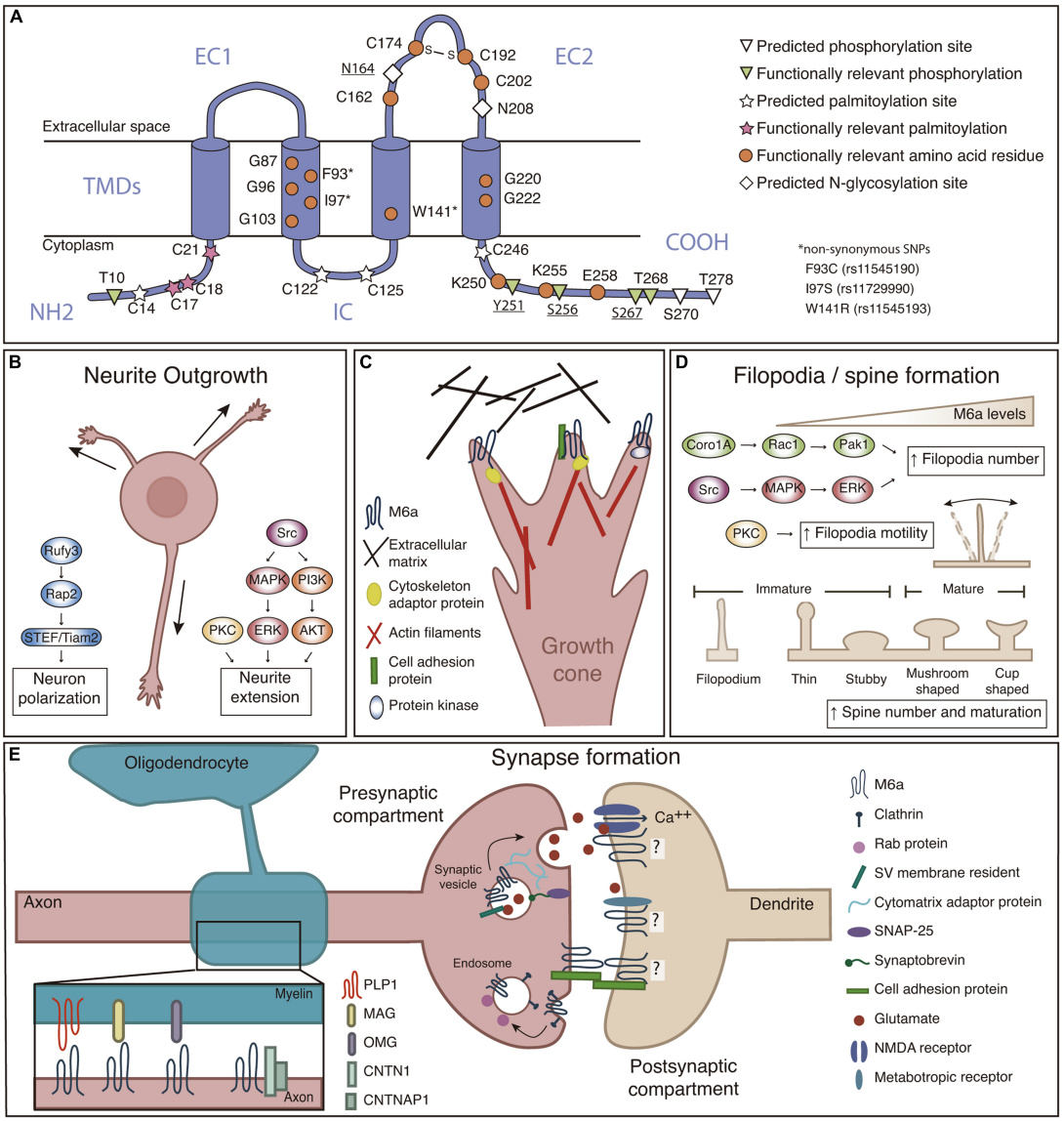

FIGURE 1 | (A) M6a structural features. M6a's topological computational model predicts four transmembrane domains (TMDs), two extracellular loops (a small one—EC1- and a large one—EC2-), an intracellular loop (IC), and N- and C-terminal ends facing the cell cytoplasm (NH2 and COOH). Predicted sites for palmitoylation (C14, C17, C18, C21, C122, C125, and C246), N-glycosylation (N164 and N208), and phosphorylation (T10, Y251, S256, S267, T268, S270, and T278) are highlighted; bold underlined sites indicate post-translational modifications which are experimentally validated. Orange circles represent amino acid residues relevant for M6a function. **(B)** M6a promotes neurite outgrowth and neuronal polarization, which involves the activation of Src/MAPK/ERK, PKC and PI3K/AKT, and Rufy3-Rap2-STEF/Tiam2 signaling pathways, respectively. **(C)** We hypothesize that M6a function depends on its association with partner proteins in specific membrane microdomains. These associations, induce auto/phosphorylation in specific C-terminal residues facing the cytoplasm, and finally promote neuronal plasticity (Fuchsova et al., 2009; Scorticati et al., 2011; Formoso et al., 2015a,b; Garcia et al., 2017; Honda et al., 2017; Aparicio et al., 2020). For example, M6a can associate with extracellular matrix proteins such as brevican and tenascin C through its extracellular loops in *trans* and/or with cell adhesion proteins (NCAM and NPTN) through its extracellular domains in *cis*, triggering its phosphorylation and therefore the recruitment of adapter proteins (such as Rap) and the activation of protein kinases that finally promote the reorganization of the cytoskeleton. **(D)** M6a promotes filopodia formation and motility through a mechanism that involves the activation of the Coro1A/Rac1/Pak1 and Src/MAPK/ERK, and PKC pathways, respectively. M6a also participates in spine formation and maturation of dendritic protrusions. **(E)** Left: Recently proposed interactions between M6a and myelin sheath proteins (PLP1, MAG, and OMG), and myelinated-axon proteins CNTN1 and CNTNAP1. Right: M6a is located at the presynaptic compartment plasma membrane, synaptic vesicle—SV—and endosomal membranes. M6a also interacts with postsynaptic glutamate receptors (like NMDA-R1 and GRM1) but its localization to the postsynaptic compartment was not experimentally confirmed yet. M6a, glycoprotein M6a; Src, Src kinase; MAPK, mitogen-activated protein kinase; ERK, extracellular signal-regulated kinase; PKC, protein kinase C; PI3K, phosphatidylinositide 3-kinase; AKT, serine/threonine-protein kinase; Rap2, Ras-related protein-2; Rufy3, Rufy 3 protein; STEF/Tiam2, T-lymphoma invasion and metastasis-inducing protein 2; NCAM, Neural cell adhesion molecule; NPTN, neuroplastin; Coro1A, coronin-1A; Rac1, Ras-related C3 botulinum toxin substrate 1; Pak1, p21-activated kinase 1; PLP1, proteolipid protein 1; MAG, myelin-associated glycoprotein; OMG, oligodendrocyte-myelin glycoprotein; CNTN1, contactin-1; CNTNAP1, contactin-associated protein 1; NMDA-R1, N-methyl-D-aspartate receptor 1; GRM1, metabotropic glutamate receptor 1; SNAP25, Synaptosomal-Associated Protein, 25 kDa.

Recent proteomic studies identified proteins associated with M6a that participate in neurite outgrowth and axon elongation (**Figures 1B,C**; Sato et al., 2011a; Huttlin et al., 2017; Aparicio et al., 2020; Haenig et al., 2020; Pourhaghighi et al., 2020). To emphasize some examples, we divided them into 3 groups: (i) Cytoplasmic proteins: which include cytoskeleton adaptor molecules and cytoskeleton organization pathways which might interact with M6a's cytoplasmic tails as Ras kinases 2, DiRas2 (Grunewald et al., 2021) and the kinases mentioned above. (ii) Cell adhesion molecules (CAMs): which mediate recognition of cellular targets, bind the cell surface to the extracellular matrix (ECM), and maintain cell shape. Examples of these molecules that could interact with M6a's extracellular loops or its transmembrane domains are neuronal cell adhesion molecule (NCAM) (Neugebauer et al., 1988), and neuroplastin, NPTN (Beesley et al., 2014). (iii) ECM proteins: which only could interact with M6a's extracellular loops: brevican (BCAN) (Miura et al., 2001), and tenascin C (TNC) (Andrews et al., 2009).

Presynaptic boutons are terminal specializations of the axon, which contain synaptic vesicles (SVs) filled with neurotransmitters. This specific compartmentalization involves the coordination of both SVs and presynaptic active zone proteins, which define regions in the membrane for the release of neurotransmitters to the synaptic cleft (Yue et al., 2014). Thus, there are three main types of proteins (i) residents of SV's membrane, such as synaptophysin (Egbujo et al., 2016), (ii) filament or adaptor proteins of the cytomatrix, such as piccolo and bassoon (Hida and Ohtsuka, 2010), and (iii) those that participate in synaptic vesicle exocytosis such as synaptosomal associated protein 25 (SNAP25) (Antonucci et al., 2016; **Figure 1E**). Roussel et al. (1998) revealed that M6a was distributed at the presynaptic membrane, in particular, on the membrane of SVs which was confirmed by proteomic analysis (Takamori et al., 2006; Taoufiq et al., 2020). Besides, M6a was also found at glutamatergic nerve terminals in the cerebellum and cerebral cortex but not in GABAergic neurons of adult brain mice. This specific-excitatory preference was also confirmed in the hippocampal formation in which M6a colocalizes with the vesicular glutamate transporter VGLUT (Cooper et al., 2008).

Recently, M6a has also been associated with other SVs and presynaptic active zone—PAZ—residents proteins, like synaptic vesicle protein 2B (SV2B), piccolo, bassoon, and synapsin 1 (Aparicio et al., 2020). Overexpression of M6a in hippocampal neurons showed a significant increment of synaptophysin puncta correlating with an increase in the number of synapses. On the contrary, neurons subjected to siRNA depletion of M6a and neurons overexpressing a truncated form of M6a at the EC2 loop exhibited a decreased number of synaptophysin puncta (Alfonso et al., 2005; Fuchsova et al., 2009; Formoso et al., 2016). Moreover, M6a internalizes and recycles back to the cell membrane via clathrin-mediated endocytosis, and localizes in Rab5, Rab7, and Rab11 positive endosomes, just like the case of SVs recycling pathways (Wu et al., 2007; Formoso et al., 2016; Garcia et al., 2017; Rosas et al., 2018). Indeed, inducing M6a acute internalization correlated with a decrease of both the number of synaptophysin puncta and synapses (Garcia et al., 2017), suggesting that M6a might be playing an active role in SV/neurotransmitter release.

M6a's Role in the Postsynaptic Formation

Straight opposed to the presynaptic terminal is the postsynaptic target. Dendritic spines, the main postsynaptic compartment, are protrusions from the dendrite shaft that receive the information from axonal terminals through different neurotransmitter receptors. Dendritic spines can show dynamic changes in number, size, shape, and movement which allow synaptic rearrangements to take place (Tonnesen and Nagerl, 2016). This plastic feature is a critical substrate for functional plasticity during pruning or learning and memory, and also for synaptic dysfunction as observed in neurodegenerative and neuropsychiatric conditions including Alzheimer's Disease (AD), autism spectral disorders (ASD), schizophrenia, and depression (Penzes et al., 2011; Bian et al., 2015; Ozcan, 2017).

According to its size and shape, dendritic spines can be classified as thin, stubby, mushroom, and cup-shaped. Moreover, according to their functionality, dendritic protussions can also be classified as immature (filopodia, thin and stubby) or mature (mushroom and cup-shaped) (**Figure 1D**). Three possible models have been proposed to explain how a synapse is formed: (i) Sotelo's model describes that a synapse could arise when an immature spine is contacted by the axon terminal inducing its development toward the mushroom type (Sotelo et al., 1975), (ii) Miller/Peters's model proposes that a presynaptic terminal directly contacts with the dendrite shaft, inducing spine outgrowth (Miller and Peters, 1981), and (iii) Filopodial model: where dendritic filopodia may actively initiate synaptogenic contacts by contacting a presynaptic terminal, thereby inducing its stabilization and subsequently maturation to the mushroom type (Yuste and Bonhoeffer, 2004; Ziv and Fisher-Lavie, 2014).

M6a has been widely described to be involved in filopodia/spine formation in different cell culture models (Alfonso et al., 2005; Sato et al., 2011b; Scorticati et al., 2011; Formoso et al., 2015b; Alvarez Julia et al., 2016; Formoso et al., 2016; Rosas et al., 2018). Two pathways have been implicated by which M6a increases filopodia density. M6a overexpression induces the activation by phosphorylation of the intracellular cascade involving the Src and MAPK/ERK pathway; and the localization of M6a within lipid rafts is compatible with this (Scorticati et al., 2011). Likewise, signaling pathways that include Rac1 and Pak1 activation through coronin1A facilitate M6a-induced filopodium formation (Alvarez Julia et al., 2016). There are key domains required for M6a to induce filopodia/spine formation (**Figure 1D**): (i) TMDs homotypic-interactions, especially commanded by particular glycine residues at TMD2 and TMD4 (Formoso et al., 2015b, 2016), (ii) a disulfide bridge at EC2 loop formed between cysteine residues C174 and C192 (Fuchsova et al., 2009), and (iii) C-terminal domain residues K250/K255/E258 (Rosas et al., 2018). Although the N-terminus is not involved in filopodia induction (Mita et al., 2015; Rosas et al., 2018), phosphorylation of certain serine/threonine residues at

N-and C-termini, T10/S256/S267/T268, proved to be necessary for filopodial motility (Brocco et al., 2010).

Although M6a induces dendritic protrusions plasticity, whether or not it is placed at the postsynaptic membrane is undetermined. For instance, M6a was identified at presynaptic membranes and enriched in glutamatergic synaptic vesicles docked to the presynaptic active zone (Roussel et al., 1998; Boyken et al., 2013). Conversely, M6a was detected in a proteomic analysis of enriched postsynaptic membrane fractions from mice brains, suggesting a postsynaptic localization for M6a (Reim et al., 2017). Besides, we described that M6a co-immunoprecipitated with integral components of the postsynaptic membranes such as metabotropic glutamate receptor 1 (GRM1), voltage-dependent anion channel 1 (VDAC1), and N-methyl-D-aspartate receptor type 1, NMDA-R1 (GR1A1) (Aparicio et al., 2020). Indeed, M6a-overexpressing neurons exhibited an increase in the number of NMDA-R1 clusters, whilst truncated forms of M6a or its depletion decreased the number of NMDA-R1 clusters (Formoso et al., 2016; Garcia et al., 2017). The colocalization of M6a and NMDA-R1 suggests that M6a acts as a scaffold protein assembling proteins and lipids to form a signaling platform on the neuronal surface (Wu et al., 2007; Scorticati et al., 2011). However, to determine whether M6a is indeed located at the postsynaptic membrane techniques such as cryo-electron microscopy and super-resolution microscopy are needed to avoid contaminations of biochemical-based techniques (Liu et al., 2019; Nosov et al., 2020).

M6a'S POTENTIAL ROLE IN NEURON-GLIA INTERACTION

M6a is enriched within cerebellar parallel and hippocampal mossy fibers, whose axons remain unmyelinated also in adulthood (Cooper et al., 2008). Nonetheless, new data suggest that M6a could participate in neuron-glia interactions. This subject exceeds the topics covered in this review, and no functional experiments were reported yet, but we would like to highlight a few insights. Pourhaghighi et al. (2020) identified associated protein complexes in adult mammal brains and built BraInMap[2]. M6a was found within a complex of 30 interacting proteins, some of which are myelin sheath proteins, including the main myelin glycoproteins PLP and MAG; or are myelin sheath associated proteins like contactin 1 and contactin associated protein 1. In agreement, we identified 20 myelin proteins in the co-immunoprecipitation complexes formed by M6a's extracellular domains and rat hippocampal samples, in which PLP was experimentally confirmed (Aparicio et al., 2020). Also, Jahn et al. (2020) identified M6a in the myelin sheath of post mortem human brains.

M6a IN SYNAPSE FUNCTION AND DYSFUNCTION

The evidence reviewed so far highlights an important role of M6a in neuronal development and synaptic plasticity. However, few reports interrogate about the role of M6a on active synapses. All of them are based on determining the cluster number of synaptophysin and/or the number of clusters between synaptophysin and NMDA-R1 on *in vitro* models (Alfonso et al., 2005; Fuchsova et al., 2009; Formoso et al., 2016; Garcia et al., 2017). For instance, endogenous M6a acute depletion using siRNA or treatments with M6a-mAb neutralizing antibodies dramatically decrease the number of synaptophysin clusters, or synaptophysin and NMDA-R1 colocalization clusters (Alfonso et al., 2005; Garcia et al., 2017). The latter suggests that M6a is not only required for the formation of synapses but also their maintenance. Evidence from M6a's relevance *in vivo* comes from the observation that several *GPM6A* variants and inadequate expression levels were associated with several neuropsychiatric disorders (see **Table 1**), thus highlighting that the impairment of M6a function contributes to disease onset or increases the risk of susceptibility.

Chronic stress induces behavioral changes in mammals, which can be evidenced by mood disorders including anxiety, claustrophobia, and depression. In this context mRNA levels of Gpm6a were decreased in the hippocampus of chronically stressed animals (Alfonso et al., 2002, 2004a,b); and then rescued with the administration of antidepressants (Alfonso et al., 2006). These are consistent with findings where chronically stress animals presented a reduction of the dendritic arborization and structural changes in the mossy fiber terminals (Cooper et al., 2008). In humans, *GPM6A* mRNA levels were also decreased in the hippocampus of depressed patients who committed suicide (Fuchsova et al., 2015). Furthermore, depressed patients treated with serotonin reuptake inhibitors showed a reduction of M6a levels in saliva compared to depressed patients under benzodiazepine treatment or no treatment at all. As a result, M6a was proposed as a mood disorder biomarker (Monteleone et al., 2020).

Gpm6a knockout mice lack obvious behavioral abnormalities but when subjected to moderate restrain stress, they presented a claustrophobia-like phenotype. These findings encouraged El-Kordi and collaborators to investigate *GPM6A* variants within claustrophobic patients. In their study they found a 3′-untranslated region variant that produced a functional mRNA that could not be silenced by neuronal miR124, thereby losing the physiological regulation of the gene (El-Kordi et al., 2013). Gregor et al. (2014) identified a *de novo* duplication of the *GPM6A* gene in a patient with learning disabilities and behavioral anomalies. Furthermore, Rao-Ruiz et al. (2015) revealed that in mice subjected to a contextual fear-memory learning task M6a was differentially up-regulated 4 h later. Until now, there was no direct relationship between M6a levels and the molecular processes underlying memory and learning formation. However, these independent findings suggest that this may warrant further investigation.

The intrinsic genetic program responsible for synapse formation and maintenance involves a correct pruning of the dendritic spines. An abnormal dendritic spine pruning during development and in adulthood contributes to the generation of synaptopathies such as ASD, schizophrenia,

[2]www.bu.edu/dbin/cnsb/mousebrain

TABLE 1 | Summary of *GPM6A* gene variants and expression levels related to disorders.

Alteration	Species	Approach	Sample	Study	Result	References
Chronic Stress	Rats	Restraint stress	HP	mRNA	↓	Alfonso et al., 2002
	Shrews	Psychosocial stress	HP	mRNA	↓	Alfonso et al., 2004a,b
	Mice	Restraint stress	HP	mRNA	↓	Alfonso et al., 2006
	Mice	Prenatal stress	HP	mRNA	↑	Monteleone et al., 2014
Claustrophobia	Mice	Gpm6a−/−		Behavioral test	↓	El-Kordi et al., 2013
	Humans			Genotyping	GPM6A variant 3'UTR	
Neuroticism	Humans			GWAS	rs17611770	Nagel et al., 2018
Depression	Humans		HP/PFC	mRNA	↓	Fuchsova et al., 2015
	Humans		Saliva	ELISA	ND and ↑	Monteleone et al., 2020
Bipolar Disorder	Humans			GWAS	rs17599018	Greenwood et al., 2012
Schizophrenia	Humans	with depression		Genotyping	rs10520303	Boks et al., 2008
	Humans			GWAS	rs1106568, rs62334820, rs13142920, rs7673823, rs6846161	Schizophrenia Working Group of the Psychiatric Genomics Consortium, 2014; Li et al., 2017; Pardiñas et al., 2018; Lam et al., 2019
Learning disability	Humans			Genotyping Microarray	GPM6A duplication	Gregor et al., 2014
Alzheimer Disease	Mice	APP/PS1 mice	OB	Proteomics	↑	Lachén-Montes et al., 2016
	Humans		HP	mRNA microarray	↓	Xu et al., 2006
	Humans	EVs	Cortical gray matter	Proteomics	↑	Muraoka et al., 2020; Quiroz-Baez et al., 2020
	Humans	EVs	CSF	Proteomics	↑	Chiasserini et al., 2020
Autistic spectrum disorder	Mice	PSD membrane fractions	Striatum and HP	Proteomics	ND	Reim et al., 2017
	Humans		CB	Proteomics	↑	Abraham et al., 2019

or AD (Penzes et al., 2011). For instance, subjects with ASD have deficits in social interactions, disruption of oral communication, and present repetitive behavior; correlated with an elevated number of dendritic spines and a late onset of the pruning process (Toro et al., 2010). Interestingly, a proteomic analysis done by Abraham et al. (2019) revealed that M6a levels were increased in samples from the cerebellum of patients with ASD. Moreover, proteomic studies showing altered M6a levels in both animal models and patients with AD contribute to a possible role in memory decline (Xu et al., 2006; Lachén-Montes et al., 2016; Chiasserini et al., 2020; Muraoka et al., 2020). Also, M6a is downregulated in the hippocampal formation whereas it is enriched in extracellular vesicles from cerebrospinal fluid (CSF) samples of AD patients suggesting an active secretion of M6a during AD progression (Xu et al., 2006; Chiasserini et al., 2020). Indeed, Muraoka et al. (2020) proposed M6a, together with ANX5, VGF, and ACTZ as a biomarker for monitoring AD progression from CSF samples (Muraoka et al., 2020).

One of the goals of genome-wide association studies is to link specific genetic variants with specific phenotypes. This information can then be used to evaluate the risk or susceptibility of a population to develop a certain disease, in diagnostic tests or to guide treatments. Indeed, single nucleotide polymorphisms (SNPs) within non-coding region of *GPM6A* have been linked to schizophrenia (Boks et al., 2008; Schizophrenia Working Group of the Psychiatric Genomics Consortium, 2014; Li et al., 2017; Pardiñas et al., 2018; Lam et al., 2019), and one variant for both neuroticism (Nagel et al., 2018) and bipolar disorder (Greenwood et al., 2012). However, there are still no reports confirming whether any of these SNPs lead to changes in M6a gene expression or function. Our lab studied 3 non-synonymous SNPs within *GPM6A's* TMD coding region reported in the dbSNP database[3]. By doing reverse genetic experiments, we demonstrated that all nsSNPs prevented M6a from being functional in neurons, impaired formation of dendritic spines and synapses owing to decreased stability, dimerization, or improper folding of the protein (Formoso et al., 2015b, 2016).

CONCLUDING REMARKS

Evidence collected over 30 years since its discovery show that glycoprotein M6a has a critical role in synapse formation,

[3]https://www.ncbi.nlm.nih.gov/snp/

plasticity, and maintenance. Previous research so far has focused on *in vitro* approaches, with only a few articles studying M6a-deficient mice. Unfortunately, in none of those studies the synaptic activity or synaptic integrity were interrogated. New data coming from "omic" and GWAS approaches in combination with basic investigation will expand our knowledge of the field and define the exact role of *GPM6A* in neuronal development and synaptopathies. This in turn will offer new routes to improve diagnosis and develop more effective treatments.

AUTHOR CONTRIBUTIONS

AL, GA, and CS were involved in bibliography revision. CS contributed to the design and conceptualization of the research topic. CS, AL, and GA wrote the manuscript. AL and GA made the figure and the table. All authors contributed to the article and approved the submitted version.

FUNDING

AL and GA were Ph.D. students. CS was a researcher from the National Council for Research of Argentina (CONICET). This work was supported by Agencia Nacional de Promoción Científica y Tecnológica (ANPCyT) BID-ANPCyT-PICT 2016-1223 and BID-ANCyT-PICT 2019-1051 to CS and BID-ANPCyT-PICT 2017-1736.

ACKNOWLEDGMENTS

We gratefully thank Dr. Karina Formoso (Institute of Metabolic and Cardiovascular Diseases, Université de Toulouse III, ISERM), Dr. Mariano M. Boccia (Laboratorio de Neurofarmacología de los Procesos de Memoria, Facultad de Farmacia y Bioquímica, UBA) and Dr. Fernán Agüero (Bioinformatics Group leader at IIBio-CONICET-UNSAM) who critically read the manuscript.

REFERENCES

Abraham, J. R., Szoko, N., Barnard, J., Rubin, R. A., Schlatzer, D., Lundberg, K., et al. (2019). Proteomic Investigations of Autism Brain Identify Known and Novel Pathogenetic Processes. *Sci. Rep.* 9:13118.

Alfonso, J., Aguero, F., Sanchez, D. O., Flugge, G., Fuchs, E., Frasch, A. C., et al. (2004a). Gene expression analysis in the hippocampal formation of tree shrews chronically treated with cortisol. *J. Neurosci. Res.* 78, 702–710. doi: 10.1002/jnr.20328

Alfonso, J., Pollevick, G. D., Van Der Hart, M. G., Flugge, G., Fuchs, E., and Frasch, A. C. (2004b). Identification of genes regulated by chronic psychosocial stress and antidepressant treatment in the hippocampus. *Eur. J. Neurosci.* 19, 659–666. doi: 10.1111/j.1460-9568.2004.03178.x

Alfonso, J., Fernandez, M. E., Cooper, B., Flugge, G., and Frasch, A. C. (2005). The stress-regulated protein M6a is a key modulator for neurite outgrowth and filopodium/spine formation. *Proc. Natl. Acad. Sci. U. S. A.* 102, 17196–17201. doi: 10.1073/pnas.0504262102

Alfonso, J., Frick, L. R., Silberman, D. M., Palumbo, M. L., Genaro, A. M., and Frasch, A. C. (2006). Regulation of hippocampal gene expression is conserved in two species subjected to different stressors and antidepressant treatments. *Biol. Psychiatry* 59, 244–251. doi: 10.1016/j.biopsych.2005.06.036

Alfonso, J., Pollevick, G. D., Castensson, A., Jazin, E., and Frasch, A. C. (2002). Analysis of gene expression in the rat hippocampus using Real Time PCR reveals high inter-individual variation in mRNA expression levels. *J. Neurosci. Res.* 67, 225–234. doi: 10.1002/jnr.10105

Alvarez Julia, A., Frasch, A. C., and Fuchsova, B. (2016). Neuronal filopodium formation induced by the membrane glycoprotein M6a (Gpm6a) is facilitated by coronin-1a, Rac1, and p21-activated kinase 1 (Pak1). *J. Neurochem.* 137, 46–61. doi: 10.1111/jnc.13552

Andrews, M. R., Czvitkovich, S., Dassie, E., Vogelaar, C. F., Faissner, A., Blits, B., et al. (2009). Alpha9 integrin promotes neurite outgrowth on tenascin-C and enhances sensory axon regeneration. *J. Neurosci.* 29, 5546–5557. doi: 10.1523/jneurosci.0759-09.2009

Antonucci, F., Corradini, I., Fossati, G., Tomasoni, R., Menna, E., and Matteoli, M. (2016). SNAP-25, a Known Presynaptic Protein with Emerging Postsynaptic Functions. *Front. Synaptic Neurosci.* 8:7. doi: 10.3389/fnsyn.2016.00007

Aparicio, G. I., Formoso, K., Leon, A., Frasch, A. C., and Scorticati, C. (2020). Identification of Potential Interacting Proteins With the Extracellular Loops of the Neuronal Glycoprotein M6a by TMT/MS. *Front. Synaptic Neurosci.* 12:28. doi: 10.3389/fnsyn.2020.00028

Baumrind, N. L., Parkinson, D., Wayne, D. B., Heuser, J. E., and Pearlman, A. L. (1992). EMA: a developmentally regulated cell-surface glycoprotein of CNS neurons that is concentrated at the leading edge of growth cones. *Dev. Dyn.* 194, 311–325. doi: 10.1002/aja.1001940407

Beesley, P. W., Herrera-Molina, R., Smalla, K. H., and Seidenbecher, C. (2014). The Neuroplastin adhesion molecules: key regulators of neuronal plasticity and synaptic function. *J. Neurochem.* 131, 268–283. doi: 10.1111/jnc.12816

Bian, W. J., Miao, W. Y., He, S. J., Qiu, Z., and Yu, X. (2015). Coordinated Spine Pruning and Maturation Mediated by Inter-Spine Competition for Cadherin/Catenin Complexes. *Cell* 162, 808–822. doi: 10.1016/j.cell.2015.07.018

Boks, M. P., Hoogendoorn, M., Jungerius, B. J., Bakker, S. C., Sommer, I. E., Sinke, R. J., et al. (2008). Do mood symptoms subdivide the schizophrenia phenotype? Association of the GMP6A gene with a depression subgroup. *Am. J. Med. Genet. B Neuropsychiatr. Genet.* 147B, 707–711. doi: 10.1002/ajmg.b.30667

Boyken, J., Gronborg, M., Riedel, D., Urlaub, H., Jahn, R., and Chua, J. J. (2013). Molecular profiling of synaptic vesicle docking sites reveals novel proteins but few differences between glutamatergic and GABAergic synapses. *Neuron* 78, 285–297. doi: 10.1016/j.neuron.2013.02.027

Brocco, M. A., Fernandez, M. E., and Frasch, A. C. (2010). Filopodial protrusions induced by glycoprotein M6a exhibit high motility and aids synapse formation. *Eur. J. Neurosci.* 31, 195–202. doi: 10.1111/j.1460-9568.2009.07064.x

Caceres, A., Ye, B., and Dotti, C. G. (2012). Neuronal polarity: demarcation, growth and commitment. *Curr. Opin. Cell Biol.* 24, 547–553. doi: 10.1016/j.ceb.2012.05.011

Chiasserini, D., Bijnsdorp, I., Bellomo, G., Orvietani, P. L., Piersma, S. R., Pham, T., et al. (2020). Proteomic analysis of extracellular vesicles in cerebrospinal fluid of patients with Alzheimer's disease. *medRxiv*. [Preprint] doi: 10.1101/2020.02.22.20026609

Claussnitzer, M., Cho, J. H., Collins, R., Cox, N. J., Dermitzakis, E. T., Hurles, M. E., et al. (2020). A brief history of human disease genetics. *Nature* 577, 179–189.

Cooper, B., Werner, H. B., and Flugge, G. (2008). Glycoprotein M6a is present in glutamatergic axons in adult rat forebrain and cerebellum. *Brain Res.* 1197, 1–12. doi: 10.1016/j.brainres.2007.11.066

Egbujo, C. N., Sinclair, D., and Hahn, C. G. (2016). Dysregulations of Synaptic Vesicle Trafficking in Schizophrenia. *Curr. Psychiatry Rep.* 18, 77.

El-Kordi, A., Kastner, A., Grube, S., Klugmann, M., Begemann, M., Sperling, S., et al. (2013). A single gene defect causing claustrophobia. *Transl. Psychiatry* 3, e254. doi: 10.1038/tp.2013.28

Fagerberg, L., Hallstrom, B. M., Oksvold, P., Kampf, C., Djureinovic, D., Odeberg, J., et al. (2014). Analysis of the human tissue-specific expression by genome-wide integration of transcriptomics and antibody-based proteomics. *Mol. Cell Proteomics* 13, 397–406. doi: 10.1074/mcp.m113.035600

Fang, P., Wang, X. J., Xue, Y., Liu, M. Q., Zeng, W. F., Zhang, Y., et al. (2016). In-depth mapping of the mouse brain N-glycoproteome reveals widespread

N-glycosylation of diverse brain proteins. *Oncotarget* 7, 38796–38809. doi: 10.18632/oncotarget.9737

Fernandez, M. E., Alfonso, J., Brocco, M. A., and Frasch, A. C. (2010). Conserved cellular function and stress-mediated regulation among members of the proteolipid protein family. *J. Neurosci. Res.* 88, 1298–1308.

Formoso, K., Billi, S. C., Frasch, A. C., and Scorticati, C. (2015a). Tyrosine 251 at the C-terminus of neuronal glycoprotein M6a is critical for neurite outgrowth. *J. Neurosci. Res.* 93, 215–229. doi: 10.1002/jnr.23482

Formoso, K., Garcia, M. D., Frasch, A. C., and Scorticati, C. (2015b). Filopodia formation driven by membrane glycoprotein M6a depends on the interaction of its transmembrane domains. *J. Neurochem.* 134, 499–512. doi: 10.1111/jnc.13153

Formoso, K., Garcia, M. D., Frasch, A. C., and Scorticati, C. (2016). Evidence for a role of glycoprotein M6a in dendritic spine formation and synaptogenesis. *Mol. Cell Neurosci.* 77, 95–104. doi: 10.1016/j.mcn.2016.10.005

Fuchsova, B., Alvarez Julia, A., Rizavi, H. S., Frasch, A. C., and Pandey, G. N. (2015). Altered expression of neuroplasticity-related genes in the brain of depressed suicides. *Neuroscience* 299, 1–17. doi: 10.1016/j.neuroscience.2015.04.057

Fuchsova, B., Fernandez, M. E., Alfonso, J., and Frasch, A. C. (2009). Cysteine residues in the large extracellular loop (EC2) are essential for the function of the stress-regulated glycoprotein M6a. *J. Biol. Chem.* 284, 32075–32088. doi: 10.1074/jbc.m109.012377

Fuentes, F., and Arregui, C. O. (2009). Microtubule and cell contact dependency of ER-bound PTP1B localization in growth cones. *Mol. Biol. Cell* 20, 1878–1889. doi: 10.1091/mbc.e08-07-0675

Garcia, M. D., Formoso, K., Aparicio, G. I., Frasch, A. C. C., and Scorticati, C. (2017). The Membrane Glycoprotein M6a Endocytic/Recycling Pathway Involves Clathrin-Mediated Endocytosis and Affects Neuronal Synapses. *Front. Mol. Neurosci.* 10:296. doi: 10.3389/fnmol.2017.00296

Greenwood, T. A., Akiskal, H. S., Akiskal, K. K., Bipolar Genome, S., and Kelsoe, J. R. (2012). Genome-wide association study of temperament in bipolar disorder reveals significant associations with three novel Loci. *Biol. Psychiatry* 72, 303–310. doi: 10.1016/j.biopsych.2012.01.018

Greer, J. M., and Lees, M. B. (2002). Myelin proteolipid protein–the first 50 years. *Int. J. Biochem. Cell Biol.* 34, 211–215. doi: 10.1016/s1357-2725(01)00136-4

Gregor, A., Kramer, J. M., Van Der Voet, M., Schanze, I., Uebe, S., Donders, R., et al. (2014). Altered GPM6A/M6 dosage impairs cognition and causes phenotypes responsive to cholesterol in human and Drosophila. *Hum. Mutat.* 35, 1495–1505. doi: 10.1002/humu.22697

Grunewald, L., Chiocchetti, A. G., Weber, H., Scholz, C. J., Schartner, C., Freudenberg, F., et al. (2021). Knockdown of the ADHD Candidate Gene Diras2 in Murine Hippocampal Primary Cells. *J. Atten. Disord.* 25, 572–583. doi: 10.1177/1087054718822129

Haenig, C., Atias, N., Taylor, A. K., Mazza, A., Schaefer, M. H., Russ, J., et al. (2020). Interactome Mapping Provides a Network of Neurodegenerative Disease Proteins and Uncovers Widespread Protein Aggregation in Affected Brains. *Cell Rep.* 32:108050. doi: 10.1016/j.celrep.2020.108050

Hida, Y., and Ohtsuka, T. (2010). CAST and ELKS proteins: structural and functional determinants of the presynaptic active zone. *J. Biochem.* 148, 131–137. doi: 10.1093/jb/mvq065

Honda, A., Ito, Y., Takahashi-Niki, K., Matsushita, N., Nozumi, M., Tabata, H., et al. (2017). Extracellular Signals Induce Glycoprotein M6a Clustering of Lipid Rafts and Associated Signaling Molecules. *J. Neurosci.* 37, 4046–4064. doi: 10.1523/jneurosci.3319-16.2017

Huminiecki, L., Lloyd, A. T., and Wolfe, K. H. (2003). Congruence of tissue expression profiles from Gene Expression Atlas, SAGEmap and TissueInfo databases. *BMC Genomics* 4:31. doi: 10.1186/1471-2164-4-31

Huttlin, E. L., Bruckner, R. J., Paulo, J. A., Cannon, J. R., Ting, L., Baltier, K., et al. (2017). Architecture of the human interactome defines protein communities and disease networks. *Nature* 545, 505–509. doi: 10.1038/nature22366

Ito, Y., Honda, A., and Igarashi, M. (2018). Glycoprotein M6a as a signaling transducer in neuronal lipid rafts. *Neurosci. Res.* 128, 19–24. doi: 10.1016/j.neures.2017.11.002

Jahn, O., Siems, S. B., Kusch, K., Hesse, D., Jung, R. B., Liepold, T., et al. (2020). The CNS Myelin Proteome: deep Profile and Persistence After Post-mortem Delay. *Front. Cell Neurosci.* 14:239. doi: 10.3389/fncel.2020.00239

Kang, R., Wan, J., Arstikaitis, P., Takahashi, H., Huang, K., Bailey, A. O., et al. (2008). Neural palmitoyl-proteomics reveals dynamic synaptic palmitoylation. *Nature* 456, 904–909. doi: 10.1038/nature07605

Lachén-Montes, M., Gonzalez-Morales, A., De Morentin, X. M., Perez-Valderrama, E., Ausin, K., Zelaya, M. V., et al. (2016). An early dysregulation of FAK and MEK/ERK signaling pathways precedes the beta-amyloid deposition in the olfactory bulb of APP/PS1 mouse model of Alzheimer's disease. *J. Proteomics* 148, 149–158. doi: 10.1016/j.jprot.2016.07.032

Lagenaur, C., Kunemund, V., Fischer, G., Fushiki, S., and Schachner, M. (1992). Monoclonal M6 antibody interferes with neurite extension of cultured neurons. *J. Neurobiol.* 23, 71–88. doi: 10.1002/neu.480230108

Lam, M., Chen, C. Y., Li, Z., Martin, A. R., Bryois, J., Ma, X., et al. (2019). Comparative genetic architectures of schizophrenia in East Asian and European populations. *Nat. Genet.* 51, 1670–1678.

Li, Z., Chen, J., Yu, H., He, L., Xu, Y., Zhang, D., et al. (2017). Genome-wide association analysis identifies 30 new susceptibility loci for schizophrenia. *Nat. Genet.* 49, 1576–1583.

Liu, Y. T., Tao, C. L., Lau, P. M., Zhou, Z. H., and Bi, G. Q. (2019). Postsynaptic protein organization revealed by electron microscopy. *Curr. Opin. Struct. Biol.* 54, 152–160. doi: 10.1016/j.sbi.2019.02.012

Martorella, M., Barford, K., Winkler, B., and Deppmann, C. D. (2017). Emergent Role of Coronin-1a in Neuronal Signaling. *Vitam. Horm.* 104, 113–131. doi: 10.1016/bs.vh.2016.10.002

Michibata, H., Okuno, T., Konishi, N., Kyono, K., Wakimoto, K., Aoki, K., et al. (2009). Human GPM6A is associated with differentiation and neuronal migration of neurons derived from human embryonic stem cells. *Stem Cells Dev.* 18, 629–639. doi: 10.1089/scd.2008.0215

Miller, M., and Peters, A. (1981). Maturation of rat visual cortex. II. A combined Golgi-electron microscope study of pyramidal neurons. *J. Comp. Neurol.* 203, 555–573. doi: 10.1002/cne.902030402

Mita, S., De Monasterio-Schrader, P., Funfschilling, U., Kawasaki, T., Mizuno, H., Iwasato, T., et al. (2015). Transcallosal Projections Require Glycoprotein M6-Dependent Neurite Growth and Guidance. *Cereb. Cortex* 25, 4111–4125. doi: 10.1093/cercor/bhu129

Miura, R., Ethell, I. M., and Yamaguchi, Y. (2001). Carbohydrate-protein interactions between HNK-1-reactive sulfoglucuronyl glycolipids and the proteoglycan lectin domain mediate neuronal cell adhesion and neurite outgrowth. *J. Neurochem.* 76, 413–424. doi: 10.1046/j.1471-4159.2001.00042.x

Monteleone, M. C., Adrover, E., Pallares, M. E., Antonelli, M. C., Frasch, A. C., and Brocco, M. A. (2014). Prenatal stress changes the glycoprotein GPM6A gene expression and induces epigenetic changes in rat offspring brain. *Epigenetics* 9, 152–160. doi: 10.4161/epi.25925

Monteleone, M. C., Billi, S. C., Viale, L., Catoira, N. P., Frasch, A. C., and Brocco, M. A. (2020). Search of brain-enriched proteins in salivary extracellular vesicles for their use as mental disease biomarkers: a pilot study of the neuronal glycoprotein M6a. *J. Affect. Disord. Rep.* 1:100003 doi: 10.1016/j.jadr.2020.100003

Mukobata, S., Hibino, T., Sugiyama, A., Urano, Y., Inatomi, A., Kanai, Y., et al. (2002). M6a acts as a nerve growth factor-gated Ca(2+) channel in neuronal differentiation. *Biochem. Biophys. Res. Commun.* 297, 722–728. doi: 10.1016/s0006-291x(02)02284-2

Muraoka, S., Deleo, A. M., Sethi, M. K., Yukawa-Takamatsu, K., Yang, Z., Ko, J., et al. (2020). Proteomic and biological profiling of extracellular vesicles from Alzheimer's disease human brain tissues. *Alzheimers Dement.* 16, 896–907. doi: 10.1002/alz.12089

Nagel, M., Jansen, P. R., Stringer, S., Watanabe, K., De Leeuw, C. A., Bryois, J., et al. (2018). Meta-analysis of genome-wide association studies for neuroticism in 449,484 individuals identifies novel genetic loci and pathways. *Nat. Genet.* 50, 920–927.

Neugebauer, K. M., Tomaselli, K. J., Lilien, J., and Reichardt, L. F. (1988). N-cadherin, NCAM, and integrins promote retinal neurite outgrowth on astrocytes in vitro. *J. Cell Biol.* 107, 1177–1187. doi: 10.1083/jcb.107.3.1177

Nosov, G., Kahms, M., and Klingauf, J. (2020). The Decade of Super-Resolution Microscopy of the Presynapse. *Front. Synaptic Neurosci.* 12:32. doi: 10.3389/fnsyn.2020.00032

Olinsky, S., Loop, B. T., Dekosky, A., Ripepi, B., Weng, W., Cummins, J., et al. (1996). Chromosomal mapping of the human M6 genes. *Genomics* 33, 532–536. doi: 10.1006/geno.1996.0231

Ozcan, A. S. (2017). Filopodia: a Rapid Structural Plasticity Substrate for Fast Learning. *Front. Synaptic Neurosci.* 9:12. doi: 10.3389/fnsyn.2017.00012

Pardiñas, A. F., Holmans, P., Pocklington, A. J., Escott-Price, V., Ripke, S., Carrera, N., et al. (2018). Common schizophrenia alleles are enriched in mutation-intolerant genes and in regions under strong background selection. *Nat. Genet.* 50, 381–389.

Penzes, P., Cahill, M. E., Jones, K. A., Vanleeuwen, J. E., and Woolfrey, K. M. (2011). Dendritic spine pathology in neuropsychiatric disorders. *Nat. Neurosci.* 14, 285–293. doi: 10.1038/nn.2741

Pourhaghighi, R., Ash, P. E. A., Phanse, S., Goebels, F., Hu, L. Z. M., Chen, S., et al. (2020). BraInMap Elucidates the Macromolecular Connectivity Landscape of Mammalian Brain. *Cell Syst.* 10:e314.

Quiroz-Baez, R., Hernandez-Ortega, K., and Martinez-Martinez, E. (2020). Insights into the proteomic profiling of extracellular vesicles for the identification of early biomarkers of neurodegeneration. *Front. Neurol.* 11:580030. doi: 10.3389/fneur.2020.580030

Rao-Ruiz, P., Carney, K. E., Pandya, N., Van Der Loo, R. J., Verheijen, M. H., Van Nierop, P., et al. (2015). Time-dependent changes in the mouse hippocampal synaptic membrane proteome after contextual fear conditioning. *Hippocampus* 25, 1250–1261. doi: 10.1002/hipo.22432

Reim, D., Distler, U., Halbedl, S., Verpelli, C., Sala, C., Bockmann, J., et al. (2017). Proteomic Analysis of Post-synaptic Density Fractions from Shank3 Mutant Mice Reveals Brain Region Specific Changes Relevant to Autism Spectrum Disorder. *Front. Mol. Neurosci.* 10:26. doi: 10.3389/fnmol.2017.00026

Rosas, N. M., Alvarez Julia, A., Alzuri, S. E., Frasch, A. C., and Fuchsova, B. (2018). Alanine Scanning Mutagenesis of the C-Terminal Cytosolic End of Gpm6a Identifies Key Residues Essential for the Formation of Filopodia. *Front. Mol. Neurosci.* 11:314. doi: 10.3389/fnmol.2018.00314

Roussel, G., Trifilieff, E., Lagenaur, C., and Nussbaum, J. L. (1998). Immunoelectron microscopic localization of the M6a antigen in rat brain. *J. Neurocytol.* 27, 695–703.

Sato, Y., Mita, S., Fukushima, N., Fujisawa, H., Saga, Y., and Hirata, T. (2011a). Induction of axon growth arrest without growth cone collapse through the N-terminal region of four-transmembrane glycoprotein M6a. *Dev. Neurobiol.* 71, 733–746. doi: 10.1002/dneu.20941

Sato, Y., Watanabe, N., Fukushima, N., Mita, S., and Hirata, T. (2011b). Actin-independent behavior and membrane deformation exhibited by the four-transmembrane protein M6a. *PLoS One* 6:e26702. doi: 10.1371/journal.pone.0026702

Schizophrenia Working Group of the Psychiatric Genomics Consortium (2014). Biological insights from 108 schizophrenia-associated genetic loci. *Nature* 511, 421–427. doi: 10.1038/nature13595

Scorticati, C., Formoso, K., and Frasch, A. C. (2011). Neuronal glycoprotein M6a induces filopodia formation via association with cholesterol-rich lipid rafts. *J. Neurochem.* 119, 521–531. doi: 10.1111/j.1471-4159.2011.07252.x

Sengpiel, F. (2018). Overview: neuroplasticity and synaptic function in neuropsychiatric disorders. *J. Physiol.* 596, 2745–2746. doi: 10.1113/jp275940

Shen, K., and Cowan, C. W. (2010). Guidance molecules in synapse formation and plasticity. *Cold Spring Harb. Perspect. Biol.* 2:a001842. doi: 10.1101/cshperspect.a001842

Sotelo, C., Hillman, D. E., Zamora, A. J., and Llinas, R. (1975). Climbing fiber deafferentation: its action on Purkinje cell dendritic spines. *Brain Res.* 98, 574–581. doi: 10.1016/0006-8993(75)90374-1

Takamori, S., Holt, M., Stenius, K., Lemke, E. A., Gronborg, M., Riedel, D., et al. (2006). Molecular anatomy of a trafficking organelle. *Cell* 127, 831–846.

Taoufiq, Z., Ninov, M., Villar-Briones, A., Wang, H. Y., Sasaki, T., Roy, M. C., et al. (2020). Hidden proteome of synaptic vesicles in the mammalian brain. *Proc. Natl. Acad. Sci. U. S. A.* 117, 33586–33596. doi: 10.1073/pnas.2011870117

Tonnesen, J., and Nagerl, U. V. (2016). Dendritic Spines as Tunable Regulators of Synaptic Signals. *Front. Psychiatry* 7:101. doi: 10.3389/fpsyt.2016.00101

Toro, R., Konyukh, M., Delorme, R., Leblond, C., Chaste, P., Fauchereau, F., et al. (2010). Key role for gene dosage and synaptic homeostasis in autism spectrum disorders. *Trends Genet.* 26, 363–372. doi: 10.1016/j.tig.2010.05.007

Torres, V. I., Vallejo, D., and Inestrosa, N. C. (2017). Emerging Synaptic Molecules as Candidates in the Etiology of Neurological Disorders. *Neural Plast.* 2017:8081758.

Tu, Y. K., Duman, J. G., and Tolias, K. F. (2018). The Adhesion-GPCR BAI1 Promotes Excitatory Synaptogenesis by Coordinating Bidirectional Trans-synaptic Signaling. *J. Neurosci.* 38, 8388–8406. doi: 10.1523/jneurosci.3461-17.2018

Ulloa, F., Cotrufo, T., Ricolo, D., Soriano, E., and Araujo, S. J. (2018). SNARE complex in axonal guidance and neuroregeneration. *Neural Regen. Res.* 13, 386–392. doi: 10.4103/1673-5374.228710

Werner, H. B., Kramer-Albers, E. M., Strenzke, N., Saher, G., Tenzer, S., Ohno-Iwashita, Y., et al. (2013). A critical role for the cholesterol-associated proteolipids PLP and M6B in myelination of the central nervous system. *Glia* 61, 567–586. doi: 10.1002/glia.22456

Wu, D. F., Koch, T., Liang, Y. J., Stumm, R., Schulz, S., Schroder, H., et al. (2007). Membrane glycoprotein M6a interacts with the micro-opioid receptor and facilitates receptor endocytosis and recycling. *J. Biol. Chem.* 282, 22239–22247. doi: 10.1074/jbc.m700941200

Xu, P. T., Li, Y. J., Qin, X. J., Scherzer, C. R., Xu, H., Schmechel, D. E., et al. (2006). Differences in apolipoprotein E3/3 and E4/4 allele-specific gene expression in hippocampus in Alzheimer disease. *Neurobiol. Dis.* 21, 256–275. doi: 10.1016/j.nbd.2005.07.004

Yu, Y., Fuscoe, J. C., Zhao, C., Guo, C., Jia, M., Qing, T., et al. (2014). A rat RNA-Seq transcriptomic BodyMap across 11 organs and 4 developmental stages. *Nat. Commun.* 5:3230.

Yue, F., Cheng, Y., Breschi, A., Vierstra, J., Wu, W., Ryba, T., et al. (2014). A comparative encyclopedia of DNA elements in the mouse genome. *Nature* 515, 355–364.

Yuste, R., and Bonhoeffer, T. (2004). Genesis of dendritic spines: insights from ultrastructural and imaging studies. *Nat. Rev. Neurosci.* 5, 24–34. doi: 10.1038/nrn1300

Zhao, J., Iida, A., Ouchi, Y., Satoh, S., and Watanabe, S. (2008). M6a is expressed in the murine neural retina and regulates neurite extension. *Mol. Vis.* 14, 1623–1630.

Ziv, N. E., and Fisher-Lavie, A. (2014). Presynaptic and postsynaptic scaffolds: dynamics fast and slow. *Neuroscientist* 20, 439–452. doi: 10.1177/1073858414523321

Conflict of Interest: The authors declare that the research was conducted in the absence of any commercial or financial relationships that could be construed as a potential conflict of interest.

Copyright © 2021 León, Aparicio and Scorticati. This is an open-access article distributed under the terms of the Creative Commons Attribution License (CC BY). The use, distribution or reproduction in other forums is permitted, provided the original author(s) and the copyright owner(s) are credited and that the original publication in this journal is cited, in accordance with accepted academic practice. No use, distribution or reproduction is permitted which does not comply with these terms.

frontiers in Synaptic Neuroscience

ORIGINAL RESEARCH
published: 03 June 2021
doi: 10.3389/fnsyn.2021.656377

Nitric Oxide Regulates GluA2-Lacking AMPAR Contribution to Synaptic Transmission of CA1 Apical but Not Basal Dendrites

Violetta O. Ivanova, Pavel M. Balaban and Natalia V. Bal*

Cellular Neurobiology of Learning Lab, Institute of Higher Nervous Activity and Neurophysiology of the Russian Academy of Science, Moscow, Russia

The mechanisms of synaptic plasticity differ in distinct local circuits. In the CA1 region of the hippocampus, the mechanisms of long-term potentiation (LTP) at apical dendrites in *stratum radiatum* and basal dendrites in *stratum oriens* involve different molecular cascades. For instance, participation of nitric oxide in LTP induction was shown to be necessary only for apical dendrites. This phenomenon may play a key role in information processing in CA1, and one of the reasons for this difference may be differing synaptic characteristics in these regions. Here, we compared the synaptic responses to stimulation of apical and basal dendrites of CA1 pyramidal neurons and found a difference in the current–voltage characteristics of these inputs, which is presumably due to a distinct contribution of GluA2-lacking AMPA receptors to synaptic transmission. In addition, we obtained data that indicate the presence of these receptors in pyramidal dendrites in both *stratum radiatum* and *stratum oriens*. We also demonstrated that inhibition of NO synthase reduced the contribution of GluA2-lacking AMPA receptors at apical but not basal dendrites, and inhibition of soluble guanylate cyclase did not affect this phenomenon.

Keywords: AMPA, nitric oxide, hippocampus, synaptic transmission, pyramidal neurons

OPEN ACCESS

Edited by:
Wayne S. Sossin,
McGill University, Canada

Reviewed by:
Anne McKinney,
McGill University, Canada
Eric Hanse,
University of Gothenburg, Sweden
Vidar Jensen,
University of Oslo, Norway

****Correspondence:***
Violetta O. Ivanova
v.o.ivanova@ihna.ru

Received: *20 January 2021*
Accepted: *19 April 2021*
Published: *03 June 2021*

Citation:
Ivanova VO, Balaban PM and Bal NV (2021) Nitric Oxide Regulates GluA2-Lacking AMPAR Contribution to Synaptic Transmission of CA1 Apical but Not Basal Dendrites. Front. Synaptic Neurosci. 13:656377. doi: 10.3389/fnsyn.2021.656377

INTRODUCTION

The CA1 region of the hippocampus is a prevailing part of the brain for studying the phenomena of synaptic plasticity. This region with its widespread projections (Cenquizca and Swanson, 2007) is a key structure for the propagation of signals from the hippocampus to other parts of the brain. The apical and basal dendrites of the CA1 pyramidal cells extend in two main directions: *stratum radiatum/stratum lacunosum moleculare* and *stratum oriens*, respectively. Most of the excitatory inputs to CA1 pyramidal neurons originate from CA3 pyramidal cells through their ipsilateral Schaffer collaterals and contralateral commissural fibers to *str. radiatum* (Van Strien et al., 2009), as well as from the entorhinal cortex through the perforant pathway into the *stratum lacunosum moleculare* (Masurkar et al., 2017).

Synaptic plasticity at basal dendrites may be an important part of information processing in CA1, since synaptic plasticity of CA1 apical dendrite synapses can be homeostatically regulated by the cell-wide history of synaptic activity (metaplasticity) including the activity of basal dendrites (Hulme et al., 2012). While synaptic plasticity at the apical dendrites of CA1 pyramidal neurons has been extensively studied, relatively little is known whether the mechanisms of synaptic plasticity are the same at basal dendrites.

Synaptic plasticity at the basal and apical dendrites of the hippocampal CA1 region has some similarities (Bradshaw et al., 2003), but the clear spatial separation of these synapses, combined with differences in the innervation of *str. radiatum* and *str. oriens*, suggests that the molecular mechanisms of plasticity may vary significantly. For instance, knockout of both the endothelial and neuronal forms of nitric oxide synthase (NOS) caused a drop in amplitude responses after induction of long-term potentiation (LTP) only at apical dendrites (Son et al., 1996), but not at basal dendrites, which is consistent with other data regarding the involvement of NOS in synaptic plasticity in *str. radiatum* and *str. oriens* (Haley et al., 1996). In addition, differences were found in the molecular cascades dependent on nitric oxide (NO): inhibition of cyclic guanosine monophosphate (cGMP), cGMP-dependent protein kinase (PKG), and soluble guanylyl cyclase (sGC) during LTP induction were demonstrated to be more effective in blocking LTP in *str. radiatum* than in *str. oriens* (Son et al., 1998). Authors suggest that this difference is due to the fact that endothelial NO synthase (eNOS) is not present in *str. oriens*, which is the main source of nitric oxide in hippocampal LTP according to O'Dell et al. (1994). However, these data contradict other studies. For instance, it was shown that there is more eNOS in *str. radiatum* than in *str. oriens* due to the higher density of blood vessels (Blackshaw et al., 2003) and that LTP maintenance requires involvement of at least one form of NOS (Son et al., 1996). It is important to note that LTP sensitivity to NO in *stratum radiatum* also depends on the stimulation protocol for LTP induction (Lu et al., 1999; Bal et al., 2017; Maltsev et al., 2019). Taken together, these data indicate that the mechanism of LTP at basal dendrites of CA1 pyramidal cells is likely to be NO-independent. However, it should be noted that the neural NOS is still present in *str. oriens* (O'Dell et al., 1994; Blackshaw et al., 2003), and application of NO donors caused cGMP production in *str. oriens* (Bartus et al., 2013), which suggests that nitric oxide has some other functions in this region.

One of the key participants in LTP is the α-amino-3-hydroxy-5-methyl-4-isoxazolepropionic acid receptor (AMPAR) which is the main provider of excitatory transmission in the mammalian CNS (Malinow and Malenka, 2002; Diering and Huganir, 2018). Most AMPARs are heterotetramers combined from the GluA1, GluA2, GluA3, and GluA4 subunits. In the adult brain, almost all GluA2 subunit mRNA undergoes posttranscriptional editing, which leads to a replacement of the neutral amino acid glutamine with positively charged arginine in the polypeptide chain of the subunit. This replacement alters the electrophysiological properties of GluA2-containing AMPARs and makes them impermeable to calcium (Higuchi et al., 1993). Nitric oxide was shown to affect the incorporation of different AMPAR subunits to the cell membrane *via* several different pathways (for review, see Ivanova et al., 2020). Thus, the interaction of nitric oxide with AMPAR subunits could be crucial in the trafficking of GluA2-lacking AMPARs [calcium-permeable (CP-AMPARs)].

In our study, we demonstrate the differences in AMPAR-NO interactions between apical and basal dendrites. We show that the contribution of CP-AMPARs to synaptic transmission in apical dendrites is higher than in basal dendrites, and the NO synthase blockade flattens this difference. This effect does not involve sGC-dependent cascades. Our results confirm previous studies demonstrating different NO-dependent mechanisms in the apical and basal dendrites of CA1 pyramidal neurons.

MATERIALS AND METHODS

Animals and Ethical Approval

All experiments followed the European Convention for the Protection of Vertebrate Animals used for Experimental and other Scientific Purposes 1986 86/609/EEC and were approved by the Ethical Committee of the Institute of Higher Nervous Activity and Neurophysiology, Russian Academy of Sciences (IHNA RAS). The mice were purchased from the Nursery for laboratory animals of the Branch of the Institute of Bioorganic Chemistry of the Russian Academy of Sciences in Pushchino. The mice were maintained in a temperature-controlled vivarium (22 ± 2°C) under a 12-h light/dark cycle (lights on at 08.00 h) with food and water *ad libitum*. All efforts were made to minimize animal suffering and to reduce the number of animals used.

Slice Preparation

Horizontal brain slices (300 μm thick) containing the ventral hippocampus and entorhinal cortex were prepared from the brains of 25–35-day-old C57Bl/6 female and male mice killed by decapitation. The slicing chamber contained an oxygenated ice-cold solution (modified from Dugue et al., 2005) composed of the following (in mM) K-gluconate, 140; N-(2-hydroxyethyl) piperazine-N′-ethanesulfonic acid (HEPES), 10; Na-gluconate, 15; ethylene glycol-bis(2-aminoethyl)-N,N,N′,N′-tetraacetic acid (EGTA), 0.2; and NaCl, 4 (pH 7.2 with KOH). Brain slices were cut using a Vibratome (Leica VT1000S, Germany). Slices were incubated for at least 40 min at 35°C before being stored at room temperature in artificial CSF (ACSF) containing the following (in mM): NaCl, 125; $NaHCO_3$, 25; KCl, 2.5; NaH_2PO_4, 1.25; $MgCl_2$, 3.9; $CaCl_2$, 1; and glucose, 25; bubbled with 95% O_2, and 5% CO_2.

Electrophysiology

Electrophysiological recording was performed in an acrylic glass perfusion chamber (Luigs and Neumann, Germany) with the bath temperature kept at 30 ± 2°C and perfused at a constant rate of 3 ml/min. Patch electrodes (resistance 4–5 MΩ) were pulled from borosilicate capillary glass (Narishige PC-100 Puller, Japan) and were filled with either a polyamine-free or a polyamine-containing solution. The polyamine-free solution consisted of the following (in mM): Cs-gluconate, 110; CsCl,

30; HEPES, 10; NaCl, 8; EGTA, 0.2; MgATP, 4; Na_3GTP, 0.3; and phosphocreatine, 10 (pH 7.3 with CsOH) osmolarity ∼290 mOsm. The polyamine-containing solution was identical except for the addition of 10 μM spermine.

CA1 pyramidal cells were identified visually using an Olympus microscope fitted with infrared differential interference contrast optics (Olympus BX51WI). Whole-cell recordings from these neurons were made in a voltage-clamp mode using the ELC-03XS amplifier (NPI Electronic, Tamm, Germany) and Clampex software (Axoclamp, Molecular Devices). Cells were held at −70 mV. Cells with unhealthy morphology and resting membrane potential above −50 mV (before correction for the liquid junction potential) were excluded from the experiments. To evoke synaptic current, glass electrodes filled with ACSF were placed in the dendritic region of *stratum radiatum* and *stratum oriens*, ∼50–100 μm from the cell body, to stimulate the inputs at interstimulus intervals of 6 s. Inhibitory synaptic transmission was blocked during recordings by adding 50 μM picrotoxin to the perfusion ACSF. In all the experiments except AMPA/NMDA ratio measurements, the NMDA-mediated component was blocked by adding 50 μM APV to the ACSF. For the experiments with NOS inhibition, slices were incubated for 40–120 min in L-NAME, 15 min in 3-bromo-7-nitroindazole or carboxy-PTIO before being placed in the perfusion chamber. Whole-cell recordings typically started 5–10 min after break-in, when the balance between intracellular milieu and patch solution was established and a steady-state current was reached, except the experiments with GluR2-lacking AMPA receptor inhibition. The stimulation intensity was adjusted to produce an EPSC with an amplitude of ∼50 pA at the beginning of each recording. The experiments were not started if there was an unstable baseline. Series resistance was monitored, and data from cells in which series resistance varied by >15% during recording were discarded from the analysis. In all the experiments, the command voltage was corrected for the liquid junction potential (−10 mV).

GluR2-Lacking AMPA Receptor Inhibition

Experiments were performed using QX-314-containing spermine-free intracellular solution. Recording started after the holding current stabilizes (1–2 min after the beginning of whole-cell recording). The amplitude of test responses stabilizes after 15–20 min of recording. The GluR2-lacking AMPA receptor antagonist Naspm (200 μM) was applied 30 min after the start of the recording. For analysis, 10 successive responses were averaged and normalized to the mean EPSC amplitude obtained between 20 and 30 min of the recording session. The degree of the blockade was evaluated as the ratio of the average steady-state current amplitude without and after Naspm application.

Current–Voltage Relationship

The experiments started after baseline stabilization (∼100 sweeps). For each holding potential point, at least 20 sweeps were collected. Responses were averaged and normalized to the mean EPSC amplitude obtained at −70 mV. To evaluate differences, the normalized values at +50 mV were compared.

Rectification Index (RI)

Experiments started after baseline stabilization (∼100 sweeps). For the −70-mV and +35-mV holding points, at least 30 and 50 sweeps were collected, respectively. The RI was calculated as the ratio of EPSCs measured at −70 mV and +35 mV ($EPSC_{-70}/EPSC_{+35}$). For each +35-mV point, only the last 30 sweeps were analyzed due to potential space clamp problems.

To test synapses for *polyamine-dependent facilitation (PdF)*, we applied four stimuli with an interstimulus interval of 33 ms ×40 for each of the inputs, 5 and 20 min after whole-cell patch formation. To evaluate changes in PdF, we normalized each of the EPSCs to the first in the train, averaged the obtained values, and separately compared the data for apical and basal dendrites in different conditions. For PdF analysis, an additional selection criterion was applied: traces with undetectable peaks of the first EPSC in the train were retracted from the analysis. The number of the retracted traces was <1% of the total number of traces.

Paired-pulse ratio was monitored by applying two stimuli with a 50-ms interstimulus interval. The experiments started after baseline stabilization (∼100 sweeps), and at least 20 sweeps were collected.

AMPA/NMDA Current Ratio

The AMPA/NMDA ratio was measured in Mg^{2+}-free ACSF. AMPA and NMDA receptor-mediated EPSCs were pharmacologically isolated by sequential bath application of APV and CNQX, respectively. First, the compound AMPAR and NMDA-mediated current was recorded in Mg^{2+}-free ASCF. After collecting at least 100 sweeps, the AMPA-mediated component was blocked by application of 50 μM CNQX. An additional 100 sweeps of the NMDA-mediated currents were collected and the NMDA nature of these currents was confirmed by subsequent application of APV. The AMPA-mediated component was obtained by subtraction of the averaged NMDA-mediated currents from the averaged compound response. For subsequent analysis, the mean amplitude of the AMPA currents was normalized to the amplitude of the NMDAR EPSCs.

Cells that did not correspond to the standard criteria of electrophysiological properties, such as input resistance, series resistance, and baseline holding current, were excluded from the analysis.

Drugs

ODQ from Sigma-Aldrich was prepared as a 25-mM stock solution in DMSO and diluted down to achieve a final bath concentration of 30 μM. 3-Bromo-7-nitroindazole (3-Br-7-ni; Enzo Life Sciences) was dissolved as a 100-mM stock in DMSO and diluted down to achieve a final bath concentration of 50 μM. Nω-Nitro-L-arginine methyl ester hydrochloride (L-NAME; Sigma-Aldrich) was prepared as a 200-mM stock in milli-Q water diluted down to achieve a final bath concentration of 200 μM. Carboxy-PTIO (2-(4-Carboxyphenyl)-4,4,5,5-tetramethylimidazoline-1-oxyl-3-oxide potassium salt) from Enzo Life Sciences was prepared as a 100-mM stock in DMSO and diluted down to achieve a final bath concentration of 50 μM. Naspm (1-naphthylacetyl spermine) was prepared as a 100-mM

stock in milli-Q water and diluted down to achieve a final bath concentration of 200 μM (Tocris Bioscience). Picrotoxin from Sigma-Aldrich was prepared as a 100-mM stock in DMSO and diluted down to achieve a final bath concentration of 50 μM. DL-2-Amino-5-phosphonopentanoic acid sodium salt (APV) from Tocris was prepared as a 100-mM stock in milli-Q water and diluted down to achieve a final bath concentration of 50 μM. CNQX disodium salt from Tocris Bioscience was prepared as a 100-mM stock in milli-Q water and diluted down to achieve a final bath concentration of 50 μM.

Statistical Analysis

Results are presented as mean ± standard error (S.E.M.) of *n* cells. All statistical tests were performed using SigmaPlot 11.0 (Systat Software Inc., USA). For pairwise comparisons (**Figures 1B,C**), one-way ANOVA was used. For multiple comparisons (**Figures 1F**, **3A,B**, **4C,D**, **5C,D**, **6**, **Supplementary Figure 1**), we used two-way ANOVA. A significant main effect or interaction was followed by *post-hoc* comparison using Multiple Comparisons vs. Control Group (Holm–Sidak test); for between-subject analysis, the untreated cells were scored as "Control Group." For **Figures 2**, **5A,B**, and **Supplementary Figure 2**, we used two-way repeated-measures ANOVA. A significant main effect or interaction was followed by *post-hoc* comparisons using Multiple Comparisons vs. Control Group (Holm–Sidak Test). For between-subject analysis, the control cells were scored as "Control Group," and for within-subject analysis all measurements were compared to the first EPSC in the train. A probability level of 0.05 or less was considered statistically significant ($^{*}p \leq 0.05$, $^{**}p \leq 0.005$).

RESULTS

Calcium-Permeable AMPA Receptors Contribute More to Synaptic Transmission at Apical Dendrites of CA1 Pyramidal Neurons Than at Basal Dendrites

First, to evaluate the contribution of GluA2-lacking AMPARs to currents in apical and basal compartments of CA1 pyramidal neurons, we measured the RI by stimulating apical and basal dendrites with glass electrodes located as shown in **Figure 1A**. The rectification index reflects inward rectification of GluA2-lacking AMPARs and is scored as the ratio of the current amplitude measured at −70 mV and +35 mV ($EPSC_{-70\,mV}/EPSC_{+35\,mV}$). We found that the rectification index in responses to stimulation of apical dendrites (RI = 3.4 ± 0.2) is significantly higher than in responses to stimulation of basal dendrites (RI = 2.5 ± 0.2; p = 0.005, one-way ANOVA, n = 14, **Figure 1C**). The current–voltage (IV) characteristics for each of the inputs supported the difference revealed by RI measurement; the apical IV demonstrated significantly higher inward rectification (p = 0.035, one-way ANOVA, n = 7, **Figure 1B**). The most common approach to detecting the contribution of GluA2-lacking AMPARs to synaptic transmission is to test sensitivity to CP-AMPAR antagonists, for example, 1-naphthylacetyl spermine trihydrochloride (Naspm). Therefore, we tested whether the responses to stimulation of apical and basal inputs are sensitive to extracellular Naspm (200 μM) application (**Figures 1D–G**). To evaluate the degree of amplitude reduction, we averaged the values from each cell in the 5-min segment at the end of the recordings (**Figure 1F**). We observed a decrease in AMPAR currents in both of the inputs (73% ± 4 of the baseline in *str. radiatum* and 83% ± 6.5 in *str. oriens*, n = 10), which may indicate the presence of CP-AMPARs in the basal and apical dendrites of CA1 pyramidal neurons. However, comparison to the untreated cells (n = 6) showed significant difference only in apical (73% ± 4 vs. 109% ± 7, p = 0.001, two-way ANOVA) but not in basal inputs (83% ± 6.5 vs. 94% ± 4, p = 0.354, two-way ANOVA). Even at physiological resting membrane potentials (∼−70 mV), a substantial portion of GluA2-lacking channels could still be blocked by polyamines during single unitary EPSCs. Thus, we used a spermine-free intracellular solution in these experiments. As a result of the endogenous polyamine washout from the dendrites, the amplitude of responses increased up to 20 min. To avoid subsequent spike generation, we added 30 μM QX-314 to the intracellular solution. Due to the different morphology of apical and basal dendrites (Benavides-Piccione et al., 2020), the response amplitude at the basal inputs tends to stabilize earlier than at the apical inputs.

In addition, Rozov and colleagues have shown previously that application of several high-frequency stimuli to the input with CP-AMPARs causes relief of the polyamine block which, in turn, results in polyamine-dependent facilitation (PdF; Rozov and Burnashev, 1999; Rozov et al., 2018). We applied a similar protocol to the apical and basal inputs of CA1 pyramidal cells and found that this type of short-term plasticity was characteristic for synapses of these cells. We applied four stimuli with an interstimulus interval of 33 ms to each of the inputs at the beginning of the recording and 20 min later. We used spermine-free and spermine-containing intracellular solutions in order to test whether polyamine washout would affect the EPSCs. For experiments with polyamine washout, we adjusted the stimuli strength after 20 min to avoid spikes due to potential space clamp problems. **Figures 2A,B** demonstrate the results of these experiments. When we used a spermine-free intracellular solution, the 3rd and 4th EPSCs in the train were significantly lower 20 min after polyamine washout than at the beginning of the recording at apical dendrites (p = 0.037 for the 3rd EPSCs and p = 0.014 for the 4th EPSCs, two-way RM ANOVA, n = 8), and we observed the same tendency at basal dendrites (p = 0.117 for the 3^{d} EPSCs and p = 0.066 for the 4th EPSCs, two-way RM ANOVA, n = 8), whereas with the presence of polyamines in the patch pipette we did not observe such differences (apical: p = 0.46 for the 3rd EPSCs and p = 0.101 for the 4th EPSCs; basal: p = 0.47 for the 3rd EPSCs and p = 0.26 for the 4th EPSCs, two-way RM ANOVA, n = 6). Thus, we showed polyamine-dependent facilitation at the synapses of CA1 pyramidal cells, which indicates the presence of CP-AMPARs at both apical and basal dendrites of these cells. However, experiments measuring the current–voltage characteristics of these inputs revealed that the CP-AMPA receptors contribute more to synaptic

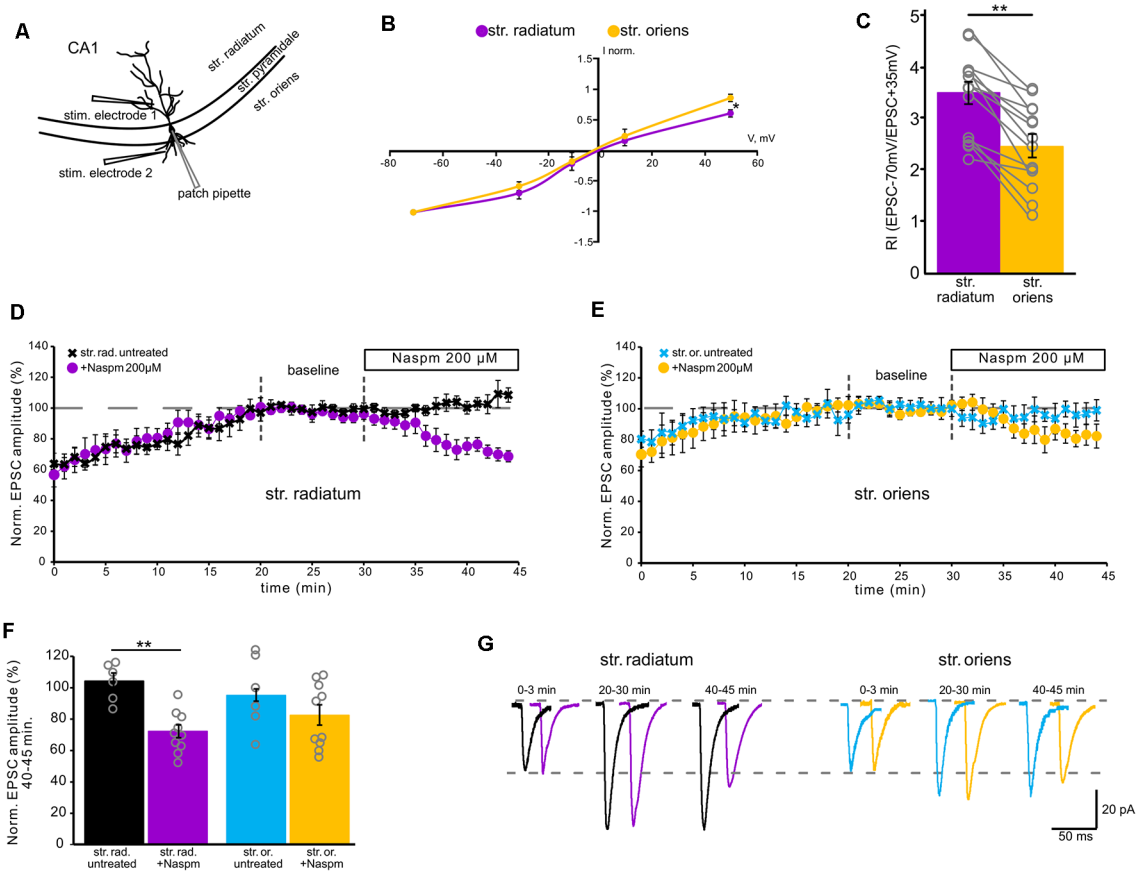

FIGURE 1 | Contribution of calcium-permeable AMPA receptors to synaptic transmission. **(A)** A schematic representation of the location of the stimulating electrode. **(B)** Current–voltage characteristics of apical (purple) and basal (orange) inputs. $n = 7$ cells from four animals, $^{*}p \leq 0.05$. **(C)** Comparison of rectification indices in *stratum radiatum* (purple) and *stratum oriens* (orange). Open gray circles represent individual data points, $n = 14$ cells from nine animals, $^{**}p \leq 0.005$. **(D)** The time course of averaged EPSC amplitude changes at apical inputs during washout of polyamine (black, $n = 6$ cells from three animals) and subsequent Naspm (200 μM) application (purple, $n = 10$ cells from eight animals), when CA1 pyramidal neurons were dialyzed with a polyamine-free intracellular solution. For analysis, 10 successive responses were averaged and normalized to the mean EPSC amplitude obtained between the 20th and 30th minutes of the recording session (baseline marked with gray dashed lines). **(E)** The same time course as **(D)** but for basal inputs. Blue, untreated cells, $n = 6$ cells from five animals. Orange, cells treated with Naspm (200 μM), ($n = 10$ cells from eight animals). **(F)** A histogram demonstrating normalized EPSCs for the last 5 min of the curves D and E. Open gray circles represent individual data points, $^{**}p \leq 0.005$. **(G)** Representative averaged traces at the indicated times of the curves D and E are shown in black and purple for apical dendrites, and in blue and orange for basal dendrites.

transmission at apical dendrites of CA1 pyramidal neurons than basal dendrites.

Nitric Oxide Synthase Blockade Alters CP-AMPAR Contribution to Currents in Apical but Not Basal Dendrites

Since nitric oxide can affect the incorporation of CP-AMPARs into the postsynaptic membrane of cells, we tested whether the blockade of its synthesis by various NO synthase inhibitors affects the characteristics of the apical and basal synapses of CA1 pyramidal cells. **Figure 3B** shows the rectification indices of the apical and basal inputs under the NO-synthase inhibitor L-NAME (200 μM), the selective inhibitor of neuronal NO-synthase 3-bromo-7-nitroindazole (50 μM), and the NO scavenger carboxy-PTIO (50 μM). The latter two inhibitors were dissolved in DMSO, and we also tested the effect on RI of DMSO alone (25 μl). A decrease in the intracellular concentration of nitric oxide significantly reduced RIs at the apical dendrites compared to control cells (DMSO: 3.1 ± 0.1, $p = 0.321$, $n = 8$; L-NAME: 2.6 ± 0.2, $p = 0.025$, $n = 8$; 3-br-7-ni: 2.4 ± 0.3, $p = 0.007$, $n = 10$; PTIO: 2.4 ± 0.3, $p = 0.002$, $n = 7$, two-way ANOVA), but not basal dendrites (DMSO: 2.1 ± 0.2, $p = 0.28$, $n = 8$; L-NAME: 2.6 ± 0.4, $p = 0.78$, $n = 8$; 3-br-7-ni: 2.1 ± 0.2, $p = 0.24$, $n = 10$; PTIO: 1.8 ± 0.1, $p = 0.07$, $n = 7$, two-way ANOVA), in various ways, thus leveling the significant difference between these two inputs. The current–voltage characteristics of the studied inputs under NOS blockade by L-NAME demonstrated a loss of inward rectification at synaptic inputs in apical but not basal dendrites ($p = 0.031$ for apical, $p = 0.4$ for basal, two-way ANOVA, $n = 7$, **Figure 3A**). We also compared the AMPA/NMDA ratio at apical and basal dendrites with

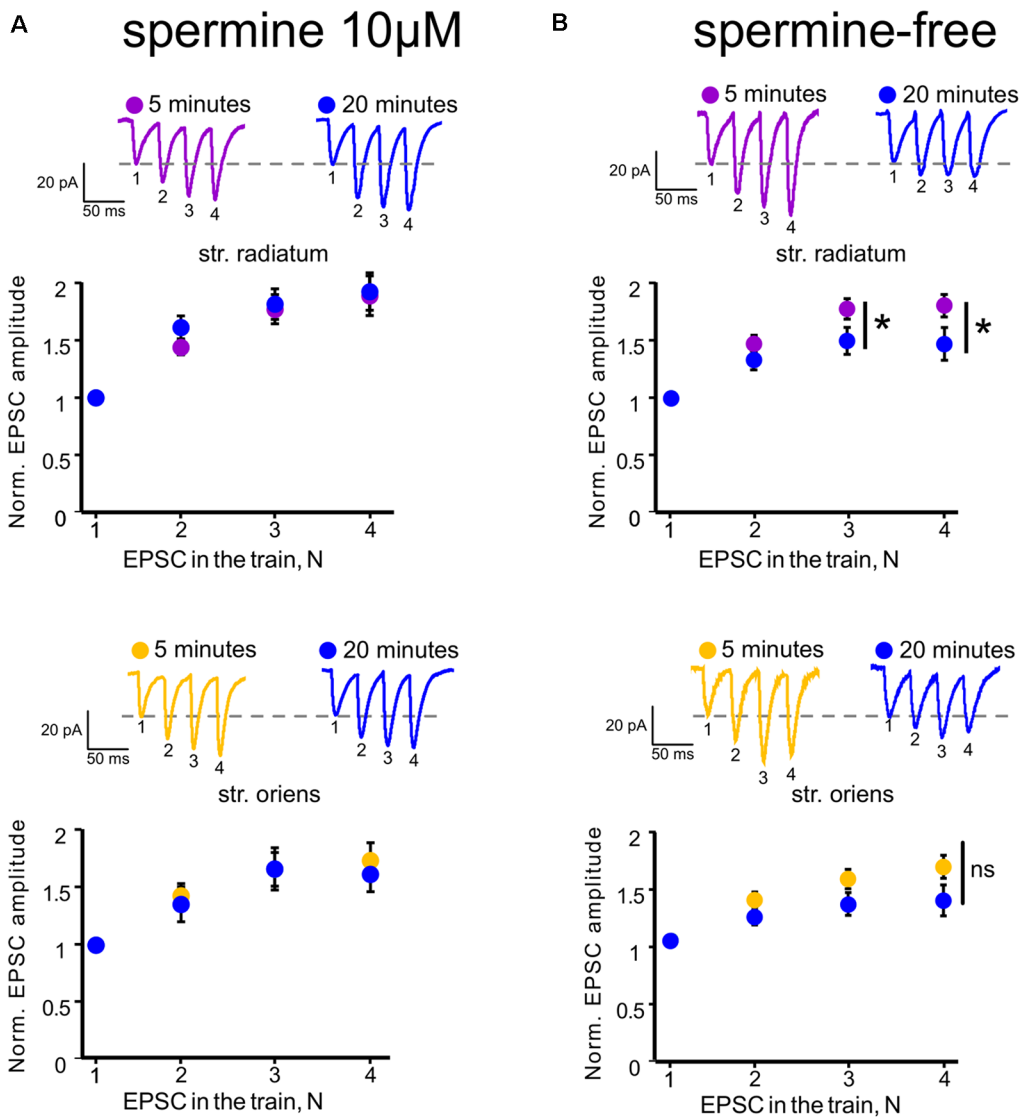

FIGURE 2 | Polyamine-dependent facilitation at the synapses of CA1 pyramidal cells. **(A)** Polyamine-dependent facilitation at apical (upper) and basal (lower) dendrites recorded with spermine-containing intracellular solution 5 and 20 min after whole-cell patch establishment, $n = 6$ cells from four animals. **(B)** Polyamine-dependent facilitation at apical (upper) and basal (lower) dendrites recorded with spermine-free intracellular solution 5 and 20 min after whole-cell patch establishment, $n = 8$ cells from five animals, $^*p \leq 0.05$; ns, nonsignificant. Averaged traces of responses to stimuli with a 33-ms interstimulus interval at the indicated times are displayed above each graph. EPSC numbering corresponds to the x-axis of each graph.

or without NOS inhibition (**Figure 5D**). In control cells, this ratio was significantly higher at apical dendrites than at basal dendrites (6.7 ± 0.6 vs. 4.9 ± 0.6, $n = 5$, $p = 0.049$, two-way ANOVA), and this difference disappeared after NOS inhibition (4.3 ± 0.8 vs. 3.9 ± 0.8, $n = 5$, $p = 0.788$, two-way ANOVA), supporting the results of the experiments with RI measurement.

Additionally, NOS inhibition prevented the drop in the current amplitude during CP-AMPAR blockade by Naspm in *str. radiatum* (109% ± 7.3 vs. 3% ± 4, $n = 10$, $p = 0.001$, two-way ANOVA, **Figure 4C**); however, in *str. oriens* we did not find a significant difference in the last 5 min of recording (89.4% ± 3.2 vs. 83% ± 6.5, $n = 10$, $p = 0.264$, two-way ANOVA, **Figure 4D**). Interestingly, the increase in the current amplitude at the beginning of the recording, which is associated with polyamine washout in both *str. radiatum* and *str. Oriens*, persisted after incubation in L-NAME (**Figures 4A,B**). This might be due to either specific mechanisms associated with polyamine washout or the possibility of NO-dependent regulation of CP-AMPAR sensitivity to polyamines. In the latter case, polyamines could still block the receptor pore but the blockade is more easily relieved which causes smaller EPSC increase and faster baseline stabilization.

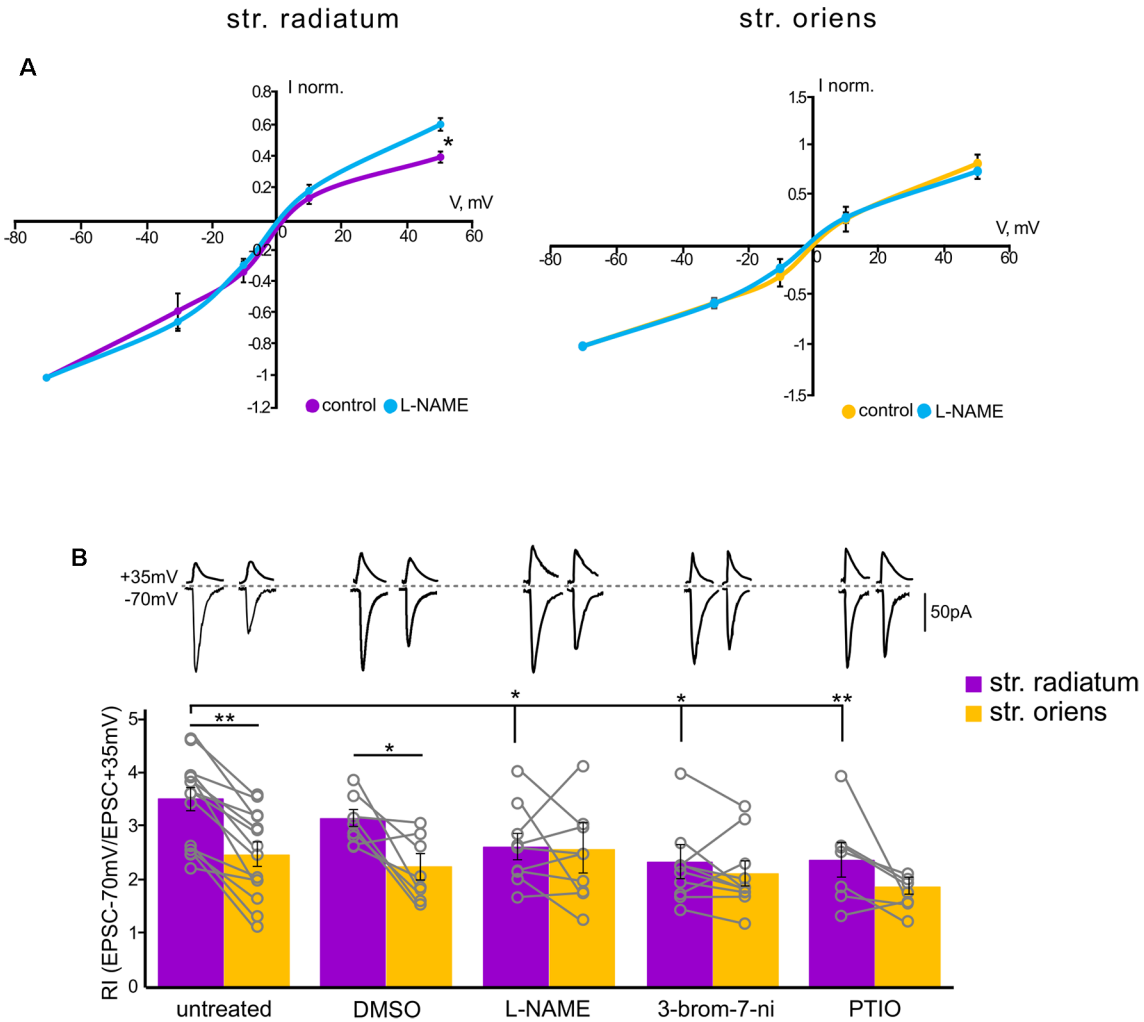

FIGURE 3 | Rectification properties of the apical and basal inputs under the NO-synthase inhibitors. **(A)** Current–voltage characteristics of apical (left) and basal (right) inputs in control cells (n = 7) and under nitric oxide synthase (NOS) blockade (n = 7), four animals, $^{*}p \leq 0.05$. **(B)** Comparison of rectification indices in *stratum radiatum* (purple) and *stratum oriens* (orange) in control cells (n = 14 cells from nine animals) and under treatment with DMSO (n = 8 cells from four animals), L-NAME (n = 8 cells from six animals), 3-bromo-7-nitroindazole (n = 10 cells from seven animals), and PTIO (n = 7 cells from four animals). Top, example traces at +35 mV and −70 mV. $^{*}p \leq 0.05$, $^{**}p \leq 0.005$. Open gray circles represent individual data points.

Next, we tested how the decrease of nitric oxide in the cell would affect polyamine-dependent facilitation at the studied inputs in the presence of spermine in the recording pipette (**Figures 5A,B**). NOS inhibition significantly affects the 4th EPSCs at apical dendrites (p = 0.006, two-way RM ANOVA, n = 7), but not at basal dendrites (p = 0.499, two-way RM ANOVA, n = 7). PdF recording was performed at the fifth minute of recording after a stable baseline was reached. Considering the wide range of nitric oxide action in the presynapse of cells (Hardingham et al., 2013), we tested whether the discovered effect was due to the presynaptic effect of nitric oxide. One of the possible approaches for evaluation of the presynaptic contribution to synaptic transmission is paired-pulse ratio measurement (Schulz et al., 1994; Christie and Jahr, 2006). Recording of paired-pulse ratio at the synapses of CA1 pyramidal cells during NOS inhibition did not reveal significant differences in these cells compared to control cells (control: 1.6 ± 0.1 in *str. radiatum*, and 1.4 ± 0.06 in *str. oriens*, n = 8; L-NAME: 1.5 ± 0.1 in *str. radiatum*, and 1.4 ± 0.07 in *str. oriens*, n = 7; 3-bromo-7-ni: 1.4 ± 0.06 in *str. radiatum*, and 1.4 ± 0.1 in *str. oriens*, n = 7). Thus, the results suggest that the disappearance of PdF in *str. radiatum* after inhibition of nitric oxide synthesis was associated with the interaction of nitric oxide with CP-AMPARs.

We examined whether the sGC-dependent pathway is involved in this interaction by treating slices with the sGC inhibitor ODQ (30 μM). We measured RIs under this condition and found that sGC inhibition did not affect the RIs of neither apical (RI = 3.5 ± 0.2, n = 5) nor basal (RI = 2.5 ± 0.3, n = 5) inputs (**Figure 6**, p = 0.027, two-way ANOVA). Next, we blocked NOS and sGC simultaneously and found that treating with L-NAME also leveled the RIs of apical (RI = 3.3 ± 0.3, n = 5)

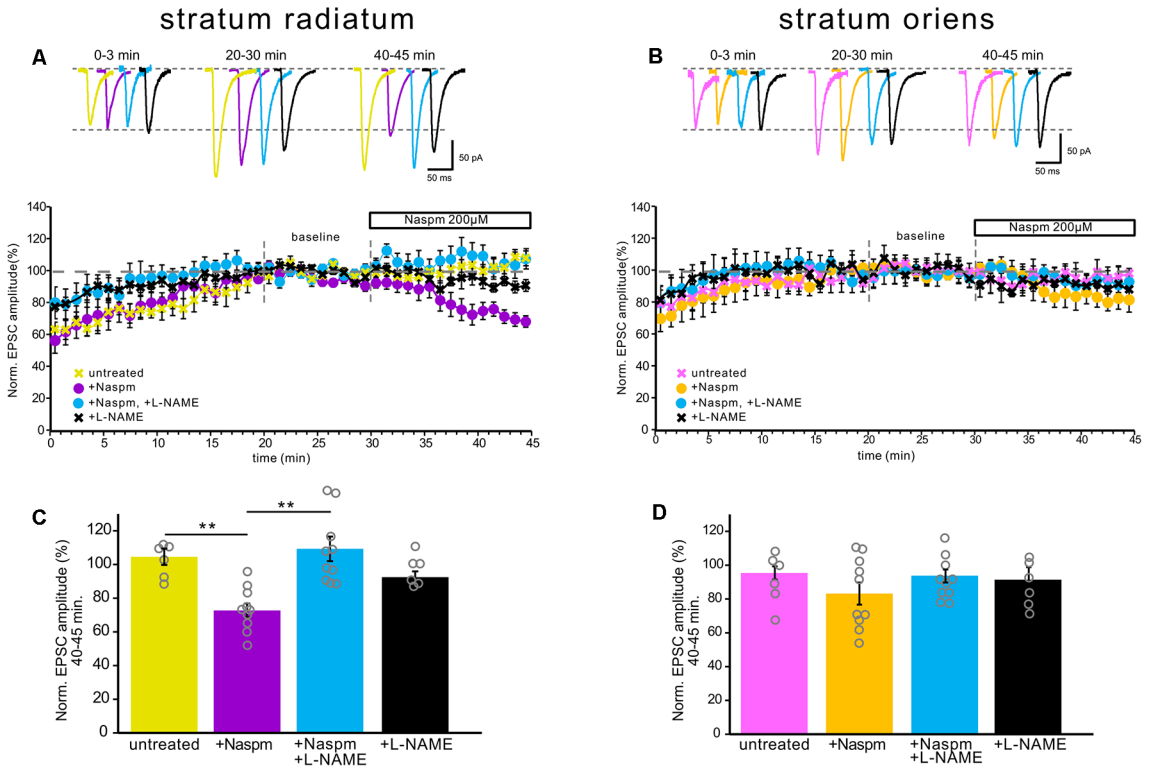

FIGURE 4 | NOS inhibition prevented CP-AMPAR current blockade by Naspm in the apical dendrites, but not in the basal dendrites. **(A)** The time course of EPSC amplitude changes in apical inputs during washout of polyamine (yellow, n = 6 cells from five animals), Naspm (200 μM) application (purple, n = 10, eight animals), and under NOS inhibition (black, n = 6 cells from four animals) and under NOS inhibition with Naspm application (blue, n = 10 cells from eight animals). For analysis, 10 successive responses were averaged and normalized to the mean EPSC amplitude obtained between 20 and 30 min of the recording session (baseline marked with gray dashed lines). Top, example traces. **(B)** The same time course as **(A)** but for basal inputs. Pink, untreated cells, n = 6 cells from five animals. Yellow, cells treated with Naspm, n = 10 cells from eight animals. Blue, cells treated with L-NAME and Naspm, n = 10 cells from eight animals. Black, cells treated with L-NAME, n = 6 cells from four animals. Top, example traces. **(C,D)** Histograms demonstrating normalized EPSCs for the last 5 min of the curves A and B, respectively. Open gray circles represent individual data points, $^{**}p \leq 0.005$.

and basal (RI = 3 ± 0.4) inputs, as in the cells treated with the NOS inhibitors alone (p = 0.680, two-way ANOVA).

DISCUSSION

In the present study, we described data supporting the presence of CP-AMPARs not only in the apical dendrites of CA1 pyramidal cells but also in the basal dendrites. Recording of basic transmission during whole-cell patch-clamp with spermine-free intracellular solution showed a gradual increase in the EPSC amplitudes at both inputs (**Figures 1D,E**), which is associated with the release of GluR2-lacking AMPARs from the polyamine block and leading to an increase in the conductance of these receptors (Rozov et al., 2012). This growth does not occur with 10 μM spermine in the patch pipette (**Supplementary Figure 3**). GluR2-lacking AMPAR blockade decreased the response amplitudes significantly in the apical dendrites and insignificantly in the basal dendrites. In addition, application of high-frequency stimulation to the inputs revealed a significant polyamine-dependent facilitation (Rozov and Burnashev, 1999; Rozov et al., 2018) in *str. radiatum*, while in *str. oriens* we observed only a tendency (**Figure 2**). However, taking into account that basal dendrites are located closer to the soma than apical dendrites, polyamines are washed out *via* the patch pipette faster. According to this, PdF at the basal inputs should slightly decrease by the fifth minute after whole-cell patch formation. Indeed, if the recording starts at ∼1 min, the p-value for the 4th EPSC decreases in basal dendrites (**Supplementary Figure 2**, p = 0.024). However, we observed a significantly higher contribution of CP-AMPARs to glutamatergic synaptic transmission in *stratum radiatum*, than in *stratum oriens* by measuring the rectification index (**Figure 1C**), which suggests that physiology or number of the receptors differs in these compartments.

The presence of GluA2-lacking AMPARs in CA1 cells prompts the question of their localization, as studies have shown different data on their presence in the postsynapse after LTP induction (Plant et al., 2006; Adesnik and Nicoll, 2007; Moult et al., 2010). Some studies have demonstrated that GluA2-lacking AMPARs constitute a small subpopulation of the synaptic AMPA receptors in non-potentiated CA1 pyramidal neurons in adult rodents (Rozov et al., 2012; Mattison et al.,

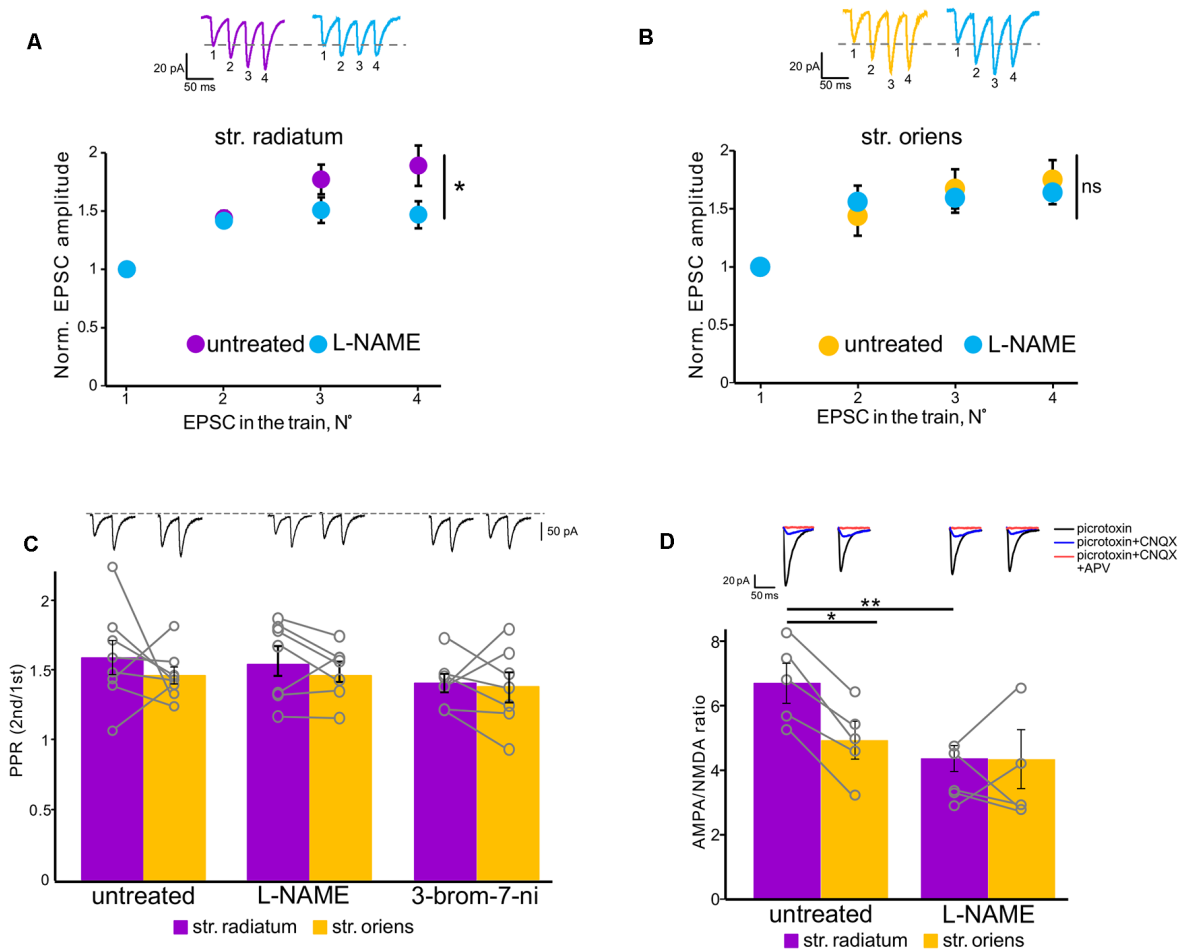

FIGURE 5 | NOS inhibition affected polyamine-dependent facilitation in the apical but not basal dendrites. **(A)** Facilitation at apical dendrites recorded with spermine-containing intracellular solution in untreated cells (purple, $n = 6$ cells from four animals) and under NOS blockade (orange, $n = 6$ cells from four animals). *$p \leq 0.05$. Top, example traces. **(B)** Basal dendrite responses recorded with spermine-containing intracellular solution in untreated cells (purple, $n = 7$ cells from four animals) and under NOS blockade (orange, $n = 7$ cells from four animals). Top, example traces. EPSC numbering corresponds to the x-axis of each graph. ns, nonsignificant. **(C)** Comparison of paired-pulse ratios in *stratum radiatum* (purple) and *stratum oriens* (orange) in untreated cells and under NOS blockade (control: $n = 8$ cells from five animals; L-NAME: $n = 7$ cells from three animals; 3-bromo-7-ni: $n = 7$ cells from three animals). Open gray circles represent individual data points. Top, example traces. **(D)** Comparison of AMPA-NMDA ratios in *stratum radiatum* (purple) and *stratum oriens* (orange) in untreated cells ($n = 5$ cells from three animals) and under NOS blockade ($n = 5$ cells from three animals). Top, example traces. *$p \leq 0.05$, **$p \leq 0.005$.

2014), and in other studies, it was shown that GluR2-lacking AMPARs in pyramidal cells in the hippocampus are replaced with GluR2-containing AMPARs in mature animals (Ho et al., 2007; Malkin et al., 2016). This discrepancy can be explained by the presence of polyamines in the patch pipette which affects the ability of GluA2-lacking AMPAR antagonists to block them (Rozov et al., 2012). In addition, the presence of polyamines in the pipette also determines the rectification characteristics of synapses with GluR2-lacking AMPARs in their membrane (Kamboj et al., 1995): the current–voltage characteristics of such synapses in the absence of spermine are linear, as in mutant GluA1-/- mice (Rozov et al., 2012).

The polyamine concentration in the patch pipette varies in different studies (Rozov et al., 2012; Mattison et al., 2014; Malkin et al., 2016). The precise concentration of intracellular free polyamines in CA1 pyramidal cells is unknown; however, it is known that the concentration varies in different regions of the rat brain (Shaskan et al., 1973), as well as in other mammals (Igarashi and Kashiwagi, 2010). In our study, we used 10 μM spermine in the intracellular solution to record the rectification properties of inputs. One can argue that the spermine concentration in our experiments was insufficient to successfully block GluR2-lacking AMPARs; however, the experiments with polyamine-dependent facilitation (**Figure 2**) indicated the opposite: 10 μM spermine in the patch pipette prevented polyamine washout from the dendritic compartments. Moreover, using 10 μM spermine-containing intracellular solution does not cause an increase in EPSC amplitude (**Supplementary Figure 3**). In addition, Hu et al. (1994) showed that 100 μM spermine inhibits [3H]L-citrulline formation, which reflects NOS activity, by ∼60% in cerebellar cells, whereas 10 μM only slightly inhibits this

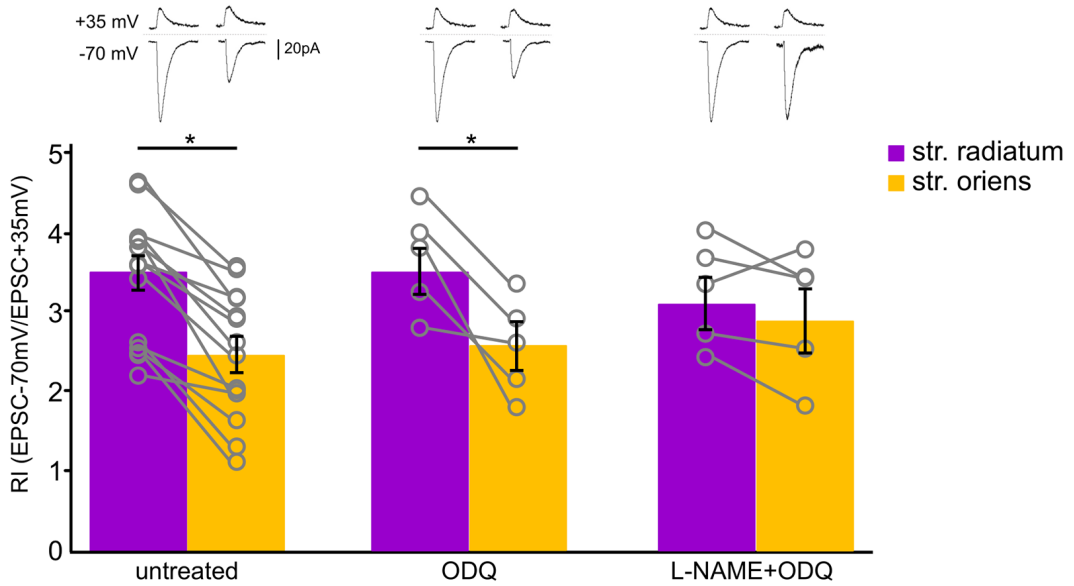

FIGURE 6 | Soluble guanylyl cyclase inhibition did not affect CP-AMPAR contribution to synaptic transmission of CA1 pyramidal cells. Comparison of rectification indices in *stratum radiatum* (purple) and *stratum oriens* (orange) in untreated cells (n = 14 cells from nine animals) and under treatment with ODQ (30 μM, n = 5 cells from three animals) and L-NAME (200 μM, n = 5 cells from three animals). Top, example traces. *$p \leq 0.05$.

reaction, **Figure 1**). This might indicate that high spermine concentration in the patch pipette can cause NOS inhibition. Indeed, when 100 μM spermine was added to the patch pipette, the difference in RIs between apical and basal dendrites of CA1 pyramidal cells was not statistically significant (apical: 3 ± 0.4; basal: 2.3 ± 0.2, n = 7, p = 0.12, two-way ANOVA; **Supplementary Figure 1**), as in the case of NOS blockade.

Nitric oxide was shown to be involved in LTP maintenance in *str. radiatum*, but not in *str. Oriens*; however, the presence of nNOS was shown in both *str. radiatum* and *str. oriens* (see the "Introduction" section). We assumed that this contrast was due to the difference in the modulation of synaptic characteristics by nitric oxide in these areas. In particular, nitric oxide could differently affect the CP-AMPAR contribution to synaptic transmission of apical and basal dendrites. We found that NOS inhibition by two different inhibitors and treatment with an NO scavenger reduced inward rectification and caused a drop in the rectification index at apical dendrites (**Figure 3**), which reflected a decrease in the contribution of GluR2-lacking AMPARs to the currents in these synapses. In addition, NOS inhibition prevented the decrease in response amplitude under Naspm treatment (**Figure 4**) and reduced the polyamine-dependent facilitation (**Figures 5A,B**), whereas, at basal inputs the NOS inhibition did not affect any of the synaptic characteristics. Thus, our data indicate that nitric oxide does not affect the contribution of GluR2-lacking AMPARs to synapses of CA1 pyramidal cell basal dendrites, while inhibition of nitric oxide synthesis significantly reduced the contribution of these receptors to apical dendrite synaptic currents. So far, it is unclear which nitric oxide-dependent mechanism exerts this effect in *str. radiatum*. For instance, the concentration of free nitric oxide in the cell can affect synthesis of intracellular polyamines (Buga et al., 1998; Boucher et al., 1999), which in turn determines the conductivity of GluR2-lacking AMPARs. However, according to our data, the increase in current amplitude during PdF under NOS inhibition disappears, which indicates an unlikelihood of an increased concentration of intracellular polyamines in apical dendrites.

Nitric oxide may also act through the regulation of CP-AMPAR trafficking or through the modification of incorporated receptors. NO inhibition could disrupt one of the possible mechanisms involved in the trafficking of AMPAR subunits: the indirect sGC-dependent pathway (Serulle et al., 2007), direct nitrosylation of GluR1 subunits (Selvakumar et al., 2013; Von Ossowski et al., 2017), or different protein–protein interactions (Chen et al., 2000; Zhang et al., 2015; for review, see Ivanova et al., 2020). One such interaction was shown for GluR2 incorporation *via* NSF-dependent declustering of the PICK1–GluR2 complex (Hanley et al., 2002; Huang et al., 2005; Sossa et al., 2007); however, in the two latter studies the NO donor application resulted in increased GluR1 surface expression (Hanley et al., 2002, **Figure 5B** and Sossa et al., 2007, **Figure 4C**); thus, there is a possibility of NSF involvement in GluR2-lacking AMPAR trafficking. We tested the cGMP-dependent pathway by blocking sGC (**Figure 6**) but did not find any differences in the rectification characteristics of the studied synapses.

Obtained results suggest that nitric oxide upregulates the CP-AMPAR sensitivity to polyamines: this might explain changes in the current–voltage relationships, decreased PdF, and persisting EPSC growth under NOS inhibition. Moreover, such modulation was demonstrated for GluR2-lacking AMPARs by the auxiliary protein stargazin (Soto et al., 2007). However, the mechanism of this modulation requires further clarification. One

possible explanation of the NOS inhibition effect is a reduced GluR2-lacking AMPAR surface expression. However, that does not explain the increase in EPSC amplitudes during polyamine washout after incubation in L-NAME.

In conclusion, this study demonstrates the effects of NOS inhibition on GluA2-lacking AMPA receptor-mediated currents at apical but not basal dendrites of the CA1 pyramidal neurons. This effect could underlie the differences in synaptic plasticity of the aforementioned synapses, although the mechanisms of this effect require further study. Many studies demonstrated differences in the mechanisms of synaptic plasticity between different neuron's compartments; the concept of a specialized "memory synapse" is discussed (Sossin, 2018). We believe that our study highlights the importance of such phenomena as synaptic heterogeneity which may underlie the features of information processing in the hippocampus. In addition, the importance of AMPA receptors for such aspects of cell life as synaptic plasticity and homeostasis is undeniable. AMPAR GluA1–4 subunit trafficking, subunit-specific protein interactions, auxiliary subunits, and posttranslational modifications could predict the types and extent of synaptic plasticity; this is the so-called "AMPA receptor code of synaptic plasticity" (Diering and Huganir, 2018), and our data reveal more details of this complex code.

DATA AVAILABILITY STATEMENT

The raw data supporting the conclusions of this article will be made available by the authors, without undue reservation.

ETHICS STATEMENT

The animal study was reviewed and approved by the Ethical committee of the Institute of Higher Nervous Activity and Neurophysiology, Russian Academy of Sciences (IHNA RAS).

AUTHOR CONTRIBUTIONS

VI designed and performed the experiments, analyzed the data, and wrote the article. PB managed the project and wrote the article. NB conceived and designed the experiments, managed the project, and wrote the article. All authors contributed to the article and approved the submitted version.

FUNDING

This work was supported by the Russian Science Foundation, grant #20-15-00398.

ACKNOWLEDGMENTS

We thank David Jappy for useful comments on the manuscript.

SUPPLEMENTARY MATERIAL

The Supplementary Material for this article can be found online at: https://www.frontiersin.org/articles/10.3389/fnsyn.2021.656377/full#supplementary-material.

REFERENCES

Adesnik, H., and Nicoll, R. A. (2007). Conservation of glutamate receptor 2-containing AMPA receptors during long-term potentiation. *J. Neurosci.* 27, 4598–4602. doi: 10.1523/JNEUROSCI.0325-07.2007

Bal, N., Roshchin, M., Salozhin, S., and Balaban, P. (2017). Nitric oxide upregulates proteasomal protein degradation in neurons. *Cell. Mol. Neurobiol.* 37, 763–769. doi: 10.1007/s10571-016-0413-9

Bartus, K., Pigott, B., and Garthwaite, J. (2013). Cellular targets of nitric oxide in the hippocampus. *PLoS One* 8:e57292. doi: 10.1371/journal.pone.0057292

Benavides-Piccione, R., Regalado-Reyes, M., Fernaud-Espinosa, I., Kastanauskaite, A., Tapia-González, S., León-Espinosa, G., et al. (2020). Differential structure of hippocampal CA1 pyramidal neurons in the human and mouse. *Cereb. Cortex* 30, 730–752. doi: 10.1093/cercor/bhz122

Blackshaw, S., Eliasson, M. J. L., Sawa, A., Watkins, C. C., Krug, D., Gupta, A., et al. (2003). Species, strain and developmental variations in hippocampal neuronal and endothelial nitric oxide synthase clarify discrepancies in nitric oxide-dependent synaptic plasticity. *Neuroscience* 119, 979–990. doi: 10.1016/s0306-4522(03)00217-3

Boucher, J. L., Moali, C., and Tenu, J. P. (1999). Nitric oxide biosynthesis, nitric oxide synthase inhibitors and arginase competition for L-arginine utilization. *Cell. Mol. Life Sci.* 55, 1015–1028. doi: 10.1007/s000180050352

Bradshaw, K. D., Emptage, N. J., and Bliss, T. V. P. (2003). A role for dendritic protein synthesis in hippocampal late LTP. *Eur. J. Neurosci.* 18, 3150–3152. doi: 10.1111/j.1460-9568.2003.03054.x

Buga, G. M., Wei, L. H., Bauer, P. M., Fukuto, J. M., and Ignarro, L. J. (1998). N(G)-hydroxy-L-arginine and nitric oxide inhibit Caco-2 tumor cell proliferation by distinct mechanisms. *Am. J. Physiol.* 275, R1256–R1264. doi: 10.1152/ajpregu.1998.275.4.R1256

Cenquizca, L. A., and Swanson, L. W. (2007). Spatial organization of direct hippocampal field CA1 axonal projections to the rest of the cerebral cortex. *Brain Res. Rev.* 56, 1–26. doi: 10.1016/j.brainresrev.2007.05.002

Chen, L., Chetkovich, D. M., Petralia, R. S., Sweeney, N. T., Kawasaki, Y., Wenthold, R. J., et al. (2000). Stargazin regulates synaptic targeting of AMPA receptors by two distinct mechanisms. *Nature* 408, 936–943. doi: 10.1038/35050030

Christie, J. M., and Jahr, C. E. (2006). Multivesicular release at Schaffer collateral-CA1 hippocampal synapses. *J. Neurosci.* 26, 210–216. doi: 10.1523/JNEUROSCI.4307-05.2006

Diering, G. H., and Huganir, R. L. (2018). The AMPA receptor code of synaptic plasticity. *Neuron* 100, 314–329. doi: 10.1016/j.neuron.2018.10.018

Dugue, G. P., Dumoulin, A., Triller, A., and Dieudonne, S. (2005). Target-dependent use of co-released inhibitory transmitters at central synapses. *J. Neurosci.* 25, 6490–6498. doi: 10.1523/JNEUROSCI.1500-05.2005

Haley, J. E., Schaible, E., Pavlidis, P., Murdock, A., and Madison, D. V. (1996). Basal and apical synapses of CA1 pyramidal cells employ different LTP induction mechanisms. *Learn. Mem.* 3, 289–295. doi: 10.1101/lm.3.4.289

Hanley, J. G., Khatri, L., Hanson, P. I., and Ziff, E. B. (2002). NSF ATPase and alpha-/beta-SNAPs disassemble the AMPA receptor-PICK1 complex. *Neuron* 34, 53–67. doi: 10.1016/s0896-6273(02)00638-4

Hardingham, N., Dachtler, J., and Fox, K. (2013). The role of nitric oxide in pre-synaptic plasticity and homeostasis. *Front. Cell. Neurosci.* 7:190. doi: 10.3389/fncel.2013.00190

Higuchi, M., Single, F. N., Köhler, M., Sommer, B., Sprengel, R., and Seeburg, P. H. (1993). RNA editing of AMPA receptor subunit GluR-B: A base-paired intron-exon structure determines position and efficiency. *Cell* 75, 1361–1370. doi: 10.1016/0092-8674(93)90622-w

Ho, M. T. W., Pelkey, K. A., Topolnik, L., Petralia, R. S., Takamiya, K., Xia, J., et al. (2007). Developmental expression of Ca2+-permeable AMPA receptors underlies depolarization-induced long-term depression at mossy fiber-CA3

pyramid synapses. *J. Neurosci.* 27, 11651–11662. doi: 10.1523/JNEUROSCI.2671-07.2007

Hu, J., Mahmoud, M. I., and El-Fakahany, E. E. (1994). Polyamines inhibit nitric oxide synthase in rat cerebellum. *Neurosci. Lett.* 175, 41–45. doi: 10.1016/0304-3940(94)91073-1

Huang, Y., Man, H. Y., Sekine-Aizawa, Y., Han, Y., Juluri, K., Luo, H., et al. (2005). S-nitrosylation of N-ethylmaleimide sensitive factor mediates surface expression of AMPA receptors. *Neuron* 46, 533–540. doi: 10.1016/j.neuron.2005.03.028

Hulme, S. R., Jones, O. D., Ireland, D. R., and & Abraham, W. C. (2012). Calcium-dependent but action potential-independent BCM-like metaplasticity in the hippocampus. *J. Neurosci.* 32, 6785–6794. doi: 10.1523/JNEUROSCI.0634-12.2012

Igarashi, K., and Kashiwagi, K. (2010). Modulation of cellular function by polyamines. *Int. J. Biochem. Cell Biol.* 42, 39–51. doi: 10.1016/j.biocel.2009.07.009

Ivanova, V. O., Balaban, P. M., and Bal, N. V. (2020). Modulation of AMPA receptors by nitric oxide in nerve cells. *Int. J. Mol. Sci.* 21:981. doi: 10.3390/ijms21030981

Kamboj, S. K., Swanson, G. T., and Cull-Candy, S. G. (1995). Intracellular spermine confers rectification on rat calcium-permeable AMPA and kainate receptors. *J. Physiol.* 486, 297–303. doi: 10.1113/jphysiol.1995.sp020812

Lu, Y. F., Kandel, E. R., and Hawkins, R. D. (1999). Nitric oxide signaling contributes to late-phase LTP and CREB phosphorylation in the hippocampus. *J. Neurosci.* 19, 10250–10261. doi: 10.1523/JNEUROSCI.19-23-10250.1999

Malinow, R., and Malenka, R. C. (2002). AMPA receptor trafficking and synaptic plasticity. *Annu. Rev. Neurosci.* 25, 103–126. doi: 10.1146/annurev.neuro.25.112701.142758

Malkin, S. L., Amakhin, D. V., Veniaminova, E. A., Kim, K. K., Zubareva, O. E., Magazanik, L. G., et al. (2016). Changes of ampa receptor properties in the neocortex and hippocampus following pilocarpine-induced status epilepticus in rats. *Neuroscience* 327, 146–155. doi: 10.1016/j.neuroscience.2016.04.024

Maltsev, A. V., Bal, N. V., and Balaban, P. M. (2019). LTP suppression by protein synthesis inhibitors is NO-dependent. *Neuropharmacology* 146, 276–288. doi: 10.1016/j.neuropharm.2018.12.009

Masurkar, A. V., Srinivas, K. V., Brann, D. H., Warren, R., Lowes, D. C., and Siegelbaum, S. A. (2017). Medial and lateral entorhinal cortex differentially excite deep versus superficial CA1 pyramidal neurons. *Cell Rep.* 18, 148–160. doi: 10.1016/j.celrep.2016.12.012

Mattison, H. A., Bagal, A. A., Mohammadi, M., Pulimood, N. S., Reich, C. G., Alger, B. E., et al. (2014). Evidence of calcium-permeable AMPA receptors in dendritic spines of CA1 pyramidal neurons. *J. Neurophysiol.* 112, 263–275. doi: 10.1152/jn.00578.2013

Moult, P. R., Cross, A., Santos, S. D., Carvalho, A. L., Lindsay, Y., Connolly, C. N., et al. (2010). Leptin regulates AMPA receptor trafficking via PTEN inhibition. *J. Neurosci.* 30, 4088–4101. doi: 10.1523/JNEUROSCI.3614-09.2010

O'Dell, T. J., Huang, P. L., Dawson, T. M., Dinerman, J. L., Snyder, S. H., Kandel, E. R., et al. (1994). Endothelial NOS and the blockade of LTP by NOS inhibitors in mice lacking neuronal NOS. *Science* 265, 542–546.

Plant, K., Pelkey, K. A., Bortolotto, Z. A., Morita, D., Terashima, A., McBain, C. J., et al. (2006). Transient incorporation of native GluR2-lacking AMPA receptors during hippocampal long-term potentiation. *Nat. Neurosci.* 9, 602–604. doi: 10.1038/nn1678

Rozov, A., and Burnashev, N. (1999). Polyamine-dependent facilitation of postsynaptic AMPA receptors counteracts paired-pulse depression. *Nature* 401, 594–598. doi: 10.1038/44151

Rozov, A., Sprengel, R., and Seeburg, P. H. (2012). GluA2-lacking AMPA receptors in hippocampal CA1 cell synapses: evidence from gene-targeted mice. *Front. Mol. Neurosci.* 5:22. doi: 10.3389/fnmol.2012.00022

Rozov, A., Zakharova, Y., Vazetdinova, A., and Valiullina-Rakhmatullina, F. (2018). The role of polyamine-dependent facilitation of calcium permeable ampars in short-term synaptic enhancement. *Front. Cell. Neurosci.* 12:345. doi: 10.3389/fncel.2018.00345

Schulz, P. E., Cook, E. P., and Johnston, D. (1994). Changes in paired-pulse facilitation suggest presynaptic involvement in long-term potentiation. *J. Neurosci.* 14, 5325–5337. doi: 10.1523/JNEUROSCI.14-09-05325.1994

Selvakumar, B., Jenkins, M. A., Hussain, N. K., Huganir, R. L., Traynelis, S. F., and Snyder, S. H. (2013). S-nitrosylation of AMPA receptor GluA1 regulates phosphorylation, single-channel conductance and endocytosis. *Proc. Natl. Acad. Sci. U S A* 110, 1077–1082. doi: 10.1073/pnas.1221295110

Serulle, Y., Zhang, S., Ninan, I., Puzzo, D., McCarthy, M., Khatri, L., et al. (2007). A GluR1-cGKII interaction regulates AMPA receptor trafficking. *Neuron* 56, 670–688. doi: 10.1016/j.neuron.2007.09.016

Shaskan, E. G., Haraszti, J. H., and Snyder, S. H. (1973). Polyamines: developmental alterations in regional disposition and metabolism in rat brain. *J. Neurochem.* 20, 1443–1452. doi: 10.1111/j.1471-4159.1973.tb00256.x

Son, H., Hawkins, R. D., Martin, K., Kiebler, M., Huang, P. L., Fishman, M. C., et al. (1996). Long-term potentiation is reduced in mice that are doubly mutant in endothelial and neuronal nitric oxide synthase. *Cell* 87, 1015–1023. doi: 10.1016/s0092-8674(00)81796-1

Son, H., Lu, Y. F., Zhuo, M., Arancio, O., Kandel, E. R., and Hawkins, R. D. (1998). The specific role of cGMP in hippocampal LTP. *Learn. Mem.* 5, 231–245.

Sossa, K. G., Beattie, J. B., and & Carroll, R. C. (2007). AMPAR exocytosis through NO modulation of PICK1. *Neuropharmacology* 53, 92–100. doi: 10.1016/j.neuropharm.2007.04.005

Sossin, W. S. (2018). Memory synapses are defined by distinct molecular complexes: a proposal. *Front. Synaptic Neurosci.* 10:5. doi: 10.3389/fnsyn.2018.00005

Soto, D., Coombs, I. D., Kelly, L., Farrant, M., and Cull-Candy, S. G. (2007). Stargazin attenuates intracellular polyamine block of calcium-permeable AMPA receptors. *Nat. Neurosci.* 10, 1260–1267. doi: 10.1038/nn1966

Van Strien, N. M., Cappaert, N. L. M., and Witter, M. P. (2009). The anatomy of memory: an interactive overview of the parahippocampal- hippocampal network. *Nat. Rev. Neurosci.* 10, 272–282. doi: 10.1038/nrn2614

Von Ossowski, L., Li, L. L., Moykkynen, T., Coleman, S. K., Courtney, M. J., and Keinanen, K. (2017). Cysteine 893 is a target of regulatory thiol modifications of GluA1 AMPA receptors. *PLoS One* 12:e0171489. doi: 10.1371/journal.pone.0171489

Zhang, P., Fu, W. Y., Fu, A. K., and Ip, N. Y. (2015). S-nitrosylation-dependent proteasomal degradation restrains Cdk5 activity to regulate hippocampal synaptic strength. *Nat. Commun.* 6:8665. doi: 10.1038/ncomms9665

Conflict of Interest: The authors declare that the research was conducted in the absence of any commercial or financial relationships that could be construed as a potential conflict of interest.

Copyright © 2021 Ivanova, Balaban and Bal. This is an open-access article distributed under the terms of the Creative Commons Attribution License (CC BY). The use, distribution or reproduction in other forums is permitted, provided the original author(s) and the copyright owner(s) are credited and that the original publication in this journal is cited, in accordance with accepted academic practice. No use, distribution or reproduction is permitted which does not comply with these terms.

frontiers in Synaptic Neuroscience

ORIGINAL RESEARCH
published: 21 September 2021
doi: 10.3389/fnsyn.2021.725880

Intracellular Properties of Deep-Layer Pyramidal Neurons in Frontal Eye Field of Macaque Monkeys

Charlotte Piette[1], Marie Vandecasteele[1], Clémentine Bosch-Bouju[1], Valérie Goubard[1], Vincent Paillé[1], Yihui Cui[1], Alexandre Mendes[1], Sylvie Perez[1], Silvana Valtcheva[1], Hao Xu[1], Pierre Pouget[2] and Laurent Venance[1]**

[1] Dynamics and Pathophysiology of Neuronal Networks Team, Center for Interdisciplinary Research in Biology (CIRB), College de France, CNRS, INSERM, PSL University, Paris, France, [2] INSERM, CNRS, Institut du Cerveau, Sorbonne Université, Paris, France

Although many details remain unknown, several positive statements can be made about the laminar distribution of primate frontal eye field (FEF) neurons with different physiological properties. Most certainly, pyramidal neurons in the deep layer of FEF that project to the brainstem carry movement and fixation signals but clear evidence also support that at least some deep-layer pyramidal neurons projecting to the superior colliculus carry visual responses. Thus, deep-layer neurons in FEF are functionally heterogeneous. Despite the useful functional distinctions between neuronal responses *in vivo*, the underlying existence of distinct cell types remain uncertain, mostly due to methodological limitations of extracellular recordings in awake behaving primates. To substantiate the functionally defined cell types encountered in the deep layer of FEF, we measured the biophysical properties of pyramidal neurons recorded intracellularly in brain slices issued from macaque monkey biopsies. Here, we found that biophysical properties recorded *in vitro* permit us to distinguish two main subtypes of regular-spiking neurons, with, respectively, low-resistance and low excitability vs. high-resistance and strong excitability. These results provide useful constraints for cognitive models of visual attention and saccade production by indicating that at least two distinct populations of deep-layer neurons exist.

Keywords: frontal eye field, primate, pyramidal cells, visual cortex, neuron classification, electrophysiology, intrinsic membrane properties

OPEN ACCESS

Edited by:
Carlos Cepeda, University of California, Los Angeles, United States

Reviewed by:
Julio Martinez-Trujillo, Western University, Canada
Jeffrey Schall, Vanderbilt University, United States

***Correspondence:**
Pierre Pouget
pierre.pouget@icm-institute.org
Laurent Venance
laurent.venance@college-de-france.fr

Received: *15 June 2021*
Accepted: *24 August 2021*
Published: *21 September 2021*

Citation:
Piette C, Vandecasteele M, Bosch-Bouju C, Goubard V, Paillé V, Cui Y, Mendes A, Perez S, Valtcheva S, Xu H, Pouget P and Venance L (2021) Intracellular Properties of Deep-Layer Pyramidal Neurons in Frontal Eye Field of Macaque Monkeys. Front. Synaptic Neurosci. 13:725880. doi: 10.3389/fnsyn.2021.725880

INTRODUCTION

It is becoming increasingly important to determine the identity of cortical neurons involved in a wide range of brain functions. The neocortex is comprised of different classes of pyramidal cells and interneurons, and distinguishing between these groups of neurons in recordings made from awake, behaving animals is a key issue. Neocortical neurons have been distinguished by their firing patterns and morphology (Connors and Gutnick, 1990; Krimer et al., 2005; Chang and Luebke, 2007; Zaitsev et al., 2012), laminar distribution (Dow, 1974; Bullier and Henry, 1979; Condé et al., 1994), molecular composition

(Cauli et al., 1997; Martina et al., 1998), functional property (González-Burgos et al., 2005), as well as developmental origin (Letinic et al., 2002). In the oculomotor field of research, it has been demonstrated that several cortical areas and subcortical regions contribute to the visual-motor mapping. One such area, the frontal eye field (FEF), contains at least three main functional types of neurons: visual, movement, and visuo-movement neurons (Goldberg and Bushnell, 1981; Bruce and Goldberg, 1985; Segraves and Goldberg, 1987; Schall, 1991; Segraves, 1992; Kodaka et al., 1997; Umeno and Goldberg, 1997; Hanes et al., 1998; DiCarlo and Maunsell, 2005). The visual and visuo-movement neurons select the target of search by increasing their firing rate in response to the presence of the target in their receptive fields (RFs) relative to when a distractor is located in their RFs (e.g., Schall and Hanes, 1993; Thompson et al., 1996). A different population of neurons, called movement neurons, increases their firing rate leading up to saccades into their movement fields (MFs) (e.g., Hanes and Schall, 1996). Finally, visuo-movement neurons also increase their firing rate leading up to saccades while they also respond to the presence of the target in RFs (Everling and Munoz, 2000; Sato et al., 2001; McPeek, 2006; Ray et al., 2009).

Some recent works have also shown that visuo-movement neurons tend to have the thinnest spikes, consistent with a role in local processing while movement neurons were found to have the widest spikes, consistent with their role in sending eye movement commands to subcortical structures such as the superior colliculus. Finally, visual neurons had wider spikes than visuo-movement neurons, consistent with their role in receiving projections from the occipital and parietal cortex (Cohen et al., 2009). These distinctions between these cell types have relied largely on firing-rate patterns or spike waveforms indirect analysis as opposed to inherent biophysical properties of the neurons being studied. As a consequence, as in the primary motor cortex where the report of thin-spiked pyramidal cells urge caution in matching extracellular recording-based and anatomically defined cell types (Lemon et al., 2021), some disagreements persist about the reliability of the distinction between FEF neuron types solely based on functional rate pattern responses (Lowe and Schall, 2018). To substantiate the functionally defined cell types encountered in FEF, we measured intracellular properties of FEF neurons recorded *in vitro* using whole-cell patch-clamp recordings in FEF acute brain slices issued from macaque monkey biopsies. The relationship between intracellular properties and functional properties of FEF is a critical missing piece of information to construct a valid physiological model of visual target selection and saccade programming.

MATERIALS AND METHODS

Ethics Statement

All experiments were carried out in accordance with the recommendations contained in the European Community Council Directives of 1986 (86/609/EEC) and the NIH Guide for the Care and Use of Laboratory Animals and were approved by the French Animal Ethics Committee of INSERM. The animals were housed under conditions of constant temperature (21 ± 1°C), humidity (55 ± 5%), and air replacement (16 times/h), on a 12-h light/12-h dark cycle with access *ad libitum* to food and water.

Animals

Biopsies were obtained at the time of their euthanasia from 8 long-tailed macaque monkeys (*Macaca fascicularis*). All animals were involved in tracer and/or lesion studies in ethically approved projects, 6 animals were 5–6 years old and their weights ranged from 3 to 5 kg. Our work benefits from these studies to obtain biopsies at the time of the terminal experiments of other studies.

Surgery and Brain Slice Preparation

Following injections of ketamine hydrochloride (25 mg/kg), atropine sulfate (0.05 mg/kg), an endotracheal tube was inserted, and the animal was placed in a stereotaxic frame. Anesthesia was maintained with 2% isoflurane in 30% O_2/air. A large craniotomy was performed over the prefrontal cortex, and a small block of tissue containing both lateral banks of arcuate sulcus (areas 8 and 46) as well as part of area 9 (Walker 1940) was carefully excised. The tissue block was placed in a 95% CO_2/5% O_2-bubbled, ice-cold solution consisting of (in mM) 125 NaCl, 2.5 KCl, 25 glucose, 25 $NaHCO_3$, 1.25 NaH_2PO_4, 2 $CaCl_2$, 1 $MgCl_2$, 1 pyruvic acid.

After the craniotomy, the animal was given an overdose of pentobarbital (30 mg/kg) and was perfused transcardially with ice-cold–modified artificial cerebrospinal fluid. A tissue block containing the portions of areas 9 and 46 non-homotopic to the first biopsy was quickly excised. Sagittal slices (330 μm) were cut using a vibrating blade microtome (VT1200S, Leica Microsystems, Nussloch, Germany). Brains were sliced in a 95% CO_2/5% O_2-bubbled, ice-cold cutting solution containing (in mM) 125 NaCl, 2.5 KCl, 25 glucose, 25 $NaHCO_3$, 1.25 NaH_2PO_4, 2 $CaCl_2$, 1 $MgCl_2$, 1 pyruvic acid, and then transferred into the same solution at 34°C for 1 h and then kept at room temperature.

Electrophysiological Recordings

Whole-cell patch-clamp recordings were performed as previously described (Paillé et al., 2013), using borosilicate glass pipettes of 4–6 MΩ resistance, filled with (in mM): 105 K-gluconate, 30 KCl, 10 HEPES, 10 phosphocreatine, 4 Mg-ATP, 0.3 Na-GTP, 0.3 EGTA (adjusted to pH 7.35 with KOH), and 0.5% biocytin. The composition of the extracellular solution was (mM): 125 NaCl, 2.5 KCl, 25 glucose, 25 $NaHCO_3$, 1.25 NaH_2PO_4, 2 $CaCl_2$, 1 $MgCl_2$, 10 μM pyruvic acid bubbled with 95% O_2 and 5% CO_2. Signals were amplified using EPC9-2 and EPC10-4 amplifiers (HEKA Elektronik, Lambrecht, Germany). All recordings were performed at 34°C, using a temperature control system (Bath-controller V, Luigs and Neumann, Ratingen, Germany) and slices were continuously superfused with extracellular solution, at a rate of 2–3 ml.min^{-1}. Slices were visualized under an Olympus BX51WI microscope (Olympus, Rungis, France), with a 4 × /0.13 objective for the placement of the stimulating electrode and a 40 × /0.80 water-immersion objective for the localization of cells for whole-cell recordings. Current–clamp recordings were sampled at 2.5 kHz and voltage–clamp recordings were

sampled at 10 kHz, with the Patchmaster v2 × 32 program (HEKA Elektronik). Glutamate transmission blockers 6-Cyano-7-nitroquinoxaline-2,3-dione (CNQX, 10 μM, Tocris, Ellisville, MO, United States) and DL-2-amino-5-phosphono-pentanoic acid (D-AP5, 50 μM, Tocris) were bath-applied and responses were measured after 5 min of application.

Electrophysiological Data Analysis

Off-line analysis was performed using Patchmaster (Heka Elektronik), Igor-Pro 6.0.3 (Wavemetrics, Lake Oswego, OR, United States) and MATLAB (The Mathworks).

Pyramidal neurons were identified in slices by their morphology and basic electrophysiological characteristics to distinguish them from interneurons (Cohen et al., 2009; Mueller et al., 2020): patched cells were pre-selected by their large soma with triangular shape through a visual inspection using infrared DIC video-microscopy. Offline analysis of AP features was then used to exclude interneurons, namely if the spike half-width was < 0.7 ms and/or the rise/decay slope ratio was < 1 in the absence of an ADP. Only cells that had a resting membrane potential (RMP) of less than −50 mV (unless spontaneously active), and an AP overshoot were included. 50 cells were retained for clustering analysis but not all cells were held for sufficient time to allow all protocols to be completed (**Supplementary Table 1**).

Passive and Active Membrane Properties

Cells were recorded in a current-clamp mode for their electrophysiological characterization. Resting membrane potential (RMP) was determined by measuring the membrane voltage in the absence of current input. For the PCA and clustering analysis, the membrane potential of spontaneously active cells was measured by excluding the spiking periods, but is not considered for the RMP comparison between clusters. A series of 500-ms hyperpolarizing and depolarizing current steps ranging from −100 in 10 pA increments were applied to the cell. For spontaneously active cells, steps were applied on top of a holding current to maintain them at rest (−60/−70 mV). Input resistance (Ri) was calculated from a single sweep as the ratio of the steady-state membrane voltage response to the current applied after injecting a small hyperpolarizing current (10–20 pA). Membrane time constant (tau) was determined on the same step by fitting the membrane potential response to a single-exponential function. Sag index was measured on a 100 pA hyperpolarizing current step and expressed as the percent of the peak voltage response that is repolarized at steady state: $(V_{peaksag} - V_{steadystate})/(V_{peak} - V_{baseline})^*100$. The rebound index was measured at the offset of the same step as the maximal positive voltage response above baseline ($V_{peak\_rebound}$) normalized by the amplitude of the steady-state response: $(V_{peak\_rebound} - V_{baseline})/(V_{peak} - V_{baseline})^*100$. The rheobase ($I_0$) was the minimal current step that evoked firing (for spontaneously active cells, it was corrected by the holding current for the PCA and clustering analysis, thus yielding negative rheobase values; for the comparison between the two clusters, rheobase was equal to 0 pA for spontaneously active cells). The delay to the first spike (from the step onset to the first spike) was measured at I_0, as well as AP properties. Action potential threshold (AP_{thres}) was chosen as the membrane potential at which the rate of voltage rise (dV/dt) reached 10 mV/ms. Action potential amplitude (AP_{amp}), rise time, and rise slope were measured from the AP_{thres} to the peak of the AP. The AP decay time and decay slope were measured from the AP_{peak} to the interpolated point where the AP decay crosses AP_{thres} ($peak_{end}$). Action potential duration (AP_{dur}) was measured as the spike width at its half-amplitude. Amplitude and duration of the afterhyperpolarization (AHP_{amp} and AHP_{dur}) were measured from the $peak_{end}$ to the through after the spike. We distinguished 1 to 3 components in the AHP: a fast component of the AHP (fAHP) present in all cells, a slower medium component (mAHP) in most cells, and an afterdepolarization (ADP) between the fAHP and the mAHP in some cells. The fAHP amplitude was measured between $peak_{end}$ and either the trough of the AHP for single-component AHPs, the onset of the mAHP (marked slowing in the voltage drop) for 2-component AHPs, or the onset of the ADP for 3-components AHPs. The ADP amplitude (when present) was measured between the end of the fAHP and the peak of the ADP. The mAHP amplitude was measured between either the end of the fAHP (2-component AHPs) or the peak of the ADP (3-component AHP), and the next trough of the AHP (see **Figure 1**). The rectification index was calculated as the ratio of the IV curve slope between −20 and 0 pA injected current over the IV curve slope between −100 and −80 pA injected current.

Subthreshold Frequency-Response Curves

We used the impedance amplitude profile (ZAP) method to characterize the resonant behavior of pyramidal cells (Puil et al., 1988; Hutcheon and Yarom, 2000). A sinewave current of fixed amplitude and 30-s duration, with a linear increase of the frequencies ranging from 0.1 to 50 Hz was used. A single zap voltage response was analyzed for each neuron. The impedance profile Z(f) was calculated from the ratio of the Fourier transforms of the voltage response and zap current; its absolute value is the impedance magnitude and its imaginary part corresponds to the phase shift between the input current and voltage response. Plotted against each other, the two components form the "impedance locus diagram". Peak in the impedance power, indicative of membrane resonance, was detected and used to define the resonant frequency (Hutcheon and Yarom, 2000). The Q factor, a measure of resonance strength, was calculated as the ratio of the impedance magnitude at the resonant frequency over the impedance magnitude at 0.5 Hz. For a more precise determination of Q, the impedance profile of each neuron was fitted with a polynomial curve (degree 8) between 0.5 and 20 Hz and the peak value was calculated. A cutoff criterion of $Q \geq 1.1$ was used to differentiate resonant from non-resonant cells (Vera et al., 2014). Frequencies below 0.5 Hz were not plotted in the impedance and phase profiles graphs to avoid low frequency distortions.

Firing Pattern Properties

The first interspike interval (ISI_{1-2}) was measured between the first and second spikes at the minimal suprathreshold current that elicited at least 2 spikes. The spike frequency adaptation

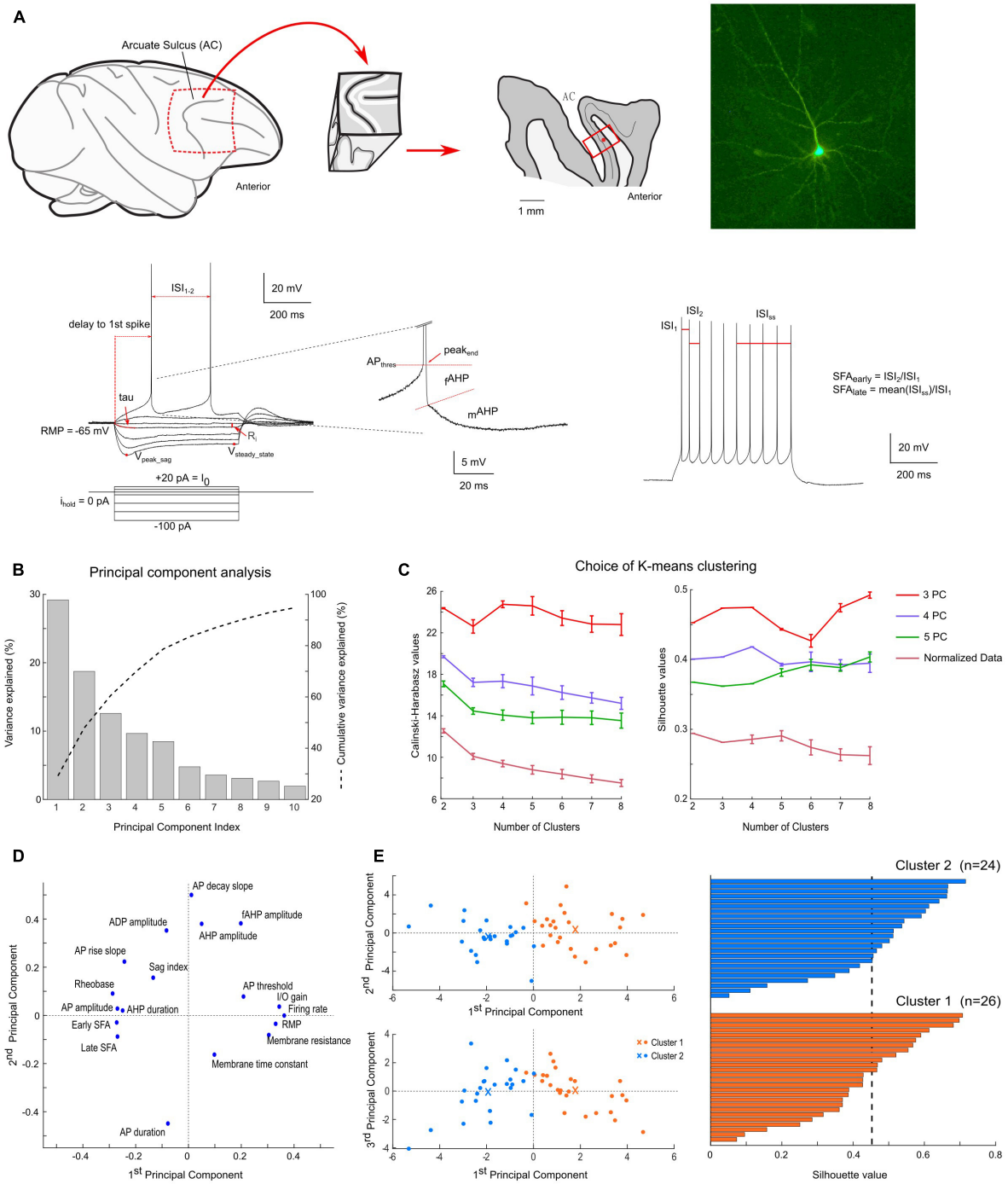

FIGURE 1 | Methodology and results of the clustering analysis. **(A)** Brain slice preparation; from left to right: sagittal view of the frontal cortex of macaque monkey (circle highlights the FEF localization, from which a biopsy is extracted), sagittal section through the FEF biopsy (layer 4 is indicated by a thin black line, the recording location is indicated by a red dot) and example of a recorded pyramidal neuron after fluorescent revelation of biocytin filling; Bottom: electrophysiological response of a pyramidal neuron to current step injections (left: up to rheobase; right: first train of at least 9 spikes; center: close-up on a spike AHP). Parameters used for analysis (in red) are further described in section "Materials and Methods." **(B)** Percentage of variance explained by each principal component of the principal component analysis. *k*-means clustering was performed on up to the first five principal components, which explained more than 80% of the total variance. **(C)** Variation of the Calinski-Harabasz index and average silhouette values as a function of the number of clusters and PCA results. These two indices were used to define the optimal number of clusters in the data. **(D)** Projection of the 18 electrophysiological parameters used for clustering on the first two principal component axes. **(E)** Results of the *k*-means clustering algorithm applied to the first three principal components with 2 clusters ($n = 26$ cells for cluster 1, in orange; and $n = 24$ for cluster 2, in blue). As visible on the projection plane (left), the first principal component contributes the most to the discrimination between the two clusters. The centroids of the clusters are indicated by orange and blue crosses. The silhouette scores (right) indicate a good level of compactness of each cluster.

indices were determined at the minimal depolarizing current step that elicited at least 9 spikes: the early spike frequency adaptation (SFA_{early}) was calculated as the ratio of the second ISI to the first ISI, and the late SFA (SFA_{late}) as the ratio of the mean of ISIs during the last half of the pulse (ISI_{ss}) to the first ISI. The firing rate at + 40 pA was calculated using the number of action potentials elicited during the 500 ms pulse (mean firing frequency), with a current injection of + 40 pA from rheobase. The f-I curve was constructed by plotting the mean firing frequency as a function of injected current. The I-O gain corresponds to the slope of the linear fit of the f-I curve, considering the first six current steps after rheobase. If there existed at least one ISI smaller than half of the mean ISI, visible at the start of the spike train, then the cell was included in the proportion of neurons displaying an initial spike doublet. For each current step, the spike frequency adaptation was measured using two different methods: as the ratio of the mean of the three last instantaneous frequencies divided by the first instantaneous frequency (similar to SFA_{late} above), or as the mean of the differences between consecutive ISIs (to minimize the influence of an initial spike doublet, if present). The spontaneous activity characteristics (mean and CV) were calculated on 30-s recording in the absence of holding current.

Responses to L2/3 Cortical Stimulation

Voltage-clamp and current-clamp responses to single L2/3 cortical stimulation were first linearly interpolated to reach a time resolution of 0.01 ms. Manually defined cursors were used to detect the onset and peak of the neuron response. When the response showed multiple peaks, the largest one defined the peak of the response. The latency of the response was defined as the interval between the timing of the largest stimulation artifact and the response onset. Extracted parameters consisted of the 20–80% rise slope (obtained from a linear fit, not defined if the response showed multiple peaks in the rising phase), half-duration, area and decay time constant (obtained from a single exponential fit, only fits of trial responses with an r-square > 0.6 were kept). Similar analyses were performed on normalized responses (normalized by the peak amplitude).

EPSPs or spiking events were recorded in response to increased stimulation currents (at least 10 trials for each stimulation current). Whenever possible, we considered the average amplitude of EPSPs eliciting a 0.7–0.9 probability of spiking and the average amplitude of EPSPs at the last stimulation current in which no spiking event was elicited to define an EPSP-spike coupling ratio, equal to the ratio of these latter two average EPSP amplitudes.

Amplitudes of paired-pulse responses in voltage-clamp were measured similarly. To characterize the short-term plasticity properties in the response train, we calculated for each interval (25, 50, 100, or 250 ms), the ratio of the amplitudes of the 2nd–10th EPSC of the train relative to the amplitude of the first EPSC.

Clustering Analysis

Clustering algorithms were used on standardized data (centered and reduced) from 50 neurons using 18 electrophysiological parameters. The parameters were: (1) RMP, (2) Membrane resistance, (3) Membrane time constant, (4) Rheobase, (5) Sag index, (6) AP threshold, (7) AP amplitude, (8) AP duration at half-width, (9) AP rise slope, (10) AP decay slope, (11) AHP amplitude, (12) fast AHP amplitude, (13) AHP amplitude, (14) AHP duration, (15) Firing rate at + 40 pA from rheobase, (16) SFA_{early}, (17) SFA_{late}, (18) I/O gain.

The average absolute correlation coefficient between these 19 parameters was 0.30, with only five pairs of parameters for which the absolute value of the correlation coefficient was superior to 0.7. To reduce the dimensionality of the dataset and remove correlations between these parameters, a principal component analysis (PCA) was performed. The first three principal components, explaining 60.5% of the variance, were retained for classification by cluster analysis (**Figure 1B**). The projection of the 18 electrophysiological parameters onto the first two principal components is indicated in **Figure 1D**.

Clustering analysis was implemented using the statistics toolbox of Matlab using the k-means algorithm, based on the squared Euclidean distance. We computed the Calinski-Harabasz index, which corresponds to the normalized ratio between the overall between-cluster variance and the overall within-cluster variance. Silhouette scores, a measure of similarity of a sample to points of its cluster when compared to points in other clusters, were measured using the squared Euclidean distance. High average silhouette scores, close to 1, indicate that the clusters are compact and distinct from each other.

Additional tests of the robustness of the clustering results were performed, by varying the number of principal components used or by directly applying the clustering algorithms on the normalized dataset. A comparison of the number of mismatches, average silhouette values and Calinski-Harabasz index is presented in **Tables 1**, **2**. Overall, the clustering results were highly consistent, with only one mismatch. Furthermore, the number of clusters was deduced from the Calinski-Harabasz index and silhouette scores (**Figure 1C**): in most cases, the optimal number of clusters was 2. Yet, a total of 4 clusters was also found to be an optimal solution when computing these indices on the first three principal components dataset.

We also verified that the quality of the recordings did not affect the clustering results, by estimating the series resistance (R_{series}) in 47 out of the 50 cells (**Supplementary Figure 1**). This parameter did not segregate with cluster identity (21 MΩ *vs.* 16.5

TABLE 1 | Comparison between different clustering algorithms.

Mismatch Counts (2 clusters)	K-3PC	K-4PC	K-5PC	K-Norm
K-3PC	0			
K-4PC	1	0		
K-5PC	1	0	0	
K-Norm	1	0	0	0
Mismatch Counts (4 clusters)	**K-3PC**	**K-4PC**	**K-5PC**	**K-Norm**
K-3PC	0			
K-4PC	15	0		
K-5PC	2	15	0	
K-Norm	3	16	1	0

TABLE 2 | Comparison of clustering quality.

2 clusters	Average silhouette	Scrambled silhouette(± SD)	Calinski-Harabasz index	Scrambled Calinski-Harabasz index (± SD)
K-3PC	0.45 ($p = 0.13$)	0.39 ± 0.05	24.4 ± 0.05 ($p = 0$)	16.2 ± 1.5
K-4PC	0.40 ($p = 0.06$)	0.33 ± 0.05	19.7 ± 0.1 ($p = 0$)	12.0 ± 1.2
K-5PC	0.37 ($p = 0.06$)	0.29 ± 0.05	17.1 ± 0.3 ($p = 0$)	9.7 ± 0.9
K-Norm	0.29 ($p = 0.03$)	0.15 ± 0.05	12.5 ± 0.2 ($p = 0$)	4.3 ± 0.4
4 clusters	**Average silhouette**	**Scrambled silhouette(± SD)**	**Calinski-Harabasz index**	**Scrambled Calinski-Harabasz index (± SD)**
K-3PC	0.47 ($p = 0.27$)	0.44 ± 0.04	24.7 ± 0.3 ($p = 0.02$)	19.6 ± 2.5
K-4PC	0.42 ($p = 0.01$)	0.36 ± 0.03	17.3 ± 0.6 ($p = 0$)	12.6 ± 1.1
K-5PC	0.37 ($p = 0.03$)	0.31 ± 0.03	14.1 ± 0.5 ($p = 0$)	9.7 ± 0.8
K-Norm	0.29 ($p = 0$)	0.13 ± 0.02	9.4 ± 0.3 ($p = 0$)	3.6 ± 0.3

MΩ, $p = 0.055$), even though there was a tendency for cluster 1 neurons to present higher series resistance (**Supplementary Figure 1A**). If this could partially explain the difference observed in spike amplitude ($p = 0.0064$), one can notice the absence of correlation between the series resistance and the input resistance, and a negative correlation between the series resistance and the rheobase ($p = 0.0116$), thus supporting the conclusions that the differences in rheobase between the two clusters are rather due to differences of input resistance rather than to differences in the quality of the recordings (**Supplementary Figure 1B**). In addition, the R_{series}/R_i ratio was below 15% for 75% of selected neurons.

Statistics

Statistical analysis was performed using Matlab 2019 (The Mathworks) or the R-based Jamovi software (The jamovi project, 2021). In all cases "n" refers to a single cell experiment from a single slice.

When comparing electrophysiological features between the two groups, reported *p*-values were calculated using a non-parametric Mann-Whitney test. Chi-square tests were used to compare the proportions of resonant neurons, or spontaneously active neurons between clusters. A 2-way repeated measures ANOVA was used to compare the I-V curves (injected current X cluster identity). A linear mixed model (LMM) was used to compare the f-I curves (fit by REML, random effect of the neuron identity and fixed effects of injected current X cluster identity tested using omnibus *F*-test with Satterthwaite method for the degrees of freedom). A generalized linear mixed model was used to compare the proportion of bursting cells (logistic model, the random effect of the neuron identity and fixed effects of injected current + cluster identity tested using omnibus chi-square tests; the interaction between factors could not be tested, as the corresponding model did not converge). LMMs were used to compare the adaptation ratio measures (fit by REML, random effect of the neuron identity and fixed effects of the number of spikes in the train × cluster identity tested using omnibus *F*-test with Satterthwaite method for the degrees of freedom). A 3-way repeated measures ANOVA was used to analyze the responses to trains of cortical stimulation (pulse number × stimulation interval × cluster identity), and 2-way repeated measures ANOVAs were further performed to analyze separately the initial and final paired pulse ratio in response to trains of stimulation (stimulation interval × cluster identity).

Histology

Biocytin (Sigma) 5 mg/ml was dissolved in the pipette solution and cells were filled during at least 20 min of recording. Subsequently, slices were fixed overnight in 2% paraformaldehyde at 4°C. Biocytin-filled cells were visualized using streptavidin-alexa488 (Invitrogen, Carlsbad, CA, United States), incubated for 2 h at room temperature. Slices were mounted on glass slides for examination under an epifluorescence microscope (DMRB, Leica).

RESULTS

Electrophysiological Classification of FEF Deep-Layer Pyramidal Neurons Using Cluster Analysis

Pyramidal neurons of the FEF deep layer ($n = 50$) were recorded by whole-cell patch-clamp at 34°C in parasagittal brain slices from tissue block containing the portions of areas 9 and 46 non-homotopic from adult macaque monkeys ($n = 8$ animals). In a subset of experiments ($n = 5$), the pyramidal nature and deep-layer localization of recorded neurons were confirmed by biocytin staining injected through the recording pipette (**Figure 1A**).

To characterize the electrophysiological properties of FEF pyramidal cells, we first applied successive hyperpolarizing and depolarizing current steps. Analysis of their responses revealed heterogeneity in both passive and active membrane properties among pyramidal neurons (**Figures 1–3**). We performed a principal component analysis, using 18 different electrophysiological parameters (see section "Materials and Methods"), for which the average correlation coefficient was 0.3. We then applied a k-means algorithm on the first three principal components, which accounted for 60.5% of the variance (**Figure 1B**). The optimal number of clusters was defined using two indices: the average silhouette score and the Calinski-Harabasz index, quantifying the compactness of each cluster using, respectively, a distance metric and the variance within and between clusters (**Figure 1C**). Two clusters of size $n = 26$

TABLE 3 | Electrophysiological properties.

Mean ± SEM	Cluster 1 ($n = 26$)	Cluster 2 ($n = 24$)	p-value (Mann-Whitney)
Resting membrane potential (mV)	−62.5 ±	−67.6 ± 0.7	***$p < 0.001$
Membrane resistance (MΩ)	432 ± 48	148 ± 14	***$p < 0.0001$
Membrane time constant (ms)	32 ± 4	24 ± 2	$p = 0.2600$
Sag Index (%)	20 ± 2	22 ± 2	$p = 0.4203$
Rebound Index (%)	35 ± 5	40 ± 6	$p = 0.4547$
Rheobase (pA)	14 ± 3	69 ± 11	***$p < 0.0001$
Delay to first spike (ms)	114 ± 15	131 ± 12	$p = 0.1180$
AP threshold (mV)	−41.4 ± 0.9	−45.9 ± 1.1	**$p = 0.0039$
AP amplitude (mV)	70.6 ± 2.6	81.4 ± 1.8	**$p = 0.0011$
AP duration at half-width (ms)	0.96 ± 0.04	1.10 ± 0.05	$p = 0.0533$
AP rise time (ms)	0.79 ± 0.02	0.82 ± 0.02	$p = 0.1151$
AP rise slope (mV.ms^{-1})	90.5 ± 3.8	100.3 ± 3.2	**$p = 0.0090$
AP decay time (ms)	1.27 ± 0.09	1.68 ± 0.14	*$p = 0.0237$
AP decay slope (mV.ms^{-1})	62.4 ± 4.7	54.4 ± 3.5	$p = 0.3173$
AP rise/decay slope ratio	1.61 ± 0.10	1.99 ± 0.12	*$p = 0.0275$
AHP amplitude (mV)	14.5 ± 0.8	12.5 ± 0.8	$p = 0.1323$
fAHP amplitude (mV)	12.3 ± 0.9	6.6 ± 0.7	***$p < 0.0001$
ADP amplitude (mV)	0.9 ± 0.2	0.99 ± 0.3	$p = 0.5574$
mAHP amplitude (mV)	2.9 ± 0.4	6.8 ± 0.8	***$p < 0.0001$
AHP duration (ms)	25 ± 3	85 ± 18	**$p = 0.0033$
ISI 1–2 (ms)	134 ± 17	150 ± 21	$p = 0.7122$
Firing rate at + 40 pA from rheobase (Hz)	24 ± 2	10 ± 1	***$p < 0.0001$
Early spike frequency adaptation	1.3 ± 0.1	2.3 ± 0.2	***$p < 0.0001$
Late spike frequency adaptation	1.9 ± 0.2	4.1 ± 0.6	***$p < 0.0001$
I/O gain (Hz.pA^{-1})	0.41 ± 0.03	0.18 ± 0.02	***$p < 0.0001$
Spontaneous frequency (Hz)	5.3 ± 1.7	0.6 ± 0.6	**$p = 0.0083$

*All data: mean ± SEM. *$p < 0.05$; **$p < 0.01$; ***$p < 0.001$.*

and $n = 24$ emerge with strongly significant differences in both their passive and active membrane properties (**Table 3** and **Figures 1**–**3**). Indeed, we first found significant differences between the two clusters in 12 out of the 18 electrophysiological parameters used for PCA (**Table 3**). Furthermore, we used this classification to evaluate whether additional electrophysiological properties—not included in the PCA—could further distinguish these two cell types.

Heterogeneity in Electrophysiological Properties

Differences in Passive Membrane Properties

Cluster 1 neurons had a significantly more depolarized RMP and higher input resistance (Ri) than cluster 2 cells (−57 ± 2 vs. −66 ± 1 mV, $p < 0.0001$ and 432 ± 48 vs. 148 ± 14 MΩ, $p < 0.0001$, respectively), and consequently a lower rheobase (3 ± 8 vs. 68 ± 12 pA, $p < 0.0001$) (**Figure 2A**). These results are well summarized in the average I-V curve profiles (**Figure 2B**), which show a larger slope for cluster 1 [2-way repeated measures ANOVA; main effect of injected current $F(10, 480) = 268.5$, $p < 0.0001$; main effect of cluster identity $F(1, 48) = 2.55$, $p = 0.1169$; interaction between injected current and cluster identity $F(10, 480) = 41.7$, $p < 0.0001$]. Moreover, cluster 1 but not cluster 2 cells displayed an inward rectification (rectification index: 2.2 ± 0.2 vs. 1.3 ± 0.1, $p < 0.0001$). These results suggest that cluster 1 neurons would be more excitable than cluster 2 cells.

Subthreshold Resonance Predominates in One Cluster

In a subset of cells ($n = 35$), the impedance amplitude profile was assessed using a chirp protocol (subthreshold current injection of a sinewave of continuously increasing frequency) between 0.1 and 50 Hz during 30 s (**Figures 2C,D**). The membrane impedance, determined by the cell morphology and voltage-gated ion channels, helps characterizing the gain but also the timing for synaptic integration at a given frequency. We took advantage of this additional protocol (not included in the PCA) to check whether the segregation also stands for impedance characteristics. In non-resonant cells (**Figure 2C**, example from cluster 1) the voltage response to the chirp stimulus decreases continuously with the stimulus frequency, whereas resonant cells (**Figure 2C**, example from cluster 2) display a preferred (resonant) frequency indicated by a maximal peak-to-peak voltage response (here ∼2 Hz). Consistently, the average profile of the impedance magnitude normalized by the impedance at 0.5 Hz presents a clear bump for cluster 2 neurons while a monotonic decrease is visible for cluster 1 neurons (**Figure 2D**). In both groups, the average phase shift increases monotonically with the oscillation frequency until reaching a plateau at 10 Hz (**Figure 2D**), but cluster 2 neurons showed a slower increase in the phase lag relative to the current, with even slightly positive phase values at the lowest frequencies, which indicate that inductive properties of ionic channels responsible for the resonance dominate over the passive low-pass filtering (**Figures 2D,E**). The degree of resonance, assessed by the Q-factor, and equal to 1 in absence of resonance, was significantly different between the two clusters ($p = 0.0203$, **Figure 2F**). Notably, 65% of pyramidal neurons of cluster 2 ($n = 11$ out of 17 cells tested) displayed a resonance (Q-factor > 1.1) at 2.13 ± 0.26 Hz ($n = 11$), while only 17% from cluster 1 (3 out 18) showed a subthreshold resonance, at a similar resonant frequency of 2.4 ± 0.5 Hz (**Figure 2G**; Chi-square test = 8.41; $p = 0.0037$). These results strengthen the validity of the clustering classification.

Action Potential Waveforms and Spike Train Properties

Cluster 1 neurons present a significantly more depolarized spike threshold (−41.4 ± 0.9 vs. −45.9 ± 1.1 mV, $p = 0.0039$), which may partially counteract the differences in passive membrane properties. Spike waveforms also differed significantly (**Figure 3A**), with cluster 1 cells showing a smaller spike amplitude (70.6 ± 2.6 vs. 81.4 ± 1.8 mV, $p = 0.0011$), a slower AP rise slope (90.5 ± 3.8 vs. 100.3 ± 3.2 mV.ms^{-1}, $p = 0.0090$) and a smaller decay time (1.27 ± 0.09 vs. 1.68 ± 0.14 ms, $p = 0.0237$). The AP was generally followed by a sequence of afterpotentials,

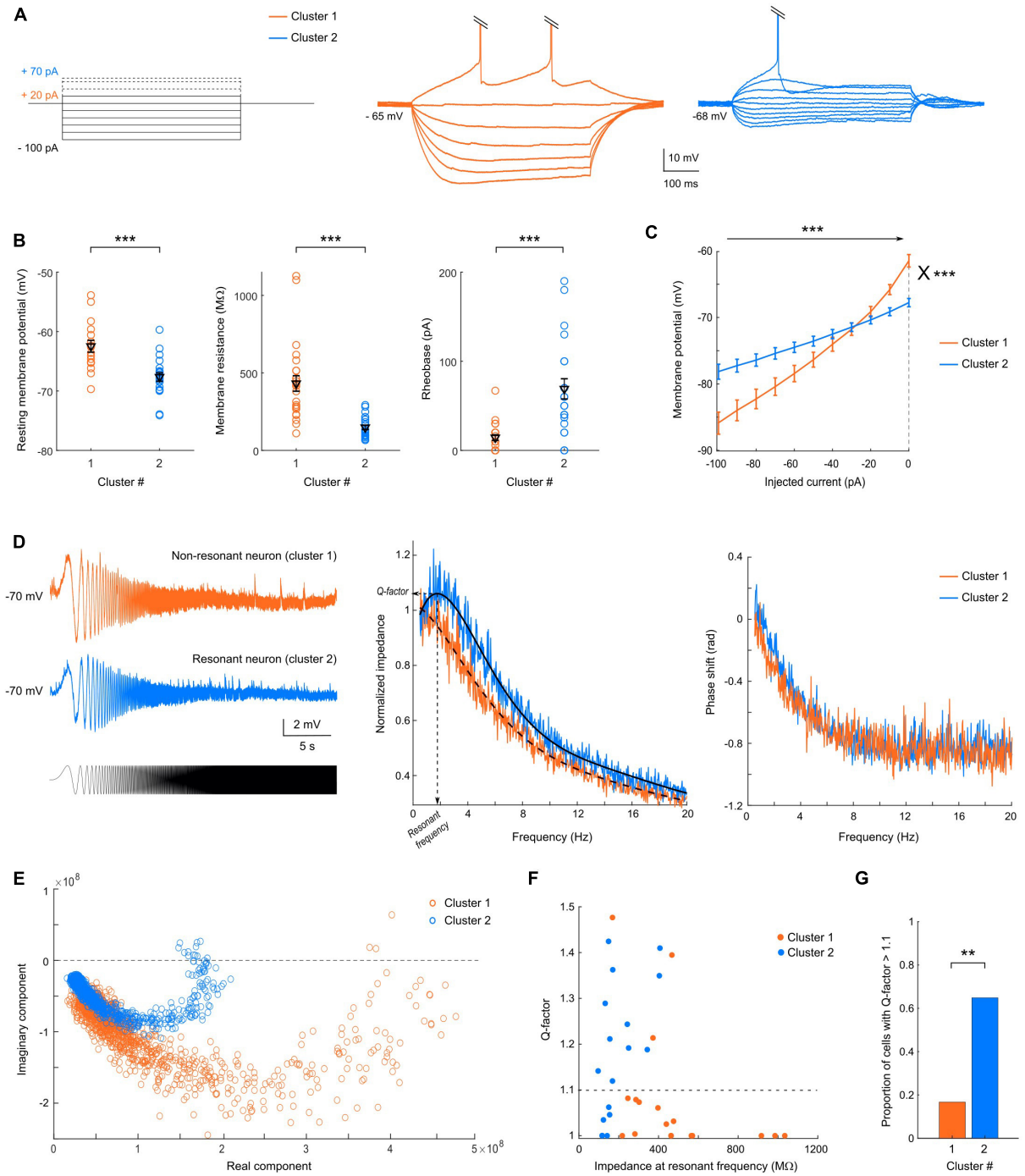

FIGURE 2 | The two clusters exhibit different passive membrane properties. **(A)** Representative responses of cluster 1 (orange, center) or cluster 2 (blue, right) neuron to current step injections (left), from –100 pA to rheobase. **(B)** Scatter plots of the passive membrane properties showing significant differences between the two clusters, with mean and SEM indicated in black. Cluster 1 neurons, indicated in orange, have a more depolarized resting membrane potential ($p < 0.001$), a higher membrane resistance ($p < 0.0001$) and a lower rheobase ($p < 0.0001$) than cluster 2 neurons, shown in blue. **(C)** Average IV-curves show an inward rectification for cluster 1, but a linear relationship between the injected current and membrane potential for cluster 2, and highlight the differences in membrane resistance and resting membrane potential. **(D)** (left) Example of voltage responses to a sinusoidal chirp current injection (bottom) for a representative non-resonant neuron belonging to cluster 1 and a resonant neuron from cluster 2. (Center) Average resonant impedance profiles for the two clusters (black: smoothing average); the resonant frequency and Q-factor are indicated for cluster 2. (right) Phase shift of the voltage waves relative to the injected current as a function of frequency. **(E)** Impedance vectors in the complex plane. The distance to the origin corresponds to the impedance magnitude and the angle with the real axis corresponds to the phase shift. Frequency increases in the clockwise direction. **(F)** Distribution of Q-factors as a function of the impedance amplitude at the resonant frequency and of the clustering classification. **(G)** Proportion of resonant cells (Q factors > 1.1), in cluster 1 and 2 (Chi-square test = 8.41; $p = 0.0037$). All data: mean ± SEM. *$p < 0.05$; **$p < 0.01$; ***$p < 0.001$.

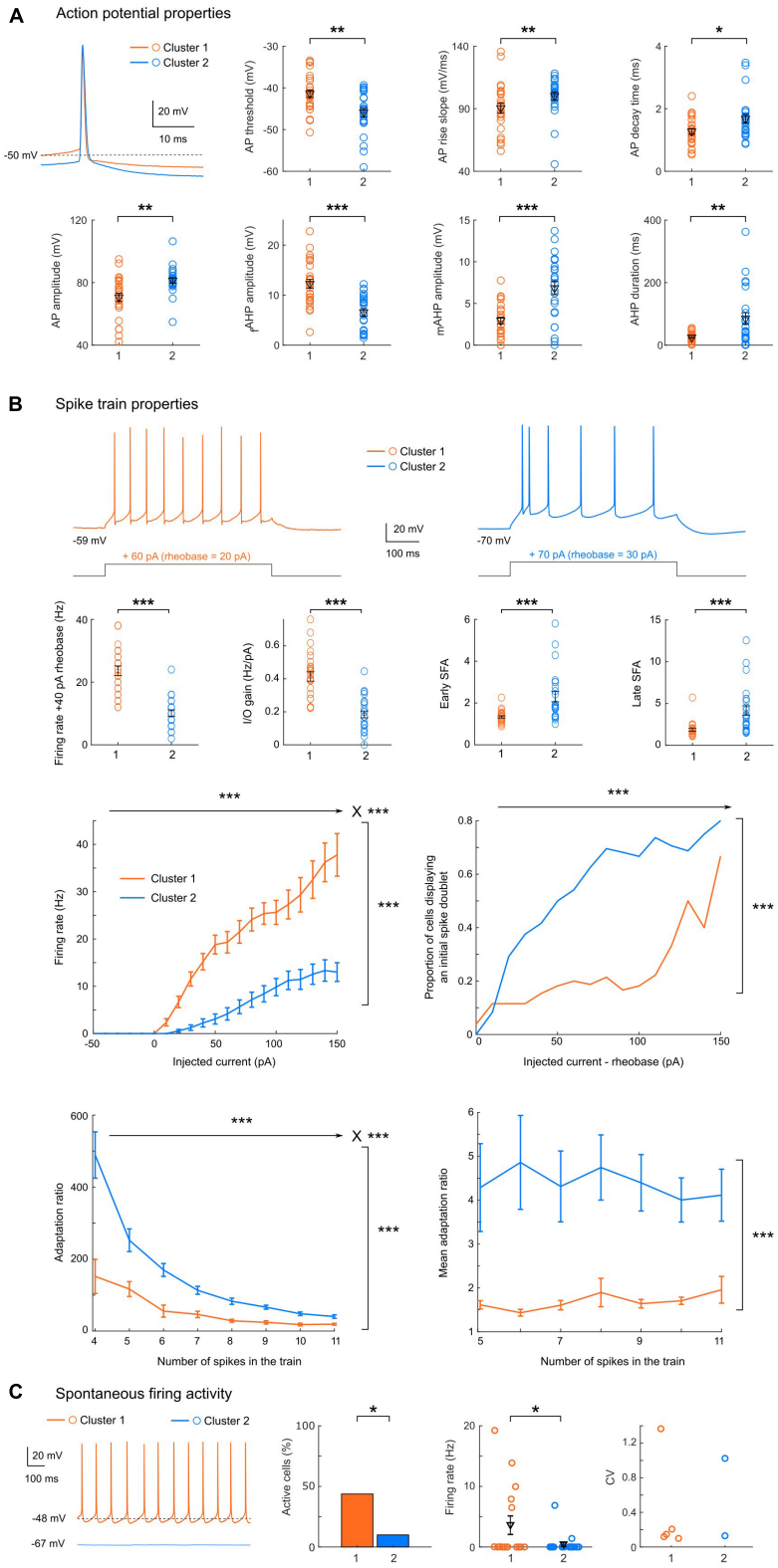

FIGURE 3 | Cluster 1 neurons have a higher excitability with less bursting and firing adaptation. **(A)** Representative action potentials for clusters 1 or 2, and scatter plots of the action potential properties showing significant differences between the two clusters, with mean and SEM indicated in black. Cluster 1 neurons have a more depolarized action potential threshold ($p = 0.0039$), a smaller AP amplitude ($p = 0.0011$), a slower rise slope ($p = 0.0090$) but a shorter decay time

(Continued)

FIGURE 3 | (Continued)
($p = 0.0237$) than cluster 2 neurons. The AHP also presented different characteristics, with a larger fast component but a smaller mAHP in cluster 1 cells ($p < 0.0001$ for both), associated to an overall shorter duration ($p = 0.0033$). **(B)** Spike train properties showing significant differences between the two clusters. Top: Representative spike trains for cluster 1 or 2, in response to a current step injection of + 40 pA above the rheobase, and scatter plots with mean and SEM indicated in black. Cluster 1 neurons display an elevated excitability (with a higher firing rate at + 40 pA from rheobase and a larger I/O gain, $p < 0.0001$ for both). In addition, the spike frequency adaptation for early and late ISIs are significantly smaller in cluster 1 neurons ($p < 0.0001$ for both). Middle: spike train mean firing rate (left, 2-way repeated measures ANOVA: $p < 0.0001$ for main effects of injected current, cluster identity and their interaction) and proportion of cells displaying an initial spike doublet (right, GLMM: $p < 0.0001$ for fixed effect of injected current and cluster identity) as a function of the injected current. Bottom: adaptation ratio measures as a function of the number of spikes in the train (left, LMM: $p < 0.0001$ for fixed effects of number of spikes, cluster identity and their interaction; right, LMM: $p = 0.001$ for fixed effect of cluster identity). **(C)** When spontaneous firing activity was monitored for 30 s (representative examples of a 1 s-epoch from each cluster are shown), the proportion of spontaneously active cells (left) was significantly higher in cluster 1 ($p = 0.0201$), and the average firing rate (center) was significantly higher than in cluster 2 ($p = 0.0202$). Both clusters displayed both regular and irregular firing cells (CV, right). All data: mean ± SEM. $^{*}p < 0.05$; $^{**}p < 0.01$; $^{***}p < 0.001$.

which are important feedback mechanisms controlling the AP duration and the refractory period: a fast AHP, followed by a depolarizing afterpotential (detected in 26/50 cells) and then a medium AHP. The fast AHP component was twice as large in cluster 1 relative to cluster 2 (12.3 ± 0.9 vs. 6.6 ± 0.7 mV, $p < 0.0001$), at the expense of the mAHP (2.9 ± 0.4 vs. 6.8 ± 0.8 mV, $p < 0.0001$). This led to an overall AHP of similar amplitude (14.5 ± 0.8 vs. 12.5 ± 0.8 ms, $p = 0.1323$), but with a significantly shorter duration in cluster 1 (25 ± 3 vs. 85 ± 18 ms, $p = 0.0011$). Importantly, we detected no significant difference in the AP duration between the two groups (0.96 ± 0.04 vs. 1.10 ± 0.05 ms, $p = 0.0533$).

In addition, the properties of spike trains evoked by suprathreshold current injections again highlighted strong differences in excitability between the two clusters (**Figure 3B**): the firing rate at + 40 pA from rheobase was higher in cluster 1 (24 ± 2 vs. 10 ± 1 Hz, $p < 0.0001$). Similarly, the I/O gain, defined as the slope between the average firing frequency and the injected current, was higher in cluster 1 (0.41 ± 0.03 vs. 0.18 ± 0.02 Hz.pA^{-1}, $p < 0.0001$). In addition, the early and late spike frequency adaptation indices, characterizing the time-dependent decrease in spike discharge rate under repetitive firing, were about twice smaller in cluster 1 neurons (respectively, 1.3 ± 0.1 vs. 2.3 ± 0.2 and 1.9 ± 0.2 vs. 4.1 ± 0.6, $p < 0.0001$ for both indices). Overall, these results indicate that cluster 2 pyramidal cells are less excitable and display stronger spike frequency adaptation compared to cluster 1 neurons. These conclusions are also supported by the distinct average profiles of the f-I curves (**Figure 3B**), displaying a higher overall activity of cluster 1 [Linear Mixed Model fixed effect of cluster identity $F(1, 48.3) = 62.7$, $p < 0.0001$] and a stronger gain [fixed effect of interaction between cluster identity and injected current $F(15, 603.6) = 24.9$, $p < 0.0001$]. The stronger adaptation observed in cluster 2 was associated with a higher proportion of cells displaying an initial burst, i.e., a spike doublet (GLMM, fixed effects of cluster identity and injected current $p < 0.0001$). To investigate the interplay between these differences in spike frequency adaptation and excitability, we measured the adaptation ratio (using two different metrics: either using the late SFA index, or the average of the differences between consecutive ISIs in order to minimize the influence of the initial spike doublet) for increasing steps intensity and compared the two clusters at intensities eliciting the same number of spikes. Both measures confirmed a markedly stronger adaptation in cluster 2 [LMM, fixed effect of cluster identity for adaptation ratio $F(1, 50.6) = 20.19$, $p < 0.0001$; fixed effect for cluster identity for mean adaptation ratio $F(1, 48.9) = 12.336$, $p = 0.001$]. In both clusters, the adaptation ratio decreased as the number of spikes in the train increased [LMM, fixed effect of number of spikes in the train: $F(7, 208) = 35.98$, $p < 0.0001$], but the decrease was stronger in cluster 2 [LMM, fixed effect of interaction $F(7, 208) = 9.23$, $p < 0.0001$]. Conversely, in both clusters the mean adaptation ratio did not depend on the number of spikes in the train [LMM, fixed effect of number of spikes $F(6, 169.8) = 0.243$, $p = 0.9615$; fixed effect of interaction: $F(6, 169.8) = 0.255$, $p = 0.9566$]. These results confirm that the difference in spike frequency adaptation between the two clusters is not simply due to their difference in excitability, which would induce a different number of spikes in the train, but probably depends on the distinct activation of specific potassium channels and/or differences in inactivation of sodium channels.

In a subset of neurons ($n = 36$), the spontaneous activity was monitored for 30 s (**Figure 3C**). The proportion of spontaneously active cells and the mean firing rate were significantly different in the 2 clusters ($p = 0.0201$, chi-square test and $p = 0.0202$, rank-sum test), with cluster 2 cells being mainly silent (2 active neurons out of 20 tested) while about half of cluster 1 cells (7 out of 16 tested) displayed spontaneous activity. Two of these cells had sporadic activity (1 spike in 30 s), while the others displayed a tonic firing (average 11.5 ± 2.3 Hz, $n = 5$, range 6.5–19.2 Hz), with a highly regular pattern (CV range: 0.099–0.21) except for one stuttering cell (CV = 1.37). Among the two active cells of cluster 2, one displayed a low firing irregular pattern (1.4 Hz, CV = 1.02) and the other a sustained regular firing pattern (6.9 Hz, CV = 0.13).

Different Integration Rules of L2/3 FEF Inputs

We next investigated whether these two groups of cells differentially integrated cortical inputs. For this purpose, we applied electrical stimulation using an electrode placed in layer 2/3 of the FEF slice and analyzed responses in deep-layer pyramidal cells (**Figure 4A**) in voltage-clamp or current-clamp.

First, the mean and SD latency of all the responses were short (on average: 3.3 ± 0.3 ms, maximum 7.8 ms, and 0.4 ± 0.05 ms, maximum 1.2 ms, $n = 34$), suggesting a monosynaptic connection. We next verified that the responses were glutamatergic, by bath application of AMPA and NMDA

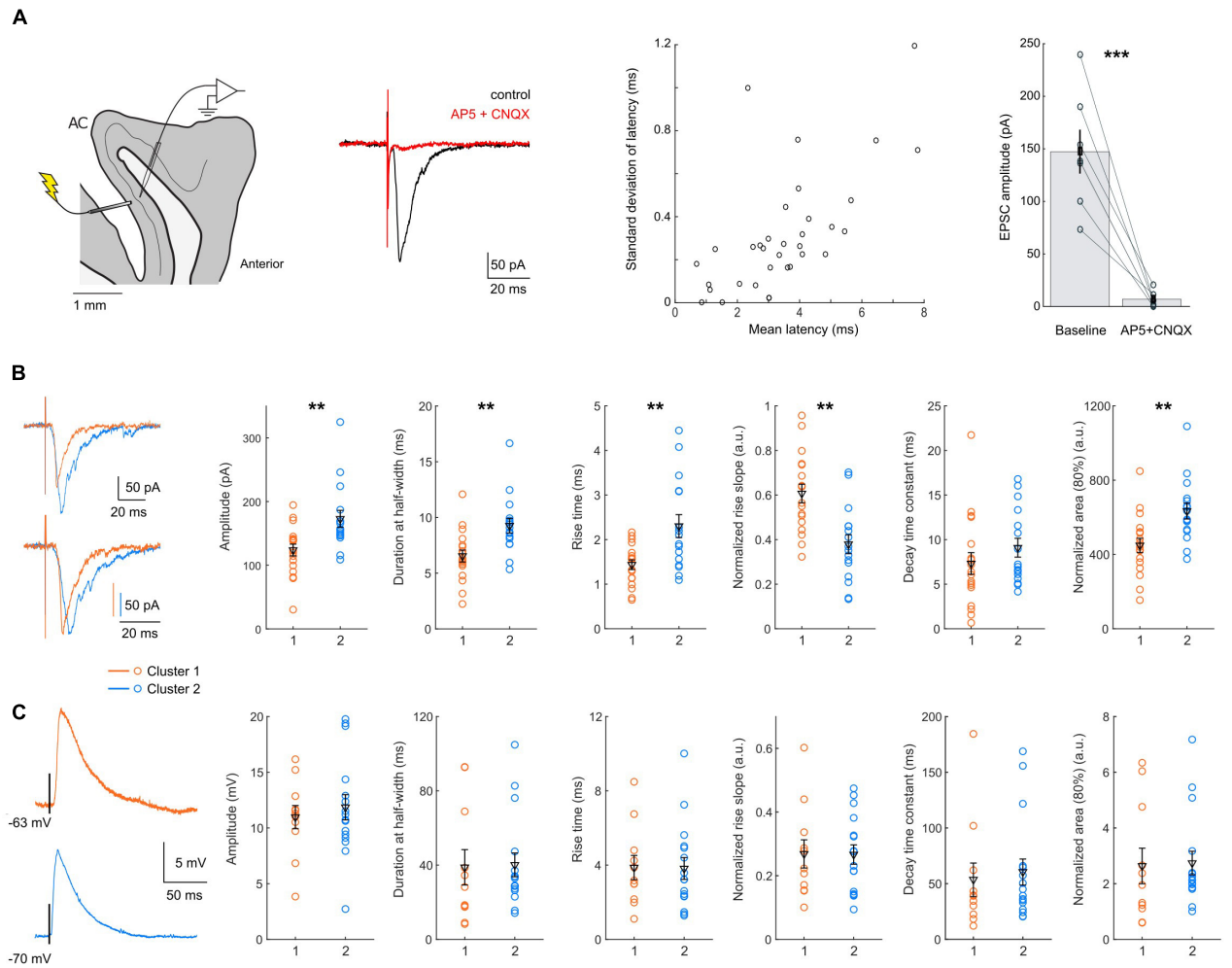

FIGURE 4 | Subthreshold responses to FEF L2/3 stimulation. **(A)** Left: diagram of the experiment configuration, and example EPSCs evoked by layer 2/3 stimulation, under control conditions (black) or in the presence of glutamate blockers (red). Center: scatter plot of the latency and SD of the latency of the responses in each cell tested ($n = 34$). Right: bath application of glutamate transmission blockers suppressed the response to layer 2/3 stimulation. **(B)** Left: example of single EPSCs recorded in cluster 1 (orange) and cluster 2 (blue) neurons, with (bottom) or without (top) amplitude normalization; Right: scatter plots of EPSC properties, with mean and SEM indicated in black. Cluster 1 neurons had EPSCs of smaller amplitude ($p = 0.0023$) and area ($p = 0.0025$), with faster kinetics: a shorter duration ($p = 0.0018$), shorter rise time ($p = 0.0083$) and faster normalized rise slope ($p = 0.0011$). **(C)** Left: example of single EPSPs recorded in cluster 1 (orange) and cluster 2 (blue) neurons. Right: scatter plots of EPSP properties, with mean and SEM indicated in black. No significant difference was detected between the EPSP properties of the two clusters. All data: mean ± SEM. $^*p < 0.05$; $^{**}p < 0.01$; $^{***}p < 0.001$.

glutamate receptor blockers (CNQX 10 μM and AP-5 50 μM). We observed a reduction of the EPSC amplitude by 94.6 ± 2.5% ($p < 0.001$, $n = 7$), effectively suppressing the response and confirming its glutamatergic nature (**Figure 4A**).

We then compared EPSC characteristics between the two clusters (**Figure 4B** and **Table 4**, $n = 18$ for cluster 1; $n = 16$ for cluster 2). The latency and the latency SD of the response were similar in both clusters (average latency: 3.2 ± 0.5 ms vs. 3.24 ± 0.3 ms, $p = 0.6169$; latency SD: 0.44 ± 0.07 ms vs. 0.37 ± 0.05 ms, $p = 0.9313$). Smaller EPSCs were recorded in cluster 1 neurons (amplitude: 124 ± 9 pA, $n = 18$ vs. 173 ± 13 pA, $n = 16$, $p = 0.0023$; area: 818 ± 7 vs. 1,109 ± 72, $p = 0.0136$), with a shorter duration at half-width (6.5 ± 0.5 ms vs. 9.3 ± 0.7 ms, $p = 0.0018$). The rise time of non-normalized EPSCs was shorter for cluster 1 neurons (1.4 ± 0.1 ms vs. 2.3 ± 0.3 ms, $p = 0.0083$), confirmed by a higher rising slope on responses normalized by their amplitude (0.61 ± 0.04 ms^{-1} vs. 0.38 ± 0.04 ms^{-1}, $p = 0.0011$). No difference was detected in EPSCs decay time constant, obtained by fitting the decay phase of the normalized EPSCs with a single exponential (7.3 ± 1.2 ms vs. 9.1 ± 1.1 ms, $p = 0.1841$). The area of normalized EPSCs also differed, with a smaller area for cluster 1 cells (449 ± 38 vs. 634 ± 43, $p = 0.0025$).

We also compared EPSP waveforms recorded in current-clamp mode (**Figure 4C** and **Table 4**, $n = 11$ for cluster 1; $n = 16$ for cluster 2). Similar to EPSCs, EPSP latencies and latency SD did not differ between cluster 1 and 2 (mean latency: 2.4 ± 0.4 ms vs. 3.0 ± 0.3 ms, $p = 0.1323$; latency SD: 0.58 ± 0.07 ms vs. 0.46 ± 0.07, $p = 0.0887$). Interestingly, the differences between

TABLE 4 | EPSCs and EPSPs properties in response to L2/3 FEF stimulation.

EPSC	Cluster 1 ($n = 18$)	Cluster 2 ($n = 16$)	p-value (Mann-Whitney)
Latency (ms)	3.2 ± 0.5	3.4 ± 0.3	$p = 0.6169$
Latency SD (ms)	0.44 ± 0.07	0.37 ± 0.05	$p = 0.9313$
Amplitude (pA)	123.8 ± 9.2	172.8 ± 13.3	$^{**}p = 0.0023$
Area 80% (10^4 pA.ms)	5.4 ± 0.7	10.2 ± 0.8	$^{***}p < 0.001$
Normalized area 80%	449 ± 38	634 ± 43	$^{**}p = 0.0025$
Duration at half-width (ms)	6.5 ± 0.5	9.3 ± 0.7	$^{**}p = 0.0018$
Rise time 20–80% (ms)	1.4 ± 0.11	2.30 ± 0.26	$^{**}p = 0.0083$
Normalized rise slope	0.61 ± 0.04	0.38 ± 0.04	$^{**}p = 0.0011$
Normalized decay time constant (ms)	7.3 ± 1.2	9.1 ± 1.1	$p = 0.1841$
EPSP	**Cluster 1 ($n = 11$)**	**Cluster 2 ($n = 16$)**	
Latency (ms)	2.4 ± 0.4	3.0 ± 0.3	$p = 0.1323$
Latency SD (ms)	0.58 ± 0.07	0.46 ± 0.07	$p = 0.0887$
Amplitude (mV)	11.0 ± 1.0	11.9 ± 1.1	$p = 0.9803$
Area 80% (10^4 mV.ms)	2.8 ± 0.7	3.1 ± 0.5	$p = 0.5373$
Normalized area 80%	2,600 ± 600	2,700 ± 400	$p = 0.5704$
Duration at half-width (ms)	38.8 ± 9.5	40.1 ± 6.4	$p = 0.6044$
Rise time 20–80% (ms)	3.9 ± 0.7	3.8 ± 0.6	$p = 0.9803$
Normalized rise slope	0.27 ± 0.04	0.27 ± 0.03	$p = 0.9410$
Normalized decay time constant (ms)	53 ± 15	60 ± 12	$p = 0.5053$

*All data: mean ± SEM. *p < 0.05; **p < 0.01; ***p < 0.001.*

cluster 1 and cluster 2 EPSCs were not detected in EPSPs. Indeed, neither the amplitude (11.0 ± 1.0 mV vs. 11.9 ± 1.1 mV, $p = 0.9803$) nor the kinetics of the EPSPs (duration at half-width: 38.8 ± 9.5 ms vs. 40.1 ± 6.4 ms, $p = 0.6044$; rise time: 3.8 ± 0.7 ms vs. 3.8 ± 0.6 ms, $p = 0.9803$) was significantly different.

We next analyzed the responses to increasing cortical stimulation strength (**Figure 5A**). We observed two main types of integration patterns: about half of the cells progressively increased their probability of firing a spike ($n = 9$ out of 19), while the other half switched abruptly from sub- to suprathreshold responses ($n = 10$ out of 19). Due to the difficulty of normalizing EPSPs responses by the stimulation current because recordings were done with different electrophysiological set-ups and stimulation electrodes, and on different slices, we chose to select the amplitude of the responses to the last stimulation current never evoking an action potential and the amplitude of the responses evoking an action potential with a 0.7–0.9 probability. Interestingly, the ratio between the amplitudes of these two responses was significantly different between the two clusters ($p = 0.0464$, **Figure 5A**), with a larger gain for cluster 2 pyramidal cells (1.2 ± 0.09, $n = 9$ vs. 1.8 ± 0.3, $n = 8$), while the EPSPs amplitudes were not significantly different (13.7 ± 2.3 mV, $n = 9$ vs. 8.8 ± 1.3 mV, $n = 9$, $p = 0.1672$; and 15.7 ± 2.3 mV, $n = 8$ vs. 13.6 ± 1.4 mV, $n = 8$, $p = 0.6730$). For suprathreshold events, the mean latency and jitter (latency SD) of evoked spikes were similar in the two clusters (cluster 1: $n = 10$; cluster 2: $n = 14$) (**Figure 5B**) ($p = 0.2658$ and $p = 0.7696$, respectively). Interestingly, in both clusters a correlation was observed between the spike latency in suprathreshold responses and the kinetics of subthreshold EPSPs (**Figure 5B**). In particular, the strong correlation with the EPSP duration at half-width segregated the neurons into two distinct groups: one with short EPSPs and fast-spiking response, and the other with slower EPSPs and evoked spikes, both groups being represented in the two clusters.

Finally, we investigated short-term plasticity properties of the responses to L2/3 FEF inputs in the 2 clusters (cluster 1: $n = 8$ neurons, cluster 2: $n = 14$ neurons) by applying trains of 10 pulses at various interpulse intervals (25, 50, 100, and 250 ms) (**Figure 6A**). Normalizing the EPSC amplitude at each successive pulse to the EPSC amplitude at the first one (**Figure 6B**) revealed that both clusters adapted their response to the train, with short-term facilitation or depression indicated by a ratio superior or inferior to 1, respectively. A 3-way ANOVA [Cluster identity X Stimulation interval X pulse number, repeated measures in each neuron; main effect of pulse number: $F(8, 160) = 40.168$, $p < 0.0001$], revealed an effect depending on the interval [main effect of interval: $F(3, 60) = 12.070$, $p < 0.0001$] and an effect depending on the clusters [main effect of cluster identity: $F(1, 20) = 8.98$, $p = 0.0071$]. Indeed, after little change in the initial paired-pulse ratio (**Figure 6C**), cluster 2 neurons displayed a strong depression instated along the train, more pronounced for shorter stimulation intervals (**Figure 6D**). Conversely, cluster 1 neurons displayed a facilitation in the initial paired-pulse ratio, independently of the stimulation interval (**Figure 6C**), which degraded along the train and turned into a depression for short stimulation intervals (**Figure 6D**). These results suggest that the two clusters identified using cell-intrinsic properties differentially integrate afferent signals from superficial cortical layers.

Validity of the Classification and Analysis for Four Clusters

The segregation obtained for two clusters was robust since only one mismatch could be detected when modifying the number of principal components used in the k-means algorithm or when performing the clustering directly on the whole normalized dataset (**Table 2**). In addition, when performing k-means classification on scrambled data, on average 7 electrophysiological parameters reached significance level (with only 2 below 0.001 and 2 between 0.01 and 0.05), while in our dataset we obtained high significance levels for 12 parameters out of 18 (with 8 below 0.001 and 4 between 0.01 and 0.05).

Since four clusters also appeared to be an optimal classification for some indicators, we also calculated the mean electrophysiological properties related to each cluster (**Table 5**), as well as the indices quantifying the robustness of the clustering method for four clusters (**Tables 1–5**). Importantly, we retrieve within the four clusters two subgroups with high resistance, more depolarized RMP and high excitability (cluster 1 and 3, $n = 10$ and 8 neurons, respectively) and two subgroups with low resistance, more hyperpolarized RMP and low excitability (cluster 2 and 4, $n = 22$ and 10 neurons, respectively). Furthermore, one can note that cluster 1 has a faster decay of its action potential (37.2 ± 3.3), twice faster than

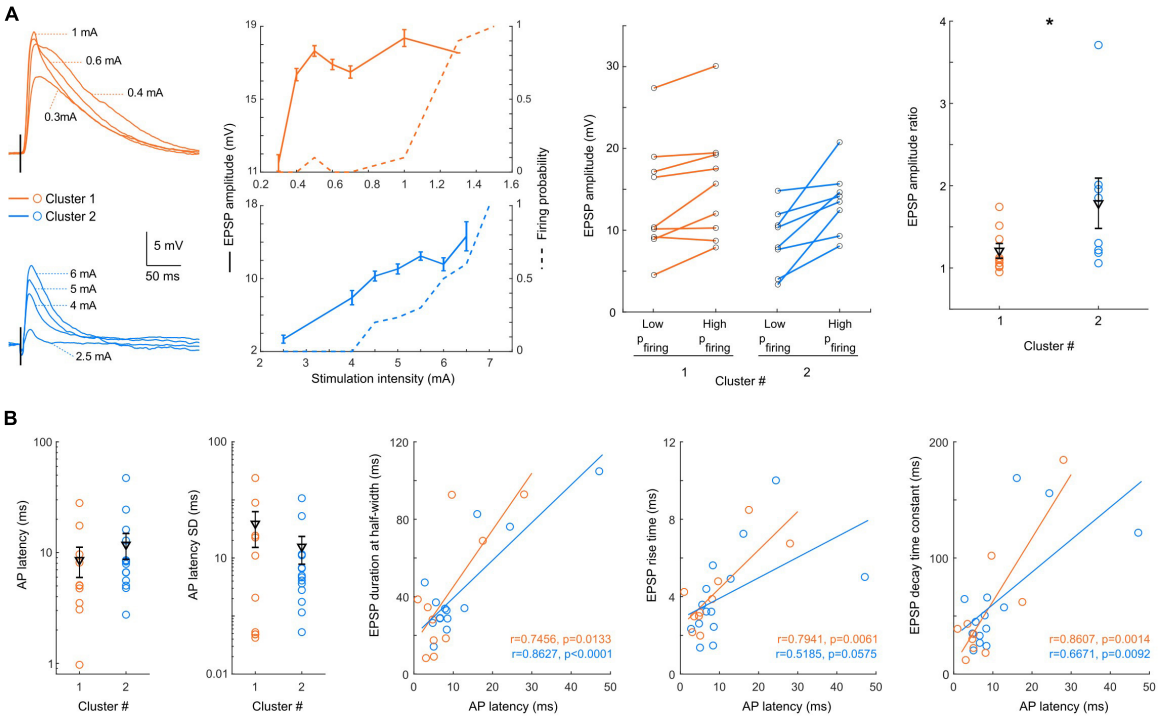

FIGURE 5 | Input/output and suprathreshold response to L2/3 stimulation. **(A)** Left: example of EPSPs (smoothed average of 10 stimulations excluding spiking events) recorded in a cluster 1 (orange) and a cluster 2 (blue) neuron in response to increasing stimulation intensity of layer 2/3, with the EPSP amplitude and probability of firing plotted as a function of stimulation amplitude for these example neurons. Center: for each neuron, the amplitude of EPSPs is plotted for a low stimulation intensity (last intensity before spiking is evoked) and a high stimulation intensity (spiking probability of 0.7–0.9). Right: the ratio between EPSP amplitudes at high/low stimulation amplitudes is significantly lower in cluster 1 neurons ($p = 0.04$). **(B)** From left to right: mean latency, and SD of the latency of spikes evoked by suprathreshold stimulation. Significant correlations are observed between the spike latency in suprathreshold responses and the kinetics (duration at half-width, rise time and decay time constant) of subthreshold EPSPs. All data: mean ± SEM. *$p < 0.05$.

cluster 3 (81.1 ± 8.5), while cluster 3 is characterized by the large amplitude of its fast AHP component (16.8 ± 1.2), about twice as large compared to the other clusters. Cluster 2 distinguishes itself by a very hyperpolarized AP threshold (−46.6 ± 1.1 mV). Cluster 4 adapts its firing pattern far more strongly compared with all three clusters, as visible in both early and late SFA indices (3.3 ± 0.4 and 6.4 ± 1, respectively), has a particularly low I/O gain and firing rate at + 40 pA from rheobase, and hence presents the lowest excitability of all subgroups. In addition, subthreshold resonance is strictly observed in the two less excitable subgroups (cluster 2: with 11 out of 17 cells and cluster 4: 3 out of 8 cells, Chi-square = 11.01; $p = 0.0117$).

DISCUSSION

Our recordings of intracellular electrophysiological properties of deep-layer pyramidal cells in FEF of macaque monkeys allowed us to distinguish two major types of regular-spiking neurons. On the one hand, the first group consists of cells with an increased excitability (depolarized RMP, higher Ri, lower rheobase, higher spontaneous and current-evoked activity, stronger I/O gain, and weaker spike frequency adaptation), with fewer resonant cells. These cells responded to superficial layer stimulation with smaller but faster EPSCs, and an initial facilitation for paired stimulations. On the other hand, the second cell type is characterized by a decreased excitability (hyperpolarized RMP and lower Ri, higher rheobase, lower spontaneous and current-evoked activity, weaker I/O gain and stronger adaptation), associated with a higher proportion of cells displaying a preferred resonant frequency at ∼2 Hz, and a higher proportion of cells initiating their spike trains with a doublet. They responded to superficial layer stimulation with stronger but slower EPSCs, and a progressive depression in response to repeated stimulations, in particular for short-time intervals.

In our sample of cells, FEF contained nearly half of each population ($n = 26$ for cluster 1 and $n = 24$ for cluster 2 out of 50 cells). Interestingly, these two types of regular-spiking pyramidal cells with notably different degree of spike adaptation have been reported in the L5 of monkey or rat prefrontal cortex or in cat association cortices (Nuñez et al., 1993; Dégenètais et al., 2002; Chang and Luebke, 2007). In addition, in these studies, a small proportion of intrinsic burst firing cells, characterized by an initial all-or-none burst at depolarizing steps, and also fast-adapting pyramidal neurons, which present a depolarizing plateau following an initial train of spikes were observed. However, we did not record any intrinsic burst firing cells or regular-spiking fast-adapting cells in FEF deep layers,

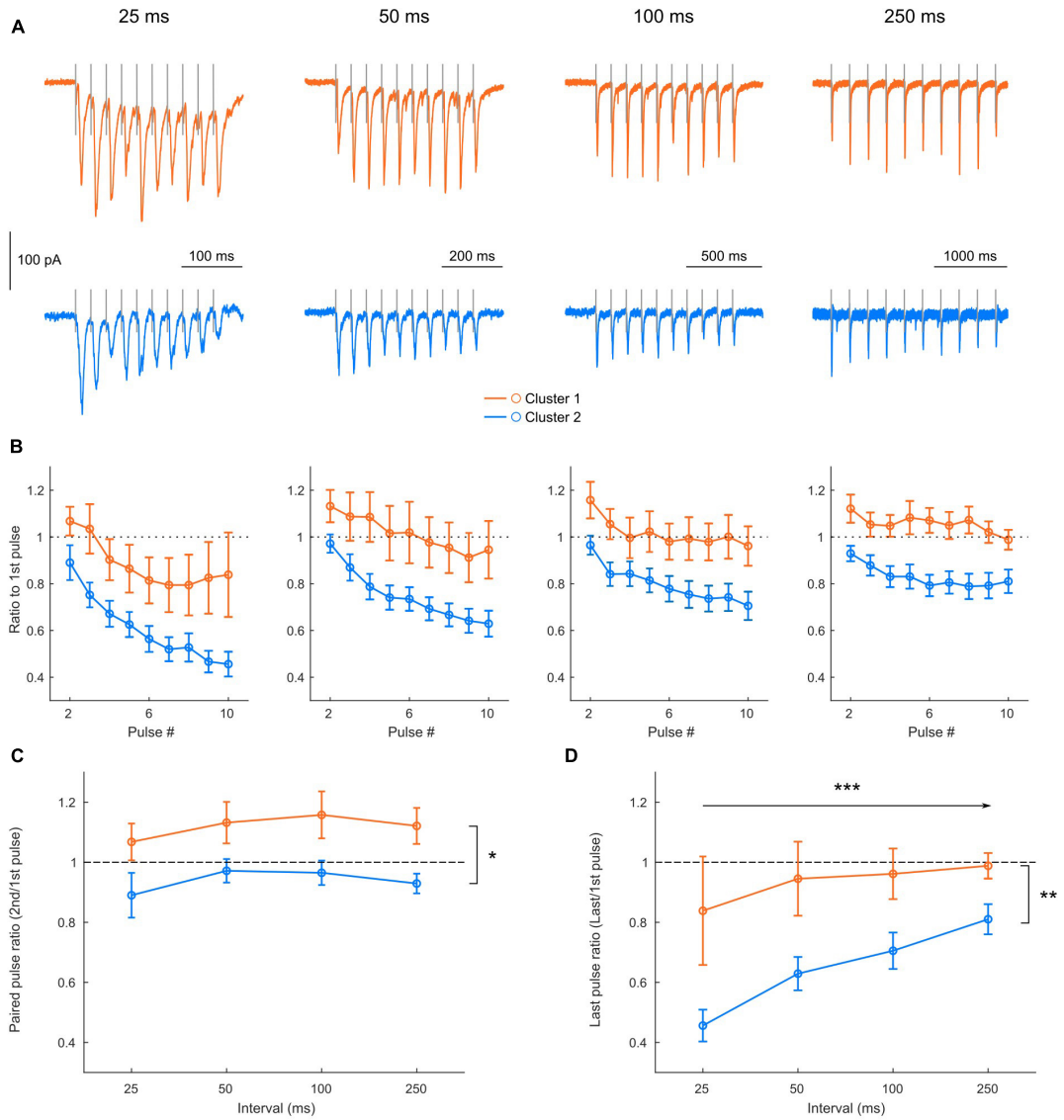

FIGURE 6 | Clusters display different short-term plasticity properties. **(A)** Example of EPSCs recorded in a cluster 1 (orange) and a cluster 2 (blue) neuron in response to trains of 10 stimulations, for increasing stimulation intervals. **(B)** Average amplitude of the EPSCs along the train (starting from the second EPSC) in cluster 1 (orange) and cluster 2 (blue) neurons, normalized in each neuron by the amplitude of the first EPSC of the train, for each stimulation interval (see 3-way ANOVA results in Results). **(C,D)** Influence of the stimulation interval on the first paired pulse ratio [**C:** EPSC2/EPSC1; 2-way repeated measures ANOVA, effect of cluster $F(1, 20) = 7.23$, $p = 0.0141$; Effect of interval $F(3, 60) = 1.7040$, $p = 0.1758$; Interaction $F(3, 60) = 0.0713$, $p = 0.9751$] and on the last pulse ratio [**D:** EPSC10/EPSC1; 2-way repeated measures ANOVA, effect of cluster $F(1, 20) = 8.20$, $p = 0.0096$; Effect of interval $F(3, 60) = 10.01$, $p < 0.0001$; Interaction $F(3, 60) = 1.66$, $p = 0.1849$]. All data: mean ± SEM. $^{*}p < 0.05$; $^{**}p < 0.01$; $^{***}p < 0.001$.

which may be due to our limited sample or specificities of the FEF. In addition to pyramidal neurons, we recorded and briefly characterized three fast-spiking interneurons (**Supplementary Figure 2** and **Supplementary Table 2**).

How can we relate these two main types of intracellular properties to the functional diversity of FEF neurons? Currently, correlations between the functional properties of FEF neurons and their anatomical and electrophysiological signatures have not been elucidated. Pioneer studies have reported three main types—visual, movement and visuo-movement neurons (Bruce and Goldberg, 1985; Schall, 1991). Yet these classes are not strictly distinct and rather form a continuum, with diverse patterns of spike rate modulation visible during a typical memory-guided saccade task (Lowe and Schall, 2018). In this perspective, the specificities of each cortical layer need to be considered, especially now that recent evidence starts to unveil the computations performed by supra-granular and deep layers, respectively (Heinzle et al., 2007; Bastos et al., 2018; Yu et al., 2019). In particular, FEF L5 pyramidal cells have been distinguished by their projecting targets, with cortico-pontine

TABLE 5 | Electrophysiological properties of four clusters.

Mean ± SEM	Cluster 1 ($n = 10$)	Cluster 2 ($n = 22$)	Cluster 3 ($n = 8$)	Cluster 4 ($n = 10$)	p-value (Kruskal-Wallis)
Resting membrane potential (mV)	−62.6 ± 1.4	−65.8 ± 0.7	−60.9 ± 3.0	−68.7 ± 1.2	$\chi^2 = 10.36$; $p = 0.0157$*1–4
Membrane resistance (MΩ)	488 ± 86	224 ± 27	467 ± 100	125 ± 14	$\chi^2 = 22.9$; $p < 0.0001$***1–4; **3–4; *1–2
Membrane time constant (ms)	39 ± 7	24 ± 3	28 ± 4	26 ± 2	$\chi^2 = 3.4$; $p = 0.34$
Rheobase (pA)	10 ± 4	42 ± 9	14 ± 5	89 ± 19	$\chi^2 = 18.1$; $p = 0.0004$***1–4; **3–4
Sag Index (%)	16 ± 4	21 ± 2	22 ± 4	25 ± 3	$\chi^2 = 4.7$; $p = 0.20$
Rebound Index (%)	−0.9 ± 8	34 ± 13	9 ± 9	88 ± 20	$\chi^2 = 18.5$; $p = 0.0003$***1–4; **3–4
AP threshold (mV)	−40.6 ± 1.2	−46.6 ± 1.1	−38.2 ± 1.4	−43.9 ± 1.0	$\chi^2 = 19.5$; $p = 0.0002$***2–3; *1–2; 3–4
AP amplitude (mV)	61.5 ± 4.0	83.7 ± 1.6	66.6 ± 3.2	80.0 ± 1.5	$\chi^2 = 29.5$ $p < 0.0001$***1–2; 2–3; *1–4; 3–4
AP duration at half-width (ms)	1.17 ± 0.09	1.02 ± 0.04	0.82 ± 0.06	1.08 ± 0.08	$\chi^2 = 9.3$; $p = 0.0253$*1–3
AP rise slope(mV.ms^{-1})	71.7 ± 4.7	106.0 ± 2.3	86.7 ± 3.9	101.7 ± 4.6	$\chi^2 = 29.3$; $p < 0.0001$***1–2; **1–4; 2–3
AP decay slope (mV.ms^{-1})	37.2 ± 3.3	60.5 ± 3.2	81.1 ± 8.5	57.4 ± 6.3	$\chi^2 = 19.4$; $p = 0.0002$***1–3; **1–2
AHP amplitude (mV)	10.7 ± 1.3	13.6 ± 0.7	17.4 ± 1.4	13.2 ± 1.3	$\chi^2 = 11.5$; $p = 0.0094$**1–3
fAHP amplitude (mV)	7.5 ± 1.0	9.0 ± 0.9	16.8 ± 1.2	7.0 ± 1.3	$\chi^2 = 17.8$; $p = 0.0005$**1–3; 2–3;3–4
ADP amplitude (mV)	0.05 ± 0.05	0.52 ± 0.1	2.2 ± 0.5	1.7 ± 0.6	$\chi^2 = 14.7$; $p = 0.0021$**1–3; *1–4
mAHP amplitude (mV)	3.3 ± 0.7	5.1 ± 0.8	2.2 ± 0.6	7.9 ± 1.1	$\chi^2 = 12.4$; $p = 0.006$**3–4; *1–4
AHP duration (ms)	25.2 ± 4.1	35.4 ± 4.9	21.9 ± 4.2	148 ± 35	$\chi^2 = 11.3$; $p = 0.0104$*1–4; 3–4
Firing rate at + 40 pA from rheobase (Hz)	24 ± 2	15 ± 1	27 ± 3.4	8 ± 1	$\chi^2 = 24.8$; $p < 0.0001$***1–4; 3–4; *1–2; 2–3
Early spike frequency adaptation	1.6 ± 0.1	1.5 ± 0.1	1.2 ± 0.1	3.3 ± 0.4	$\chi^2 = 26.3$; $p < 0.0001$***2–4; 3–4; *1–4
Late spike frequency adaptation	2.6 ± 0.4	2.1 ± 0.2	1.5 ± 0.1	6.4 ± 1	$\chi^2 = 27.6$; $p < 0.0001$***2–4; 3–4; *1–3
I/O gain (Hz.pA^{-1})	0.41 ± 0.04	0.27 ± 0.03	0.48 ± 0.07	0.15 ± 0.03	$\chi^2 = 21.4$; $p < 0.0001$***3–4; **1–4; *2–3
Spontaneous frequency (Hz)	6.8 ± 3.0	1.7 ± 1.0	5.8 ± 3.7	0	$\chi^2 = 7.3$; $p = 0.062$

*All data: mean ± SEM. *$p < 0.05$; **$p < 0.01$; ***$p < 0.001$.*

neurons carrying in half-cases movement-related information (Segraves and Goldberg, 1987; Segraves, 1992), and corticotectal neurons projecting to the superior colliculus carrying cognitive and sensory-related information (Sommer and Wurtz, 2000). It would be far too simplistic to try mapping our two clusters to these highly heterogeneous functional categories. However, we can still draw hypotheses between the characteristics found by our classification and the distinct activity (transient or sustained) and response patterns (with or without a delay) reported within these three main categories.

On the one hand, cluster 1 neurons with their higher excitability profile appear as a preferred candidate over less excitable regular-spiking pyramidal neurons to encode precise and persistent information, similarly to what was concluded with the help of a computational model in the retrosplenial cortex (Brennan et al., 2020). Spike frequency adaptation has also been shown to destabilize persistent firing (Carter and Wang, 2007). Thus, the features of cluster 1 neurons in the FEF may facilitate the production of tonic discharge in the continuous presence of inputs such as during fixation (Izawa and Suzuki, 2014), or ramping sustained activity when an accumulation of evidence on the sensory target position is being processed, as well as in persistent firing linked to attention (Moore and Fallah, 2001; Armstrong et al., 2009) or in the slow return to baseline following the saccade (Hanes et al., 1995; Lowe and Schall, 2018). On the other hand, cluster 2 pyramidal cells would require stronger inputs to produce an output spiking response, because of their higher rheobase and lower input resistance. Yet, their output may then be more reliably transmitted to downstream targets due to the higher propensity of these cells to spike high-frequency doublets. In addition, due to their high spike-frequency adaptation, their responses may remain clipped to the time of the stimulus, which could be either the visual target or the saccade command. They could thus become active at the end of the hypothesized "winner-take-all competition process" that may be at stake during the saccade generation process (Itti and Koch, 2000; Thompson and Bichot, 2005). Thus, cluster 2 neurons could contribute preferentially to movement generation or participate in feedforward target sensory processing, while cluster 1 neurons would rather provide feedback information to supra-granular layers, controlling for example working memory maintenance (Bastos et al., 2018).

In addition to differences in intrinsic properties, significant differences in evoked EPSC kinetics were observed between the two clusters. Yet these differences were no longer visible in current-clamp recordings at the somatic level. This may be explained "passively" by the high resistance of cluster 1 cells, which may counteract the smaller elicited currents evoked under L2/3 stimulation or it could be linked to homeostatic processes, that actively lowered the excitatory drive of those intrinsically more excitable neurons (Debanne et al., 2019). In addition, these results cannot exclude differential integration patterns at the dendritic level, especially given that dendrites and the soma appear more strongly compartmentalized in primates (Beaulieu-Laroche et al., 2018).

Interestingly, we also found a wide range of mean latency and latency SD when a single action potential was evoked by L2/3 stimulation, with overlaps between the two clusters,

that could be correlated to EPSP kinetics. Our results showed that the highest temporal precision of the spiking response relative to the stimulation time was found in cells whose EPSPs have a short halfwidth, rise time or decay time constant, in agreement with model predictions (Rodriguez-Molina et al., 2007). Importantly, the variability in the spike latency could endow neurons with different functional roles. Indeed, if the nature of L2/3 inputs has not been elucidated, the computational model of Heinzle et al. (2007) provide useful hypotheses, suggesting that L2/3 neurons transform the visual saliency map, carried by layer 4 neurons, into an attentional signal, sending the position of the selected target to L5 neurons, while also possibly generating a motor plan due to feedback connections. In addition, *in vivo* recordings have shown that the peak activity of visual or movement-related neurons varied across categories (Lowe and Schall, 2018). One could hypothesize that neurons presenting short-latency evoked spikes would be preferentially involved in the generation of the pre-saccadic bump of activity, while neurons with longer-latency spikes may be associated with less "clipped" activity relative to the visual input or the saccade production.

In addition, the short-term plasticity observed between L2/3 and deep-layer excitatory connections is dominated by depression for short-time intervals, as observed in other cortical areas across different species. This general property of the cortical microcircuit has been described as a means for gain control, producing equal post-synaptic responses to rapidly or slowly firing afferents, and generating an enhanced sensitivity to fast changes in presynaptic firing rate (Abbott et al., 1997). This phenomenon may be particularly crucial on the one hand for some movement-related FEF neurons that generate a punctual and transient response, either before or immediately after the saccade. Such activity may thus be aided by the stronger depression observed in cluster 2 neurons which also strongly adapt their firing rates. On the other hand, cluster 1 neurons, which present smaller short-term depression, with even an initial facilitation at the start of repeated L2/3 stimulation trains, may transmit action potentials more reliably during bursts of activity. This mechanism could act in synergy with their small firing rate adaptation, to maintain tonic discharge patterns, such as in the case of fixation neurons (Izawa and Suzuki, 2014) or during delays in which attention or memory-related information needs to be maintained (Bruce and Goldberg, 1985; Sommer and Wurtz, 2000). Yet, several questions remain unresolved relative to the synaptic properties of L2/3-L5 fast-spiking interneurons and L5 recurrent excitatory connections, that could also contribute to shaping persistent activity patterns at the network level (Yoon et al., 2020).

In our recordings, 40% of pyramidal neurons displayed subthreshold resonance at about 2 Hz, with a significant majority present in the low-resistance cluster. This proportion is similar to the one found in a recent study on human cortical pyramidal cells (Moradi Chameh et al., 2021). If such subthreshold resonance is usually associated with the expression of Ih currents (Beaulieu-Laroche et al., 2018; Moradi Chameh et al., 2021), we did not find significant correlations between the existence of a large sag voltage and low-frequency resonance when considering all resonant and non-resonant neurons. This may indicate that additional ionic currents such as the persistent Na^+ current may also drive the subthreshold resonance observed here. In the presence of high levels of fluctuations, as observed *in vivo* in cortical circuits, such subthreshold resonance may also turn into or at least favor a firing-rate resonance (Brunel et al., 2003), making cluster 2 neurons likely candidates in participating to theta-coupling with V4 during visual search (Yan and Zhou, 2019) as well as to higher gamma coupling during attentional tasks (Gregoriou et al., 2009). As previously reported, few neurons in layer 5 of FEF project to visual cortex (V4 or inferotemporal area) and very few if any of these neurons have axons that also terminate in the superior colliculus (Pouget et al., 2009). These results have been seen as strong suggestions that deep neurons of FEF that project to visual cortex are to be considered a feedforward or intermediate type of pathways. In the same vein, we consider that these data are consistent with the hypothesis that the signal in extrastriate cortex received from FEF relates to target selection and not saccade planning and could be sent by a majority of cluster 2 neurons, also in agreement with their electrophysiological properties as discussed above. Altogether, these frequency couplings may optimize the postsynaptic impact between FEF and V4 (Gregoriou et al., 2009) or between FEF and anterior cingulate cortices during sensorimotor mapping (Babapoor-Farrokhran et al., 2017).

Notably, our clustering analysis did not highlight a difference in spike width, as reported by some studies using extracellular recordings. Yet, this feature used for classifying movement and visual neurons vs. visuo-movement neurons, which would have the thinnest spikes (Cohen et al., 2009; Ding and Gold, 2012; Thiele et al., 2016), still remain debated, as a more recent study report no significant difference (Lowe and Schall, 2018). In addition, correlations between intracellular recordings and extracellular waveforms should be subjected to a careful interpretation: only about 50% of the variance could be explained by the intracellular features according to a recent study (Xu and Baker, 2018), while external factors such as the distance to the recorded cells and the filtering properties of the extracellular matrix need also to be considered (Nelson et al., 2013).

A future step in the characterization of FEF neuronal subpopulation would be to examine their morphological features and whether they segregate with electrophysiological clusters. First of all, this would allow to rigorously confirm the pyramidal nature of all recorded neurons. Indeed, our spike shape criteria to exclude interneurons cannot discriminate broad spiking interneurons, such as VIP cells—though from proportion alone, combined with visual targeting of pyramidal soma shapes in slices, it is highly unlikely that their number would populate a cluster representing 50% of our sample. Secondly, a morphological quantification would be particularly relevant since two groups of L5 pyramidal cells, retrogradely labeled by horseradish peroxidase injections into the superior colliculus, have previously been distinguished based on the size of their soma (Fries, 1984), a morphological feature that can be related to the input resistance, for which our two clusters strongly differ. In addition, differences in axonal conduction times have been reported (Segraves and Goldberg, 1987; Segraves, 1992)

with fixation and movement neurons having longer and shorter conduction times, respectively. These results could potentially map our electrophysiological distinctions, since on the one hand, cluster 1 cells, which we hypothesize to be in part fixation neurons due to their discharge pattern, have a high input resistance, and could thus have a smaller soma and a narrower axon, with longer conduction times. On the other hand, cluster 2 neurons, that could send target or saccade signaling, would be larger and have shorter conduction times, because of their high input resistance.

If our electrophysiological recordings targeted FEF L5, one cannot exclude that a minority of recorded neurons were situated at the border between L5/L6. More importantly, the origin of our two clusters could emerge from the existence of gradients within L5, determined for instance by soma depth, projection target and/or dendritic complexity. Interestingly, the considerable electrophysiological differences observed within our sample echoes the large variability reported in human neocortical L5 pyramidal cells (Moradi Chameh et al., 2021), that could partially be explained by a gradient in dendritic complexity (with thick or thin-tufted pyramidal cells at the two extremes).

Some precautions should be taken into consideration for comparing our *in vitro* electrophysiological results with *in vivo* recordings. It thus remains to strengthen the existence of such neuronal clusters using *in vivo* intracellular recordings in non-anesthetized primates. Indeed, we examined the neuronal properties *in vitro* in brain slices maintained at 34°C, thus 3°C below physiological temperature, to increase the viability of the brain slices, but this is known to affect AP kinetics or spiking frequency (Thompson et al., 1985). Nevertheless, if we can expect modified absolute values for intrinsic and active membrane properties for *in vivo* conditions, the belonging of FEF deep layer pyramidal cells to at least two clusters should be confirmed since most of membrane properties evolve linearly with decreasing temperatures, at least in the 37–33°C range (Thompson et al., 1985). Also, the dendritic tree damage caused by slice preparation and the choice of ionic concentrations can influence the membrane properties. In particular, lower calcium concentration can modify the propensity for generating high-frequency spike bursts (Brumberg et al., 2000), which were not visible in our recordings. Finally, we used square current steps to standardize experimental conditions and to extract membrane properties and repetitive firing features that are critical and lacking for modeling studies. Nevertheless, such responses are not readily translatable into *in vivo* firing characteristics; the links we draw between the data from each preparation can only be tentative, and would need to be tested using stimulation protocols that better mimic task-related activity (or conclusively investigated using *in vivo* patch-clamp).

To conclude, the ability to distinguish types of neurons in FEF is necessary to understand whether the visual to motor transformation occurs within or across distinct neuron types. We found that intracellular properties of deep-layer pyramidal cells in FEF of macaque monkeys allow classifying two majors cell types. These results are important to better account for the existence of a functional micro-circuit playing a key role in sensorimotor transformation within the FEF.

DATA AVAILABILITY STATEMENT

The original contributions presented in the study are included in the article/**Supplementary Material**, further inquiries can be directed to the corresponding author/s.

ETHICS STATEMENT

The animal study was reviewed and approved by the European Community Council Directives of 1986 (86/609/EEC) and the NIH Guide for the Care and Use of Laboratory Animals and were approved by the French Animal Ethics Committee of INSERM.

AUTHOR CONTRIBUTIONS

PP, LV, MV, and CP: conceptualization, writing, review, and editing. CP, MV, CB-B, VG, VP, YC, AM, SP, SV, HX, and LV: investigation and analysis. PP and LV: supervision. All authors contributed to the article and approved the submitted version.

FUNDING

CP was a Research Fellow of the Ecole Normale Supérieure (Paris, France).

ACKNOWLEDGMENTS

We acknowledge Carine Karachi and Chantal François to give access to the primate biopsies at the end of their protocols and their help during the surgeries; France Maloumian for her help to prepare the figures. We also acknowledge the contributions of Collège de France, Inserm, CNRS that aided the efforts of the authors.

SUPPLEMENTARY MATERIAL

The Supplementary Material for this article can be found online at: https://www.frontiersin.org/articles/10.3389/fnsyn.2021.725880/full#supplementary-material

Supplementary Figure 1 | R_{series} does not segregate with cluster identity. **(A)** R_{series} scatterplots of neurons in each cluster, with mean and SEM indicated in black. For both two (left) or four (right) clusters, the difference between groups is non-significant (left: Mann-Whitney test, $p = 0.0555$; right: Kruskal-Wallis test, $p = 0.101$). **(B)** R_{series} scatterplots with each parameter of the PCA that is significantly different between the two clusters. The correlation coefficient and *p*-value (Pearson's correlation), calculated with all neurons (clusters pooled) is indicated above each graph.

Supplementary Figure 2 | Fast spiking interneurons recorded in FEF Layer 5. Electrophysiological response of a fast spiking interneuron to current step injections (left: from −100 pA, 10 pA-steps up to rheobase; center: +40 pA above rheobase; right: I–V curve).

REFERENCES

Abbott, L. F., Varela, J. A., Sen, K., and Nelson, S. B. (1997). Synaptic depression and cortical gain control. *Science* 275, 220–224. doi: 10.1126/science.275.5297.221

Armstrong, K. M., Chang, M. H., and Moore, T. (2009). Selection and maintenance of spatial information by frontal eye field neurons. *J. Neurosci.* 29, 15621–15629. doi: 10.1523/JNEUROSCI.4465-09.2009

Babapoor-Farrokhran, S., Vinck, M., Womelsdorf, T., and Everling, S. (2017). Theta and beta synchrony coordinate frontal eye fields and anterior cingulate cortex during sensorimotor mapping. *Nat. Commun.* 8 :13967. doi: 10.1038/ncomms13967

Bastos, A. M., Loonis, R., Kornblith, S., Lundqvist, M., and Miller, E. K. (2018). Laminar recordings in frontal cortex suggest distinct layers for maintenance and control of working memory. *Proc. Natl. Acad. Sci. U.S.A.* 115, 1117–1122. doi: 10.1073/pnas.1710323115

Beaulieu-Laroche, L., Toloza, E. H. S., van der Goes, M.-S., Lafourcade, M., Barnagian, D., Williams, Z. M., et al. (2018). Enhanced dendritic compartmentalization in human cortical neurons. *Cell* 175, 643–651.e14. doi: 10.1016/j.cell.2018.08.045

Brennan, E. K. W., Sudhakar, S. K., Jedrasiak-Cape, I., John, T. T., and Ahmed, O. J. (2020). Hyperexcitable Neurons Enable Precise and Persistent Information Encoding in the Superficial Retrosplenial Cortex. *Cell Rep* 30, 1598–1612.e8. doi: 10.1016/j.celrep.2019.12.093

Bruce, C. J., and Goldberg, M. E. (1985). Primate frontal eye fields. I. Single neurons discharging before saccades. *J. Neurophysiol.* 53, 603–635. doi: 10.1152/jn.1985.53.3.603

Brumberg, J. C., Nowak, L. G., and McCormick, D. A. (2000). Ionic mechanisms underlying repetitive high-frequency burst firing in supragranular cortical neurons. *J. Neurosci.* 20, 4829–4843. doi: 10.1523/JNEUROSCI.20-13-04829.2000

Brunel, N., Hakim, V., and Richardson, M. (2003). Firing-rate resonance in a generalized integrate-and-fire neuron with subthreshold resonance. *Phys. Rev. E Stat. Nonlin. Soft. Matter. Phys.* 67:051916. doi: 10.1103/PhysRevE.67.051916

Bullier, J., and Henry, G. H. (1979). Laminar distribution of first-order neurons and afferent terminals in cat striate cortex. *J. Neurophysiol.* 42, 1271–1281. doi: 10.1152/jn.1979.42.5.1271

Carter, E., and Wang, X.-J. (2007). Cannabinoid-mediated disinhibition and working memory: dynamical interplay of multiple feedback mechanisms in a continuous attractor model of prefrontal cortex. *Cereb. Cortex* 17, i16–i26. doi: 10.1093/cercor/bhm103

Cauli, B., Audinat, E., Lambolez, B., Angulo, M. C., Ropert, N., Tsuzuki, K., et al. (1997). Molecular and physiological diversity of cortical nonpyramidal cells. *J. Neurosci.* 17, 3894–3906. doi: 10.1523/JNEUROSCI.17-10-03894.1997

Chang, Y.-M., and Luebke, J. I. (2007). Electrophysiological diversity of layer 5 pyramidal cells in the prefrontal cortex of the rhesus monkey: in vitro slice studies. *J. Neurophysiol.* 98, 2622–2632. doi: 10.1152/jn.00585.2007

Cohen, J. Y., Pouget, P., Heitz, R. P., Woodman, G. F., and Schall, J. D. (2009). Biophysical support for functionally distinct cell types in the frontal eye field. *J. Neurophysiol.* 101, 912–916. doi: 10.1152/jn.90272.2008

Condé, F., Lund, J. S., Jacobowitz, D. M., Baimbridge, K. G., and Lewis, D. A. (1994). Local circuit neurons immunoreactive for calretinin, calbindin D-28k or parvalbumin in monkey prefronatal cortex: distribution and morphology. *J. Comp. Neurol.* 341, 95–116. doi: 10.1002/cne.903410109

Connors, B. W., and Gutnick, M. J. (1990). Intrinsic firing patterns of diverse neocortical neurons. *Trends Neurosci.* 13, 99–104. doi: 10.1016/0166-2236(90)90185-D

Debanne, D., Inglebert, Y., and Russier, M. (2019). Plasticity of intrinsic neuronal excitability. *Curr. Opin. Neurobiol.* 54, 73–82. doi: 10.1016/j.conb.2018.09.001

Dégenètais, E., Thierry, A.-M., Glowinski, J., and Gioanni, Y. (2002). electrophysiological properties of pyramidal neurons in the rat prefrontal cortex: an in vivo intracellular recording study. *Cereb. Cortex* 12, 1–16. doi: 10.1093/cercor/12.1.1

DiCarlo, J. J., and Maunsell, J. H. R. (2005). Using neuronal latency to determine sensory–motor processing pathways in reaction time tasks. *J. Neurophysiol.* 93, 2974–2986. doi: 10.1152/jn.00508.2004

Ding, L., and Gold, J. I. (2012). Neural correlates of perceptual decision making before, during, and after decision commitment in monkey frontal eye field. *Cereb. Cortex* 22, 1052–1067. doi: 10.1093/cercor/bhr178

Dow, B. M. (1974). Functional classes of cells and their laminar distribution in monkey visual cortex. *J. Neurophysiol.* 37, 927–946. doi: 10.1152/jn.1974.37.5.927

Everling, S., and Munoz, D. P. (2000). Neuronal correlates for preparatory set associated with pro-saccades and anti-saccades in the primate frontal eye field. *J. Neurosci.* 20, 387–400. doi: 10.1523/JNEUROSCI.20-01-00387.2000

Fries, W. (1984). Cortical projections to the superior colliculus in the macaque monkey: a retrograde study using horseradish peroxidase. *J. Comp. Neurol.* 230, 55–76. doi: 10.1002/cne.902300106

Goldberg, M. E., and Bushnell, M. C. (1981). Behavioral enhancement of visual responses in monkey cerebral cortex. II. Modulation in frontal eye fields specifically related to saccades. *J. Neurophysiol.* 46, 773–787. doi: 10.1152/jn.1981.46.4.773

González-Burgos, G., Krimer, L. S., Povysheva, N. V., Barrionuevo, G., and Lewis, D. A. (2005). Functional properties of fast spiking interneurons and their synaptic connections with pyramidal cells in primate dorsolateral prefrontal cortex. *J. Neurophysiol.* 93, 942–953. doi: 10.1152/jn.00787.2004

Gregoriou, G. G., Gotts, S. J., Zhou, H., and Desimone, R. (2009). High-frequency, long-range coupling between prefrontal and visual cortex during attention. *Science* 324, 1207–1210. doi: 10.1126/science.1171402

Hanes, D. P., Patterson, W. F., and Schall, J. D. (1998). Role of frontal eye fields in countermanding saccades: visual, movement, and fixation activity. *J. Neurophysiol.* 79, 817–834. doi: 10.1152/jn.1998.79.2.817

Hanes, D. P., and Schall, J. D. (1996). Neural control of voluntary movement initiation. *Science* 274, 427–430. doi: 10.1126/science.274.5286.427

Hanes, D. P., Thompson, K. G., and Schall, J. D. (1995). Relationship of presaccadic activity in frontal eye field and supplementary eye field to saccade initiation in macaque: poisson spike train analysis. *Exp. Brain Res.* 103, 85–96. doi: 10.1007/BF00241967

Heinzle, J., Hepp, K., and Martin, K. A. C. (2007). A microcircuit model of the frontal eye fields. *J. Neurosci.* 27, 9341–9353. doi: 10.1523/JNEUROSCI.0974-07.2007

Hutcheon, B., and Yarom, Y. (2000). Resonance, oscillation and the intrinsic frequency preferences of neurons. *Trends Neurosci.* 23, 216–222. doi: 10.1016/S0166-2236(00)01547-2

Itti, L., and Koch, C. (2000). A saliency-based search mechanism for overt and covert shifts of visual attention. *Vis. Res.* 40, 1489–1506. doi: 10.1016/S0042-6989(99)00163-7

Izawa, Y., and Suzuki, H. (2014). Activity of fixation neurons in the monkey frontal eye field during smooth pursuit eye movements. *J. Neurophysiol.* 112, 249–262. doi: 10.1152/jn.00816.2013

Kodaka, Y., Mikami, A., and Kubota, K. (1997). Neuronal activity in the frontal eye field of the monkey is modulated while attention is focused on to a stimulus in the peripheral visual field, irrespective of eye movement. *Neurosci. Res.* 28, 291–298. doi: 10.1016/S0168-0102(97)00055-2

Krimer, L. S., Zaitsev, A. V., Czanner, G., Kröner, S., González-Burgos, G., Povysheva, N. V., et al. (2005). Cluster analysis–based physiological classification and morphological properties of inhibitory neurons in layers 2–3 of monkey dorsolateral prefrontal cortex. *J. Neurophysiol.* 94, 3009–3022. doi: 10.1152/jn.00156.2005

Lemon, R. N., Baker, S. N., and Kraskov, A. (2021). Classification of cortical neurons by spike shape and the identification of pyramidal neurons. *Cereb. Cortex* bhab147. doi: 10.1093/cercor/bhab147

Letinic, K., Zoncu, R., and Rakic, P. (2002). Origin of GABAergic neurons in the human neocortex. *Nature* 417, 645–649. doi: 10.1038/nature00779

Lowe, K. A., and Schall, J. D. (2018). Functional categories of visuomotor neurons in macaque frontal eye field. *eNeuro* 5, 1–21. doi: 10.1523/ENEURO.0131-18.2018

Martina, M., Schultz, J. H., Ehmke, H., Monyer, H., and Jonas, P. (1998). Functional and molecular differences between voltage-gated K^+ channels of fast-spiking interneurons and pyramidal neurons of rat hippocampus. *J. Neurosci.* 18, 8111–8125. doi: 10.1523/JNEUROSCI.18-20-08111.1998

McPeek, R. M. (2006). Incomplete suppression of distractor-related activity in the frontal eye field results in curved saccades. *J. Neurophysiol.* 96, 2699–2711. doi: 10.1152/jn.00564.2006

Moore, T., and Fallah, M. (2001). Control of eye movements and spatial attention. *Proc. Natl. Acad. Sci. U.S.A.* 98, 1273–1276.

Moradi Chameh, H., Rich, S., Wang, L., Chen, F.-D., Zhang, L., Carlen, P. L., et al. (2021). Diversity amongst human cortical pyramidal neurons revealed via their sag currents and frequency preferences. *Nat. Commun.* 12:2497. doi: 10.1038/s41467-021-22741-9

Mueller, A., Krock, R. M., Shepard, S., and Moore, T. (2020). Dopamine receptor expression among local and visual cortex-projecting frontal eye field neurons. *Cereb. Cortex* 30, 148–164. doi: 10.1093/cercor/bhz078

Nelson, M. J., Bosch, C., Venance, L., and Pouget, P. (2013). Microscale inhomogeneity of brain tissue distorts electrical signal propagation. *J. Neurosci.* 33, 2821–2827. doi: 10.1523/JNEUROSCI.3502-12.2013

Nuñez, A., Amzica, F., and Steriade, M. (1993). Electrophysiology of cat association cortical cells *in vivo*: intrinsic properties and synaptic responses. *J. Neurophysiol.* 70, 418–430. doi: 10.1152/jn.1993.70.1.418

Paillé, V., Fino, E., Du, K., Morera Herreras, T., Perez, S., Hellgren Kotaleski, J., et al. (2013). GABAergic circuits control spike-timing-dependent plasticity. *J. Neurosci.* 33, 9353–9363. doi: 10.1523/JNEUROSCI.5796-12.2013

Pouget, P., Stepniewska, I., Crowder, E. A., Leslie, M. W., Emeric, E. E., Nelson, M. J., et al. (2009). Visual and motor connectivity and the distribution of calcium-binding proteins in macaque frontal eye field: implications for saccade target selection. *Front. Neuroanat.* 3:2. doi: 10.3389/neuro.05.002.2009

Puil, E., Gimbarzvesky, B., and Spigelman, I. (1988). Primary involvement of K+ conductance in membrane resonance of trigeminal root ganglion neuron. *J. Neurophysiol.* 59, 77–89. doi: 10.1152/jn.1988.59.1.77

Ray, S., Pouget, P., and Schall, J. D. (2009). Functional distinction between visuomovement and movement neurons in macaque frontal eye field during saccade countermanding. *J. Neurophysiol.* 102, 3091–3100. doi: 10.1152/jn.00270.2009

Rodriguez-Molina, V. M., Aertsen, A., and Heck, D. H. (2007). Spike timing and reliability in cortical pyramidal neurons: effects of EPSC kinetics, input synchronization and background noise on spike timing. *PLoS One* 2:e319. doi: 10.1371/journal.pone.0000319

Sato, T., Murthy, A., Thompson, K. G., and Schall, J. D. (2001). Search efficiency but not response interference affects visual selection in frontal eye field. *Neuron* 30, 583–591. doi: 10.1016/S0896-6273(01)00304-X

Schall, J. D. (1991). Neuronal activity related to visually guided saccades in the frontal eye fields of rhesus monkeys: comparison with supplementary eye fields. *J. Neurophysiol.* 66, 559–579. doi: 10.1152/jn.1991.66.2.559

Schall, J. D., and Hanes, D. P. (1993). Neural basis of saccade target selection in frontal eye field during visual search. *Nature* 366, 467–469. doi: 10.1038/366467a0

Segraves, M. A. (1992). Activity of monkey frontal eye field neurons projecting to oculomotor regions of the pons. *J. Neurophysiol.* 68, 1967–1985. doi: 10.1152/jn.1992.68.6.1967

Segraves, M. A., and Goldberg, M. E. (1987). Functional properties of corticotectal neurons in the monkey's frontal eye field. *J. Neurophysiol.* 58, 1387–1419. doi: 10.1152/jn.1987.58.6.1387

Sommer, M. A., and Wurtz, R. H. (2000). Composition and topographic organization of signals sent from the frontal eye field to the superior colliculus. *J. Neurophysiol.* 83, 1979–2001. doi: 10.1152/jn.2000.83.4.1979

The jamovi project (2021). *jamovi (Version 1.6) [Computer Software]. version 1.2.27.0*. Available online at: https://www.jamovi.org (accessed February 8, 2021).

Thiele, A., Brandt, C., Dasilva, M., Gotthardt, S., Chicharro, D., Panzeri, S., et al. (2016). Attention induced gain stabilization in broad and narrow-spiking cells in the frontal eye-field of macaque monkeys. *J. Neurosci.* 36, 7601–7612. doi: 10.1523/JNEUROSCI.0872-16.2016

Thompson, K. G., and Bichot, N. P. (2005). "A visual salience map in the primate frontal eye field," in *Progress in Brain Research Development, Dynamics and Pathology of Neuronal Networks: From Molecules to Functional Circuits*, eds J. van Pelt, M. Kamermans, C. N. Levelt, A. van Ooyen, G. J. A. Ramakers, and P. R. Roelfsema (Amsterdam: Elsevier), 249–262. doi: 10.1016/S0079-6123(04)47019-8

Thompson, K. G., Hanes, D. P., Bichot, N. P., and Schall, J. D. (1996). Perceptual and motor processing stages identified in the activity of macaque frontal eye field neurons during visual search. *J. Neurophysiol.* 76, 4040–4055. doi: 10.1152/jn.1996.76.6.4040

Thompson, S. M., Masukawa, L. M., and Prince, D. A. (1985). Temperature dependence of intrinsic membrane properties and synaptic potentials in hippocampal CA1 neurons *in vitro*. *J. Neurosci.* 5, 817–824. doi: 10.1523/JNEUROSCI.05-03-00817.1985

Umeno, M. M., and Goldberg, M. E. (1997). Spatial processing in the monkey frontal eye field. I. Predictive visual responses. *J. Neurophysiol.* 78, 1373–1383. doi: 10.1152/jn.1997.78.3.1373

Vera, J., Pezzoli, M., Pereira, U., Bacigalupo, J., and Sanhueza, M. (2014). Electrical resonance in the θ frequency range in olfactory amygdala neurons. *PLoS One* 9:e85826. doi: 10.1371/journal.pone.0085826

Xu, W., and Baker, S. N. (2018). In vitro characterization of intrinsic properties and local synaptic inputs to pyramidal neurons in macaque primary motor cortex. *Eur. J. Neurosci.* 48, 2071–2083. doi: 10.1111/ejn.14076

Yan, T., and Zhou, H.-H. (2019). Synchronization between frontal eye field and area V4 during free-gaze visual search. *Zool. Res.* 40, 394–403. doi: 10.24272/j.issn.2095-8137.2019.055

Yoon, J. Y., Lee, H. R., Ho, W.-K., and Lee, S.-H. (2020). Disparities in short-term depression among prefrontal cortex synapses sustain persistent activity in a balanced network. *Cereb. Cortex* 30, 113–134. doi: 10.1093/cercor/bhz076

Yu, Y., Huber, L., Yang, J., Jangraw, D. C., Handwerker, D. A., Molfese, P. J., et al. (2019). Layer-specific activation of sensory input and predictive feedback in the human primary somatosensory cortex. *Sci. Adv.* 5:eaav9053. doi: 10.1126/sciadv.aav9053

Zaitsev, A. V., Povysheva, N. V., Gonzalez-Burgos, G., and Lewis, D. A. (2012). Electrophysiological classes of layer 2/3 pyramidal cells in monkey prefrontal cortex. *J. Neurophysiol.* 108, 595–609. doi: 10.1152/jn.00859.2011

Conflict of Interest: The authors declare that the research was conducted in the absence of any commercial or financial relationships that could be construed as a potential conflict of interest.

Publisher's Note: All claims expressed in this article are solely those of the authors and do not necessarily represent those of their affiliated organizations, or those of the publisher, the editors and the reviewers. Any product that may be evaluated in this article, or claim that may be made by its manufacturer, is not guaranteed or endorsed by the publisher.

Copyright © 2021 Piette, Vandecasteele, Bosch-Bouju, Goubard, Paillé, Cui, Mendes, Perez, Valtcheva, Xu, Pouget and Venance. This is an open-access article distributed under the terms of the Creative Commons Attribution License (CC BY). The use, distribution or reproduction in other forums is permitted, provided the original author(s) and the copyright owner(s) are credited and that the original publication in this journal is cited, in accordance with accepted academic practice. No use, distribution or reproduction is permitted which does not comply with these terms.

frontiers in Synaptic Neuroscience

ORIGINAL RESEARCH
published: 11 January 2022
doi: 10.3389/fnsyn.2021.769228

Spindle-Shaped Neurons in the Human Posteromedial (Precuneus) Cortex

Francisco Javier Fuentealba-Villarroel[1,2†], Josué Renner[1,3†], Arlete Hilbig[4], Oliver J. Bruton[5] and Alberto A. Rasia-Filho[1,2,3*]*

[1] Department of Basic Sciences/Physiology, Universidade Federal de Ciências da Saúde de Porto Alegre, Porto Alegre, Brazil, [2] Graduate Program in Neuroscience, Universidade Federal do Rio Grande do Sul, Porto Alegre, Brazil, [3] Graduate Program in Biosciences, Universidade Federal de Ciências da Saúde de Porto Alegre, Porto Alegre, Brazil, [4] Department of Medical Clinics/Neurology, Universidade Federal de Ciências da Saúde de Porto Alegre, Porto Alegre, Brazil, [5] Carl von Ossietzky Universität Oldenburg, Oldenburg, Germany

The human posteromedial cortex (PMC), which includes the precuneus (PC), represents a multimodal brain area implicated in emotion, conscious awareness, spatial cognition, and social behavior. Here, we describe the presence of Nissl-stained elongated spindle-shaped neurons (suggestive of von Economo neurons, VENs) in the cortical layer V of the anterior and central PC of adult humans. The adapted "single-section" Golgi method for *postmortem* tissue was used to study these neurons close to pyramidal ones in layer V until merging with layer VI polymorphic cells. From three-dimensional (3D) reconstructed images, we describe the cell body, two main longitudinally oriented ascending and descending dendrites as well as the occurrence of spines from proximal to distal segments. The primary dendritic shafts give rise to thin collateral branches with a radial orientation, and pleomorphic spines were observed with a sparse to moderate density along the dendritic length. Other spindle-shaped cells were observed with straight dendritic shafts and rare branches or with an axon emerging from the soma. We discuss the morphology of these cells and those considered VENs in cortical areas forming integrated brain networks for higher-order activities. The presence of spindle-shaped neurons and the current discussion on the morphology of putative VENs address the need for an in-depth neurochemical and transcriptomic characterization of the PC cytoarchitecture. These findings would include these spindle-shaped cells in the synaptic and information processing by the default mode network and for general intelligence in healthy individuals and in neuropsychiatric disorders involving the PC in the context of the PMC functioning.

Keywords: human brain (cerebral cortex), cytology (CY), default mode network (DMN), dendritic spines, 3D reconstruction, general intelligence (*g*), von Economo neuron (VEN)

OPEN ACCESS

Edited by:
Joachim H. R. Lübke, Julich Research Centre, Helmholtz Association of German Research Centres (HZ), Germany

Reviewed by:
Nathaniel Heintz, The Rockefeller University, United States
Zdravko Petanjek, University of Zagreb, Croatia

***Correspondence:**
Oliver J. Bruton
oliver.bruton@uni-oldenburg.de
Alberto A. Rasia-Filho
aarf@ufcspa.edu.br; rasiafilho@yahoo.com

† These authors have contributed equally to this work

Received: *01 September 2021*
Accepted: *29 November 2021*
Published: *11 January 2022*

Citation:
Fuentealba-Villarroel FJ, Renner J, Hilbig A, Bruton OJ and Rasia-Filho AA (2022) Spindle-Shaped Neurons in the Human Posteromedial (Precuneus) Cortex. Front. Synaptic Neurosci. 13:769228. doi: 10.3389/fnsyn.2021.769228

INTRODUCTION

Von Economo neurons (VENs) have a peculiar phylogenetic and ontogenetic development and are characterized by an elongated spindle-shaped or rod-shaped cell body mainly found in the cortical layer V of restricted brain areas of some species, including humans and other primates, but not in all mammals (Nimchinsky et al., 1995; Allman et al., 2005, 2010; Hakeem et al., 2009; Cauda et al., 2014; Raghanti et al., 2015; Hodge et al., 2020; Jacob et al., 2021). In humans, VENs have been reported

mainly in the anterior cingulate cortex (ACC) and frontoinsular cortex (FI; Raghanti et al., 2015; Banovac et al., 2019, 2021; Correa-Júnior et al., 2020 and references therein), but also in the dorsolateral prefrontal cortex (Brodmann area 9; Fajardo et al., 2008) and in the medial frontopolar prefrontal cortex (Brodmann area 10; González-Acosta et al., 2018). VENs might correspond to ∼3% of all neurons in layer V in the ACC (Fajardo et al., 2008; see comments about their relative abundance in Banovac et al., 2021), being more numerous in the ACC and FI of humans than in apes (Allman et al., 2010).

Human VENs show features of excitatory projecting neurons (Nimchinsky et al., 1995; Evrard et al., 2012; Hodge et al., 2020). They may provide fast interconnections between neocortical areas, such as the ACC and FI cortices (Craig, 2009), and recent transcriptomic data suggest that human VENs may project to extratelencephalic, subcortical targets (Hodge et al., 2020). In gorillas, VENs also project to the inferior frontal gyrus, inferotemporal cortex, laterally to the hippocampus, as well as to the septum and amygdala (Allman et al., 2010). VENs innervate the midbrain periaqueductal gray and the parabrachial nucleus of dorsolateral pons of monkeys (discussed in Evrard et al., 2012), and may link emotion and control of sympathetic/parasympathetic sites in brainstem and spinal cord regions (Cobos and Seeley, 2015; Jacot-Descombes et al., 2020).

The identification of cells as VENs (or putative ones) has been based on Nissl/thionin staining (Nimchinsky et al., 1995; Raghanti et al., 2015), Golgi impregnation (Watson et al., 2006; Banovac et al., 2019, 2021; Correa-Júnior et al., 2020), intracellular biocytin (Hodge et al., 2020), retrograde labeling with cholera toxin b and Alexa 594 fluorescent dextran nanoinjection (Evrard et al., 2012), immunoreactivity for different biochemical biomarkers including neurotransmitters' receptors, neuropeptides, and transcription factors (Allman et al., 2005, 2010; Stimpson et al., 2011; Dijkstra et al., 2018), and/or different gene expressions (Allman et al., 2010; Evrard et al., 2012; Cobos and Seeley, 2015; Yang et al., 2019; Hodge et al., 2020). VENs are morphologically different from neighboring pyramidal neurons (Allman et al., 2005; Watson et al., 2006) and are larger than layer VI "fusiform" neurons (Nimchinsky et al., 1999). Although having some molecular profile in common with layer V pyramidal and fork neurons, human putative VENs showed distinctive intrinsic membrane properties in the FI (Hodge et al., 2020) and transcriptomic characteristics in the ACC (Yang et al., 2019). These data are fundamental to integrate morphological and genetic characteristics to identify phenotype-associated cells and to test the proposed functional roles for VENs in main control neural networks (Bruton, 2021), as well as their vulnerability in diseases with social and emotional deficits (Allman et al., 2005; Cauda et al., 2014; Raghanti et al., 2015).

The shape of VENs is also characterized by the presence of two main perpendicularly oriented thick primary dendritic shafts, one ascending toward more superficial cortical layers and another descending toward the inner cortical layer (Allman et al., 2005; Watson et al., 2006; Evrard et al., 2012; Seeley et al., 2012; Raghanti et al., 2015). Indeed, the human ACC is a region where the cell body and the primary dendrites of VENs were identified using different morphological, neurochemical, and transcriptomic approaches. Based on these data to guide the use of the Golgi method, the three-dimensional (3D) reconstruction of Golgi-impregnated layer V VENs indicated the heterogeneity of dendrites and spines of these cells in this brain area. That is, ACC VENs were described in a morphological *continuum* from sparsely branched (as previously reported by Watson et al., 2006) to more extensively ramified cells with varied collateral branches and differences in the distribution, density, and shape of dendritic spines (Correa-Júnior et al., 2020). On the other hand, VENs should have a brush-like aspect for the descending dendrites with an axon in the ACC and in the FI, a morphological characteristic that was evidenced in the first drawings of these Golgi-impregnated neurons (Banovac et al., 2019, 2021; note the aspect of the axonal ramification in the original drawing from Ramón y Cajal shown as Figure 1 in Banovac et al., 2021). Dendrites and spines in VENs are important cellular elements to be studied because the geometry and biophysical properties of both are linked to the synaptic integration, strength, and plasticity (Yuste, 2010; Rochefort and Konnerth, 2012; Spruston et al., 2013; Hayashi-Takagi et al., 2015; Rollenhagen and Lübke, 2016; Tønnesen and Nägerl, 2016; Nakahata and Yasuda, 2018) for broad information processing in healthy individuals and in neurodegenerative diseases (Herms and Dorostkar, 2016). Dendritic spines are complex elements that can enhance the connectivity between neurons and increase the packing density of synapses without increasing the overall volume of the brain (Bourne and Harris, 2009). Moreover, dendritic spines are specialized postsynaptic units for most excitatory inputs (Spruston et al., 2013; Brusco et al., 2014; Helm et al., 2021; but see Kubota et al., 2016 for the impact of inhibitory GABAergic terminals on spines), whose complexity is evident in the human brain (Cajal, 1909-1911; Yuste, 2013; Dall'Oglio et al., 2015).

The neuroanatomical and cytoarchitectonic maps of the posteromedial cortex (PMC), including the subdivisions of the precuneus (PC, former "quadrate lobule of Foville"), represent current research avenues on multimodal integrative areas in the human brain. The anatomical and functional development of the PC as well as the adjacent medioventral areas in the PMC may have played a significant role in human brain evolution for somatosensory processing, motor behavior, mental imagery, attentional shift, self-awareness, and judgments about other persons' mental states, social and cognitive specializations (Wenderoth et al., 2005; Denny et al., 2012; Bruner et al., 2014, 2017a,b). The human PMC may include the PC, the posterior cingulate cortex (Brodmann area, BA, 23), the retrosplenial cortex in the posterior callosal sulcus (areas 29 and 30), and the transitional zone (area 31) between the PC and the posterior cingulate cortex (Margulies et al., 2009). Some features are remarkable: (1) bulging of the parietal surface during the first year of life in *Homo sapiens* is a morphogenetic stage absent in chimpanzees and Neandertals, (2) the deep parietal areas show discrete cytoarchitectural differences between human and non-human primates, and (3) the extension of the PC is the principal source of midsagittal brain variability in adult humans (Bruner et al., 2014, 2017a,b and references therein). In midsagittal sections, the PC is a fully differentiated isocortex located in

the superior parietal cortex, posterior to the postcentral sulcus and the marginal ramus of the cingulate sulcus, anterior to the parieto-occipital fissure and the cuneus, above the subparietal sulcus and adjacent to the transition area to the posterior cingulate and the retrosplenial cortex (Cavanna and Trimble, 2006; Scheperjans et al., 2008a,b; Margulies et al., 2009; Mai et al., 2016; Bruner et al., 2017a). Nevertheless, the human PC varies in its geometry (mostly in its longitudinal dimensions), in the patterns of convolution, and how sulci extend within it (Bruner et al., 2014, 2017a).

The human PC has been referred to as BA 7 (or 7m, further divided in 7a and 7b for its anterior and posterior parts, respectively) or, according to the von Economo and Koskinas cytoarchitectonic atlas, numbered as areas 62–64 (or P*Em*, P*Ep*, and P*Ey*; c.f. Triarhou, 2009). The human PC would include BAs 7 and 31 or, additionally, the 23 and 30 ones (e.g., see plates 72 and 77 in Mai et al., 2016; but see data in Cavanna and Trimble, 2006 and references therein). Otherwise, the cytoarchitectonic parcellation of structurally distinct microanatomical areas identified a heterogeneous medial border for the 7A, 7P, and 7M parts in the human PC, considering the existence of interindividual anatomical variability and interhemispheric topographic asymmetries (Scheperjans et al., 2008a,b). These PC parts would be located posterior to the postcentral sulcus, where areas 5L and 5M would still be occupying a variable volume of the anterior part of the Brodmann PC 7a (Scheperjans et al., 2008a,b). Functionally, the PC is a multimodal integrative heterogeneous area as revealed by resting-state functional MRI data (Margulies et al., 2009). That is, (1) the anterior PC can be a sensorimotor region connected with the superior parietal cortex, paracentral lobule, and motor cortex, also including the insula; (2) the central PC can be a cognitive/associative/multimodal zone connected to the dorsolateral prefrontal, dorsomedial prefrontal, and multimodal lateral inferior parietal cortex; and (3) the posterior PC is connected with contiguous visual cortical regions (Margulies et al., 2009).

Considering that VENs occur in cortical areas for higher sensorial and motor integration, emotional and cognitive functions, intuition and social behavior elaboration, and flexibility, we looked for the presence of "spindle-shaped" cells, which would be suggestive of VENs, in the human PMC. Our intention is not to cause a potential confusion with other uses of the term "spindle neurons" (also mentioned in Watson et al., 2006) or "spindle-transformed pyramidal cells" (as extensively reviewed in Banovac et al., 2021). Rather, we describe the morphology of these neurons in layer V until merging with layer VI of the human PC based on their Nissl-stained and Golgi-impregnated features while we do not have complete data for their definitive neurochemical and transcriptomic characterization and classification. Here, we studied the anterior and central regions of the PC (BA 7), which correspond approximately to fMRI chosen regions of interest/"seeds" 5–7 and 9–11 within the PC (Margulies et al., 2009; seeds data 11 and 15 from *SI Appendix* were visually compared and considered as central PC). Our samples included the tissue posterior to the postcentral sulcus, mostly corresponding to the PC (although areas 5L and 5M would also be included; Scheperjans et al., 2008a,b), and a small part of the transitional area 31 in the ventral limit close to the subparietal sulcus (but not advancing to the posterior cingulate cortex). First, we used Nissl staining to identify neurons with a characteristic elongated spindle-shaped cell body close to pyramidal neurons in the PC cortical layer V and in the transition to layer VI. Afterward, two-dimensional (2D) and 3D reconstructions of Golgi-impregnated spindle-shapled neurons evidenced two main shafts oriented perpendicularly, corresponding to the ascending and descending primary dendrites in these cells. We discuss the morphology of putative VENs in other human brain areas, the need for additional classification of these PC spindle-shaped cells as well as the implications for the local cytoarchitectonics and the functional possibilities for the presence of spindle-shaped (or putative VENs) in the human PC for both the "default mode network" (DMN) and high multimodal cortical processing.

MATERIALS AND METHODS

The present procedure was adapted from the description published in Correa-Júnior et al. (2020).

Subjects

The subjects were two men and one woman reportedly healthy neurologically and psychiatrically, with no previous neurosurgical interventions. Age, sex, *postmortem* interval, and cause of death are shown in **Table 1**. The next of kin provided written informed consent for brain donation during an autopsy at the morgue, as well as provided the donors' clinical and comorbidities information. Each subject was screened for cognitive decline using the "Informant Questionnaire on Cognitive Decline in the Elderly" (IQCODE; Neto et al., 2017). This validated interview procedure has a cut-off point scores indicative of dementia of $\geq$3.27 or 3.48 in the Brazilian population (Sanchez and Lourenço, 2009; Carrabba et al., 2015). Only cases below these values were included in the present study (**Table 1**). Brain tissue was also analyzed histologically and immunohistochemically by a neurologist/neuropathologist (AH) to confirm the absence of common vascular lesions or evident neurodegenerative disorders other than primary age-related alterations.

All ethical and legal procedures were carried out in accordance with the international regulatory standards based on the Helsinki Declaration of 1964. The privacy rights of subjects were observed at all times. There is no potentially identifiable data for any individual included in this article. The Brazilian Ethics Committee from the Federal University of Health Sciences of Porto Alegre (UFCSPA; #62336116.6.0000.5345, 18718719.7.0000.5345, and 06273619.7.0000.5345) and the Federal University of Rio Grande do Sul (#18718719.7.3001.5347) approved this study.

Tissue Processing and the Nissl Staining Procedure

Brains were kept immersed in 10% laboratory-grade, unbuffered formaldehyde solution at room temperature (RT) for

TABLE 1 | Characteristics of the human cases.

Cases (code#)	Age (years)	Sex	PMI (hours)	IQCODE	Cause of death	Tissue fixation	Technique
2	91	F	6–20	1.32	Pneumonia	Immersion	Thionin/Golgi
3	79	M	6–20	3.15	Cardiac Arrest	Immersion	Thionin/Golgi
4	49	M	6–20	3.00	Undetermined	Immersion	Thionin/Golgi

PMI, postmortem interval; F, female; M, male.

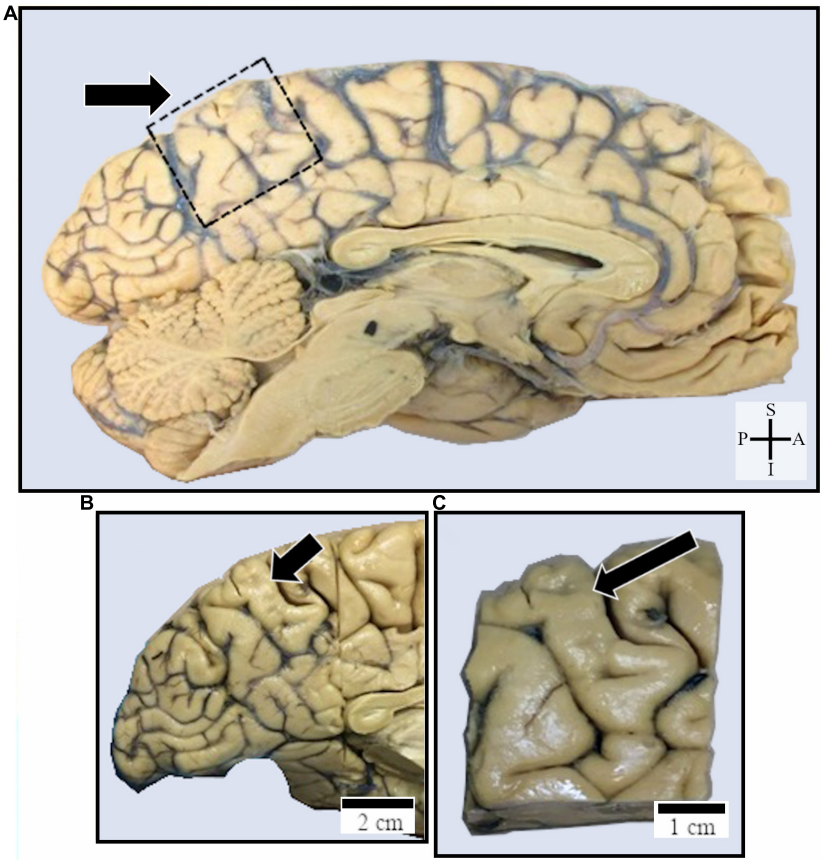

FIGURE 1 | (A) Midsagittal section to show the macroscopic location of the human posteromedial cortex where the precuneus (PC, pointed by an arrow and delimited within a dashed square) was studied near the transition zone to the posterior cingulate cortex. **(B,C)** Higher magnification images of the human PC where samples were obtained for the identification of spindle-shaped neurons in cortical layer V (shown in the following figures). Coordinates: A, anterior; I, inferior; P, posterior; S, superior. Scales are shown in the figure.

approximately 6 years before study. The PC was located in the dorsal portion of the PMC, posterior to the marginal ramus of the cingulate sulcus, anterior to the parieto-occipital fissure and the cuneus, and including the subparietal sulcus as anatomical reference, as mentioned above (**Figure 1**; Margulies et al., 2009; Mai et al., 2016; Bruner et al., 2017a). The anterior and central PC in the left hemisphere (the side available in these samples) were studied from 41.5 to 73.6 mm posterior to the midpoint of the anterior commissure (Mai et al., 2008, 2016; **Figures 2**, **3**).

At the beginning of this study, tissue blocks were sectioned and post-fixed at RT for 30 days using phosphate buffer solution (PBS, 0.1 M, pH = 7.4), 4% formaldehyde, and 1.5% picric acid. Samples were coronally sectioned with a vibrating microtome (1000S; Leica, Germany) in an alternating fashion. One series was sectioned at 50 μm for the Nissl technique, the other at 200 μm for the Golgi method.

The Nissl staining identified the cortical layers and different cells in the PC (**Figures 2**, **3**). That is, sections were (1) placed on gelatin-coated slides and left to dry at RT for 1 day; (2) then, slides were immersed in a 4% formaldehyde in PBS for 1 week at 4°C and protected from light; (3) dried for 1 day at RT and immersed in a 70% ethanol solution for 1 day; (4) immersed in increasing concentrations of ethanol and cleared in absolute xylene; (5) immersed in decreasing solutions of ethanol and washed in distilled water; (7) immersed in a solution of 0.25% cresyl violet (Merck, Germany) for 2 min; (7) immersed in distilled water to remove excessive dying, and in solutions of

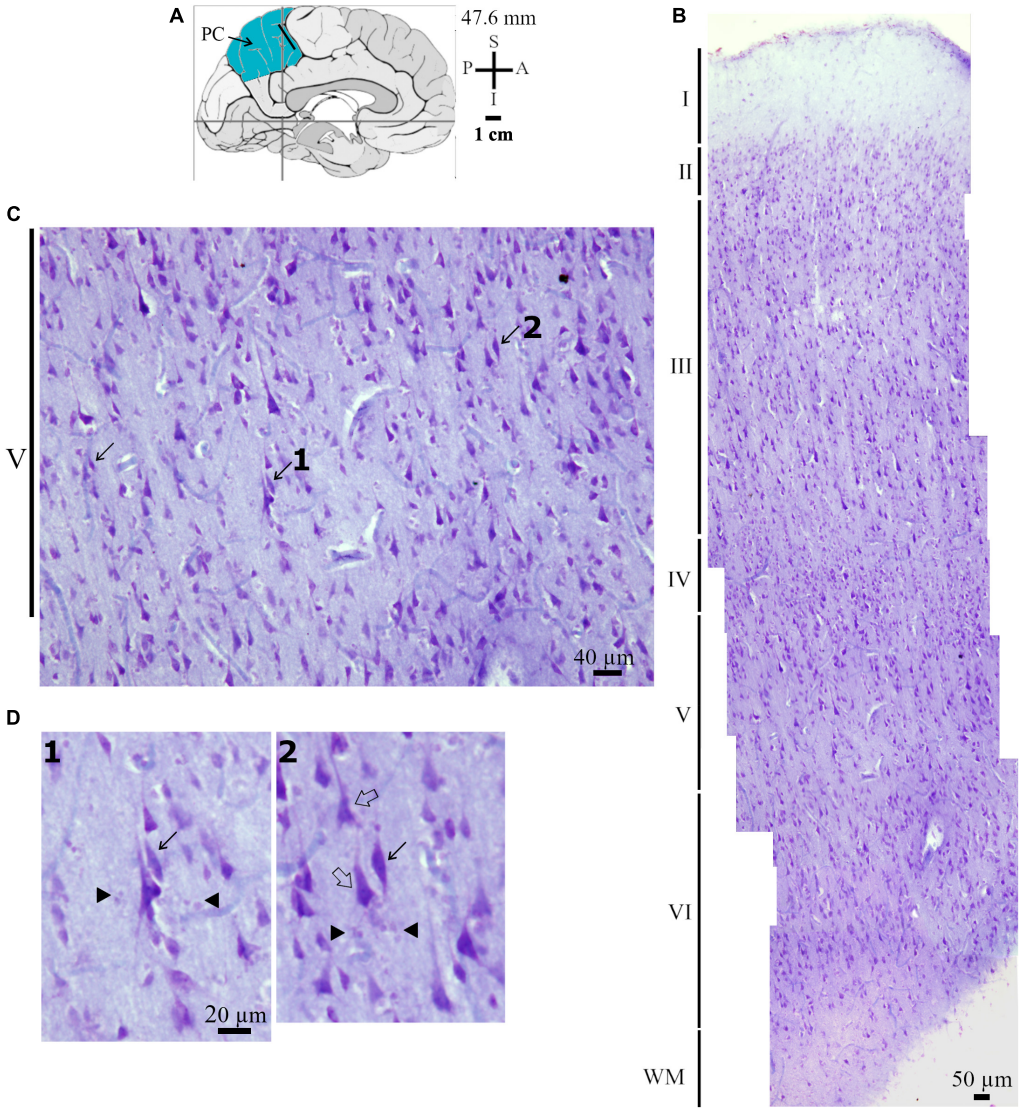

FIGURE 2 | (A) Schematic drawing of the medial view of the human brain and the location of the anterior region of the precuneus (PC, highlighted in blue), in this case 47.6 mm posterior to the midpoint of the anterior commissure. The dark bar indicates approximately the place where histological data were obtained. Adapted from Mai et al. (2008, 2016). Coordinates: I, inferior; L, lateral; M, medial; S, superior. **(B)** Photomicrograph of Nissl-stained cells in layers I to VI in the anterior PC. WM, white matter. **(C)** Photomicrograph in higher magnification of Nissl-stained cells in the layer V of the human PC as shown in **(B)**. The spindle-shaped neurons (pointed by solid arrows) are close to pyramidal neurons and other local cells in the cortical layer V and in the transition to layer VI. **(D)** Further details for the morphology of the spindle-shaped neurons pointed and numbered 1 and 2 in **(C)**. Note their characteristic elongated cell body and two perpendicularly oriented primary dendrites, one with an ascending and another with a descending spatial orientation in the neuropil. Compare these spindle-shaped cells to the neighboring stained pyramidal neurons (examples indicated by an open arrow). Adjacent glia cells are also present (indicated by a solid arrow head). Scales are shown in each figure. Image adjustment of contrast and brightness made with Photoshop CS3 (Adobe Systems, Inc., United States).

increasing ethanol concentration; (8) dipped in a solution of 95% ethanol with 1% acetic acid and absolute xylene; and (9) mounted with synthetic balsam (Soldan, Brazil) and coverslipped.

The Golgi Method and the Two-Dimensional and Three-Dimensional Image Reconstruction Procedures

We used the "single-section" Golgi method adapted for long-term fixed *postmortem* human brain (Dall'Oglio et al., 2010 on the original Gabbott and Somogyi, 1984; developed for 3D image processing by Reberger et al., 2018) as previously done for the characterization of neurons and dendritic spines in both subcortical (amygdaloid nuclei) and cortical human brain areas (Dall'Oglio et al., 2013, 2015; Vásquez et al., 2018; Correa-Júnior et al., 2020; Rasia-Filho et al., 2021). Brain sections were sectioned and kept immersed in the same post-fixation solution as mentioned above for three more days. Afterward, sections were: (1) rinsed in PBS and immersed in a solution of 0.1% osmium tetroxide (Sigma Chemicals Co., United States)

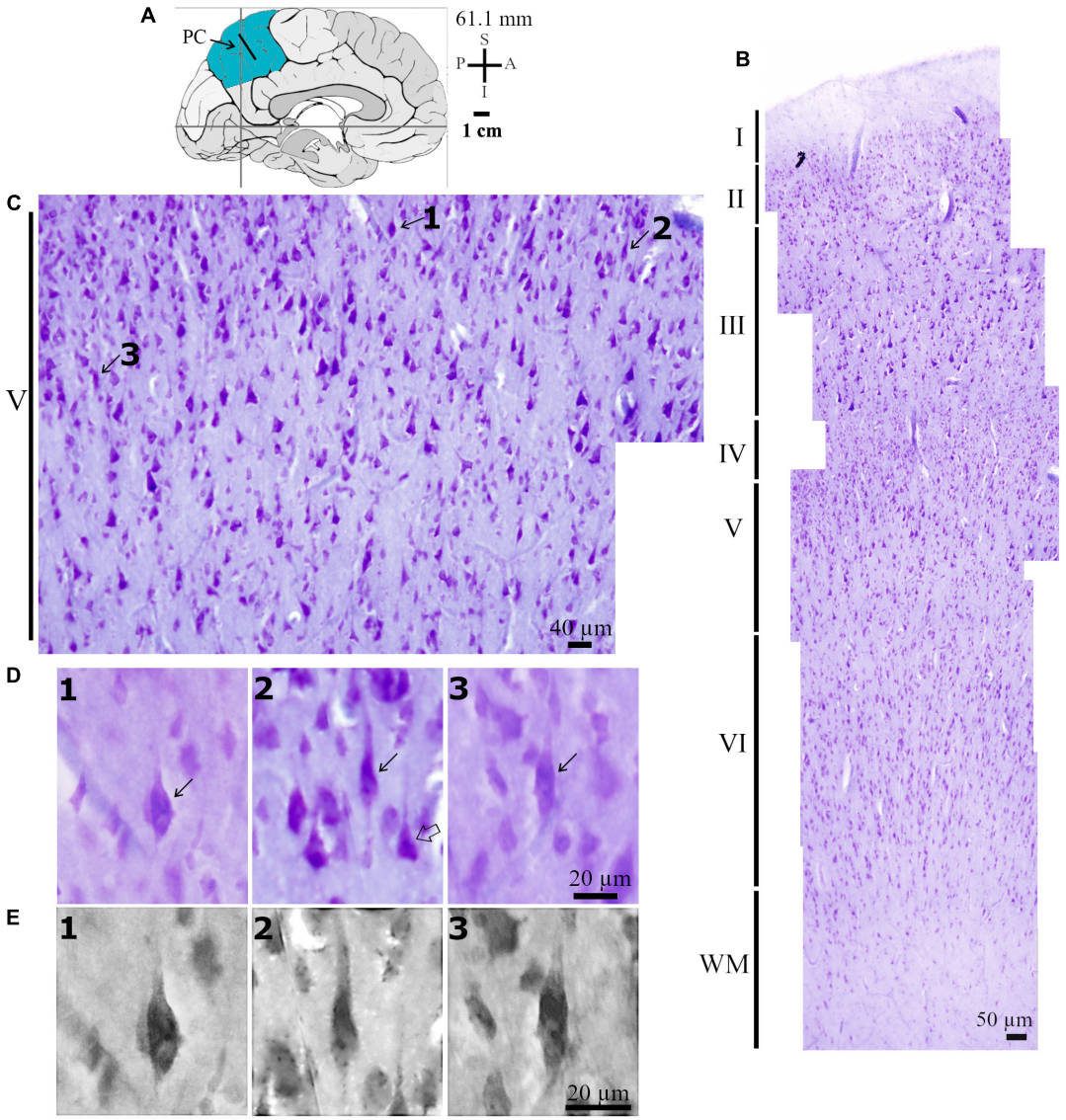

FIGURE 3 | (A) Left: Schematic drawing of the medial view of the human brain and the location of the central region of the precuneus (PC, highlighted in blue), in this case 61.1 mm posterior to the midpoint of the anterior commissure. The dark bar indicates approximately the place where histological data were obtained. Adapted from Mai et al. (2008, 2016). Coordinates: I, inferior; L, lateral; M, medial; S, superior. **(B)** Photomicrograph of Nissl-stained cells in layers I to VI in the intermediate PC. WM, white matter. **(C)** Photomicrograph in higher magnification of Nissl-stained cells in the layer V of the human PC as shown in **(B)**. The spindle-shaped neurons (numbered 1–3 and pointed by solid arrows) are close to pyramidal neurons and other local cells in the cortical layer V and in the transition to layer VI. **(D)** Further detail for the morphology of these spindle-shaped neurons indicated in **(C)**. Note their characteristic elongated cell body and two perpendicularly oriented primary dendrites, one with an ascending and another with a descending spatial orientation in the neuropil. Compare these spindle-shaped cells to the neighboring stained pyramidal neurons (example indicated by open arrow). **(E)** Higher magnification of the same spindle-shaped neurons shown in **(D)** to evidence the aspect of their chromatin and nucleolus. Scales are shown in each figure. Image adjustment of contrast and brightness made with Photoshop CS3 (Adobe Systems, Inc., United States).

in PBS for 20 min; (2) rinsed in PBS and immersed in 3% potassium dichromate (Merck) at 4°C in the dark for 2 days; (3) rinsed in distilled water, "sandwiched" between coverslips, placed in a solution of 1.5% silver nitrate (Merck) at RT for 1 day and protected from light; (4) washed in distilled water, placed on gelatin-coated histological slides, dried at RT, dehydrated in an ascending series of ethanol, cleared in ethanol and absolute xylene; and (5) covered with non-acidic synthetic balsam (refractive index = 1.518–1.521, Permount Mounting Medium, EMS, United States or similar product, Soldan, Brazil) and coverslipped.

We used the following criteria to select Golgi-impregnated neurons for further study: (1) cells should have their soma located within the boundaries of the PC; (2) spindle-shaped cells should be near to pyramidal neurons in the cortical layer V until the transition to layer VI; (3) cells should have two main primary

dendrites oriented vertically toward the white matter and apical surface; (4) cells should be relatively "isolated" in the neuropil to allow its best visualization; (5) dendrites should have defined borders and, as much as possible, be tapering after branching or at distal locations; and (6) dendritic spines should be visible and morphologically distinct than unspecific silver precipitated in the section background.

The general morphology of PC neurons was studied at 260× (using an objective planapochromatic lens UPlanSApo 0.6 NA, Olympus, Japan) using a light microscope (Olympus BX-61, Japan) equipped with a *z*-stepping motor and coupled to a CCDDP72 high-performance camera (Olympus, Japan). Each image was acquired after advancing 0.5 μm for each *z* stack, under high resolution (1360 × 1024 pixels), and submitted to dynamic deconvolution using the Image Pro Plus 7.0 software (Media Cybernetics, United States) during the acquisition process (Dall'Oglio et al., 2013; Reberger et al., 2018). Files were recorded as .TIFF files. The selected images were converted to 8-bit monochromatic pictures before processing (Correa-Júnior et al., 2020). We initially elaborated a 2D reconstruction of the cell body and dendrites of Golgi-impregnated neurons by summing microscopic images at sequential focal planes. Small adjustments of brightness and background contrast were made in final reconstructed images using Adobe Photoshop CS3 software (Adobe Systems, Inc., United States) and/or Neuromantic free software (v1.6.3 programmed in Borland C++ Builder, University of Reading, United Kingdom), without altering the original neuronal features.

Based on this 2D general shape reconstruction, we proceeded next to the 3D reconstruction of selected neurons in accordance with the procedure described in Correa-Júnior et al. (2020). That is, we used the Neuromantic software (as mentioned above), and a semi-automatic tracing of the cell body and dendrites was done for the original stack of microscopic images acquired along with the three spatial coordinates. Reconstructions were achieved as a sequence of 3D points with an ASCII-based format representing dendritic trees as a series of connected cylinders of varying radii identified by orthogonally lines from edge-to-edge (Myatt et al., 2012). The luminosity was inverted to evidence the dendritic shafts details contrasting with the background. Contrast was adjusted for the visualization of thin branches using the algorithm and image processing described in Myatt et al. (2012). Final reconstructions were saved as SWC format (Parekh and Ascoli, 2013). Morphometric data were obtained using the L-Measure free software (Scorcioni et al., 2008) on the 3D reconstructed images. Values were calculated for the cell body length, main diameter and volume, the dendritic diameter of the primary shafts, total number of branches (i.e., the sum obtained starting from primary dendrites, including segments between branching points, and toward the end of main or collateral branches), total length, and total volume of the dendritic tree. However, it must be mentioned that measurements of the neuronal cell body and dendrites can be affected by the fixation procedure and the tissue shrinkage due to each technique used. The morphometric values shown in **Figure 8** might not be the actual ones (as occurs *in vivo*) due to unavoidable changes in the nervous tissue following death and the various steps for the present histological processing (Dall'Oglio et al., 2010, 2013, 2015; Reberger et al., 2018; see also Zeba et al., 2008 for additional discussion).

The 3D reconstruction of dendritic spines was done using brightfield images acquired at a final magnification of 1300× using an 100× oil immersion objective lens (planapochromatic UPlanSApo 1.4 NA, Olympus, Japan). Each image was saved with high resolution (2070 × 1548 pixels) and submitted to dynamic deconvolution using the Image Pro Plus 7.0 software. Spines were imaged from proximal to distal branches. Data were obtained by controlling the focus in the *z* axis and acquiring *z*-stacks at sequential 0.1 μm steps. Corresponding images were stored as .TIFF files and converted to 8-bit monochromatic pictures. Each spiny dendritic segment imaged consisted of approximately 100–200 sequential frames (Correa-Júnior et al., 2020).

Following Reberger et al. (2018), spines were 3D reconstructed using an algorithm processed in the MATLAB software (R2105b, The MathWorks, United States). I.e., "after processing the gray scale slices independently or using a median 3D filters in smaller subvolumes, images were processed using the following steps: (a) outlier removal; (b) edge enhancement using a variant of the 'unsharp masking method' and image filtering approach based on domain transforms ('edge-aware'); (c) binarization using an adaptive thresholding approach; (d) pruning false positives (i.e., correction for the maintenance or removal of small objects in the image of interest if they are a dendritic segment and spine or an obvious artifact); (e) 2D flood-fill operation for each slice of the binary volume; (f) tricubic interpolation to smooth transitions between adjacent slices; and (g) visualization of the final volume of the sampled images containing the selected dendritic shafts and their spines" (Vásquez et al., 2018) using the "Fiji" Image J software (Schindelin et al., 2012) with the "Volume Viewer" plug-in.[1] Images had final adjustments of brightness and contrast made in Photoshop CS3 without altering spine counting or classification (Correa-Júnior et al., 2020).

The identification and classification of each type of 3D-reconstructed dendritic spine was based on previous descriptions (Fiala and Harris, 1999; Arellano et al., 2007a,b; Brusco et al., 2014; González-Ramírez et al., 2014; Dall'Oglio et al., 2015; Vásquez et al., 2018; Correa-Júnior et al., 2020; Rasia-Filho et al., 2021). By rotating the reconstructed images, spines were observed at different angles to determine occurrence from proximal to distal dendrites, number, shape, and size (Reberger et al., 2018). For each spine, we considered: (1) the presence, length, and diameter of a neck, (2) the number of protrusions from a single stalk, (3) the head diameter, and (4) the head shape. According to these morphological features, spines were classified as (1) thin (2) stubby, (3) wide, (4) mushroom-like, (5) ramified, and (6) with a transitional aspect between these classes or as "atypical" (or "multiform") spines with more complex and varied shapes (Dall'Oglio et al., 2015 and references therein). Tiny protrusions extending from the head of a spine were classified as spinules (Brusco et al., 2014; Zaccard et al., 2020; Petralia et al., 2021).

[1] https://imagej.nih.gov/ij/plugins/volumeviewer.html

All computational procedures were run using Windows Microsoft® (version 10), Intel® Core™ i7-8750H CPU @2.20 GHz, 16.0 GB RAM memory, NVIDIA® GeForce GTX 1050 Ti with 4 GB for image processing.

RESULTS

The Nissl-stained sections served to identify the cortical cytoarchitectonics and the cell body shape of neurons in layer V in the anterior and central regions of the human PC (**Figures 2**, **3**). Our interest was initially centered in Nissl-stained cells with an elongated spindle-shaped or rod-shaped cell body with two symmetric, vertically oriented primary dendritic shafts emerging at opposite somatic poles. The cell body shape of these cells should be similar to those reported previously for putative VENs (e.g., Nimchinsky et al., 1995; Allman et al., 2005, 2010; Hodge et al., 2020). We observed these cells in the PC layer V and in the transition to layer VI close to pyramidal neurons, which ranged from small and intermediate to large size, and glial cells (**Figures 2C**, **3C**). Nissl-stained spindle-shaped neurons displayed a longitudinal cell body length similar to some neighboring pyramidal neurons (**Figures 2D**, **3D**) as well as the characteristic neuronal chromatin aspect and a prominent nucleolus (**Figure 3E**).

There are limitations for the Golgi method when studying adult human *postmortem* samples. That is, not all cells were completely impregnated in the human PC, and it was not possible to reliably determine the presence of an axon and its ramification in all neurons. Few well-impregnated spindle-shaped neurons randomly fulfilled the inclusion criteria for further study. Descriptive data are provided for these available neurons without further statistical comparisons. The three subjects studied here had neurons in layer V showing the spindle-shaped soma and two primary dendrites, but few cells were well-impregnated. We selected the Nissl staining and the best Golgi-impregnated spindle-shaped neurons that we could obtain, shown in **Figures 2–10** and **Supplementary Figures 1–3** from

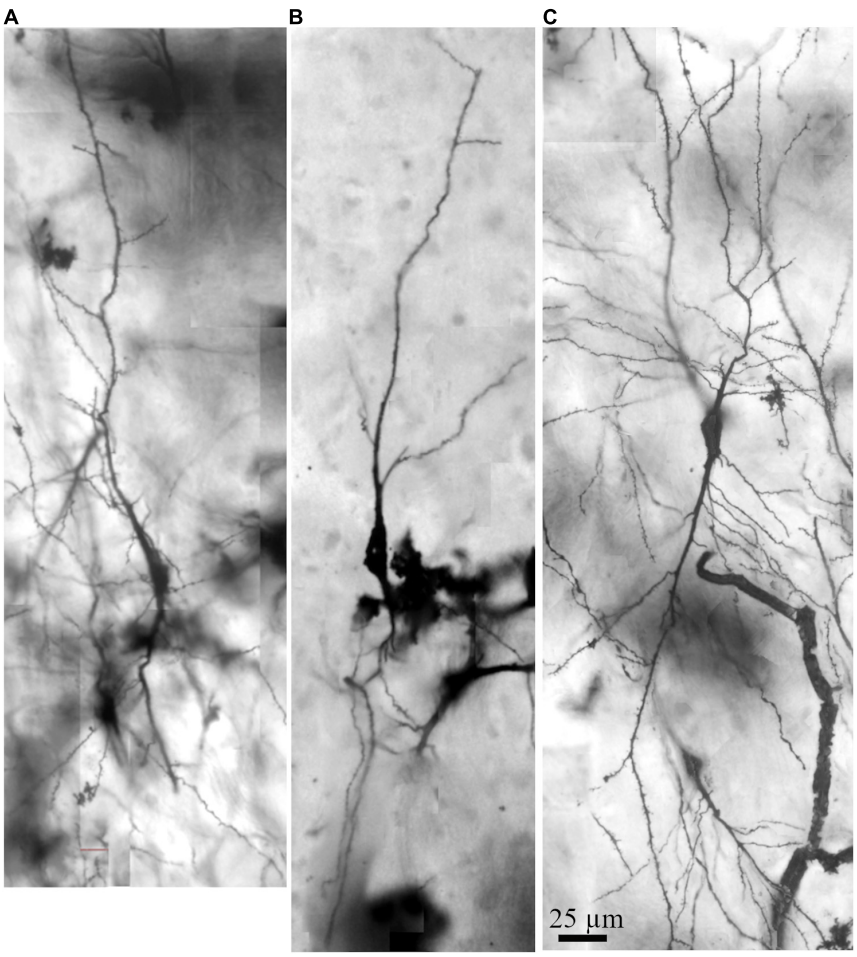

FIGURE 4 | Photomicrographic composition of Golgi-impregnated spindle-shaped neurons from layer V and in the transition to layer VI in the human precuneus observed using brightfield microscopy. **(A–C)** Neurons show a spindle-shaped soma with vertically oriented main primary dendritic shafts at opposite poles and the dendritic ramification in one focal plane. These neurons were 2D and 3D reconstructed and are shown in **Figures 5–8** and **Supplementary Figures 1–3**. Dendritic spines are not quite visible at this magnification. Image adjustment of contrast and brightness made with Photoshop CS3 (Adobe Systems, Inc., United States).

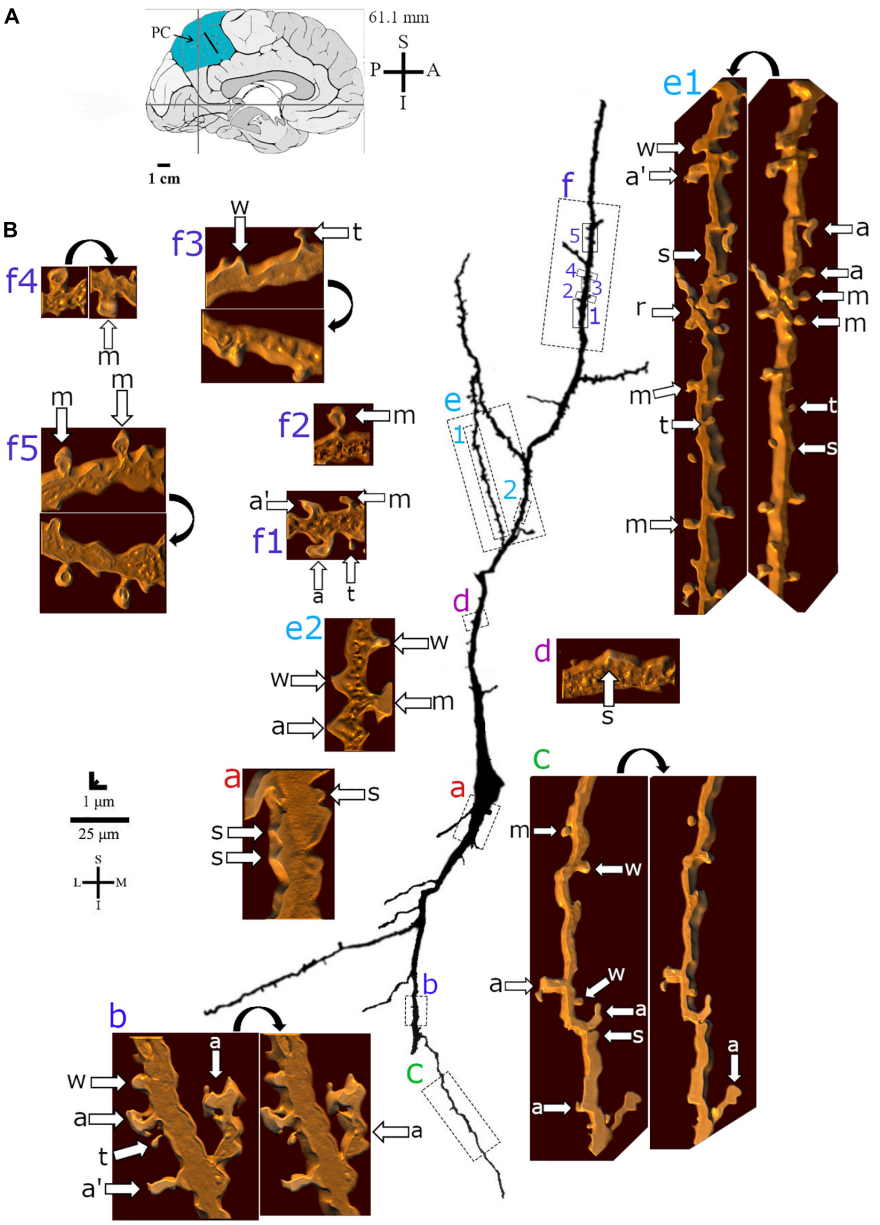

FIGURE 5 | (A) Left: Schematic drawing of the medial view of the human brain showing the location of the precuneus (PC, highlighted in blue), central region, 61.1 mm posterior to the midpoint of the anterior commissure. Adapted from Mai et al. (2008, 2016). **(B)** Two-dimensional (for the overall shape) and 3D (for the dendritic and spine details) image reconstructions of serial brightfield photomicrographs of a Golgi-impregnated spindle-shaped neuron from layer V in the human PC (pial surface at the top). Note the cell body shape, the main ascending and descending primary dendrites with a straight course and few ramifications. Proximal to distal dendritic segments (identified by colored letters from "a" to "f") were sampled and their spines are shown at higher magnification in the adjacent corresponding boxes. Note the distribution of low to moderate density of spines as well as the variety of their shapes. Spines were classified as stubby (s), wide (w), thin (t), mushroom (m), ramified (r), with a transitional (t), or atypical aspect (a). Spine types are indicated by arrows at different rotating angles. An apostrophe with the corresponding spine indicates the presence of a spinule. Image adjustment of contrast made with Photoshop CS3 (Adobe Systems, Inc., United States). Coordinates in **(A,B)**: I, inferior; L, lateral; M, medial; S, superior. Scale = 25 µm for the 2D reconstruction and 1 µm for the 3D reconstructions.

case #4 (described in **Table 1**). For example, in 7 serial sections from this specific case, we found 15 randomly impregnated pyramidal neurons (one example is shown in **Supplementary Figure 4**, most of the others were not completely impregnated) and 8 spindle-shaped cells (5 of them are shown here, the others had only the cell body and short "cut-off" proximal dendritic branches visible). The sampled spindle-shaped neurons were observed along the anterior or the central parts of the PC (see legends of the corresponding **Figures 2–10**). We also observed some small fusiform and other pleomorphic neurons, including a spindle- to rod-shaped cell, in layer VI of the human central part of the PC (**Figures 11**, **12**), as described below.

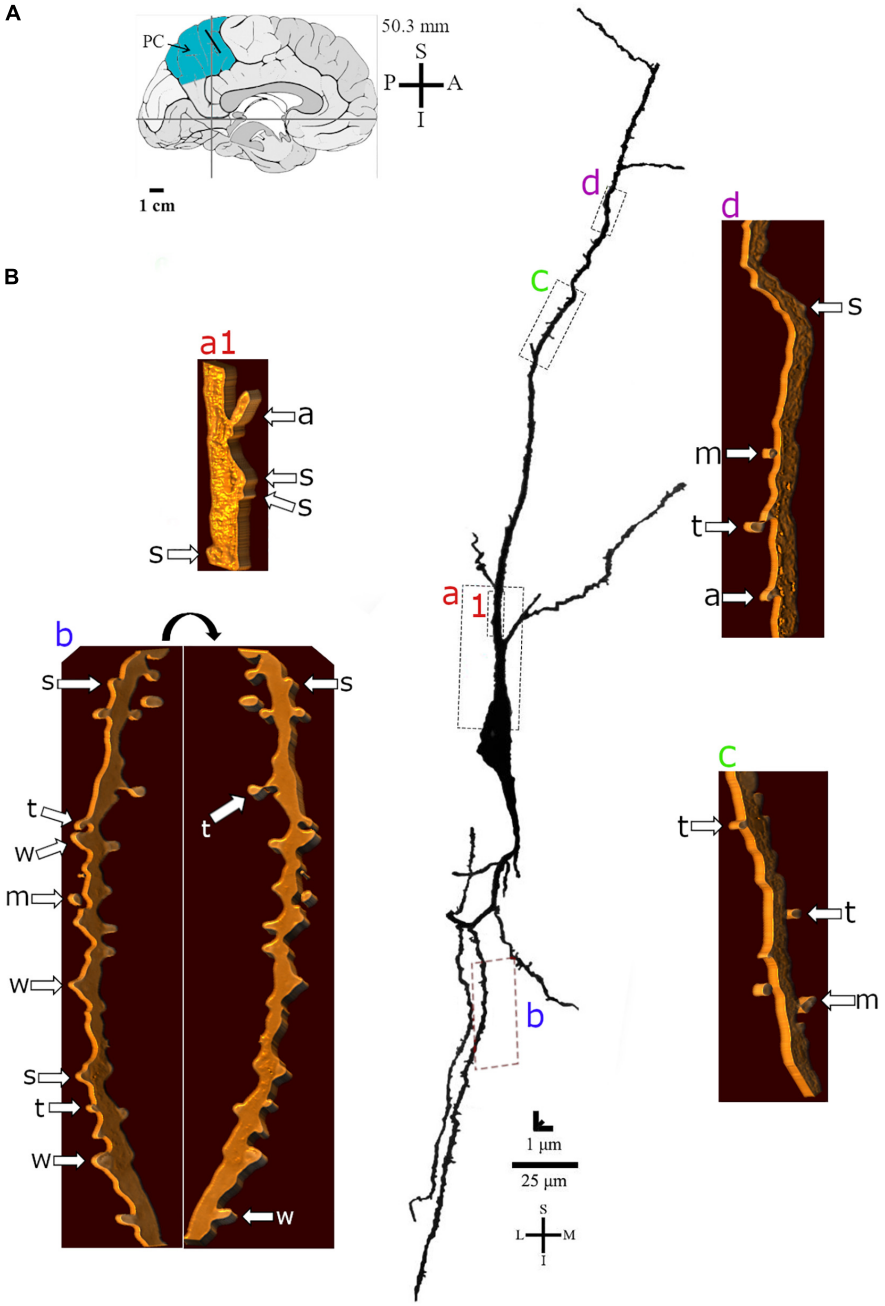

FIGURE 6 | (A) Left: Schematic drawing of the medial view of the human brain showing the location of the precuneus (PC, highlighted in blue), anterior region, 50.3 mm posterior to the midpoint of the anterior commissure. Adapted from Mai et al. (2008, 2016). **(B)** Two-dimensional (for the overall shape) and 3D (for the dendritic and spine details) image reconstructions of serial brightfield photomicrographs of a Golgi-impregnated spindle-shaped neuron from layer V in the human PC (pial surface at the top). Note the cell body shape, the main ascending and descending primary dendrites with a straight course and ramifications. Proximal to distal dendritic segments (identified by colored letters from "a" to "d") were sampled and their spines are shown at higher magnification in the adjacent corresponding boxes. Note the sparse distribution and density of spines. Spines were classified as stubby (s), wide (w), thin (t), mushroom (m), with a transitional (t), or atypical aspect (a). Spine types are indicated at different rotating angles. Image adjustment of contrast made with Photoshop CS3 (Adobe Systems, Inc., United States). Coordinates in **(A,B)**: I, inferior; L, lateral; M, medial; S, superior. Scale = 25 μm for the 2D reconstruction and 1 μm for the 3D reconstructions.

Using the Golgi results, we performed the 3D reconstruction of three spindle-shaped neurons found in layer V and in the transition to layer VI to evidence their dendritic and spines features in the human PC (**Figures 4–8**). The characteristic aspect of the cell body at different viewing angles and the preferred vertical orientation of the two main dendritic shafts of these cells are shown in **Supplementary Figures 1–3**. These neurons have a similar cell body shape, but show some differences in the

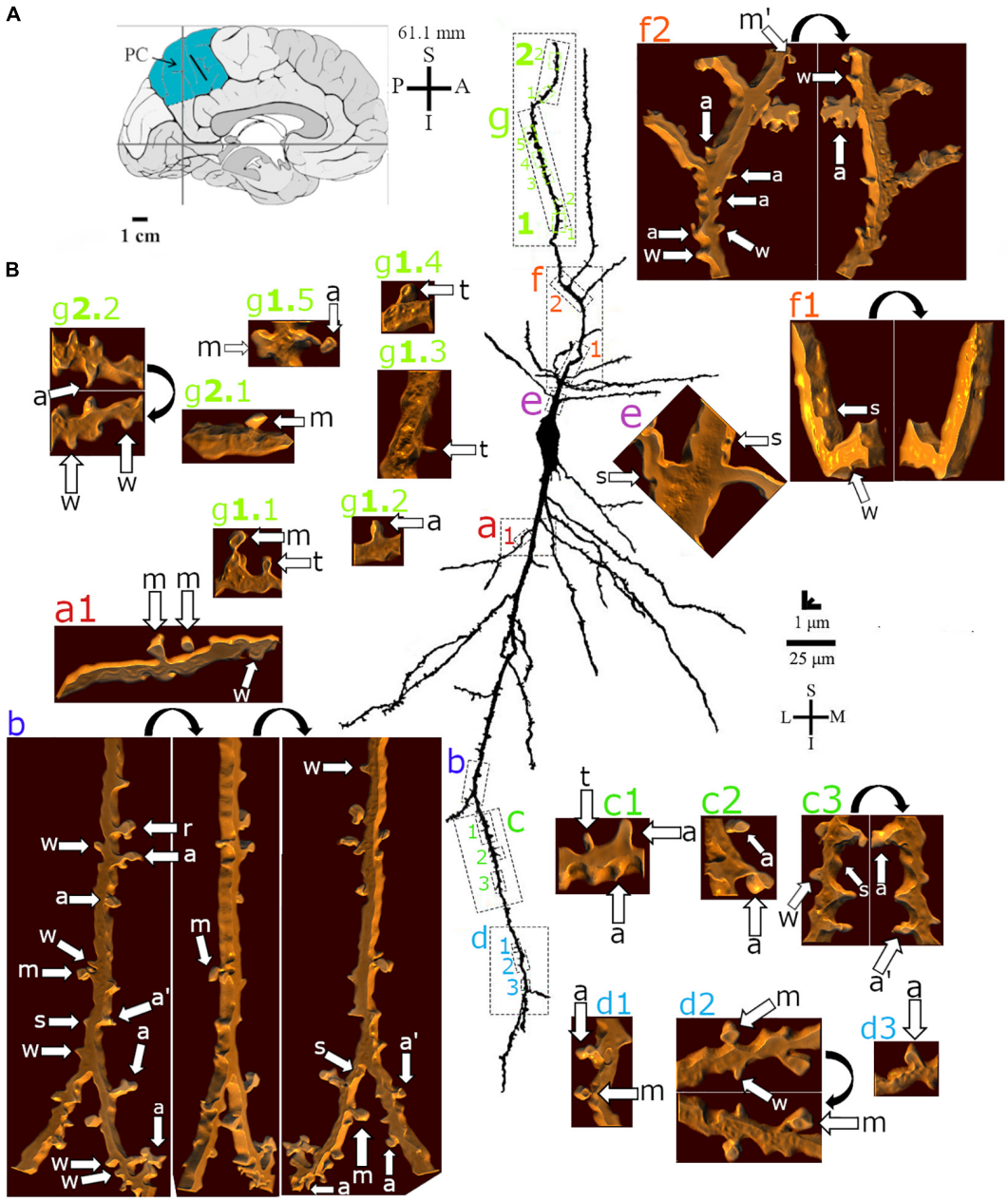

FIGURE 7 | (A) Left: Schematic drawing of the medial view of the human brain showing the location of the precuneus (PC, highlighted in blue), central region, 61.1 mm posterior to the midpoint of the anterior commissure. Adapted from Mai et al. (2008, 2016). **(B)** Two-dimensional (for the overall shape) and 3D (for the dendritic and spine details) image reconstructions of serial brightfield photomicrographs of a Golgi-impregnated spindle-shaped neuron in the layer V in transition to layer VI in the human PC (pial surface at the top). Note the cell body shape, the main ascending and descending primary dendrites with more profuse branching points and radial ramifications. Proximal to distal dendritic segments (identified by colored letters from "a" to "g") were sampled and their spines are shown at higher magnification in the adjacent corresponding boxes. Note the distribution of low to moderate density of spines as well as the variety of their shapes. Spines were classified as stubby (s), wide (w), thin (t), mushroom (m), ramified (r), with a transitional (t), or atypical aspect (a). Dendritic segments and spine types are indicated at different rotating angles. An apostrophe with the corresponding spine indicates the presence of a spinule. Image adjustment of contrast made with Photoshop CS3 (Adobe Systems, Inc., United States). Coordinates in **(A,B)**: I, inferior; L, lateral; M, medial; S, superior. Scale = 25 µm for the 2D reconstruction and 1 µm for the 3D reconstructions.

dendritic branching pattern (**Figures 4–8**). That is, although they have two main longitudinal ascending and descending shafts with a straight course, dendrites varied in the number and aspect of the collateral branches (**Figure 8** for comparison). Spindle-shaped neurons can have few collateral dendritic branches with an oblique orientation (**Figures 5**, **6**) or display more profuse ramification in both ascending and descending dendrites and collateral branches with a higher radial extension (**Figure 7**).

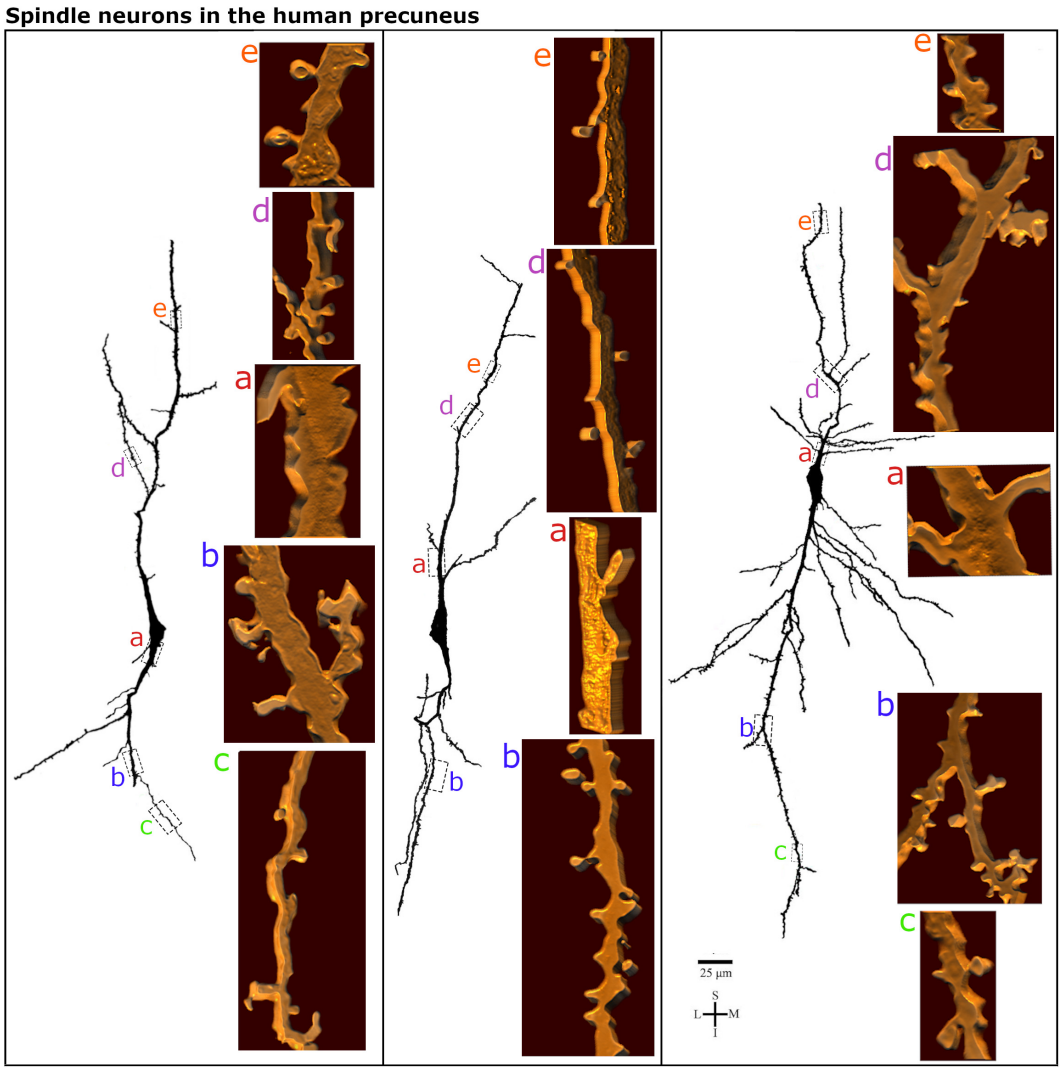

Cell body			
Axial lenght (µm)	33.7	35.7	34.6
Maximum diameter (µm)	9.8	9.7	14.8
Area (µm^2)	627.4	761.1	1083.7
Volume (µm^3)	1068.7	1437.1	2830.9
Dendrites			
Number of branches	32	30	61
Maximum diameter (µm)	3.7	4.5	8.7
Total dendritic lenght (µm)	836.8	957.5	2450.3
Total dendritic area (µm^2)	3328	3364	10213.2
Total dendritic volume (µm^3)	1311.8	1197.5	4135.5

FIGURE 8 | (Top) Comparison of the morphological features for the dendrites of spindle-shaped neurons in the human precuneus cortex shown in **Figures 5–7**. Compare the branching pattern of the spindle-shaped cell in the right with the others. Pleomorphic spines are shown from proximal to distal segments in these cells. Image adjustment of contrast made with Photoshop CS3 (Adobe Systems, Inc., United States). **(Bottom)** Quantitative data were obtained from these cells. Morphometrical data refer to the cell body parameters (note the similar axial length) and features of both ascending and descending dendrites (note the values for the neuron in the right compared to the others).

Morphometric data were obtained to exemplify the present observations (**Figure 8**). It is also worth noting that the spindle-shaped neurons shown in **Figures 5–7** required 54, 142, and 31 serial *z* stacks (0.5 μm each) for their 3D reconstruction, respectively (**Supplementary Figures 1–3**). That is, these neurons can display a 3D dendritic extension restricted to the same vertical axis where the cell body is or can also exhibit obliquely oriented dendritic branches with a higher extension toward the surrounding volume. For example, the spindle-shaped neuron shown in **Figure 6** has more branches along the *z*-axis (and therefore needed more *z* stacks for its imaging), which is observed at different rotation angles after 3D reconstruction (**Supplementary Figure 2**).

Dendritic spines showed a variety of shapes and sizes intermingled in the same dendritic segments (**Figures 5e1**, **6b,d**, **7b**). Spine types ranged from small to large (**Figures 6a1,b**) with stubby, wide, thin, mushroom, ramified, transitional aspects or more complex shapes with different neck thickness and/or multiple bulbous structures (**Figures 5e1**, **7f2** right).

Mushroom spines showed heads with a bulbous or a perforated-like aspect (**Figure 5e1**, left). Spines with transitional or atypical aspects showed diverse shapes (**Figures 5b,c**, **7b,c2,d1**). Among them, there is a double spine with a neck and a bulb followed by a second neck giving rise to another ending bulb (**Figure 5c**, left image, "a" in the right side of the dendrite). Pleomorphic spines were found from proximal to distal ascending and descending dendrites, showing a sparse to moderate density toward more distal segments (**Figures 5–7**). Spines occurred either isolated or grouped (**Figures 5b,c**, **7b,f2**) in the main and collateral dendritic branches (**Figures 5b,e**, **6b,c**, **7b–d,g**). Spinules were also observed in different spine types (**Figures 5e1,f1**, **7b,c3**).

There were some additional features for the spindle-shaped neurons in layer V and in the transition to layer VI in the human PC. We have also observed a spindle-shaped neuron (longitudinal length and higher diameter of 37 and 19 μm, respectively) with straight dendritic branches devoid of main ramifications in both ascending and descending branches and with a moderate density of small spines (**Figure 9**), and another spindle-shaped neuron (longitudinal length and higher diameter of 38 and 19 μm, respectively) with a delicate axon emerging from the cell body, close to the descending primary dendrite, and with few spines along the dendritic shafts (**Figure 10**). The axon in this latter cell emerges from a short hillock, is directed to the inner cortical layer, has a tiny aspect and few ramifications at approximate right angles (**Figure 10**).

Lastly, Golgi-impregnated cells with varied cell body shapes occur in the polymorphic layer VI of the human PC (**Figures 11A,B**). Some fusiform cells are smaller than layer V spindle-shaped neurons (compare the scale bar in **Figure 11** and in **Figures 5–7**). For example, the cell body of two small fusiform neurons, measured after the cellular 2D reconstruction, had 18 and 20 μm for the longitudinal length and 8 and 9 μm for the higher diameter (**Figures 11A,B**, respectively). These neurons also show two vertically oriented primary dendrites arising from opposite somatic poles, but very short dendritic branches with a restrict extension in the neuropil (**Figure 11A**).

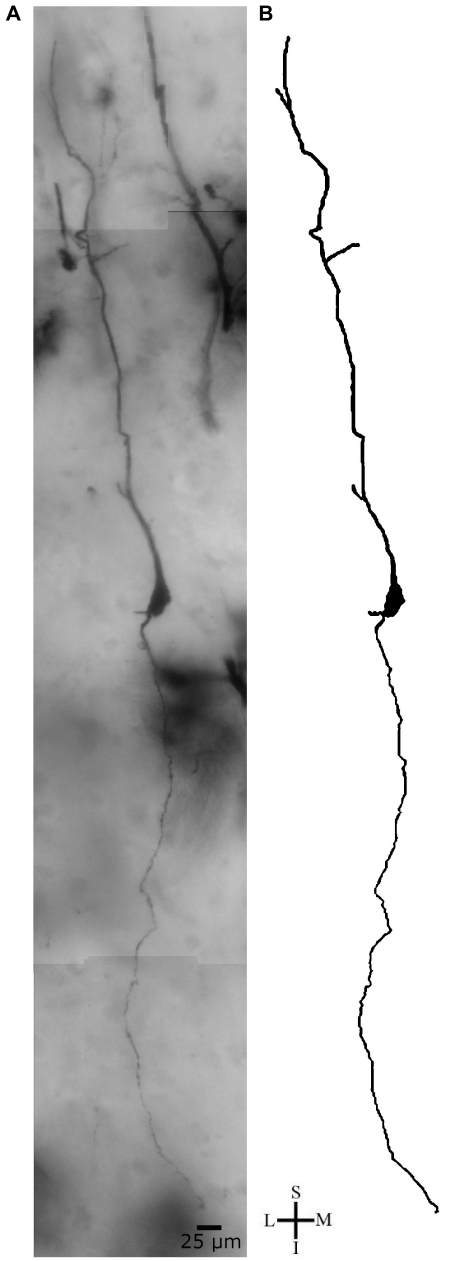

FIGURE 9 | (A) Photomicrographic composition of a Golgi-impregnated spindle-shaped neuron from layer V in the transition to layer VI in the human precuneus (central region, 61.1 mm posterior to the midpoint of the anterior commissure) observed using brightfield microscopy. **(B)** Two-dimensional image reconstruction of the same neuron in **(A)** (pial surface at the top). Note the cell body shape and the two main ascending and descending primary dendrites with rare branching points. Image reconstructed using the Neuromantic software (University of Reading, United Kingdom) with adjustment of contrast made with Photoshop CS3 (Adobe Systems, Inc., United States). Coordinates in **(A,B)**: I, inferior; L, lateral; M, medial; S, superior. Scale = 25 μm.

Some of the thin collateral branches radiate in various angles and show an oblique to horizontal projection (**Figure 11B**). Other fusiform cell displays two main primary dendritic shafts

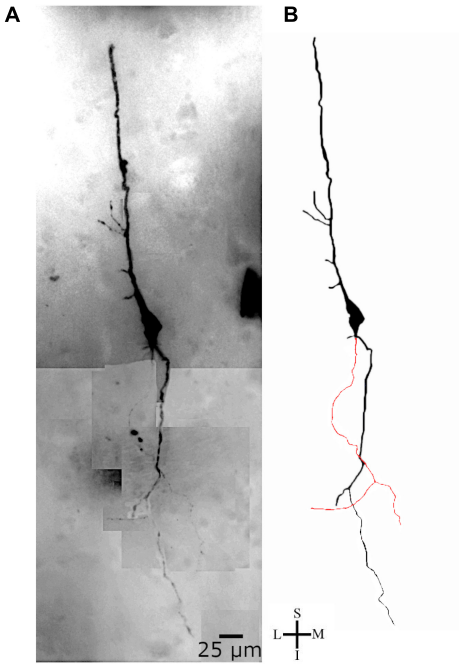

FIGURE 10 | (A) Photomicrographic composition of a Golgi-impregnated spindle-shaped neuron from layer V in the transition to layer VI in the human precuneus (central region, 61.1 mm posterior to the midpoint of the anterior commissure) observed using brightfield microscopy. **(B)** Two-dimensional image reconstruction of the same neuron in **(A)** (pial surface at the top). Note the cell body shape, two main ascending and descending primary dendrites with various branching points, and the presence of a delicate axon (colored in red) emerging from the soma, close to the descending dendrite, and ramifying at approximate right angles. Image reconstructed using the Neuromantic software (University of Reading, United Kingdom) with adjustment of contrast made with Photoshop CS3 (Adobe Systems, Inc., United States). Coordinates in **(A,B)**: I, inferior; L, lateral; M, medial; S, superior. Scale = 25 µm.

but also other small primary branches that alter the shape of the cell body (**Figure 11C**, neuron in dark). This latter cell was observed adjacent to a "modified pyramidal neuron" (MPN, according to Braak, 1980; **Figure 11C**, arrow head) in this inner layer. Interestingly, an elongated spindle- to rod-shaped neuron (longitudinal length and higher diameter of 41 and 16 µm, respectively) was found at the deeper part of layer VI in the PC (**Figure 12**). This spiny cell has two thick primary dendrites. The descending one is thicker than the ascending shaft, gives rise to two secondary branches with radially oriented collaterals, and a segment that appears to be the axon hillock. The ascending dendrite has a longer extension and some collaterals that radiate to the adjacent neuropil. There is a third dendritic branch, thinner than the others, emerging from the cell body and directed to the top of the section (**Figure 12**).

DISCUSSION

We describe the presence and the morphological features of Nissl-stained and Golgi-impregnated spindle-shaped neurons in the anterior and central regions of the PC in the human PMC. They were found close to pyramidal cells in the cortical layer V and in the transition to pleomorphic layer VI. In the PC, these spindle-shaped neurons display a similar cell body shape and two primary dendritic branches with a longitudinal spatial orientation as putative VENs described in other human brain areas (Nimchinsky et al., 1995; Allman et al., 2005, 2010; Watson et al., 2006; Fajardo et al., 2008; Cobos and Seeley, 2015; Raghanti et al., 2015). Nevertheless, the neurochemical and transcriptomic identity of these cells have to be determined to establish their definite classification. Here, we will discuss the morphology of VENs and critically compare our Golgi data with those from other authors (Watson et al., 2006; Banovac et al., 2019, 2021) as well as with other congruent approaches that have been used to identify human VENs in the ACC and FI. These PC layer V spindle-shaped neurons showed few dendritic branches in the main ascending and descending dendritic shafts or a more ramified aspect with collateral dendrites at different angles and extension along the surrounding neuropil. In addition, dendritic spines ranged from sparse to moderate from proximal to distal segments. We observed intermingled spines of varied shapes and sizes, as well as the presence of spinules after 3D reconstruction. These results would add to the cytoarchitecture and to the synaptic and information processing in the human PC integrated in multimodal networks relevant for the DMN and general intelligence (*g*) in the human brain. These findings also underscore the need for an in-depth characterization of these spindle-shaped (or putative VENs) in both healthy individuals and in neurological and psychiatric conditions involving the PC in the context of the PMC functioning, as commented below.

Neurons Might Be Classified as Von Economo Neurons by Concurring Techniques

There is an important current discussion on what can be considered a VEN based on morphological criteria (Nissl and Golgi techniques), after using *in situ* hybridization and immunohistochemistry assays for VEN-associated distinctive expression of cellular markers and/or by employing single nucleus RNA sequencing to obtain transcriptome data and to predict cellular functional properties. In a recent paper, Banovac et al. (2019) defined "VENs on Golgi staining as a neuron with the following morphological features: an elongated, stick-like cell body gradually continuing into thick apical and basal stem, a brush-like basal stem arborization and an axon origin distant from the cell body," i.e., at least 100 µm away from the cell nucleus. These authors also recommended that "the identification of von Economo's specialized cells in other cortical regions and non-primates should be done by demonstrating the dendritic and axonal morphology or by identifying specific markers or marker combinations that would enable the identification of VENs without relying solely on morphology" (Banovac et al., 2021).

Let us comment on the current data that include the cell body, the dendritic and axonal morphology with the identification of VEN markers focusing in cells from the layer V of the human ACC and FI. We will exclude small fusiform or MPNs in layer VI from the present discussion. First, it is important to consider

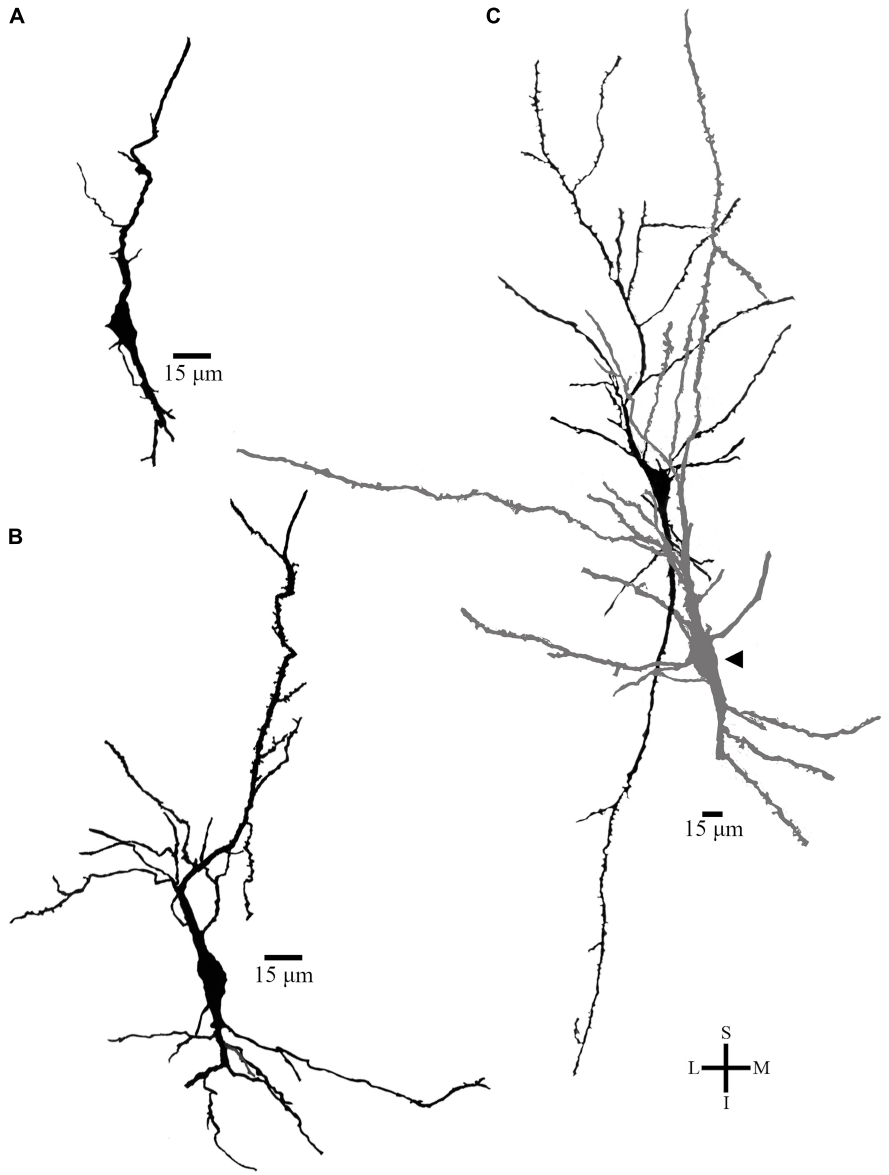

FIGURE 11 | (A,B) Two-dimensional image reconstruction of serial brightfield photomicrographs showing the overall shape of Golgi-impregnated neurons from the pleomorphic layer VI in the human precuneus (central region, 61.1 mm posterior to the midpoint of the anterior commissure, pial surface at the top). Note the fusiform cell body shape, short ascending, and descending primary dendrites with variable ramification and collateral branches. In **(C)**, a different fusiform cell (in dark) displays two main primary dendritic shafts but also some additional small primary branches that alter the shape of the cell body. The arrow points to a "modified pyramidal neuron" (in gray) according to Braak (1980). Note the scale bar for this figure and compare it to the ones presented for layer V spindle-shaped neurons in this same brain area (**Figures 5–8**). Image adjustments made with Photoshop CS3 (Adobe Systems, Inc., United States).

that von Economo and Koskinas identified "VENs" in humans using the Nissl staining (see Figures 4 and 5 in Banovac et al., 2021). That is, it was the cell body shape, its relative size compared to adjacent cells, and the aspect of two main primary dendrites of these neurons located in the layer V of restricted brain areas that led to the identification of "VENs as VENs." The "stick- or corkscrew-shaped cell body were clearly distinguishable from other spindle-shaped cells found throughout the cerebral cortex" (Banovac et al., 2021). This cell body shape described by von Economo and Koskinas resembles the elongated soma of neurons previously drawn by Ramón y Cajal (Figure 1 from Banovac et al., 2021). However, it is also possible to observe a certain variability in the cell body shape of VENs drawn by Ramón y Cajal, including a likely "spindle" aspect (compare the cell body shape and the descending dendrites originating an evident axon in the four VENs marked as C and D in Figure 1 from Banovac et al., 2021; data from the FI of a 1-month-old human girl). Afterward, Nimchinsky et al. (1995) described Nissl-stained spindle neurons in the layer Vb of the human ACC with "…a basal dendrite that was at least as thick as its apical dendrite…." These "spindle

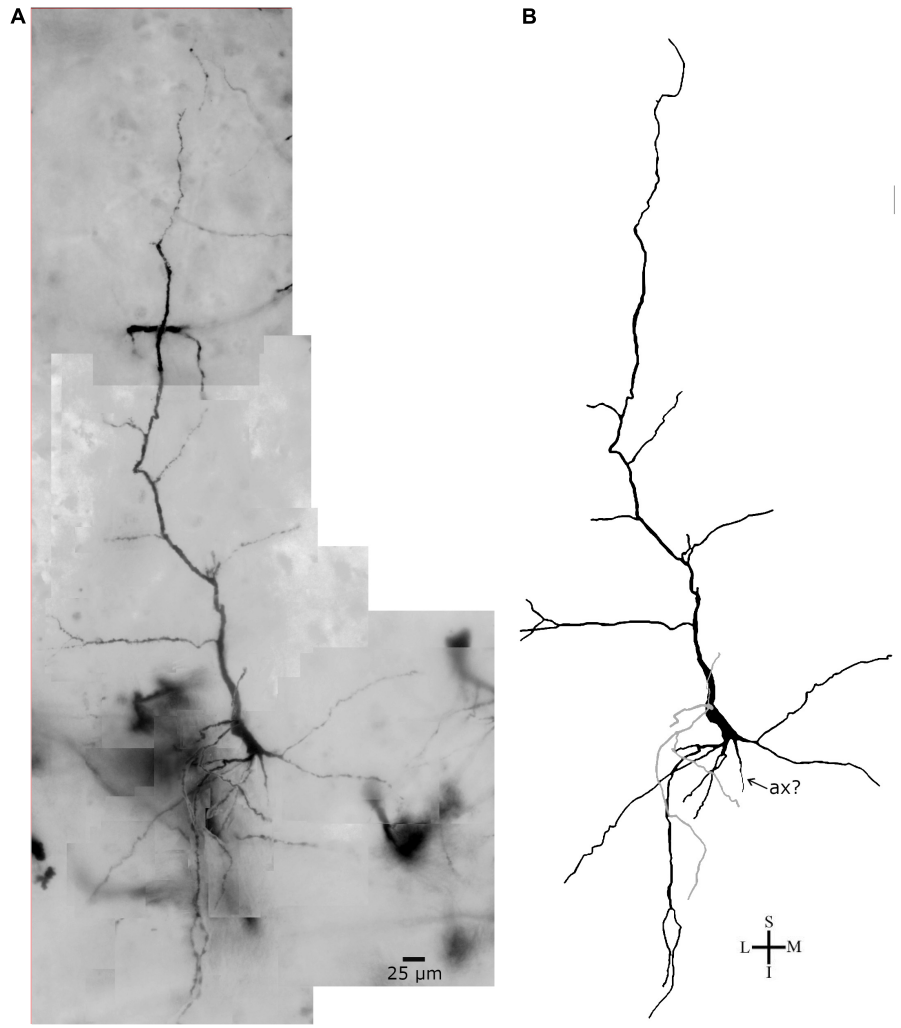

FIGURE 12 | (A) Photomicrographic composition of a Golgi-impregnated spindle- to rod-shaped neuron from the inner layer VI in the human precuneus (central region, 61.1 mm posterior to the midpoint of the anterior commissure) observed using brightfield microscopy. **(B)** Two-dimensional image reconstruction of the same neuron in **(A)** (pial surface at the top). Note the elongated cell body shape, two main longitudinally oriented primary dendrites with various branching points, a third thinner primary dendrite arising from the cell body (colored in gray). Note the thick aspect of the descending primary dendrite, its ramification in secondary branches, and a process that would be an axon hillock (ax, indicated by an arrow). The axon extent or its ramification are not visible. Image reconstructed using the Neuromantic software (University of Reading, United Kingdom) with adjustment of contrast made with Photoshop CS3 (Adobe Systems, Inc., United States). Coordinates in **(A,B)**: I, inferior; L, lateral; M, medial; S, superior. Scale = 25 µm.

neurons were readily distinguishable from pyramidal neurons and exhibited a variety of morphologies. Some were very slender and elongate, with apical and basal dendrites nearly as thick as the soma at its widest point. Others were shorter, more stout, and usually curved. Occasionally, neurons were encountered with a bifid basal dendrite or a third major dendrite emerging from the soma. In addition, lipofuscin deposits were common and were occasionally so large that they distorted the shape of an otherwise very slender neuron... The significance of this cellular variability is not clear, but it might be related to the cytoarchitectonic variability in this region..." (see additional examples in Figure 4D from Jacot-Descombes et al., 2020).

While maintaining the particular elongated somatic aspect and two main primary dendrites at opposite somatic poles, some variability for the rod and spindle shapes of the cell body of putative VENs in cortical layer V could be observed using additional techniques in human samples (e.g., for transcriptomic-related data, see Figure 1a, right image, and Figures 2b and 2c in Hodge et al., 2020; Figure 1A for the rod and spindle cell body shape of neurons expressing specific genes shown in Figures 4B′ and C′ in Yang et al., 2019; for the different immunocytochemical stainings of VENs, including cell body shape and primary dendrites, see Figure 3 in Allman et al., 2005; the cell body variability in Figures 10B and 11B in Allman et al., 2010; the somatic shape and primary dendrites in Figures 3D and 3F as well as the immunohistochemistry images in Figures 4D and 4F in Dijkstra et al., 2018; and, the immunostaining pattern shown in Figures 2A and 2B in Stimpson et al., 2011). Human

PC neurons are also examples of some spindle-shaped cells in the human brain in Figure 3A (Correa-Júnior et al., 2020), and this cell body feature directed further study of the ACC VENs shown in Figures 3B–D and Figures 4–8 in this report. Also worth noting are the cell body shape of a NeuN/SMI-32 double-immunolabeled VEN shown in Figure 11B in Banovac et al. (2019), the cell body shapes of presumed VENs after *in situ* mRNA hybridization (and high level expression) of FEZF2 in the FI layer V (Figure 4D″ in Cobos and Seeley, 2015), and the fact that, using Golgi-Cox sections to identify VENs in the deep part of layer V and the upper part of layer VI in the human ACC, "most VENs had a more spindle-shaped cell body, and the point of demarcation between the soma and the stems was more apparent" (Banovac et al., 2019).

These findings would accompany the distinction made when classifying VENs, bipolar ovoid and rhomboid-shaped cell bodies or, if one considers the various results for putative VENs in cortical layer V, the identification of human VENs with a cell body shape with some variability between stick-like or rod and spindle shapes, for example. There is also some similarity between the cell body shape (used as the morphological parameter in this case) of a layer V "VEN" included in the original study of von Economo and Koskinas (shown in the bottom left of Figure 4 in Banovac et al., 2021) and the "bipolar" neuron (not considered a "VEN") shown in Figure 10A (leftmost neuron) from Banovac et al. (2019). A parallel discussion could be done on VENs shapes and markers in the macaque monkey (e.g., see Figures 2A and D–G, and Figures S1 E′, F′, and F″ in Evrard et al., 2012). Moreover, the 3D reconstruction is a useful procedure that can provide complementary data to 2D images. When observed at different rotation angles, the cell body shape of the same 3D reconstructed Golgi-impregnated VEN can show a spindle-shape or a slender aspect (for example, see the three Supplementary Figures in 3D animation in Correa-Júnior et al., 2020 and the present **Supplementary Figures 1–3**).

Von Economo neurons, fork cells, and a subset of pyramidal cells are transcriptomically similar to one another in the human FI (Hodge et al., 2020), and layer V VENs express some markers that can also be found in fork cells and large pyramidal neurons in the human ACC or FI (Allman et al., 2010; Stimpson et al., 2011; Dijkstra et al., 2018). A within cell class phenotypic variability may occur for VENs since not all of them are immunolabeled by the same marker at the same time in the FI layer V (see Figure 11B in Allman et al., 2010; Cobos and Seeley, 2015). These data would question how layer V VENs are a morphological diversification of an evolutionarily conserved cell type, a morphological modification of pyramidal neurons (as a spindle-transformed cell) or represent a regionally distinctive and selectivelly evolved specialized cell type in the human cerebral cortex (Allman et al., 2005; Cobos and Seeley, 2015; Banovac et al., 2019, 2021; Yang et al., 2019; Hodge et al., 2020).

Notably, thick-tufted layer V pyramidal neurons are a heterogeneous class of cells, but are morphologically different from their neighboring VENs (Watson et al., 2006; compare with Ramaswamy and Markram, 2015; Cembrowski and Spruston, 2019; Rasia-Filho et al., 2021); see also comments on the likely coexistence of discrete and continuous variations that underlie cell-type diversity in BRAIN Initiative Cell Census Network (BICCN), 2021. VENs emerge mainly after birth, increase in number until age 4 years (Allman et al., 2005), and can be susceptible to alterations in some neuropsychiatric disorders (as described below). Compared to pyramidal neurons, a recent transcriptomic profile study identified 344 genes with VEN-associated expression in the human ACC, including 215 higher and 129 lower expression genes, some for morphogenesis, dendritic branching and axon myelination or for neurological and psychiatric disorders in humans (Yang et al., 2019). Human ACC VENs have four lower expression genes (HPCA, HPCAL1, RALGDS, and NUBP2) that directly interact with RHOA, an important regulator of dendritic morphogenesis (Yang et al., 2019). Accordingly, "the single large basal dendrite of VEN might have resulted from a transformation of the genetic programs during evolution for pyramidal neuron development to modify the basal dendrite in order to concentrate its growth in the primary component and suppress the secondary and tertiary branching" (Yang et al., 2019 and references therein). In these cells, the MEF2C high expression is also expected to reduce the density of dendritic spines, whereas many myelination-related genes (such as MBP and PLP1) showed VEN-increased expression (Yang et al., 2019). This latter would make difficult the reliable identification of the VEN axon and to trace its pathway and ramification after myelinization using the Golgi method, specially in samples obtained from adults. Some of these proposed implications for selective gene expression are supported by the morphological data obtained on dendrites and spines of putative VENs, compared to pyramidal neurons, in the human ACC reported by Watson et al. (2006).

As occurs for the cell body shape, VENs would also display heterogeneity in the dendritic architecture. Banovac et al. (2019) proposed the division of VENs in two groups based on peak total dendritic length, i.e., small VENs with 1500–2500 μm, and large VENs with 5000–6000 μm. Correa-Júnior et al. (2020) suggested a *continuum* of branching patterns. Therefore, it would be interesting to consider how dendrites and spines can alter their shape, even within the same class of neuron, due to region-specific specializations and according to the local processing of the synaptic demand from different neural circuits. For example, there are clear variations in the branching pattern of basal dendrites, the length and distal apical ramification with a tuft aspect if pyramidal neurons are located in the superficial or deeper parts of the layer V in the rat frontal cortex (Morishima and Kawaguchi, 2006). Human pyramidal neurons also show a heterogeneity in dendritic morphology with four different main apical branching patterns in the hippocampal CA1 area (Benavides-Piccione et al., 2020). The axon in these cells can emerge either from the soma (66% of the cases) or from the initial portion of a basal dendrite (44% of the cases; Benavides-Piccione et al., 2020). Therefore, it would be plausible that a certain degree of plasticity and heterogeneity would also occur for VENs in specific areas, including the morphological features of their cell body shape (as mentioned above), dendritic branching, and spine features in the human brain. The 3D reconstruction of Golgi-impregnated VENs located in the layer V of the human ACC indicates a

continuum of dendritic and spine heterogeneity, ranging from less ramified to more branched ones, also including the presence and density of pleomorphic dendritic spines (Correa-Júnior et al., 2020). As mentioned in Cobos and Seeley (2015), "human VENs may be a heterogeneous population comprising projection neurons with diverse targets including the contralateral cortex." These are possibilities that deserve further development and interpretation with the available morphological data (Watson et al., 2006; Banovac et al., 2019, 2021; Correa-Júnior et al., 2020).

Let us consider again the fact that the cell body shape and the aspect of the primary dendrites served to identify putative VENs in the layer V of ACC and FI using different histological, neurochemical and transcriptomic markers, although there is not a single specific marker for these cells currently. Watson et al. (2006) used the characteristic cell body shape as one criteria for the identification of layer V human VENs, as follows: "The criteria for classifying a neuron as a VEN was an elongated, large soma in layer 5 of the FI or ACC, a prominent basal dendrite, and symmetrical morphology along the horizontal and vertical axes of the cell. . . . We further constrained the category to include only those neurons that had no additional dendrites or branching for a half-soma's distance along the length of the proximal dendrites." Even with this inclusion criteria, it would be that neurons in the layer V of the ACC shown in Watson et al. (2006) or in Correa-Júnior et al. (2020) are not identical to the MPN in the layer V of the prefrontal cortex (shown in Figure 3, right side, from Banovac et al., 2021). The neuron shown in Banovac et al. (2021) is a spindle-shaped cell with two ascending and descending dendrites devoid of any ramification along their long course, whereas the spindle-shaped neuron in Figure 4 from Correa-Júnior et al. (2020) displays a sparse ramification and no visible axon hillock arising from the cell body, for example. On the other hand, one spindle-shaped neuron in the PC (**Figure 9**) has both dendrites with a straight course and a scarce radial arborization, apparently more restricted than the neuron shown as a VEN in the ACC by Watson et al. (2006; shown in **Figure 4B**). This PC neuron would resemble the dendritic features of the neuron classified as a prefrontal MPN by Banovac et al. (2021; shown in **Figure 3**, right side). Let us also remember that VENs have been considered a subclass of MPNs (Banovac et al., 2019).

The description of the tuft aspect of the descending dendritic branches, from where the axon is observed (Banovac et al., 2019, 2021), is an important morphological feature evidenced in the original Golgi study of VENs, and the efforts to look for these specific cells in the human brain are impressive (Banovac et al., 2021). Notwithstanding, additional images for the descending dendrites in putative VENs have been reported. For example, an elongated rod-shaped neuron, classified as VEN and labeled with an antibody to vasopressin 1a receptor in the ACC of an adult male human, displayed a main descending dendrite with no tuft or brush-like branches (visible along approximately 100 μm in Figure 3a in Allman et al., 2005). The same was found for two layer V rod-shaped and spindle-shaped VENs in the FI of a human male after immunocytochemical staining for DISC-1 (showing a straight descending dendrite visible along approximately 100 μm in the left neuron in the Figure 11B from Allman et al., 2010) and for a rod-shaped neuron stained for neuromedin B (with a straight descending dendrite visible along approximately 125 μm in Figure 10C in Allman et al., 2010). Hodge et al. (2020) provided the transcriptomic evidence that VENs are regionally specialized extratelencephalic-projecting excitatory neurons and included a biocytin-filled putative layer V VEN from the FI of an adult human in their report. This is the first electrophysiological single neuron patch clamp recording for human putative VENs, whose data were obtained from *ex vivo* peri-tumor insula tissue brain slices from a single human donor. These authors described some distinctive intrinsic membrane properties for putative VENs relative to neighboring pyramidal neurons. The local putative VEN had "the expected large spindle-shaped morphology with large caliber bipolar dendrites that extended into layer 6 (descending trunk), as well as toward the pial surface into upper layer 3 (ascending trunk). Dendritic branching was very simple, but with notable short and wispy lateral branches concentrated proximal to the soma. The axon could not be readily distinguished from these finer dendrites" (shown in Figure 5C in Hodge et al., 2020). Considering the likelihood of morphological heterogeneity within the same class of neurons (e.g., as occurs in pyramidal ones, Cembrowski and Spruston, 2019; Benavides-Piccione et al., 2020; Rasia-Filho et al., 2021), it would be plausible to consider that the description of some morphological variability for the dendrites of VENs would not be conflicting; rather, they would be complementary to the original descriptions of these cells. The integration of multiple approaches and criteria are need to reach a consensus in this field (Banovac et al., 2021).

There are few data on the axonal morphology of human VENs (but see relevant figures in Banovac et al., 2019, 2021). The adapted Golgi method used here for human *postmortem* brain (Dall'Oglio et al., 2010, 2015; Vásquez et al., 2018; Rasia-Filho et al., 2021) does not always provide the identification of the axon to trace its origin and ramification, which was also mentioned in Correa-Júnior et al. (2020). We described the diffuse axonal pattern (which would imply that the observed fibers would be not myelinated) in the neuropil of the human medial amygdaloid nucleus, and identified the axon hillock emerging from the cell body or in close primary dendrite in some local cells using this same Golgi technique (Dall'Oglio et al., 2013). However, the aspect of the axon is a limitation in the present study. In our samples (**Figures 4**–**7**), we were not confident to determine that a segment with varied tapering aspect would be an axon arising from a distal dendrite without having additional morphological evidence for the axonal diameter, angle of ramification, and caliber after branching (as shown by Ramón y Cajal in Figure 1 from Banovac et al., 2021) or having other supporting data from immunolabeled components of the axonal cytoskeleton, anterograde or retrograde tracing, intracellular dye, and/or electrophysiological recordings.

On the other hand, there was a spindle-shaped neuron in the PC with an axon hillock arising from the cell body (**Figure 10**). This would characterize it as a MPN according to Banovac et al. (2021). It is very important to determine if all VENs in the human FI and ACC (and, then, for all VENs to be considered true "VENs" in other areas of the human cerebral cortex) must have an

axon arising from a brush-like basal stem arborization (Banovac et al., 2019, 2021). Most histological, immunocytochemical, *in situ* hybridization, single nucleus RNA sequencing, and electrophysiological data will have to be reconsidered according to these results and checked for these specific basal dendritic and axonal characteristics. Alternatively, there might be a growing body of evidence in the literature that would indicate that layer V stick-like, rod- and/or spindle-shaped neurons are likely phenotypes of VENs that, independently of the determination of the strict aspect for their dendritic branching pattern, have been congruently reported as specialized cells with functional implications and abnormalities in various neuropathological conditions (see Figure 2 in Seeley, 2008; the morphological aspect of the soma and proximal dendrites of VENs in Figure 7 from Raghanti et al., 2015; Figure 2A and data in Jacot-Descombes et al., 2020; and, Table 2 from Banovac et al., 2021).

The morphological description provided by Banovac et al. (2019, 2021) for VENs is an important piece for studying these cells. From other approaches, some variability in the spindle- to rod-shaped cell body or in the aspect of the descending dendrite of the cells identified as VENs were also obtained and/or are expected to occur. In this regard, the cellular components of the layer V of the PC represent an interesting area open to further research in the human brain. Here, spindle-shaped neurons might represent a spectrum that ranges from a morphology of two straight dendrites and rare ramification (**Figure 9**) or with an axon arising from the cell body (**Figure 10**) to a more profuse dendritic ramification, with various collateral branches and a radial extension, and no visible axon hillock in the cell body (**Figures 6**, **7**). There are some hypotheses to be considered. These two former cells would resemble the description of MPNs (Banovac et al., 2021), the others would be a subtype of VENs. It would be also possible that VENs would show heterogeneity in their dendritic features, including "simple" forms observed in the ACC (Watson et al., 2006) to small and large VENs in terms of total dendritic length (Banovac et al., 2019). The possibility that spindle-shaped neurons can be VENs is consistent with the visualization of this cell body type by Ramón y Cajal in the FI. The length and aspect of the descending dendrites of putative VENs would allow some heterogeneity, as observed in rod-shaped neurons with a straight descending dendrite immunolabeled with antibodies to vasopressin 1a receptor, DISC-1, and for neuromedin B (Allman et al., 2005, 2010), after patch clamp recording and intracellular dye injection of a putative VEN with a large spindle-shaped soma and with no descending dendritic tuft (Hodge et al., 2020), and in rod-shaped neurons with a brush-like basal stem arborization and an axon origin distant from the cell body (Banovac et al., 2019, 2021). It is possible that not all spindle-shaped cell body cells be defined as VENs (Banovac et al., 2021), but putative VENs in layer V would be spindle-shaped, rod-shaped, stick, or corkscrew cells with regional specializations as observed with concurring techniques and neurochemical, electrophysiological, transcriptomic, and neuropathological characteristics (Allman et al., 2005, 2010; Raghanti et al., 2015; Yang et al., 2019; Hodge et al., 2020; Jacot-Descombes et al., 2020).

To advance this field, *Patch-seq* transcriptomes, a method relying on sequencing somatic RNA of single patch-clamp-recorded neurons, would help to identify if neuron types previously considered homogenous would be set into distinct subtypes (Fuzik et al., 2016; see a description on the difficulties related to the electrophysiological study of human VENs in Hodge et al., 2020). Highly multiplexed, high-resolution brain-wide cell type mapping, and high-throughput spatially resolved transcriptomics approaches would provide data to integrate individual cell type variability and connectivity-mapping information in specific brain areas (Close et al., 2021). These complementary experimental approaches can contribute with relevant data toward a unified, consensual neuronal classification based on a high-throughput single-cell transcriptomic-based taxonomy, building a probabilistic definition (Yuste et al., 2020) of spindle-shaped neurons as VENs (or not) in different brain areas and testing for intra- and inter-type variability in the phenotype of VENs at different ages. Importantly, "…the existence of cell states, spatial gradients of phenotypes and mixtures of differences and similarities in cross-species comparisons present challenges to a discrete and categorical perspective on defining cell types. Prematurely adopting an inflexible definition of types will obscure the significance of observed phenotypic variability and its biological interpretation…" while might exist a "… core and intermediate cells or the description of a cell type as a continuous trajectory in transcriptomic space" (Yuste et al., 2020).

It will be also crucial to determine if VENs emerge by differentiation of a prior cell within a cortical layer or migrate along the development toward specific parts of the cerebral mantle (Allman et al., 2005). We will have to determine if VENs exist only in cortical layer V. If so, it is interesting to question whether the spindle- to rod-shaped neuron observed in the inner layer VI of the PC (**Figure 12**) would resemble the shape of a layer V VEN or represents another molecularly different neuronal type in this polymorphic layer.

Morphological Implications for Spindle-Shaped Neurons (or Putative Von Economo Neurons) in the Human Precuneus

Currently, there is no human or monkey neuron morphologically classified as VENs in the PC layer V available at the open database "NeuroMorpho.Org" (version 8.1.25, released 2021-07-22, content: 151,303 neurons), where 70 reconstructed neurons are labeled as pyramidal ones in the layer III of Brodmann parietal area 7a of the rhesus monkey, and 14 reconstructed neurons in the layer III of Brodmann parietal area 7a of the baboon and vervet monkeys (original references available at http://neuromorpho.org/KeywordResult.jsp?count=70&keywords=%22%20area%207a%22 and http://neuromorpho.org/KeywordResult.jsp?count=14&keywords=%22brodmann%20area%207%22). Indeed, the cellular complexity, the inherent difficulties, and the technical limitations for studying the human *postmortem* brain tissue were reported previously (e.g., Dall'Oglio et al., 2013; Reberger et al., 2018; Vásquez et al., 2018

and references therein; see also the effect of the embedding medium and tissue shrinkage in the VENs spiral-shaped and corkscrew aspect of primary dendrites in Banovac et al., 2019).

The emergence of VENs is not related to the relative brain size or encephalization of the studied species (Allman et al., 2010). There is a possibility that VENs might be associated with the mechanical challenges associated with larger, gyrencephalic brains along with other evolutionary adaptations (Jacob et al., 2021). Human VENs with sparse dendritic trees and symmetric ascending and descending main shafts were considered computationally simple compared to layer V pyramidal neurons, likely receiving few inputs within individual minicolumns for a rapid cortical radial signal transmission (Watson et al., 2006). Currently, VENs with particular neurochemical profiles, heterogeneous dendritic geometry and spine features can be part of a more complex scenario than previously perceived. VENs with more branched ascending and descending dendrites (Banovac et al., 2019; Correa-Júnior et al., 2020) can have additional biophysical properties with a higher surface for synaptic processing and plasticity modulated by pleomorphic spines. Together with the intrinsic properties of putative VENs' membrane (Hodge et al., 2020), the increased dendritic arbor might provide further possibilities for the connectivity repertoire, computational power, and elaboration of information by these cells, as described for other neuron types (Oakley et al., 2001; Wen et al., 2009; Spruston et al., 2013; Brunel et al., 2014; Eyal et al., 2016; Rollenhagen and Lübke, 2016).

Von Economo neurons express dopamine D3 and D5 receptors, serotonin-1b and −2b receptors (Watson, 2006), GABA receptor subunit θ, adrenoreceptor α-1A (Dijkstra et al., 2018), activating transcription factor 3 of the CREB protein family, interleukin-4 receptor, and neuromedin B with a possible connection of interoception/visceral states and social awareness (Allman et al., 2010; Stimpson et al., 2011; Raghanti et al., 2015). The distribution of transmitter receptors in more superficial or deeper cortical layers in the human PC ("7A of the superior parietal lobule") suggests that ascending and descending dendrites from layer V cells may be modulated by different excitatory and inhibitory synaptic inputs (Palomero-Gallagher and Zilles, 2019). It remains to be determined whether VENs have dendritic domains with different integrative, linear and non-linear properties, and specific neurochemically modulated firing pattern as well as if VENs have heterogeneous morphological and functional features related to their intracortical or extratelencephalic projections.

Furthermore, the presence, distribution, number, size, and shape of dendritic spines from proximal to distal dendritic segments in the PC spindle-shaped neurons need to be taken into account and compared to other VENs functional properties and electrophysiology in the future. Activity-driven changes in dendritic spines can occur in a region-specific manner and according to each network and neuron-specific synaptic demand, stability, and plasticity (Benavides-Piccione et al., 2002; Chen et al., 2011; Araya et al., 2014; Hayashi-Takagi et al., 2015; Kasai et al., 2021). The spine-free dendritic zones are important for the synaptic integration (Kubota et al., 2016), but spines can provide additional properties for the modulation of neural circuitries and balancing the multimodal information processing. Spines with different forms (including those with convoluted structure) can differ in their impact on the fine-tuned synaptic processing by having different postsynaptic density composition, number and type of postsynaptic receptors, subcellular components and organization, electrical and biochemical compartmentalization, clustering pattern, degree of cooperativity between adjacent spines and the parent dendrite, and impact on the neuronal voltage and output frequency (Rochefort and Konnerth, 2012; Yadav et al., 2012; Yuste, 2013; Stewart et al., 2014; Dall'Oglio et al., 2015; Tønnesen and Nägerl, 2016; Berry and Nedivi, 2017; Lu and Zuo, 2017; Nakahata and Yasuda, 2018). Spinules, also found in PC spindle-shaped neurons, are active functional elements for synaptic development and maintenance that add to the neuronal plasticity repertoire and rapid integration of signals (Petralia et al., 2018, 2021). For example, NMDA activation can increase spinule number, length, and contact with distal presynaptic elements (Zaccard et al., 2020). There is a new avenue for research to establish the functional relation of layer V spindle-shaped neurons within the local cytoarchitecture of PC, including the activity of adjacent pyramidal and other "non-pyramidal" neurons and glia cells, in this same and in the adjacent cortical layers where ascending and descending dendrites are present.

Possible Functional Implications for Spindle-Shaped Neurons (or Putative Von Economo Neurons) in the Precuneus Within Integrated Brain Networks

The possibility of existence of VENs in the human PC is compelling. Some interesting points deserve further discussion. That is, primates have evolved cognitive mechanisms to understand and analyze complex social interactions (Freiwald, 2020). Among the multiple cellular components with an intrinsic connectivity and functional networks in the human cerebral cortex (see further discussion in van den Heuvel et al., 2015), some large-scale circuits have been studied for their roles in resting state, attention and task-related activity or cognitive functions (Ng et al., 2016; Deming and Koenigs, 2020; Forlim et al., 2020; Kolb and Whishaw, 2021). High signal coherence within these networks makes the sub-components functionally coupled along varied timeframes (Ng et al., 2016 and references therein), such as in the DMN, which comprises the PC (Cavanna and Trimble, 2006) and the posterior cingulate cortex, the medial prefrontal cortex, and the bilateral intraparietal cortex/angular gyrus; in the "salience network" (SN), including the bilateral anterior insula and the dorsal ACC; and, in the "executive control network" (ECN) including the "frontoparietal network" (FPN) composed of bilateral middle frontal gyri and supramarginal gyri/inferior parietal lobe (Hidalgo-Lopez et al., 2021 and references therein), the intraparietal sulcus, and dorsal prefrontal cortex (Ptak, 2012; Deming and Koenigs, 2020). The PC was also included in the ECN/frontoparietal control system for moment-to-moment tasks (Kolb and Whishaw, 2021).

As a hub region of the human brain, the PMC components have been implicated in a broad array of cognitive and emotional

processes (Cavanna and Trimble, 2006; Cavanna, 2007; Yang et al., 2014; Zhang et al., 2014). Multimodal information processing is reflected in the patterns of functional connectivity of brain regions. The PMC can be subdivided into clusters exhibiting connectivity profiles that are positively and negatively correlated with areas of the DMN, with a gradual transition for the PMC's functional connectivity in the dorsal–ventral and anterior–posterior directions (Cauda et al., 2010). I.e., the dorsal–anterior parts were associated with regions subserving the control of attentional mechanisms, while the dorsal–posterior PMC, encompassing sections of Broadman areas 7 and 31, was identified as a constituent of a FPN related to visual–spatial motion control (Cauda et al., 2010). On the other hand, the ventral–anterior PMC-compartment (Broadman areas 23, 30, and 31) showed specific connections with a network strongly resemblant of the task-negative DMN, while the central-posterior PMC (containing parts of Broadman area 7) displayed links with a network related to visual information processing (Cauda et al., 2010). Employing diffusion tensor imaging and fiber tracking for the PMC, the dorsal–anterior PMC was linked up with sensorimotor areas whereas the dorsal–posterior portion was heavily tied to regions engaged in visual processing (Zhang et al., 2014). Another distinction was detected between the dorsal–central and dorsal–ventral PMC, with the former representing an associative area and the latter emerging as a transitional area between different circuitries as indicated by its highly varied set of cortical links (Zhang et al., 2014). The ventral-most section displayed extensive associations with limbic areas (Zhang et al., 2014). Taken together, these results underscore the PMC's relevance for a multitude of interacting, yet dissociable brain networks relevant for higher-level cognition. Notably, the human PC has one of the highest resting metabolic rates in the cerebral cortex and elaborates sensorimotor, visual, and cognitive/associative information (Margulies et al., 2009), also including self-centered mental imagery and consciousness (Cavanna, 2007), empathy and perspective-taking (Zebarjadi et al., 2021), working memory (altered in cases of mild cognitive impairment, MCI, Yokosawa et al., 2020), episodic memory retrieval (Cavanna and Trimble, 2006), and metacognition processing (Ye et al., 2018).

In accordance with its involvement in cognitive functions, the human PC has been found to play a role in *g* (both structurally and functionally, see Menary et al., 2013; Basten et al., 2015; Hilger et al., 2017; Takeuchi et al., 2018). The construct of *g*, which is best conceptualized as "a distillate obtained from many diverse abilities" (Jensen, 1998), is regarded as the single best predictor of scholastic and vocational achievements as well as other socially relevant outcomes (Gottfredson, 1997; Jensen, 1998). Due to its association with neurological variables (Penke et al., 2012; Gignac and Bates, 2017), *g* has become a major focus of investigation (Haier, 2016), and the influential "Parieto-Frontal Integration Theory" (Jung and Haier, 2007) posits that *g* is closely related to a task-invariant network comprising a circumscribed set of brain regions. Several lines of evidence support the existence of such a domain-general network (Basten et al., 2015; Hugdahl et al., 2015). Regions often implicated in the latter include prefrontal areas such as the dorsolateral prefrontal cortex, the ACC and anterior insula, as well as parietal areas such as the intraparietal sulcus and PC (Jung and Haier, 2007; Niendam et al., 2012; Basten et al., 2015; Assem et al., 2020; Martínez and Colom, 2021). As its prefrontal regions exhibit an intriguing overlap with those ones to which human VENs are restricted, the existence of VENs in the parietal portion of the "process-invariant network" associated with *g* has been predicted (Bruton, 2021). The plausibility of this prediction, suggested by the present findings, is underscored by the fact that the PMC has been shown to play a role in two intrinsic connectivity networks (ICNs) known to substantially relate to *g*: namely, the central executive network (CEN) and the DMN (Cauda et al., 2010; Utevsky et al., 2014; Dubois et al., 2018; Uddin et al., 2019). The ability to activate the CEN while efficiently deactivating the DMN has been found to predict higher levels of *g* and abilities known to be highly saturated with *g*, such as working memory (Anticevic et al., 2012; Basten et al., 2013; Gignac, 2014; Koshino et al., 2014; Sherman et al., 2014; Bruton, 2021; DeSerisy et al., 2021). Thus, the DMN's relevance for *g* may stem from the fact that the insufficient and inefficient attenuation of this network may interfere with the successful employment of externally oriented, task-related attentional resources – a task accomplished by the ECN (Anticevic et al., 2012; Basten et al., 2013; Hugdahl et al., 2015; Bruton, 2021).

In this context, Bruton (2021) elaborated another possibility regarding the functional role of human VENs integrated in brain circuits. It was hypothesized that VENs might contribute to the emergence of *g* by functioning as cerebral pacemakers that promptly establish the coherence of neuronal oscillations (Bruton, 2021). This conjecture is grounded in the "communication-through-coherence" hypothesis which contends that the interaction between connected neuronal populations is limited to temporal slots of synchronized oscillations (Fries, 2005, 2015). VENs would thus transmit rhythmic signal bursts across large distances that, after arriving at their targeted neuronal populations, entrain the latter to the signaled rhythm, thereby implementing oscillatory coherence. In this manner, VENs might function as so-called "herald neurons" which allow for the undelayed processing of subsequently arriving, more complex signals (Bruton, 2021). This conceptualization might also help to elucidate the VENs presumed role in switching between the anticorrelated ECN and DMN (Menon and Uddin, 2010; Bruton, 2021). These VENs would facilitate the unobstructed communication between critical frontal and parietal regions and subdivisions implicated in the ECN and DMN, respectively (Bruton, 2021). Instead of directly activating the ECN while disabling the DMN (Sridharan et al., 2008), VENs (as "herald neurons") would rapidly establish coherence of oscillations between core regions of both networks prior to the phase of actual switching, leading to more efficient functional dissociation and thus decreased DMN interference with task-relevant mental activity originating from the ECN (Anticevic et al., 2012; Bruton, 2021). The fact that different subdivisions of the PMC, including the PC, have been implicated in different ICNs (Margulies et al., 2009; Yang et al., 2014; Kolb and Whishaw, 2021) underlines the importance of efficient internetwork communication especially in this particular parietal

area to which VENs could significantly participate in (for additional data on PMC and PC connectome, tractography and white matter dissection, see Baker et al., 2018; Assem et al., 2020; Jitsuishi and Yamaguchi, 2021). An intriguing objective for future research would be to establish whether the observed variation in dendritic architecture and spine features of spindle-shaped neurons, if they are VENs, exhibit individual differences and whether they are correlated with human cognition as reflected by constructs such as *g*.

Vulnerability of Von Economo Neurons and the Pathological Findings Involving the Human Precuneus

The PC is also directly or indirectly affected by neuropsychiatric disorders in which VENs would show vulnerability or pathological involvement (Nimchinsky et al., 1995; Allman et al., 2001, 2005; Watson, 2006; Cauda et al., 2014; Raghanti et al., 2015; Jacot-Descombes et al., 2020). Putative VENs are affected in the behavioral variant of the frontotemporal dementia with hindered social–emotional functions (Seeley et al., 2006; Seeley, 2008; Santillo and Englund, 2014; Gami-Patel et al., 2019; Lin et al., 2019); in cases of agenesis of the corpus callosum with impairment in humor and judgment of scenes of social interactions; in the bipolar disorder (reviewed in Cauda et al., 2014; Raghanti et al., 2015) and autism spectrum disorder (Allman et al., 2005), and in familial dysautonomia with mood impairments (Jacot-Descombes et al., 2020).

Von Economo neurons were also related to schizophrenia (Krause et al., 2017). The protein encoded by the gene DISC1 (disrupted in schizophrenia) had an evolutionary change in the line leading to humans, is related to neuronal migration and dendritic branching, and is preferentially expressed by VENs (Allman et al., 2010; Cauda et al., 2014; see the GWAS atlas at https://atlas.ctglab.nl for current data on current DISC1 associations). In addition, reduced resting-state connectivity in the PC was correlated with apathy in patients with schizophrenia (Forlim et al., 2020). Apathy is a motivational disorder incurring reduced or loss of goal-directed behavior, goal-directed cognitive processes, and emotion (Forlim et al., 2020). In this regard, the PC connectivity was correlated with the severity of these symptoms and with alterations in the subjective experience of a continuous sense of the self, regarded as dysfunctional interactions between relevant brain regions (Forlim et al., 2020). On the other hand, in few cases when epilepsy originated in the PC there were heterogeneous ictal symptoms, including body movement sensation or body image disturbance, somatosensory and visual auras, vestibular manifestations, eye movements, complex motor behaviors, and bilateral asymmetric tonic and hypermotor seizures (Harroud et al., 2017; Yang et al., 2018).

A meta-analysis of functional MRI task-related activity of psychopathy drew attention to the increased activity predominantly in midline cortical regions overlapping with the DMN (i.e., dorsomedial prefrontal cortex, posterior cingulate, and PC) as well as with the medial temporal lobe (Deming and Koenigs, 2020). Psychopathy was negatively related to neural activity in dorsal ACC and was positively related to neural activity in a bilateral portion of medial parietal and occipital cortex (including posterior cingulate and PC), bilateral dorsomedial prefrontal cortex, right inferior frontal gyrus, right posterior orbitofrontal cortex, right medial temporal cortex (including amygdala), right hippocampus, and right parahippocampal gyrus (Deming and Koenigs, 2020). Whereas DMN increases activity during self-referential processing and decreases activity during externally focused, non-self-referential tasks, FPN increases activity during cognitively demanding, externally focused tasks (Deming and Koenigs, 2020). The SN, which is particularly important for detecting salient external stimuli, would be responsible for switching between the two anticorrelated networks, DMN and FPN (Deming and Koenigs, 2020). In psychopathy, both the DMN components posterior cingulate cortex and PC not only are overactive across a variety of tasks but also less functionally and structurally connected to other DMN regions, including dorsomedial and ventromedial prefrontal cortex and other regions of the FPN (Deming and Koenigs, 2020). One possibility is that psychopathic individuals fail to deactivate midline DMN regions during externally focused tasks and such failure could result in increased competition between DMN and externally oriented attention networks (such as FPN), disrupting the shift of attention to the external task, and leading to corresponding performance deficits (Deming and Koenigs, 2020).

The PC neurons and circuitries can also be damaged in Alzheimer's disease (AD; Gefen et al., 2018; Berron et al., 2020; but see also Nelson et al., 2009). Metabolic reduction or hypoperfusion of the PC can be found in the early stages of AD, even before clinical diagnosis of dementia (Thomas et al., 2019). It is possible that hypoperfusion begins largely in PC and spreads to the parietal cortex and cingulate gyrus along with progression of the AD to other cortical areas (Aghakhanyan et al., 2018). The PC is involved in working memory and its deactivation is associated with early MCI assessed by a validated clinical screening instrument for cognitive decline (Yokosawa et al., 2020). Moreover, the PC seems to be a region with high vulnerability to β-amyloid (Aβ) deposition, showing major Aβ load in Aβ-PET and in association with cognitive decline in MCI and AD patients compared with healthy controls (Aghakhanyan et al., 2018). White matter microstructure alteration occurs in the early stage of amyloid pathology and the strongest association was found in PC and the corpus callosum (Collij et al., 2021). The study of the cellular components of the PC and the timely diagnosis of an altered function in this brain area would direct new treatments to alleviate or prevent the progress of MCI and AD in the future.

In conclusion, we describe the presence of Nissl-stained spindle-shaped neurons in the anterior and central regions of the human PC with a cell body aspect in layer V compatible with putative VENs, as described in other brain areas. The Golgi morphological identity of these cells has now to be complemented with relevant neurochemical, electrophysiological, and transcriptomic-based identification

for unified cell type classification. Using the Golgi method, the PC spindle-shaped neurons in layer V and in the transition to layer VI have a dendritic architecture and spine diversity that suggest additional functional implications for the local cytoarchitecture and for the synaptic and information processing in integrated networks for higher-order activities (such as the DMN and *g*) in this multimodal complex area. Additional studies can elucidate the transcriptomic features of the PC spindle-shaped (or putative VENs) and compare them with other cells in the human ACC and FI, considering network circuits demands with particular local features and/or diversity in the morphological and functional cellular specializations in the human brain. This will be an important achievement also for the comprehension of neuropsychiatric disorders involving the PC in the context of the PMC functioning.

DATA AVAILABILITY STATEMENT

The datasets presented in this study can be found in online repositories. The names of the repository/repositories and accession number(s) can be found below: Raw data included in this manuscript were generated at the UFCSPA (Brazil) and are available from the authors. Data were originally presented and registered as a M.Sc. Thesis (2018) as follows: Fuentealba Villarroel, F.J. "Estudo sobre os neurônios de von Economo do pré-cúneo humano" (in Portuguese), Graduation in Neurosciences, Universidade Federal do Rio Grande do Sul (UFRGS), Brazil, publicly registered at https://www.lume.ufrgs.br/handle/10183/193616.

ETHICS STATEMENT

The studies involving human participants were reviewed and approved by the Brazilian Ethics Committee from the Federal University of Health Sciences of Porto Alegre (UFCSPA; #62336116.6.0000.5345, 18718719.7.0000.5345, and 06273619.7.0000.5345) and the Federal University of Rio Grande do Sul (#18718719.7.3001.5347). The next of kin of the patients/participants provided their written informed consent for brain donation during autopsy.

AUTHOR CONTRIBUTIONS

FJF-V, JR, AH, and AAR-F: study concept and design. FJF-V, JR, and AAR-F: acquisition of data and two-dimensional reconstructions. JR and AAR-F: three-dimensional reconstructions. FJF-V, JR, AH, OJB, and AAR-F: critical interpretation of data and discussion and elaboration of the manuscript. All authors contributed to the article and approved the submitted version.

FUNDING

Grants from the Brazilian Agencies CAPES and CNPq (Brazilian Ministry of Science Technology and Innovation "RRID"), Grant/Award Number: 314352/2020-1, SCR_002876. Support for article fee payment from the Universität Oldenburg, Oldenburg, Germany.

ACKNOWLEDGMENTS

Authors are thankful to Lucila L. Gutierrez and Nivaldo D. Correa-Júnior (UFCSPA, Brazil) for their participation in our first Golgi experiments, and to Diego Rovaris (USP, Brazil) for his advices on the use of the GWAS database.

SUPPLEMENTARY MATERIAL

The Supplementary Material for this article can be found online at: https://www.frontiersin.org/articles/10.3389/fnsyn.2021.769228/full#supplementary-material

Supplementary Figure 1 | Three-dimensional reconstruction of layer V Golgi-impregnated from the human precuneus cortex (corresponding to **Figure 5**).

Supplementary Figure 2 | Three-dimensional reconstruction of layer V Golgi-impregnated from the human precuneus cortex (corresponding to **Figure 6**).

Supplementary Figure 3 | Three-dimensional reconstruction of layer V and in the transition to layer VI Golgi-impregnated from the human precuneus cortex (corresponding to **Figure 7**).

Supplementary Figure 4 | Golgi-impregnated layer V pyramidal neuron from the human precuneus cortex (central region, 61.1 mm posterior to the midpoint of the anterior commissure).

REFERENCES

Aghakhanyan, G., Vergallo, A., Gennaro, M., Mazzarri, S., Guidoccio, F., Radicchi, C., et al. (2018). The precuneus – a witness for excessive Aβ gathering in Alzheimer's disease pathology. *Neurodegener. Dis.* 18, 302–309. doi: 10.1159/000492945

Allman, J. M., Hakeem, A., Erwin, J. M., Nimchinsky, E., and Hof, P. (2001). The anterior cingulate cortex. The evolution of an interface between emotion and cognition. *Ann. N. Y. Acad. Sci.* 935, 107–117. doi: 10.1111/j.1749-6632.2001.tb03476.x

Allman, J. M., Tetreault, N. A., Hakeem, A. Y., Manaye, K. F., Semendeferi, K., Erwin, J. M., et al. (2010). The von Economo neurons in frontoinsular and anterior cingulate cortex in great apes and humans. *Brain Struct. Funct.* 214, 495–517. doi: 10.1007/s00429-010-0254-0

Allman, J. M., Watson, K. K., Tetreault, N. A., and Hakeem, A. Y. (2005). Intuition and autism: a possible role for von Economo neurons. *Trends Cogn. Sci.* 9, 367–373. doi: 10.1016/j.tics.2005.06.008

Anticevic, A., Cole, M. W., Murray, J. D., Corlett, P. R., Wang, X. J., and Krystal, J. H. (2012). The role of default network deactivation in cognition and disease. *Trends Cogn. Sci.* 16, 584–592. doi: 10.1016/j.tics.2012.10.008

Araya, R., Vogels, T. P., and Yuste, R. (2014). Spine neck length and synaptic efficacy. *Proc. Nat. Acad. Sci. U.S.A.* 111, E2895–E2904. doi: 10.1073/pnas.1321869111

Arellano, J. I., Benavides-Piccione, R., DeFelipe, J., and Yuste, R. (2007a). Ultrastructure of dendritic spines: correlation between synaptic and spine morphologies. *Front. Neurosci.* 1:131–143. doi: 10.3389/neuro.01.1.1.010.2007

Arellano, J. I., Espinosa, A., Fairén, A., Yuste, R., and DeFelipe, J. (2007b). Non-synaptic dendritic spines in neocortex. *Neuroscience* 145, 464–469. doi: 10.1016/j.neuroscience.2006.12.015

Assem, M., Glasser, M. F., Van Essen, D. C., and Duncan, J. (2020). A domain-general cognitive core defined in multimodally parcellated human cortex. *Cereb. Cortex* 30, 4361–4380. doi: 10.1093/cercor/bhaa023

Baker, C. M., Burks, J. D., Briggs, R. G., Conner, A. K., Glenn, C. A., Manohar, K., et al. (2018). A connectomic atlas of the human cerebrum – chapter 8: the posterior cingulate cortex, medial parietal lobe, and parieto-occipital sulcus. *Oper. Neurosurg. (Hagerstown)* 15:S350–S371. doi: 10.1093/ons/opy262

Banovac, I., Sedmak, D., Džaja, D., Jalšovec, D., Jovanov Miloševiæ, N., Rašin, M. R., et al. (2019). Somato-dendritic morphology and axon origin site specify von Economo neurons as a subclass of modified pyramidal neurons in the human anterior cingulate cortex. *J. Anat.* 235, 651–669. doi: 10.1111/joa.13068

Banovac, I., Sedmak, D., Judaš, M., and Petanjek, Z. (2021). Von Economo neurons – primate-specific or commonplace in the mammalian brain? *Front. Neural Circuits* 15:714611. doi: 10.3389/fncir.2021.714611

Basten, U., Hilger, K., and Fiebach, C. J. (2015). Where smart brains are different: a quantitative meta-analysis of functional and structural brain imaging studies on intelligence. *Intelligence* 51, 10–27. doi: 10.1016/j.intell.2015.04.009

Basten, U., Stelzel, C., and Fiebach, C. J. (2013). Intelligence is differentially related to neural effort in the task-positive and the task-negative brain network. *Intelligence* 41, 517–528. doi: 10.1016/j.intell.2013.07.006

Benavides-Piccione, R., Ballesteros-Yáñez, I., DeFelipe, J., and Yuste, R. (2002). Cortical area and species differences in dendritic spine morphology. *J. Neurocytol.* 31, 337–346.

Benavides-Piccione, R., Regalado-Reyes, M., Fernaud-Espinosa, I., Kastanauskaite, A., Tapia-González, S., León-Espinosa, G., et al. (2020). Differential structure of hippocampal CA1 pyramidal neurons in the human and mouse. *Cereb. Cortex* 30, 730–752.

Berron, D., van Westen, D., Ossenkoppele, R., Strandberg, O., and Hansson, O. (2020). Medial temporal lobe connectivity and its associations with cognition in early Alzheimer's disease. *Brain* 143, 1233–1248. doi: 10.1093/brain/awaa068

Berry, K. P., and Nedivi, E. (2017). Spine dynamics: are they all the same? *Neuron* 96, 43–55. doi: 10.1016/j.neuron.2017.08.008

Bourne, J. N., and Harris, K. M. (2009). "Ultrastructural analysis of spine plasticity," in *Encyclopedia Of Neuroscience*, ed. L. R. Squire (New York, NY: Elsevier), 11–17. doi: 10.1016/b978-008045046-9.01771-x

Braak, H. (1980). *Architectonics of the Human Telencephalic Cortex*. Berlin: Springer-Verlag.

BRAIN Initiative Cell Census Network (BICCN) (2021). A multimodal cell census and atlas of the mammalian primary motor cortex. *Nature* 598, 86–102. doi: 10.1038/s41586-021-03950-0

Brunel, N., Hakim, V., and Richardson, M. J. R. (2014). Single neuron dynamics and computation. *Curr. Opin. Neurobiol.* 25, 149–155. doi: 10.1016/j.conb.2014.01.005

Bruner, E., Pereira-Pedro, A. S., Chen, X., and Rilling, J. K. (2017a). Precuneus proportions and cortical folding: a morphometric evaluation on diverse human sample. *Ann. Anat.* 211, 120–128. doi: 10.1016/j.aanat.2017.02.003

Bruner, E., Preuss, T. M., Chen, X., and Rilling, J. K. (2017b). Evidence for expansion of the precuneus in human evolution. *Brain Struct. Funct.* 222, 1053–1060. doi: 10.1007/s00429-015-1172-y

Bruner, E., Rangel de Lázaro, G., de la Cuétara, J. M., Martín-Loeches, M., Colom, R., and Jacobs, H. I. (2014). Midsagittal brain variation and MRI shape analysis of the precuneus in adult individuals. *J. Anat.* 224, 367–376. doi: 10.1111/joa.12155

Brusco, J., Merlo, S., Ikeda, ÉT., Petralia, R. S., Kachar, B., Rasia-Filho, A. A., et al. (2014). Inhibitory and multisynaptic spines, and hemispherical synaptic specialization in the posterodorsal medial amygdala of male and female rats. *J. Comp. Neurol* 522, 2075–2088. doi: 10.1002/cne.23518

Bruton, O. J. (2021). Is there a "g-neuron"? Establishing a systematic link between general intelligence (g) and the von Economo neuron. *Intelligence* 86, 101540. doi: 10.1016/j.intell.2021.101540

Cajal, R. (1909-1911). *Histologie Du Système Nerveux De L'homme Et Des Vertébrés*. Paris: Maloine.

Carrabba, L. H. G., Menta, C., Fasolin, E. M., Loureiro, F., and Gomes, I. (2015). Características psicométricas das versões completa e reduzida do IQCODE-BR em idosos de baixa renda e escolaridade. *Rev. Bras. Geriat. Gerontol.* 18, 715–723. doi: 10.1590/1809-9823.2015.14034

Cauda, F., Geminiani, G. C., and Vercelli, A. (2014). Evolutionary appearance of von Economo's neurons in the mammalian cerebral cortex. *Front. Hum. Neurosci.* 8:104. doi: 10.3389/fnhum.2014.00104

Cauda, F., Geminiani, G., D'Agata, F., Sacco, K., Duca, S., Bagshaw, A. P., et al. (2010). Functional connectivity of the posteromedial cortex. *PLoS One* 5:e13107. doi: 10.1371/journal.pone.0013107

Cavanna, A. E. (2007). The precuneus and consciousness. *CNS Spectr.* 12, 545–552. doi: 10.1017/S1092852900021295

Cavanna, A. E., and Trimble, M. R. (2006). The precuneus: a review of its functional anatomy and behavioral correlates. *Brain* 129, 564–583. doi: 10.1093/brain/awl004

Cembrowski, M. S., and Spruston, N. (2019). Heterogeneity within classical cell types is the rule: lessons from hippocampal pyramidal neurons. *Nat. Rev. Neurosci.* 20, 193–204. doi: 10.1038/s41583-019-0125-5

Chen, X., Leischner, U., Rochefort, N. L., Nelken, I., and Konnerth, A. (2011). Functional mapping of single spines in cortical neurons in vivo. *Nature* 475, 501–505. doi: 10.1038/nature10193

Close, J. L., Long, B. R., and Zeng, H. (2021). Spatially resolved transcriptomics in neuroscience. *Nat. Methods* 18, 23–25. doi: 10.1038/s41592-020-01040-z

Cobos, I., and Seeley, W. W. (2015). Human von Economo neurons express transcription factors associated with Layer V subcerebral projection neurons. *Cereb. Cortex* 25, 213–220. doi: 10.1093/cercor/bht219

Collij, L. E., Ingala, S., Top, H., Wottschel, V., Stickney, K. E., Tomassen, J., et al. (2021). White matter microstructure disruption in early stage amyloid pathology. *Alzheimers Dement.* 13:e12124. doi: 10.1002/dad2.12124

Correa-Júnior, N. D., Renner, J., Fuentealba-Villarroel, F., Hilbig, A., and Rasia-Filho, A. A. (2020). Dendritic and spine heterogeneity of von Economo neurons in the human cingulate cortex. *Front. Synapt. Neurosci.* 12:25. doi: 10.3389/fnsyn.2020.00025

Craig, A. D. (2009). How do you feel now? The anterior insula and human awareness. *Nat. Rev. Neurosci.* 10, 59–70. doi: 10.1038/nrn2555

Dall'Oglio, A., Dutra, A. C., Moreira, J. E., and Rasia-Filho, A. A. (2015). The human medial amygdala: structure, diversity, and complexity of dendritic spines. *J. Anat.* 227, 440–459. doi: 10.1111/joa.12358

Dall'Oglio, A., Ferme, D., Brusco, J., Moreira, J. E., and Rasia-Filho, A. A. (2010). The "single-section" Golgi method adapted for formalin-fixed human brain and light microscopy. *J. Neurosci. Methods* 189, 51–55. doi: 10.1016/j.jneumeth.2010.03.018

Dall'Oglio, A., Xavier, L. L., Hilbig, A., Ferme, D., Moreira, J. E., Achaval, M., et al. (2013). Cellular components of the human medial amygdaloid nucleus. *J. Comp. Neurol.* 521, 589–611. doi: 10.1002/cne.23192

Deming, P., and Koenigs, M. (2020). Functional neural correlates of psychopathy: a meta-analysis of MRI data. *Transl. Psychiatry* 10:133. doi: 10.1038/s41398-020-0816-8

Denny, B. T., Kober, H., Wager, T. D., and Ochsner, K. N. (2012). A meta-analysis of functional neuroimaging studies of self- and other judgments reveals a spatial gradient for mentalizing in medial prefrontal cortex. *J. Cogn. Neurosci.* 24, 1742–1752. doi: 10.1162/jocn_a_00233

DeSerisy, M., Ramphal, B., Pagliaccio, D., Raffanello, E., Tau, G., Marsh, R., et al. (2021). Frontoparietal and default mode network connectivity varies with age and intelligence. *Develop. Cogn. Neurosci.* 48:100928. doi: 10.1016/j.dcn.2021.100928

Dijkstra, A. A., Lin, L. C., Nana, A. L., Gaus, S. E., and Seeley, W. W. (2018). von Economo neurons and fork cells: a neurochemical signature linked to monoaminergic function. *Cereb. Cortex* 28, 131–144. doi: 10.1093/cercor/bhw358

Dubois, J., Galdi, P., Paul, L. K., and Adolphs, R. (2018). A distributed brain network predicts general intelligence from resting-state human neuroimaging data. *Phil. Trans. R. Soc. B Biol. Sci.* 373:20170284. doi: 10.1098/rstb.2017.0284

Evrard, H. C., Forro, T., and Logothetis, N. K. (2012). von Economo neurons in the anterior insula of the macaque monkey. *Neuron* 74, 482–489. doi: 10.1016/j.neuron.2012.03.003

Eyal, G., Verhoog, M. B., Testa-Silva, G., Deitcher, Y., Lodder, J. C., Benavides-Piccione, R., et al. (2016). Unique membrane properties and enhanced signal

processing in human neocortical neurons. *eLife* 5:e16553. doi: 10.7554/eLife.16553

Fajardo, C., Escobar, M. I., Buriticá, E., Arteaga, G., Umbarila, J., Casanova, M. F., et al. (2008). von Economo neurons are present in the dorsolateral (dysgranular) prefrontal cortex of humans. *Neurosci. Lett.* 435, 215–218. doi: 10.1016/j.neulet.2008.02.048

Fiala, J. C., and Harris, K. M. (1999). "Dendrite structure," in *Dendrites*, eds G. Stuart, N. Spruston, and M. Häusser (New York, NY: Oxford University Press), 1–34.

Forlim, C. G., Klock, L., Bächle, J., Stoll, L., Giemsa, P., Fuchs, M., et al. (2020). Reduced resting-state connectivity in the precuneus is correlated with apathy in patients with schizophrenia. *Sci. Rep.* 10:2616. doi: 10.1038/s41598-020-59393-6

Freiwald, W. A. (2020). Social interaction networks in the primate brain. *Curr. Opin. Neurobiol.* 65, 49–58. doi: 10.1016/j.conb.2020.08.012

Fries, P. (2005). A mechanism for cognitive dynamics: neuronal communication through neuronal coherence. *Trends Cogn. Sci.* 9, 474–480. doi: 10.1016/j.tics.2005.08.011

Fries, P. (2015). Rhythms for cognition: communication through coherence. *Neuron* 88, 220–235. doi: 10.1016/j.neuron.2015.09.034

Fuzik, J., Zeisel, A., Máté, Z., Calvigioni, D., Yanagawa, Y., Szabó, G., et al. (2016). Integration of electrophysiological recordings with single-cell RNA-seq data identifies neuronal subtypes. *Nat. Biotech.* 34, 175–183. doi: 10.1038/nbt.3443

Gabbott, P. L., and Somogyi, J. (1984). The 'single' section Golgi-impregnation procedure: methodological description. *J. Neurosci. Methods* 11, 221–230. doi: 10.1016/0165-0270(84)90084-0

Gami-Patel, P., van Dijken, I., van Swieten, J. C., Pijnenburg, Y. A. L., Netherlands Brain Bank, Rozemuller, A. J. M., et al. (2019). von Economo neurons are part of a larger neuronal population that are selectively vulnerable in C9orf72 frontotemporal dementia. *Neuropathol. Appl. Neurobiol.* 45, 671–680. doi: 10.1111/nan.12558

Gefen, T., Papastefan, S. T., Rezvanian, A., Bigio, E. H., Weintraub, S., Rogalski, E., et al. (2018). Von Economo neurons of the anterior cingulate across the lifespan and in Alzheimer's disease. *Cortex* 99, 69–77. doi: 10.1016/j.cortex.2017.10.015

Gignac, G. E. (2014). Fluid intelligence shares closer to 60% of its variance with working memory capacity and is a better indicator of general intelligence. *Intelligence* 47, 122–133. doi: 10.1016/j.intell.2014.09.004

Gignac, G. E., and Bates, T. C. (2017). Brain volume and intelligence: the moderating role of intelligence measurement quality. *Intelligence* 64, 18–29. doi: 10.1016/j.intell.2017.06.004

González-Acosta, C. A., Escobar, M. I., Casanova, M. F., Pimienta, H. J., and Buriticá, E. (2018). Von Economo neurons in the human medial frontopolar cortex. *Front. Neuroanat.* 12:64. doi: 10.3389/fnana.2018.00064

González-Ramírez, M. M., Velázquez-Zamora, D. A., Olvera-Cortés, M. E., and González-Burgos, I. (2014). Changes in the plastic properties of hippocampal dendritic spines underlie the attenuation of place learning in healthy aged rats. *Neurobiol. Learn. Mem.* 109, 94–103. doi: 10.1016/j.nlm.2013.11.017

Gottfredson, L. S. (1997). Why g matters: the complexity of everyday life. *Intelligence* 24, 79–132. doi: 10.1016/S0160-2896(97)90014-3

Haier, R. J. (2016). *The Neuroscience Of Intelligence*. Cambridge: Cambridge University Press.

Hakeem, A. Y., Sherwood, C. C., Bonar, C. J., Butti, C., Hof, P. R., and Allman, J. M. (2009). von Economo neurons in the elephant brain. *Anat. Rec.* 292, 242–248. doi: 10.1002/ar.20829

Harroud, A., Boucher, O., Tran, T. P. Y., Harris, L., Hall, J., Dubeau, F., et al. (2017). Precuneal epilepsy: clinical features and surgical outcome. *Epilepsy Behav.* 73, 77–82. doi: 10.1016/j.yebeh.2017.05.018

Hayashi-Takagi, A., Yagishita, S., Nakamura, M., Shirai, F., Wu, Y. I., Loshbaugh, A. L., et al. (2015). Labelling and optical erasure of synaptic memory traces in the motor cortex. *Nature* 525, 333–338. doi: 10.1038/nature15257

Helm, M. S., Dankovich, T. M., Mandad, S., Rammner, B., Jähne, S., Salimi, V., et al. (2021). A large-scale nanoscopy and biochemistry analysis of postsynaptic dendritic spines. *Nat. Neurosci.* 24, 1151–1162.

Herms, J., and Dorostkar, M. M. (2016). Dendritic spine pathology in neurodegenerative diseases. *Ann. Rev. Pathol.* 11, 221–250. doi: 10.1146/annurev-pathol-012615-044216

Hidalgo-Lopez, E., Zeidman, P., Harris, T., Razi, A., and Pletzer, B. (2021). Spectral dynamic causal modelling in healthy women reveals brain connectivity changes along the menstrual cycle. *Commun. Biol.* 4:954. doi: 10.1038/s42003-021-02447-w

Hilger, K., Ekman, M., Fiebach, C. J., and Basten, U. (2017). Efficient hubs in the intelligent brain: Nodal efficiency of hub regions in the salience network is associated with general intelligence. *Intelligence* 60, 10–25. doi: 10.1016/j.intell.2016.11.001

Hodge, R. D., Miller, J. A., Novotny, M., Kalmbach, B. E., Ting, J. T., Bakken, T. E., et al. (2020). Transcriptomic evidence that von Economo neurons are regionally specialized extratelencephalic-projecting excitatory neurons. *Nat. Commun.* 11:1172. doi: 10.1038/s41467-020-14952-3

Hugdahl, K., Raichle, M. E., Mitra, A., and Specht, K. (2015). On the existence of a generalized non-specific task-dependent network. *Front. Hum. Neurosci.* 9:430. doi: 10.3389/fnhum.2015.00430

Jacob, J., Kent, M., Benson-Amram, S., Herculano-Houzel, S., Raghanti, M. A., Ploppert, E., et al. (2021). Cytoarchitectural characteristics associated with cognitive flexibility in raccoons. *J. Comp. Neurol.* 529, 3375–3388. doi: 10.1002/cne.25197

Jacot-Descombes, S., Keshav, N., Brosch, C. M. S., Wicinski, B., Warda, T., Norcliffe-Kaufmann, L., et al. (2020). von Economo neuron pathology in familial dysautonomia: quantitative assessment and possible implications. *J. Neuropathol. Exper. Neurol.* 79, 1072–1083. doi: 10.1093/jnen/nlaa095

Jensen, A. R. (1998). *The g Factor: The Science of Mental Ability*. Westport, CT: Praeger.

Jitsuishi, T., and Yamaguchi, A. (2021). Posterior precuneus is highly connected to medial temporal lobe revealed by tractography and white matter dissection. *Neuroscience* 466, 173–185. doi: 10.1016/j.neuroscience.2021.05.009

Jung, R. E., and Haier, R. J. (2007). The parieto-frontal integration theory (P-FIT) of intelligence: converging neuroimaging evidence. *Behav. Brain Sci.* 30, 135–187. doi: 10.1017/S0140525X07001185

Kasai, H., Ziv, N. E., Okazaki, H., Yagishita, S., and Toyoizumi, T. (2021). Spine dynamics in the brain, mental disorders and artificial neural networks. *Nat. Rev. Neurosci.* 22, 407–422. doi: 10.1038/s41583-021-00467-3

Kolb, B., and Whishaw, I. Q. (2021). *Fundamentals of Human Neuropsychology*. New York, NY: Worth Publishers.

Koshino, H., Minamoto, T., Yaoi, K., Osaka, M., and Osaka, N. (2014). Coactivation of the default mode network regions and working memory network regions during task preparation. *Sci. Rep.* 4, 1–8. doi: 10.1038/srep05954

Krause, M., Theiss, C., and Brüne, M. (2017). Ultrastructural alterations of von Economo neurons in the anterior cingulate cortex in schizophrenia. *Anat. Rec.* 300, 2017–2024. doi: 10.1002/ar.23635

Kubota, Y., Karube, F., Nomura, M., and Kawaguchi, Y. (2016). The diversity of cortical inhibitory synapses. *Front. Neural Circuits* 10:27. doi: 10.3389/fncir.2016.00027

Lin, L. C., Nana, A. L., Hepker, M., Hwang, J. L., Gaus, S. E., Spina, S., et al. (2019). Preferential tau aggregation in von economo neurons and fork cells in frontotemporal lobar degeneration with specific MAPT variants. *Acta Neuropathol. Commun.* 7:159. doi: 10.1186/s40478-019-0809-0

Lu, J., and Zuo, Y. (2017). Clustered structural and functional plasticity of dendritic spines. *Brain Res. Bull.* 129, 18–22. doi: 10.1016/j.brainresbull.2016.09.008

Mai, J. K., Majtanik, M., and Paxinos, G. (2016). *Atlas Of The Human Brain*. New York, NY: Academic Press.

Mai, J. K., Paxinos, G., and Voss, T. (2008). *Atlas Of The Human Brain*. New York, NY: Academic Press.

Margulies, D. S., Vincent, J. L., Kelly, C., Lohmann, G., Uddin, L. Q., Biswal, B. B., et al. (2009). Precuneus shares intrinsic functional architecture in humans and monkeys. *Proc. Natl. Acad. Sci. U.S.A.* 106, 20069–20074. doi: 10.1073/pnas.0905314106

Martínez, K., and Colom, R. (2021). "Imaging the intelligence of humans," in *The Cambridge Handbook of Intelligence and Cognitive Neuroscience*, eds A. K. Barbey, S. Karama, and R. J. Haier (Cambridge: Cambridge University Press).

Menary, K., Collins, P. F., Porter, J. N., Muetzel, R., Olson, E. A., Kumar, V., et al. (2013). Associations between cortical thickness and general intelligence in children, adolescents and young adults. *Intelligence* 41, 597–606. doi: 10.1016/j.intell.2013.07.010

Menon, V., and Uddin, L. Q. (2010). Saliency, switching, attention and control: a network model of insula function. *Brain Struct. Funct.* 214, 655–667. doi: 10.1007/s00429-010-0262-0

Morishima, M., and Kawaguchi, Y. (2006). Recurrent connection patterns of corticostriatal pyramidal cells in frontal cortex. *J. Neurosci.* 26, 4394–4405. doi: 10.1523/jneurosci.0252-06.2006

Myatt, D. R., Hadlington, T., Ascoli, G. A., and Nasuto, S. J. (2012). Neuromantic – from semi-manual to semi-automatic reconstruction of neuron morphology. *Front. Neuroinformat.* 6:4. doi: 10.3389/fninf.2012.00004

Nakahata, Y., and Yasuda, R. (2018). Plasticity of spine structure: local signaling, translation and cytoskeletal reorganization. *Front. Synaptic Neurosci.* 10:29. doi: 10.3389/fnsyn.2018.00029

Nelson, P. T., Abner, E. L., Scheff, S. W., Schmitt, F. A., Kryscio, R. J., Jicha, G. A., et al. (2009). Alzheimer's-type neuropathology in the precuneus is not increased relative to other areas of neocortex across a range of cognitive impairment. *Neurosci. Lett.* 450, 336–339. doi: 10.1016/j.neulet.2008.11.006

Neto, E. R., Fonseca, M. K., Guedes, A. C. B., Oliveira, F. H., Hilbig, A., and Fernandez, L. L. (2017). Neuropathological findings in entorhinal cortex of subjects aged 50 years or older and their correlation with dementia in a sample from Southern Brazil. *Dement. Neuropsychol.* 11, 24–31. doi: 10.1590/1980-57642016dn11-010005

Ng, K. K., Lo, J. C., Lim, J. K. W., Chee, M. W. L., and Zhou, J. (2016). Reduced functional segregation between the default mode network and the executive control network in healthy older adults: a longitudinal study. *NeuroImage* 133, 321–330. doi: 10.1016/j.neuroimage.2016.03.029

Niendam, T. A., Laird, A. R., Ray, K. L., Dean, Y. M., Glahn, D. C., and Carter, C. S. (2012). Meta-analytic evidence for a superordinate cognitive control network subserving diverse executive functions. *Cogn. Affect. Behav. Neurosci.* 12, 241–268. doi: 10.3758/s13415-011-0083-5

Nimchinsky, E. A., Gilissen, E., Allman, J. M., Perl, D. P., Erwin, J. M., and Hof, P. R. (1999). A neuronal morphologic type unique to humans and great apes. *Proc.Natl. Acad. Sci. U.S.A.* 96, 5268–5273. doi: 10.1073/pnas.96.9.5268

Nimchinsky, E. A., Vogt, B. A., Morrison, J. H., and Hof, P. R. (1995). Spindle neurons of the human anterior cingulate cortex. *J. Comp. Neurol.* 355, 27–37. doi: 10.1002/cne.903550106

Oakley, J. C., Schwindt, P. C., and Crill, W. E. (2001). Dendritic calcium spikes in layer 5 pyramidal neurons amplify and limit transmission of ligand gated dendritic current to soma. *J. Neurophysiol.* 86, 514–527. doi: 10.1152/jn.2001.86.1.514

Palomero-Gallagher, N., and Zilles, K. (2019). Cortical layers: Cyto-, myelo-, receptor- and synaptic architecture in human cortical areas. *NeuroImage* S1053-8119, 30682–30691. doi: 10.1016/j.neuroimage.2017.08.035

Parekh, R., and Ascoli, G. A. (2013). Neuronal morphology goes digital: a research hub for cellular and system neuroscience. *Neuron* 77, 1017–1038. doi: 10.1016/j.neuron.2013.03.008

Penke, L., Maniega, S. M., Bastin, M. E., Hernández, M. V., Murray, C., Royle, N. A., et al. (2012). Brain white matter tract integrity as a neural foundation for general intelligence. *Mol. Psychiatry* 17:1026. doi: 10.1038/mp.2012.66

Petralia, R. S., Wang, Y. X., Mattson, M. P., and Yao, P. J. (2018). Invaginating structures in mammalian synapses. *Front. Synaptic Neurosci.* 10:4. doi: 10.3389/fnsyn.2018.00004

Petralia, R. S., Yao, P. J., Kapogiannis, D., and Wang, Y.-X. (2021). Invaginating structures in synapses – Perspective. *Front. Synaptic Neurosci.* 13:685052. doi: 10.3389/fnsyn.2021.685052

Ptak, R. (2012). The frontoparietal attention network of the human brain: action, saliency, and a priority map of the environment. *Neuroscientist* 18, 502–515. doi: 10.1177/1073858411409051

Raghanti, M. A., Spurlock, L. B., Treichler, F. R., Weigel, S. E., Stimmelmayr, R., Butti, C., et al. (2015). An analysis of von Economo neurons in the cerebral cortex of cetaceans, artiodactyls, and perissodactyls. *Brain Struct. Funct.* 220, 2303–2314. doi: 10.1007/s00429-014-0792-y

Ramaswamy, S., and Markram, H. (2015). Anatomy and physiology of the thick-tufted layer 5 pyramidal neuron. *Front. Cell. Neurosci.* 9:233. doi: 10.3389/fncel.2015.00233

Rasia-Filho, A. A., Guerra, K. T. K., Vásquez, C. E., Dall'Oglio, A., Reberger, R., Jung, C. R., et al. (2021). The subcortical-allocortical-neocortical continuum for the emergence and morphological heterogeneity of pyramidal neurons in the human brain. *Front. Synaptic Neurosci.* 13:616607. doi: 10.3389/fnsyn.2021.616607

Reberger, R., DallOglio, A., Jung, C. R., and Rasia-Filho, A. A. (2018). Structure and diversity of human dendritic spines evidenced by a new three-dimensional reconstruction procedure for Golgi staining and light microscopy. *J. Neurosci. Methods* 293, 27–36. doi: 10.1016/j.jneumeth.2017.09.001

Rochefort, N. L., and Konnerth, A. (2012). Dendritic spines: from structure to in vivo function. *EMBO Rep.* 13, 699–708. doi: 10.1038/embor.2012.102

Rollenhagen, A., and Lübke, J. H. R. (2016). "Dendritic elaboration: morphology and chemistry," in *Neuroscience in the 21st Century*, eds D. W. Pfaff and N. D. Volkow (New York, NY: Springer), 225–264. doi: 10.1007/978-1-4939-3474-4_11

Sanchez, M. A. S., and Lourenço, R. A. (2009). Informant questionnaire on cognitive decline in the elderly (IQCODE): adaptação transcultural para uso no Brasil. *Cad. Saúde Púb.* 25, 1455–1465. doi: 10.1590/s0102-311x2009000700003

Santillo, A. F., and Englund, E. (2014). Greater loss of von Economo neurons than loss of layer II and III neurons in behavioral variant frontotemporal dementia. *Am. J. Neurodegener. Dis.* 3, 64–71.

Scheperjans, F., Eickhoff, S. B., Hömke, L., Mohlberg, H., Hermann, K., Amunts, K., et al. (2008a). Probabilistic maps, morphometry, and variability of cytoarchitectonic areas in the human superior parietal cortex. *Cereb. Cortex* 18, 2141–2157. doi: 10.1093/cercor/bhm241

Scheperjans, F., Hermann, K., Eickhoff, S. B., Amunts, K., Schleicher, A., and Zilles, K. (2008b). Observer-independent cytoarchitectonic mapping of the human superior parietal cortex. *Cereb. Cortex* 18, 846–867. doi: 10.1093/cercor/bhm116

Schindelin, J., Arganda-Carreras, I., Frise, E., Kaynig, V., Longair, M., Pietzsch, T., et al. (2012). Fiji: an open-source platform for biological-image analysis. *Nat. Methods* 9, 676–682. doi: 10.1038/nmeth.2019

Scorcioni, R., Polavaram, S., and Ascoli, G. A. (2008). L-Measure: a web-accessible tool for the analysis, comparison and search of digital reconstructions of neuronal morphologies. *Nat. Prot.* 3, 866–876. doi: 10.1038/nprot.2008.51

Seeley, W. W. (2008). Selective functional, regional, and neuronal vulnerability in frontotemporal dementia. *Curr. Opin. Neurol.* 21, 701–707. doi: 10.1097/WCO.0b013e3283168e2d

Seeley, W. W., Carlin, D. A., Allman, J. M., Macedo, M. N., Bush, C., Miller, B. L., et al. (2006). Early frontotemporal dementia targets neurons unique to apes and humans. *Ann. Neurol.* 60, 660–667. doi: 10.1002/ana.21055

Seeley, W. W., Merkle, F. T., Gaus, S. E., Craig, A. D., Allman, J. M., and Hof, P. R. (2012). Distinctive neurons of the anterior cingulate and frontoinsular cortex: a historical perspective. *Cereb. Cortex* 22, 245–250. doi: 10.1093/cercor/bhr005

Sherman, L. E., Rudie, J. D., Pfeifer, J. H., Masten, C. L., McNealy, K., and Dapretto, M. (2014). Development of the default mode and central executive networks across early adolescence: a longitudinal study. *Dev. Cogn. Neurosci.* 10, 148–159. doi: 10.1016/j.dcn.2014.08.002

Spruston, N., Häusser, M., and Stuart, G. (2013). "Information processing in dendrites and spines," in *Fundamental Neuroscience*, eds L. R. Squire, D. Berg, F. E. Bloom, S. du, A. Ghosh Lac, and N. C. Spitzer (Waltham, MA: Academic Press), 231–260. doi: 10.1016/b978-0-12-385870-2.00011-1

Sridharan, D., Levitin, D. J., and Menon, V. (2008). A critical role for the right fronto-insular cortex in switching between central-executive and default-mode networks. *Proc. Natl. Acad. Sci. U.S.A.* 105, 12569–12574. doi: 10.1073/pnas.0800005105

Stewart, M. G., Popov, V. I., Kraev, I. V., Medvedev, N., and Davies, H. A. (2014). "Structure and complexity of the synapse and dendritic spine," in *The Synapse*, eds V. Pickel and M. Segal (New York, NY: Academic Press), 1–20. doi: 10.1016/b978-0-12-418675-0.00001-8

Stimpson, C. D., Tetreault, N. A., Allman, J. M., Jacobs, B., Butti, C., Hof, P. R., et al. (2011). Biochemical specificity of von Economo neurons in hominoids. *Am. J. Hum. Biol.* 23, 22–28. doi: 10.1002/ajhb.21135

Takeuchi, H., Taki, Y., Nouchi, R., Yokoyama, R., Kotozaki, Y., Nakagawa, S., et al. (2018). General intelligence is associated with working memory-related brain activity: new evidence from a large sample study. *Brain Struct. Funct.* 223, 4243–4258. doi: 10.1007/s00429-018-1747-5

Thomas, B., Sheelakumari, R., Kannath, S., Sarma, S., and Menon, R. N. (2019). Regional cerebral blood flow in the posterior cingulate and precuneus and the entorhinal cortical atrophy score differentiate mild cognitive impairment and dementia due to Alzheimer disease. *Am. J. Neuroradiol.* 40, 1658–1664. doi: 10.3174/ajnr.A6219

Tønnesen, J., and Nägerl, V. (2016). Dendritic spines as tunable regulators of synaptic signals. *Front. Psych.* 7:101. doi: 10.3389/fpsyt.2016.00101

Triarhou, L. C. (2009). *Von Economo and Koskinas' Atlas of Cytoarchitectonics of the Adult Human Cerebral Cortex*. Basel: Karger.

Uddin, L. Q., Yeo, B. T., and Spreng, R. N. (2019). Towards a universal taxonomy of macro-scale functional human brain networks. *Brain Topogr.* 32, 926–942. doi: 10.1007/s10548-019-00744-6

Utevsky, A. V., Smith, D. V., and Huettel, S. A. (2014). Precuneus is a functional core of the default-mode network. *J. Neurosci.* 34, 932–940. doi: 10.1523/JNEUROSCI.4227-13.2014

van den Heuvel, M. P., Scholtens, L. H., Feldman Barrett, L., Hilgetagm, C. C., and de Reus, M. A. (2015). Bridging cytoarchitectonics and connectomics in human cerebral cortex. *J. Neurosci.* 35, 13943–13948. doi: 10.1523/JNEUROSCI.2630-15.2015

Vásquez, C. E., Reberger, R., Dall'Oglio, A., Calcagnotto, M. E., and Rasia-Filho, A. A. (2018). Neuronal types of the human cortical amygdaloid nucleus. *J. Comp. Neurol.* 526, 2776–2801. doi: 10.1002/cne.24527

Watson, K. K. (2006). *The von Economo Neurons: From cells to Behavior*. Ph.D Thesis. Pasadena, CA: California Institute of Technology.

Watson, K. K., Jones, T. K., and Allman, J. M. (2006). Dendritic architecture of the von Economo neurons. *Neuroscience* 141, 1107–1112. doi: 10.1016/j.neuroscience.2006.04.084

Wen, Q., Stepanyants, A., Elston, G. N., Grosberg, A. Y., and Chklovskii, D. B. (2009). Maximization of the connectivity repertoire as a statistical principle governing the shapes of dendritic arbors. *Proc. Natl. Acad. Sci. U.S.A.* 106, 12536–12541. doi: 10.1073/pnas.0901530106

Wenderoth, N., Debaere, F., Sunaert, S., and Swinnen, S. P. (2005). The role of anterior cingulate cortex and precuneus in the coordination of motor behaviour. *Eur. J. Neurosci.* 22, 235–246. doi: 10.1111/j.1460-9568.2005.04176.x

Yadav, A., Gao, Y. Z., Rodriguez, A., Dickstein, D. L., Wearne, S. L., Luebke, J. I., et al. (2012). Morphologic evidence for spatially clustered spines in apical dendrites of monkey neocortical pyramidal cells. *J. Comp. Neurol.* 520, 2888–2902. doi: 10.1002/cne.23070

Yang, L., Yang, Y., Yuan, J., Sun, Y., Dai, J., and Su, B. (2019). Transcriptomic landscape of von Economo neurons in human anterior cingulate cortex revealed by microdissected-cell RNA sequencing. *Cereb. Cortex* 29, 838–851. doi: 10.1093/cercor/bhy286

Yang, Y., Wang, H., Zhou, W., Qian, T., Sun, W., and Zhao, G. (2018). Electroclinical characteristics of seizures arising from the precuneus based on stereoelectroencephalography (SEEG). *BMC Neurol.* 18:110. doi: 10.1186/s12883-018-1119-z

Yang, Z., Craddock, R. C., Margulies, D. S., Yan, C. G., and Milham, M. P. (2014). Common intrinsic connectivity states among posteromedial cortex subdivisions: insights from analysis of temporal dynamics. *NeuroImage* 93, 124–137. doi: 10.1016/j.neuroimage.2014.02.014

Ye, Q., Zou, F., Lau, H., Hu, Y., and Kwok, S. C. (2018). Causal evidence for mnemonic metacognition in human precuneus. *J. Neurosci.* 38, 6379–6387. doi: 10.1523/JNEUROSCI.0660-18.2018

Yokosawa, K., Kimura, K., Takase, R., Murakami, Y., and Boasen, J. (2020). Functional decline of the precuneus associated with mild cognitive impairment: magnetoencephalographic observations. *PLoS One* 15:e0239577. doi: 10.1371/journal.pone.023957

Yuste, R. (2010). *Dendritic Spines*. Cambridge: The MIT Press.

Yuste, R. (2013). Electrical compartmentalization in dendritic spines. *Ann. Rev. Neurosci.* 36, 429–449. doi: 10.1146/annurev-neuro-062111-150455

Yuste, R., Hawrylycz, M., Aalling, N., Aguilar-Valles, A., Arendt, D., Armañanzas, R., et al. (2020). A community-based transcriptomics classification and nomenclature of neocortical cell types. *Nat. Neurosci.* 23, 1456–1468. doi: 10.1038/s41593-020-0685-8

Zaccard, C. R., Shapiro, L., Martin-de-Saavedra, M. D., Pratt, C., Myczek, K., Song, A., et al. (2020). Rapid 3D enhanced resolution microscopy reveals diversity in dendritic spinule dynamics, regulation, and function. *Neuron* 107, 522–537. doi: 10.1016/j.neuron.2020.04.025

Zeba, M., Jovanov-Miloseviæ, N., and Petanjek, Z. (2008). Quantitative analysis of basal dendritic tree of layer III pyramidal neurons in different areas of adult human frontal cortex. *Coll. Antropol.* 32(Suppl. 1), 161–169.

Zebarjadi, N., Adler, E., Kluge, A., Jääskeläinen, I. P., Sams, M., and Levy, J. (2021). Rhythmic neural patterns during empathy to vicarious pain: beyond the affective-cognitive empathy dichotomy. *Front. Hum. Neurosci.* 15:708107. doi: 10.3389/fnhum.2021.708107

Zhang, Y., Fan, L., Zhang, Y., Wang, J., Zhu, M., Zhang, Y., et al. (2014). Connectivity-based parcellation of the human posteromedial cortex. *Cereb. Cortex* 24, 719–727. doi: 10.1093/cercor/bhs353

Conflict of Interest: The authors declare that the research was conducted in the absence of any commercial or financial relationships that could be construed as a potential conflict of interest.

Publisher's Note: All claims expressed in this article are solely those of the authors and do not necessarily represent those of their affiliated organizations, or those of the publisher, the editors and the reviewers. Any product that may be evaluated in this article, or claim that may be made by its manufacturer, is not guaranteed or endorsed by the publisher.

Copyright © 2022 Fuentealba-Villarroel, Renner, Hilbig, Bruton and Rasia-Filho. This is an open-access article distributed under the terms of the Creative Commons Attribution License (CC BY). The use, distribution or reproduction in other forums is permitted, provided the original author(s) and the copyright owner(s) are credited and that the original publication in this journal is cited, in accordance with accepted academic practice. No use, distribution or reproduction is permitted which does not comply with these terms.

frontiers | Frontiers in Synaptic Neuroscience

TYPE Original Research
PUBLISHED 17 November 2022
DOI 10.3389/fnsyn.2022.1056308

Check for updates

OPEN ACCESS

EDITED BY
Ka Wan Li,
VU Amsterdam, Netherlands

REVIEWED BY
Jan Van Weering,
Center for Neurogenomics and Cognitive Research, Netherlands
Natali Lujan Chanaday Ricagni,
University of Pennsylvania, United States

*CORRESPONDENCE
Christoph Körber
koerber@uni-heidelberg.de

RECEIVED 28 September 2022
ACCEPTED 03 November 2022
PUBLISHED 17 November 2022

CITATION
Paksoy A, Hoppe S, Dörflinger Y, Horstmann H, Sätzler K and Körber C (2022) Effects of the clathrin inhibitor Pitstop-2 on synaptic vesicle recycling at a central synapse *in vivo*. *Front. Synaptic Neurosci.* 14:1056308. doi: 10.3389/fnsyn.2022.1056308

COPYRIGHT
© 2022 Paksoy, Hoppe, Dörflinger, Horstmann, Sätzler and Körber. This is an open-access article distributed under the terms of the Creative Commons Attribution License (CC BY). The use, distribution or reproduction in other forums is permitted, provided the original author(s) and the copyright owner(s) are credited and that the original publication in this journal is cited, in accordance with accepted academic practice. No use, distribution or reproduction is permitted which does not comply with these terms.

Effects of the clathrin inhibitor Pitstop-2 on synaptic vesicle recycling at a central synapse *in vivo*

Alp Paksoy[1], Simone Hoppe[1], Yvette Dörflinger[1], Heinz Horstmann[1], Kurt Sätzler[2] and Christoph Körber[1]*

[1]Department of Functional Neuroanatomy, Institute of Anatomy and Cell Biology, Heidelberg University, Heidelberg, Germany, [2]School of Biomedical Sciences, University of Ulster, Coleraine, United Kingdom

Four modes of endocytosis and subsequent synaptic vesicle (SV) recycling have been described at the presynapse to ensure the availability of SVs for synaptic release. However, it is unclear to what extend these modes operate under physiological activity patterns *in vivo*. The coat protein clathrin can regenerate SVs either directly from the plasma membrane (PM) via clathrin-mediated endocytosis (CME), or indirectly from synaptic endosomes by SV budding. Here, we examined the role of clathrin in SV recycling under physiological conditions by applying the clathrin inhibitor Pitstop-2 to the calyx of Held, a synapse optimized for high frequency synaptic transmission in the auditory brainstem, *in vivo*. The effects of clathrin-inhibition on SV recycling were investigated by serial sectioning scanning electron microscopy (S^3EM) and 3D reconstructions of endocytic structures labeled by the endocytosis marker horseradish peroxidase (HRP). We observed large endosomal compartments as well as HRP-filled, black SVs (bSVs) that have been recently recycled. The application of Pitstop-2 led to reduced bSV but not large endosome density, increased volumes of large endosomes and shifts in the localization of both types of endocytic compartments within the synapse. These changes after perturbation of clathrin function suggest that clathrin plays a role in SV recycling from both, the PM and large endosomes, under physiological activity patterns, *in vivo*.

KEYWORDS

3D reconstruction, calyx of Held synapse, clathrin, electron microscopy, synaptic vesicle cycle

Introduction

Local SV recycling at the presynapse is an essential process for the maintenance of neurotransmission (Ceccarelli et al., 1973; Heuser and Reese, 1973). However, the exact molecular mechanisms underlying SV recycling are still not completely understood, especially *in vivo* (for review see Kokotos and Cousin, 2015; Watanabe and Boucrot, 2017; Chanaday et al., 2019; Ivanova and Cousin, 2022). Till date, four different, mutually non-exclusive mechanisms for synaptic endocytosis have been described. CME retrieves individual SVs with the help of a clathrin coat directly from the PM (Heuser and Reese, 1973; Murthy and De Camilli, 2003; Logiudice et al., 2009). During activity dependent bulk endocytosis (ADBE), a large piece of presynaptic membrane is taken-up from the PM to form an endosome from which SVs can bud (e.g., Miller and Heuser, 1984; Holt et al., 2003; Wu and Wu, 2007; Kokotos and Cousin, 2015). Ultrafast endocytosis (UFE) retrieves a portion of the PM equivalent to 4 SVs, which is much less than ADBE (Watanabe et al., 2013, 2014). During kiss-and-run, a fusion pore is transiently opened without full collapse of the SV into the PM. This allows the retrieval of the SV as a whole (Gandhi and Stevens, 2003; He et al., 2006; Zhang et al., 2009). Different endocytosis modes have been linked to distinct levels of activity; CME and UFE for example are thought to operate at low to moderate synaptic activity levels, while ADBE is suggested to be employed only during periods of high synaptic activity (Balaji and Ryan, 2007; Zhu et al., 2009; Leitz and Kavalali, 2011, 2014; Watanabe et al., 2013; Delvendahl et al., 2016; Chanaday and Kavalali, 2018). However, it is not clear which of these mechanism(s) is operating *in vivo*, under physiological activity patterns, as most studies have been conducted in cultured neurons or brain slices (e.g., de Lange et al., 2003; Granseth et al., 2006; Kim and Ryan, 2009; Watanabe et al., 2013, 2014; Soykan et al., 2017). We therefore sought out to examine endocytosis *in vivo* in a synapse optimized for high frequency synaptic transmission.

A prime model synapse operating at high frequencies is the calyx of Held, a giant, glutamatergic, axosomatic synapse formed between the globular bushy cells of the contralateral anterior ventral cochlear nucleus and the principal cells of the medial nucleus of the trapezoid body (MNTB) in the auditory brainstem. The calyx of hearing animals can faithfully transmit signals at frequencies of several hundred Hertz but has to undergo extensive structural and functional remodeling around the onset of hearing, in order to meet the requirements of processing airborne sounds (Borst and Soria van Hoeve, 2012). Two different forms of endocytic compartments have been identified at the calyx using the endocytosis marker HRP: large tubular or cisternal endosomes and recently recycled SVs (termed bSVs from here on) (de Lange et al., 2003; Körber et al., 2012), although their origin, in particular which endocytosis mechanism(s) has been operational, remained elusive.

To gain further insights into the mechanisms of SV recycling employed during physiological, high frequency synaptic transmission, we examined the role of clathrin at the calyx of Held *in vivo*. Therefore, we applied the clathrin inhibitor Pitstop-2 (von Kleist et al., 2011) alongside with HRP to the MNTB of early hearing rats just after the onset of hearing, a time at which the mature pattern of signal transmission has been established at the calyx (Crins et al., 2011; Sonntag et al., 2011). The rats were subjected to environmental noise inducing physiological synaptic transmission patterns at the calyx. Synaptic endocytosis in response to this stimulation was examined by electron microscopy and 3D analysis of the size and distribution of HRP-filled bSVs and large endosomes. Application of Pitstop-2 led to a decrease in bSV density, an increased volume of large endosomes and a shift in bSV and large endosome localization toward the presynaptic membrane.

Materials and methods

Stereotaxic injections

All experiments were conducted in accordance with the German federal law and the EU directive 2010/63. The protocols were approved by the local authority (Regierungspräsidium Karlsruhe). Sprague Dawley rats of either sex were injected at P12/13 with either HRP only (10 mg/ml in PBS, SERVA, Heidelberg, Germany), HRP supplemented with 1% DMSO or HRP along with Pitstop-2 (120 μM, Sigma) into the MNTB as described previously (Körber et al., 2012). In brief, rats were anesthetized, transferred into a non-traumatic stereotaxic frame (Kopf Instruments, Tujunga, CA) and 2 μl of marker or drug solution were injected to the following coordinates relative to bregma and midline (x, y, z in mm): 0.95, –6.4, –7.6. Pitstop-2 was delivered in a two-step injection. First, Pitstop-2 was administered to the MNTB alone and only in the second injection, 15 min after the first one, Pitstop-2 was co-injected with HRP to the identical coordinates. The rats remained anesthetized between the two injections. After surgery, rats recovered quickly and behaved normally while they were exposed to standard laboratory environmental noise (radio, air conditioner, human conversation) for 30 min.

Fixation and tissue processing

Rats were deeply anesthetized and transcardially perfused with 15 ml of PBS followed by 15 ml PFA (4% in PBS). The brain was removed and post-fixed at 4°C over night. The brainstem was cut into 100 μm thick sections including the MNTB on a vibratome (Sigmann Elektronik, Hüffenhardt, Germany). The sections were prepared for the DAB reaction as described previously (Körber et al., 2012). In brief, the sections were

incubated in α-D-glucose (2 mg/ml) and 3,3′diaminobenzidine (DAB) (1.4 mg/ml) dissolved in PBS for 20 min in the dark. *Aspergillus* glucose oxidase (0.1 mg/ml, SERVA) was added to start the DAB polymerization. The DAB reaction was stopped after 1 h by incubating the sections in cacodylic acid (100 mM) for 30 min. The MNTB was excised and post-fixed for 1 h in 1.5% potassium-ferry-cyanide and 2% osmium tetroxide on ice in the dark. The samples were rinsed three times in distilled water, dehydrated in an ascending series of ethanol, incubated in epoxy/propylenoxide (1:1) over night and embedded in epoxy resin, which was polymerized at 60°C for 36 h.

Serial section scanning electron microscopy

Serial section scanning electron microscopy (S^3EM) was performed as described before (Horstmann et al., 2012). Ribbons of 20 serial sections (40 nm) were cut through the MNTB using an Ultracut S ultramicrotome (Leica) equipped with a diamond knife angled at 45° (Diatome, Biel, Switzerland). Sections were collected on clean silicon wafers (Si-Mat Silicon Materials, Landsberg, Germany) that were glow discharged for 30 s right before tissue sectioning. Tissue compression due to sectioning was neutralized by exposure to chloroform vapor. The samples were dried and stained following a modified Reynolds-procedure [saturated uranyl acetate solution (16 min) followed by lead citrate (8 min)]. Scanning electron microscopy was performed using a LEO Gemini 1530 equipped with a field emission gun and an ATLAS scanning generator (Zeiss) using the InLens detector at the following settings: 3.6 mm working distance, 30 μm aperture and 2 keV acceleration voltage. Images of 2632 × 2632 pixels were taken at a pixel size of 3.8 nm (dwell time 25.6 μs).

Data analysis

Images were only taken from tissue that did not show signs of mechanical damage due to the injection procedure. Calyces were randomly chosen within the MNTB. However, since continuous supply of HRP during the loading period is crucial for the study of endocytosis, only calyces fully surrounded by HRP were considered for further analysis. 18-22 consecutive EM sections were manually aligned according to prominent structures present in consecutive sections for 3D reconstruction using OpenCAR software (Sätzler et al., 2002). The PM, the innervation side and the large endosomal compartments were manually contoured in each aligned section. In order to evade artifacts intrinsic to the imaging process, only large endosomes spanning no less than two consecutive sections (80 nm) were considered for 3D reconstruction. bSVs were identified by their round morphology, uniform black labeling and SV-like diameter. We controlled for variability in the DAB reaction by measuring intensity profiles of randomly chosen bSVs. bSVs were only considered for further analysis if intensity values were homogeneous along the profile (as opposed to the two distinct intensity peaks observed at the membrane of non-labeled SVs) and at least 1.5-fold higher than those of non-labeled SV membrane peaks. bSVs were reconstructed as spheres based on their diameter (Sätzler et al., 2002). 3D reconstructions were performed following the Delaunay method (Boissonnat and Geiger, 1992). OpenCARnEval, a command-line version of OpenCAR, provided numerical readouts of the structural features using batch scripts.

Statistics

The population means and standard deviations (SD) of each experimental group were estimated by equal weighing of the averages and SDs of the individual synapses within the group as described previously (Körber et al., 2012). Utilizing these normal population estimates, we analyzed the two population means according to their differences and similarities by establishing the 95% confidence interval for the differences between two group means of normally distributed data (Berry, 1995). Since volumes of large endosomes were not normally distributed, they were first log transformed and differences in large endosome volume were calculated from the transformed data. The positions of large endosome and bSVs within the synapse were determined by classifying them as either closer to the innervation side or to the backside of the synapse (Körber et al., 2012). We compared the proportions of large endosomes or bSVs that were closer to either side by approximating the measured β-density of proportions in each experiment via a normal distribution (Berry, 1995). These approximations were used to determine the corresponding confidence intervals as described above. Data is represented as mean ± SEM. Significance in object densities, cell average-based endosome volumes and cell average-based distances was assigned by one-way ANOVA or nested one-way ANOVA as indicated, using Prism 9 software (GraphPad). Q-Q-plots were generated using R software. The experimental distributions obtained under the various conditions were compared to two simulated conditions assuming either identical distributions (**Figure 5**, red lines) or similar, not significantly different distributions (**Figure 5**, blue lines). The similar, not significantly different distributions were obtained by linear regression of the quantiles of the compared distributions.

Results

The functional relevance of CME for SV recycling has recently been challenged (Kim and Ryan, 2009; Kononenko et al., 2014; Watanabe et al., 2014; Delvendahl et al., 2016;

Soykan et al., 2017; Yu et al., 2018). We therefore examined the effect of the clathrin inhibitor Pitstop-2 (von Kleist et al., 2011) on synaptic endocytosis and SV recycling at the calyx of Held synapse *in vivo*. Pitstop-2 was applied together with HRP by stereotaxic injection into the MNTB of anesthetized rats. After recovery from anesthesia, the rats were subjected to environmental noise for 30 min, which provides physiological stimulation to the calyx of Held synapse. The properties of HRP filled presynaptic endocytic compartments, identified by the DAB reaction product, were examined by S^3EM (Horstmann et al., 2012) (**Figure 1**). In order to examine the mechanisms of endocytosis active during high frequency synaptic activity induced by a physiological stimulus (airborne sound), we used early hearing rats at P12/13 that had already established the mature pattern of synaptic transmission at the calyx (Crins et al., 2011; Sonntag et al., 2011). Throughout the study, we compared the results of Pitstop-2 application to two independent control groups: rats injected only with HRP, and rats injected with HRP supplemented with 1% DMSO which was used to dissolve Pitstop-2.

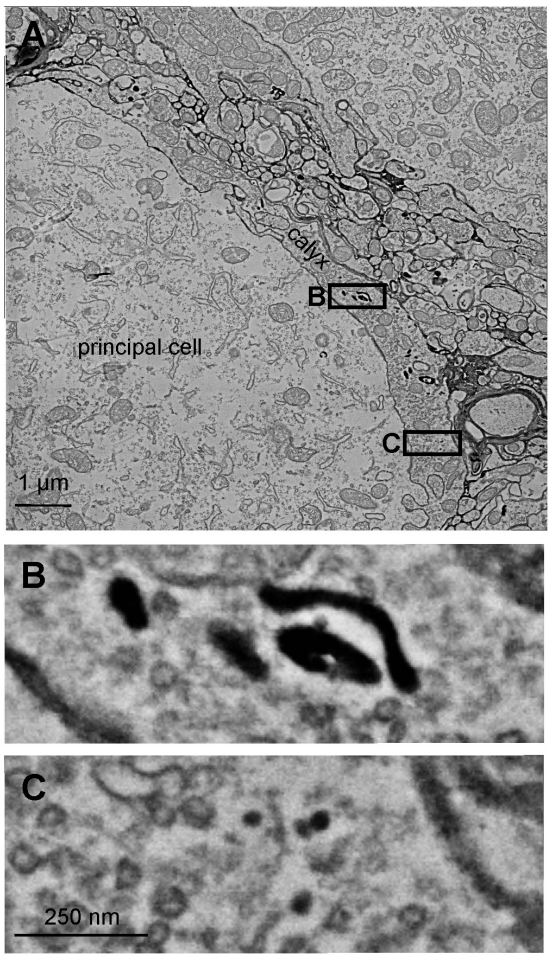

FIGURE 1
In vivo application of HRP labels endocytic structures at the calyx of Held synapse. **(A)** EM image of a P12 calyx of Held surrounded by HRP reaction product. Endocytic compartments are evident in the calyx as well as the MNTB principal cell. **(B,C)** Higher magnifications from the framed areas in **(A)** showing large endosomes **(B)** and bSVs **(C)**, respectively. Scale bar is 1 µm **(A)** or 250 nm **(B,C)**.

Pitstop-2 does not block synaptic vesicle recycling *in vivo*

The application of HRP *in vivo* resulted in the labeling of two forms of endocytic structures – large endosomes (**Figure 1B**) and bSVs (**Figure 1C**) (Körber et al., 2012) – irrespective of the presence of Pitstop-2 (**Figure 2**). Large endosomes were defined as HRP-labeled structures spanning at least two consecutive sections. Both types of endocytic compartments were detected throughout the calyx volume, in the vicinity of the innervation side as well as in areas toward the backside of the synapse (see below). The presence of bSVs, which have been generated either directly via CME or via budding from HRP-filled endosomes, suggests that SV recycling persists in the presence of Pitstop-2 although clathrin function is impaired (**Figure 2B**). Analysis of the densities of endocytic compartments, however, revealed a moderate decrease in bSV density after Pitstop-2 application (Pitstop-2: 30.73 ± 5.20 bSVs/µm^3, HRP only: 82.33 ± 17.06 bSVs/µm^3, HRP and DMSO: 46.69 ± 3.15 bSVs/µm^3; p = 0.019, one-way ANOVA, Dunnett's *post hoc* test: HRP only vs. HRP and DMSO: $p > 0.05$, HRP only vs. Pitstop-2: p = 0.013) (**Figure 3A**), which was not due to a sampling bias caused by differences in the reconstructed calyx volume (HRP only: 7.42 ± 1.19 µm^3, HRP and DMSO: 11.62 ± 1.55 µm^3, Pitstop-2: 5.96 ± 2.69 µm^3; p = 0.14, one-way ANOVA). A block of SV recycling during ongoing synaptic transmission would eventually lead to the loss of SVs in the recycling pool and thus the mobilization and exocytosis of reserve pool SVs. Since these cannot be regenerated either under these conditions, block of SV recycling should eventually lead to a reduction in SV density in general. In order to assess such a loss in SV density, we quantified the density of non-labeled SVs (nl-SVs) in the reconstructed calyx segments, but did not observe a reduction upon Pitstop-2 application (HRP only: 705 ± 109 nl-SVs/µm^3, HRP and DMSO: 760 ± 84 nl-SVs/µm^3, Pitstop-2: 719 ± 97 nl-SVs/µm^3; p = 0.91, one-way ANOVA) (**Figure 3C**). Moreover, the total SV density (sum of bSVs and nl-Sv per calyx volume) was unaffected by Pitstop-2 application (HRP only: 787 ± 121 SVs/µm^3, HRP and DMSO: 807 ± 85 SVs/µm^3, Pitstop-2: 750 ± 101 SVs/µm^3; p = 0.92, one-way ANOVA) (**Figure 3D**). However, the total SV density is dominated by the density of nl-SVs, which is approximately 10 times higher than the bSV density, and thus occludes the moderate reduction in bSV density.

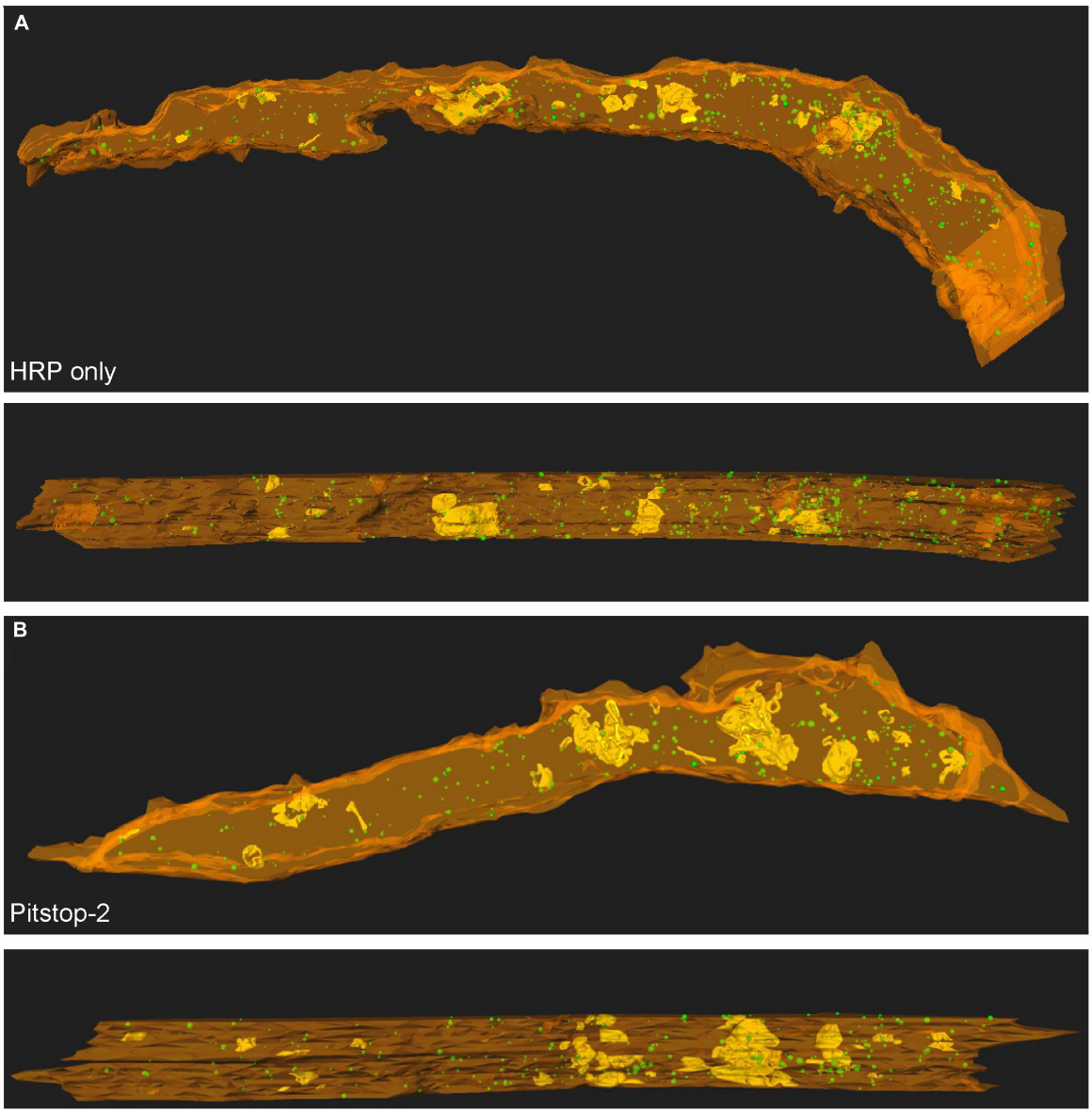

FIGURE 2
Large endosomes and recently recycled bSVs are located throughout the calyx volume, irrespecitve of the presence or absence of Pitstop-2. **(A)** 3D reconstructions of endocytic compartments in a calyx of Held segment at P12/13 in the absence of Pitstop-2 (HRP only control). **(B)** 3D reconstructions of endocytic compartments in a calyx of Held segment at P12/13 in the presence of Pitstop-2. PM appears in orange, large endosomes are depicted in yellow and bSVs as green spheres. The innervation side is facing the bottom (top) or the front (bottom).

Despite the moderate decrease specifically in bSV density, we did not observe alterations in the density of large endosomes after Pitstop-2 application (Pitstop-2: 5.55 ± 2.06 endosomes/μm^3, HRP only: 5.80 ± 0.68 endosomes/μm^3, HRP and DMSO: 3.14 ± 0.45 endosomes/μm^3; p = 0.9841, one-way ANOVA) (Figure 3B). Pitstop-2 application thus resulted in a moderate but specific reduction of the density of one type of endocytic compartments – bSVs – without effecting the density of the other type – large endosomes – in calyx of Held synapses.

Pitstop-2 impairs the volume regulation of large endosomes

Although the density of large endosomes was unaffected by Pitstop-2 application, the volume of large endosomes was significantly increased in calyces treated with Pitstop-2 (measured values: Pitstop-2: 0.00145 ± 0.001 μm^3 compared to 0.00084 ± 0.00104 μm^3 and 0.00094 ± 0.00171 μm^3 in the HRP only and HRP and DMSO groups, respectively, shown as cumulative probability plot; Figure 4A; n = 104–152 endosomes

10.3389/fnsyn.2022.1056308

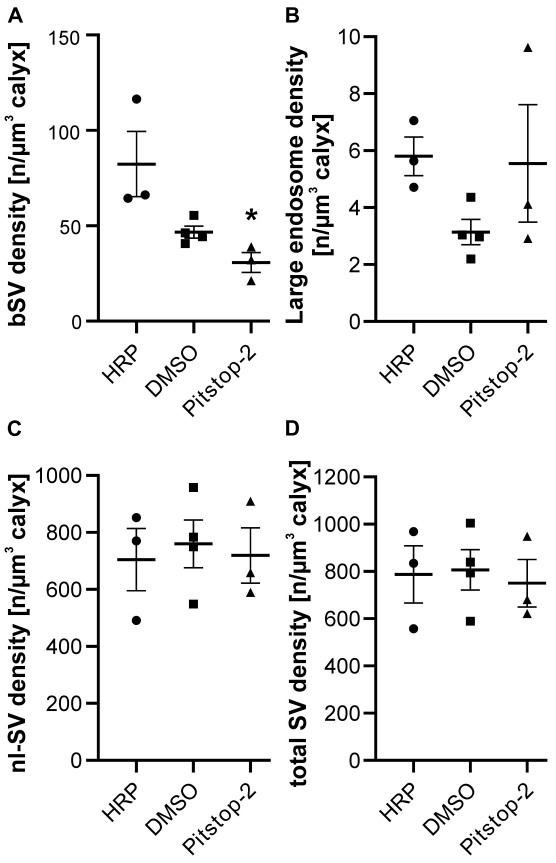

FIGURE 3
The density of large endosomes is unchanged after Pitstop-2 treatment while the density of bSVs decreases. **(A–D)** Quantification of the effects of Pitstop-2 on the density of bSVs **(A)**, large endosomes **(B)**, non-labeled SV (nl-SVs) **(C)** and total SVs (bSVs + nl-SVs) **(D)** at the calyx of Held [number of endosomes or SVs per μm^3 calyx volume, n = 3–4 calyces/group, 1 calyx/animal; * = $p < 0.05$ one-way ANOVA followed by Dunnett's *post hoc* test (HRP only vs. Pitstop-2)].

from 3 to 4 calyces/group, 1 calyx/animal; $d = 0.73$; $p < 0.05$ compared to both control groups based on confidence intervals of log transformed data; log transformed values: Pitstop-2: 0.01374 ± 0.00014 μm^3, HRP only: 0.01277 ± 0.00009 μm^3 HRP and DMSO: 0.01311 ± 0.00009 μm^3; 3-4 calyces/group, 1 calyx/animal; $p = 0.038$ nested one-way ANOVA and Dunnett's *post hoc* test, HRP only vs. Pitstop-2; **Figure 4B**). This increase in volume can be caused by two effects, which are not mutually exclusive. Either the application of Pitstop-2 induces a shift in the endocytosis mechanism toward clathrin-independent mechanisms such as ADBE and UFE due to impairment of CME at the PM, or the clathrin-dependent budding of bSVs from large endosomes is perturbed in the presence of Pitstop-2. Irrespective of the actual mechanism, these results show that clathrin is important for the size regulation of large (recycling) endosomes.

Effects of Pitstop-2 on the localization of endocytic compartments

In addition to the density of endocytic compartments, we also investigated their localization within the synapse. This measure can provide insights into the location of endocytosis and/or the internal trafficking of recently endocytosed compartments. Therefore, we measured the distances from individual large endosomes and bSVs to the PM at the innervation side and at the back of the synapse. Although the back of the calyx seems to be an unlikely place for compensatory endocytosis, we frequently observe endocytic compartments of either type that are located closer to the back of the calyx than to the innervation side. This does not necessarily mean that the actual endocytosis event occurred at the back of the calyx. Instead, the compartment could have been trafficked to the backside. Moreover, such observations can be caused by the complex geometry of the calyx with its varying thickness and protrusions, which can hamper distance measurements between endocytic compartments and the innervation side. We thus also analyzed the distance to the back of the calyx to provide a more complete description of an endocytic compartment's localization inside the calyx. The distance measurements toward both sides of the calyx were highly variable, even within single calyces, and did not show significant differences between Pitstop-2 treated calyces and control synapses (**Table 1**, nested one-way ANOVA). Although the cell-average based analysis of distances between the endocytic compartments and the PM did not yield significant results, changes in the distribution of the distance measurements could have been occluded in the analysis. We therefore performed a Q-Q-plot analysis which provides a sensitive way to detect such changes in measurement distributions between experimental conditions (**Figure 5**). The experimentally derived Q-Q-plots were compared to two simulated distributions assuming either identical (**Figure 5**, red lines) or similar, statistically not different, distributions (**Figure 5**, blue lines, see Materials and methods) between the experimental conditions. However, the Q-Q-plot analysis did not reveal any differences between individual distance distributions, since our data always resembled the case of a similar, not significantly different distribution (**Figure 5**, compare data points to blue lines).

In a final step, we considered the complex morphology of the calyx, especially its variable thickness and the presence of protrusions at the innervation side (see above) (Sätzler et al., 2002), and sorted the endocytic compartments into two categories: those being closer to the innervation side, i.e., the AZs, and those being closer to the back of the calyx. The sorting was based on whether the distance of a given endocytic compartment was shorter to the innervation side or the backside of the calyx and compensates for variability in distance measurement distributions due to variations in calyx morphology (Körber et al., 2012). Application of Pitstop-2

resulted in a shift of large endosomes toward the innervation side (Figure 6). The large endosomes were similarly distributed among the control groups (percentage of large endosomes closer to the innervation side: HRP only: 38.8 ± 4.1%, HRP and DMSO: 37.3 ± 3.9%), but the application of Pitstop-2 increased the fraction of large endosomes closer to the innervation side to 54.5 ± 4.9% (d = 0.64; $p < 0.05$ weighted mean analysis, Pitstop-2 different from both control groups) (Figure 6C). Additional to the effect of Pitstop-2 on the localization of large endosomes, it also altered the localization of bSVs, resulting in a mild shift of the bSV distribution toward the innervation side (percentage of bSVs closer to the innervation side: HRP only: 39.0 ± 1.2%, HRP and DMSO: 40 ± 1.1%, Pitstop-2: 44.1 ± 2.0%; d = 0.21; $p < 0.05$ weighted mean analysis, Pitstop-2 different from both control groups) (Figure 6C). Thus, impairing clathrin function by Pitstop-2 induced changes in the localization of endocytic structures, irrespective of the compartment type, at the calyx of Held *in vivo*. This suggests that clathrin may be important for different mechanisms of SV regeneration, CME and budding from large endosomes, under physiological activity patterns.

Discussion

In the present study, we show that perturbing clathrin function results in the impairment of SV recycling at the calyx of Held synapse under physiological activity, *in vivo*. 3D EM analysis of endocytic structures revealed that application of the clathrin inhibitor Pitstop-2 impaired SV recycling via CME and/or budding from large endosomes. Our investigation of endocytic compartments relied on HRP, which is applied extracellularly and taken up into the presynapse by endocytosis. At the calyx of Held, we confirmed two types of HRP-labeled endocytic structures: bSVs and large endosomes (de Lange et al., 2003; Denker et al., 2011; Körber et al., 2012). bSVs are either created by CME or via budding from large, recycling endosomes. The large endosomes, however, can be generated by

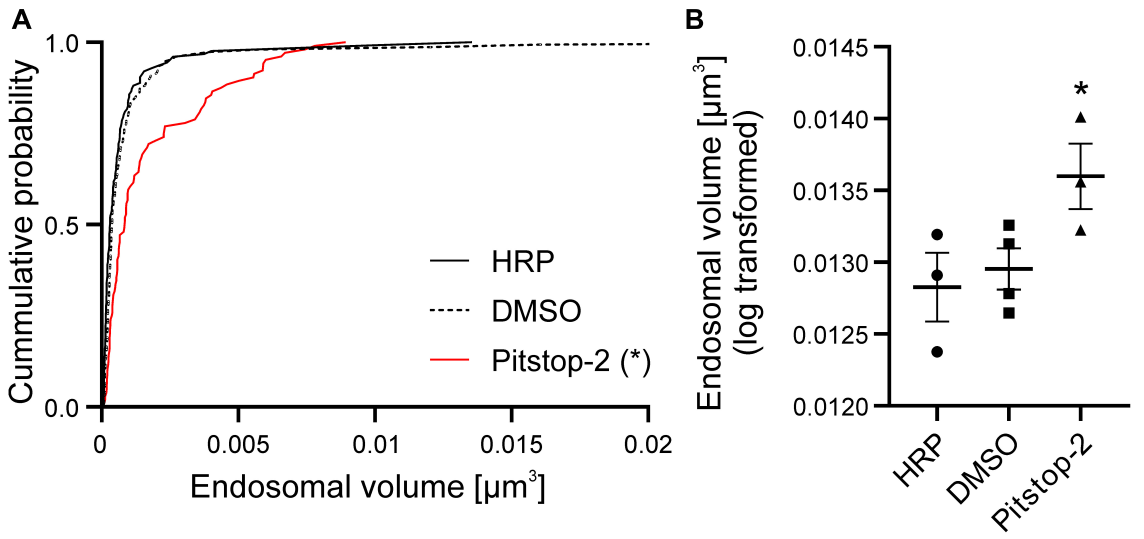

FIGURE 4
The volume of large endosomes is increased at the calyx of Held upon application of Pitstop-2. **(A)** Cumulative probability plot of all large endosome volumes observed in the presence and absence of Pitstop-2 (n = 104–152 endosomes from 3 to 4 calyces/group, 1 calyx/animal; * = $p < 0.05$, Pitstop-2 treatment significantly different from both controls). **(B)** Quantification of log transformed endosome volumes [n = 3–4 calyces/group, 1 calyx/animal; * = $p < 0.05$ nested one-way ANOVA followed by Dunnett's *post hoc* test (HRP only vs. Pitstop-2)].

TABLE 1 Distance measurements between endocytic structures and the PM at either the innervation side or the back of the synapse.

Experimental groups	HRP only	HRP+DMSO	Pitstop-2	Nested one-way ANOVA
Mean				
bSV- innervation side	518 ± 66	839 ± 216	644 ± 303	0.59
bSV- back of the synapse	183 ± 14	310 ± 59	221 ± 51	0.24
Large endosome-innervation side	183 ± 14	310 ± 59	221 ± 51	0.13
Large endosome-back of the synapse	115 ± 3	232 ± 43	179 ± 56	0.14

Cell-based average distances, given as mean ± SEM in nm.

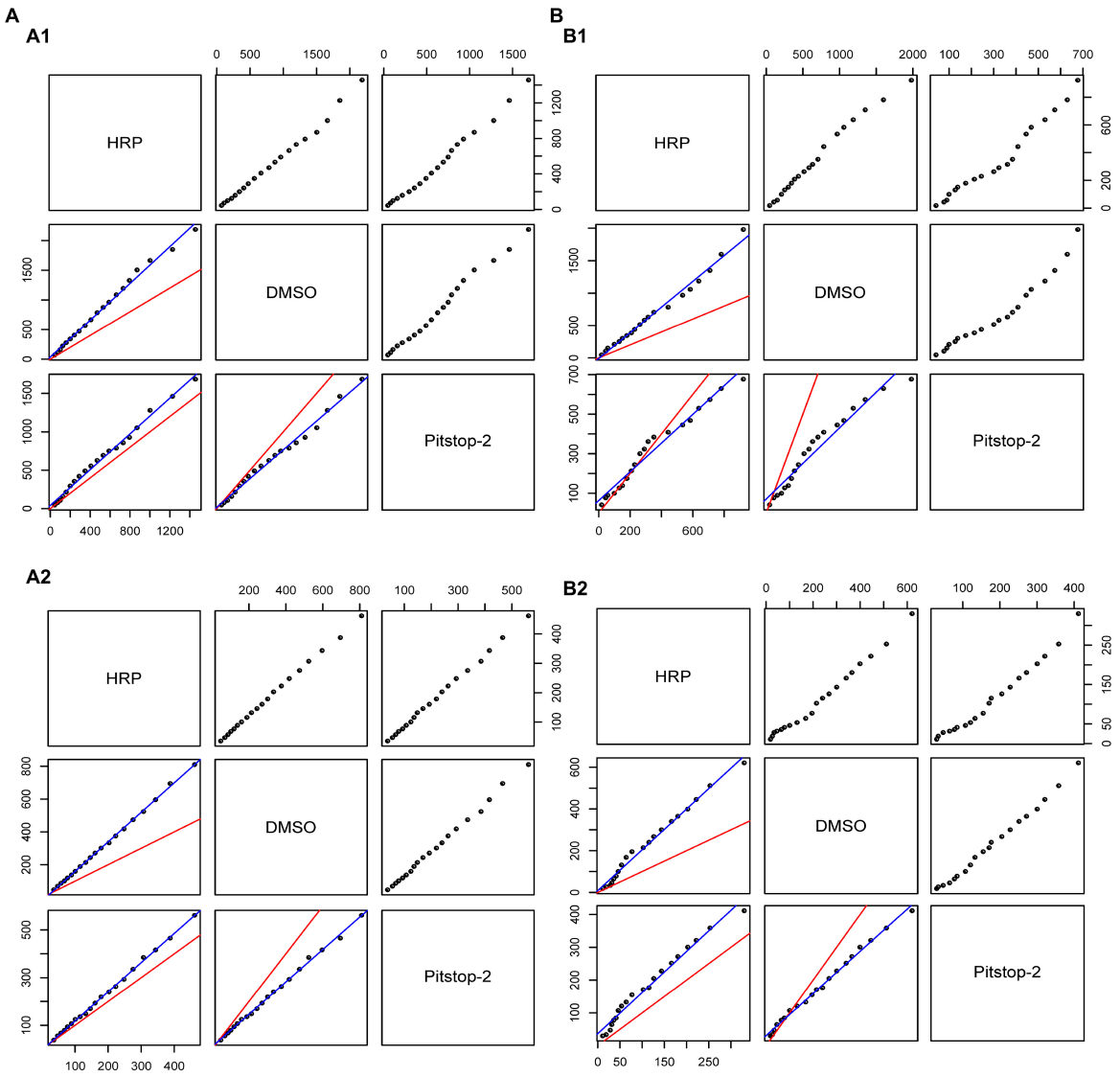

FIGURE 5
The distances between endocytic compartments and the PM at the innervation side or backside are insensitive to Pitstop-2 treatment. **(A,B)** Quantile-Quantile plots for probability distributions of mean distances from bSVs **(A)** and large endosomes **(B)** to the PM at the innervation side **(A1,B1)** and to the PM at the back of the synapse **(A2,B2)** in comparison between control and treatment groups. The red line represents the case of identical distributions, whereas the blue line represents similar, statistically not significantly different distributions (see Materials and methods) (n = 3–4 calyces/group, 1 calyx/animal).

three distinct mechanisms: first, by the fusion of CME-derived vesicles either with each other or with early endosomes, second, by ADBE and third, by UFE (Richards et al., 2000; Rizzoli et al., 2006; Cheung et al., 2010; Hoopmann et al., 2010; Watanabe et al., 2013, 2014; Kokotos and Cousin, 2015). They are then either broken-up into SVs (Watanabe et al., 2014) or designated for lysosomal degradation, possibly after some time spend as a recycling endosome at the presynapse (Rizzoli, 2014).

In the auditory system, the physiological requirements on SV recycling change depending on the presence or absence of airborne sounds, as the former induces synaptic transmission at frequencies of more than 300 Hz for prolonged times (Kopp-Scheinpflug et al., 2008). The data presented here shows that clathrin is involved in the recycling of SVs and thus comprises one mechanism to meet the synaptic requirements of sound processing.

Dynamics of large endosomes *in vivo*

Multiple mechanisms can lead to the formation of the large endosomes observed at calyx of Held *in vivo*

10.3389/fnsyn.2022.1056308

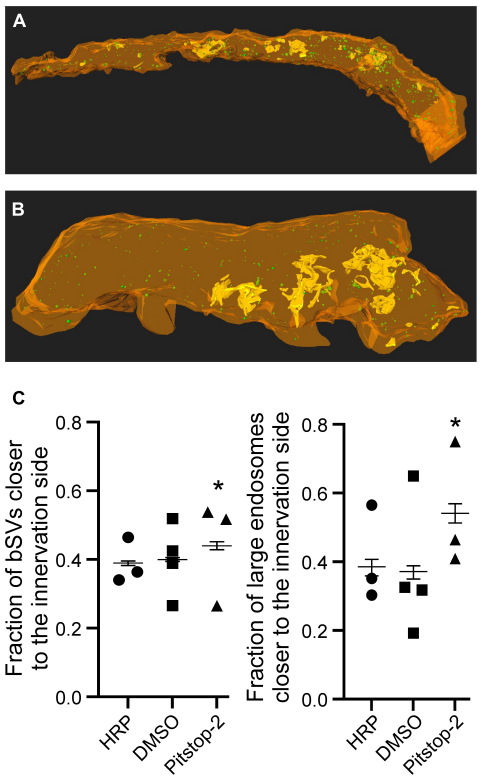

FIGURE 6
Application of Pitstop-2 alters the localization of large endosomes and bSVs at the calyx of Held. **(A)** 3D reconstruction of the endocytic compartments in the absence of Pitstop-2. **(B)** 3D reconstruction of the endocytic compartments in the presence of Pitstop-2. PM appears in orange, large endosomes are depicted in yellow and bSVs as green spheres. The innervation side is facing the bottom. **(C)** Quantification of the effects of Pitstop-2 on the localization of bSVs (left) and large endosomes (right) Please note that the weighted means are depicted. (n = 3–4 calyces/group, 1 calyx/animal; * = $p < 0.05$, Pitstop-2 different from both control groups).

(de Lange et al., 2003; Denker et al., 2011; Körber et al., 2012). Large endosomes are thought to endure for some time at the synapse, acting as sorting and/or recycling endosomes before they are transported back to the soma and follow the lysosomal route (reviewed in Rizzoli, 2014). Of note, small endosomes derived from UFE have been shown to degrade within seconds (Watanabe et al., 2013, 2014). The data shown here demonstrates that the application of Pitstop-2 affects large endosome volume and localization within the synapse without changing their density, implying that both parameters are depending on proper clathrin function. We observed a Pitstop-2-induced shift of large endosomes toward the innervation side of the calyx. This could imply that processes resulting in large endosome generation (see above) happen more often at the innervation side. However, an increase in endosome formation at the innervation side should have resulted in a concomitant increase in large endosome number and thus density in the calyces treated with Pitstop-2. We did not observe such an increase, but cannot formally exclude this possibility as small increases in endosome density could have been occluded by its relatively large variability. Moreover, the endosome density would have remained constant if an increase in endosome formation at the innervations side is accompanied by a decrease in endosome formation/transport at/to the back of the calyx. Nevertheless, a shift in endosome localization toward the innervation side is in line with a change to Pitstop-2-insensitive mechanisms of SV recycling which are expected to take place in proximity of AZs at the PM of the innervation (reviewed in Soykan et al., 2016; Chanaday et al., 2019).

In addition to the shift in localization, we observed an increase in the volume of large endosomes in synapses treated with Pitstop-2. This could be caused by a stronger employment of clathrin-independent endocytosis (CIE) modes such as UFE and ADBE and a consequential build-up of large endosomes, or by a decrease in clathrin-dependent SV budding from large endosomes. Both scenarios are in accordance with a dual role for clathrin in endocytosis and SV recycling at the calyx of Held *in vivo*.

Regeneration of synaptic vesicles *in vivo*

Clathrin-mediated endocytosis (CME) has been regarded as the major mechanism of synaptic endocytosis during moderate synaptic activity. However, this view has been challenged by an increasing number of studies showing that CIE mechanisms play important roles under these conditions (reviewed in Soykan et al., 2017; Milosevic, 2018; Chanaday et al., 2019). Nevertheless, CIE mechanisms like UFE and ADBE likely require clathrin to dissolve the larger endosomes into SVs (Watanabe et al., 2014). Our results on bSV density and localization show that the application of Pitstop-2 reduced bSV density and shifted bSV localization toward the PM at the calyx of Held *in vivo*. Interestingly, we did not observe a reduction in the density of nl-SVs, probably due to the large number of SV at the calyx of Held (see Sätzler et al., 2002) and the relatively short incubation time of Pitstop-2 at the calyx (see below). However, the effects of Pitstop-2 application on the density and localization of bSVs suggest that different mechanisms of SV re-formation operate at the calyx, likely depending on the physiological demand on SV recycling in the presence or absence of sound perception.

The moderate reduction in bSV density observed upon Pitstop-2 application shows that at least a fraction of SV re-formation is clathrin-dependent. This could be either due to CME or clathrin-dependent SV budding from endosomes. Concomitant to the decrease in bSV density, we observed a shift in bSV localization toward the innervation side, suggesting that those SVs that are recycled in the presence of Pitstop-2

are located preferentially in a position favorable for future rounds of exocytosis. This preference is not surprising given the demand SVs for synaptic transmission during sound perception (de Lange et al., 2003; Borst and Soria van Hoeve, 2012; Körber et al., 2012). Of note, recently recycled SVs have also been shown to be randomly located in the presynaptic terminal of the neuromuscular junction (Rizzoli and Betz, 2004). However, the observed increase in large endosome volume upon Pitstop-2 treatment suggests that the reduction in bSV density is at least partially due to impairments in endosomal volume reduction by clathrin-dependent SV budding and that at least a part of the bSVs observed in the vincinity of the innervation side in the presence of Pitstop-2 is generated via CME.

Budding of SVs from endosomes is mechanistically different from CME as it requires AP-1 and/or AP-3 complexes instead of the AP-2 complex necessary for CME (Kim and Ryan, 2009; Glyvuk et al., 2010; Newell-Litwa et al., 2010; Kononenko et al., 2014). Thus, Pitstop-2 may preferentially impair AP-1/AP-3-dependent SV budding from large endosomes while AP-2-dependent CME prevails at least partially in the presence of Pitstop-2. However, we cannot rule out that bSVs were generated via CIE or another, yet unknown, Pitstop-2 insensitive budding mechanism. Interestingly, knock-down of the AP-2 complex in cultured hippocampal neurons slowed down endocytosis but did not fully block it (Kim and Ryan, 2009) suggesting alternative mechanisms of endocytosis operating at the PM. In line with this finding, intracellular application of Pitstop-1, a non-membrane permeable clathrin inhibitor (von Kleist et al., 2011), to the calyx also slowed down endocytosis without inhibiting it completely (Yue et al., 2017).

Limitations and conclusion

Despite the effects of Pitstop-2 on SV recycling presented here, we would like to mention that the pharmacokinetics of Pitstop-2 *in vivo* are unknown. This poses a limitation to our approach as we cannot formally rule out that the concentration of Pitstop-2 at the synapse was too low to completely block clathrin-dependent processes. We therefore limited our analyses of Pitstop-2-induced effects to 30 min. after a single application. However, the fact that we were able to detect changes in the structure, density and localization of endocytic compartments after Pitstop-2 application implies that our approach interfered with clathrin function and resulted in an at least partial block of clathrin-dependent mechanisms. Nevertheless, long-term inhibition of clathrin by continuous application of Pitstop-2 (e.g., via an osmotic pump) and its effects on SV recycling and the usage of the reserve pool will be an interesting topic for future studies. Of note, two biochemical studies have raised doubts about the specificity of Pitstop-2 as a clathrin inhibitor (Dutta et al., 2012; Willox et al., 2014). However, there are also numerous studies showing Pitstop-2 to specifically block clathrin-dependent processes in neurons (von Kleist et al., 2011; Merriam et al., 2013; Neef et al., 2014; Missig et al., 2017; DiCello et al., 2019; Gomez et al., 2021; Zhang et al., 2021; Jaramillo-Polanco et al., 2022). Nevertheless, potential off target effects of Pitstop-2 need to be considered with respect to our results. There have been concerns regarding the proposed interaction sides of Pitstop-2 within the N-terminal domain of clathrin (Willox et al., 2014). Since we were not interested in the function of individual clathrin-domains, this concern does not affect the interpretation of our data as long as Pitstop-2 inhibits clathrin in some way. Moreover, it has also been reported that the application of Pitstop-2 prevented the clathrin-independent endocytosis of the major histocompatibility complex I (MHC I) (Dutta et al., 2012), which could interfere with our results. Clathrin-independent MHC I endocytosis is not well understood, but requires Arf6-GDP (Montealegre and van Endert, 2019). In neurons, Arf6 regulates the number of SVs and cisternal endosomes at the presynapse. Knock-down of Arf6 or its pharmacological inhibition result in a decrease in the number of SVs with a simultaneous increase in the number of docked SVs as well as the accumulation of cisternal endosomes in cultured hippocampal synapses (Tagliatti et al., 2016). If Pitstop-2 inhibits CIE via an Arf6-dependent mechanism, we should have observed the accumulation of cisternal/large endosomes at the calyx and/or a general reduction of the total number of SVs. Although we could have potentially missed a small reduction in SV number (see above), the increase in cisternal/large endosome number in hippocampal synapses is substantial and would have probably been detected in our experiments. Since we neither observed a reduction in total SV number nor an increase in the number of cisternal/large endosomes upon Pitstop-2 application, we conclude that a possible inhibition of Arf6-dependent CIE by Pitstop-2 does not interfere with our interpretation of the data presented. However, other Arf6-independent CIE processes include ADBE and UFE. The block of these two processes should have resulted in a decreased number of large endosomes, which we did not observe either. Thus, the present data obtained by our pharmacological approach likely allows us to draw valid conclusions about the nature of clathrin function during high frequency synaptic transmission *in vivo*.

The investigation of endocytic compartments by EM provides the best possible resolution but limits the investigation to a single time point per animal and thus precludes attempts to follow the fate of a given endocytic compartment over time. Further studies using, e.g., fluorescent endocytosis markers in combination with advanced imaging methods such as micro-endoscopy will shed light on such questions. Additionally, further studies that do not rely on the pharmacological inhibition of clathrin will be required to identify the precise nature of the clathrin-dependent mechanisms engaged in SV recycling *in vivo*. Lastly, our approach does not allow to discriminate SV recycling in response to sound processing from SV recycling under spontaneous activity. Although such

a correlation would be highly desirable, it is hampered by the fact that hearing rats vocalize and it is thus very difficult to insulate them from sound perception. Correlations are further complicated by the high spontaneous activity of the calyx of Held even in the absence of sound perception (Kopp-Scheinpflug et al., 2008). Thus, even limiting analysis to calyces with high densities of endocytic compartment would not faithfully separate those with high spontaneous activities from those active due to sound processing.

Despite these limitations, we have shown that clathrin-dependent SV recycling from the PM and/or endosomal compartments accounts for at least a fraction of the regenerated SVs at the calyx of Held *in vivo*. Presumably, both pathways are active at the mature calyx in order to meet the high demand on SV recycling due to the processing of airborne sounds which requires faithful synaptic transmission at frequencies of several hundred Hertz for a prolonged time. We thus conclude that clathrin-mediated SV recycling is an integral part of the SV regeneration strategy at a central high frequency synapse *in vivo*.

Data availability statement

The raw data supporting the conclusions of this article will be made available by the authors, without undue reservation.

Ethics statement

The animal study was reviewed and approved by Regierungspräsidium Karlsruhe.

Author contributions

CK conceived the project. AP, SH, YD, and HH performed the research. AP, KS, and CK analyzed the data. AP and CK wrote the manuscript with inputs from all authors. All authors contributed to the article and approved the submitted version.

Funding

This study was supported by a Deutsche Forschungsgemeinschaft Priority Program 1608 "Ultrafast and temporally precise information processing: Normal and dysfunctional hearing" grant to CK. The publication of this article was supported by the Deutsche Forschungsgemeinschaft and Heidelberg University within the "Open Access Publishing" funding program.

Acknowledgments

We are grateful to Marion Schmitt for excellent technical assistance.

Conflict of interest

The authors declare that the research was conducted in the absence of any commercial or financial relationships that could be construed as a potential conflict of interest.

Publisher's note

All claims expressed in this article are solely those of the authors and do not necessarily represent those of their affiliated organizations, or those of the publisher, the editors and the reviewers. Any product that may be evaluated in this article, or claim that may be made by its manufacturer, is not guaranteed or endorsed by the publisher.

References

Balaji, J., and Ryan, T. A. (2007). Single-vesicle imaging reveals that synaptic vesicle exocytosis and endocytosis are coupled by a single stochastic mode. *Proc. Natl. Acad. Sci. U.S.A.* 104, 20576–20581. doi: 10.1073/pnas.0707574105

Berry, D. A. (1995). *Statistics: A bayesian perspective*. Duxbury, MA: Duxbury Press.

Boissonnat, J.-D., and Geiger, B. (1992). *Three dimensional reconstruction of complex shapes based on the delaunay triangulation*. [Research Report] RR-1697. Bordeaux: INRIA.

Borst, J. G., and Soria van Hoeve, J. (2012). The calyx of Held synapse: From model synapse to auditory relay. *Annu. Rev. Physiol.* 74, 199–224.

Ceccarelli, B., Hurlbut, W. P., and Mauro, A. (1973). Turnover of transmitter and synaptic vesicles at the frog neuromuscular junction. *J. Cell Biol.* 57, 499–524.

Chanaday, N. L., and Kavalali, E. T. (2018). Optical detection of three modes of endocytosis at hippocampal synapses. *Elife* 7:e36097. doi: 10.7554/eLife.36097

Chanaday, N. L., Cousin, M., Milosevic, I., Watanabe, S., and Morgan, J. (2019). the synaptic vesicle cycle revisited: New insights into the modes and mechanisms. *J. Neurosci.* 39, 8209–8216. doi: 10.1523/JNEUROSCI.1158-19.2019

Cheung, G., Jupp, O. J., and Cousin, M. A. (2010). Activity-dependent bulk endocytosis and clathrin-dependent endocytosis replenish specific synaptic vesicle pools in central nerve terminals. *J. Neurosci.* 30, 8151–8161.

Crins, T. T., Rusu, S. I., Rodríguez-Contreras, A., and Borst, J. G. (2011). Developmental changes in short-term plasticity at the rat calyx of Held synapse. *J. Neurosci.* 31, 11706–11717.

de Lange, R. P., de Roos, A. D., and Borst, J. G. (2003). Two modes of vesicle recycling in the rat calyx of Held. *J. Neurosci.* 23, 10164–10173.

Delvendahl, I., Vyleta, N. P., von Gersdorff, H., and Hallermann, S. (2016). Fast, temperature-sensitive and clathrin-independent endocytosis at central synapses. *Neuron* 90, 492–498. doi: 10.1016/j.neuron.2016.03.013

Denker, A., Bethani, I., Kröhnert, K., Körber, C., Horstmann, H., Wilhelm, B. G., et al. (2011). A small pool of vesicles maintains synaptic activity in vivo. *Proc. Natl. Acad. Sci. U.S.A.* 108, 17177–17182.

DiCello, J. J., Rajasekhar, P., Eriksson, E. M., Saito, A., Gondin, A. B., Veldhuis, N. A., et al. (2019). Clathri and GRK2/3 inhibitors block δ-opioid receptor internalization in myenteric neurons and inhibit neuromuscular transmission in the mouse colon. *Am. J. Physiol. Gastrointest. Liver Physiol.* 317, G79–G89. doi: 10.1152/ajpgi.00085.2019

Dutta, D., Williamson, C. D., Cole, N. B., and Donaldson, J. G. (2012). Pitstop 2 is a potent inhibitor of clathrin-independent endocytosis. *PLoS One* 7:e45799. doi: 10.1371/journal.pone.0045799

Gandhi, S. P., and Stevens, C. F. (2003). Three modes of synaptic vesicular recycling revealed by single-vesicle imaging. *Nature* 423, 607–613. doi: 10.1038/nature01677

Glyvuk, N., Tsytsyura, Y., Geumann, C., D'Hooge, R., Hüve, J., Kratzke, M., et al. (2010). AP-1/sigma1B-adaptin mediates endosomal synaptic vesicle recycling, learning and memory. *Embo J.* 29, 1318–1330. doi: 10.1038/emboj.2010.15

Gomez, K., Ran, D., Madura, C. L., Moutal, A., and Khanna, R. (2021). Non-SUMOylated CRMP2 decreases Na(V)1.7 currents via the endocytic proteins Numb, Nedd4-2 and Eps15. *Mol. Brain* 14:20. doi: 10.1186/s13041-020-00714-1

Granseth, B., Odermatt, B., Royle, S. J., and Lagnado, L. (2006). Clathrin-mediated endocytosis is the dominant mechanism of vesicle retrieval at hippocampal synapses. *Neuron* 51, 773–786.

He, L., Wu, X.-S., Mohan, R., and Wu, L.-G. (2006). Two modes of fusion pore opening revealed by cell-attached recordings at a synapse. *Nature* 444, 102–105. doi: 10.1038/nature05250

Heuser, J. E., and Reese, T. S. (1973). Evidence for recycling of synaptic vesicle membrane during transmitter release at the frog neuromuscular junction. *J. Cell Biol.* 57, 315–344.

Holt, M., Cooke, A., Wu, M. M., and Lagnado, L. (2003). Bulk membrane retrieval in the synaptic terminal of retinal bipolar cells. *J. Neurosci.* 23, 1329–1339.

Hoopmann, P., Punge, A., Barysch, S. V., Westphal, V., Bückers, J., Opazo, F., et al. (2010). Endosomal sorting of readily releasable synaptic vesicles. *Proc. Natl. Acad. Sci. U.S.A.* 107, 19055–19060.

Horstmann, H., Körber, C., Sätzler, K., Aydin, D., and Kuner, T. (2012). Serial section scanning electron microscopy (S3EM) on silicon wafers for ultra-structural volume imaging of cells and tissues. *PLoS One* 7:e35172. doi: 10.1371/journal.pone.0035172

Ivanova, D., and Cousin, M. A. (2022). Synaptic vesicle recycling and the endolysosomal System: A reappraisal of form and function. *Front. Synaptic Neurosci.* 14:826098. doi: 10.3389/fnsyn.2022.826098

Jaramillo-Polanco, J., Lopez-Lopez, C., Yu, Y., Neary, E., Hegron, A., Canals, M., et al. (2022). Opioid-induced pronociceptive signaling in the gastrointestinal tract is mediated by delta-opioid receptor signaling. *J. Neurosci.* 42, 3316–3328. doi: 10.1523/JNEUROSCI.2098-21.2022

Kim, S. H., and Ryan, T. A. (2009). Synaptic vesicle recycling at CNS snapses without AP-2. *J. Neurosci.* 29, 3865–3874. doi: 10.1523/JNEUROSCI.5639-08.2009

Kokotos, A. C., and Cousin, M. A. (2015). Synaptic vesicle generation from central nerve terminal endosomes. *Traffic* 16, 229–240.

Kononenko, N. L., Puchkov, D., Classen, G. A., Walter, A. M., Pechstein, A., Sawade, L., et al. (2014). Clathrin/AP-2 mediate synaptic vesicle reformation from endosome-like vacuoles but are not essential for membrane retrieval at central synapses. *Neuron* 82, 981–988. doi: 10.1016/j.neuron.2014.05.007

Kopp-Scheinpflug, C., Tolnai, S., Malmierca, M. S., and Rübsamen, R. (2008). The medial nucleus of the trapezoid body: Comparative physiology. *Neuroscience* 154, 160–170.

Körber, C., Horstmann, H., Sätzler, K., and Kuner, T. (2012). Endocytic structures and synaptic vesicle recycling at a central synapse in awake rats. *Traffic* 13, 1601–1611. doi: 10.1111/tra.12007

Leitz, J., and Kavalali, E. T. (2011). Ca2+ influx slows single synaptic vesicle endocytosis. *J. Neurosci.* 31, 16318–16326.

Leitz, J., and Kavalali, E. T. (2014). Fast retrieval and autonomous regulation of single spontaneously recycling synaptic vesicles. *Elife* 3:e03658. doi: 10.7554/eLife.03658

Logiudice, L., Sterling, P., and Matthews, G. (2009). Vesicle recycling at ribbon synapses in the finely branched axon terminals of mouse retinal bipolar neurons. *Neuroscience* 164, 1546–1556. doi: 10.1016/j.neuroscience.2009.09.023

Merriam, L. A., Baran, C. N., Girard, B. M., Hardwick, J. C., May, V., and Parsons, R. L. (2013). Pituitary adenylate cyclase 1 receptor internalization and endosomal signaling mediate the pituitary adenylate cyclase activating polypeptide-induced increase in guinea pig cardiac neuron excitability. *J. Neurosci.* 33, 4614–4622. doi: 10.1523/JNEUROSCI.4999-12.2013

Miller, T. M., and Heuser, J. E. (1984). Endocytosis of synaptic vesicle membrane at the frog neuromuscular junction. *J. Cell Biol.* 98, 685–698.

Milosevic, I. (2018). Revisiting the role of clathrin-mediated endoytosis in synaptic vesicle recycling. *Front. Cell. Neurosci.* 12:27. doi: 10.3389/fncel.2018.00027

Missig, G., Mei, L., Vizzard, M. A., Braas, K. M., Waschek, J. A., Ressler, K. J., et al. (2017). Parabrachial pituitary adenylate cyclase-activating polypeptide activation of amygdala endosomal extracellular signal-regulated kinase signaling regulates the emotional component of pain. *Biol. Psychiatry* 81, 671–682. doi: 10.1016/j.biopsych.2016.08.025

Montealegre, S., and van Endert, P. M. (2019). Endocytic recycling of MHC class I molecules in non-professional antigen presenting and dendritic cells. *Front. Immunol.* 9:3098. doi: 10.3389/fimmu.2018.03098

Murthy, V. N., and De Camilli, P. (2003). Cell biology of the presynaptic terminal. *Annu. Rev. Neurosci.* 26, 701–728.

Neef, J., Jung, S., Wong, A. B., Reuter, K., Pangrsic, T., Chakrabarti, R., et al. (2014). Modes and regulation of endocytic membrane retrieval in mouse auditory hair cells. *J. Neurosci.* 34, 705–716. doi: 10.1523/JNEUROSCI.3313-13.2014

Newell-Litwa, K., Chintala, S., Jenkins, S., Pare, J.-F., McGaha, L., Smith, Y., et al. (2010). Hermansky-pudlak protein complexes, AP-3 and BLOC-1, differentially regulate presynaptic composition in the striatum and hippocampus. *J. Neurosci.* 30, 820–831. doi: 10.1523/JNEUROSCI.3400-09.2010

Richards, D. A., Guatimosim, C., and Betz, W. J. (2000). Two endocytic recycling routes selectively fill two vesicle pools in frog motor nerve terminals. *Neuron* 27, 551–559. doi: 10.1016/s0896-6273(00)00065-9

Rizzoli, S. O. (2014). Synaptic vesicle recycling: Steps and principles. *Embo J.* 33, 788–822. doi: 10.1002/embj.201386357

Rizzoli, S. O., and Betz, W. J. (2004). The structural organization of the readily releasable pool of synaptic vesicles. *Science* 303, 2037–2039.

Rizzoli, S. O., Bethani, I., Zwilling, D., Wenzel, D., Siddiqui, T. J., Brandhorst, D., et al. (2006). Evidence for early endosome-like fusion of recently endocytosed synaptic vesicles. *Traffic* 7, 1163–1176. doi: 10.1111/j.1600-0854.2006.00466.x

Sätzler, K., Söhl, L. F., Bollmann, J. H., Borst, J. G. G., Frotscher, M., Sakmann, B., et al. (2002). Three-dimensional reconstruction of a calyx of held and its postsynaptic principal neuron in the medial nucleus of the trapezoid body. *J. Neurosci.* 22, 10567–10579. doi: 10.1523/JNEUROSCI.22-24-10567.2002

Sonntag, M., Englitz, B., Typlt, M., and Rübsamen, R. (2011). The calyx of held develops adult-like dynamics and reliability by hearing onset in the mouse in vivo. *J. Neurosci.* 31, 6699–6709. doi: 10.1523/JNEUROSCI.0575-11.2011

Soykan, T., Kaempf, N., Sakaba, T., Vollweiter, D., Goerdeler, F., Puchkov, D., et al. (2017). Synaptic vesicle endocytosis occurs on multiple timescales and is mediated by formin-dependent actin assembly. *Neuron* 93, 854–866.e4. doi: 10.1016/j.neuron.2017.02.011

Soykan, T., Maritzen, T., and Haucke, V. (2016). Modes and mechanisms of synaptic vesicle recycling. *Curr. Opin. Neurobiol.* 39, 17–23.

Tagliatti, E., Fadda, M., Falace, A., Benfenati, F., and Fassio, A. (2016). Arf6 regulates the cycling and the readily releasable pool of synaptic vesicles at hippocampal synapse. *Elife* 5:e10116. doi: 10.7554/eLife.10116

von Kleist, L., Stahlschmidt, W., Bulut, H., Gromova, K., Puchkov, D., Robertson, M. J., et al. (2011). Role of the clathrin terminal domain in regulating coated pit dynamics revealed by small molecule inhibition. *Cell* 146, 471–484. doi: 10.1016/j.cell.2011.06.025

Watanabe, S., and Boucrot, E. (2017). Fast and ultrafast endocytosis. *Curr. Opin. Cell Biol.* 47, 64–71.

Watanabe, S., Rost, B. R., Camacho-Pérez, M., Davis, M. W., Söhl-Kielczynski, B., Rosenmund, C., et al. (2013). Ultrafast endocytosis at mouse hippocampal synapses. *Nature* 504, 242–247.

Watanabe, S., Trimbuch, T., Camacho-Pérez, M., Rost, B. R., Brokowski, B., Söhl-Kielczynski, B., et al. (2014). Clathrin regenerates synaptic vesicles from endosomes. *Nature* 515, 228–233.

Willox, A. K., Sahraoui, Y. M. E., and Royle, S. J. (2014). Non-specificity of Pitstop 2 in clathrin-mediated endocytosis. *Biol. Open* 3, 326–331. doi: 10.1242/bio.20147955

Wu, W., and Wu, L.-G. (2007). Rapid bulk endocytosis and its kinetics of fission pore closure at a central synapse. *Proc. Natl. Acad. Sci.* 104, 10234–10239. doi: 10.1073/pnas.0611512104

Yu, S-c, Jánosi, B., Liewald, J. F., Wabnig, S., and Gottschalk, A. (2018). Endophilin A and B join forces with clathrin to mediate synaptic vesicle recycling in *Caenorhabditis elegans*. *Front. Mol. Neurosci.* 11:196. doi: 10.3389/fnmol.2018.00196

Yue, H. Y., Bieberich, E., and Xu, J. (2017). Promotion of endocytosis efficiency through an ATP-independent mechanism at rat calyx of Held terminals. *J. Physiol.* 595, 5265–5284. doi: 10.1113/JP274275

Zhang, Q., Li, Y., and Tsien, R. W. (2009). The dynamic control of kiss-and-run and vesicular reuse probed with single nanoparticles. *Science* 323, 1448–1453.

Zhang, Y., Zhu, J., Xu, H., Yi, Q., Yan, L., Ye, L., et al. (2021). Time-dependent internalization of s100b by mesenchymal stem cells via the pathways of clathrin- and lipid raft-mediated endocytosis. *Front. Cell Dev. Biol.* 9:674995. doi: 10.3389/fcell.2021.674995

Zhu, Y., Xu, J., and Heinemann, S. F. (2009). Two pathways of synaptic vesicle retrieval revealed by single-vesicle imaging. *Neuron* 61, 397–411. doi: 10.1016/j.neuron.2008.12.024

frontiers | Frontiers in Synaptic Neuroscience

TYPE Original Research
PUBLISHED 12 May 2023
DOI 10.3389/fnsyn.2023.1176864

Check for updates

OPEN ACCESS

EDITED BY
Karri P. Lamsa,
University of Szeged, Hungary

REVIEWED BY
Iria Gonzalez Dopeso-Reyes,
UMR 5535 Institut de Génétique Moléculaire de Montpellier, France
Thomas J. Younts,
University College London, United Kingdom
Sofía Vallés,
Instituto de Investigaciones Bioquímicas de Bahía Blanca, Argentina

*CORRESPONDENCE
Susana Cohen-Cory
✉ scohenco@uci.edu

RECEIVED 01 March 2023
ACCEPTED 25 April 2023
PUBLISHED 12 May 2023

CITATION
Del Rio R Jr, Serrano RG, Gomez E, Martinez JC, Edward MA, Santos RA, Diaz KS and Cohen-Cory S (2023) Cell-autonomous and differential endocannabinoid signaling impacts the development of presynaptic retinal ganglion cell axon connectivity *in vivo*. *Front. Synaptic Neurosci.* 15:1176864. doi: 10.3389/fnsyn.2023.1176864

COPYRIGHT
© 2023 Del Rio, Serrano, Gomez, Martinez, Edward, Santos, Diaz and Cohen-Cory. This is an open-access article distributed under the terms of the Creative Commons Attribution License (CC BY). The use, distribution or reproduction in other forums is permitted, provided the original author(s) and the copyright owner(s) are credited and that the original publication in this journal is cited, in accordance with accepted academic practice. No use, distribution or reproduction is permitted which does not comply with these terms.

Cell-autonomous and differential endocannabinoid signaling impacts the development of presynaptic retinal ganglion cell axon connectivity *in vivo*

Rodrigo Del Rio Jr., Rosa G. Serrano, Eric Gomez, Joshua C. Martinez, Marina A. Edward, Rommel A. Santos, Kenneth S. Diaz and Susana Cohen-Cory*

Department of Neurobiology and Behavior, University of California, Irvine, Irvine, CA, United States

Cannabis exposure during gestation evokes significant molecular modifications to neurodevelopmental programs leading to neurophysiological and behavioral abnormalities in humans. The main neuronal receptor for Δ^9-tetrahydrocannabinol (THC) is the type-1 cannabinoid receptor CB_1R, one of the most abundant G-protein-coupled receptors in the nervous system. While THC is the major psychoactive phytocannabinoid, endocannabinoids (eCBs) are the endogenous ligands of CB_1R and are known to act as retrograde messengers to modulate synaptic plasticity at different time scales in the adult brain. Accumulating evidence indicates that eCB signaling through activation of CB_1R plays a central role in neural development. During development, most CB_1R localized to axons of projection neurons, and in mice eCB signaling impacts axon fasciculation. Understanding of eCB-mediated structural plasticity during development, however, requires the identification of the precise spatial and temporal dynamics of CB_1R-mediated modifications at the level of individual neurons in the intact brain. Here, the cell-autonomous role of CB_1R and the effects of CB_1R-mediated eCB signaling were investigated using targeted single-cell knockdown and pharmacologic treatments in *Xenopus*. We imaged axonal arbors of retinal ganglion cells (RGCs) in real time following downregulation of CB_1R *via* morpholino (MO) knockdown. We also analyzed RGC axons with altered eCB signaling following treatment with URB597, a selective inhibitor of the enzyme that degrades Anandamide (AEA), or JZL184, an inhibitor of the enzyme that blocks 2-Arachidonoylglycerol (2-AG) hydrolysis, at two distinct stages of retinotectal development. Our results demonstrate that CB_1R knockdown impacts RGC axon branching at their target and that differential 2-AG and AEA-mediated eCB signaling contributes to presynaptic structural connectivity at the time that axons terminate and when retinotectal synaptic connections are made.

Altering CB_1R levels through CB_1R MO knockdown similarly impacted dendritic morphology of tectal neurons, thus supporting both pre- and postsynaptic cell-autonomous roles for CB_1R-mediated eCB signaling.

KEYWORDS

***Xenopus laevis*, live imaging, optic tectum, knockdown, anandamide (AEA), 2-Arachidonoylglycerol (2-AG)**

Introduction

About 2.5–5.0 percent of pregnant women in the US report using cannabis during gestation, yet little is known about the effects of cannabinoid exposure during pregnancy (Henschke, 2019). Various large-scale longitudinal linkage studies have demonstrated potential consequences that include low birth weight, impulsivity and hyperactivity in children, and higher rates of anxiety, depression and in drug abuse later in life (Calvigioni et al., 2014). Similarly, maternal cannabinoid exposure during lactation may impact brain development postnatally due to its high concentration in breast milk, eight times that of a mother's plasma levels (Henschke, 2019). It is therefore important to have a clear understanding of the roles of endocannabinoids (eCBs) and their receptors during early neuronal differentiation to better understand the biological mechanisms involved in cannabis use and the functional consequences of cannabinoid exposure on the developing brain. A large number of studies have shown that eCBs have critical functions in fetal and postnatal brain development, neuronal connectivity, and glial cell differentiation (Berghuis et al., 2007; Harkany et al., 2007, 2008a,b; Martinez et al., 2020; Marinelli et al., 2023). eCBs are important neuromodulators of multiple central neurotransmitter systems that are essential for fetal brain development (Gaffuri et al., 2012). eCBs released from post-synaptic neurons serve as retrograde signals that suppress neurotransmitter release at cortical synapses (Freund et al., 2003), but also can act in a non-retrograde and/or autocrine manner to modulate synaptic function and can interact with other neuromodulatory systems (Castillo et al., 2012). Dissociated cell cultures, mouse, and zebrafish models with targeted deletion of the cannabinoid receptor type-1 (CB_1R) have shown that neurite extension and axon fasciculation are affected by altered cannabinoid signaling (Mulder et al., 2008; Watson et al., 2008; Wu et al., 2010). In the visual system, pharmacological activation or blockade of CB_1R activity can modulate growth cone morphology of cortical and retinal neurons in culture and affects the topographic organization of retinal projections in the brain of knockout mice (Argaw et al., 2011). Because eCBs dynamically regulate brain development, the timing and duration of cannabinoid exposure may have differential effects on developing neurons, and long-term consequences may vary depending on the cellular context. Studies are therefore needed to characterize roles of eCB signaling at multiple stages of brain and neural development in intact organisms especially given that exogenously administered cannabinoids possess medicinal properties and their recreational and therapeutic use in the management of nausea and vomiting during pregnancy is on the rise (Henschke, 2019). Here, we characterized cellular mechanisms by which eCB signaling modulates neural circuit development *in vivo* by differentiating cell-autonomous effects versus global effects of pharmacologic treatments. Moreover, our *in vivo* single-cell analysis allowed us to distinguish between the influence of cannabinoids on developing synaptic circuits at distinct times of development.

Endocannabinoids (eCBs) are lipophilic molecules, which are thought to be synthesized on demand from plasma membrane components through multiple biosynthetic pathways (Freitas et al., 2018). Dietary polyunsaturated fatty acids (PUFAs) serve as precursors for eCBs in the brain. Arachidonic acid (AA), the principal n-6 PUFA in the brain, is produced from linoleic acid (LA), and serves as the precursor to anandamide (AEA), an important eCB that has been implicated in several aspects of neural development (Harkany et al., 2007; Maccarrone et al., 2014; Anderson et al., 2015). Similar to AEA, docosahexaenoic acid (DHA, 22:6n-3), a n-3 polyunsaturated fatty acid (n-3 PUFA) and an essential component of the central nervous system (CNS), is also synthesized from dietary precursors such as α-linolenic acid (ALA) (Freitas et al., 2018). Previous work from our laboratory assessed how depriving such dietary PUFAs from adult maternal *Xenopus* frogs affects retinotectal development. Using *Xenopus* as a model, we demonstrated that maternal n-3 PUFA deficiency significantly alters the morphology and early connectivity of developing central neurons in the progeny, coincident with reduced embryonic brain DHA levels and a decrease in BDNF-mediated neurotrophic support (Igarashi et al., 2015). Maternal dietary DHA supplementation was able to rapidly reverse the n-3 PUFA mediated developmental deficits (Igarashi et al., 2015). AEA, similarly to DHA derivatives in the brain, is synthesized by the N-acyl phosphatidylethanolamine-specific phospholipase D (NAPE-PLD) and hydrolyzed by fatty acid amide hydrolase (FAAH). Another major eCB that can also bind CB_1R with high affinity is 2-Arachidonoylglycerol (2-AG), synthetized by hydrolysis from diacylglycerols (DAGs) by two lipases, DAGLα and DAGLβ, and hydrolyzed by monoacylglycerol lipase (MAGL). Here, we used the relative simplicity of the *Xenopus* visual system to examine basic underlying cellular mechanisms by which n-6 PUFA-derived eCBs modulate presynaptic connectivity. We explored how altered cannabinoid signaling can adversely affect presynaptic retinal ganglion cell (RGC) axons at distinct epochs of development, specifically during axon targeting and during the development of structural and functional brain connectivity. By examining dynamic cellular changes in presynaptic connectivity in postmitotic neurons we were able to differentiate effects of endocannabinoids in the

intact, developing brain, and to correlate structural with functional changes.

Materials and methods

Animals

Xenopus laevis tadpoles were obtained by either *in vitro* fertilization of oocytes or by natural mating of adult females primed with human chorionic gonadotropin. Female and male pairs were left to mate overnight and embryos were collected following 12 h post-injection. Tadpoles were raised in rearing solution [60 mM NaCl, 0.67 mM KCl, 0.34 mM $Ca(NO_3)_2$, 0.83 mM $MgSO_4$, 10 mM HEPES, pH 7.4, and 40 mg/l gentamicin] plus 0.001% phenylthiocarbamide to halt melanocyte pigmentation, with a 12-h light and dark cycle. Tadpoles from stage 38/39 (2.5 to 3 days post-fertilization at 20°C) to stage 45 (5 days post-fertilization at 20°C) were anesthetized during experimental manipulations with 0.05% tricaine methanesulfonate (Finquel; Argent Laboratories, Redmond, WA, USA). Staging of embryos was performed according to Nieuwkoop and Faber (1956). The sex of tadpoles used for experimentation and analyses was random and unknown, as gonadal differentiation in *Xenopus laevis* begins well after stage 49 (Piprek et al., 2017), 9 to 13 days postfertilization. Animal procedures were approved by the Institutional Animal Care and Use Committee of the University of California, Irvine (Animal Welfare Assurance Number A3416–01).

Immunohistochemistry

Stage 42 to stage 47 tadpoles were euthanized with tricaine methanesulfonate and fixed in 4% paraformaldehyde in 0.1 M phosphate buffer, pH 7.5, for 2 h. For coronal sections, tadpoles were cryoprotected in 30% sucrose overnight and embedded in OCT compound (Sakura Finetek, Torrance, CA, USA), and 25-μm cryostat sections were obtained. Coronal sections at the level of the optic tectum were incubated with a rabbit polyclonal antibody against a synthetic peptide from the N-terminal extracellular region of human CB_1 receptor (1:200 dilution; Cayman Chemicals) or a rabbit polyclonal antibody against the cannabinoid receptor CB_1(1–77) (1:250 dilution, Cat# 209550, Calbiochem). CB_1R primary antibodies were visualized using goat anti-rabbit Alexa 488 secondary antibodies (1:500 dilution; Invitrogen, Eugene, OR, USA). The specificity of CB_1R antibodies (1:500 dilution) to recognize endogenous *Xenopus* CB_1R was previously tested and confirmed by Western blot analysis: a band of∼60 kDa was detected by anti- CB_1R antibodies in stage 45 *Xenopus* brain lysates similar to the chick brain (da Silva Sampaio et al., 2018).

Transfection of morpholinos or plasmids

Downregulation of CB_1R expression was performed using lissamine-tagged morpholino anti-sense oligonucleotides (300 nmol, Genetools, Philomath, OR, USA) to block protein translation in *Xenopus* tadpoles similar to published studies (Santos et al., 2018), a treatment that results in 40–60% reduction in protein levels. A morpholino (MO) against *Xenopus laevis* cannabinoid receptor 1 *Cnr1* mRNA was designed with the sequence 5′-GGCCATCCAGAATTGACTTCATTAC-3′ as described in Zheng et al. (2015). A standard lissamine-tagged control morpholino oligonucleotide with the following sequence 5′-CCTCTTACCTCAgTTACAATTTATA-3′ with no known targeting effects was used for control comparisons. Targeted downregulation of CB_1R expression in developing RGCs or in tectal neurons was achieved using single-cell electroporation in developing *Xenopus* tadpoles (Liu and Haas, 2011). Prior to electroporation, tadpoles were anesthetized with 0.05% tricaine methanesulfonate. A CUY-21 edit stimulator was used to electroporate and transfect individual RGCs or tectal neurons of stage 42–43 tadpoles. RGCs or tectal neurons were co-electroporated with lissamine-tagged CB_1R MO (150 nmol pipette concentration) and a cell-filling dye Alexa Fluor 488 dextran, 3,000 MW (2 mg/111 μl pipette concentration, Invitrogen, Eugene, OR, USA), with one electroporation performed per tadpole. Reagents were loaded onto an aluminosilicate pipette (AF100-64-10, 1.00 mm, 0.64 mm, 10 cm) with a pulled tapered-tip with an opening of about 0.5 μm. Neurons transfected with a standard lissamine-tagged control MO (100 nmol pipette concentration) and Alexa Fluor 488 dextran were used as a control comparison with CB_1R MO transfected neurons. Tadpoles were then raised at 22°C until stage 45 (1 day later). Co-transfections of lissamine-tagged morpholinos and Alexa 488 dextran were confirmed *via* fluorescence microscopy. In some tadpoles, leaky single-cell electroporations resulted in more than one transfected neuron. Only tadpoles with individual RGC axons or tectal neurons double-labeled with lissamine and Alexa 488 dextran in the optic tectum were selected for two-photon confocal imaging and analysis (Santos et al., 2018).

Transfection of RGCs with plasmids by electroporation to visualize axon arbors and presynaptic sites

A 2–5 μL mix of Green fluorescent protein (GFP)-synaptobrevin and tdTomato plasmids at equimolar amounts (1 μg/μL) were loaded into an aluminosilicate glass capillary needle and mounted onto a three-axis manual micromanipulator. Tadpoles at stage 28–32 were anesthetized with 0.05% tricaine methanesulfonate and placed in an anesthetic-saturated Sylgard cushion with a custom-made trench. Tadpoles were mounted on their side, with the right eye up, using a standard size harp slice grid. A second micromanipulator holding a pair of cathode and anode copper electrodes were placed 0.1 mm apart to span the diameter of the eye. About 1–2 nL of DNA mix was pressure injected into the anterior chamber near the lens at 20 psi and 15 ms duration using a Picospritzer III pipet holder. A Grass SD9 stimulator was used to simultaneously deliver single currents of 40 V, 200 Hz, 2 ms delay, and 2 ms duration. Tadpoles recovered in fresh rearing solution immediately after electroporation. Tadpoles at stages 39–45 were screened and those with single RGCs expressing tdTomato and punctate GFP-syb in their axon terminals were selected and used for experimentation and imaging.

Pharmacologic manipulations of endocannabinoid levels

We used two experimental paradigms to compare the potential effects of increased AEA signaling with those of 2-AG during RGC axon targeting, branching and presynaptic differentiation in intact animals. Swimming *Xenopus laevis* tadpoles were treated with URB597 an inhibitor of FAAH, or JZL184 a potent inhibitor of MAGL-2, at two distinct stages of visual system development; at stage 38–39 when RGC axons target the optic tectum and at stage 45, when they begin to actively branch. Tadpoles starting at stage 38–39 were reared in multi-well plates in the presence of either URB597 (2.5 μM in 0.1% Dimethyl sulfoxide (DMSO) in rearing solution; Cayman Chemicals, Ann Arbor, MI, USA), JZL184 (2.5 μM in 0.1% DMSO in rearing solution; Cayman Chemicals), or vehicle solution (0.1% in DMSO) for a total of 3 days (until stage 45) in the presence of the drug, with replenishment of fresh pharmacologic agent and rearing solution every 24 h. The concentration of the pharmacologic agents used is within the lowest concentration range shown to be effective and elicit differential effects on sensorimotor function in *Xenopus* tadpoles and zebrafish larvae (Miraucourt et al., 2016; Khara et al., 2022). Tadpoles were then imaged *in vivo* every 24 h for 3 days beginning at stage 45 and reared between observation intervals in the absence of the drug treatment. For pharmacologic treatment of tadpoles beginning at stage 45, tadpoles with single RGCs expressing tdTomato and punctate GFP-synaptobrevin in their axon terminals were first imaged (0 h) and then immediately transferred to fresh rearing solution with either vehicle (0.1% DMSO), URB597 (2.5 μM), or JZL184 (2.5 μM). Tadpoles were reared for 24 h in the presence of the drug and then anesthetized to obtain a second imaging time point (24 h). After the second imaging, tadpoles were returned to fresh rearing solution with fresh drug, reared for 24 h and then imaged (48 h imaging time point). In a subset of experiments aimed to assess the acute effects of drug treatment, stage 45 tadpoles with single RGCs expressing tdTomato and punctate GFP-synaptobrevin in their axon terminals were anesthetized after the initial imaging and 1 nL of vehicle solution or 1 nL of a 50 μM solution of URB597 was injected into the ventricle and lateral side of the tectal neuropil. Tadpoles were then transferred to fresh rearing solution for recovery and were then imaged 6, 12 and 24 h after initial imaging, at stage 45.

Fatty acid analysis of tadpole samples

A total of twenty tadpoles per experimental condition, either at stage 38–39 or at stage 45, were treated as above with either URB597 (2.5 μM in 0.1% DMSO in rearing solution; Cayman Chemicals, Ann Arbor, MI, USA), JZL184 (2.5 μM in 0.1% DMSO in rearing solution; Cayman Chemicals), or vehicle solution (0.1% DMSO) for 1 h. Tadpoles were then transferred to fresh rearing solution without the drug, anesthetized in 0.05% Finquel, quickly rinsed to remove most of the rearing solution containing the drug, and immediately frozen until further processing for fatty acid analysis. Frozen tadpole samples were homogenized, extracted and processed for liquid chromatography-mass spectrometry (LC/MS-MS) analyses as in Torrens et al. (2023). Triplicate experiments were used for the statistical analysis of data. One-way and two-way ANOVA with Tukey's multiple comparison tests were used to statistical analysis of data. Results were considered significant in comparison to control when $p \leq 0.05$.

In vivo real-time confocal microscopy imaging

At stage 45, tadpoles were anesthetized with 0.05% tricaine methanesulfonate and mounted in a 35 × 10-mm Petri dish containing an agar cushion (2.5% w/v agar gel in 1× MR). Tadpoles were screened with 10× and 20× objective lenses using an epifluorescence microscope for the presence of fluorescently labeled RGC axons innervating the contralateral side of the optic tectum or individual tectal neurons in the optic tectum. Tadpoles were transferred to a custom-made anesthetic-saturated Sylgard chamber and positioned in place using a standard size harp slice grid. Imaging of tadpoles co-transfected with MOs and Alexa 488 dextran was performed using an inverted laser scanning LSM780 confocal microscope (Zeiss), equipped with a MaiTai Ti: Sapphire multiphoton laser system and a 63× objective. Tadpoles were imaged over the course of 3 days, at 24-h intervals. A two-photon wavelength of 760 to 780 was used to image the Alexa 488 cell-filling dye in RGC axons or in tectal neurons in the midbrain. Neurons in tadpoles co-transfected with tdTomato and GFP-synaptobrevin were imaged using a Nikon PCM2000 laser-scanning confocal microscope equipped with Argon and HeNe lasers. To assess the effects of long-term drug treatment, tadpoles were first imaged at stage 45 and every 24 h later over the course of 2 days. To assess the acute effects of treatment, tadpoles were imaged at 6, 12 and 24 h after the initial imaging at stage 45. Images were collected in a 1 μm interval throughout the extent of the arbor. Tadpoles were allowed to recover in fresh rearing solution immediately after imaging.

Neuronal arbor analysis

In brief, three-dimensional images of fluorescently-labeled RGC axon or tectal neuron dendritic arbors were manually reconstructed blind to treatment using the Neuromantic tracing software version 1.7.5 (Myatt et al., 2012). Each axonal or dendritic arbor was reconstructed plane-by-plane from the image z-stack and was then measured and analyzed using the Neuromantic software. Branch tips were identified as the terminal ends of primary axons or dendrites. The total arbor including branch tips was thresholded, binarized, and skeletonized with the Neuromantic software so that the arbor was represented as a single pixel width. Processes of more than 5 μm in length were considered branches, while processes less than 5 μm were categorized as filopodia (Alsina et al., 2001; Marshak et al., 2007; Manitt et al., 2009). To measure the number of GFP-synaptobrevin puncta in GFP-synaptobrevin and tdTomato double-labeled axons, overlapped images were digitized, selected for color (yellow; locations of complete red and green overlay with hue and pixel intensity values between 16–67 and 150–255, respectively) and binarized as in Alsina et al. (2001) using the MetaMorph software (Molecular Devices, Inc., San Jose, CA, USA). GFP-synaptobrevin labeled puncta of 0.5–1.0 μm^2 in size (size

of smallest puncta observed) and 150–255 pixel intensity values were considered single synaptic clusters. The number of pixels representing the GFP-synaptobrevin puncta were counted with MetaMorph (Alsina et al., 2001) and normalized by the length of the axon arbor. Similar synaptic cluster values were obtained by digital or manual counting of yellow puncta. Student's *t*-tests and one-way ANOVA with Tukey's or Sidak's multiple comparison tests were used for the statistical analysis of the data. Results were considered significant in comparison to control as follows: $^{*}p \leq 0.05$, $^{**}p \leq 0.005$, $^{***}p \leq 0.001$, unless otherwise indicated on the graph.

Visual avoidance task

Stage 45 tadpoles were placed in a 14 cm×15 cm glass Petri dish, with darkened walls, filled with 80 ml of modified rearing solution at room temperature. The dish was placed on a monitor screen and a solid, opaque box was placed over the monitor to eliminate outside light. A camera was affixed to the opening at the top of the box for video recording. Visual stimuli were produced by a custom-written program modified and adapted from published protocols (Dong et al., 2009; Khakhalin et al., 2014). Four tadpoles were placed in the Petri dish per trial for each of the experimental conditions. A video loop containing randomly distributed black circles of 0.3 mm radius was projected on a white background. This size was found to produce optimal responses to the stimulus as shown in Nagel et al. (2015). Swimming tadpoles were exposed to the moving circles for a period of 30 s per trial for a total of six trials per tadpole. The tadpole's response to every circle encountered was analyzed blind to treatment, with frame-by-frame replay of recorded behaviors, by tracing each tadpole's swimming path. Tadpoles were observed to freeze, swim in circles, and/or swim away by altering their direction, speed, or both when presented with stimuli. These responses were counted as visual reactions to the stimuli. Failure to alter the swimming path, move away from the circle or a lack of freezing behavior was considered a failure to respond. Experiments were performed during the light phase of the 12-h light-dark cycle. Treatments were identical to those of drug treatment and *in vivo* imaging studies with the exception that tadpoles were exposed to pharmacologic agents in rearing solution beginning at stage 45 and tested for the behavioral task 24 h later. The behavior of a total of 20–24 tadpoles was analyzed per condition from three independent experiments: Student's *t*-tests and one-way ANOVA with Tukey's multiple comparison tests were used for the statistical analysis of the data. Results of behavioral analysis were considered significant as follows: $^{*}p \leq 0.05$, $^{**}p \leq 0.005$, $^{***}p \leq 0.001$.

Results

CB_1R expression in the retina and midbrain of *Xenopus* tadpoles

Studies have shown that the endocannabinoid receptor CB_1R is dynamically regulated during the development of *Xenopus laevis* embryos, with its mRNA being detected as early as stage 28 and protein at stage 41 (Migliarini et al., 2006). To define cell-autonomous roles for the CB_1 receptor during retinotectal development, we first set out to confirm CB_1R expression in *Xenopus* at the time when retinotectal circuits begin to form. We performed immunohistochemistry on coronal sections of stage 42 and stage 45 tadpoles using two distinct polyclonal antibodies against CB_1R that showed consistent immunoreactivity patterns. In the *Xenopus* eye, strong CB_1R expression localized to the RGC, inner plexiform and inner nuclear layers (**Figures 1A, B**) in agreement with published studies (Miraucourt et al., 2016), as well as in the optic nerve (**Figure 1C**). CB_1R immunoreactivity was also strongly localized to cell bodies and neuropil within the *Xenopus* midbrain and hindbrain (**Figures 1D–F**). As illustrated in **Figure 1G**, individual neuronal cell bodies and processes projecting to the neuropil could be distinguished by their strong CB_1R immunoreactivity. Little CB_1R immunoreactivity was detected near the ciliary margin of the retina, where retinal precursor cells localize at these stages (**Figure 1A**), and was similarly absent in the proliferative areas of the brain (**Figures 1D–G**). Thus, the expression patterns of CB_1R in *Xenopus* are consistent with potential pre- and postsynaptic cell-autonomous roles in postmitotic neurons in the developing visual system.

Cell-autonomous CB_1R signaling impacts RGC axon morphology

A number of studies support roles for CB_1R signaling during RGC differentiation and function in *Xenopus* as in other species (Martella et al., 2016; Miraucourt et al., 2016; Middleton et al., 2019; Elul et al., 2022). However, direct effects of CB_1R -mediated endocannabinoid signaling in the development of visual central connectivity have not been demonstrated. Here, we examined potential CB_1R cell-autonomous effects by downregulating its expression through targeted CB_1R MO knockdown in tadpoles at the time when retinotectal connections form. Single-cell co-electroporation of lissamine-tagged Control or CB_1R MO together with Alexa 488 dextran was used to downregulate CB_1R expression at stage 43 and visualize individual RGC axons as they terminate in the optic tectum beginning at stage 45, 24 h after MO transfection. While axons from RGCs transfected with the CB_1R MO targeted normally within the tectal neuropil, their branching patterns and morphologies differed from those of RGCs in tadpoles transfected with Control MO (**Figure 2**). Qualitatively, axons from RGCs with CB_1R knockdown had more branches that terminated in growth cones and/or took abnormal turns (**Figure 2A**). When quantifying the total number of branches in axons imaged 48 h after transfection, axons from RGCs with CB_1R knockdown had significantly fewer branches when compared to axons from RGCs transfected with Control MO (Control MO 19.61 ± 2.72 branches, CB_1R MO 8.0 ± 1.41 branches; n = 23 axons per condition, with one axon imaged per tadpole; **Figure 2B**). To determine the time course of the knockdown effect, a smaller sample of tadpoles with targeted RGC MO knockdown were imaged over the course of 3 days, beginning at stage 45, 24 h after transfection. Axon branch number was significantly lower in RGCs with CB_1R MO knockdown at the first imaging interval and remained low when compared to controls at the end of the observation period, while

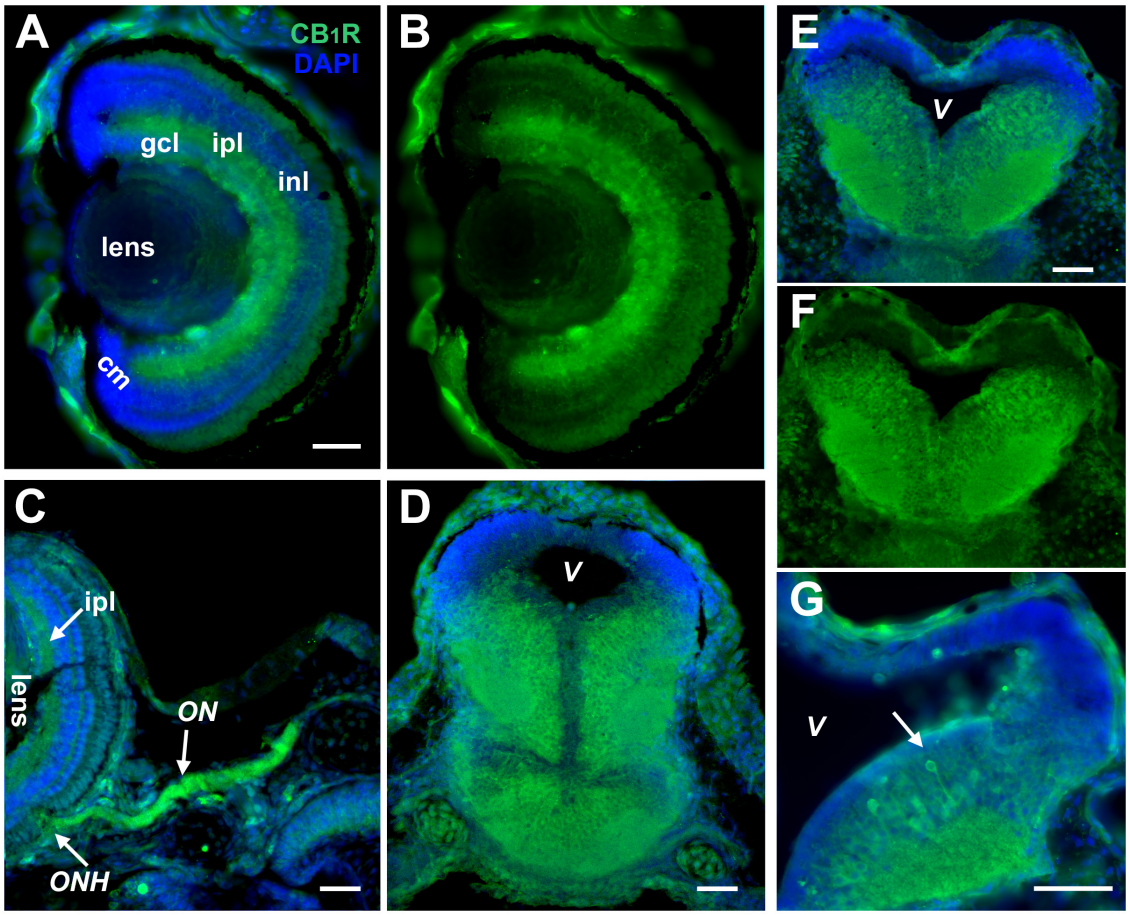

FIGURE 1
CB_1R expression in the developing *Xenopus* visual system. **(A,B)** Coronal section of a retina of a stage 45 tadpole shows localization of strongest CB_1R immunoreactivity (green) in the ganglion cell layer (gcl), inner nuclear layer (inl), and the inner plexiform layer (ipl). The cellular layers are clearly denoted by the DAPI staining in **(A)** (blue). Note the absence of CB_1R immunoreactivity in the ciliary margin (cm). **(C)** Strong CB_1R immunoreactivity is also observed in the optic nerve head (ONH) where RGC axons exit the retina, and along the optic nerve (ON). **(D–F)** CB_1R expression in the brain is illustrated by the coronal sections of midbrain **(D)**, caudal midbrain **(E,F)** and rostral hindbrain **(G)** where CB_1R immunoreactivity (green) localizes to cell bodies that lay medially and in the adjacent neuropil of stage 43 to stage 45 tadpoles. Note the individual neuronal cell bodies and processes projecting to the neuropil with strong CB_1R immunoreactivity (**G**, arrow). In **(D,E,G)**, the DAPI staining highlights the lower CB_1R immunoreactivity in the proliferative zones near the ventricle (V) and its absence in the dorsal-most portion of the brain. Scale bars = 50 μm. Similar patterns of CB_1R immunoreactivity were obtained with two commercial antibodies to CB_1R (**A,B,E–G**; Cayman Chemicals, and **C,D**; Calbiochem).

control RGC axons tended to increase their branch number over the course of 3 days ($n = 12$ axons for Control MO, $n = 11$ axons for CB_1R MO, one axon imaged per tadpole; **Figure 2C**). These results demonstrate that presynaptic RGCs that express CB_1Rs are capable to respond cell-autonomously to acute alterations in eCB signaling.

Endocannabinoid levels and pharmacologic manipulation in *Xenopus* embryos and tadpoles

To further examine effects of altered endocannabinoid signaling on presynaptic retinotectal connectivity, we exposed tadpoles to pharmacologic agents starting at two distinct stages of development, at stage 38/39, when the first RGC axons travel to and begin to innervate the optic tectum (Holt and Harris, 1983), and at stage 45 when retinotectal connections actively form (Alsina et al., 2001). Tadpoles at these stages were evaluated for fatty acid content to determine endogenous levels and confirm the efficacy of the treatment. Tadpoles were treated with URB597 (2.5 μM), a selective inhibitor of FAAH, the enzyme that degrades AEA and related compounds, or JZL184 (2.5 μM), a potent and selective inhibitor of MAGL, the enzyme that blocks 2-AG hydrolysis. In control, vehicle-treated tadpoles, levels of AEA, palmitoylethanolamide (PEA) and oleoylethanolamide (OEA) were lower at stage 38 and increased by stage 45 (**Table 1**). URB597 treatment at stage 38 did not significantly change the levels of AEA, PEA, OEA or 2-AG (**Table 1**). However, at stage 45, URB597 treatment significantly increased AEA and OEA levels but did not change PEA or 2-AG levels when compared to vehicle or JZL184-treated tadpoles (**Table 1**), indicating the efficacy of the FAAH inhibitor treatment and suggesting that fatty acid synthesis and metabolism are dynamically regulated. Similar to AEA, levels of 2-AG were lower in stage 38 tadpoles than at stage 45 but were orders of magnitude higher than those of AEA at both stages (Stage 38; AEA approx. 20 pg/mg of protein, 2-AG approx. 470 ng/mg

10.3389/fnsyn.2023.1176864

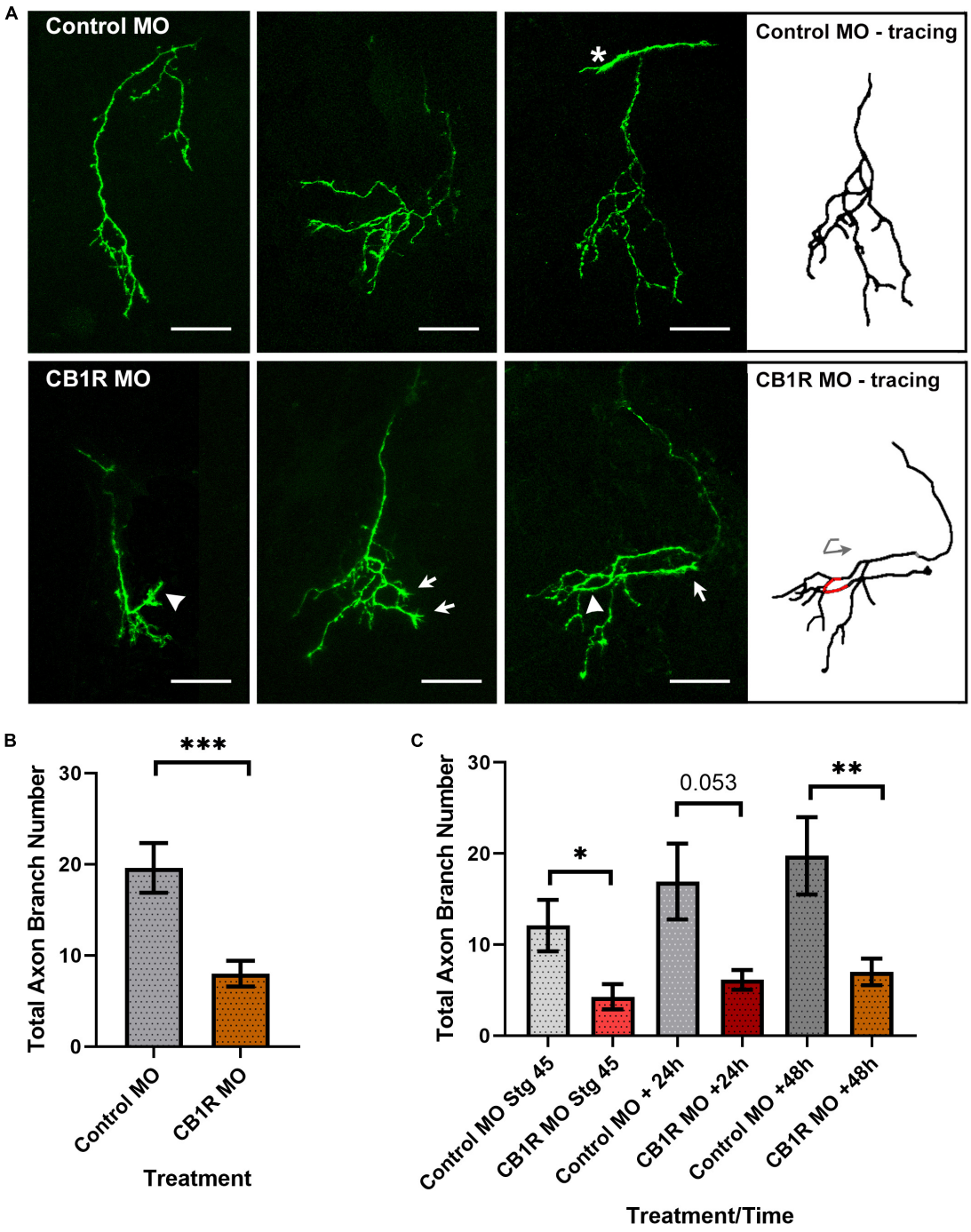

FIGURE 2

CB_1R downregulation alters RGC axon morphology. **(A)** Projections of three individual RGC axons transfected with Control MO (top) or CB_1R MO (bottom) imaged *in vivo* by two-photon confocal microscopy. While axons from RGCs transfected with the CB_1R MO targeted normally within the tectal neuropil, their branching patterns and morphologies differed from those of RGCs in tadpoles transfected with Control MO. Qualitatively, axons from RGCs with CB_1R knockdown had more branches that terminated in growth cones (arrows) and/or took abnormal turns (arrowheads). The tracing for the third CB_1R MO sample axon better illustrates the abnormal turn (red; curved arrow) taken by the axon. The asterisk in the third Control MO sample points to the growth cone of a targeting RGC axon. Scale bars = 50 μm. **(B)** Quantitatively, axons from RGCs with CB_1R knockdown had significantly fewer branches when compared to axons from RGCs transfected with Control MO 48 h after transfection (n = 23 axons per condition, one axon per tadpole). **(C)** When imaging over the course of 3 days, axon branch number was significantly lower in RGCs with CB_1R MO knockdown at the initial imaging (stage 45), with a trend at the 24-h imaging interval (+24 h) and remaining significantly lower when compared to controls at the end of the imaging period (+48 h). Control MO n = 12; CB_1R MO n = 11. Mean ± SEM. *$p \leq 0.05$, **$p \leq 0.005$, ***$p \leq 0.001$.

protein; Table 1). Interestingly, treatment of tadpoles with JZL184 significantly increased 2-AG levels at stage 38 when compared to vehicle or URB597-treated tadpoles but not at stage 45 (Table 1), again suggesting a differential, dynamic regulation 2-AG synthesis and metabolism during development. Levels of AEA, PEA or OEA were not significantly different in JZL184 treated tadpoles from

those in vehicle-treated tadpoles at either of the two stages analyzed (Table 1), eliminating the possibility of off-target effects.

Rate of axon branching is selectively increased after URB597 treatment in actively branching RGCs

To further evaluate how endocannabinoid receptor activation impacts RGC axon morphology at the time that retinotectal connections form, we examined potential changes in RGC axon targeting, branching and synaptic differentiation upon changes in eCB levels by imaging individual RGC axons co-expressing tdTomato and GFP-synaptobrevin as they innervate the tectal neuropil in stage 45 tadpoles. We used URB597 to increase endogenous AEA levels in the brain. Microinjection of a single, acute dose of URB597 (1 nL of 50 μM solution) into the optic tectum resulted in a rapid change in RGC axon morphology at the target within the first 6 h after treatment when compared to vehicle-injected controls (Figures 3A, B). The number of branches and the rate of RGC axon branching (change in branch number) in URB597 treated tadpoles was significantly higher than in controls during the first 6 h after treatment (0–6 h; Control 105.5 ± 5.4%; URB597 152.1 ± 5.9%, p = 0.0002; Figure 3C). While URB597-treated axons continued to branch and increased their complexity at the 12- and 24-h imaging time points (Figure 3B), the rate of axon branching returned to that of control levels by the 12-h imaging time point (Figure 3C). Thus, the effects of acute increase in eCB signaling, as a result from blocking hydrolysis of AEA and related eCBs by the FAAH inhibitor, were rapid and involved a significant remodeling of axon arbors. To further evaluate effects of a more chronic treatment, we exposed tadpoles to URB597 for a period of 48 h at stage 45 when axons actively branch. Immediately after initial imaging, we reared stage 45 tadpoles with RGCs expressing tdTomato and GFP-synaptobrevin in URB597 (2.5 μM in rearing solution) for 2 days. RGC axons in URB597-treated tadpoles significantly increased their number of branches during the first 24 h of treatment when compared to controls, resulting in RGC axons with a significantly higher branch number than those in control tadpoles by 24 and 48 h (Figures 4A, B, D). The observation that RGC axons in URB597-treated tadpoles showed a fast response to URB597 treatment (at 24 h) but did not further increase their number of branches by 48 h, again indicate a rapid effect of the drug treatment. Imaging of RGC axons also showed that during the first 24 h of treatment, GFP-synaptobrevin puncta were added at rate to maintain the normal density of presynaptic sites in the more elaborate RGC axon arbors (Figures 4A, B, E). Specifically, as axons in URB597-treated tadpoles branched more rapidly during the first 24 h of treatment (Change in branch number 0–24 h: Control 146.7 ± 16.4%, URB597 242.3 ± 60.2%; p = 0.043, not shown graphically), the number of GFP-synaptobrevin puncta in those axons increased at a rate to maintain a similar density in the more branched arbors when compared with axons from control tadpoles (Change in GFP-syb puncta/length 0–24 h: Control 151.8 ± 60.6%; URB597 163.7 ± 31.1%; p = 0.854; Figure 4E).

To evaluate whether altered endocannabinoid levels and signaling influence RGC axons not only as they branch but also as they travel to the tectum and before they begin to branch, tadpoles co-electroporated with tdTomato plus GFP-synaptobrevin expression plasmids were then treated with URB597 beginning at stage 38 and every 24 h after for 2 days until they reached stage 45. Tadpoles were then transferred to fresh rearing medium without the drug and imaged at that stage (stage 45; 0 h) and 24 and 48 h later. Treatment of young tadpoles with URB597 resulted in RGC axons with similar morphologies to those in aged matched control tadpoles by stage 45 but failed to increase their branch number over the course of 2 days (Figures 5A, B). In contrast to the effects of treatment beginning at stage 45, the number of axon branches was significantly lower in RGCs at the 48-h imaging time point in tadpoles treated with URB597 at stage 38 when compared to RGCs in control tadpoles at the same stage (Figure 5D). Surprisingly, even though chronic treatment with URB597 in tadpoles at stage 38 resulted in RGC axons with more immature axon morphologies at stage 45, those RGC axons had a significantly higher density of GFP-synaptobrevin labeled presynaptic sites than axons in control tadpoles at all imaging intervals (GFP-syb puncta/20 μm: Control 0 h 2.18 ± 0.5, URB597 0 h 4.8 ± 1.1; Control 24 h 3.26 ± 0.9, URB597 24 h 8.02 ± 1.6; Control 48 h 3.36 ± 1.2, URB597 48 h 8.17 ± 1.3, $p \leq 0.05$, n = 9 axons for control, n = 7 axons for URB597, Figure 5E). Together these results indicate that endogenous AEA participates in axon branching and synaptic differentiation and that differential effects at distinct stages of axon development may reflect differential activation and/or desensitization of CB_1R or of the eCB system during development.

TABLE 1 Fatty acid analysis of tadpole samples.

	Fatty acid	Concentration	(pg/mg)	Concentration (ng/mg)
	AEA	PEA	OEA	2-AG
Stage 38 treatment				
DMSO	19.5 ± 7.5	986.0 ± 139	102.4 ± 13.1	466.2 ± 39.1
URB597	24.8 ± 4.8	1,231 ± 114	193.6 ± 33.9	325.3 ± 45.2
JZL184	48.16 ± 5.4	1,282 ± 243	216.9 ± 19.3	886.5 ± 133*
Stage 45 treatment				
DMSO	90.3 ± 23.2	2,012 ± 220	501 ± 13.6	1,263 ± 107
URB597	224.5 ± 53.5**	4,124 ± 1633	931 ± 225.2*	1,553 ± 363
JZL184	76.0 ± 21.5	3,074 ± 407	412.8 ± 83.5	940 ± 226

One-way and two-way ANOVA with Tukey's multiple comparison tests show significant differences between JZL184 versus DMSO and URB597 treated tadpoles at stage 38 (*$p \leq 0.05$), and URB597 versus DMSO and JZL184 treated tadpoles at stage 45 (**$p \leq 0.005$). OEA levels are also significantly increased by the URB597 treatment at stage 45 (*$p \leq 0.05$). No other significant difference among groups either at stage 38 or stage 45 was found. Mean ± SEM.

Early JZL184 treatment interferes with axon branching and induces pathfinding errors in RGC axons as they target in the optic tectum

To evaluate potential differential effects of AEA and 2-AG-mediated endocannabinoid signaling on RGC axons, a similar

10.3389/fnsyn.2023.1176864

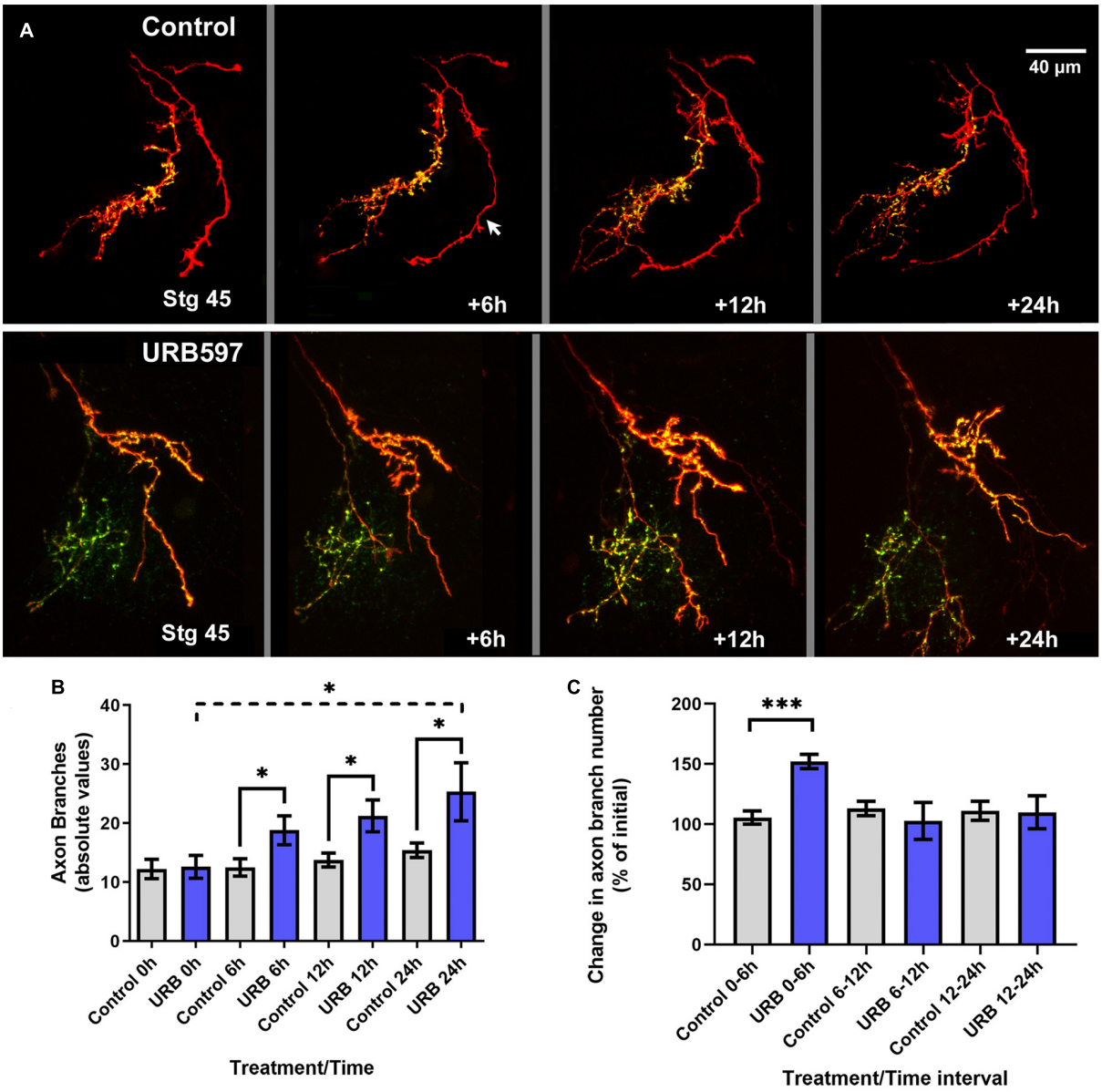

FIGURE 3
Rapid and transient branching response by RGC axons to acute tectal URB597 treatment. **(A)** Tadpoles with RGC axons co-expressing tdTomato and GFP-synaptobrevin received an acute, localized injection of URB597 into the optic tectum at stage 45 and were imaged by confocal microscopy 6, 12 and 24 h after initial imaging (stg 45, time 0 h). Two sample arbors in a control tadpole (top panel) and in a tadpole with tectal injection of URB597 (bottom panel) illustrate the changes in dynamic branching and in the number and localization of GFP-labeled pre-synaptic sites in the axon arbors. In the control sample, one axon expresses tdTomato only (arrow). Scale bar = 40 µm. **(B)** Quantitative analysis of total branch number shows that RGC axons had significantly more branches in the URB597-treated tadpoles during first 6 h after treatment than RGC axons in control tadpoles, a significant difference that was maintained for 24 h. **(C)** The rate of axon branching, expressed as the change in branch number per imaging interval, was significantly higher during the first 6 h after URB597 tectal injection and returned to a similar rate to those in control tadpoles at the 6–12- and 12–24-h imaging intervals. Control n = 12 axons, URB597 n = 7 axons. Analysis by Student's t-tests. Mean ± SEM. *$p \leq 0.05$, ***$p \leq 0.001$.

protocol was used to increase endogenous 2-AG levels by adding JZL184, a MAGL inhibitor, to the rearing solution either at stage 45 or stage 38. In contrast to URB597 treatment, treatment of stage 45 tadpoles with JZL184 over the course of 2 days resulted in RGC axons with similar number of branches at all observation time points when compared to controls (Figures 4C–E). While no significant changes in RGC axon branch number or branch dynamics were observed in tadpoles exposed to JZL184 at stage 45, axons were simpler and less branched than controls when treatment was initiated at stage 38. In JZL184-treated tadpoles, RGC axon branch number was significantly lower than controls at the 48-h imaging time point (Figures 5C, D). Moreover, we observed that treatment of tadpoles with JZL184 at stage 38 resulted in RGC axons with more branching and axon pathfinding errors, including abnormal crossing to the ipsilateral optic tectum (Figures 6A–C). Quantitatively RGC axon arbors in stage 38 JZL184-treated tadpoles did not differ in the overall number branches they possessed from those in URB597 treated tadpoles, however, axon

10.3389/fnsyn.2023.1176864

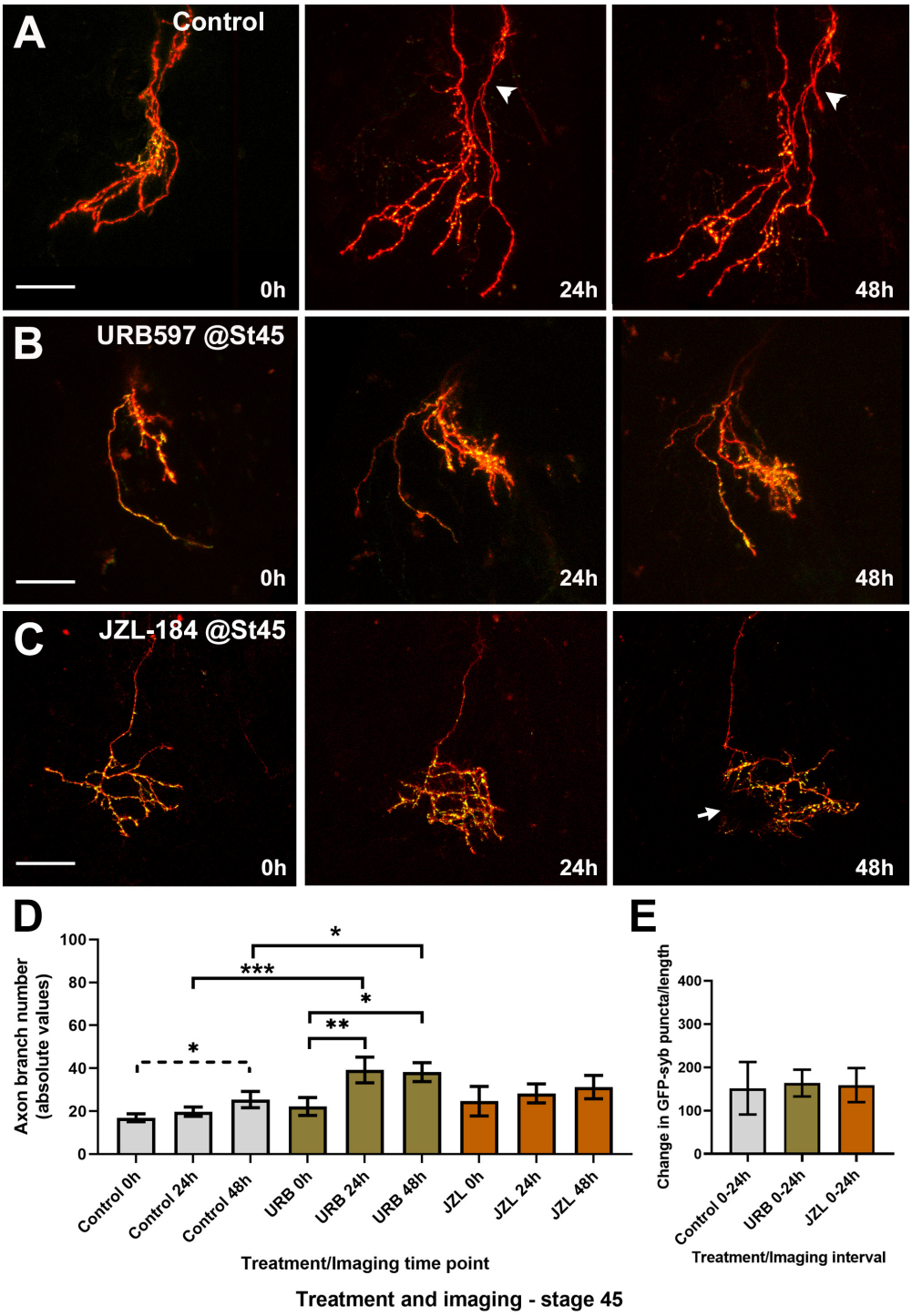

FIGURE 4
Global URB597 treatment at stage 45 increases the complexity of actively branching RGCs *in vivo*. **(A–C)** Sample RGC axons in stage 45 tadpoles transfected with tdTomato and GFP-synaptobrevin plasmids. Tadpoles imaged *in vivo* at stage 45 before (0 h), and 24, and 48 h after vehicle (**A**; Control), URB597 **(B)**, or JZL184 **(C)** bath treatment. RGC axons gradually increased their number of branches over a period of 48 h. Arrowhead in **(A)**, points to a second axon. Arrow in **(C)** points to an area of the arbor obscured by a pigment cell. Scale bars = 50 μm. **(D)** Quantitative analysis of branch number in RGC axons in URB597-treated tadpoles shows a faster and significant increase in branch number during the first 24 h of treatment, resulting in a higher number of branches by 24 and 48 h vs. controls (n = 10 axons per condition). No significant difference in the number of branches was observed for axons in JZL184 treated tadpoles at any observation interval when compared to axons in control tadpoles. **(E)** The density of GFP-synaptobrevin puncta per arbor was calculated as the number of puncta per 20 μm. No significant difference in puncta density before and 24 h after treatment (change in GFP-synaptobrevin puncta/length 0–24 h) was observed in axons from URB597- or JZL184-treated tadpoles when compared to controls. Analysis by ANOVA with Sidak's multiple comparisons tests and Student's t-test. Mean ± SEM, $*p \leq 0.05$, $**p \leq 0.005$, $***p \leq 0.001$.

10.3389/fnsyn.2023.1176864

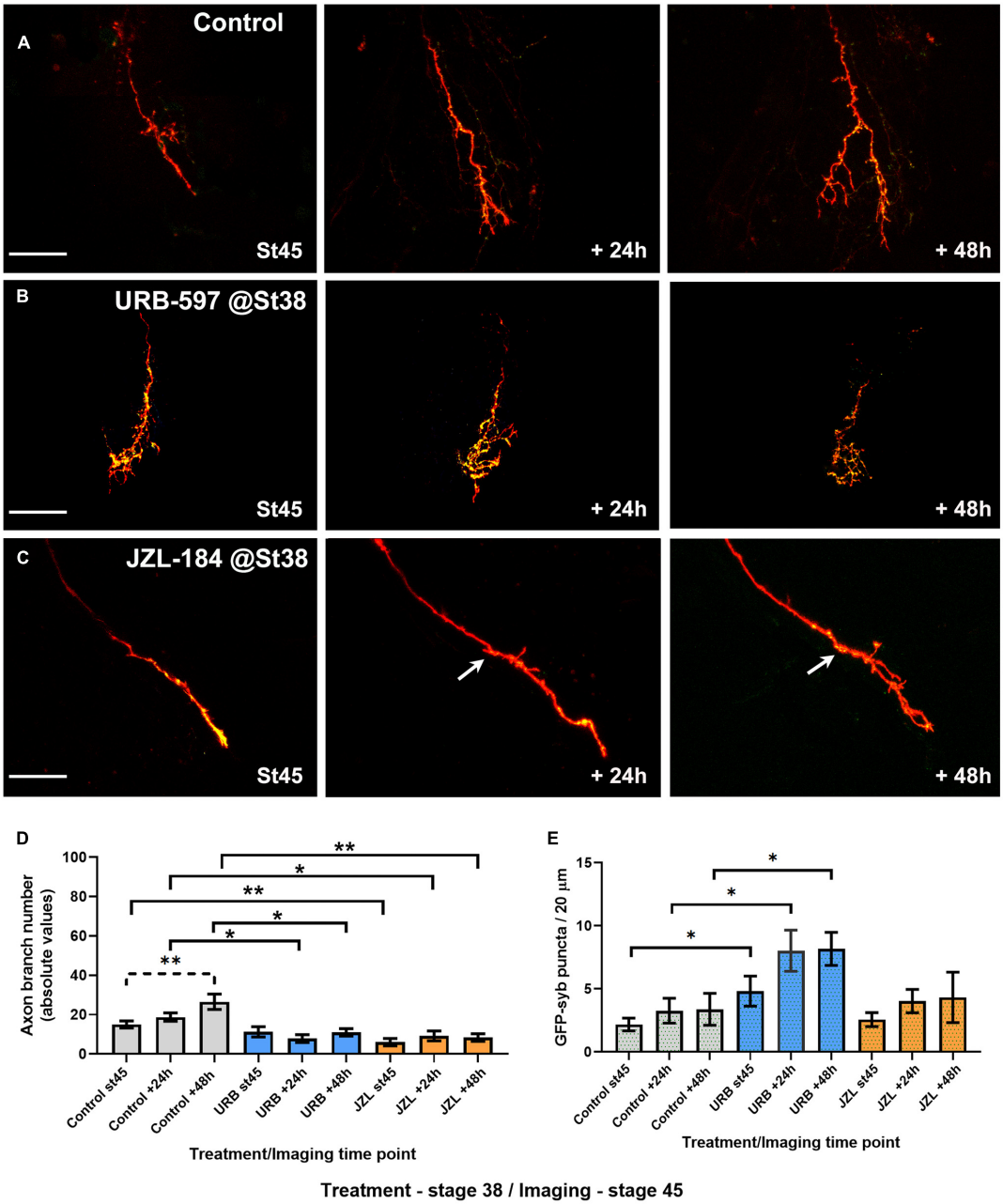

FIGURE 5
URB597 or JZL184 treatment during early axon pathfinding and targeting results in RGC axons with much simpler morphologies as they branch at their target. Tadpoles were treated with URB597 or JZL184 beginning at stage 38 until stage 45, when tadpoles with RGC axons expressing tdTomato and GFP-synaptobrevin were imaged for three consecutive days in the absence of the drug. **(A–C)** Sample RGC axons in tadpoles treated with vehicle solution (**A**; Control), URB597 **(B)** or JZL184 **(C)** imaged *in vivo* by confocal microscopy at stage 45, and 24, and 48 h after first imaging. Arrow in **(C)** points to the first branching point of the axon. Scale bars = 50 µm. **(D)** Quantitative analysis of branch number in RGC axons of tadpoles exposed to the drugs from stage 38 to stage 45 showed that RGC axons in both JZL184 and URB597-treated tadpoles failed to increase their branch number over the course of 48 h when compared to controls (n = 11 axons per condition). Axons in control-treated tadpoles significantly increased their branch number over the 48-h imaging period. **(E)** The density of GFP-synaptobrevin puncta per arbor was calculated as the number of puncta per 20 µm. When compared to controls, axons in URB597-treated tadpoles had a significant higher puncta density at all imaging intervals. Analysis by ANOVA with Sidak's multiple comparisons tests. Mean ± SEM, *$p \leq 0.05$, **$p \leq 0.005$.

branches made more abnormal turns within the neuropil and/or branched more locally in JZL184 treated tadpoles than in URB597-treated and control tadpoles (Figure 6D). The density of GFP-synaptobrevin labeled presynaptic sites in axons from JZL184-treated tadpoles was not significantly different from control tadpoles at any of the imaging intervals (GFP-syb puncta/20 µm: Control 0 h 2.18 ± 0.5, JZL184 0 h 2.56 ± 0.55; Control 24 h 3.26 ± 0.9, JZL184 24 h 4.02 ± 0.9; Control 48 h 3.36 ± 1.2, JZL184 48 h 4.31 ± 1.8, $p \leq 0.05$, n = 9 axons per condition, Figure 5E). Together, these results indicate that differential AEA- and 2-AG-mediated endocannabinoid signaling at distinct times of development impacts RGC axon arbor morphological and synaptic

10.3389/fnsyn.2023.1176864

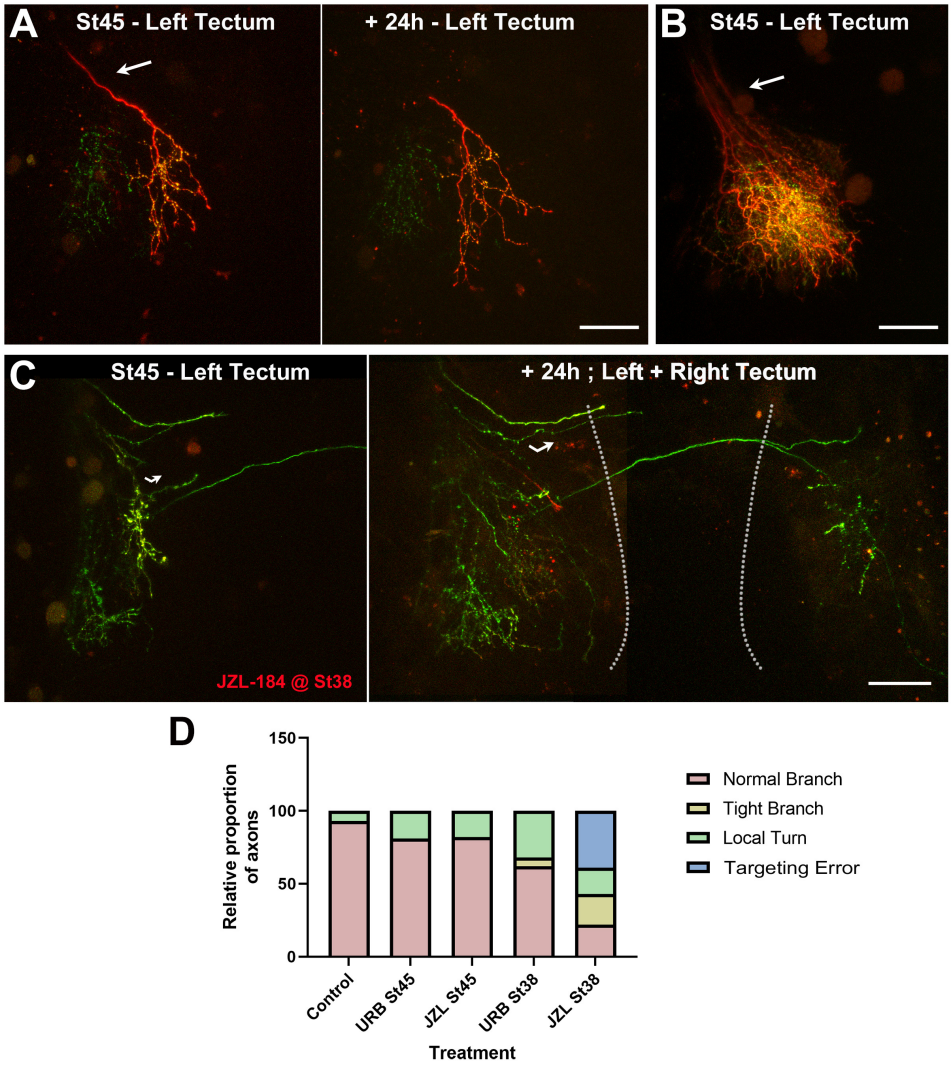

FIGURE 6
Targeting errors in arborizing RGC axons induced by early JZL184 treatment. **(A–C)** Confocal projections of RGC axons branching in the optic tectum of control **(A,B)** and JZL184-treated **(C)** tadpoles imaged at stage 45. **(A,B)** The examples of control tadpoles with individual axons at stage 45 and +24 h **(A)**, or multiple axons at stage 45 **(B)** illustrate how RGC axons enter the optic tectum through the optic tract (arrows) with similar directionality before they branch. **(C)** Confocal images of the optic tectum of a tadpole treated with JZL184 beginning at stage 38 show RGC axons with apparent targeting errors within the contralateral hemisphere at stage 45 (left panel, curved arrow), and reveal abnormal crossing of axons to the ipsilateral hemisphere 24 h after initial imaging (right panel; stitched image). The dashed lines delineate the two midbrain hemispheres. Scale bars = 100 μm. **(D)** While quantitatively RGC axon arbors in tadpoles treated with URB597 and JZL184 at stage 38 differ in the overall number of branches they possessed at stage 45 (**Figure 5**), in proportion axon arbors were also observed to make abnormal turns (local turns) within the neuropil and/or to branch more locally (tight branch) when treatment began at stage 38. Moreover, in proportion more RGC axons in tadpoles treated with JZL184 projected aberrantly, showing abnormal ipsilateral crossing (targeting errors). Control n = 14, URB597 at stage 45 n = 16, JZL184 at stage 45 n = 11, URB597 at stage 38 n = 19, JZL184 at stage 38 n = 28. Statistical analysis by chi-square, difference in outcome among groups $p \leq 0.0001$.

differentiation at the time that active *Xenopus* retinotectal synaptic connections are made.

Cell-autonomous CB_1R signaling also contributes to the structural differentiation of postsynaptic tectal neurons

Studies have shown that CB_1R expression is high in glutamatergic projection neurons during development and then decreases as glutamatergic circuits mature (Vitalis et al., 2008), consistent with our observation of a CB_1R -mediated presynaptic action on RGCs in a differentiating retinotectal circuit. To also examine whether CB_1R signaling can directly impact postsynaptic neurons in the visual system, we examined the morphological differentiation of tectal neurons with targeted CB_1R knockdown (**Figure 7**). Single-cell co-electroporation of lissamine-tagged Control or CB_1R MO together with Alexa 488 dextran in the brain of stage 43 tadpoles was used to downregulate CB_1R expression and visualize individual tectal neurons beginning at stage 45, 24 h after MO transfection. At stage 45, tectal neurons with CB_1R

knockdown had a similar dendrite branch number as control MO-transfected neurons (Control MO 21.74 ± 2.47 branches, n = 45 neurons, CB_1R MO 17.40 ± 2.85 branches, n = 42 neurons; **Figure 7B**). However, while control tectal neurons continued to branch and significantly increase their number of branches 24 and 48 h after the first imaging, neurons with CB_1R MO knockdown failed to increase their branch numbers and length over the course of 2 days (**Figures 7C, E**), and were significantly simpler than controls by 48 h (**Figures 7B, D**). Thus, altering CB_1R-mediated endocannabinoid signaling can also impact dendritic morphology and connectivity of postsynaptic tectal neurons cell-autonomously, although with a different time scale (significant at the 48-h imaging time point, **Figures 7B, D**) when compared to the cell-autonomous effects on presynaptic RGCs (significant at the first imaging time point, **Figure 2C**).

Altering AEA levels enhanced visually guided responses

To determine the functional consequence of altered cannabinoid signaling during active RGC axon branching and synapse formation, and to correlate structural changes with functional changes at the same developmental stage, we used a visually-guided behavioral assay to measure responses to visual stimulation. Tadpoles at stage 45 were treated with vehicle (0.1% DMSO in rearing solution), URB597 (2.5 μM) or JZL184 (2.5 μM) for 24 h prior to behavioral testing. The tadpoles' response to advancing stimuli (video loop of moving black dots) was measured and quantified as percent positive responses per total interactions with potential stimuli (see section "Materials and methods"). The avoidance response to stimulus in tadpoles treated with URB597, which would increase AEA levels, was significantly higher than that of tadpoles exposed to vehicle control or JZL184 for 24 h (**Figure 8**). Thus, structural changes in RGC axon arbors as caused by the URB597 treatment (**Figures 3**, **4**) correlate with functional behavioral changes in visual responses to stimulus.

Discussion

Our studies characterized the differential effects of eCBs on differentiating RGC axons at distinct times of development *in vivo*, demonstrating not only cell-autonomous effects of CB_1R signaling on RGCs, but also that global and rapid changes in AEA and 2-AG levels and signaling in developing tadpoles can differentially influence RGC axon growth and connectivity in the intact developing organism.

Developmental studies have shown that CB_1R is high evolutionary conserved among species and is highly expressed in the developing brain of multiple vertebrate species, from zebrafish to mammals (Lam et al., 2006; Martella et al., 2016; da Silva Sampaio et al., 2018). *Xenopus laevis* CB_1R has 74% nucleotide sequence identity and 83% amino acid sequence identity with human CB_1R (Cottone et al., 2003). In *Xenopus*, *cnr1* expression is relatively low from gastrula to neurula stages and increases five-fold by stage 34–35, during the early tailbud stage (Zheng et al., 2015). CB_1R knockdown in early *Xenopus* embryos, at the four-cell stage, induces developmental eye defects by stage 41, supporting a role for CB_1R signaling in retinal development and differentiation (Zheng et al., 2015). Moreover, recent studies have shown that exposure of whole brain preparations of young tadpoles to CB_1R agonists alter the growth cone structure of RGCs as they travel through the optic tract (Elul et al., 2022), while pharmacological activation of the CB_1R in *Xenopus* tadpoles at later stages increases RGC firing response to visual stimulation (Miraucourt et al., 2016). Functional analyses in zebrafish also support a role for eCBs in normal vision (Martella et al., 2016). Using *Xenopus*, we provide further evidence that endocannabinoids can differentially impact the structure and connectivity of RGCs at distinct times of development and that RGCs are capable to respond to changes in cannabinoid signaling cell-autonomously.

While CB_1R has been detected in embryonic and postnatal neuronal progenitors in rodents, expression levels in differentiating and migrating progenitors in all species is very low compared to expression levels in newly differentiated neurons (Harkany et al., 2008a; Vitalis et al., 2008; Gaffuri et al., 2012). In agreement with observation of CB_1R enrichment in differentiating neurons, our immunohistochemical studies showed that the eCB receptor CB_1R is expressed in *Xenopus* tadpoles at higher levels in differentiated postmitotic neurons in the visual system (**Figure 1** and see Miraucourt et al., 2016). In stage 45 tadpoles, a time when functional visual circuit connections form, CB_1R immunoreactivity is absent in precursor cells near the ventricle and in the dorso-caudal midbrain but is highly expressed in newly differentiated cells in the midbrain and in the tectal neuropil. In retina, CB_1R immunoreactivity is observed from time when RGCs extend axons to the brain (stage 42) to when they make functional synaptic connections with tectal cells (stage 45 to 47). Thus, the expression patterns of CB_1R in the *Xenopus* visual system indicate that postmitotic RGCs can directly respond to CB_1R signaling similar to those in mammals and other vertebrate species.

Similar to effects on proliferation, the effects of CB_1R activation and eCB signaling on neurite outgrowth have mostly been analyzed using neuroblastoma-derived cell lines and primary neuronal cultures, with somewhat conflicting results (Gaffuri et al., 2012). For example, some studies have shown that CB_1R activation has a positive effect on FGF2 and N-cadherin mediated neurite outgrowth of neurons in culture, an effect that may be mediated by 2-AG activity (Williams et al., 2003). In contrast, other groups have shown negative effects of CB_1R activation on BDNF-induced neurite outgrowth in inhibitory neurons in culture as well as in axon and dendrite growth in CB_1R-transfected neurons *in vitro* (Berghuis et al., 2005; Vitalis et al., 2008). Evidence from pyramidal neurons in culture treated with eCB agonists (AEA, ACEA) and inverse agonists (AM251) indicates that neurons require an eCB tone to initiate axonal polarization and that eCB signaling interferes with axon branching (Mulder et al., 2008). Other studies have shown that THC can affect cytoskeletal dynamics by modulating the expression of microtubule binding proteins that are necessary for axon growth (Tortoriello et al., 2014), while evidence also indicates that acute CB_1R activation results in rapid contraction of the neuronal actomyosin cytoskeleton in hippocampal cells in culture (Roland et al., 2014). Pharmacologic studies also show that CB_1R agonists attenuated activity-dependent remodeling of dendritic spines in mature cortical neurons in culture (Njoo et al., 2015). Thus, while most studies implicate the eCB system in

10.3389/fnsyn.2023.1176864

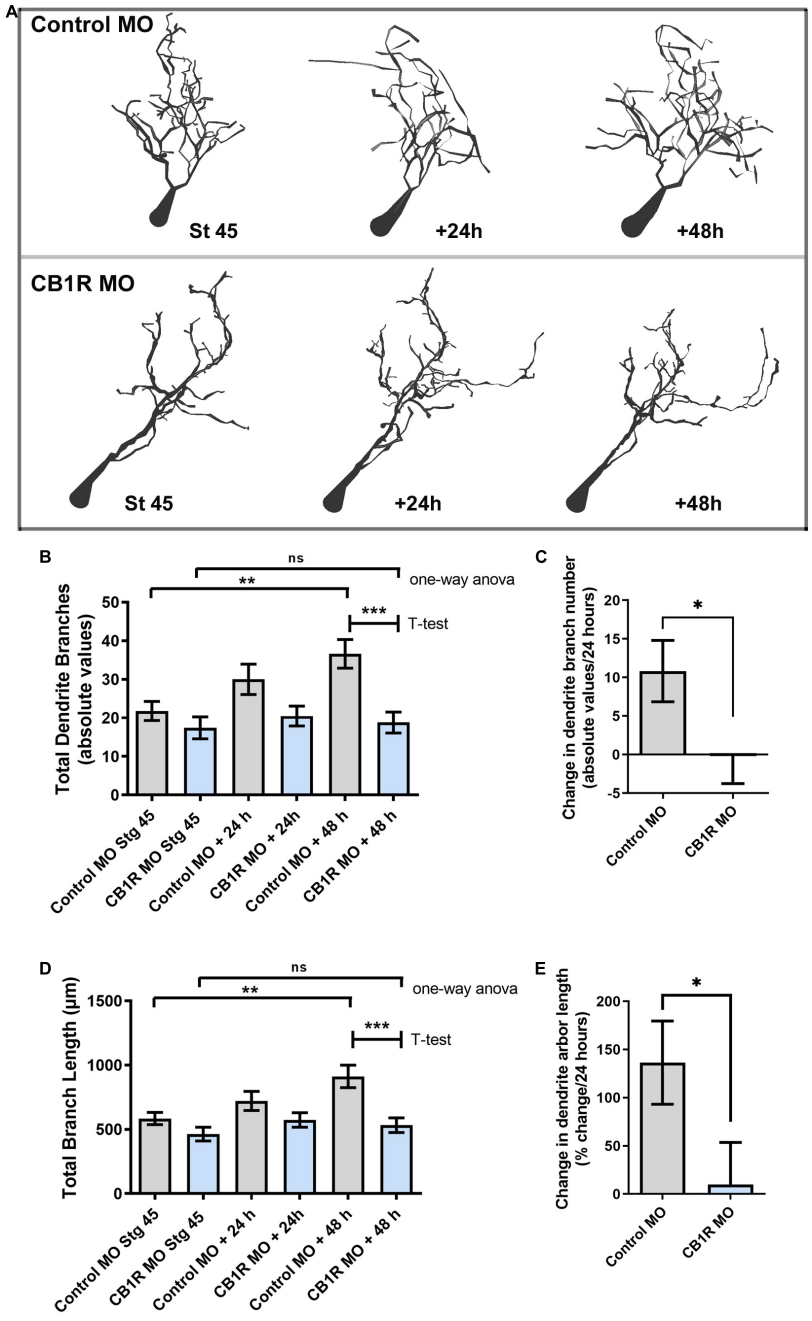

FIGURE 7
Single-cell CB_1R knockdown decreases the branching and growth of tectal neurons *in vivo*. **(A)** Tracings of sample neurons in stage 45 tadpoles transfected with Alexa 488 dextran and lissamine-tagged Control MO or CB_1R MO and imaged *in vivo* by two-photon confocal microscopy over the course of 3 days. Dendritic arbors were digitally reconstructed in three-dimensions using the Neuromantic tracing software and rendered for illustration purposes using Adobe Photoshop. **(B)** Dendritic arbors of neurons with CB_1R MO had a similar number of branches as Control MO neurons at stage 45 after but possessed a significantly a lower number of branches than controls by the 48-h imaging time point. **(C)** Quantifying the rate of branch addition as the change in branch number in every 24 h-imaging intervals showed that neurons transfected with Control MO increased their complexity by adding new branches, neurons transfected CB_1R MO failed to increase the complexity of their dendritic arbor. **(D,E)** Quantification of total dendritic arbor length reveals that tectal neurons with CB_1R MO fail to increase their dendritic arbor length **(D)** and grow at a lower rate **(E)** than Control MO transfected neurons (n = 29 neurons per condition). Statistical analysis by one-way ANOVA and Student's t-test. Mean ± SEM. *$p \leq 0.05$, **$p \leq 0.005$, ***$p \leq 0.001$.

establishing and maintaining a polarized morphology in developing neurons and in axon growth through cytoskeletal modifications, it remains unclear how developing neural circuits are dynamically shaped in the intact developing embryo, again highlighting the need to examine effects in more natural physiological settings.

Previous studies from our laboratory on the analysis of RGC axon growth and targeting demonstrate differential *in vivo* versus *in vitro* responses of RGC axon growth cones to axon guidance molecules. Specifically, by imaging RGC axon growth cones in Stage 40 *Xenopus* tadpoles right before they begin

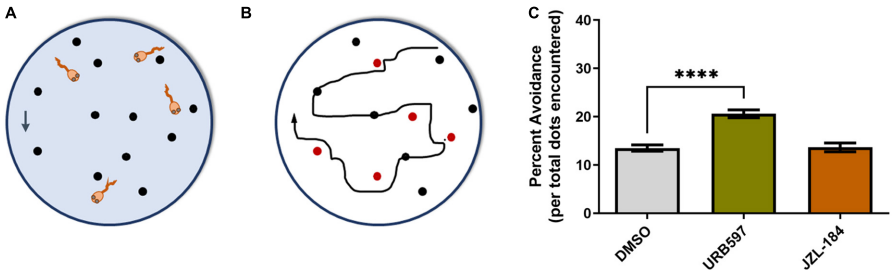

FIGURE 8
URB597 treatment enhances visually guided responses. **(A)** Schematic of the visual avoidance task. Tadpoles at stage 45, treated with vehicle (0.1% DMSO in rearing solution), URB597 or JZL184, were tested for their ability to alter their swimming behavior upon encountering moving dots (arrow depicts downward movement of dots). **(B)** The tadpole's swimming path and responses to advancing stimuli (black and red circles) were tracked and analyzed. A tadpole freezing response upon coinciding with the stimulus (red circles) or changing its swimming direction and speed was considered active avoidance. **(C)** Tadpoles treated with URB597 had increased avoidance responses to the presentation of the stimulus 24 h post-treatment when compared to vehicle treated controls. Control n = 24 tadpoles, URB597 n = 20 tadpoles, JZL184 n = 20 tadpoles. Mean ± SEM. ****$p \leq 0.0001$.

to arborize, we showed that netrin-1 impacts early axon arbor differentiation by altering branching responses at their optic tectal target and inhibiting growth cone advancement within the target (Shirkey et al., 2012). These effects on RGC axons were not recapitulated in culture on growth cones exposed to netrin-1 (Shirkey et al., 2012). Thus, the differential *in vivo* versus *in vitro* effects indicates that neurons need to integrate multiple cues in their local *in vivo* environment to modulate axon elongation, targeting and branching. Here, we demonstrate that both single-cell downregulation of CB_1R expression as well as acute and chronic alterations in eCB levels in intact *Xenopus* tadpoles during RGC axon targeting and branching significantly impact RGC axons. Cell-autonomous downregulation of CB_1R in postmitotic RGCs at the time they terminate in the optic tectum interfered with normal axon branching and resulted in RGC axons that abnormally retained terminal growth cones. Thus, negative regulation of CB_1R function resulted in similar but less penetrant phenotypes to those observed on RGC axons after cell-autonomous alterations in BDNF-mediated TrkB signaling (Marshak et al., 2007), a molecular pathway that has been linked to eCB signaling (Maison et al., 2009; Yeh et al., 2017), but more penetrant phenotypes than after downregulation of DCC-mediated netrin signaling (Manitt et al., 2009; Shirkey et al., 2012), a mechanism that has been linked to CB_1R -mediated growth cone steering (Argaw et al., 2011).

A role for eCB signaling in axon fasciculation and pathfinding has been suggested based on observations of diffuse thalamocortical and corticothalamic tracts in adult CB_1R knockout mice and fasciculation deficits in callosal and corticofugal projections in neonatal CB_1R knockout mice using fiber bundle analyses (Mulder et al., 2008; Wu et al., 2010). These analyses of mutant mice, while demonstrating that eCB signaling is important for axon growth, were not able to unequivocally demonstrate whether effects on axon fasciculation are independent of neural differentiation and did not distinguish from other potential global or time-dependent effects on growing axons. In the current studies, brain microinjection of URB597 resulted in a rapid increase in RGC axon branch number at the target within the first 6 h after treatment when compared to vehicle-injected controls (**Figure 2**). The effect on axon branch number was rapid, with axons then continuing to remodel at a normal rate and increasing their number of branches by 12 and 24 h. Thus, the effects of acute increase in eCB signaling, as would result from blocking hydrolysis of AEA and related eCBs by the FAAH inhibitor, are rapid and seem to involve a significant remodeling of axon arbors. These rapid effects are supported by the effects of prolonged, global treatment in tadpoles exposed to URB597 for 48 h. URB597 treatment at stage 45 resulted in a significant increase in the rate of axon branching 24 h after initial treatment, similar to the effect we observed after acute treatment but with a longer onset. In contrast, axon branch number was significantly lower over time in tadpoles that were treated with URB597 beginning at stage 38 and imaged at stage 45 when compared to controls as axons failed to branch. However, even though axons remained simpler than controls when tadpoles were treated with URB597 early as they path-find, the density of GFP-synaptobrevin labeled presynaptic sites was significantly higher than that in control axons. Thus, while the early increase in AEA levels and signaling interfered with subsequent axon branching at the target, it also positively impacted synapse number.

Neuronal responses to altered eCB levels and signaling may depend on the expression levels of key enzymes responsible for their synthesis and degradation and on the local environment where the neuron grows (Aguirre et al., 2019). FAAH is expressed in the retina of multiple vertebrate species (Yazulla et al., 1999; Glaser et al., 2005), and the enzymes responsible for the synthesis (DAGLα) and the degradation (MAGL) of 2-AG are expressed in multiple rodent retinal cell types during development, including RGCs (Cecyre et al., 2014). Developmental expression of both FAAH and MAGL has been characterized in zebrafish larva at stages when retinotectal connections are made, paralleling CB_1R expression and function in vision in this same species (Martella et al., 2016). Even though tissue-specific expression of AEA or 2-AG biosynthetic and catabolic enzymes has not been directly demonstrated in *Xenopus laevis*, FAAH and DAGLα transcripts can be detected in developing embryos and tadpoles (Session et al., 2016). In *Xenopus*, AEA activation of the CB_1R has been demonstrated to occur as early as stage 41 (Migliarini et al., 2006), while bath application of CB_1R agonists has been found to directly enhance RGC excitability within the retina of stage 45 tadpoles without the need for retinotectal feedback (Miraucourt et al., 2016). Here, we used similar protocols to increase endogenous AEA levels

with URB597 or 2-AG levels by adding JZL184, a MAGL inhibitor, in tadpoles at stage 38 or stage 45. While no significant changes in axon branch number or branch dynamics were observed in tadpoles exposed to JZL184 at stage 45, axons were simpler and less branched than controls when treatment was initiated at stage 38. Moreover, early JZL184 treatment induced significant pathfinding errors in a subset of RGC axons at the target, abnormally crossing to the opposite side of the optic tectum. These effects coincide with the timing at which JZL184 treatment significantly increases endogenous 2-AG levels in tadpoles, thus supporting the idea that presynaptic RGC axons that express CB_1Rs are capable to respond to acute alterations in eCB signaling but that effects of AEA and 2-AG are distinct and depend on the developmental stage. That AEA and 2-AG differentially impact *Xenopus* RGC axon navigation and branching through direct CB_1R signaling on RGCs, however, remains to be established.

It is likely that pharmacologic and genetic manipulations which alter eCB levels and signaling impact not only RGCs but most neurons and glia throughout the CNS. The effects of pharmacologic manipulation in young tadpoles may also depend on the global ability of the drug treatment to affect multiple/different circuits at distinct times of development, as suggested by the differential effects of the drug treatments on the levels of AEA, 2-AG and other fatty acid metabolites on the whole tadpole organism. However, our studies show that downregulation of CB_1R in single, developing pre- and postsynaptic neurons in the otherwise intact brain of living animals is sufficient to alter their connectivity at the time that synaptic connections are made. That altered connectivity is induced by time-dependent changes in eCB levels and signaling is also supported by our observations that a short exposure to drugs that interfere with FAAH function, and thus increase eCB levels, results in functional changes in the visual circuit as measured by our visual avoidance task; results that are similar to those of more chronic manipulations in *Xenopus* tadpoles (Miraucourt et al., 2016). Moreover, effects of JZL184 treatment on misrouting of targeting *Xenopus* RGC axons support a role for eCB signaling in axon navigation effects, as shown for CB_1R knockout mice where axon fasciculation of corticothalamic and thalamocortical axons is altered possibly through altered 2-AG signaling (Wu et al., 2010). Similarly, pathfinding errors that include increased contralateral crossing of spinal axons in zebrafish larvae with CB_1R MO knockdown (Watson et al., 2008), support a role for eCB-mediated CB_1R signaling in guiding developing axons. Understanding how cannabinoid signaling can induced cell-autonomous changes in connectivity in the developing brain is of significance, especially as negative regulation of cannabinoid receptor expression and function has been correlated with THC/cannabis consumption (Tortoriello et al., 2014; Silva et al., 2015). Our single-cell analysis of CB_1R function in *Xenopus* expands our understanding of how cell-autonomous CB_1R-mediated eCB signaling in single neurons, and how global alterations in eCB levels in a developing embryo, can impact pre- and postsynaptic neuronal connectivity in the intact brain.

Data availability statement

The raw data supporting the conclusions of this article will be made available by the authors, without undue reservation.

Ethics statement

This animal study was reviewed and approved by the Institutional Animal Care and Use Committee of the University of California, Irvine (Animal Welfare Assurance Number: A3416–01).

Author contributions

SC-C, RDR, and RAS conceived the project. RDR and RGS conducted knockdown and imaging experiments. RDR, EG, and JM conducted pharmacologic experiments. ME conducted behavioral experiments. RAS conducted imaging and immunohistochemical experiments. RDR, EG, JM, ME, KD, and SC-C analyzed data and the Impact of Cannabinoids Across Lifespan (ICAL) Center for the Study of Cannabis at UCI ran the LC/MS analysis. SC-C wrote the manuscript with input from all authors. All authors contributed to the article and approved the submitted version.

Funding

This work was funded in part a National Eye Institute grant EY011912 to SC-C and a National Institute on Drug Abuse, ICAL: Impact of Cannabinoids Across Lifespan Center grant P50DA044118-01 to Daniele Piomelli, and an NSF GRFP DGE-1321846 award to RAS.

Acknowledgments

We thank Alexa Torrens for assisting with fatty acid analysis, and Eduardo Munoz, Kevin Donohue, and Ginger Short for help with initial aspects of this project. We are also grateful to Dr. Daniele Piomelli for his support and for helpful comments on the project. This study was made possible in part through access to the Optical Biology Core Facility of the Developmental Biology Center, a shared resource supported by the Cancer Center Support Grant (CA-62203) and Center for Complex Biological Systems Support Grant (GM-076516).

Conflict of interest

The authors declare that the research was conducted in the absence of any commercial or financial relationships that could be construed as a potential conflict of interest.

Publisher's note

All claims expressed in this article are solely those of the authors and do not necessarily represent those of their affiliated organizations, or those of the publisher, the editors and the reviewers. Any product that may be evaluated in this article, or claim that may be made by its manufacturer, is not guaranteed or endorsed by the publisher.

References

Aguirre, E. C., Gaveglio, V. L., and Pasquare, S. J. (2019). The endocannabinoid system is present in rod outer segments from retina and is modulated by light. *Mol. Neurobiol.* 56, 7284–7295. doi: 10.1007/s12035-019-1603-5

Alsina, B., Vu, T., and Cohen-Cory, S. (2001). Visualizing synapse formation in arborizing optic axons in vivo: dynamics and modulation by BDNF. *Nat. Neurosci.* 4, 1093–1101. doi: 10.1038/nn735

Anderson, G. R., Aoto, J., Tabuchi, K., Foldy, C., Covy, J., Yee, A. X., et al. (2015). Beta-neurexins control neural circuits by regulating synaptic endocannabinoid signaling. *Cell* 162, 593–606.

Argaw, A., Duff, G., Zabouri, N., Cecyre, B., Chaine, N., Cherif, H., et al. (2011). Concerted action of CB1 cannabinoid receptor and deleted in colorectal cancer in axon guidance. *J. Neurosci.* 31, 1489–1499. doi: 10.1523/JNEUROSCI.4134-09.2011

Berghuis, P., Dobszay, M. B., Wang, X., Spano, S., Ledda, F., Sousa, K. M., et al. (2005). Endocannabinoids regulate interneuron migration and morphogenesis by transactivating the TrkB receptor. *Proc. Natl. Acad. Sci. U. S. A.* 102, 19115–19120. doi: 10.1073/pnas.0509494102

Berghuis, P., Rajnicek, A. M., Morozov, Y. M., Ross, R. A., Mulder, J., Urban, G. M., et al. (2007). Hardwiring the brain: endocannabinoids shape neuronal connectivity. *Science* 316, 1212–1216. doi: 10.1126/science.1137406

Calvigioni, D., Hurd, Y. L., Harkany, T., and Keimpema, E. (2014). Neuronal substrates and functional consequences of prenatal cannabis exposure. *Eur. Child Adolesc. Psychiatry* 23, 931–941. doi: 10.1007/s00787-014-0550-y

Castillo, P. E., Younts, T. J., Chavez, A. E., and Hashimotodani, Y. (2012). Endocannabinoid signaling and synaptic function. *Neuron* 76, 70–81. doi: 10.1016/j.neuron.2012.09.020

Cecyre, B., Monette, M., Beudjekian, L., Casanova, C., and Bouchard, J. F. (2014). Localization of diacylglycerol lipase alpha and monoacylglycerol lipase during postnatal development of the rat retina. *Front. Neuroanat.* 8:150. doi: 10.3389/fnana.2014.00150

Cottone, E., Salio, C., Conrath, M., and Franzoni, M. F. (2003). Xenopus laevis CB1 cannabinoid receptor: molecular cloning and mRNA distribution in the central nervous system. *J. Comp. Neurol.* 464, 487–496. doi: 10.1002/cne.10808

da Silva Sampaio, L., Kubrusly, R. C. C., Colli, Y. P., Trindade, P. P., Ribeiro-Resende, V. T., Einicker-Lamas, M., et al. (2018). Cannabinoid receptor type 1 expression in the developing avian retina: morphological and functional correlation with the dopaminergic system. *Front. Cell Neurosci.* 12:58. doi: 10.3389/fncel.2018.00058

Dong, W., Lee, R. H., Xu, H., Yang, S., Pratt, K. G., Cao, V., et al. (2009). Visual avoidance in Xenopus tadpoles is correlated with the maturation of visual responses in the optic tectum. *J. Neurophysiol.* 101, 803–815. doi: 10.1152/jn.90848.2008

Elul, T., Lim, J., Hanton, K., Lui, A., Jones, K., Chen, G., et al. (2022). Cannabinoid Receptor Type 1 regulates growth cone filopodia and axon dispersion in the optic tract of Xenopus laevis tadpoles. *Eur. J. Neurosci.* 55, 989–1001. doi: 10.1111/ejn.15603

Freitas, H. R., Isaac, A. R., Malcher-Lopes, R., Diaz, B. L., Trevenzoli, I. H., and De Melo Reis, R. A. (2018). Polyunsaturated fatty acids and endocannabinoids in health and disease. *Nutr. Neurosci.* 21, 695–714. doi: 10.1080/1028415X.2017.1347373

Freund, T. F., Katona, I., and Piomelli, D. (2003). Role of endogenous cannabinoids in synaptic signaling. *Physiol. Rev.* 83, 1017–1066. doi: 10.1152/physrev.00004.2003

Gaffuri, A. L., Ladarre, D., and Lenkei, Z. (2012). Type-1 cannabinoid receptor signaling in neuronal development. *Pharmacology* 90, 19–39. doi: 10.1159/000339075

Glaser, S. T., Deutsch, D. G., Studholme, K. M., Zimov, S., and Yazulla, S. (2005). Endocannabinoids in the intact retina: 3 H-anandamide uptake, fatty acid amide hydrolase immunoreactivity and hydrolysis of anandamide. *Vis. Neurosci.* 22, 693–705. doi: 10.1017/S0952523805226020

Harkany, T., Guzman, M., Galve-Roperh, I., Berghuis, P., Devi, L. A., and Mackie, K. (2007). The emerging functions of endocannabinoid signaling during CNS development. *Trends Pharmacol. Sci.* 28, 83–92. doi: 10.1016/j.tips.2006.12.004

Harkany, T., Keimpema, E., Barabas, K., and Mulder, J. (2008a). Endocannabinoid functions controlling neuronal specification during brain development. *Mol. Cell Endocrinol.* 286(1–2 Suppl. 1), S84–S90. doi: 10.1016/j.mce.2008.02.011

Harkany, T., Mackie, K., and Doherty, P. (2008b). Wiring and firing neuronal networks: endocannabinoids take center stage. *Curr. Opin. Neurobiol.* 18, 338–345. doi: 10.1016/j.conb.2008.08.007

Henschke, P. (2019). Cannabis: an ancient friend or foe? What works and doesn't work. *Semin. Fetal Neonatal. Med.* 24, 149–154. doi: 10.1016/j.siny.2019.02.001

Holt, C. E., and Harris, W. A. (1983). Order in the initial retinotectal map in Xenopus: a new technique for labelling growing nerve fibres. *Nature* 301, 150–152. doi: 10.1038/301150a0

Igarashi, M., Santos, R. A., and Cohen-Cory, S. (2015). Impact of maternal n-3 polyunsaturated fatty acid deficiency on dendritic arbor morphology and connectivity of developing Xenopus laevis central neurons in vivo. *J. Neurosci.* 35, 6079–6092. doi: 10.1523/JNEUROSCI.4102-14.2015

Khakhalin, A. S., Koren, D., Gu, J., Xu, H., and Aizenman, C. D. (2014). Excitation and inhibition in recurrent networks mediate collision avoidance in Xenopus tadpoles. *Eur. J. Neurosci.* 40, 2948–2962. doi: 10.1111/ejn.12664

Khara, L. S., Amin, M. R., and Ali, D. W. (2022). Inhibiting the endocannabinoid degrading enzymes FAAH and MAGL during zebrafish embryogenesis alters sensorimotor function. *J. Exp. Biol.* 225, jeb244146. doi: 10.1242/jeb.244146

Lam, C. S., Rastegar, S., and Strahle, U. (2006). Distribution of cannabinoid receptor 1 in the CNS of zebrafish. *Neuroscience* 138, 83–95. doi: 10.1016/j.neuroscience.2005.10.069

Liu, X. F., and Haas, K. (2011). Single-cell electroporation in Xenopus. *Cold Spring Harb. Protoc.* 2011:db.to065607. doi: 10.1101/pdb.top065607

Maccarrone, M., Guzman, M., Mackie, K., Doherty, P., and Harkany, T. (2014). Programming of neural cells by (endo)cannabinoids: from physiological rules to emerging therapies. *Nat. Rev. Neurosci.* 15, 786–801. doi: 10.1038/nrn3846.nrn3846

Maison, P., Walker, D. J., Walsh, F. S., Williams, G., and Doherty, P. (2009). BDNF regulates neuronal sensitivity to endocannabinoids. *Neurosci. Lett.* 467, 90–94. doi: 10.1016/j.neulet.2009.10.011

Manitt, C., Nikolakopoulou, A. M., Almario, D. R., Nguyen, S. A., and Cohen-Cory, S. (2009). Netrin participates in the development of retinotectal synaptic connectivity by modulating axon arborization and synapse formation in the developing brain. *J. Neurosci.* 29, 11065–11077. doi: 10.1523/JNEUROSCI.0947-09.2009

Marinelli, S., Marrone, M. C., Di Domenico, M., and Marinelli, S. (2023). Endocannabinoid signaling in microglia. *Glia* 71, 71–90. doi: 10.1002/glia.24281

Marshak, S., Nikolakopoulou, A. M., Dirks, R., Martens, G. J., and Cohen-Cory, S. (2007). Cell-autonomous TrkB signaling in presynaptic retinal ganglion cells mediates axon arbor growth and synapse maturation during the establishment of retinotectal synaptic connectivity. *J. Neurosci.* 27, 2444–2456. doi: 10.1523/JNEUROSCI.4434-06.2007

Martella, A., Sepe, R. M., Silvestri, C., Zang, J., Fasano, G., Carnevali, O., et al. (2016). Important role of endocannabinoid signaling in the development of functional vision and locomotion in zebrafish. *FASEB J.* 30, 4275–4288. doi: 10.1096/fj.201600602R

Martinez, L. R., Black, K. C., Webb, B. T., Bell, A., Baygani, S. K., Mier, T. J., et al. (2020). Components of endocannabinoid signaling system are expressed in the perinatal mouse cerebellum and required for its normal development. *eNeuro* 7:ENEURO.0471-19.2020. doi: 10.1523/ENEURO.0471-19.2020

Middleton, T. P., Huang, J. Y., and Protti, D. A. (2019). Cannabinoids modulate light signaling in ON-sustained retinal ganglion cells of the mouse. *Front. Neural Circ.* 13:37. doi: 10.3389/fncir.2019.00037

Migliarini, B., Marucci, G., Ghelfi, F., and Carnevali, O. (2006). Endocannabinoid system in Xenopus laevis development: CB1 receptor dynamics. *FEBS Lett.* 580, 1941–1945. doi: 10.1016/j.febslet.2006.02.057

Miraucourt, L. S., Tsui, J., Gobert, D., Desjardins, J. F., Schohl, A., Sild, M., et al. (2016). Endocannabinoid signaling enhances visual responses through modulation of intracellular chloride levels in retinal ganglion cells. *Elife* 5:e15932. doi: 10.7554/eLife.15932

Mulder, J., Aguado, T., Keimpema, E., Barabas, K., Ballester Rosado, C. J., Nguyen, L., et al. (2008). Endocannabinoid signaling controls pyramidal cell specification and long-range axon patterning. *Proc. Natl. Acad. Sci. U. S. A.* 105, 8760–8765. doi: 10.1073/pnas.0803545105

Myatt, D. R., Hadlington, T., Ascoli, G. A., and Nasuto, S. J. (2012). Neuromantic - from semi-manual to semi-automatic reconstruction of neuron morphology. *Front. Neuroinform.* 6:4. doi: 10.3389/fninf.2012.00004

Nagel, A. N., Marshak, S., Manitt, C., Santos, R. A., Piercy, M. A., Mortero, S. D., et al. (2015). Netrin-1 directs dendritic growth and connectivity of vertebrate central neurons in vivo. *Neural Dev.* 10:14. doi: 10.1186/s13064-015-0041-y

Nieuwkoop, P. D., and Faber, J. (1956). *Normal Table of Xenopus laevis*. The Netherlands: Elsevier North Holland.

Njoo, C., Agarwal, N., Lutz, B., and Kuner, R. (2015). The cannabinoid receptor CB1 interacts with the WAVE1 complex and plays a role in actin dynamics and structural plasticity in neurons. *PLoS Biol.* 13:e1002286. doi: 10.1371/journal.pbio.1002286

Piprek, R. P., Kloc, M., Tassan, J. P., and Kubiak, J. Z. (2017). Development of Xenopus laevis bipotential gonads into testis or ovary is driven by sex-specific cell-cell interactions, proliferation rate, cell migration and deposition of extracellular matrix. *Dev. Biol.* 432, 298–310. doi: 10.1016/j.ydbio.2017.10.020

Roland, A. B., Ricobaraza, A., Carrel, D., Jordan, B. M., Rico, F., Simon, A., et al. (2014). Cannabinoid-induced actomyosin contractility shapes neuronal morphology and growth. *Elife* 3:e03159. doi: 10.7554/eLife.03159

Santos, R. A., Fuertes, A. J. C., Short, G., Donohue, K. C., Shao, H., Quintanilla, J., et al. (2018). DSCAM differentially modulates pre- and postsynaptic structural and functional central connectivity during visual system wiring. *Neural Dev.* 13:22. doi: 10.1186/s13064-018-0118-5

Session, A. M., Uno, Y., Kwon, T., Chapman, J. A., Toyoda, A., Takahashi, S., et al. (2016). Genome evolution in the allotetraploid frog Xenopus laevis. *Nature* 538, 336–343. doi: 10.1038/nature19840

Shirkey, N. J., Manitt, C., Zuniga, L., and Cohen-Cory, S. (2012). Dynamic responses of Xenopus retinal ganglion cell axon growth cones to netrin-1 as they innervate their in vivo target. *Dev. Neurobiol.* 72, 628–648. doi: 10.1002/dneu.20967

Silva, L., Harte-Hargrove, L., Izenwasser, S., Frank, A., Wade, D., and Dow-Edwards, D. (2015). Sex-specific alterations in hippocampal cannabinoid 1 receptor expression following adolescent delta-9-tetrahydrocannabinol treatment in the rat. *Neurosci. Lett.* 602, 89–94. doi: 10.1016/j.neulet.2015.06.033

Torrens, A., Ruiz, C. M., Martinez, M. X., Tagne, A. M., Roy, P., Grimes, D., et al. (2023). Nasal accumulation and metabolism of Delta(9)-tetrahydrocannabinol following aerosol ('vaping') administration in an adolescent rat model. *Pharmacol. Res.* 187:106600. doi: 10.1016/j.phrs.2022.106600

Tortoriello, G., Morris, C. V., Alpar, A., Fuzik, J., Shirran, S. L., Calvigioni, D., et al. (2014). Miswiring the brain: delta9-tetrahydrocannabinol disrupts cortical development by inducing an SCG10/stathmin-2 degradation pathway. *EMBO J.* 33, 668–685. doi: 10.1002/embj.201386035

Vitalis, T., Laine, J., Simon, A., Roland, A., Leterrier, C., and Lenkei, Z. (2008). The type 1 cannabinoid receptor is highly expressed in embryonic cortical projection neurons and negatively regulates neurite growth in vitro. *Eur. J. Neurosci.* 28, 1705–1718. doi: 10.1111/j.1460-9568.2008.06484.x

Watson, S., Chambers, D., Hobbs, C., Doherty, P., and Graham, A. (2008). The endocannabinoid receptor, CB1, is required for normal axonal growth and fasciculation. *Mol. Cell Neurosci.* 38, 89–97. doi: 10.1016/j.mcn.2008.02.001

Williams, E. J., Walsh, F. S., and Doherty, P. (2003). The FGF receptor uses the endocannabinoid signaling system to couple to an axonal growth response. *J. Cell Biol.* 160, 481–486. doi: 10.1083/jcb.200210164

Wu, C. S., Zhu, J., Wager-Miller, J., Wang, S., O'Leary, D., Monory, K., et al. (2010). Requirement of cannabinoid CB(1) receptors in cortical pyramidal neurons for appropriate development of corticothalamic and thalamocortical projections. *Eur. J. Neurosci.* 32, 693–706. doi: 10.1111/j.1460-9568.2010.07337.x

Yazulla, S., Studholme, K. M., McIntosh, H. H., and Deutsch, D. G. (1999). Immunocytochemical localization of cannabinoid CB1 receptor and fatty acid amide hydrolase in rat retina. *J. Comp. Neurol* 415, 80–90. doi: 10.1002/(sici)1096-9861(19991206)415:1<80::aid-cne6>3.0.co;2-h

Yeh, M. L., Selvam, R., and Levine, E. S. (2017). BDNF-induced endocannabinoid release modulates neocortical glutamatergic neurotransmission. *Synapse* 71:10.1002/syn.21962. doi: 10.1002/syn.21962

Zheng, X., Suzuki, T., Takahashi, C., Nishida, E., and Kusakabe, M. (2015). cnrip1 is a regulator of eye and neural development in Xenopus laevis. *Genes Cells* 20, 324–339. doi: 10.1111/gtc.12225

frontiers | Frontiers in Synaptic Neuroscience

TYPE Original Research
PUBLISHED 24 May 2023
DOI 10.3389/fnsyn.2023.1156777

Check for updates

OPEN ACCESS

EDITED BY
Dirk Feldmeyer,
Helmholtz Association of German Research Centres (HZ), Germany

REVIEWED BY
Michael F. Jackson,
University of Manitoba, Canada
Xiangping Chu,
University of Missouri–Kansas City, United States

*CORRESPONDENCE
Sanjay S. Kumar
✉ sanjay.kumar@med.fsu.edu

RECEIVED 01 February 2023
ACCEPTED 10 May 2023
PUBLISHED 24 May 2023

CITATION
Beesley S, Gunjan A and Kumar SS (2023) Visualizing the triheteromeric N-methyl-D-aspartate receptor subunit composition.
Front. Synaptic Neurosci. 15:1156777.
doi: 10.3389/fnsyn.2023.1156777

COPYRIGHT
© 2023 Beesley, Gunjan and Kumar. This is an open-access article distributed under the terms of the Creative Commons Attribution License (CC BY). The use, distribution or reproduction in other forums is permitted, provided the original author(s) and the copyright owner(s) are credited and that the original publication in this journal is cited, in accordance with accepted academic practice. No use, distribution or reproduction is permitted which does not comply with these terms.

Visualizing the triheteromeric N-methyl-D-aspartate receptor subunit composition

Stephen Beesley, Akash Gunjan and Sanjay S. Kumar*

Department of Biomedical Sciences, College of Medicine and Program in Neuroscience, Florida State University, Tallahassee, FL, United States

N-methyl-D-aspartate receptors (NMDARs) are one of three ligand-gated ionotropic channels that transduce the effects of neurotransmitter glutamate at excitatory synapses within the central nervous system. Their ability to influx Ca^{2+} into cells, unlike mature AMPA or kainate receptors, implicates them in a variety of processes ranging from synaptic plasticity to cell death. Many of the receptor's capabilities, including binding glutamate and regulating Ca^{2+} influx, have been attributed to their subunit composition, determined putatively using cell biology, electrophysiology and/or pharmacology. Here, we show that subunit composition of synaptic NMDARs can also be readily visualized in acute brain slices (rat) using highly specific antibodies directed against extracellular epitopes of the subunit proteins and high-resolution confocal microscopy. This has helped confirm the expression of triheteromeric *t*-NMDARs (containing GluN1, GluN2, and GluN3 subunits) at synapses for the first time and reconcile functional differences with diheteromeric *d*-NMDARs (containing GluN1 and GluN2 subunits) described previously. Even though structural information about individual receptors is still diffraction limited, fluorescently tagged receptor subunit puncta coalesce with precision at various magnifications and/or with the postsynaptic density (PSD-95) but not the presynaptic active zone marker Bassoon. These data are particularly relevant for identifying GluN3A-containing *t*-NMDARs that are highly Ca^{2+} permeable and whose expression at excitatory synapses renders neurons vulnerable to excitotoxicity and cell death. Imaging NMDAR subunit proteins at synapses not only offers firsthand insights into subunit composition to correlate function but may also help identify zones of vulnerability within brain structures underlying neurodegenerative diseases like Temporal Lobe Epilepsy.

KEYWORDS

NMDA receptors, subunit composition, *t*-NMDARs, visualizing subunit composition, immunohistochemistry, confocal microscopy, GluN3

Introduction

N-methyl-D-aspartate receptors are remarkably functionally diverse– capable of modulating their kinetic and voltage-dependent properties for serving either as integrators or coincident detectors of synaptic activity to screening monovalent and divalent cations for regulating their selective permeabilities to bring about synaptic plasticity (Pilli and Kumar, 2014; Beesley et al., 2020b). Apart from glutamate, their endogenous ligand,

they bind a host of molecules ranging from glycine and D-serine, their co-agonists, to ketamine, phencyclidine and zinc which modulate their function in ways still not fully understood. This diversity in function is attributed to unique assemblies of four subunit proteins that constitute the receptor's subunit composition (Kumar, 2016). NMDAR subunit composition has hitherto been determined indirectly using cell biology, electrophysiology and/or pharmacology because imaging individual receptors or their subunits directly has proven difficult due to limitations in spatial resolution brought about by diffraction. This has hindered explorations into the role and locus of expression (presynaptic/postsynaptic) of the GluN3 subunit and its integration with GluN1 and GluN2 to make *t*-NMDARs in the brain. The recent availability of highly specific antibodies directed against extracellular epitopes of the subunit proteins has provided the opportunity for imaging their colocalization at synapses using high-resolution confocal microscopy as a means of examining subunit composition and testing specific hypotheses regarding their expression.

Glutamatergic NMDARs are heterotetrameric proteins comprising different combinations of the GluN1, GluN2 (A-D), and GluN3 (A-B) subunits derived from distinct gene families (*Grin1-Grin3*). All NMDARs contain one or more of the obligatory GluN1 subunits, which when assembled with GluN2 subunits of the same type, give rise to conventional diheteromeric (*d*-) NMDARs (e.g., GluN1-2A-1-2A). Note, however, that GluN3-containing *d*-NMDARs (e.g., GluN1-3A-1-3A), unlike their GluN2-containing counterparts, have been shown using expression systems to be activated by glycine but not glutamate, have reduced Ca^{2+} permeability, and believed to express presynaptically (Chatterton et al., 2002; Matsuda et al., 2002; Grand et al., 2018). Triheteromeric NMDARs, by contrast, contain three different types of subunits (e.g., GluN1-2A-1-2B), and include receptors that are composed of one or more subunits from each of the three gene families, designated *t*-NMDARs (Kumar, 2016) (e.g., GluN1-2A-3A-2A). We showed previously that GluN3-containing *t*-NMDARs in the brain can be distinguished from GluN2-containing *d*-NMDARs electrophysiologically, have reduced affinity for Mg^{2+} and increased selectivity for Ca^{2+} over Na^{+}, making them highly Ca^{2+} permeable (Pilli and Kumar, 2012; Beesley et al., 2020b; Kumar and Kumar, 2021). These receptors are blocked by the pan-NMDAR antagonist D-(-)-2-Amino-5-phosphonopentanoic acid (D-AP5) and by D-serine, a potential gliotransmitter and a co-agonist of conventional NMDARs (Kumar, 2016; Beesley et al., 2019, 2020a). To obtain visual confirmation of the expression and colocalization of GluN1, GluN2, and GluN3 subunits to make *t*-NMDARs in native tissue, we immunoassayed individual subunit proteins in acutely cut slices of the rat brain (50 μm thick) with fluorescently tagged antibodies (**Supplementary Table 1**) and imaged them on a high-resolution confocal microscope. We looked specifically in the medial entorhinal area (MEA) where we had initially characterized the voltage-dependent properties of these receptors using electrophysiology, measured their Ca^{2+} permeability (Beesley et al., 2019, 2020b) and confirmed expression of the GluN3A protein and its colocalization with GluN1 and GluN2 (A and/or B) subunits (Kumar, 2016) using coimmunoprecipitation experiments (Beesley et al., 2019) and area specific tissue analysis (ASTA) (Beesley et al., 2022). Additionally, we determined whether these subunit proteins colocalized with PSD-95 or Bassoon, to determine the postsynaptic/presynaptic locus of their expression. The immunostained puncta imaged likely represent an ensemble of ∼10–20 NMDARs per synapse (Kumar and Huguenard, 2001; Goncalves et al., 2020; Li et al., 2021). Cross reactivity between different colored channels was minimized using appropriate secondary antibodies and fluorophores.

The premise of the current work is to determine whether: (a) NMDAR subunits can be individually visualized through immunohistochemistry in acute brain slices; (b) the subunit proteins co-express and overlap spatially to putatively inform about the subunit composition of the underlying receptors; (c) the subunits overlap with Bassoon and/or PSD-95 to inform about their pre- and/or postsynaptic colocalization. This type of imaging is qualitative in nature and precludes any meaningful quantitation because the images acquired pertain to only a single optical section from a stack of confocal-acquired images (collapsing the stack makes the puncta difficult to resolve because their size in the z-plane is at most the size of the minimum optical thickness possible on the scope). Furthermore, differences in the antigenicity of the fluorophore-conjugated antibodies required adjustment of intensity levels for each of the fluorophores imaged to effectively declutter and resolve the individual puncta. Thus, in addition to minimizing cross immunofluorescence of the fluorophore-conjugated antibodies, we had to optimize imaging using the luminescence/contrast correction parameters for each of the channels separately such that only the brightest puncta for each fluorophore could be visualized. This may jeopardize the accurate counting/estimation of subunit puncta and/or synapses on dendrites in the regions imaged, and hence the goal of this study is restricted to establishing/confirming whether subunit proteins for assembling *t*-NMDARs are expressed by the brain and determining the locus of their expression. Quantitation of expression levels is therefore beyond the scope of the current work and may require more sophisticated approaches like FRET (fluorescence resonance energy transfer) imaging and/or electron microscopy.

Materials and methods

All experiments were carried out in accordance with the *National Institutes of Health Guide for Care and Use of Laboratory Animals* and were approved by the Florida State University Institutional Animal Care Committee. Although no experiments were conducted on live animals, we have followed the recommendations in the ARRIVE guidelines.

Brain fixation and slicing

As described previously (Beesley et al., 2020a, 2022), Sprague-Dawley rats (male, postnatal day 40–90, 160–190 g, $N = 4$) were deeply anesthetized with urethane (1.5 mg/kg; i.p.) prior to intra-aortal fixation with 4% paraformaldehyde (PFA) in a 0.1 M phosphate buffer solution (PB; pH 7.4; 4°C) following an initial flush with ice-cold saline (0.9%, 4°C). Brains were removed and post-fixed overnight in PFA before being transferred to a 30% sucrose solution in PB until equilibration. Horizontal slices

(50 μm-thick) were cut on a cryostat and the sections (six series comprising of 12 sections per series) collected in a cryoprotectant solution consisting of 30% ethylene glycol and 25% glycerol in 50 mM PB. The cut sections were stored at –20°C until processed or analyzed.

Imaging

Immunofluorescence

Cryo-protected brain slices fixed in PFA were trimmed to retain the regions of interest (MEA and hippocampus) and washed in PB (0.1 M; 2, 5 min rinses), main rinse solution (MRS: 0.1 M PB, 0.1M glycine, 0.5% Triton X-100; 3, 10 min rinses) before being exposed to a blocking solution (0.1 M PB, 0.5% Triton X-100, 2% goat serum, 2% bovine serum albumin) for a minimum of 1 h on a shaker. Slices were then exposed to the primary antibody (**Supplementary Table 1**) in blocking solution overnight at room temperature under agitation. Slices were then washed in PB (3, 5 min rinses), MRS (3, 10 min rinses) before being exposed to the secondary antibodies (**Supplementary Table 2**) in blocking solution for 2 h under agitation. For multi-antigen immunolabeling, primary and secondary antibodies from differing host species were generally incubated together e.g., GluN1 (*guinea pig*) and GluN2A (*rabbit*). However, as many of the primary antibodies used were raised in rabbit, we did sequential primary-secondary antibody incubations with intermittent exposures to an unconjugated goat anti-rabbit secondary antibody to saturate as many epitopes on the primary as possible. For example, to assay for GluN2A and GluN3A subunit proteins in rat with primary antibodies made in rabbit, we first incubated the tissue with rabbit anti-GluN1 primary antibody overnight, washed with PB and MRS before exposing it to goat anti-rabbit Alexa-488 secondary antibody for 2 h. Following this step and washes with PB and MRS, the tissue was incubated with an unconjugated goat anti-rabbit secondary antibody for 2 h before being washed again in PB and MRS and exposed to the second rabbit anti-GluN3A primary overnight. Finally, following PB and MRS washes, the tissue was incubated with the third goat anti-rabbit Alexa-594 secondary antibody for 2 h before being rewashed in PB and MRS and readied for mounting on glass slides using vectashield mounting media with or without DAPI (Vector Laboratories, CA, USA). This sequential incubation protocol enabled successful labeling of multiple antigens despite the limitation of finding primary antibodies made in different host species. MAP2 protein was immunolabeled by incubating slices overnight in a rabbit primary (**Supplementary Table 1**) in blocking solution. They were washed in MRS (3, 10 min rinses) the following day and incubated in goat anti-rabbit biotin for 2 h and streptavidin 647 (all in blocking solution; **Supplementary Table 2**) for 2 h with intermittent washes in MRS (3, 10 min rinses). Each immunofluorescence assay was repeated at least twice with brain sections taken from different series.

The glass mounted slides were stored at 4°C in the dark until imaged on a confocal laser-scanning microscope (Zeiss LSM 880) using a Plan-Apochromat 63x/1.40 oil DIC M27 objective with appropriate excitation/emission filters for the secondary antibodies listed in **Supplementary Table 2**. During initial microscope setup (line averaging: 4; pixel dwell: 2.67–5.33 μs; resolution: assigned by software) the fluorophore with the longest wavelength imaged in an experiment (e.g., 647 nm) was assigned 1 Airy unit and the pinhole size corresponding to this setting (e.g., 64 μm) was used for each of the other fluorophores imaged under high magnification. Laser intensity and optical gain was set based on the fluorophores imaged such that the energy used for excitation saturated as few of the pixels as possible. The acquired images were minimally processed using Zen 2012 SP1 (black edition; Carl Zeiss) software where we took advantage of the digital zoom (with interpolation) to enlarge them, assign channel colors to the fluorophores, and optimize intensity and contrast (using the range indicator function) so that only the brightest signals/puncta could be visualized without background clutter. These likely represent protein agglomerations on spine heads that are at just the right orientation in the optical plane to maximize viewing. We used the program's built-in (Min/Max and Best Fit) functions to guide us in optimizing the imaging of each channel separately using the luminescence/contrast correction parameters (Gamma/Black/White) as exemplified in **Supplementary Figure 6**. Colocalization/overlap of protein puncta was ascertained using these independently optimized images at high/low digital zooms and depicted in figure form throughout the manuscript for various experimental conditions and controls. Furthermore, we make no distinctions between object and pixel based colocalization given the high magnification used for visualization of the subunits and do not construe colocalization alone to be indicative of protein-protein interactions. Unless indicated otherwise, images used in the figures are from a single optical section in a z-stack of ∼10–15 sections per brain slice (section thickness: ∼5.8 μm; interval 0.48 μm; see **Figure 4B**).

Cell culture and transfection

Human embryonic kidney (HEK) 293 cells were grown to 80% confluence in six-well plates in DMEM (Dulbecco's Modified Eagle Medium) containing fetal bovine serum at 37°C and 5% CO_2 and transfected with fluorescent protein-tagged GluN subunit-specific plasmids using jetPRIME transfection reagent (Polyplus) as per the manufacturer's instructions. The following plasmids were used for transfections: GluN1, pEYFP-NR1a (Addgene plasmid # 17928) (Luo et al., 2002); GluN2A, pCI-EGFP-NR2a wt (Addgene, plasmid # 45445) (Barria and Malinow, 2002); GluN3A, pcDNA3.1-NR3A-eGFP, which we constructed for this study as follows: Plasmid pGEMHE-NR3A-eGFP designed for *in vitro* transcription was a generous gift of Dr. Ehud Isacoff, University of California at Berkely (Ulbrich and Isacoff, 2008). The NR3A-EGFP fusion gene from this plasmid was excised using BamH1 and *Not*I restriction enzymes and ligated in frame into the corresponding restriction sites in the multiple cloning site of the mammalian expression vector pcDNA3.1 V5-A to generate the pcDNA3.1-NR3A-eGFP plasmid. After verifying the cloning junctions and part of the coding sequence by Sanger sequencing, this plasmid was used in our study for HEK 293 cell transfections. A total of 72 h post-transfection, cells were washed once in phosphate buffered saline and lysed in 20 μl 1x SDS sample buffer (in mM): 50 Tris (pH 6.8), 10% glycerol, 2.5 EDTA (pH 8), 2% SDS, 2.5% β-mercaptoethanol, 2 mg bromophenol blue, boiled for 5 min at 100°C and centrifuged for 1 min at 16,000 g.

Cell Biology

Immunoblotting

For assaying NMDAR subunits, a 6% polyacrylamide gel was used. Total HEK cell protein was added to the gel and allowed to migrate in running buffer (in mM): 25 Tris, 191 glycine, 0.1% SDS at 180V for approximately 75 min, or until the dye front ran off the gel. The gel was then transferred to polyvinylidene difluoride (PVDF) membrane using a transfer buffer (in mM): 25 Tris, 191 glycine at 75V for 90 min at 4°C. The membrane was then blocked for 30 min in 5% fat-free milk in Tris-buffered saline (TBS) and incubated with the primary antibody (**Supplementary Table 1**) overnight at room temperature under gentle agitation. Following removal of the primary antibody on the following day, the membrane was washed in TBS with Tween-20 (TBST; in mM: 50 Tris, 150 NaCl pH 7.4–7.6, 0.05% Tween-20; 3, 5 min rinses) and incubated with the secondary antibody [donkey anti-rabbit IRDye 680RD or donkey anti-guinea pig IRDye 680RD (LI-COR)] for 1 h in the dark at room temperature under gentle agitation. Membranes were rewashed in TBST (3, 5 min rinses) and then imaged on a LiCor Odyssey CLx imager. To rule out cross reactivity, primary antibodies (anti-GluN3A, anti-GluN1 and anti-GluN2A) were added sequentially to the membrane and intermingled with separate imaging sessions i.e., anti-GluN3A, donkey anti-rabbit IRDye 680RD exposure → imaging session #1 → anti-GluN1, anti-guinea pig IRDye 680RD exposure → imaging session #2 → anti-GluN2a, donkey anti-rabbit IRDye 680RD → imaging session #3 (see **Supplementary Table 1**).

Statistical tests

Unless otherwise noted, statistical significance was measured with a nested *t*-test (GraphPad Prism 9). Error bars in the figures represent standard error of the mean.

Data availability

All data generated and/or analyzed during this study are included in this published article. Note that the low magnification images in the figures represent *raw data* used for analysis of proteins imaged under enlargement of regions identified in these images. However, TIFF versions of the images used and/or analyzed during the current study are available from the corresponding author on reasonable request.

Results

GluN1 and GluN3 subunit proteins colocalize with PSD-95 on dendrites

To determine synaptic versus extrasynaptic expression of the critical glycine-binding subunits of *t*-NMDARs (GluN1 and GluN3) in the MEA, we immunoassayed neuron-specific dendrites with microtubule-associated protein 2 (MAP2), postsynaptic density with PSD-95 protein which is exclusively localized to mature glutamatergic synapses (Prange et al., 2004; Zheng et al., 2011), and either GluN1 (**Figure 1A**) or GluN3A (**Figure 1B**). The dendritic marker enables delineation from the soma (identified with the nuclear stain DAPI, or 4′,6-diamidino-2-phenylindole, *top row*, **Figure 1A**) and lends perspective to the relative location of putative synapses through PSD-95 immunolabeling. Note the punctate expression of the postsynaptic marker relative to the dendrite at various magnifications (*top row*, **Figure 1A**) and the precision with which the GluN1 protein puncta tend to coalesce (*arrowheads*, *middle row*, **Figure 1A**). Not all PSDs appeared to contain GluN1 (*circled yellow*, *middle row*, **Figure 1A**), suggestive of nascent synapses (Washbourne et al., 2002). Alterations in the pseudo color antigen key for the proteins imaged facilitate the gauging of their colocalization (*middle and bottom rows*, **Figure 1A**). Note the preponderance of GluN3A protein puncta, which like GluN1, colocalize nicely with PSD-95 (arrowheads, *all rows*, **Figure 1B**). Together, these data show the synaptic expression of both GluN1 and GluN3A proteins in the MEA through their colocalization with postsynaptic marker PSD-95.

To validate our imaging data in the MEA, we also assayed the hippocampus where GluN3A expression was established using area specific tissue analysis (ASTA) (Beesley et al., 2022). Consistent with these studies, we found widespread expression of GluN3A protein puncta that colocalized with PSD-95 throughout CA1 to CA3 (**Figure 2A**), although the high magnification used for their visualization precluded quantification of their relative abundance in these subfields. Note the dendritic enmeshing of cell bodies in what appears to be *stratum pyramidale* (*top row*, **Figure 2A**) and the coalescing of GluN3A puncta with PSD-95 at the level of the dendrites in the neuropil at various magnifications (*bottom rows*, *arrowheads*, **Figure 2A**). The average PSD-95 density in the MEA was 0.056 ± 0.006 puncta per μm^2 (mean ± s.e.m, $N = 4$ animals; **Figure 2B**) and the average diameter (0.402 ± 0.006 μm) and cross-sectional area (0.131 ± 0.004 μm^2) of these puncta ($n = 178$ and 177, respectively, **Figure 2B**) were similar to those reported in the literature (Sheng and Hoogenraad, 2007; Kim and Sheng, 2009). Interestingly, GluN3A subunit protein puncta were on average smaller in diameter and cross-sectional area (0.350 ± 0.011 μm and 0.104 ± 0.006 μm^2, respectively, $n = 80$, $N = 3$; **Figure 2C**) compared with PSD-95 (**Figure 2B**), although these differences turned out to be not statistically significant ($p = 0.21$ and 0.24, respectively, nested *t*-test). Despite minor variations in size due to spine orientation etc., the consistency of the averaged data with electron microscopy studies reported in the literature lend confidence to our imagining the colocalization of distinct NMDAR subunits at a single synapse.

GluN1, GluN2, and GluN3 subunit proteins colocalize postsynaptically for making *t*-NMDARs

Having established postsynaptic expression of the glycine binding GluN1 and GluN3A subunits independently, we sought to determine their colocalization with glutamate binding GluN2 subunits to make *t*-NMDARs. Given that we could only image four fluorophores at a time, we chose to immunoassay GluN1, GluN2A,

10.3389/fnsyn.2023.1156777

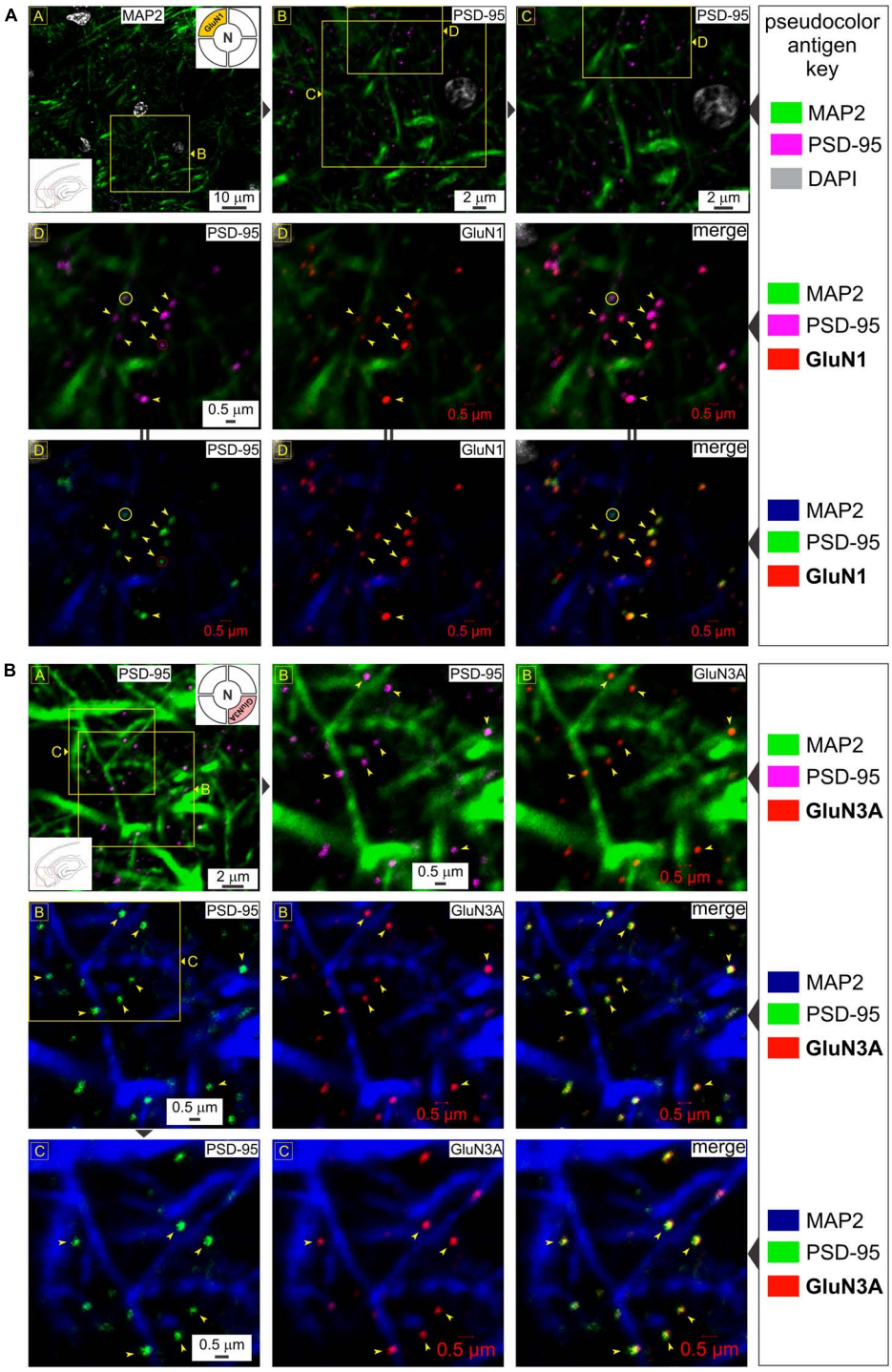

FIGURE 1
Glycine-binding GluN1 and GluN3A subunit proteins colocalize with the postsynaptic marker PSD-95. **(A)** *Top row*: Immunolabeling of postsynaptic density (PSD-95) puncta in the medial entorhinal area [MEA, also referred to as *area entorhinalis pars medialis* in the literature; red box in the bottom left *inset* of image in R (*row*) 1, C (*column*) 1] relative to dendrites immunolabeled with MAP2 at the indicated enlargements (lettered boxes in yellow; images magnified successively are linked with ▶). Nuclei are labeled with DAPI. In this and subsequent figures, the *pseudocolor antigen key* indicates the color assignment for the antigens/fluorophores imaged/depicted and alterations in color assignment (marked by || between images) are to aid in gauging colocalization of the proteins imaged. *Middle and bottom rows*: Immunolabeling of GluN1 subunit protein of the NMDAR (N; top right *inset* of image in R1C1) and their colocalization (*arrowheads*) with PSD-95 (*merged images* in R2C3 and R3C3) at putative synapses on dendrites (*red circles*). Note that not all PSDs contain GluN1 (*yellow circles*). **(B)** Immunolabeling of PSD-95 puncta (images in R1C1, R1C2, R2C1, and R3C1) and GluN3A (top right *inset* in R1C1) subunit protein (images in R1C3, R2C2, and R3C2) and their colocalization (arrowheads) with PSD-95 (*merged images* in R2C3 and R3C3) at the indicated enlargements (lettered boxes in yellow). Note that the schematics of brain slices embedded as insets within images and keys in this and all subsequent figures, provide locational information of the regions imaged (*red boxes*) and approximately where within these regions the images depicted are taken from (*yellow boxes*). We have been consistent in recording from the same location within the MEA, and hence, some insets convey just region-specific information.

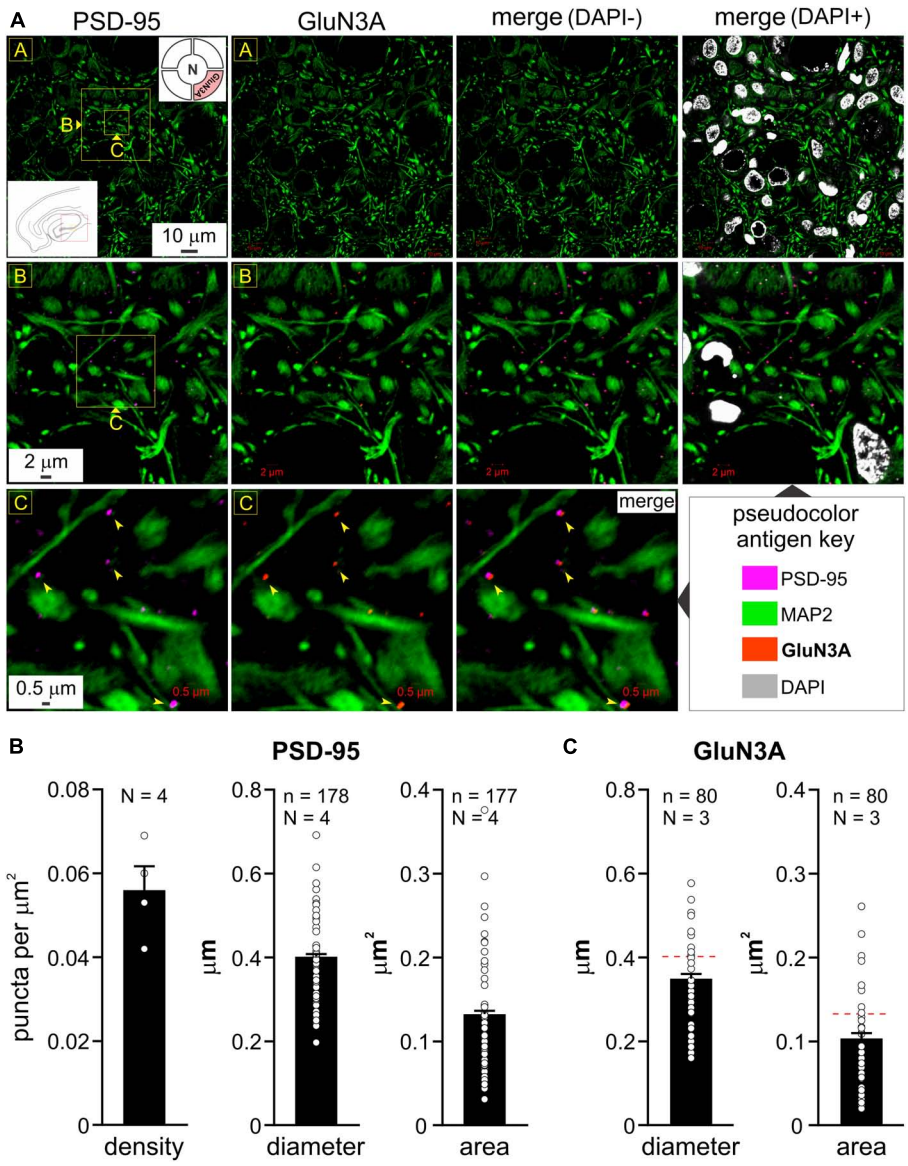

FIGURE 2
Colocalization of GluN3A subunit protein with postsynaptic density (PSD-95) in the hippocampus and quantitation of puncta in the medial entorhinal area (MEA). **(A)** Immunolabeling of PSD-95 puncta (images in R1C1, R2C1, and R3C1) and GluN3A (top right *inset* in R1C1) subunit protein (images in R1C2, R2C2, and R3C2) and their colocalization with PSD-95 (*merged images* in R1C3-C4, R2C3-C4, and R3C3; *arrowheads*) in the hippocampus (CA1-3; red box in the bottom left *inset* of image in R1C1) relative to dendrites immunolabeled with MAP2 at the indicated enlargements (*lettered boxes in yellow*). Nuclei, labeled with DAPI, indicate cell density within the neuropil. **(B,C)** Histograms of average density, diameter, and area of PSD-95 **(B)** and GluN3A **(C)** puncta in the MEA (error bars indicate s.e.m; n, number of puncta measured; N, animals used). Density estimates **(B)** were only made for PSD-95 from various non-overlapping regions within MEA imaged at differing magnifications. GluN3A subunit protein puncta were on average smaller in diameter and cross-sectional area compared with PSD-95 [hatched red line, **(C)**], although these differences were not statistically significant, p = 0.21 and 0.24, respectively, nested t-test.

and GluN3A subunit proteins along with MAP2, knowing that both GluN1 and GluN3A puncta coalesce precisely with the postsynaptic marker PSD-95. GluN1, GluN2A, and GluN3A subunit protein puncta in the MEA were imaged separately at various enlargements and merged to assay colocalization (*top two rows*, **Figure 3A**). Note that GluN1 and GluN3A puncta coalesce precisely with the GluN2 puncta, and this is better appreciated by altering the pseudocolor antigen key at higher magnifications (*arrowheads, bottom three rows*, **Figure 3A**). The *merge matrix* depicted in **Figure 3B** enables pairwise assessment of colocalization of the GluN1, GluN2A, and GluN3A subunit proteins at a single synapse on a dendrite at the highest level of magnification (note changes in color of the merged channels aid in assessing overlap). The merged images in the rightmost column of **Figure 3B** offer the first glimpses of the *t*-NMDAR subunit composition, comprising two glycine binding subunits (GluN1 and GluN3A) and two glutamate binding subunits (GluN2A) as described previously (Pilli and Kumar, 2012; Kumar, 2016; Beesley et al., 2019). To probe colocalization of these subunit proteins further, we delved deeper into the tissue moving from optical section 7 (**Figures 3A, B**) to 13 (**Figures 4A, B**; *inset*, *bottom*

right panel, **Figure 4B**). As before, there was clear colocalization of the GluN1, GluN2A and GluN3A subunit protein puncta at various magnifications (*arrowheads*, *top two rows*, **Figure 4A**) and the high signal to noise ratio even permitted visualization of spinous protrusions (putative spine heads) emanating from the MAP2 labeled dendrites (*white arrowheads in bottom two rows*, **Figure 4A**) that seem to contain the sites (PSD, *demarcated by yellow arrowheads in third row from top*, **Figure 4A**) at which the three subunit proteins colocalize (*bottom two rows*, **Figure 4A**). The merge matrix shown in **Figure 4B** enables pairwise assessment of this colocalization at high magnification (note the change in pseudocolor antigen key).

To reconfirm their postsynaptic origin, we immunoassayed for GluN3A and GluN2A subunit proteins together with MAP2 and PSD-95 in a separate set of experiments looking into the MEA (**Figure 5A**) and hippocampus (**Figure 5B**). GluN3A and GluN2A puncta colocalize with PSD-95 at the level of the dendrites, as can be seen by correlating the merged images of GluN2A and GluN3A (*rightmost column*, **Figure 5**) with PSD-95 (*leftmost column*, **Figure 5**) at various magnifications (*top three rows*, *yellow arrowheads*, **Figures 5A, B**), although not all subunits colocalize with PSD-95 or with each other (*yellow circles*, **Figure 5A**). Interestingly, we found conspicuous dense immunolabeling of GluN2A and GluN3A subunit proteins, but not PSD-95, in the perikaryon of the cell bodies (*white arrowheads*, *rows 4 and 5*, **Figure 5A**), but not the nucleus, that attests to the specificity of the antibodies used and serves as an internal control for colocalization of subunit puncta with the postsynaptic marker. We found a similar pattern of immunolabeling in the hippocampus (**Figure 5B**). Note the precision with which the coalesced subunits align with the postsynaptic marker at the level of the dendrite under high magnification (*bottom row*, **Figure 5B**). Together, these data provide firsthand evidence of the coalescing of GluN1, GluN2A, and GluN3A subunit proteins for making *t*-NMDARs postsynaptically.

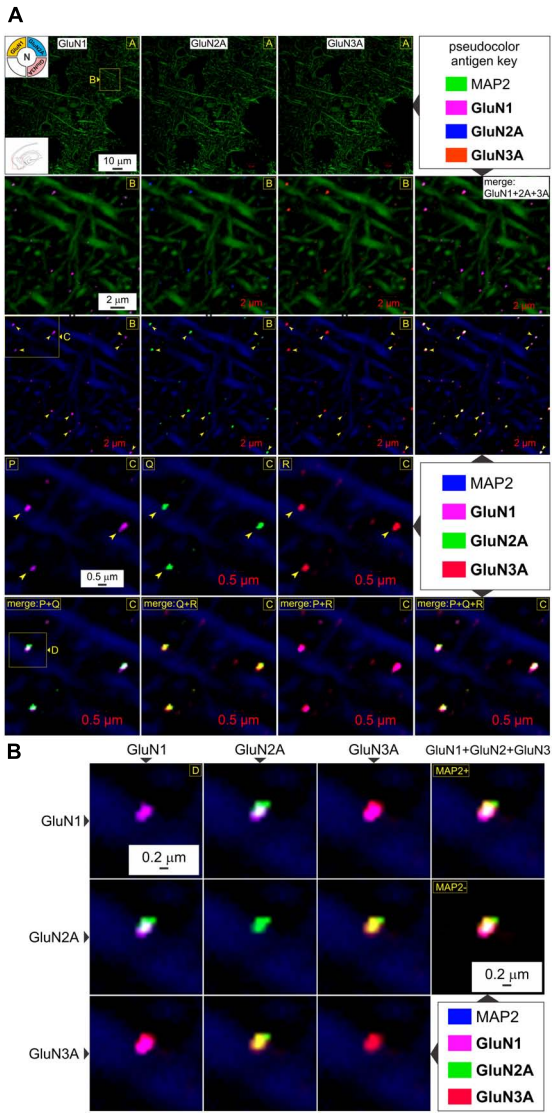

FIGURE 3
GluN1, GluN2A, and GluN3A subunit proteins colocalize for making *t*-NMDARs in the MEA. **(A)** Quadruple immunolabeling of GluN1 (images in R1-4C1), GluN2A (images in R1-4C2), and GluN3A (images in R1-4C3) subunit protein puncta relative to dendrites immunolabeled with MAP2 in the MEA (red box in the bottom left *inset* of image in R1C1) and their pairwise and triplicate colocalization (*merged images* in R2-3C4, R5C1-4) for making *t*-NMDARs (top left *inset* in R1C1) at the indicated enlargements (*lettered boxes in yellow*). Arrowheads point to representative examples of individual subunit puncta or their colocalization. Changes in the *pseudocolor antigen key* (marked by || between images) are to aid in gauging colocalization of the proteins imaged. **(B)** The *merge matrix* for pairwise assessment of GluN1, GluN2A, and GluN3A subunit protein colocalization at a single synapse on a dendrite at the highest level of magnification. The merged images in the rightmost column (R1-2C4) showcase *t*-NMDAR subunit composition, comprising glycine binding subunits (GluN1 and GluN3A) coalescing with glutamate binding subunits (GluN2A).

GluN1 and GluN3 subunits do not colocalize with the presynaptic marker Bassoon

To rule out the possibility of presynaptic *t*-NMDAR expression, we immunoassayed separately for the glycine binding subunits GluN1 (mandatory for making NMDARs) and GluN3A, together with the dendritic marker MAP2 and Bassoon, one of two (the other being Piccolo) very large scaffolding proteins of the cytomatrix assembled at the active zone of excitatory and inhibitory synapses where neurotransmitter is released (Richter et al., 1999; Gundelfinger et al., 2015). We found extensive labeling of Bassoon throughout the MEA neuropil which stood out from the labeling for PSD-95 and/or GluN1 at various magnifications (**Figure 6**). Bassoon labeled puncta were restricted mostly to intradendritic spaces and paired, but not colocalized, with PSD-95 (*red circles*, *top row*, **Figure 6A**) and/or GluN1 (*yellow circles with embedded arrowheads*, **Figures 6A–C**). Note the distinction between colocalization of GluN1 puncta with PSD-95, and together, their pairing with a clearly separated Bassoon (**Figures 6B, C**). The separation between PSD-95 and Bassoon varied between pairings and likely depends on the orientation of the synapse within the optical plane. Not all GluN1/PSD-95 colocalizations could be associated with visible Bassoon puncta (*yellow circles*, **Figures 6A–C**) and conversely, not all Bassoon puncta were associated with PSD-95 and/or GluN1. To more closely examine

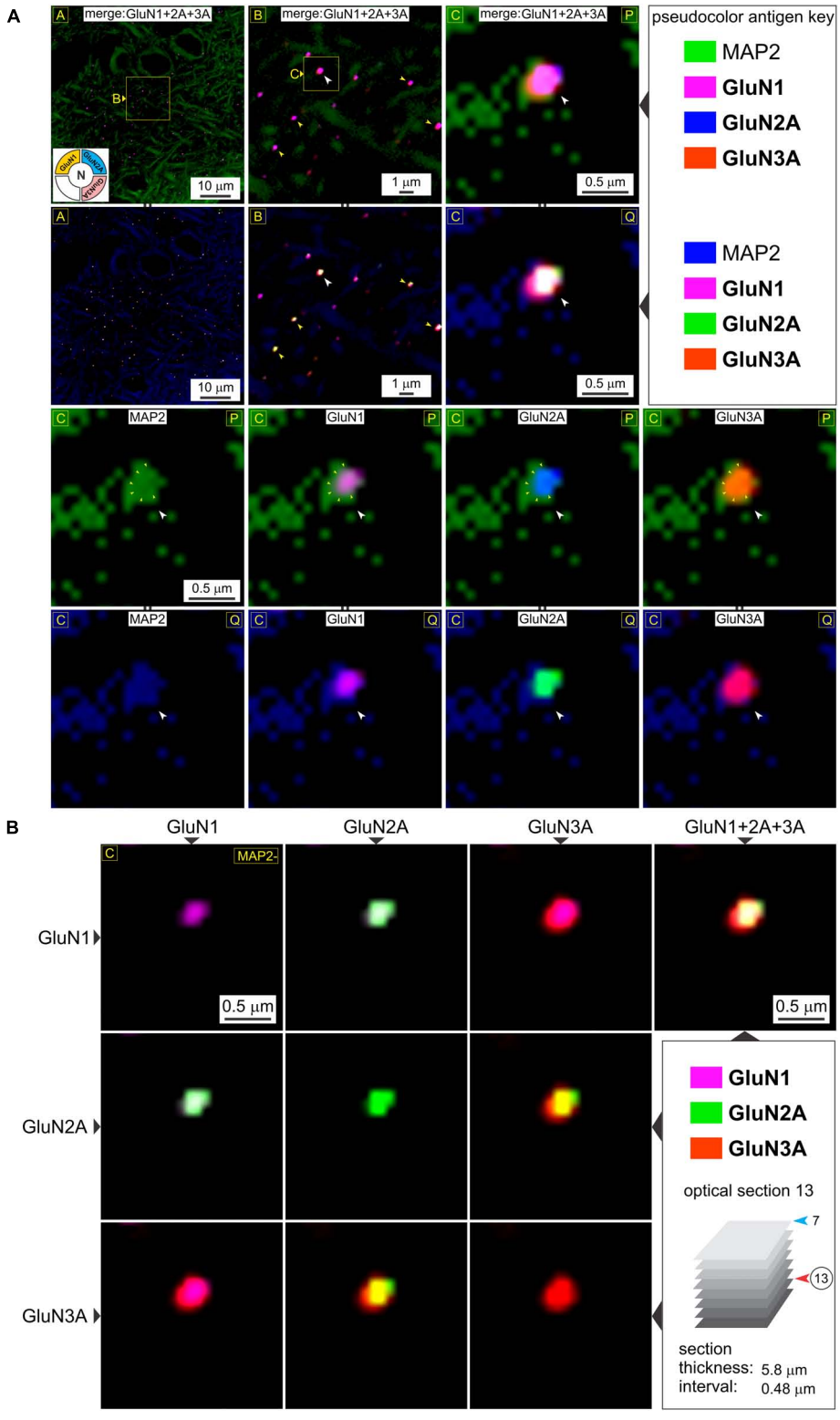

FIGURE 4
A closer look at *t*-NMDAR subunit composition. **(A)** Consistency in immunolabeling of colocalized GluN1, GluN2A, and GluN3A subunit protein puncta (*merged images* in R1-2C1-3) relative to dendrites (MAP) in deeper potions of the medial entorhinal area (MEA) [optical section 13 versus 7 in previous figure; *see bottom right panel* in **(B)**] at the indicated enlargements (*lettered boxes in yellow*). Arrowheads (in images at the top two rows) point to representative examples of subunit colocalization and changes in the *pseudocolor antigen key* (marked by || between images; R2C1-3, R4C1-4) are to aid in gauging colocalization of the proteins imaged. An example of a putative spine head emanating from the dendrite at high magnification (*images* in R1-2C3, R3-4C1-4) containing a postsynaptic density (PSD) (outlined by the small yellow arrowheads in images R3C1-4) where the individual subunits (white arrowheads, R3-4C1-4) appear to coalesce. **(B)** The *merge matrix* for pairwise assessment of GluN1, GluN2A, and GluN3A subunit protein colocalization at a single synapse at the highest level of magnification. The merged image in the rightmost column (R1C4) showcases *t*-NMDAR subunit composition (Note differences in *pseudocolor antigen key* with **Figure 3B**).

10.3389/fnsyn.2023.1156777

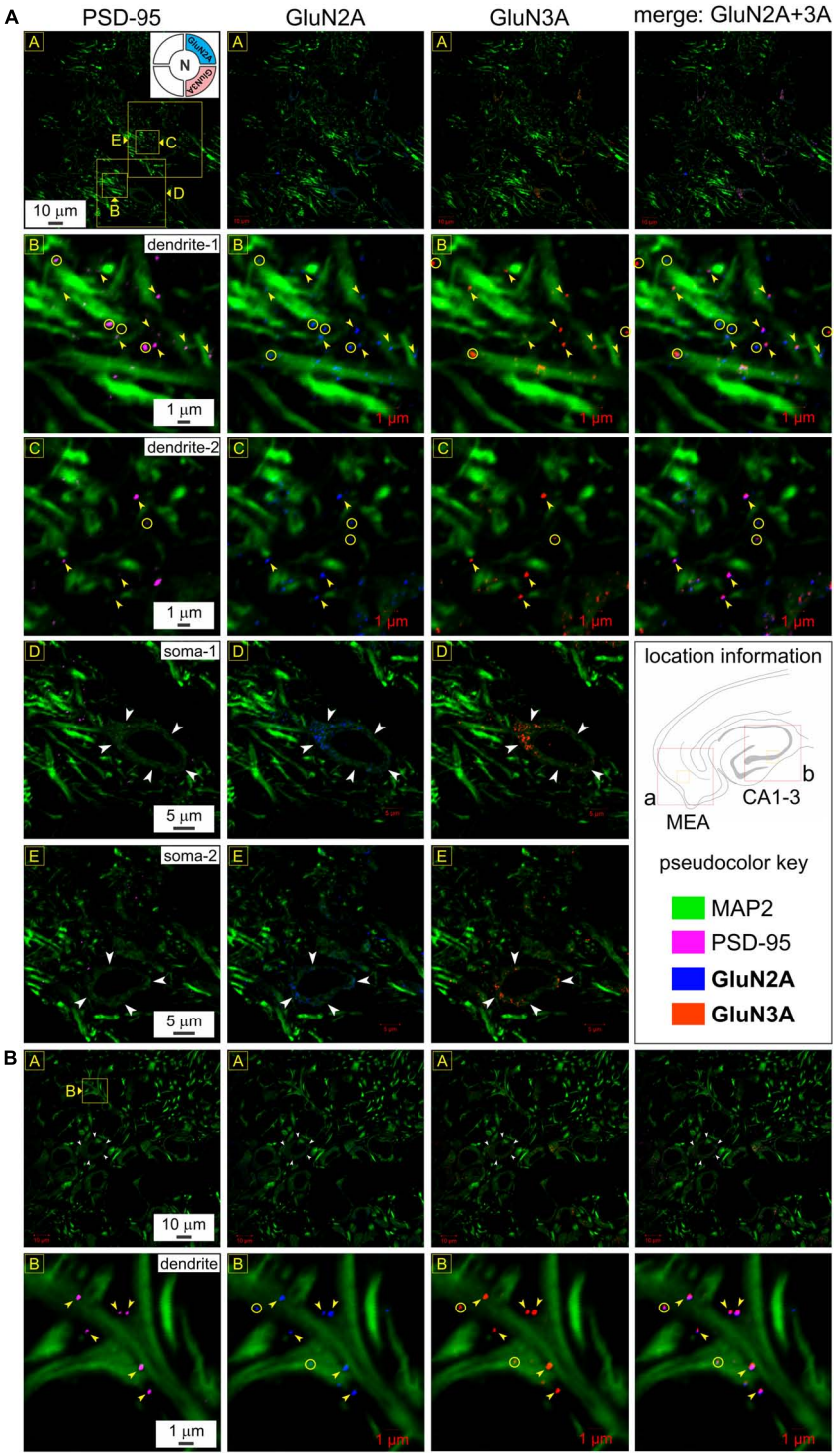

FIGURE 5

Postsynaptic expression and colocalization of glutamate binding (GluN2A) and glycine binding (GluN3A) subunits in medial entorhinal area (MEA) and hippocampus. **(A)** Immunolabeling of GluN2A and GluN3A subunit proteins and their colocalization with postsynaptic density (PSD-95) to reconfirm their postsynaptic expression in MEA **(A)** and the hippocampus **(B)** at various levels of enlargement (*lettered boxes in yellow*). GluN3A and GluN2A puncta colocalize with PSD-95 at the level of the dendrites (MAP2; R2-3C1-4), as can be seen by correlating the merged images of GluN2A and GluN3A (*rightmost column* of images, R1-3C4) with PSD-95 (*leftmost column* of images, R1-3C1) at the indicated magnifications. Yellow arrowheads point to representative examples of individual subunit puncta, their colocalization with each other and with PSD-95. Note that not all subunits colocalize with PSD-95 or with each other (*yellow circles*). Dense immunolabeling of GluN2A and GluN3A subunit proteins, but not PSD-95, in the perikaryon of the cell bodies (*white arrowheads*, R4-5C1-3), but not the nucleus (internal control for colocalization of subunits with the postsynaptic marker). **(B)** Somatic (*white arrowheads*, R1C1-4) and dendritic (*yellow arrowheads*, R2C1-4) immunolabeling of GluN2A and GluN3A subunit proteins in the hippocampus (CA1-3) follow the pattern observed in MEA **(A)**. Note how the coalesced subunits (R1-2C4) align with the postsynaptic marker (R1-2C1) at the level of the dendrite under high magnification (yellow arrowheads, *bottom row*). Not all colocalization could be associated with a visible PSD (yellow circles, *bottom row*).

the colocalization of GluN1/PSD-95 puncta and their separation from the presynaptic marker Bassoon, we looked at single synapses under high magnification (**Figures 6D–F**). Note the location of Bassoon (*yellow arrowheads*, *both rows*, **Figure 6D**) relative to PSD-95 (*white arrowheads*, *both rows*, **Figure 6D**) and GluN1 (*orange arrowheads*, *both rows*, **Figure 6D**), with or without the dendrite (MAP2) in the background (*top and bottom rows, respectively*, **Figure 6D**). The enlarged images (**Figures 6E, F**), with the pseudocolor antigen key altered to assess colocalization, clearly show that the presynaptic marker Bassoon is separated from the postsynaptic marker PSD-95, defining the synapse, and that colocalization of GluN1 is with PSD-95 but not Bassoon. We noted additionally that expression of the GluN1 puncta relative to PSD-95 (P) and Bassoon (B) might be indicative of synaptic orientation (*dotted lines with arrows*, **Figures 6E, F**) in the optical plane imaged. To confirm if GluN3A subunit protein follows the GluN1 pattern of expression, we immunoassayed for it together with the dendritic marker MAP2 and Bassoon (**Figure 7**). Like GluN1, GluN3A also colocalized with PSD-95 and both pair but do not coalesce with Bassoon independently or as a single unit at various magnifications (*top two rows*, *yellow circles*, **Figure 7A**). The high magnification images (**Figure 7B**) clearly show that the presynaptic marker Bassoon (*yellow arrowheads*, **Figure 7B**) is again separated from the postsynaptic marker PSD-95 (*white arrowheads*, **Figure 7B**) at the level of single synapses, and that colocalization of GluN3A (*orange arrowheads*, **Figure 7B**) is with PSD-95 but not Bassoon. Together, these data confirm the postsynaptic expression of GluN1 and GluN3 subunit proteins and by extension of *t*-NMDARs of which they are comprised.

Control experiments

Even though agglomerations of subunit puncta with PSD-95 or among themselves cannot be attributed to chance given the number of colocalizations, we nonetheless performed three specific types of control experiments to legitimize these occurrences.

Antibody controls

To revalidate in house, the specificity of the commercially obtained *primary antibodies* against *t*-NMDAR subunits and to rule out any cross reactivity between them, we expressed GluN1, GluN2A, and GluN3A subunits individually in HEK 293 cells using fluorescent protein-tagged, subunit-specific plasmids (see cell *culture and transfection* in Methods) and assayed for them sequentially using the commercially obtained primary antibodies following visual verification of their expression (**Supplementary Table 1**; see *immunoblotting* in the *cell biology* section of Methods). Our results suggest that the antibodies recognize their respective antigens with high specificity and little to no cross reactivity (**Supplementary Figure 1**).

Histology controls

To rule out cross reactivity of fluorophore-conjugated *secondary antibodies* with incorrect primary antibodies and to gauge non-specific immunofluorescence. For this, we immunolabeled MAP2 with a rabbit primary (**Supplementary Table 1**) and a goat anti-rabbit biotin/streptavidin 647 secondary (**Supplementary Table 2**) to visualize dendrites, followed by immunolabeling of GluN1 with a guinea pig primary and incubations with a goat anti-guinea pig Alexa 555 secondary and an additional unconjugated goat anti-rabbit secondary (to saturate as many epitopes on the first primary as possible). We then assayed for cross immunofluorescence of the other fluorophore-conjugated secondary antibodies used in our protocols–goat anti-rabbit Alexa 594 and goat anti-rabbit Alexa 488 under high magnification. There was little to no cross immunofluorescence of the secondaries with the primaries, thereby validating their specificity and our approach for sequential immunolabeling of antigens (**Supplementary Figure 2A**; also see section on *immunofluorescence* in Methods). We reassessed this again by immunolabeling PSD-95 and GluN1 with rabbit and guinea pig primaries (**Supplementary Table 1**) and visualizing them with goat anti-rabbit Alexa 488 and goat anti-guinea pig Alexa 555 secondary antibodies, respectively (**Supplementary Table 2**), followed by incubation with an unconjugated goat anti-rabbit antibody. We then assayed for cross immunofluorescence of the goat anti-rabbit biotin-streptavidin 647 (secondary only) and goat anti-rabbit Alexa 594 secondary. As before, there was little to no cross immunofluorescence of the fluorophore-conjugated secondaries with the primaries (**Supplementary Figure 2B**).

Region and tissue-specific controls

NMDAR subunit controls were assayed in this study by evaluating their expression patterns in brain areas other than the MEA and hippocampus and in non-neuronal tissue. For region-specific controls, we assayed for the expression of GluN1, GluN2A, and GluN3A subunits in the medulla oblongata (**Supplementary Figure 3**) and the cerebellum (Farrant et al., 1994; Llansola et al., 2005; **Supplementary Figure 4**) and used liver tissue as our non-neuronal control (**Supplementary Figure 5**). There was sparse expression of all three subunits in both the medulla and cerebellum compared to either the MEA or hippocampus. In the cell-dense neuropil of the medulla, we found both somatic and dendritic expression of GluN1, GluN2A and GluN3A subunit proteins in punctate form (**Supplementary Figures 3A, B**) that coalesced occasionally to make putative *t*-NMDARs (**Supplementary Figure 3C**) and conventional GluN1/GluN2A-containing *d*-NMDARs (**Supplementary Figure 3D**). However, unlike MEA or hippocampus, we also observed for the first time, co-expression of GluN3A with GluN2A, but not GluN1, suggesting that the two subunits can come together as dimers (**Supplementary Figure 3E**). Whether these can dimerize further to make functional NMDARs is unknown. This pattern of expression was also observed in the cerebellum proper (**Supplementary Figures 4A, B**) with the expression of putative *d*- and *t*-NMDARs (**Supplementary Figures 4C, D**) and GluN2A/GluN3A dimers. As in the medulla, we estimated ∼50% of the dimers to be GluN2A/GluN3A expressing (**Supplementary Figure 4E**), 10% to be GluN1/GluN2A expressing and the rest as expressing all three subunits, given that we found few, if any, dimers containing just GluN1 and GluN3A. The expression of NMDAR subunits in the liver (non-neuronal control tissue) was even sparser than in the cerebellum or medulla, but not totally absent (**Supplementary Figure 5**). Furthermore, the MAP2 antibody which showed specificity for dendritic processes associated with neurons (as opposed to astroglia) in brain tissue, likely immunolabeled a variant of MAP2 protein in liver

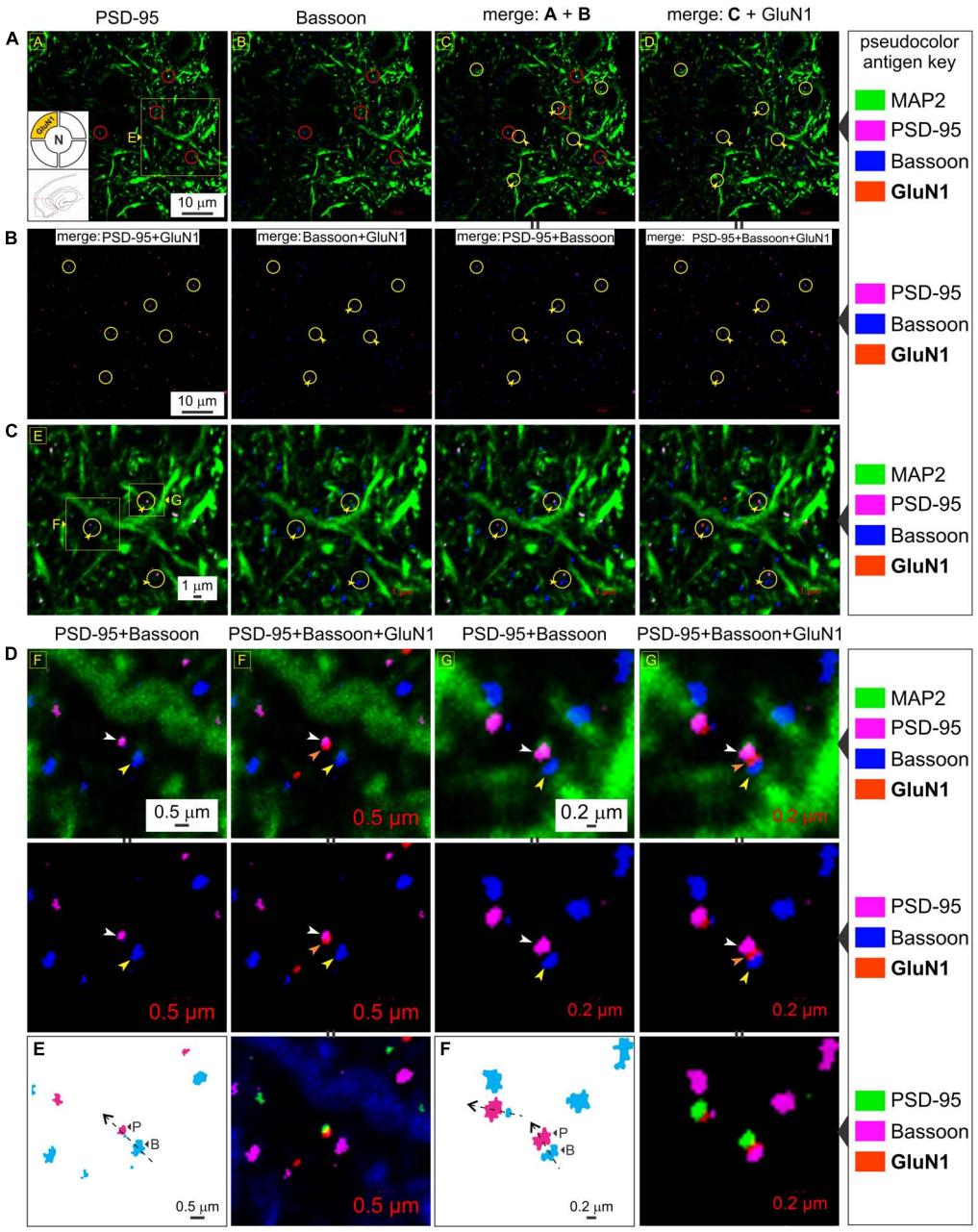

FIGURE 6
The GluN1 subunit protein colocalizes with postsynaptic density (PSD-95) but not the presynaptic marker Bassoon. **(A–C)** Quadruple immunolabeling of GluN1 (mandatory subunit of all NMDARs), PSD-95 (postsynaptic marker), Bassoon (presynaptic marker) and MAP2 (dendrite) in the medial entorhinal area (MEA) highlighting the separation between pre- and postsynaptic markers (*red circles* in a) and/or GluN1 [*yellow circles with embedded arrowheads* in **(A–C)**] and the dendritic colocalization of GluN1 subunit protein with PSD-95 but not Bassoon [rightmost columns in **(A–C)**] at the indicated enlargements (*lettered boxes in yellow*). Note the distinction between colocalization of GluN1 puncta with PSD-95, and together, their pairing with a clearly separated Bassoon. Changes in the *pseudocolor antigen key* [marked by || between images in **(A,B)**] are to aid in gauging colocalization of the proteins imaged. **(D–F)** Expression of GluN1 subunit protein puncta (*orange arrowheads*) relative to PSD-95 (*white arrowheads*) and Bassoon (*yellow arrowheads*) at single synapses under high magnifications **(D,E)**. The *pseudocolor antigen key* is altered to aid gauging of colocalization of the proteins imaged [marked by || between images in **(D–F)**]. The GluN1 puncta outlined in **(E,F)** relative to PSD-95 (P) and Bassoon (B) is indicative of synaptic orientation (*dotted lines with arrows*) in the optical plane imaged.

tissue revealing hepatocytes (confirmed using the nuclear DAPI stain; Supplementary Figure 5A). Expression of GluN1 within the cell bodies of hepatocytes and/or non-parenchymal liver cells was higher than the expression of GluN2A and GluN3A combined, and these subunit puncta could only be visualized properly under high magnifications (bottom row of images in Supplementary Figures 5A, B) given their sparse expression. We occasionally came across puncta containing the GluN1, GluN2A, and GluN3A subunit proteins needed for making *t*-NMDARs, although a large majority of the puncta were GluN2A/GluN3A dimers devoid of GluN1 (white arrow heads point to missing subunits; Supplementary Figure 5A, immunolabeled with MAP2).

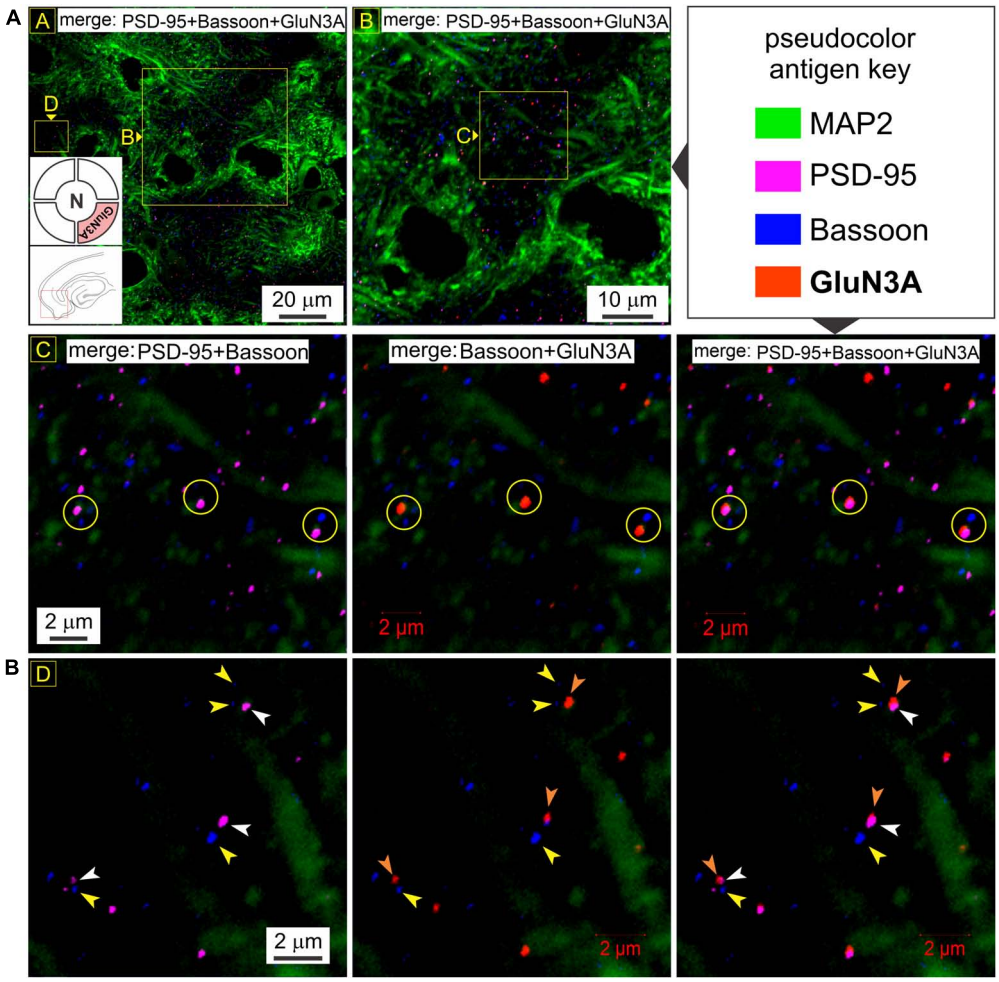

FIGURE 7
GluN3A subunit protein also colocalizes with postsynaptic density (PSD-95) but not Bassoon. **(A)** Quadruple immunolabeling of GluN3A (required for making *t*-NMDARs), PSD-95 (postsynaptic marker), Bassoon (presynaptic marker) and MAP2 (dendrite) in the medial entorhinal area (MEA) showing the separation between pre- and postsynaptic markers (R2C1) and/or GluN3A (top two rows; *yellow circles* in R2C1-3) and the dendritic colocalization of GluN3A subunit protein with PSD-95 but not Bassoon (*merged images* in R1C1-2 and R2C2-3) at the indicated enlargements (*lettered boxes in yellow*). **(B)** Dendritic expression of GluN3A subunit protein puncta (*orange arrowheads*) relative to PSD-95 (*white arrowheads*) and Bassoon (*yellow arrowheads*) at single synapses under high magnification. Note that GluN3A subunit puncta colocalize with PSD-95 and together paired with but well-separated from Bassoon, defining functional synapses.

Many of these dimers were in the cytoplasm, judging from their expression relative to the well-demarcated nuclei (labeled with DAPI; **Supplementary Figure 5B**). Together, these data constitute regional and tissue-specific controls for the NMDAR subunit proteins assayed in the MEA and hippocampus.

Discussion

Visualizing receptor subunit composition is essential for reconciling electrophysiological, cell biological and pharmacological data with function. This is especially true for NMDARs that are functionally very diverse. Studies of recombinant receptors have suggested that variations in subunit composition endow NMDARs with their functional diversity (Cull-Candy et al., 2001; Paoletti et al., 2013) although the precise makeup of native receptors and their expression patterns in the brain has remained largely unknown. The discovery and cloning of the GluN3 subunits (GluN3A-B), the final members of the NMDAR family, augmented the functional diversity of conventional glutamate-activated GluN1/GluN2(A-D) containing NMDARs by introducing unconventional glycine-activated GluN1/GluN3(A-B) NMDARs that were originally thought to form relatively Ca^{2+}-impermeable cation channels and be expressed presynaptically (Das et al., 1998; Chatterton et al., 2002; Perez-Otano and Rodriguez-Moreno, 2019; Crawley et al., 2022). We showed previously that the GluN3 subunit can combine with GluN1 and GluN2 (A and/or B) to make glutamate activated *t*-NMDARs which are distinguishable from GluN2-containing *d*-NMDARs electrophysiologically (have excitatory postsynaptic currents with markedly different current-voltage relationships), have reduced affinity for Mg^{2+}, and increased selectivity for Ca^{2+} over Na^{+}, making them highly Ca^{2+} permeable (Pilli and Kumar, 2012, 2014; Beesley et al., 2019, 2020b; Kumar and Kumar, 2021). These receptors are blocked by the pan-NMDAR antagonist D-(-)-2-Amino-5-phosphonopentanoic acid (D-AP5) and by D-serine,

a potential gliotransmitter and a co-agonist of conventional NMDARs (Kumar, 2016; Beesley et al., 2019, 2020a). Furthermore, we showed that NMDAR subunit composition can vary, not only between different types of neurons, but also between different synaptic inputs onto a neuron and even at a single synapse and that these differences are specific to NMDARs but not coexpressed α-amino-3-hydroxy-5-methyl-4-isoxazolepropionic acid receptors (AMPARs) (Kumar and Huguenard, 2003; Pilli and Kumar, 2012).

The present study is an attempt at visualizing *t*-NMDAR subunit composition at excitatory synaptic inputs onto pyramidal neurons in the medial entorhinal cortex, a hub of spatial navigation (Hafting et al., 2005) and memory consolidation, interfacing the hippocampus, where memories are initially formed, and the neocortex, where they are eventually rendered for permanent storage (Iijima et al., 1996; Tronson and Taylor, 2007). Our data provide direct evidence for colocalization of the two glycine binding subunit proteins, GluN1 and GluN3A, with glutamate binding GluN2A subunits for making synaptic *t*-NMDARs. Note that colocalization alone does not imply interaction and it is conceivable for these subunits to assemble separately as GluN1/GluN3A and GluN1/GluN2A *d*-NMDARs, but unlikely, because of the different neurotransmitters required for their activation and the perpetually desensitized state in which GluN1/GluN3A *d*-NMDARs would find themselves given the continuous albeit controlled availability of glycine at the synaptic cleft and/or be rendered permanently antagonized by ambient D-serine *in vivo* (Berger et al., 1998; Chatterton et al., 2002; Pilli and Kumar, 2012) c.f. excitatory glycine GluN1/GluN3A receptors (eGlyRs) (Grand et al., 2018; Otsu et al., 2019; Bossi et al., 2022). Moreover, PSD-95 binds specifically with the GluN2 subunit of the NMDARs and serves as a multidomain anchoring protein for many scaffolding and structural proteins postsynaptically (Sweatt, 2008; Stanic et al., 2015) thereby increasing the likelihood of its interaction with GluN3. The alternate possibility of *t*-NMDARs assembling with GluN1/GluN2A *d*-NMDARs at single synapses however, cannot be ruled out because both receptor types are activatable by glutamate and blocking synaptic *t*-NMDARs in the MEA pharmacologically has been shown to unmask *d*-NMDARs, with all responses being antagonized by D-AP5 (Beesley et al., 2019). Colocalization of functionally distinct NMDAR subtypes at individual synaptic inputs likely enhances the repertoire of neurons for information processing and plasticity within the entorhinal cortex (Pilli and Kumar, 2014). Our data also establish the postsynaptic locus of expression of these receptors by examining the colocalization of various subunits with PSD-95 but not with the presynaptic marker Bassoon. Although we could not resolve finer details of region and/or lamina specific information owing to the high magnifications used for visualization, we did not observe subunit puncta to colocalize individually or as a cohort with Bassoon, thereby ruling out presynaptic expression of these receptors within the MEA and/or CA1-3 hippocampus.

An upshot of this work is the possibility of visually analyzing pathology underlying neurodegenerative disorders like temporal lobe epilepsy (TLE) from the synaptic/receptor perspective. For example, we have previously shown how *t*-NMDARs, by virtue of their increased selectivity for Ca^{2+} render neurons vulnerable to excitotoxic damage and contribute to the pathology (vulnerability and pattern of neuronal loss) and by extension to the pathophysiology (Ca^{2+}-induced excitotoxicity) underlying TLE (Beesley et al., 2020a; Kumar and Kumar, 2021). By assaying the spatial expression of their subunit proteins (GluN1, GluN2A, GluN2B, and GluN3A) using area-specific tissue analysis (ASTA), a novel methodology for harvesting brain chads from hard-to-reach regions within brain slices for Western blotting, we recently showed that GluN3A was expressed in a gradient along the mid-lateral extent of layer three MEA and along the CA1-subicular axis in the hippocampus, unlike GluN1 and GluN2A which were uniformly distributed. The expression profile of GluN3A defined the "zones of vulnerability" in these regions where there was significant cell loss and neurodegeneration, hallmark features of the disease (Beesley et al., 2022). Thus, the GluN3A expression pattern was indicative of the spatial extent of the pathology in the hippocampus and entorhinal cortex implicating *t*-NMDARs in TLE pathogenesis. Future studies will be able to use the methodology described here to examine spatiotemporal changes in the expression patterns of specific NMDAR subunit proteins visually as a function of disease progression by incorporating data from epileptic animal models to better characterize TLE pathology.

The paucity of subunit-specific compounds has been the bane of NMDAR research until recently, especially for triheteromeric receptors, hindering characterization of their biophysical and functional properties and assessments of their expression and role in the brain. This has even stymied progress on seeking molecules with which to pursue therapeutic options for a wide variety of diseases that implicate them (Paoletti and Neyton, 2007; Stroebel et al., 2018). Furthermore, many of the compounds available for NMDAR subunit pharmacology are not specific enough and there is a niche for alternative approaches to assess subunit composition. The present study, undertaken in the spirit of seeing is believing, is aimed at fulfilling this niche through direct visualization of subunit composition using subunit-specific antibodies and high-resolution confocal microscopy as described in this work.

Data availability statement

The original contributions presented in this study are included in the article/ **Supplementary material**, further inquiries can be directed to the corresponding author.

Ethics statement

The animal study was reviewed and approved by Florida State University Institutional Animal Care Committee.

Author contributions

SK and SB designed and analyzed all experiments outlined in this manuscript. SB contributed to all the cell biology, histology, and confocal microscopy. AG contributed to transfections of HEK cells with plasmids for heterologous expression of GluN subunits to validate the specificity of the antibodies used in this work and provided guidance with microscopy. SK contributed to the electrophysiological assessment of *t*-NMDAR function and writing

the manuscript. All authors contributed to the article and approved the submitted version.

Funding

This work was supported in part by grants from the College of Medicine at Florida State University, the Pediatric Epilepsy Research Foundation (PERF), and the National Institutes of Health (R01NS097802) to SK.

Acknowledgments

We acknowledge Dr. Johanna Paik for challenging us to demonstrate visually the assembly of the three distinct subunit proteins (GluN1-3) that go into making *t*-NMDARs during many a staff room discussion 4 years ago that got us started on this project of visualizing NMDAR subunit composition. Our thanks extend to Dr. Serena Giovinazzi from the Gunjan lab for constructing, sequencing, and testing the GluN3A transfection plasmid for expression by fluorescence microscopy and Western blotting. We are indebted to Ruth Didier for her expert guidance and assistance with confocal microscopy and Prof. Tom Houpt for his critical comments and invaluable feedback on our manuscript.

Conflict of interest

The authors declare that the research was conducted in the absence of any commercial or financial relationships that could be construed as a potential conflict of interest.

Publisher's note

All claims expressed in this article are solely those of the authors and do not necessarily represent those of their affiliated organizations, or those of the publisher, the editors and the reviewers. Any product that may be evaluated in this article, or claim that may be made by its manufacturer, is not guaranteed or endorsed by the publisher.

Supplementary material

The Supplementary Material for this article can be found online at: https://www.frontiersin.org/articles/10.3389/fnsyn.2023.1156777/full#supplementary-material

References

Barria, A., and Malinow, R. (2002). Subunit-specific NMDA receptor trafficking to synapses. *Neuron* 35, 345–353. doi: 10.1016/s0896-6273(02)00776-6

Beesley, S., Sullenberger, T., Crotty, K., Ailani, R., D'Orio, C., Evans, K., et al. (2020a). D-serine mitigates cell loss associated with temporal lobe epilepsy. *Nat. Commun.* 11:4966. doi: 10.1038/s41467-020-18757-2

Beesley, S., Sullenberger, T., and Kumar, S. S. (2020b). The GluN3 subunit regulates ion selectivity within native N-methyl-Daspartate receptors. *IBRO Rep.* 9, 147–156. doi: 10.1016/j.ibror.2020.07.009

Beesley, S., Sullenberger, T., Lee, C., and Kumar, S. S. (2022). GluN3 subunit expression correlates with increased vulnerability of hippocampus and entorhinal cortex to neurodegeneration in a model of temporal lobe epilepsy. *J. Neurophysiol.* 127, 1496–1510. doi: 10.1152/jn.00070.2022

Beesley, S., Sullenberger, T., Pilli, J., Abbasi, S., Gunjan, A., and Kumar, S. S. (2019). Colocalization of distinct NMDA receptor subtypes at excitatory synapses in the entorhinal cortex. *J. Neurophysiol.* 121, 238–254. doi: 10.1152/jn.00468.2018

Berger, A. J., Dieudonne, S., and Ascher, P. (1998). Glycine uptake governs glycine site occupancy at NMDA receptors of excitatory synapses. *J. Neurophysiol.* 80, 3336–3340. doi: 10.1152/jn.1998.80.6.3336

Bossi, S., Dhanasobhon, D., Ellis-Davies, G. C. R., Frontera, J., de Brito Van, Velze, M., et al. (2022). GluN3A excitatory glycine receptors control adult cortical and amygdalar circuits. *Neuron* 110, 2438–2454.e8. doi: 10.1016/j.neuron.2022.05.016.

Chatterton, J. E., Awobuluyi, M., Premkumar, L. S., Takahashi, H., Talantova, M., Shin, Y., et al. (2002). Excitatory glycine receptors containing the NR3 family of NMDA receptor subunits. *Nature* 415, 793–798. doi: 10.1038/nature715

Crawley, O., Conde-Dusman, M. J., and Perez-Otano, I. (2022). GluN3A NMDA receptor subunits: more enigmatic than ever? *J. Physiol.* 600, 261–276. doi: 10.1113/JP280879

Cull-Candy, S., Brickley, S., and Farrant, M. (2001). NMDA receptor subunits: diversity, development and disease. *Curr. Opin. Neurobiol.* 11, 327–335. doi: 10.1016/s0959-4388(00)00215-4

Das, S., Sasaki, Y. F., Rothe, T., Premkumar, L. S., Takasu, M., Crandall, J. E., et al. (1998). Increased NMDA current and spine density in mice lacking the NMDA receptor subunit NR3A. *Nature* 393, 377–381. doi: 10.1038/30748

Farrant, M., Feldmeyer, D., Takahashi, T., and Cull-Candy, S. G. (1994). NMDA-receptor channel diversity in the developing cerebellum. *Nature* 368, 335–339. doi: 10.1038/368335a0

Goncalves, J., Bartol, T. M., Camus, C., Levet, F., Menegolla, A. P., Sejnowski, T. J., et al. (2020). Nanoscale co-organization and coactivation of AMPAR, NMDAR, and mGluR at excitatory synapses. *Proc. Natl. Acad. Sci. U S A.* 117, 14503–14511. doi: 10.1073/pnas.1922563117

Grand, T., Abi Gerges, S., David, M., Diana, M. A., and Paoletti, P. (2018). Unmasking GluN1/GluN3A excitatory glycine NMDA receptors. *Nat. Commun.* 9:4769. doi: 10.1038/s41467-018-07236-4

Gundelfinger, E. D., Reissner, C., and Garner, C. C. (2015). Role of bassoon and piccolo in assembly and molecular organization of the active zone. *Front. Synaptic Neurosci.* 7:19. doi: 10.3389/fnsyn.2015.00019

Hafting, T., Fyhn, M., Molden, S., Moser, M. B., and Moser, E. I. (2005). Microstructure of a spatial map in the entorhinal cortex. *Nature* 436, 801–806. doi: 10.1038/nature03721

Iijima, T., Witter, M. P., Ichikawa, M., Tominaga, T., Kajiwara, R., and Matsumoto, G. (1996). Entorhinal-hippocampal interactions revealed by real-time imaging. *Science* 272, 1176–1179. doi: 10.1126/science.272.5265.1176

Kim, E., and Sheng, M. (2009). The postsynaptic density. *Curr. Biol.* 19, R723–R724. doi: 10.1016/j.cub.2009.07.047

Kumar, S., and Kumar, S. S. (2021). A model for predicting cation selectivity and permeability in AMPA and NMDA receptors based on receptor subunit composition. *Front. Synaptic Neurosci.* 13:779759. doi: 10.3389/fnsyn.2021.779759

Kumar, S. S. (2016). "Functional detection of novel triheteromeric NMDA receptors," in *Ionotropic Glutamate Receptor Technologies*, ed. G. K. Popescu (New York, NY: Springer), 71–80.

Kumar, S. S., and Huguenard, J. R. (2001). Properties of excitatory synaptic connections mediated by the corpus callosum in the developing rat neocortex. *J. Neurophysiol.* 86, 2973–2985. doi: 10.1152/jn.2001.86.6.2973

Kumar, S. S., and Huguenard, J. R. (2003). Pathway-specific differences in subunit composition of synaptic NMDA receptors on pyramidal neurons in neocortex. *J. Neurosci.* 23, 10074–10083.

Li, S., Raychaudhuri, S., Lee, S. A., Brockmann, M. M., Wang, J., Kusick, G., et al. (2021). Asynchronous release sites align with NMDA receptors in mouse hippocampal synapses. *Nat. Commun.* 12:677. doi: 10.1038/s41467-021-21004-x

Llansola, M., Sanchez-Perez, A., Cauli, O., and Felipo, V. (2005). Modulation of NMDA receptors in the cerebellum. 1. properties of the NMDA receptor that modulate its function. *Cerebellum* 4, 154–161. doi: 10.1080/14734220510007996

Luo, J. H., Fu, Z. Y., Losi, G., Kim, B. G., Prybylowski, K., Vissel, B., et al. (2002). Functional expression of distinct NMDA channel subunits tagged with green fluorescent protein in hippocampal neurons in culture. *Neuropharmacology* 42, 306–318. doi: 10.1016/s0028-3908(01)00188-5

Matsuda, K., Kamiya, Y., Matsuda, S., and Yuzaki, M. (2002). Cloning and characterization of a novel NMDA receptor subunit NR3B: a dominant subunit that reduces calcium permeability. *Brain Res. Mol. Brain Res.* 100, 43–52. doi: 10.1016/s0169-328x(02)00173-0

Otsu, Y., Darcq, E., Pietrajtis, K., Matyas, F., Schwartz, E., Bessaih, T., et al. (2019). Control of aversion by glycine-gated GluN1/GluN3A NMDA receptors in the adult medial habenula. *Science* 366, 250–254. doi: 10.1126/science.aax1522

Paoletti, P., Bellone, C., and Zhou, Q. (2013). NMDA receptor subunit diversity: impact on receptor properties, synaptic plasticity and disease. *Nat. Rev. Neurosci.* 14, 383–400. doi: 10.1038/nrn3504

Paoletti, P., and Neyton, J. (2007). NMDA receptor subunits: function and pharmacology. *Curr. Opin. Pharmacol.* 7, 39–47. doi: 10.1016/j.coph.2006.08.011

Perez-Otano, I., and Rodriguez-Moreno, A. (2019). Presynaptic NMDARs and astrocytes ally to control circuit-specific information flow. *Proc. Natl. Acad. Sci. U S A.* 116, 13166–13168. doi: 10.1073/pnas.1908293116

Pilli, J., and Kumar, S. S. (2012). Triheteromeric N-methyl-D-aspartate receptors differentiate synaptic inputs onto pyramidal neurons in somatosensory cortex: involvement of the GluN3A subunit. *Neuroscience* 222, 75–88. doi: 10.1016/j.neuroscience.2012.07.020

Pilli, J., and Kumar, S. S. (2014). Potentiation of convergent synaptic inputs onto pyramidal neurons in somatosensory cortex: dependence on brain wave frequencies and NMDA receptor subunit composition. *Neuroscience* 272, 271–285. doi: 10.1016/j.neuroscience.2014.04.062

Prange, O., Wong, T. P., Gerrow, K., Wang, Y. T., and El-Husseini, A. (2004). A balance between excitatory and inhibitory synapses is controlled by PSD-95 and neuroligin. *Proc. Natl. Acad. Sci. U S A.* 101, 13915–13920. doi: 10.1073/pnas.0405939101

Richter, K., Langnaese, K., Kreutz, M. R., Olias, G., Zhai, R., Scheich, H., et al. (1999). Presynaptic cytomatrix protein bassoon is localized at both excitatory and inhibitory synapses of rat brain. *J. Comp. Neurol.* 408, 437–448.

Sheng, M., and Hoogenraad, C. C. (2007). The postsynaptic architecture of excitatory synapses: a more quantitative view. *Annu. Rev. Biochem.* 76, 823–847. doi: 10.1146/annurev.biochem.76.060805.160029

Stanic, J., Carta, M., Eberini, I., Pelucchi, S., Marcello, E., Genazzani, A. A., et al. (2015). Rabphilin 3A retains NMDA receptors at synaptic sites through interaction with GluN2A/PSD-95 complex. *Nat. Commun.* 6:10181. doi: 10.1038/ncomms10181

Stroebel, D., Casado, M., and Paoletti, P. (2018). Triheteromeric NMDA receptors: from structure to synaptic physiology. *Curr. Opin. Physiol.* 2, 1–12. doi: 10.1016/j.cophys.2017.12.004

Sweatt, J. D. (2008). *Learning and Memory : a Comprehensive Reference*. Oxford: Academic Press.

Tronson, N. C., and Taylor, J. R. (2007). Molecular mechanisms of memory reconsolidation. *Nat. Rev. Neurosci.* 8, 262–275. doi: 10.1038/nrn2090

Ulbrich, M. H., and Isacoff, E. Y. (2008). Rules of engagement for NMDA receptor subunits. *Proc. Natl. Acad. Sci. U S A.* 105, 14163–14168. doi: 10.1073/pnas.0802075105

Washbourne, P., Bennett, J. E., and McAllister, A. K. (2002). Rapid recruitment of NMDA receptor transport packets to nascent synapses. *Nat. Neurosci.* 5, 751–759. doi: 10.1038/nn883

Zheng, C. Y., Seabold, G. K., Horak, M., and Petralia, R. S. (2011). MAGUKs, synaptic development, and synaptic plasticity. *Neuroscientist* 17, 493–512. doi: 10.1177/1073858410386384

frontiers | Frontiers in Synaptic Neuroscience

TYPE Original Research
PUBLISHED 30 May 2023
DOI 10.3389/fnsyn.2023.1198159

Check for updates

OPEN ACCESS

EDITED BY
Alfredo Kirkwood,
Johns Hopkins University, United States

REVIEWED BY
Corette J. Wierenga,
Radboud University, Netherlands
Andrew Lutas,
National Institute of Diabetes and Digestive and Kidney Diseases (NIH), United States

*CORRESPONDENCE
Thomas Mittmann
✉ mittmann@uni-mainz.de

RECEIVED 31 March 2023
ACCEPTED 05 May 2023
PUBLISHED 30 May 2023

CITATION
Ueberbach T, Simacek CA, Tegeder I, Kirischuk S and Mittmann T (2023) Tonic activation of $GABA_B$ receptors via GAT-3 mediated GABA release reduces network activity in the developing somatosensory cortex in GAD67-GFP mice.
Front. Synaptic Neurosci. 15:1198159.
doi: 10.3389/fnsyn.2023.1198159

COPYRIGHT
© 2023 Ueberbach, Simacek, Tegeder, Kirischuk and Mittmann. This is an open-access article distributed under the terms of the Creative Commons Attribution License (CC BY). The use, distribution or reproduction in other forums is permitted, provided the original author(s) and the copyright owner(s) are credited and that the original publication in this journal is cited, in accordance with accepted academic practice. No use, distribution or reproduction is permitted which does not comply with these terms.

Tonic activation of $GABA_B$ receptors via GAT-3 mediated GABA release reduces network activity in the developing somatosensory cortex in GAD67-GFP mice

Timo Ueberbach[1], Clara A. Simacek[1], Irmgard Tegeder[2], Sergei Kirischuk[1] and Thomas Mittmann[1]*

[1]Institute for Physiology, University Medical Center of the Johannes Gutenberg-University, Mainz, Germany, [2]Institute of Clinical Pharmacology, Faculty of Medicine, Goethe-University, Frankfurt, Germany

The efficiency of neocortical information processing critically depends on the balance between the glutamatergic (excitatory, E) and GABAergic (inhibitory, I) synaptic transmission. A transient imbalance of the E/I-ratio during early development might lead to neuropsychiatric disorders later in life. The transgenic glutamic acid decarboxylase 67-green fluorescent protein (GAD67-GFP) mouse line (KI) was developed to selectively visualize GABAergic interneurons in the CNS. However, haplodeficiency of the GAD67 enzyme, the main GABA synthetizing enzyme in the brain, temporarily leads to a low GABA level in the developing brain of these animals. However, KI mice did not demonstrate any epileptic activity and only few and mild behavioral deficits. In the present study we investigated how the developing somatosensory cortex of KI-mice compensates the reduced GABA level to prevent brain hyperexcitability. Whole-cell patch clamp recordings from layer 2/3 pyramidal neurons at P14 and at P21 revealed a reduced frequency of miniature inhibitory postsynaptic currents (mIPSCs) in KI mice without any change in amplitude or kinetics. Interestingly, mEPSC frequencies were also decreased, while the E/I-ratio was nevertheless shifted toward excitation. Surprisingly, multi-electrode-recordings (MEA) from acute slices revealed a decreased spontaneous neuronal network activity in KI mice compared to wild-type (WT) littermates, pointing to a compensatory mechanism that prevents hyperexcitability. Blockade of $GABA_B$ receptors ($GABA_B$Rs) with CGP55845 strongly increased the frequency of mEPSCs in KI, but failed to affect mIPSCs in any genotype or age. It also induced a membrane depolarization in P14 KI, but not in P21 KI or WT mice. MEA recordings in presence of CGP55845 revealed comparable levels of network activity in both genotypes, indicating that tonically activated $GABA_B$Rs balance neuronal activity in P14 KI cortex despite the reduced GABA levels. Blockade

of GABA transporter 3 (GAT-3) reproduced the CGP55845 effects suggesting that tonic activation of $GABA_BRs$ is mediated by ambient GABA released via GAT-3 operating in reverse mode. We conclude that GAT-3-mediated GABA release leads to tonic activation of both pre- and postsynaptic $GABA_BRs$ and restricts neuronal excitability in the developing cortex to compensate for reduced neuronal GABA synthesis. Since GAT-3 is predominantly located in astrocytes, GAD67 haplodeficiency may potentially stimulate astrocytic GABA synthesis through GAD67-independent pathways.

KEYWORDS

GABA, $GABA_B$ receptors, somatosensory cortex, E/I balance, presynaptic, postsynaptic, GAT-3, neurodevelopmental disorders

1. Introduction

Gamma-aminobutyric acid (GABA), the main inhibitory neurotransmitter in the mature CNS, fulfills trophic functions during development (Meier et al., 1983; Represa and Ben-Ari, 2005) and gradual maturation of GABAergic system has been implicated in the timing of the critical period in sensory systems (for review, see Jiang et al., 2005). A reduced level of GABA can strongly impact brain functions both during development and in adulthood. Under healthy conditions the brain balances the strengths of glutamatergic excitation (E) vs. GABAergic inhibition (I), establishing an appropriate E/I balance. However, this E/I balance can be disturbed during development and throughout life. Numerous studies suggested that a transient E/I imbalance during early development cause structural and functional developmental malfunctions and manifests in behavioral deficits in adult rodents (for review, see Eichler and Meier, 2008; Ghatak et al., 2021). In humans those disbalanced states of the developing brain have been associated with neuropsychiatric diseases like autism-spectrum disorders (ASD) and schizophrenia, or promote epileptogenesis (Turrigiano and Nelson, 2004; Eichler and Meier, 2008; Naaijen et al., 2017; Bassetti et al., 2021; Kirischuk, 2022). However, we have previously observed an impaired GABAergic signaling in the contralateral cortical hemisphere in adolescent mice early after traumatic brain injury (TBI), resulting in a shift of the cortical E/I ratio toward excitation (Le Prieult et al., 2017). Such a trauma-induced E/I- imbalance was linked to the development of post traumatic epilepsy (Pavlov et al., 2011; Le Prieult et al., 2017; Dulla and Pitkanen, 2021; Ihbe et al., 2022). However, we found that expression of a presynaptic voltage-gated calcium channel (CaV1.3) in somatostatin-positive interneurons counterbalances the early impaired GABAergic inhibition and hyperactivity on the cortical network after TBI (Ihbe et al., 2022). In search for compensatory mechanisms, which can rebalance the E/I ratio in the cortex, the present study made use of the GAD67-GFP knock-in mouse line (KI), a well-established mouse model to study GABAergic interneurons in living tissues (Tamamaki et al., 2003). This mouse line significantly contributed to a better understanding of the role of GABAergic interneurons on normal brain development and also under pathological conditions like ASD, schizophrenia or TBI (Gandhi et al., 2008; Curley et al., 2013; Ihbe et al., 2022). However, the GFP labeling comes with the cost of one functional copy of the GAD1 Gen which codes the GAD67 glutamate decarboxylase enzyme, the main producer of GABA in the developing CNS (Erlander et al., 1991; Erlander and Tobin, 1991; Gonzales et al., 1991). As a consequence, the lack of one functional copy of the GAD1 gen leads to a reduced expression of the GAD67 enzyme and in turn a decreased GABA concentration in the CNS (Tamamaki et al., 2003). We hypothesized that the GABA shortage will shift the E/I ratio away from physiological equilibrium. Indeed, on the behavioral level several studies demonstrated changes in social behavior, like hyperactivity, ADHD-like behavior and changes in response to olfactory sensory stimuli in KI mice (Janitzky et al., 2009; Bruxel et al., 2016). However, the KI mouse line was not shown to generate more epileptic seizures compared to their wild type littermates (Tamamaki et al., 2003), which indicates potential compensatory mechanisms to prevent chronical hyperexcitability and epileptogenesis. Here we investigated the strength of the excitatory and inhibitory neurotransmission in layers 2/3 pyramidal neurons in the somatosensory cortex of young, developing KI-mice using electrophysiological patch-clamp recordings. In addition, we recorded cortical network activity in acute cortical slices using multi-electrode array (MEA) techniques. Surprisingly, although we observed reduced GABA levels and an elevated E/I ratio in the cortex of KI mice at P14, the MEA recordings disclosed a reduced neuronal network activity. To address the underlying mechanism(s), we assessed effects of blocking $GABA_BRs$ or the GABA transporter 3 (GAT-3). The results suggest that the suppressed cortical network activity in the KI mice at P14 resulted from an inhibition of the glutamatergic excitatory transmission via tonically activated pre- and postsynaptic GABA-B-receptors ($GABA_BRs$), and that the ambient GABA required to activate those $GABA_BRs$ was released through reverse operating GAT-3. Since GAT-3 is mainly expressed in astrocytes (Minelli et al., 1996) and was shown to have neuroprotective effects after brain trauma in rodents (Cho et al., 2022), we propose that low cortical GABA concentrations in young KI mice stimulates GABA efflux from astrocytes, thereby stabilizing neuronal network activity despite an observed GABA shortage.

2. Materials and methods

2.1. Animals and ethical statement

Juvenile, transgenic heterozygous GAD67-GFP positive (KI) mice (n = 41) and their GAD67-GFP negative (WT) littermates (n = 38) were used in two age groups on either postnatal days 14/15 (P14) or on the postnatal days 21/22 (P21).

This mouse line was originally generated by Tamamaki et al. (2003). For the present experiments we crossed KI- with wild-type C57BL/6N- mice. During preparation of the cortical tissue from the offspring (see section "2.3 Slice preparation") each brain was optically inspected for presence or absence of GFP-positive cells. This was done by the experimenter in a non-blinded approach and by use of a fluorescent lamp (SFA Light Head, Nightsea, Hatfield, PA, USA) in the area of the cerebellum. Animals were kept under standard 12 h day/night rhythm at a constant temperature of 23°C with an *ad libitum* supply of food and water. The experiments were designed to restrict the number of animals that were used in this study to the necessary minimum, and all experiments were performed in accordance with German and European laws of animal welfare in science (2010/63/EU).

2.2. ELISA

The cortical GABA-concentration was examined by ELISA experiments using whole cortex lysates from KI and their WT littermates. Mice were deeply anesthetized with 4% isoflurane and decapitated. Next, the brains were quickly removed, the cortex isolated and frozen in liquid nitrogen. Cortex lysates were produced using an electrical homogenizer adding 1.5 ml N-PER Neuronal Protein extraction reagent (Thermo Fisher Scientific, Waltham, MA, USA) with the addition of the Halt Protease and Phosphatase Inhibition cocktail (1:100; Thermo Fisher Scientific, Waltham, MA, USA). After keeping the samples at 4°C for 1 h they were centrifuged at 13,000 rpm for 20 min at 4°C. The supernatant was used for further analysis. Samples were adjusted to a protein concentration of 1.5 mg/ml. The GABA concentration was measured with a GABA sandwich Elisa kit (Abcam, Cambridge, England). The fluorescence signals were measured using a plate reader (Infinite M1000, Tecan, Switzerland).

2.3. Slice preparation

Mice were deeply anesthetized with 4% isoflurane and decapitated. The brain was removed and transferred into ice cold oxygenated (95% O_2 and 5% CO_2) cutting artificial cerebrospinal fluid (cACSF) containing (in mM): 87 NaCl, 37.5 choline chloride, 2.5 KCl, 7$MgSO_4$ × 7H_2O, 0.5 $CaCl_2$ × H_2O, 1.25 NaH_2PO_4 × H_2O, 25 $NaHCO_3$, and 25 d-glucose; pH: 7.4 (ingredients purchased from Carl Roth, Karlsruhe, Germany).

Brains were cut into 350 µm coronal slices for patch-clamp experiments and 400 µm for MEA recordings using a vibratome (VT1200 S, Leica, Wetzlar, Germany). Brain slices containing the somatosensory cortex were collected and incubated for 20 min in cACSF at 37°C and additional 40 min in normal ACSF (ACSF) containing (in mM): 125 NaCl, 2.5 KCl, 1 $MgSO_4$ × 7 H_2O, 2 $CaCl_2$ × H_2O, 1.25 NaH_2PO_4 × H_2O, 25 $NaHCO_3$, and 25 d-glucose; pH: 7.4 (ingredients purchased from Carl Roth, Karlsruhe, Germany) at room temperature.

2.4. Multi-electrode array recordings

Spontaneous neuronal activity was recorded using a 2-chamber MEA system (MEA2100 System, Multi Channel Systems MCS GmbH, Kusterdingen, Germany). A chip consists of 60 electrodes (59 recording electrodes, 1 internal reference, 60MEA200/30iR; Multi Channel Systems MCS GmbH, Kusterdingen, Germany) with a distance of 200 µm between electrodes. The diameter of each recording electrode was 30 µm.

The cortical slices were placed on the chip in a way that the top border of the slice was aligned with the border of the top electrode row (see **Figure 1B**). Electrode rows two and three corresponded to cortical layers 2/3 were used for recordings and analysis. The location of the somatosensory cortex was identified according to the mouse brain atlas by Paxinos and Franklin (2004).

Slices were fixed on the MEA chip using a platinum grid and constantly perfused with oxygenated ACSF at a flow rate of 1.5 ml/min using a centrifugal pump (Gilson international, Berlin, Germany). The recording chamber containing ACSF was heated to 32°C. The slices equilibrated on the chip for 30 min before starting the electrophysiological recordings. Spontaneous activity was sampled at 25 kHz. The raw data were filtered using a Butterworth high-pass second order filter with a 200 Hz cut-off. The cortical spontaneous network activity was recorded for 5 min. Every event crossing the 5-fold standard deviation (SD) of the noise was considered as a spike. Spike detection was performed using Multichannel Analyzer 2.18 software (Multi Channel Systems MCS GmbH, Kusterdingen, Germany).

2.5. Whole-cell patch-clamp recordings

Brain slices were transferred into the recording chamber mounted on an upright microscope (Olympus, BX50WI, Shinjuku, Japan). The slices were constantly perfused with oxygenated ACSF using a gravity-driven system with a flow rate of 1.5 ml/min.

All electrophysiological signals were recorded using an Axopatch-200B amplifier and Clampex 11.2 software (Molecular Devices, San José, CA, USA). Pipettes were pulled using a DMZ Zeitz-Puller (Planegg, Germany). The resistance of the glass pipettes ranged between 3 and 10 MOhm when filled with the intra-pipette solution. Depending on the experiment, two different intracellular solutions were used. The potassium-based intracellular solution contained (in mM) K-gluconate, 140; KCl, 8; $MgCl_2$ × 6 H_2O, 2; Na_2ATP, 4; Na_2GTP hydrate, 0.3; Na_2Phosphocreatin, 10; HEPES Potassium salt, 10. The cesium-based intracellular solution contained (in mM) Cs-gluconate, 125; CsCl, 5; EGTA, 10; $MgCl_2$, 2; Na_2ATP, 2; Na_2GTP, 0.4; HEPES, 10; N-Ethyl lidocaine bromide (QX-314), 5. The pH was set to 7.3 by KOH and CsOH for K^+- and Cs^+-based solutions, respectively.

Slices were optically inspected with a low magnification objective (5X, Zeiss, Oberkochen, Germany) to identify the area

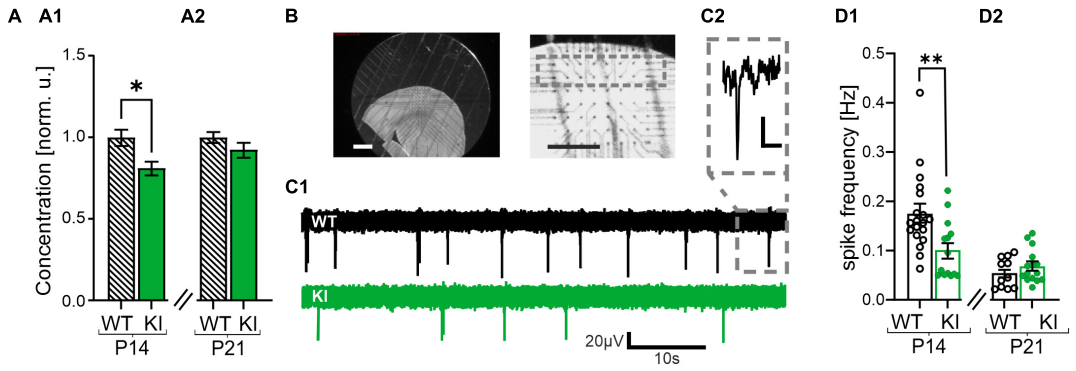

FIGURE 1
Reduced gamma-aminobutyric acid (GABA) concentration and impaired spontaneous network activity in somatosensory cortex of KI-mice. **(A)** GABA concentration in whole cortex lysates of P14 **(A1)** and P21 KI mice **(A2)** normalized to wild-type (WT) littermates and recorded by ELISA. Note the reduced GABA concentration in KI mice at P14. **(B)** Representative images of an acute cortical brain slice placed on the multi-electrode array (MEA) Chip (left and middle). The gray square represents the recording area, layers 2/3. Scale bars = 10 mm. **(C1)** Representative voltage traces of WT (above) and KI (below) mice at P14 recorded with the MEA. **(C2)** The inset shows a spike event at higher magnification, Scale bar = 20 µV/10 ms **(D1)** Mean spontaneous spike frequency in WT and KI mice at P14 and at P21 **(D2)**. Note the reduced frequency in P14 KI animals compared to WT littermates.

of the somatosensory cortex. Next, individual pyramidal neurons were optically selected for the desired patch-clamp recordings in cortical layers 2/3 using a 40X objective (Olympus, Shinjuku, Japan). Recordings started at least 5 min after establishing the whole-cell configuration to allow the proper wash-in of the intra-pipette solution. For measurements in current-clamp mode the recorded pyramidal neurons were kept at their resting membrane potential and the K^+-based intrapipette solution was used. We used a stimulation protocol with a pulse duration of 500 ms and gradually increasing current steps ranging from −20 to +480 pA. Input resistance and passive membrane properties were calculated from the hyperpolarization steps and applying a mono-exponential fit. The first action potential (AP) was used to analyze the functional properties of APs, including threshold, risetime and amplitude. The frequency of the APs was calculated from the maximum number of APs observed during a 500 ms depolarizing current step.

Both, miniature inhibitory postsynaptic currents (mIPSCs) and miniature excitatory postsynaptic currents (mEPSCs), were recorded under voltage clamp conditions with a cesium-based intrapipette solution. The bathing solution contained tetrodotoxin (TTX, 1 µM), a selective blocker of voltage-gated Na^+ channels, and it contained 2-amino-5-phosphonovalerinans acid (DAP-5, 25 µM), an antagonist of NMDA receptors. The recorded neurons were initially voltage-clamped to a holding potential of −70 mV. For mEPSCs, the cells were kept at −60 mV, which is the reversal potential for $GABA_A$-receptor-mediated currents. The mIPSCs were recorded at a holding potential of +10 mV, which is the reversal potential of AMPA-receptor-mediated currents. Serial resistance compensation was not applied. The mIPSC/mEPSC signals were recorded at least for 5 min. Signals were filtered at 3 kHz and sampled at 25 kHz. All electrophysiological data were analyzed using the Clampfit11 software (Molecular Devices, San José, CA, USA). The specific antagonists of $GABA_B$Rs, CGP55845, and of GABA transporters GAT-3, SNAP5114, as well as the specific $GABA_B$R-agonist Baclofen were provided by Tocris (Bio-Techne, Wiesbaden, Germany). All other chemicals were purchased by Carl Roth (Karlsruhe, Germany).

2.6. Statistics

All data were analyzed using Excel 2019 (Microsoft, USA) and GaphPad Prism software (San Diego, CA, USA). Results are presented as mean ± standard error of the mean (SEM). If not otherwise noted, a pairwise Mann-Whitney Test was performed for non-parametric distributions. For comparison of more than two experimental groups we performed a Kruskal-Wallis Test with Dunn's multiple comparison (mentioned in the text). Statistical significant differences between experimental groups are displayed by asterisks $^*P < 0.05$; $^{**}P < 0.01$; $^{***}P < 0.001$.

3. Results

3.1. GAD67-GFP KI mice show lower network activity compared to WT littermates

GAD67 is the main neuronal GABA synthesizing enzyme in early development (Greif et al., 1991). Haplodeficiency of this enzyme in the present KI-mouse model was reported to result in a reduction of GABA concentration in the whole brain (Tamamaki et al., 2003). First, we verified the previous finding of a reduced GABA concentration in this mouse model by performing a GABA ELISA experiment of whole brain lysates. As expected, we observed a reduced GABA concentration in the cortex of young KI mice at P14 compared to their aged-matched WT littermates (0.8 ± 0.04 in KI as compared with WT, $n = 7$, $p = 0.0175$, **Figure 1A1**). This reduction was no longer visible at the age of 21 days (0.9 ± 0.04 in KI as compared with WT, $n = 7$, $p = 0.3829$, **Figure 1A2**). Theoretically, such a reduction in the concentration of the main inhibitory neurotransmitter GABA at P14 should boost cortical network activity. We tested this hypothesis by performing MEA recordings from the somatosensory cortex and recording of spontaneous spiking frequency in the tissue (**Figures 1B, C1, C2**).

To our surprise we observed a reduced spontaneous spiking frequency in cortical slices from P14 KI mice compared to their WT littermates (KI: 0.1 ± 0.02 Hz, n = 14; WT: 0.2 ± 0.02 Hz, n = 19, p = 0.0025; **Figure 1D1**). This effect was transient, since no significant differences were observed in the cortex from older mice at P21 (WT: 0.05 ± 0.01 Hz, n = 11; KI: 0.07 ± 0.01 Hz, n = 15, p = 0.413, **Figure 1D2**). The observed hypoactivity at P14 likely originates from a compensatory mechanism to protect cortical networks from hyperactivity that would arise from GABA-deficiency in the P14 KI mice. This mechanism might include intrinsic neuronal alterations like changes in passive or active membrane properties, and/or an altered network excitability mediated by changes in synaptic functions.

3.2. No changes in active and passive membrane properties between KI and WT mice

To investigate whether the observed differences in spontaneous network activities are caused by alterations of the intrinsic membrane properties, we performed whole-cell patch-clamp recordings from visually identified pyramidal neurons in layers 2/3 of the somatosensory cortex. The passive membrane properties revealed no significant changes between the genotypes (**Supplementary Table 1**). Next, we analyzed functional properties of evoked action potentials (APs), including amplitude, threshold and rise-time. Although the AP threshold and the maximal firing rate of APs were significantly altered between WT and KI mice at P21 (**Supplementary Table 1**), those findings cannot explain the reduced spontaneous network activity in KI mice at P14. So, we conclude that GAD67 haplodeficiency does not affect the passive and active membrane properties of pyramidal neurons to explain the altered spontaneous network activity in the somatosensory cortex at P14.

3.3. Altered basal synaptic transmission in KI mice caused an increased E/I ratio in P14, but not in P21 mice

Next, we focused on synaptic neurotransmission in the somatosensory cortex of the KI mice. We explored potential changes in excitatory and inhibitory synaptic currents and performed whole-cell patch-clamp experiments to recorded mEPSCs and mIPSCs in presence of 1 μM TTX, a blocker of voltage-gated Na^+ channels, and 25 μM DAP-5, an antagonist of NMDA receptors. The cesium-based intracellular solution allowed us to exclusively record GABAergic mIPSCs at a holding potential of +10 mV as well as exclusively glutamatergic mEPSCs at holding potential of −60 mV from the same recorded neuron (see section "2 Materials and methods").

Interestingly, the glutamatergic, AMPA-receptor-mediated mEPSCs revealed a reduced frequency in KI mice compared to their littermates in both age groups (WT, P14: 3.9 ± 0.2 Hz, n = 7; KI, P14: 2.8 ± 0.3 Hz, n = 9, p = 0.0115; WT, P21: 3.9 ± 0.2 Hz, n = 8; KI, P21: 2.7 ± 0.2 Hz, n = 7, p = 0.0022, **Figures 2A, C1, C2**). Neither amplitudes nor kinetics of the mEPSCs were significantly different in KI and WT mice (**Supplementary Table 2**). As expected from the haplodeficiency of GAD67, the frequency of $GABA_A$ receptor-mediated mIPSCs was also reduced in KI mice compared to WT littermates in both age groups (WT, P14: 3 ± 0.5 Hz, n = 8; KI, P14: 1.4 ± 0.2 Hz, n = 11, p = 0.0068; WT, P21: 3.5 ± 0.5 Hz, n = 8; KI, P21: 2.2 ± 0.3 Hz, n = 7, p = 0.0401, **Figures 2B, D1, D2**). Again, the amplitudes and kinetics of mIPSCs were comparable between WT and KI animals (**Supplementary Table 2**). Although both, excitatory and inhibitory synaptic inputs were reduced in KI mice, the E/I-ratio, defined as the ratio of the frequency of mEPSCs vs. mIPSC was significantly higher at P14 (WT, P14: 1.4 ± 0.2, n = 7; KI, P14: 2.8 ± 0.5, n = 9, p = 0.0079, **Figure 2E1**). Interestingly, this imbalance was transient and no longer visible at P21 (WT, P21: 1.3 ± 0.2, n = 8; KI, P21: 1.5 ± 0.3, n = 7, p = 0.7789, **Figure 2E2**). To ensure that the observed differences in mPSC frequencies were not biased by a lower detection of small-amplitude events, we also compared the 10% of events with the highest signal amplitude. The kinetics and amplitudes of these events were not different between genotypes (**Supplementary Table 3**), confirming the reduction only in frequencies of miniature postsynaptic currents. We conclude that the E/I ratio in the somatosensory cortex of KI mice at P14 is shifted toward stronger excitation (**Figure 2E1**), despite the overall reduced network activity (**Figure 1D1**). This on the first view contradictory finding suggests the existence of an additional mechanism to counterbalance the elevated E/I-ratio. GABA can activate both, ionotropic $GABA_A$ receptors as well as metabotropic (inhibitory) $GABA_BR$. We hypothesized that the latter one would be the key candidate to mediate the downscaling of neuronal network activity through ambient GABA.

3.4. $GABA_BRs$ are tonically activated on glutamatergic presynapses in KI mice

$GABA_BRs$ are G_i protein-coupled receptors, which can modulate the frequency of both, mEPSCs and mIPSCs (Alten et al., 2022). To test the role $GABA_BRs$ on the frequency of mEPSCs, we performed whole-cell patch-clamp recordings with a K^+-based intracellular solution. First, we recorded the baseline mEPSCs in drug-free aCSF. Next, we bath-applied the $GABA_BR$ agonist Baclofen (10 μM) followed by the $GABA_BR$ antagonist CGP55845 (1 μM). Baclofen significantly decreased the frequency of mEPSCs in all experimental groups normalized to control conditions (Kruskal-Wallis Test with Dunn's multiple comparison, $p < 0.05$), except for the P14 KI mice, which however, showed a similar trend (**Figures 3A, B1, B2**). Notably, Baclofen had a significantly weaker effect on KI mice tissue at the age of P21 compared to WT controls (WT, P14: 0.6 ± 0.06, n = 9; KI, P14: 0.8 ± 0.06, n = 12 p = 0.0585; WT, P21: 0.4 ± 0.04, n = 11; KI, P21: 0.6 ± 0.06, n = 7, p = 0.0165, **Figure 3B2**). This indicates that additional activation of $GABA_BRs$ through baclofen is less effective at glutamatergic synapses of the KI mice at P14 and P21, suggesting that $GABA_BRs$ were already tonically activated by ambient GABA.

Next, we tested if presynaptic $GABA_BRs$ were indeed activated by ambient GABA. We bath applied the specific $GABA_BR$-antagonist CGP55845 (1 μM) and observed no changes in the frequency of mEPSCs in WT mice. This suggested that presynaptic $GABA_BRs$ at glutamatergic terminals of WT mice are not strongly

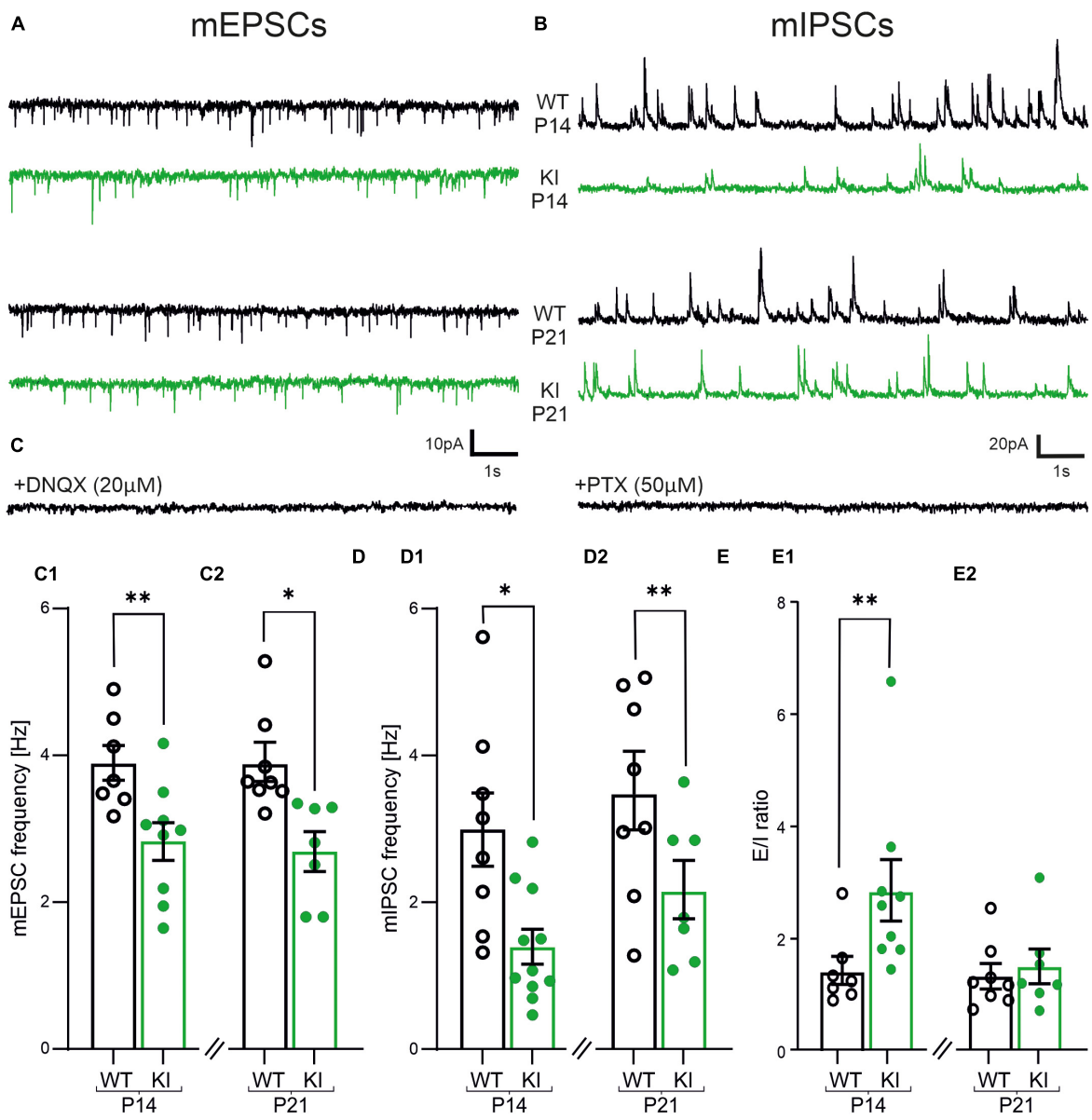

FIGURE 2
Impaired frequencies of miniature excitatory postsynaptic currents (mEPSCs) and miniature inhibitory postsynaptic currents (mIPSCs) and imbalanced E/I-ratio in layers 2/3 pyramidal cells of KI mice. **(A)** Representative traces of mEPSCs recorded at −60 mV in the presence of 25 µM DAP-5 and 1 µM TTX. DNQX (20 µM, bottom trace) completely abolished all inward currents confirming that they are AMPA-receptor dominated. **(B)** Representative traces of mIPSCs recorded at +10 mV from same neurons as shown in **(A)**. Picrotoxin (PTX, 50 µM, bottom trace) abolished all signals proving that they are originating from $GABA_A$-receptor activity. **(C)** Summary graph showing the mean frequency of mEPSCs, which are reduced in P14 **(C1)** and P21 **(C2)** KI-mice. **(D)** The mean frequency of mIPSCs is also reduced in P14 **(D1)** and P21 **(D2)** KI-mice compared to WT littermates. **(E)** Summary graph of the ratio from the frequency of mEPSCs vs. mIPSCs, which is increased at P14 **(E1)**.

activated by ambient GABA. In contrast, CGP55845 significantly increased the frequencies of mEPSCs in KI animals in both age groups (WT, P14: 1 ± 0.04-fold, n = 9; KI, P14: 2.5 ± 0.4-fold, n = 12, p = 0.0018; WT, P21: 0.7 ± 0.05-fold, n = 11; KI, P21: 1.6 ± 0.3-fold, n = 7, p = 0.003, **Figures 3A1, A2, C1, C2**). We also compared the absolute frequency of mEPSCs in the presence of CGP55845. At both age groups, we could no longer detect a significant difference of the mEPSCs frequency between genotypes in the presence of CGP55845 ($p > 0.05$). This suggested that presynaptic $GABA_BRs$ are tonically activated in KI mice, thereby inhibiting the glutamatergic strength in the cortical network.

3.5. No tonic presynaptic inhibition at GABAergic synapses in KI mice

Next, we performed similar experiments with the cesium-based intracellular solution to examine any presynaptic effect of $GABA_BRs$ on GABAergic synapses in KI mice. Baclofen strongly reduced the frequency of mIPSCs compared to control conditions in both, WT and KI mice at both ages (**Figures 4A1, A2**) (Kruskal-Wallis Test with Dunn's multiple comparison; $p < 0.05$). However, no significant difference was observed between the two genotypes (WT, P14: 0.6 ± 0.05, n = 7; KI, P14: 0.6 ± 0.04, n = 8,

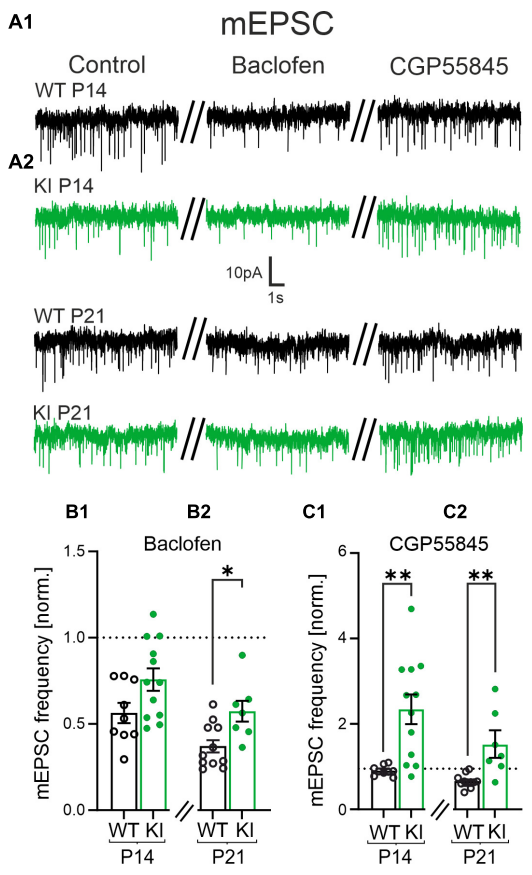

FIGURE 3
The reduced frequency of miniature excitatory postsynaptic currents (mEPSCs) is mediated by activity from presynaptic $GABA_B$ receptors ($GABA_BRs$) at glutamatergic synapses. **(A)** Representative mEPSCs of P14 and P21 mice under control condition (left), in presence of Baclofen (10 μM, middle) and in CGP55845 (1 μM, right trace). **(B1,B2)** Summary diagrams of the relative mean frequency of mEPSCs in presence of the $GABA_BR$ agonist Baclofen normalized to the recordings made in control artificial cerebrospinal fluid (ACSF). **(B2)** Note the significantly smaller reduction in the frequency in wild-type (WT)-animals at P21. **(C1,C2)** The $GABA_BR$- antagonist CGP55845 restored the mEPSC frequency back to control levels in WT mice at P14 and at P21. Note, CGP55845 strongly increased the mEPSC frequency in KI-mice above the level of the control data.

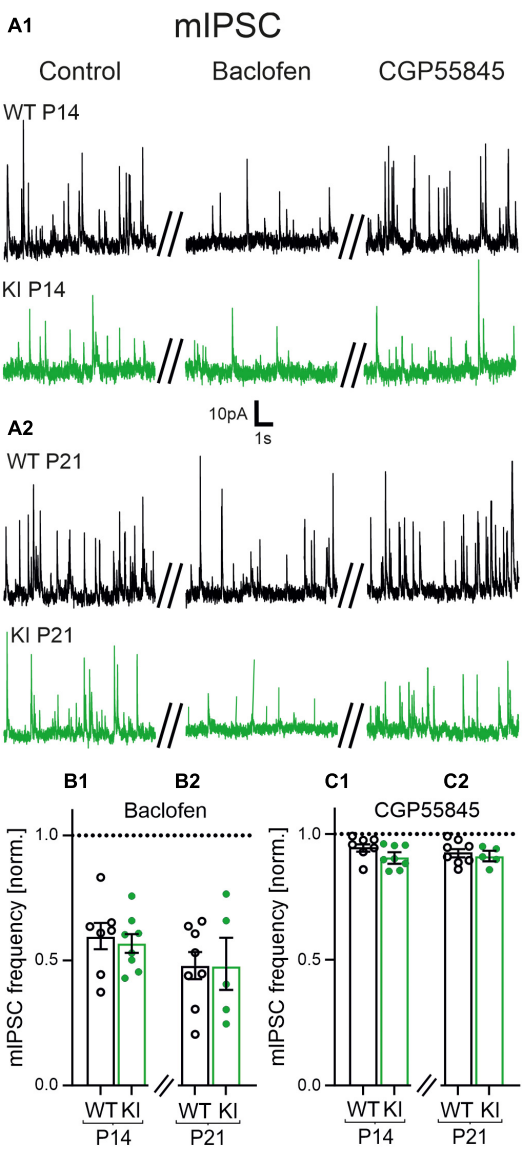

FIGURE 4
Role of $GABA_B$ receptors ($GABA_BRs$) for the impaired frequency of miniature inhibitory postsynaptic currents (mIPSCs) at inhibitory synapses. **(A1,A2)** Representative current traces of mIPSCs of P14 and P21 mice under control condition (left), in the presence of Baclofen (10 μM, middle) and CGP55845 (1 μM, right). **(B1,B2)** Baclofen decreased the mean relative frequency of mIPSCs in all age groups and genotypes. Data were normalized to corresponding control signals in control artificial cerebrospinal fluid (ACSF). **(C1,C2)** CGP55845 rescued the frequency of mIPSCs back to the level of the corresponding control recordings in all age groups and genotypes.

p = 0.6126; WT, P21: 0.5 ± 0.05, n = 8; KI, P21: 0.5 ± 0.09, n = 5, p = 0.9999, **Figures 4B1, B2**). Hence, GABAergic synapses express functional $GABA_BRs$ independent of genotypes and age. Interestingly, and in contrast to the glutamatergic system, blockade of $GABA_BRs$ with CGP55845 failed to increase the frequency of mIPSCs in KI mice of both age groups compared to their WT littermates (WT, P14: 1 ± 0.02, n = 7; KI, P14: 0.9 ± 0.01, n = 8, p = 0.0939; WT, P21: 0.9 ± 0.02, n = 8; KI, P21: 0.9 ± 0.01, n = 5, p = 0.6216, **Figures 4C1, C2**). To substantiate the results, we also compared the absolute frequency of mIPSCs in the presence of CGP55845. The mIPSC frequency was still significantly different between the two genotypes in both age groups ($p < 0.05$). This indicates that GABAergic synapses are functionally not affected by tonic inputs from presynaptic $GABA_BR$. Together with the results on glutamatergic synapses we conclude that tonically activated $GABA_BRs$ in KI mice inhibit the excitatory synaptic drive, thereby reducing network excitability.

3.6. Tonic activation of postsynaptic $GABA_BRs$ in KI mice

Postsynaptic $GABA_BRs$ can also affect neuronal signaling (Tao et al., 2013; Gerrard et al., 2018; Shaye et al., 2021; Bassetti, 2022). Therefore, we investigated a potential contribution of postsynaptic $GABA_BRs$ in our mouse model. First, we performed whole-cell patch clamp experiments to disclose changes in the holding current of pyramidal neurons induced by Baclofen or CGP55845. We used a K^+-based intracellular solution and voltage-clamped the

neurons to a holding potential of −60 mV. The $GABA_BR$ agonist Baclofen shifted the holding current toward a hyperpolarization in both genotypes, indicating expression of functional $GABA_BRs$ at the postsynaptic site. The Baclofen-induced shift was not different between KI and WT mice at P14 (WT, P14: 56 ± 15 pA, n = 9; KI, P14: 60 ± 6 pA, n = 12 p = 0.31; **Figures 5A1, B1**), however, it was smaller in KI animals at P21 compared to their age matched littermates (WT, P21: 82 ± 8 pA, n = 11; KI, P21: 53 ± 7 pA, n = 7, p = 0.0285, **Figures 5A2, B2**). The $GABA_BR$-antagonist CGP55845 reversed the effects of Baclofen in WT mice at both ages and in KI mice at P21. Notably, CGP55845 induced a significant shift of the holding current toward depolarization at P14 in the KI mice (**Figure 5A1**). This indicates an existence of tonically activated $GABA_BRs$ at the postsynaptic site of P14 KI (WT, P14: 5 ± 5 pA, n = 9; KI, P14: −26 ± 4 pA, n = 12 p = 0.0002; WT, P21: −4 ± 6 pA, n = 11; KI, P21: 8 ± −5 pA, n = 7, p = 0.6119, **Figures 5A1, A2, C1, C2**). Together, tonic $GABA_BR$-mediated postsynaptic inhibition in concert with stronger tonic presynaptic inhibition at glutamatergic synapses could explain the overall reduction of network excitability in the cortex of KI mice at P14. These data also provide a possible explanation for the compensation of the network activity at P21 (see **Figure 1**). The loss of the tonic postsynaptic $GABA_BR$-mediated inhibition in the P21 KI can lead to compensation of the network activity at P21.

3.7. Tonic $GABA_BR$ activation mediated decreased network activity in KI mice

To further verify the proposed mechanism, we measured cortical spontaneous network activity in presence of Baclofen (10 μM) or CGP55845 (1 μM) in MEA recordings of acute slice. As already shown in **Figure 1**, the spontaneous firing frequency was impaired in KI-mice at P14 compared to WT-controls (WT, P14: 0.2 ± 0.03 Hz, n = 8; KI, P14: 0.1 ± 0.02, n = 9, p = 0.0206; **Figure 6B1**). In presence of the $GABA_BR$-agonist we could not observe differences in spontaneous network activity between KI and WT mice at P14 (**Figure 6D1**). However, Baclofen had a significantly weaker effect on the cortical activity in KI-mice at P21 when compared to WT-animals of the same age (WT, P21: 0.02 ± 0.002 Hz, n = 5; KI, P21: 0.03 ± 0.005 Hz, n = 6, p = 0.0087; **Figure 6D2**). This indicates an already activation of $GABA_B$-Rs in KI-animals. In presence of the $GABA_BR$-blocker we observed no significant difference in spontaneous activity between KI and WT mice in both age groups (WT, P14: 0.2 ± 0.03 Hz, n = 8; KI, P14: 0.3 ± 0.04 Hz, n = 9, p = 0.3213; WT, P21: 0.07 ± 0.007 Hz, n = 5; KI, P21: 0.07 ± 0.006, n = 6, p = 0.8896; **Figures 6F1, F2**). In summary, the increased tonic activation of $GABA_BRs$ in the cortex of KI mice at P14 mediated the reduction of spontaneous network activity, despite the reduction in total amount of GABA and the observed shift of E/I ratio toward excitation.

3.8. GAT-3 provides GABA for the tonic $GABA_BR$ activation

The haplodeficiency in GAD67 in our KI-mice leads to a reduced neuronal GABA synthesis, so we speculated on alternative

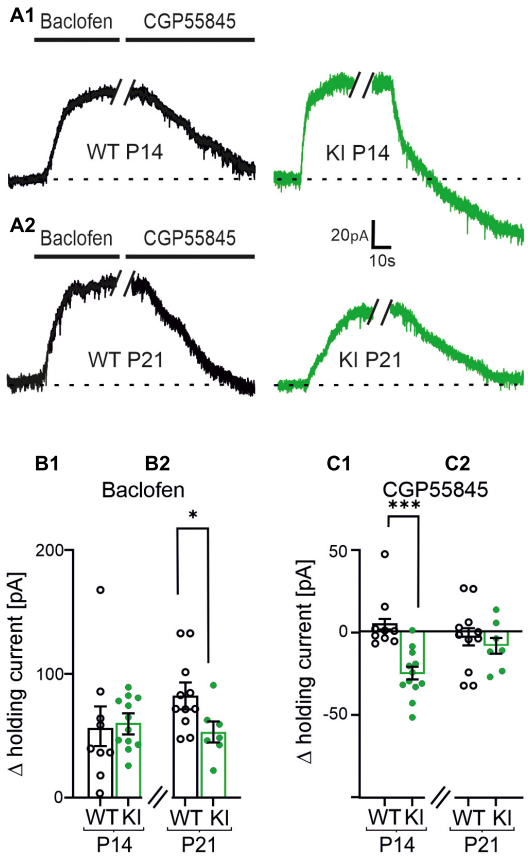

FIGURE 5
Postsynaptic $GABA_B$ receptors ($GABA_BRs$) shift the holding current of layers 2/3 pyramidal cells during voltage-clamp recordings. **(A1,A2)** Representative current traces of voltage clamped pyramidal neurons at constant holding potential of −60 mV in P14 and P21 wild-type (WT)- and KI-mice under control conditions, in presence of Baclofen (10 μM) or CGP55845 (1 μM). **(B1,B2)** Summary diagram of the mean changes in holding current induced by Baclofen or CGP55845. Baclofen shifted the holding current corresponding to a hyperpolarization of the cells. Note, the hyperpolarization was significantly weaker expressed in P21 KI mice as compared to WT littermates **(B2)**. **(C1,C2)** Effect of CGP55845 on the shift of the holding current. The $GABA_BR$-antagonist reversed the effect of Baclofen. Importantly, CGP55845 induced a current shift, which even corresponds to a depolarization of the cells in P14 KI mice.

main sources for the generation of the ambient GABA in these animals. Our experiments so far provided evidence that ambient GABA activates $GABA_BRs$ on glutamatergic pre- and post-synapses to compensate for the impaired GABAergic inhibition. In the cerebral cortex the GABA transporter 3 (GAT-3) has been shown to operate in reverse mode, i.e., releasing GABA, under resting conditions (Kinney, 2005). As GAT-3 is predominantly localized at astrocytes (Minelli et al., 1996) and GAD67 expression in astrocytes is very low (Schousboe et al., 1992), we hypothesized that a reduction of neuronal GAD67-mediated GABA synthesis may facilitate GABA efflux via GAT-3.

To test this hypothesis, we recorded mEPSCs using a potassium K^+-based intracellular solution (**Figures 7A, C1**). Then we incubated the slices with SNAP5114 (50 μM), a selective GAT-3 blocker. In presence of the GAT-3 blocker no differences in the frequencies of mEPSCs were observed in KI- compared to WT-mice (WT, P14: 2.2 ± 0.2 Hz, n = 11; KI, P14: 2.44 ± 0.13 Hz,

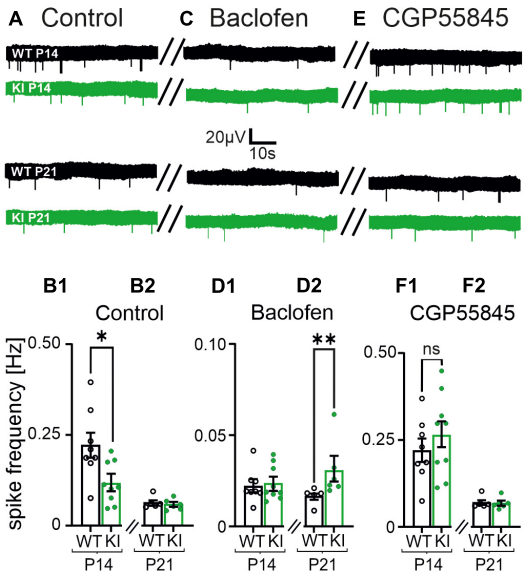

FIGURE 6
Spontaneous cortical network activity of acute coronal brain slices is affected by Baclofen and CGP55845. **(A)** Representative voltage traces from multi-electrode array (MEA) recordings under control conditions in P14 and P21 mice (left column traces). **(B1,B2)** The mean spike frequency is impaired in KI mice at P14 in normal artificial cerebrospinal fluid (ACSF). **(C)** Representative voltage traces in presence of Baclofen (10 μM, middle column). **(D1,D2)** Baclofen further reduced the mean spike frequencies. Note, the impairment is weaker in KI mice at P21 compared to wild-type (WT) littermates. **(E)** Representative voltage traces in presence of CGP55845 (1 μM). **(F1,F2)** CGP55845 rescued the level of spontaneous activity back to control levels in P21 mice. Note the spike frequencies are no longer significantly different between KI and WT mice at P14.

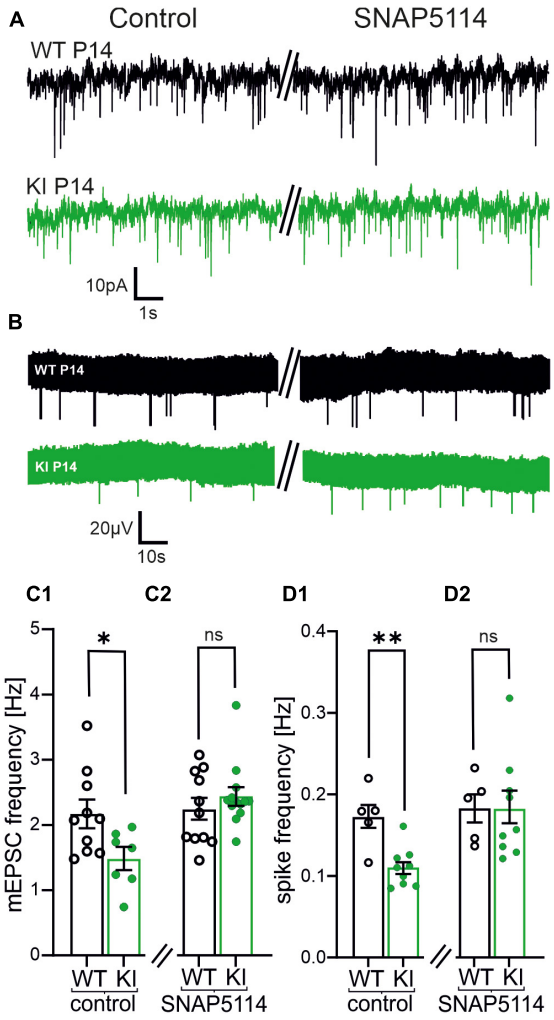

FIGURE 7
Blockade of the astrocytic transporter GABA transporter 3 (GAT-3) increases both, frequency of miniature excitatory postsynaptic currents (mEPSCs) and spontaneous activity in KI mice at P14. **(A)** Representative traces of mEPSCs in controls (left) and after incubation of SNAP5114 (50 μM, right). **(B)** Representative voltage traces of spontaneous activity by multi-electrode array (MEA) recordings under control conditions (left) and after incubation with SNAP5114 (right). **(C1,C2)** Summary diagram of the mean frequency of mEPSCs in KI and WI mice in controls and in the presence of SNAP5114. Note that the mEPSC frequency recovers to a level similar to wild-type (WT)-mice in presence of the GABA transporter 3 (GAT-3)-blocker in KI animals **(C2)**. **(D1,D2)** Summary diagram of the mean spontaneous activity in the cortical slice in KI and WI mice in controls and in presence of SNAP5114. Also, the spontaneous activity increases to the level of WT-mice in SNAP5114 **(D2)**.

n = 13, p = 0.5029, **Figures 7A, C2**). To corroborate this result, we also performed MEA recordings from P14 cortical slices (**Figures 7B, D1**). Similar to the effects on mEPSCs, SNAP-5114 led to a comparable spontaneous network activity in KI mice and WT littermates (WT, P14: 0.2 ± 0.02 Hz, n = 5; KI, P14: 0.2 ± 0.02, n = 9, p = 0.7972; **Figures 7B, D2**). Finally, we tested whether GAT-3-mediated GABA efflux was able to evoke a tonic activation of $GABA_BRs$. Indeed, in presence of the GAT-3 blocker, any $GABA_BR$ inhibition through CGP55845 failed to affect the frequency of mEPSCs (WT, P14: 2.5 ± 0.2 Hz, n = 4; KI, P14: 2.6 ± 0.1 Hz, n = 4, p = 0.4857; **Supplementary Figure 1**). These results suggest that GAT-3 mediated efflux is the main source of extracellular GABA under these conditions, and GABA efflux prevented any cortical hyperactivity in the brains of young KI mice at P14.

4. Discussion

4.1. Transient reduction of GABA level in KI mice

The present heterozygous GAD67 (GFP)-mouse line (KI) was previously shown to express reduced concentrations of cortical GABA at P14 (Tamamaki et al., 2003). GABA levels in the present study were measured in whole cortex lysates using ELISA techniques, which does not allow to delineate changes in $[GABA]_i$ in a cell type-specific manner. However, as GABA in the CNS is mostly located in GABAergic interneurons (Del Rio et al., 1992), our ELISA data suggested a low GABA availability and hence low GABAergic synaptic function in cortical networks of KI-mice. Indeed, the frequency of mIPSCs was significantly reduced in KI mice, indicating a weaker phasic GABAergic drive. Notably, weakening of inhibitory drive was not reflected by an increase in spiking activity of our acute coronal brain slices (**Figure 1**). Also, the intrinsic membrane and firing properties of pyramidal neurons

were not altered between WT- and KI- mice. Therefore, we focused on potential functional changes in synaptic neurotransmission.

4.2. Changes of basal glutamatergic and GABAergic synaptic transmission

The frequency of mIPSCs as well as mEPSCs were significantly reduced in KI cortex. Reduction in frequency of mIPSCs (**Figure 2**) is in good agreement with previous reports on mouse models with a reduced GABA synthesis (Lau and Murthy, 2012; Lazarus et al., 2015). One might expect that this reduction of GABAergic inhibition would lead to exaggerated excitatory glutamatergic activity in the network. Instead, we also observed a reduction in the frequency of glutamatergic mEPSCs in the KI animals.

Low synaptic levels of GABA might also reduce filling of presynaptic vesicles with GABA (Zhou et al., 2000; Engel et al., 2001) and hence reduce the amplitudes of mIPSCs. Indeed, this has been reported for homozygous GAD1 knockout mice models by others (Lau and Murthy, 2012). However, the mIPSC amplitudes in our recordings were not different in KI-animals at P14 or at P21 (**Supplementary Table 2**). The differences likely arise from use of homozygous tissue plus cell cultures or slice cultures, in which the synaptic connectivity is likely to be altered as compared to our acute slice model from hemizygous GAD67 KI mice. Another possible explanation could be a compensatory upregulation of postsynaptic $GABA_A$ receptors. In this case, we would also not see changes in the amplitude of mIPSCs.

Alterations in the subunit composition of postsynaptic receptors is known to be a possible postsynaptic compensatory mechanism to adjust synaptic strength (charge transfer). For example, this has been shown in neurodevelopmental disorders (Han et al., 2014; Hammer et al., 2015) (for review see: Kirischuk, 2022). In our KI-mouse model we did not observe significant differences in amplitude or kinetics of both, mIPSCs and mEPSCs between the genotypes (**Supplementary Table 2**). Consequently, changes in subunit composition of postsynaptic AMPA- as well as of $GABA_A$ receptors are unlikely causing the reduced network activity in our KI mouse model.

4.3. Elevated E/I ratio associated with a reduced network activity

The reduced frequency of both mEPSCs and mIPSCs can affect the E/I ratio in KI-mice. An E/I imbalance was earlier observed in several animal models of neurological disorders (Rubenstein and Merzenich, 2003; Ghatak et al., 2021). Indeed, we also detected an increased E/I ratio in the KI mice at P14, but not at P21. This transient shift of E/I ratio toward more excitation resulted from a relatively stronger reduction in the inhibitory drive of KI mice (**Figure 2**). The frequency of mIPSCs increased with maturation from P14 to P21 in KI mice, thereby stabilizing the E/I ratio to WT levels at P21. One reason for this recovery might be that during maturation an additional GABA-synthesizing enzyme, GAD-65, is functionally expressed in synapses of neurons (Kiser et al., 1998) thereby increasing the level of GABA in the cortex.

Theoretically, the observed shift in E/I balance toward excitation should promote hyperactivity in the cortical networks. However, we observed a decrease in neuronal network activity (**Figure 1**). This is likely a result of an additional compensatory mechanism in the cortex of KI-mice to counterbalance the potential hyperexcitability. Elevated E/I ratios in cortical networks were also observed in various genetic mouse models of autism, which was also interpreted as a homeostatic stabilization mechanism of synaptic drive rather than driving network hyperexcitability (Antoine et al., 2019). Altered GABAergic functions were also observed during visual processing in humans suffering from ASD, and they were modulated by $GABA_BR$ activity (Huang et al., 2022). In a tumor suppressor gene 2 (Tsc2±) mouse ASD model both, the tonic pre- and postsynaptic $GABA_BRs$ were shown to modulate the E/I ratio (Bassetti et al., 2020). However, so far the present KI mouse model was never reported to show an ASD-like behavior, which indicates that at least one additional cellular an mechanism is required to develop ASD phenotype.

4.4. Role of presynaptic $GABA_BRs$ on basal synaptic transmission

$GABA_B$ receptors are already expressed in the embryonic cortex (Turgeon and Albin, 1994). They fulfill trophic functions during early development as well as phasic and tonic synaptic transmission in mature brain (for recent review see: Bassetti, 2022). As $GABA_BRs$ are metabotropic Gi-coupled receptors, their activation leads to a suppression of the adenylate cyclase as well as to the opening of specific K^+ channels (GIRK-channels) and to the inhibition of presynaptic Ca^{2+} channels (for review: Padgett and Slesinger, 2010). In line with these actions of $GABA_BRs$ we observed a reduction in frequency of glutamatergic mEPSCs in presence of the $GABA_BR$ agonist in all experimental groups. Blockade of $GABA_BRs$ with CGP55845 exclusively increased the frequency of mEPSCs in KI mice, which is strong evidence that glutamatergic presynapses in KI-mice tissue are tonically inhibited by ambient GABA. Our data indicate that GABAergic synapses also express functional $GABA_BRs$ in both genotypes and age groups. However, the blockade of $GABA_BRs$ had no effect on the mIPSC frequency indicating that the receptors are not activated by ambient GABA. From these experiments we conclude that the decreased mIPSC frequencies in KI mice are most likely a consequence of reduced intracellular GABA concentration, and this might lead to a decreased number of presynaptic vesicles, thereby reducing the readily releasable pool (RRP).

4.5. $GABA_BR$-mediated postsynaptic inhibition

Baclofen increased the holding current of pyramidal neurons in all experimental groups confirming others that pyramidal neurons express functional postsynaptic $GABA_BRs$ (Terunuma et al., 2014). Interestingly, when $GABA_BRs$ were blocked with GGP55845, we observed a significant depolarization in the KI mice tissue only

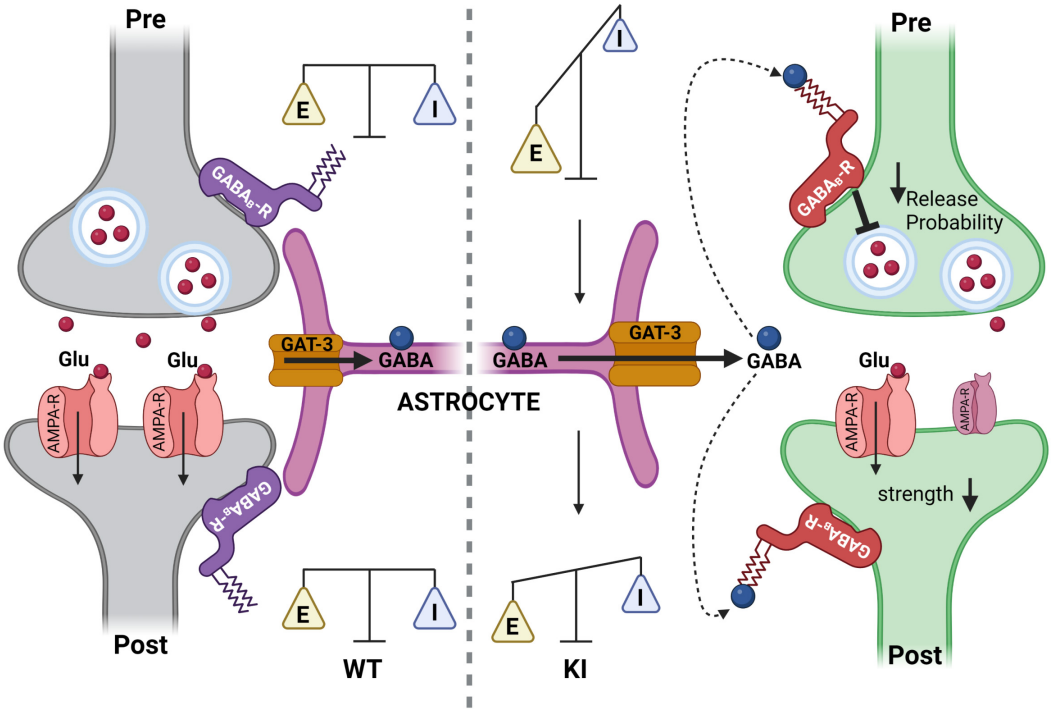

FIGURE 8
Summary cartoon illustrating the mechanism to counterbalance a temporal neuronal gamma-aminobutyric acid (GABA) deficit in KI mice at P14 through activation of tonic pre- and postsynaptic GABAB receptors ($GABA_BRs$) at glutamatergic synapses in the somatosensory cortex. **(Left)** Glutamatergic synapse of the somatosensory cortex in a wild-type (WT)-mouse at P14. GABA is taken up normally via GAT1 into GABAergic neurons (not shown) and via GABA transporter 3 (GAT-3) (orange) into astrocytes (purple). Subsequently, $GABA_BRs$ (blue) are not activated. **(Right)** Glutamatergic synapse of the somatosensory cortex in a KI mice at P14. Astrocytes express the GAT-3 transporter, which is operating in reverse mode. The extrasynaptic GABA, released via GAT-3, can activate pre- and postsynaptic $GABA_BRs$. This activation of $GABA_BRs$ leads to a decreased presynaptic glutamate release and decreased postsynaptic strength to counterbalance network activity, thereby preventing hyperexcitability in a GABA-deficient cortex (Figure created with Biorender.com).

at P14, suggesting tonic activation of postsynaptic $GABA_BRs$ in mice with a haploinsufficiency for GAD67 at P14, but not in WT mice. It should be noted that although our data indicated $GABA_BR$ activation at the post-synapse of KI-mice at P14, we could not detect any changes in resting membrane potential or input resistance in these neurons. Still, this may be a result from the cellular localization of the $GABA_BR$ located directly on dendrites of the neurons (Booker et al., 2013).

So far, the data suggested the following cellular model (**Figure 8**) to balance the cortical network in KI-mice at P14: $GABA_BRs$ were tonically activated by ambient GABA in mice with a haplodeficiency of GAD67 at P14. This led to a reduction in strength of presynaptic glutamatergic inputs. In parallel, tonically activated $GABA_BRs$ on the postsynaptic site also functionally inhibited the excitatory pyramidal neurons. This might act as a compensatory mechanism to shift the E/I balance toward inhibition, thereby protecting the cortex from network hyperactivity. Tonic $GABA_BR$ activation is no longer present at the post-synapse at P21 (**Figure 5**) and shows at least a trend of reduction in the pre-synapse (**Figure 3**). Both results can be mediated by a negative feedback mechanism, which might occur due to the increased tonic activation of $GABA_BRs$ at P14. This could lead to internalization of $GABA_BRs$, which impairs their impact on neuronal activity.

4.6. $GABA_BR$ dependent network activity

Tonically activated $GABA_BRs$ can reduce the cortical network activity (see **Figure 6**). The slightly higher spontaneous activity under the presence of Baclofen in slices of KI at P21 could result from a reduced expression of functional $GABA_BRs$ in pyramidal neurons at this age. This would agree with the theory raised above, that in KI at P21 $GABA_BR$ have a decreased influence on the neuronal activity. When all $GABA_BRs$ were blocked with CGP55845, we could not observe any changes between the experimental groups. This indicated that on the network level tonically activated $GABA_BRs$ stabilize the E/I ratio of single neurons at the cost of a decreased network activity, even in case of a reduced GABA synthesis like in the KI mouse. This raises the question of the putative GABA source.

4.7. GAT-3-mediated GABA release

In hippocampus, synaptically released GABA is the main source of extracellular GABA $[GABA]_e$. GAT1 operating in uptake mode is the dominant transporter that keeps $[GABA]_e$ low and prevents activation of extrasynaptic $GABA_A$ and $GABA_BRs$ (Jensen et al., 2003; Glykys and Mody, 2007). In the cerebral cortex however, GAT-3-mediated GABA efflux can be observed even

under resting conditions (Kinney, 2005; Kirmse and Kirischuk, 2006). GATs transport one GABA molecule with one Cl^- and two Na^+ ions (Attwell et al., 1993; Kristensen et al., 2011). As GABA is predominantly uncharged under physiological pH, the transport process is electrogenic and depends on three transmembrane gradients: Cl^-, Na^+ and GABA. The reduced GABAergic synaptic activity in the KI mice suggests a lower $[GABA]_e$ and higher transmembrane GABA gradient. The latter might facilitate the observed tonic GAT-3-mediated GABA efflux in the cerebral cortex (Kinney, 2005), and is compatible with our observation: blockade of GAT3 shifted both, the frequency of mEPSCs and the network spiking activity back to the level of WT-controls. Moreover, when the $GABA_BR$ antagonist CGP55845 was applied on top of the GAT-3 inhibitor SNAP-5114, it did not affect the neuronal activity, confirming that GAT-3-mediated GABA release is the main mechanism that sets the strength of $GABA_BR$-mediated inhibition in the cortex of KI mice. Interestingly, the GAT3 mediated increase in GABA level did not activate $GABA_B$ receptors at inhibitory terminals. As an explanation for this we cannot exclude that GABAergic terminals express modified $GABA_BRs$, which are less-sensitive to GABA. However, since extracellular GABA is likely released via astrocytic GAT3, we propose that the spatial distribution of GAT3 and/or intra-astrocytic signaling, for example through changes in Na^+ concentration, underlies the uneven activation of $GABA_BRs$.

5. Conclusion

Reduction of phasic GABA release in the KI mice is compensated by non-synaptic GAT-3-mediated GABA release. This leads to tonic activation of presynaptic $GABA_BRs$ selectively at glutamatergic synapses, and in turn protects against cortical hyperactivity in this mouse model of neuronal GABA-deficiency. While GABA transporters like GAT-1 are localized predominantly on neurons, GAT-3 is expressed by astrocytes (Minelli et al., 1995; Minelli et al., 1996). GAT-3-mediated GABA release from astrocytes has been shown in several brain regions (for review see: Kilb and Kirischuk, 2022), and it was shown to have neuroprotective effects in animal models of brain injury (Cho et al., 2022). Elevation of intra-astrocytic Na^+ leads to switching GAT-3 into GABA efflux mode (Heja et al., 2009; Heja et al., 2012). This mechanism could explain an increased extrasynaptic GABA release in the present KI mice model, since the increased E/I ratio at P14 would likely lead to stronger glutamate uptake by astrocytes, which in turn would facilitate GABA release. In addition, astrocytes are capable to synthesize GABA in a GAD67 independent manner from a monoamine putrescine (Jo et al., 2014; Kwak et al., 2020). It is tempting to speculate that the reduced neuronal GABA level in GAD67-GFP mice may be detected by astrocytes, resulting in facilitated GABA synthesis via GAD67-independent pathways resulting in a stronger non-synaptic GABA release. However, further investigations are required to verify this hypothesis.

Data availability statement

The raw data supporting the conclusions of this article will be made available by the authors, without undue reservation.

Ethics statement

All animal experiments conducted in this study were in accordance with national and European laws for the use of animals in research (2010/63/EU) and were approved by the local ethical committee.

Author contributions

IT, SK, and TM planned the research. TU and CS performed and analyzed the experiments. TU, CS, IT, SK, and TM wrote the manuscript. All authors have read and approved the final manuscript.

Funding

This work was supported by a grant of the Deutsche Forschungsgemeinschaft to TM and IT (CRC1080, C02).

Acknowledgments

We thank the Simone Dahms-Praetorius for professional technical assistance.

Conflict of interest

The authors declare that the research was conducted in the absence of any commercial or financial relationships that could be construed as a potential conflict of interest.

Publisher's note

All claims expressed in this article are solely those of the authors and do not necessarily represent those of their affiliated organizations, or those of the publisher, the editors and the reviewers. Any product that may be evaluated in this article, or claim that may be made by its manufacturer, is not guaranteed or endorsed by the publisher.

Supplementary material

The Supplementary Material for this article can be found online at: https://www.frontiersin.org/articles/10.3389/fnsyn.2023.1198159/full#supplementary-material

References

Alten, B., Guzikowski, N. J., Zurawski, Z., Hamm, H. E., and Kavalali, E. T. (2022). Presynaptic mechanisms underlying GABA(B)-receptor-mediated inhibition of spontaneous neurotransmitter release. *Cell Rep.* 38:110255. doi: 10.1016/j.celrep.2021.110255

Antoine, M. W., Langberg, T., Schnepel, P., and Feldman, D. E. (2019). Increased excitation-inhibition ratio stabilizes synapse and circuit excitability in four autism mouse models. *Neuron* 101, 648–661.e4. doi: 10.1016/j.neuron.2018.12.026

Attwell, D., Barbour, B., and Szatkowski, M. (1993). Nonvesicular release of neurotransmitter. *Neuron* 11, 401–407. doi: 10.1016/0896-6273(93)90145-H

Bassetti, D. (2022). Keeping the balance: GABA(B) receptors in the developing brain and beyond. *Brain Sci.* 12:419. doi: 10.3390/brainsci12040419

Bassetti, D., Lombardi, A., Kirischuk, S., and Luhmann, H. J. (2020). Haploinsufficiency of Tsc2 leads to hyperexcitability of medial prefrontal cortex via weakening of tonic GABAB receptor-mediated inhibition. *Cereb. Cortex* 30, 6313–6324. doi: 10.1093/cercor/bhaa187

Bassetti, D., Luhmann, H. J., and Kirischuk, S. (2021). Presynaptic GABA(B) receptor-mediated network excitation in the medial prefrontal cortex of Tsc2(+/-) mice. *Pflugers Arch* 473, 1261–1271. doi: 10.1007/s00424-021-02576-5

Booker, S. A., Gross, A., Althof, D., Shigemoto, R., Bettler, B., Frotscher, M., et al. (2013). Differential GABAB-receptor-mediated effects in perisomatic- and dendrite-targeting parvalbumin interneurons. *J Neurosci* 33, 7961–7974. doi: 10.1523/JNEUROSCI.1186-12.2013

Bruxel, E. M., Akutagava-Martins, G. C., Salatino-Oliveira, A., Genro, J. P., Zeni, C. P., Polanczyk, G. V., et al. (2016). GAD1 gene polymorphisms are associated with hyperactivity in attention-deficit/hyperactivity disorder. *Am. J. Med. Genet. B Neuropsychiatr. Genet.* 171, 1099–1104. doi: 10.1002/ajmg.b.32489

Cho, F. S., Vainchtein, I. D., Voskobiynyk, Y., Morningstar, A. R., Aparicio, F., Higashikubo, B., et al. (2022). Enhancing GAT-3 in thalamic astrocytes promotes resilience to brain injury in rodents. *Sci. Transl. Med.* 14:eabj4310. doi: 10.1126/scitranslmed.abj4310

Curley, A. A., Eggan, S. M., Lazarus, M. S., Huang, Z. J., Volk, D. W., and Lewis, D. A. (2013). Role of glutamic acid decarboxylase 67 in regulating cortical parvalbumin and GABA membrane transporter 1 expression: implications for schizophrenia. *Neurobiol. Dis.* 50, 179–186. doi: 10.1016/j.nbd.2012.10.018

Del Rio, J. A., Soriano, E., and Ferrer, I. (1992). Development of GABA-immunoreactivity in the neocortex of the mouse. *J. Comp. Neurol.* 326, 501–526. doi: 10.1002/cne.903260403

Dulla, C. G., and Pitkanen, A. (2021). Novel approaches to prevent epileptogenesis after traumatic brain injury. *Neurotherapeutics* 18, 1582–1601. doi: 10.1007/s13311-021-01119-1

Eichler, S. A., and Meier, J. C. (2008). E-I balance and human diseases - from molecules to networking. *Front. Mol. Neurosci.* 1:2. doi: 10.3389/neuro.02.002.2008

Engel, D., Pahner, I., Schulze, K., Frahm, C., Jarry, H., Ahnert-Hilger, G., et al. (2001). Plasticity of rat central inhibitory synapses through GABA metabolism. *J Physiol* 535(Pt. 2), 473–482. doi: 10.1111/j.1469-7793.2001.00473.x

Erlander, M. G., Tillakaratne, N. J., Feldblum, S., Patel, N., and Tobin, A. J. (1991). Two genes encode distinct glutamate decarboxylases. *Neuron* 7, 91–100. doi: 10.1016/0896-6273(91)90077-D

Erlander, M. G., and Tobin, A. J. (1991). The structural and functional heterogeneity of glutamic acid decarboxylase: a review. *Neurochem. Res.* 16, 215–226. doi: 10.1007/BF00966084

Gandhi, S. P., Yanagawa, Y., and Stryker, M. P. (2008). Delayed plasticity of inhibitory neurons in developing visual cortex. *Proc. Natl. Acad. Sci. U.S.A.* 105, 16797–16802. doi: 10.1073/pnas.0806159105

Gerrard, L. B., Tantirigama, M. L. S., and Bekkers, J. M. (2018). Pre- and postsynaptic activation of GABA(B) receptors modulates principal cell excitation in the piriform cortex. *Front. Cell Neurosci.* 12:28. doi: 10.3389/fncel.2018.00028

Ghatak, S., Talantova, M., McKercher, S. R., and Lipton, S. A. (2021). Novel therapeutic approach for excitatory/inhibitory imbalance in neurodevelopmental and neurodegenerative diseases. *Annu. Rev. Pharmacol. Toxicol.* 61, 701–721. doi: 10.1146/annurev-pharmtox-032320-015420

Glykys, J., and Mody, I. (2007). The main source of ambient GABA responsible for tonic inhibition in the mouse hippocampus. *J. Physiol.* 582(Pt. 3), 1163–1178. doi: 10.1113/jphysiol.2007.134460

Gonzales, C., Kaufman, D. L., Tobin, A. J., and Chesselet, M. F. (1991). Distribution of glutamic acid decarboxylase (Mr 67,000) in the basal ganglia of the rat: an immunohistochemical study with a selective cDNA-generated polyclonal antibody. *J. Neurocytol.* 20, 953–961. doi: 10.1007/BF01187913

Greif, K. F., Erlander, M. G., Tillakaratne, N. J., and Tobin, A. J. (1991). Postnatal expression of glutamate decarboxylases in developing rat cerebellum. *Neurochem. Res.* 16, 235–242. doi: 10.1007/BF00966086

Hammer, M., Krueger-Burg, D., Tuffy, L. P., Cooper, B. H., Taschenberger, H., Goswami, S. P., et al. (2015). Perturbed hippocampal synaptic inhibition and gamma-oscillations in a neuroligin-4 knockout mouse model of autism. *Cell Rep.* 13, 516–523. doi: 10.1016/j.celrep.2015.09.011

Han, S., Tai, C., Jones, C. J., Scheuer, T., and Catterall, W. A. (2014). Enhancement of inhibitory neurotransmission by GABAA receptors having alpha2,3-subunits ameliorates behavioral deficits in a mouse model of autism. *Neuron* 81, 1282–1289. doi: 10.1016/j.neuron.2014.01.016

Heja, L., Barabas, P., Nyitrai, G., Kekesi, K. A., Lasztoczi, B., Toke, O., et al. (2009). Glutamate uptake triggers transporter-mediated GABA release from astrocytes. *PLoS One* 4:e7153. doi: 10.1371/journal.pone.0007153

Heja, L., Nyitrai, G., Kekesi, O., Dobolyi, A., Szabo, P., Fiath, R., et al. (2012). Astrocytes convert network excitation to tonic inhibition of neurons. *BMC Biol.* 10:26. doi: 10.1186/1741-7007-10-26

Huang, Q., Pereira, A. C., Velthuis, H., Wong, N. M. L., Ellis, C. L., Ponteduro, F. M., et al. (2022). GABA(B) receptor modulation of visual sensory processing in adults with and without autism spectrum disorder. *Sci. Transl. Med.* 14:eabg7859. doi: 10.1126/scitranslmed.abg7859

Ihbe, N., Le Prieult, F., Wang, Q., Distler, U., Sielaff, M., Tenzer, S., et al. (2022). Adaptive mechanisms of somatostatin-positive interneurons after traumatic brain injury through a switch of alpha subunits in L-type voltage-gated calcium channels. *Cereb. Cortex* 32, 1093–1109. doi: 10.1093/cercor/bhab268

Janitzky, K., Stork, O., Lux, A., Yanagawa, Y., Schwegler, H., and Linke, R. (2009). Behavioral effects and pattern of brain c-fos mRNA induced by 2,5-dihydro-2,4,5-trimethylthiazoline, a component of fox feces odor in GAD67-GFP knock-in C57BL/6 mice. *Behav. Brain Res.* 202, 218–224. doi: 10.1016/j.bbr.2009.03.038

Jensen, K., Chiu, C. S., Sokolova, I., Lester, H. A., and Mody, I. (2003). GABA transporter-1 (GAT1)-deficient mice: differential tonic activation of GABAA versus GABAB receptors in the hippocampus. *J. Neurophysiol.* 90, 2690–2701. doi: 10.1152/jn.00240.2003

Jiang, B., Huang, Z. J., Morales, B., and Kirkwood, A. (2005). Maturation of GABAergic transmission and the timing of plasticity in visual cortex. *Brain Res. Brain Res. Rev.* 50, 126–133. doi: 10.1016/j.brainresrev.2005.05.007

Jo, S., Yarishkin, O., Hwang, Y. J., Chun, Y. E., Park, M., Woo, D. H., et al. (2014). GABA from reactive astrocytes impairs memory in mouse models of Alzheimer's disease. *Nat. Med.* 20, 886–896. doi: 10.1038/nm.3639

Kilb, W., and Kirischuk, S. (2022). GABA release from astrocytes in health and disease. *Int. J. Mol. Sci.* 23:15859. doi: 10.3390/ijms232415859

Kinney, G. A. (2005). GAT-3 transporters regulate inhibition in the neocortex. *J. Neurophysiol.* 94, 4533–4537. doi: 10.1152/jn.00420.2005

Kirischuk, S. (2022). Keeping excitation-inhibition ratio in balance. *Int. J. Mol. Sci.* 23:5746. doi: 10.3390/ijms23105746

Kirmse, K., and Kirischuk, S. (2006). Ambient GABA constrains the strength of GABAergic synapses at Cajal-Retzius cells in the developing visual cortex. *J. Neurosci.* 26, 4216–4227. doi: 10.1523/JNEUROSCI.0589-06.2006

Kiser, P. J., Cooper, N. G., and Mower, G. D. (1998). Expression of two forms of glutamic acid decarboxylase (GAD67 and GAD65) during postnatal development of rat somatosensory barrel cortex. *J. Comp. Neurol.* 402, 62–74. doi: 10.1002/(SICI)1096-9861(19981207)402:1<62::AID-CNE5>3.0.CO;2-M

Kristensen, A. S., Andersen, J., Jorgensen, T. N., Sorensen, L., Eriksen, J., Loland, C. J., et al. (2011). SLC6 neurotransmitter transporters: structure, function, and regulation. *Pharmacol. Rev.* 63, 585–640. doi: 10.1124/pr.108.000869

Kwak, H., Koh, W., Kim, S., Song, K., Shin, J. I., Lee, J. M., et al. (2020). Astrocytes control sensory acuity via tonic inhibition in the thalamus. *Neuron* 108, 691.e–706.e. doi: 10.1016/j.neuron.2020.08.013

Lau, C. G., and Murthy, V. N. (2012). Activity-dependent regulation of inhibition via GAD67. *J. Neurosci.* 32, 8521–8531. doi: 10.1523/JNEUROSCI.1245-12.2012

Lazarus, M. S., Krishnan, K., and Huang, Z. J. (2015). GAD67 deficiency in parvalbumin interneurons produces deficits in inhibitory transmission and network disinhibition in mouse prefrontal cortex. *Cereb. Cortex* 25, 1290–1296. doi: 10.1093/cercor/bht322

Le Prieult, F., Thal, S. C., Engelhard, K., Imbrosci, B., and Mittmann, T. (2017). Acute cortical transhemispheric diaschisis after unilateral traumatic brain injury. *J. Neurotrauma* 34, 1097–1110. doi: 10.1089/neu.2016.4575

Meier, E., Drejer, J., and Schousboe, A. (1983). Trophic actions of GABA on the development of physiologically active GABA receptors. *Adv. Biochem. Psychopharmacol.* 37, 47–58.

Minelli, A., Brecha, N. C., Karschin, C., DeBiasi, S., and Conti, F. (1995). GAT-1, a high-affinity GABA plasma membrane transporter, is localized to neurons and astroglia in the cerebral cortex. *J. Neurosci.* 15, 7734–7746. doi: 10.1523/JNEUROSCI.15-11-07734.1995

Minelli, A., DeBiasi, S., Brecha, N. C., Zuccarello, L. V., and Conti, F. (1996). GAT-3, a high-affinity GABA plasma membrane transporter, is localized to astrocytic processes, and it is not confined to the vicinity of GABAergic synapses in the cerebral cortex. *J. Neurosci.* 16, 6255–6264. doi: 10.1523/JNEUROSCI.16-19-06255.1996

Naaijen, J., Bralten, J., Poelmans, G., Image consortium, Glennon, J., and Franke, B. (2017). Glutamatergic and GABAergic gene sets in attention-deficit/hyperactivity disorder: association to overlapping traits in ADHD and autism. *Transl. Psychiatry* 7:e999. doi: 10.1038/tp.2016.273

Padgett, C. L., and Slesinger, P. A. (2010). GABAB receptor coupling to G-proteins and ion channels. *Adv. Pharmacol.* 58, 123–147. doi: 10.1016/S1054-3589(10)58006-2

Pavlov, I., Huusko, N., Drexel, M., Kirchmair, E., Sperk, G., Pitkanen, A., et al. (2011). Progressive loss of phasic, but not tonic, GABAA receptor-mediated inhibition in dentate granule cells in a model of post-traumatic epilepsy in rats. *Neuroscience* 194, 208–219. doi: 10.1016/j.neuroscience.2011.07.074

Paxinos, G., and Franklin, K. B. J. (2004). *The mouse brain in stereotaxic coordinates*. Amsterdam: Elsevier Academic Press.

Represa, A., and Ben-Ari, Y. (2005). Trophic actions of GABA on neuronal development. *Trends Neurosci.* 28, 278–283. doi: 10.1016/j.tins.2005.03.010

Rubenstein, J. L., and Merzenich, M. M. (2003). Model of autism: increased ratio of excitation/inhibition in key neural systems. *Genes Brain Behav.* 2, 255–267. doi: 10.1034/j.1601-183X.2003.00037.x

Schousboe, A., Westergaard, N., Sonnewald, U., Petersen, S. B., Yu, A. C., and Hertz, L. (1992). Regulatory role of astrocytes for neuronal biosynthesis and homeostasis of glutamate and GABA. *Prog. Brain Res.* 94, 199–211. doi: 10.1016/S0079-6123(08)61751-3

Shaye, H., Stauch, B., Gati, C., and Cherezov, V. (2021). Molecular mechanisms of metabotropic GABA(B) receptor function. *Sci. Adv.* 7:eabg3362. doi: 10.1126/sciadv.abg3362

Tamamaki, N., Yanagawa, Y., Tomioka, R., Miyazaki, J., Obata, K., and Kaneko, T. (2003). Green fluorescent protein expression and colocalization with calretinin, parvalbumin, and somatostatin in the GAD67-GFP knock-in mouse. *J. Comp. Neurol.* 467, 60–79. doi: 10.1002/cne.10905

Tao, W., Higgs, M. H., Spain, W. J., and Ransom, C. B. (2013). Postsynaptic GABAB receptors enhance extrasynaptic GABAA receptor function in dentate gyrus granule cells. *J. Neurosci.* 33, 3738–3743. doi: 10.1523/JNEUROSCI.4829-12.2013

Terunuma, M., Revilla-Sanchez, R. I, Quadros, M., Deng, Q., Deeb, T. Z., Lumb, M., et al. (2014). Postsynaptic GABAB receptor activity regulates excitatory neuronal architecture and spatial memory. *J. Neurosci.* 34, 804–816. doi: 10.1523/JNEUROSCI.3320-13.2013

Turgeon, S. M., and Albin, R. L. (1994). Postnatal ontogeny of GABAB binding in rat brain. *Neuroscience* 62, 601–613. doi: 10.1016/0306-4522(94)90392-1

Turrigiano, G. G., and Nelson, S. B. (2004). Homeostatic plasticity in the developing nervous system. *Nat. Rev. Neurosci.* 5, 97–107. doi: 10.1038/nrn1327

Zhou, Q., Petersen, C. C., and Nicoll, R. A. (2000). Effects of reduced vesicular filling on synaptic transmission in rat hippocampal neurones. *J. Physiol.* 525 Pt 1(Pt. 1), 195–206. doi: 10.1111/j.1469-7793.2000.t01-1-00195.x

frontiers | Frontiers in Synaptic Neuroscience

TYPE Mini Review
PUBLISHED 07 December 2023
DOI 10.3389/fnsyn.2023.1250753

Check for updates

OPEN ACCESS

EDITED BY
Karri P. Lamsa,
University of Szeged, Hungary

REVIEWED BY
Irmgard Tegeder,
Goethe University Frankfurt, Germany
Emilio J. Galván,
Instituto Politécnico Nacional de México (CINVESTAV), Mexico
Michael M. Kohl,
University of Glasgow, United Kingdom
Nelson Rebola,
INSERM U1127 Institut du Cerveau et de la Moelle épinière (ICM), France

*CORRESPONDENCE
Charlotte Piette
✉ charlotte.piette@college-de-france.fr
Laurent Venance
✉ laurent.venance@college-de-france.fr

RECEIVED 30 June 2023
ACCEPTED 20 November 2023
PUBLISHED 07 December 2023

CITATION
Piette C, Gervasi N and Venance L (2023) Synaptic plasticity through a naturalistic lens. *Front. Synaptic Neurosci.* 15:1250753. doi: 10.3389/fnsyn.2023.1250753

COPYRIGHT
© 2023 Piette, Gervasi and Venance. This is an open-access article distributed under the terms of the Creative Commons Attribution License (CC BY). The use, distribution or reproduction in other forums is permitted, provided the original author(s) and the copyright owner(s) are credited and that the original publication in this journal is cited, in accordance with accepted academic practice. No use, distribution or reproduction is permitted which does not comply with these terms.

Synaptic plasticity through a naturalistic lens

Charlotte Piette*, Nicolas Gervasi and Laurent Venance*

Center for Interdisciplinary Research in Biology (CIRB), College de France, CNRS, INSERM, Université PSL, Paris, France

From the myriad of studies on neuronal plasticity, investigating its underlying molecular mechanisms up to its behavioral relevance, a very complex landscape has emerged. Recent efforts have been achieved toward more naturalistic investigations as an attempt to better capture the synaptic plasticity underpinning of learning and memory, which has been fostered by the development of *in vivo* electrophysiological and imaging tools. In this review, we examine these naturalistic investigations, by devoting a first part to synaptic plasticity rules issued from naturalistic *in vivo*-like activity patterns. We next give an overview of the novel tools, which enable an increased spatio-temporal specificity for detecting and manipulating plasticity expressed at individual spines up to neuronal circuit level during behavior. Finally, we put particular emphasis on works considering brain-body communication loops and macroscale contributors to synaptic plasticity, such as body internal states and brain energy metabolism.

KEYWORDS

synaptic plasticity, *in vivo*-like patterns, neuromodulation, learning, memory, spike-timing dependent plasticity, neuroenergetic, body internal states

Background

There is an increasing body of evidence in favor of the neuronal plasticity (synaptic, intrinsic and/or structural) and memory hypothesis (Martin and Morris, 2002; Josselyn and Tonegawa, 2020). Synaptic plasticity rules were first investigated *in vitro*, in which neuronal activity patterns can be exactly controlled. Although some rules have been validated *in vivo*, further clarification is needed on how *in vivo* neuronal activity causes synaptic plasticity. Furthermore, the diversity of plasticity rules and profiles expressed within an individual neuron or a given circuit, the plasticitome (McFarlan et al., 2023), calls for a clearer understanding of their specific functions and also of their interplay during learning. In the light of recent studies, this review aims at highlighting how naturalistic investigations of synaptic plasticity can provide a critical insight into the plasticity and memory research field.

From neuronal activity patterns to plasticity rules

Multiple plasticity induction protocols, more or less inspired by *in vivo* activity patterns, have been used both *in vitro* and *in vivo* to unveil the spatio-temporal constraints of synaptic plasticity expression in neuronal networks and dissect their molecular determinants. High-frequency stimulation (HFS) is still widely used because it induces reliable and (generally) potent plasticity ((long-term potentiation, LTP, or long-term depression, LTD) LTP or LTD depending on brain areas, neuronal subtypes). Although HFS can somehow mimic some sensory epochs, HFS appears in most conditions rather as an artificial cell conditioning paradigm because of its high and regular stimulation frequency (100 Hz), and duration (typically

1 s repeated several times). Yet, it is crucial to study the effects of stimulation protocols using natural activity patterns, obtained from *in vivo* electrophysiological recordings (Paulsen and Sejnowski, 2000). Indeed, it will inform on which activity patterns are sufficient and effective at inducing plasticity during learning *in vivo*, hence uncovering naturalistic plasticity rules. In addition, it enables to identify molecular determinants (partially different from those recruited by HFS-induced plasticity), that could later be used for manipulating plasticity expression *in vivo*.

First attempts of realistic stimulations came with theta-burst stimulations, determined from *in vivo* recordings of place cells showing theta rhythm linked to memory storage. Later on, *in vivo* recordings of cortical neurons displaying low frequency firing (<5 Hz) and the discovery of backpropagating action potential (bAP), a signal that could bind presynaptic and postsynaptic activity for plasticity induction, led to spike-timing dependent plasticity (STDP) paradigms (Feldman, 2012; Debanne and Inglebert, 2023). Temporally ordered coincident neuronal activity was postulated by Donald Hebb as the critical driver of long-lasting modifications between neurons (Sejnowski, 1999). Its experimental validation came with the discovery that repeated presynaptic activity preceding post-synaptic activity within a few tens of milliseconds could induce LTP, while the converse temporal order led to LTD; aka Hebbian STDP. Since then, multiple polarity and forms of STDP have been described (Feldman, 2012). Classically, STDP is induced with 100–150 presynaptic and postsynaptic pairings at low frequency (1–2 Hz). However, various forms of STDP aiming at mimicking more *in vivo*-like activity (Debanne and Inglebert, 2023) were also evoked using smaller number of pairings (5–30) (Froemke et al., 2006; Cui et al., 2015, 2016; Cepeda-Prado et al., 2022) as expected in single-trial or one-shot learning (Piette et al., 2020), more complex spiking sequences, such as spike triplets or quadruplets (Froemke and Dan, 2002; Mendes et al., 2020), or *in vivo* spiking patterns replayed between two neighboring neurons *in vitro* (Isaac et al., 2009). STDP was also translated *in vivo* by associating natural sensory stimulation that activates afferents combined with evoked or spontaneous spiking of a single cortical neuron (Yao and Dan, 2001; Meliza and Dan, 2006; Jacob et al., 2007).

STDP rules usually rely on the repetition of precisely timed presynaptic and postsynaptic spikes *in vitro*. Yet the exact contribution of spike timing relative to firing rate in eliciting synaptic plasticity *in vivo* is still debated (Graupner et al., 2016). Related to this, it was shown that plasticity rules vary across cerebellar regions, with a precise time interval of 120 ms between parallel fiber and climbing fiber inputs allowing for plasticity expression in the flocculus (known to receive error signals at this delay during oculomotor learning), while a broader range of intervals are permissive for plasticity expression in the vermis, implicated in a wider variety of learning paradigms (Suvrathan et al., 2016). In addition, cortico-striatal STDPs show different sensitivity to spike timing jitter *in vitro*: endocannabinoid-dependent plasticities (endocannabinoid-LTD and endocannabinoid-LTP) are more robust to spike timing variability compared to NMDA-LTP (Cui et al., 2018). Such differential sensitivities between endocannabinoid-LTP and NMDA-LTP (induced by few pairings, 5–15, versus 100 pairings, respectively) could underlie different functions, at different stages of learning as sequential activity patterns become more and more stereotyped (Thorn et al., 2010; Figure 1).

Furthermore, STDP faces two major interrogations questioning its physiological relevance: (i) Can plasticity only be induced by a global feedback signal, such as a bAP, resulting from the activation of a critical number of synapses? This would contradict the fact that a limited number of synapses could be subjected to plasticity. Also, this implies that only digital (bAP) but not analog signals induce plasticity; (ii) How can the compressed timescale (typically, pairings intervals are <50 milliseconds and repeated at 1 Hz) in which STDP occurs be compatible with behavioral timescales (subseconds to minutes)? Indeed, if STDP is sensitive to correlations of tens or hundreds of milliseconds (Feldman, 2012), temporal associations between different stimuli during learning are typically in the subsecond/minute range (Drew and Abbott, 2006).

The first point has been addressed in different ways. Paired subthreshold events can induce long-term plasticity, such that bAP would not be necessary for plasticity expression (Fino et al., 2009; Brandalise and Gerber, 2014) and strong post-synaptic depolarization was shown to induce sufficient intracellular Ca^{2+} rise, due to dendritic non-linearities, to evoke long-term plasticity (Holthoff et al., 2004; Hardie and Spruston, 2009). Therefore, digital (bAPs) as well as analog (EPSPs) signals can induce *in vitro* plasticity. Because bAPs are attenuated differently among neuronal subtypes, and along the dendritic arbor, in part depending on the level of excitatory and inhibitory synaptic inputs, their contribution is likely to vary *in vivo* (Waters and Helmchen, 2004). Hence, delimiting the exact role and spatial extension of digital and analog signals for triggering synaptic plasticity *in vivo* requires further investigation. This consideration also led to the study of more naturalistic forms of STDP, dependent upon the temporal correlation between two distinct presynaptic afferences, the input-timing-dependent plasticity (ITDP), using timing rules that mapped synaptic delays caused by neural network architecture (Dudman et al., 2007; Cho et al., 2012; Basu et al., 2013; Mehaffey and Doupe, 2015; Leroy et al., 2017; Figure 1). ITDP can be viewed as a physiological upgrade of STDP since it does not rely on an artificial post-synaptic injection of current necessary to create the bAP (see the critical view of STDP in Lisman and Spruston, 2010), but on paired activation of presynaptic inputs triggering sub- or suprathreshold activity in the postsynaptic element.

Regarding the second point, even though the compressed (milliseconds) timescale of STDP is compatible with replay episodes in sleep for learning specific temporal sequences (Debanne and Inglebert, 2023; George et al., 2023), the search for factors contributing to enlarge its temporal window put a strong emphasis on nonlinear slow-timescale mechanisms (e.g. CaMKII and calcineurin) (O'Donnell, 2023) and on the three-factor learning rule (Frémaux and Gerstner, 2016; Edelmann et al., 2017; Foncelle et al., 2018; Brzosko et al., 2019). Indeed, STDP has been originally described as a two-factor rule relying on paired activity in the presynaptic and postsynaptic elements (two-factor) to fulfill Hebb's postulate, and was later augmented to a third-factor rule to include neuromodulators (e.g. dopamine, noradrenaline or acetylcholine), neurotransmitters (GABA or endocannabinoids), neuropeptides (BDNF) or glia (astrocytes), which efficiently modulate plasticity and can enlarge the temporal window of STDP expression. Indeed, repeated co-activation

Abbreviations: bAP, backpropagating action potential; BTSP, behavioral timescale plasticity; ITDP, input-timing-dependent plasticity; HFS, high-frequency stimulation; LTP, long-term potentiation; STDP, spike-timing dependent plasticity.

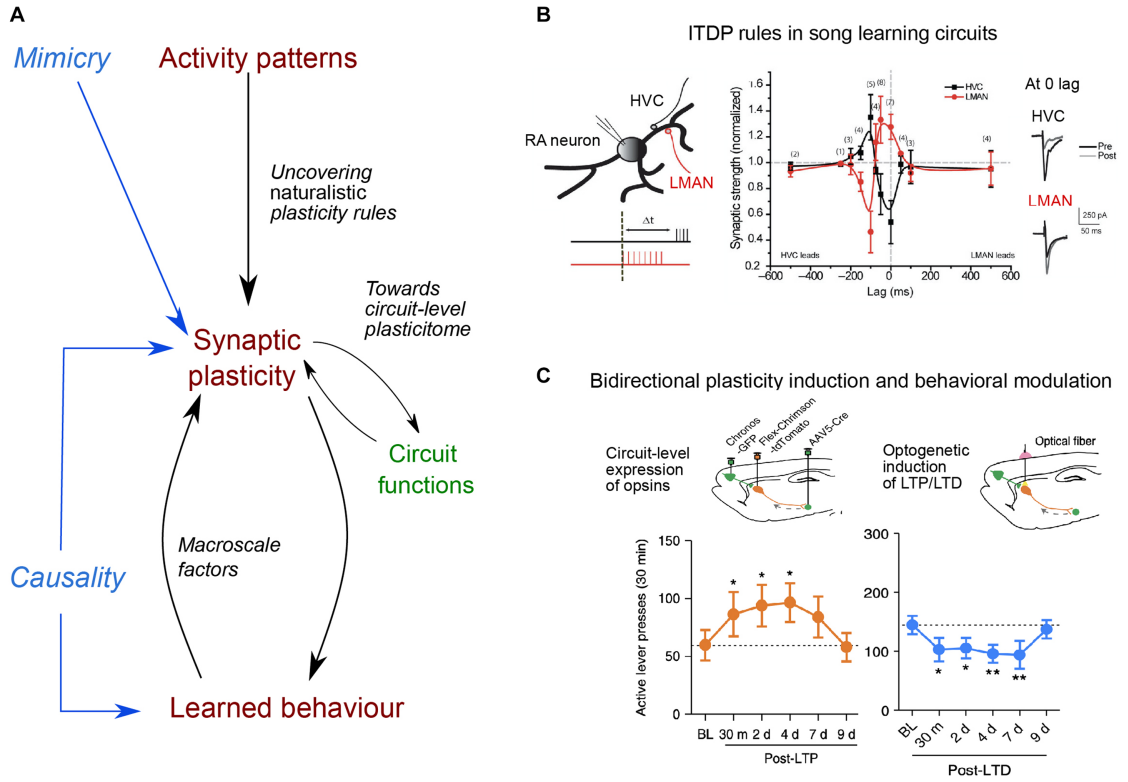

FIGURE 1
Main directions of investigation for uncovering naturalistic plasticity rules, their circuit functions and causal link to learned behavior. **(A)** Uncovering naturalistic synaptic plasticity rules needs to rely on *in vivo* activity patterns, by considering the rate and timing of naturally incoming inputs, which can then be replayed *in vitro*. Mimicry experiments aim to mimic naturalistic stimulation, compatible with synaptic plasticity expression. Next, understanding the function of synaptic plasticity expression in a given circuit remains a major challenge. Different forms of plasticity, occurring at different synapses, expressed at different timescales and relying on different molecular cascades (constituting the plasticitome) may be evoked within a single event and hence requires a circuit-level investigation, that further considers the presence of third factors (e.g., neuromodulators, neuropeptides or glial cells), and also of macroscale factors (such as body–brain internal states or neuroenergetic load). Finally, determining causal links between synaptic plasticity and learned behavior has remained limited to stereotypical behavior. **(B)** Example of naturalistic stimulation, based on singing-related activity, leading to opposing heterosynaptic plasticity in the songbird cortex (robust nucleus of the arcopallium, RA), in which two inputs critical for song learning converge: afferences from premotor HVC (dark) and one from LMANN (red): when one input is potentiated, the other is depressed, and direction of plasticity (*y*-axis) shows a strong dependence on the relative timing of stimulation (lag, *x*-axis). Example traces of excitatory post-synaptic potentials (EPSC) pre and post-stimulation are displayed for 0ms time lag. Adapted from Mehaffey and Doupe (2015). **(C)** Example of an evoked-bidirectional plasticity and induced-behavioral changes. LTP or LTD were induced at cortico-striatal synapses *in vivo*, using optogenetic tools and virally-mediated expression of excitatory opsins in medial prefrontal cortex and dorsomedial striatum (top schemas). Induction of LTP and LTD led rats trained to self-administer ethanol to actively press more the lever over several days post-plasticity induction protocol, leading to increased ethanol intake (orange trace), or long-lasting reduction of their number of lever presses (blue trace) their number of lever presses (blue trace), respectively. Adapted from Ma et al. (2018).

of synaptic activities, together with dopamine release, leave eligibility traces for about 1 s at cortico-striatal synapses (Yagishita et al., 2014), 5 s in the neocortex (He et al., 2015) or even up to 10 min in the hippocampus (Brzosko et al., 2015; Fuchsberger et al., 2022).

Lastly, a naturalistic plasticity rule was recently uncovered at CA3-CA1 synapses, both *in vitro* and *in vivo*, which no longer requires repetitions and co-activation of presynaptic and postsynaptic elements (Bittner et al., 2017; Priestley et al., 2022; Fan et al., 2023). Synaptic inputs from CA3 place cells are potentiated by the occurrence of a single Ca^{2+} dendritic plateau, produced at distal dendrites. Importantly, the temporal overlap between the two signals can span the second timescale and their temporal order does not impact plasticity expression. The dendritic plateau potential appears as an instructive signal, evoked by specific circumstances (reduced dendritic inhibition, permissive neuromodulatory signaling, strong inputs), occurring for instance during exploration of a novel environment (Priestley et al., 2022) or of a context in which specific task-related information is carried by a given position (Zhao et al., 2022). Due to behavioral timescale plasticity (BTSP) asymmetric time course (Bittner et al., 2017; Magee and Grienberger, 2020), predictive information might be encoded.

This overview presented several refinements aiming at approaching naturalistic synaptic plasticity rules. This effort should be continued, especially since our understanding of synaptic plasticity rules remains mostly defined at the scale of an entire synaptic pathway and focuses on a given population of excitatory or projecting neurons. In this direction, considering interactions between neighboring neurons has unveiled a variety of heterosynaptic plasticity mechanisms (Chistiakova et al., 2015; Mendes et al., 2020). These can influence the net plasticity outcome of a given circuit when interactions between inhibitory and excitatory neurons are examined (D'Amour and Froemke, 2015; Hiratani and Fukai, 2017). Heterogeneities in plasticity expression at the neuronal level can arise from a neuron's prior and ongoing activity (Han et al., 2007) or its dendritic architecture, in

particular the distribution of active inhibitory and excitatory synapses (Harvey and Svoboda, 2007; El-Boustani et al., 2018) or compartmentalized changes in dendritic excitability (Losonczy et al., 2008). These additional considerations reinforce the need to detect input-specific signals from both somatic and dendritic compartments, that could serve as proxies for local synaptic plasticity expression.

This overview also pointed out the importance of reinforcing the translation between *in vivo* and *in vitro* recordings, keeping in mind discrepancies relative to ionic composition (Inglebert et al., 2020), metabolic substrates (Dembitskaya et al., 2022), neuromodulator concentrations or spontaneous activity levels, as well as body-brain internal states, which constitute key factors affecting plasticity induction thresholds, as will be discussed below.

Toward the uncovering and manipulation of a learning-induced plasticitome

In parallel to extracting synaptic plasticity rules evoked by natural *in vivo*-like activity patterns, a vast number of studies has uncovered learning-induced synaptic changes, hence directly examining synaptic plasticity in naturalistic settings. Detection of synaptic changes historically relied on *in vivo* electrophysiological recordings of synaptic efficacy using electrical stimulation yet lacking cell-type specificity and often restricted to a single circuit, or from *ex vivo* saturation/occlusion experiments or measures of AMPA/NMDAR ratio, which cannot provide a full account of synaptic temporal dynamics. The development of optical stimulation combined with spatial- and cell-specific expression of opsins partially lifted the first limitation: as an example, cortico-striatal plasticity monitored *in vivo* during an auditory discrimination task, based on the selective optogenetic stimulation of cortical neurons along the tonotopic axis, revealed spatially selective plasticity induction depending on reward contingencies (Xiong et al., 2015). Combined with c-Fos labeling of both presynaptic and postsynaptic cells active during fear conditioning, *ex vivo* recordings showed an occlusion of LTP between engram cells, along with changes in presynaptic release probability (Choi et al., 2018). Notably, the all-optical approach combined with imaging of subthreshold membrane potential dynamics and opto-stimulation of afferences allows plasticity detection at the circuit-level (Fan et al., 2023). It could further be extended, by probing multiple regions simultaneously using novel imaging tools, such as light beads microscopy, enabling large volumetric recording of neuronal activity (Demas et al., 2021). In addition, a key advantage of optical approaches is their combinatorial power, by juxtaposing the dynamics of optical sensors and labeling of active cells during behavioral tasks. Typically, to better capture the full temporal dynamics of synaptic plasticity expression, calcium and voltage sensors, which can track initial signatures of synaptic changes, could be combined with sensors related to downstream cascades such as CamKII (Lee et al., 2009) or PKA (Gervasi et al., 2010), which inform on long-term plasticity expression and maintenance *in vivo*. Furthermore, the development of presynaptic vesicular release sensors, which are currently effective *in vitro* (Ferro et al., 2017) should also help investigating the often-neglected presynaptic plasticity loci. Although these tools offer unprecedented access to detailed naturalistic plasticitomes, they also have their own limitations and caveats. Indeed, the expression of opsins combined with viral vectors is not without cell specificity confounds and toxicity-related issues (Miyashita et al., 2013). In addition, opsins or fluorescent sensors can alter natural synaptic dynamics, depending for instance on their expression levels (Jackman et al., 2014).

Chronic tracking of structural dynamics in spine numbers and shapes using *in vivo* 2-photon imaging (Pfeiffer et al., 2018), i.e. structural plasticity, can be used as proxy for synaptic strength (Holtmaat and Svoboda, 2009). Dual-eGRASP, a split fluorescent protein that emits fluorescence only when presynaptic and postsynaptic eGRASP components are physically attached in the synaptic cleft (Choi et al., 2018, 2021), combined with the *Fos* promoter-driven tetracycline transactivator system (Mayford and Reijmers, 2015), allows to track longitudinally *in vivo* synapses between pre and post-synaptic neurons active or not during learning (Lee et al., 2023). Other avenues, down to *in vivo* tracking of receptor dynamics, have also been opened (Matsuo et al., 2008; Zhang et al., 2015) and can be envisaged simultaneously across thousands of synapses (Graves et al., 2021).

Beyond the detailed characterization of plasticity expression *in vivo* during learning, the demonstration of a causality between plasticity expression and learned behavior now represents a current grail in neurophysiology, such that bidirectional behavioral modifications can be caused by bidirectional manipulation of synaptic efficacy. Currently, only a couple of studies has achieved such bidirectional control: a conditioned fear response was, respectively, erased and restored upon depotentiation and re-potentiation of the auditory inputs to the lateral amygdala (Nabavi et al., 2014). Likewise, cortico-striatal opto-induced-LTP and -LTD promoted and decreased, respectively, alcohol-seeking behavior (Ma et al., 2018; Figure 1). Optogenetically-induced depotentiation of LTP, initially induced by auditory fear conditioning, suppressed fear responses to the conditioned stimulus (Kim et al., 2007). Furthermore, with two auditory stimuli underlying two different memories, opto-potentiation and -depotentiation of synapses shared within each specific cell assembly selectively restored or impaired the retrieval of one memory while sparing the other (Abdou et al., 2018). These causal manipulations should now aim at triggering reversible synaptic changes using naturalistic plasticity induction protocols, instead of classical low or high-frequency stimulation. In addition, to further nail down causality at the synapse-level, a specific ChR2 expression on recently activated synapses could allow more physiological excitation, by mimicking *in vivo* occurring calcium transients, compared to full somatic activation (Gobbo et al., 2017). In the future, one could even imagine modulating bidirectionally and reversibly the excitability of individual spines or dendritic branches during learning, for instance through targeted expression of both hyperpolarizing and excitatory opsins. Yet, an ongoing issue of manipulating synaptic efficacy relates to its specificity, and the absence of interference with other synaptic mechanisms or basal neurotransmission, as well as the possibility to cause other pathological changes or evoke compensatory mechanisms. Therefore, the development of spatio-temporally precise manipulations, with sensor expression impacting the least physiological dynamics, remains of critical importance.

Finally, instead of directly manipulating synaptic weights to cause behavioral changes, mimicry experiments currently (and somehow paradoxically) offer more naturalistic settings for testing

the memory and synaptic plasticity hypothesis. Indeed, mimicry consists of artificially stimulating neuronal circuits *in vivo* (without undergoing any kind of experience) and triggering behavioral changes. The stimulation mimics putative activity patterns during a real learning experience and can therefore bridge naturalistic synaptic plasticity rules described above and their behavioral relevance. At this day, only associations between conditioned and unconditioned stimuli were mimicked. Building up on previous works in which a partial sensory experience combined with opto-stimulation created artificial memories (Josselyn and Tonegawa, 2020), an artificial memory was generated by combining patterned stimulation of olfactory glomeruli with the stimulation of distinct inputs to the ventral tegmental area that mediated either aversion or reward (Vetere et al., 2019). A next challenge will be to move from neuronal assemblies down to the synaptic level in these same simple behavioral paradigms (using tools described above; Gobbo et al., 2017), and to generalize to more complex learning, using naturalistic sequences of neuronal activation.

The (almost) overlooked of synaptic plasticity research: the body–brain communication loops and neuroenergetics

In synaptic plasticity, besides the two "Hebbian" factors (presynaptic and postsynaptic activities), a third "neoHebbian" factor allows the stabilization and shaping of plasticity maps. This third factor gathered well-defined elements such as neurotransmitters/neuromodulators, neuropeptides, fatty acids or glial cells (reviewed in: Frémaux and Gerstner, 2016; Foncelle et al., 2018; Brzosko et al., 2019). Here, we chose to focus on macroscale factors, defined by integrated body–brain communication loops, also in relation to external states (Kanwal et al., 2021; Flavell et al., 2022). Indeed, the brain receives massive sensorimotor feedback from the body, such as heartbeat (Hsueh et al., 2023), blood pressure, respiratory rate (Folschweiller and Sauer, 2023), gastric fullness, internal temperature or visceral pain. During active behavioral states, the integration of these feedbacks engages widespread circuits. Macroscale factors also include sleep–wake, circadian or seasonal-related rhythms, as well as metabolic (thirst and feeding) states. These factors are mediated by brain–body endocrine communication, metabolic substrates and associated signaling molecules, and recruit neuromodulators, glial or immune cells. As an illustration, the general body state changes during exercise can favor plasticity expression. Weak theta-pattern stimulation of the hippocampus, which does not produce LTP in control rats, induces LTP in rats housed with a running wheel (Farmer et al., 2004). Voluntary exercise, by increasing theta oscillation and lowering LTP induction threshold, may prime the network to promote synaptic plasticity *in vitro* and *in vivo* (van Praag et al., 1999).

Secretory molecules and vesicles released by organs such as skeletal muscle, adipose tissue, liver and gut are part of the body–brain feedback (Pedersen and Febbraio, 2012). These molecules, such as FNDC5/irisin, adiponectin, or IL-6, cross the blood–brain barrier, (i) induce changes in neurotrophins such as BDNF or EGF-1, associated with improvements in hippocampus plasticity, spatial memory, and object recognition (Vaynman et al., 2004; Gomes da Silva et al., 2010), (ii) modulate the cerebrovasculature, allowing improvements in energy metabolism, delivery of oxygen, nutrients, neurotrophins and other factors promoting learning and memory, and (iii) act on plasticity through the increased number, cell body size and arborization length of astrocytes, (Saur et al., 2014), impairment of microglia (Vukovic et al., 2012) and increased neurogenesis (van Praag et al., 1999).

Among the macroscale factors that could control plasticity expression, neuroenergetics has received particular attention. Synaptic activity is the most energy-consuming process in the brain (Attwell and Laughlin, 2001). Synaptic energy supply is provided on-demand (Kasischke et al., 2004; Chuquet et al., 2010; Ruminot et al., 2017) by neuronal glycolysis and/or glial-derived lactate (via the astrocyte-neuron lactate shuttle) (Magistretti and Allaman, 2018; Bonvento and Bolanos, 2021). Synaptic plasticity and learned behavior depend on the metabolic reservoir. This is well illustrated under food restriction, in flies, with a trade-off between long-term memory establishment and survival (Mery and Kawecki, 2005; Plaçais and Preat, 2013). Long-term neuronal reconfigurations, leading to behavioral changes, mediated by feeding state have also been identified in *C. elegans* (Takeishi et al., 2020) and in the Etruscan shrew (Ray et al., 2020). In addition, top-down adaptations have also been identified between synaptic plasticity induction and energy uptake mechanisms following learning, with vascular adaptations (Lacoste et al., 2014), glial recruitment (Genoud et al., 2006), altered expression of insulin-sensitive glucose or lactate transporters (Tadi et al., 2015; Ashrafi et al., 2017) and mitochondrial activity (Todorova and Blokland, 2017). Interestingly, flies increase their energy intake following multiple trials training, leading to a dopamine-mediated upregulation of cellular metabolism driving LTP in the brain region involved in long-term memory (Plaçais et al., 2017). Dissecting precisely how the energy available and the nature of metabolic substrates – especially lactate and/or glucose-can control synaptic plasticity expression has been the subject of several works (Newman et al., 2011; Suzuki et al., 2011; Murphy-Royal et al., 2020); of note, lactate is also a signaling metabolite and as such acts on neuronal excitability and plasticity via NMDA receptors and or hydroxycarboxylic acid receptor type-1 (HCAR1) (Magistretti and Allaman, 2018). In particular, during learning, the neuronal computational load at play may be more or less intense, raising the possibility that plasticity induction could be more or less metabolically demanding and therefore requires different metabolic pathways. Indeed, lactate supply was required for high stimulation load activity patterns (theta-burst-induced LTP) in CA3-CA1 circuit, whereas glucose was sufficient for less demanding neural computation (low-frequency STDP paradigm) (Dembitskaya et al., 2022). Interestingly, this switch in metabolic substrates was also visible *in vivo* when novel object exploration required a higher attentional and cognitive load and for the corresponding *in vivo* LTP expression (Dembitskaya et al., 2022; Figure 2). It remains to examine how glucose and lactate intervene as exclusive or combined fueling in various engrams depending on the body internal states (diet, emotions, effort) and how global energy is regionally redistributed to meet cellular metabolism (Bruckmaier et al., 2020). More generally, investigating how synaptic plasticity induction and maintenance can be controlled by specific diets (ketone-based or high-fat diet) and is altered in various metabolic diseases (obesity, diabetes, but also neurodegenerative diseases) might provide further mechanistic understanding of body–brain interactions. Yet, as these

10.3389/fnsyn.2023.1250753

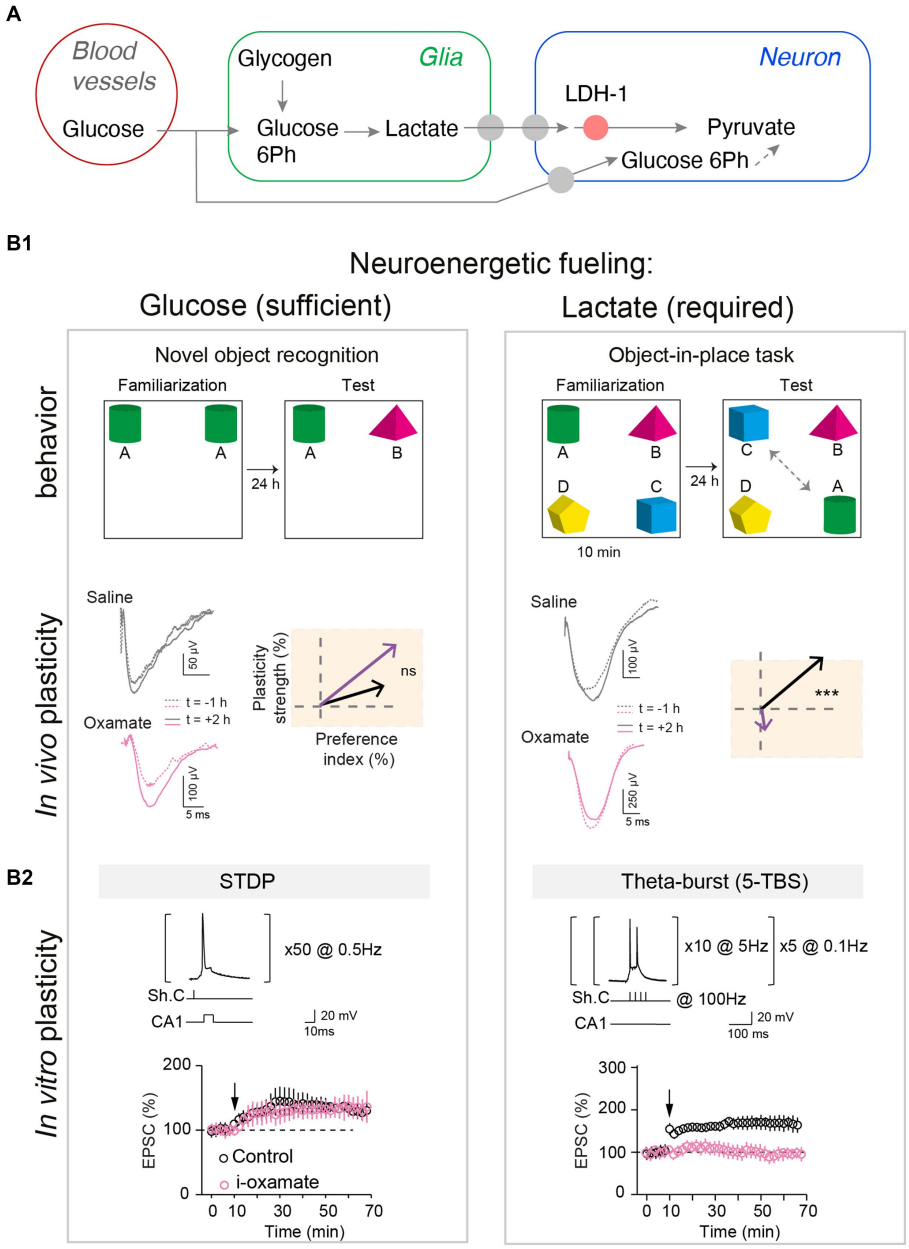

FIGURE 2
Glucose and lactate metabolisms are differently engaged in neuronal fueling for plasticity expression and memory. **(A)** Main steps of the glucose and the glia-derived lactate transports: astrocytic glycogen catalysis into glucose-6-phosphate and then lactate, lactate entry in neurons via monocarboxylate transporters, and lactate conversion into pyruvate by the neuronal lactate dehydrogenase (LDH-1). **(B1)** Lactate metabolism is necessary for learning cognitive tasks requiring high attentional load as exemplified in the object-in-place task (with four objects) and for expressing the corresponding *in vivo* hippocampal LTP, but glucose is sufficient for a less demanding task such as a simple novel object recognition (with two objects). Rats were injected bilaterally, via cannulas implanted above hippocampal CA1 layer, with either saline or oxamate (50 mM), an inhibitor of the neuronal LDH preventing the conversion of lactate into pyruvate, before familiarization step. Rats with saline performed equally well in both tasks whereas rats receiving oxamate did not detect novelty in the object-in-place task (illustrated by a low preference index value) and did not express LTP (averaged vectors: *y*-axis indicates LTP versus LTD expression and *x*-axis the learning performance evaluated with the preference index). *In vivo* synaptic plasticity during behavioral task with evoked-field-EPSP recorded before familiarization (baseline) and 2 hours after familiarization to determine synaptic changes, in relation with behavior. **(B2)** Lactate metabolism is mandatory to fuel the demanding neural computations implicated in NMDA receptor-mediated LTP forms in hippocampus triggered by theta-burst stimulations, while glucose metabolism is sufficient for lighter forms of LTP, based on less and lower-frequency stimulations. The structure of the plasticity induction protocols and the averaged time-course of the synaptic weight after theta-burst stimulation and STDP protocols are illustrated. Oxamate was applied intracellularly (via the patch-clamp pipette) in the sole recorded neuron, and LDH inhibition shows distinct effects on theta-burst stimulation and STDP expression since it prevented theta-burst stimulation-induced LTP but not STDP-induced LTP. In conclusion, scaling of the computational and cognitive loads requires the metabolism of glia-derived lactate to match the neuroenergetic needs of sustained neuronal activity patterns and high cognitive load, and for less demanding plasticity and learning paradigms, glucose suffices as an energy substrate. Adapted from Dembitskaya et al. (2022).

body–brain communication loops and macroscale factors usually fluctuate on slower timescales relative to synaptic activation, evidence for their causal interplay might be particularly challenging to achieve.

Conclusion

This mini-review presented key avenues, initiated in the synaptic plasticity and memory research field, that put forward a naturalistic viewpoint. This naturalistic lens was first directed at presenting naturalistic synaptic plasticity rules, based on *in vivo* neuronal activity patterns recorded during learning experience, which can then be dissected *in vitro* and/or *in vivo*. Next, it focused on current advances for uncovering naturalistic plasticitomes, i.e. induced by the animal's own experience, which can provide detailed spatio-temporal characterizations of synaptic plasticity. Finally, besides well-defined third factors (neuromodulators, neuropeptides or glia), this-mini review emphasized that macroscale factors (internal states and the neuronal energy fueling with glucose and lactate metabolisms) can interplay with synaptic plasticity, and hence participate in defining a complex naturalistic context that shapes synaptic plasticity expression during behavior. The next challenges will be to further nail down the relevant synaptic plasticity rules and associated signaling cascades engaged *in vivo*, by investigating causal interactions between neuronal activity patterns, plasticity maps and behavioral consequences. To further enlarge our naturalistic lens on synaptic plasticity, feasibility of mimicry and causality demonstrations should be tested on complex and natural behaviors, such as episodic-like memory or procedural learning. More attention should also be drawn to the existence and contribution of macroscale factors with the major difficulty of their inextricable bounds to natural behaviors and causal manipulations.

Author contributions

CP wrote the first draft of the "From neuronal activity patterns to plasticity rules" and "Toward the uncovering of a learning-induced plasticitome" sections, and design the Figure 1. LV and NG wrote the "The (almost) overlooked of synaptic plasticity research: the body–brain communication loops and neuroenergetics" section. LV redraft the whole manuscript, and design the Figure 2. All authors wrote "background" and "conclusions" sections, and have edited and corrected the manuscript.

Funding

This work was supported by grants from the Agence Nationale pour la Recherche (grants ANR EngFlea), the LabEx Paris-Sciences et Lettres (PSL) and Collège de France.

Conflict of interest

The authors declare that the research was conducted in the absence of any commercial or financial relationships that could be construed as a potential conflict of interest.

Publisher's note

All claims expressed in this article are solely those of the authors and do not necessarily represent those of their affiliated organizations, or those of the publisher, the editors and the reviewers. Any product that may be evaluated in this article, or claim that may be made by its manufacturer, is not guaranteed or endorsed by the publisher.

References

Abdou, K., Shehata, M., Choko, K., Nishizono, H., Matsuo, M., Muramatsu, S. I., et al. (2018). Synapse-specific representation of the identity of overlapping memory engrams. *Science* 360, 1227–1231. doi: 10.1126/science.aat3810

Ashrafi, G., Wu, Z., Farrell, R. J., and Ryan, T. A. (2017). GLUT4 mobilization supports energetic demands of active synapses. *Neuron* 93, 606–615.e3. doi: 10.1016/j.neuron.2016.12.020

Attwell, D., and Laughlin, S. B. (2001). An energy budget for signaling in the grey matter of the brain. *J. Cerebral Blood Flow Metabolism* 21, 1133–1145. doi: 10.1097/00004647-200110000-00001

Basu, J., Srinivas, K. V., Cheung, S. K., Taniguchi, H., Huang, Z. J., and Siegelbaum, S. A. (2013). A cortico-hippocampal learning rule shapes inhibitory microcircuit activity to enhance hippocampal information flow. *Neuron* 79, 1208–1221. doi: 10.1016/j.neuron.2013.07.001

Bittner, K. C., Milstein, A. D., Grienberger, C., Romani, S., and Magee, J. C. (2017). Behavioral time scale synaptic plasticity underlies CA1 place fields. *Science* 357, 1033–1036. doi: 10.1126/science.aan3846

Bonvento, G., and Bolanos, J. P. (2021). Astrocyte-neuron metabolic cooperation shapes brain activity. *Cell Metab.* 33, 1546–1564. doi: 10.1016/j.cmet.2021.07.006

Brandalise, F., and Gerber, U. (2014). Mossy fiber-evoked subthreshold responses induce timing-dependent plasticity at hippocampal CA3 recurrent synapses. *Proc. Natl. Acad. Sci.* 111, 4303–4308. doi: 10.1073/pnas.1317667111

Bruckmaier, M., Tachtsidis, I., Phan, P., and Lavie, N. (2020). Attention and capacity limits in perception: a cellular metabolism account. *J. Neurosci.* 40, 6801–6811. doi: 10.1523/jneurosci.2368-19.2020

Brzosko, Z., Mierau, S. B., and Paulsen, O. (2019). Neuromodulation of spike-timing-dependent plasticity: past, present, and future. *Neuron* 103, 563–581. doi: 10.1016/j.neuron.2019.05.041

Brzosko, Z., Schultz, W., and Paulsen, O. (2015). Retroactive modulation of spike timing-dependent plasticity by dopamine. *Elife* 4:e09685. doi: 10.7554/elife.09685

Cepeda-Prado, E. A., Khodaie, B., Quiceno, G. D., Beythien, S., Edelmann, E., and Lessmann, V. (2022). Calcium-permeable AMPA receptors mediate timing-dependent LTP elicited by low repeat coincident pre- and postsynaptic activity at schaffer collateral-CA1 synapses. *Cereb. Cortex* 32, 1682–1703. doi: 10.1093/cercor/bhab306

Chistiakova, M., Bannon, N. M., Chen, J.-Y., Bazhenov, M., and Volgushev, M. (2015). Homeostatic role of heterosynaptic plasticity: models and experiments. *Front. Comput. Neurosci.* 9:89. doi: 10.3389/fncom.2015.00089

Cho, J.-H., Bayazitov, I. T., Meloni, E. G., Myers, K. M., Carlezon, W. A., Zakharenko, S. S., et al. (2012). Coactivation of thalamic and cortical pathways induces input timing–dependent plasticity in amygdala. *Nat. Neurosci.* 15, 113–122. doi: 10.1038/nn.2993

Choi, D. I., Kim, J., Lee, H., Kim, J., Sung, Y., Choi, J. E., et al. (2021). Synaptic correlates of associative fear memory in the lateral amygdala. *Neuron* 109, 2717–2726.e3. doi: 10.1016/j.neuron.2021.07.003

Choi, J.-H., Sim, S.-E., Kim, J., Choi, D. I., Oh, J., Ye, S., et al. (2018). Interregional synaptic maps among engram cells underlie memory formation. *Science* 360, 430–435. doi: 10.1126/science.aas9204

Chuquet, J., Quilichini, P., Nimchinsky, E. A., and Buzsaki, G. (2010). Predominant enhancement of glucose uptake in astrocytes versus neurons during activation of the somatosensory cortex. *J. Neurosci.* 30, 15298–15303. doi: 10.1523/JNEUROSCI.0762-10.2010

Cui, Y., Paillé, V., Xu, H., Genet, S., Delord, B., Fino, E., et al. (2015). Endocannabinoids mediate bidirectional striatal spike-timing-dependent plasticity. *J. Physiol.* 593, 2833–2849. doi: 10.1113/jp270324

Cui, Y., Prokin, I., Mendes, A., Berry, H., and Venance, L. (2018). Robustness of STDP to spike timing jitter. *Sci. Rep.* 8:8139. doi: 10.1038/s41598-018-26436-y

Cui, Y., Prokin, I., Xu, H., Delord, B., Genet, S., Venance, L., et al. (2016). Endocannabinoid dynamics gate spike-timing dependent depression and potentiation. *Elife* 5:e13185. doi: 10.7554/elife.13185

D'amour, J. A., and Froemke, R. C. (2015). Inhibitory and excitatory spike-timing-dependent plasticity in the auditory cortex. *Neuron* 86, 514–528. doi: 10.1016/j.neuron.2015.03.014

Debanne, D., and Inglebert, Y. (2023). Spike timing-dependent plasticity and memory. *Curr. Opin. Neurobiol.* 80:102707. doi: 10.1016/j.conb.2023.102707

Demas, J., Manley, J., Tejera, F., Barber, K., Kim, H., Traub, F. M., et al. (2021). High-speed, cortex-wide volumetric recording of neuroactivity at cellular resolution using light beads microscopy. *Nat. Methods* 18, 1103–1111. doi: 10.1038/s41592-021-01239-8

Dembitskaya, Y., Piette, C., Perez, S., Berry, H., Magistretti, P. J., and Venance, L. (2022). Lactate supply overtakes glucose when neural computational and cognitive loads scale up. *Proc. Natl. Acad. Sci.* 119:e2212004119. doi: 10.1073/pnas.2212004119

Drew, P. J., and Abbott, L. F. (2006). Extending the effects of spike-timing-dependent plasticity to behavioral timescales. *Proc. Natl. Acad. Sci. U. S. A.* 103, 8876–8881. doi: 10.1073/pnas.0600676103

Dudman, J. T., Tsay, D., and Siegelbaum, S. A. (2007). A role for synaptic inputs at distal dendrites: instructive signals for hippocampal long-term plasticity. *Neuron* 56, 866–879. doi: 10.1016/j.neuron.2007.10.020

Edelmann, E., Cepeda-Prado, E., and Leßmann, V. (2017). Coexistence of multiple types of synaptic plasticity in individual hippocampal CA1 pyramidal neurons. *Front. Synaptic Neurosci.* 9:7. doi: 10.3389/fnsyn.2017.00007

El-Boustani, S., Ip, J. P., Breton-Provencher, V., Knott, G. W., Okuno, H., Bito, H., et al. (2018). Locally coordinated synaptic plasticity of visual cortex neurons in vivo. *Science* 360, 1349–1354. doi: 10.1126/science.aao0862

Fan, L. Z., Kim, D. K., Jennings, J. H., Tian, H., Wang, P. Y., Ramakrishnan, C., et al. (2023). All-optical physiology resolves a synaptic basis for behavioral timescale plasticity. *Cells* 186, 543–559.e19. doi: 10.1016/j.cell.2022.12.035

Farmer, J., Zhao, X., van Praag, H., Wodtke, K., Gage, F. H., and Christie, B. R. (2004). Effects of voluntary exercise on synaptic plasticity and gene expression in the dentate gyrus of adult male Sprague–Dawley rats in vivo. *Neuroscience* 124, 71–79. doi: 10.1016/j.neuroscience.2003.09.029

Feldman, D. E. (2012). The spike-timing dependence of plasticity. *Neuron* 75, 556–571. doi: 10.1016/j.neuron.2012.08.001

Ferro, M., Lamanna, J., Ripamonti, M., Racchetti, G., Arena, A., Spadini, S., et al. (2017). Functional mapping of brain synapses by the enriching activity-marker SynaptoZip. *Nat. Commun.* 8:1229. doi: 10.1038/s41467-017-01335-4

Fino, E., Deniau, J.-M., and Venance, L. (2009). Brief subthreshold events can act as Hebbian signals for long-term plasticity. *PLoS One* 4:e6557. doi: 10.1371/journal.pone.0006557

Flavell, S. W., Gogolla, N., Lovett-Barron, M., and Zelikowsky, M. (2022). The emergence and influence of internal states. *Neuron* 110, 2545–2570. doi: 10.1016/j.neuron.2022.04.030

Folschweiller, S., and Sauer, J.-F. (2023). Behavioral state-dependent modulation of prefrontal cortex activity by respiration. *J. Neurosci.* 43, 4795–4807. doi: 10.1523/jneurosci.2075-22.2023

Foncelle, A., Mendes, A., Jędrzejewska-Szmek, J., Valtcheva, S., Berry, H., Blackwell, K. T., et al. (2018). Modulation of spike-timing dependent plasticity: towards the inclusion of a third factor in computational models. *Front. Comput. Neurosci.* 12:49. doi: 10.3389/fncom.2018.00049

Frémaux, N., and Gerstner, W. (2016). Neuromodulated spike-timing-dependent plasticity, and theory of three-factor learning rules. *Front. Neural Circ.* 9:85. doi: 10.3389/fncir.2015.00085

Froemke, R. C., and Dan, Y. (2002). Spike-timing-dependent synaptic modification induced by natural spike trains. *Nature* 416, 433–438. doi: 10.1038/416433a

Froemke, R. C., Tsay, I. A., Raad, M., Long, J. D., and Dan, Y. (2006). Contribution of individual spikes in burst-induced long-term synaptic modification. *J. Neurophysiol.* 95, 1620–1629. doi: 10.1152/jn.00910.2005

Fuchsberger, T., Clopath, C., Jarzebowski, P., Brzosko, Z., Wang, H., and Paulsen, O. (2022). Postsynaptic burst reactivation of hippocampal neurons enables associative plasticity of temporally discontiguous inputs. *Elife* 11:e81071. doi: 10.7554/elife.81071

Genoud, C., Quairiaux, C., Steiner, P., Hirling, H., Welker, E., and Knott, G. W. (2006). Plasticity of astrocytic coverage and glutamate transporter expression in adult mouse cortex. *PLoS Biol.* 4:e343. doi: 10.1371/journal.pbio.0040343

George, T. M., de Cothi, W., Stachenfeld, K. L., and Barry, C. (2023). Rapid learning of predictive maps with STDP and theta phase precession. *Elife* 12:e80663. doi: 10.7554/elife.80663

Gervasi, N., Tchénio, P., and Preat, T. (2010). PKA dynamics in a drosophila learning center: coincidence detection by rutabaga adenylyl cyclase and spatial regulation by dunce phosphodiesterase. *Neuron* 65, 516–529. doi: 10.1016/j.neuron.2010.01.014

Gobbo, F., Marchetti, L., Jacob, A., Pinto, B., Binini, N., Pecoraro Bisogni, F., et al. (2017). Activity-dependent expression of channelrhodopsin at neuronal synapses. *Nat. Commun.* 8:1629. doi: 10.1038/s41467-017-01699-7

Gomes da Silva, S., Unsain, N., Mascó, D. H., Toscano-Silva, M., de Amorim, H. A., Silva Araújo, B. H., et al. (2010). Early exercise promotes positive hippocampal plasticity and improves spatial memory in the adult life of rats. *Hippocampus* 22, 347–358. doi: 10.1002/hipo.20903

Graupner, M., Wallisch, P., and Ostojic, S. (2016). Natural firing patterns imply low sensitivity of synaptic plasticity to spike timing compared with firing rate. *J. Neurosci.* 36, 11238–11258. doi: 10.1523/jneurosci.0104-16.2016

Graves, A. R., Roth, R. H., Tan, H. L., Zhu, Q., Bygrave, A. M., Lopez-Ortega, E., et al. (2021). Visualizing synaptic plasticity in vivo by large-scale imaging of endogenous AMPA receptors. *Elife* 10:e66809. doi: 10.7554/elife.66809

Han, J.-H., Kushner, S. A., Yiu, A. P., Cole, C. J., Matynia, A., Brown, R. A., et al. (2007). Neuronal competition and selection during memory formation. *Science* 316, 457–460. doi: 10.1126/science.1139438

Hardie, J., and Spruston, N. (2009). Synaptic depolarization is more effective than back-propagating action potentials during induction of associative long-term potentiation in hippocampal pyramidal neurons. *J. Neurosci.* 29, 3233–3241. doi: 10.1523/JNEUROSCI.6000-08.2009

Harvey, C. D., and Svoboda, K. (2007). Locally dynamic synaptic learning rules in pyramidal neuron dendrites. *Nature* 450, 1195–1200. doi: 10.1038/nature06416

He, K., Huertas, M., Hong, S. Z., Tie, X., Hell, J. W., Shouval, H., et al. (2015). Distinct eligibility traces for LTP and Ltd in cortical synapses. *Neuron* 88, 528–538. doi: 10.1016/j.neuron.2015.09.037

Hiratani, N., and Fukai, T. (2017). Detailed dendritic excitatory/inhibitory balance through heterosynaptic spike-timing-dependent plasticity. *J. Neurosci.* 37, 12106–12122. doi: 10.1523/jneurosci.0027-17.2017

Holthoff, K., Kovalchuk, Y., Yuste, R., and Konnerth, A. (2004). Single-shock ltd by local dendritic spikes in pyramidal neurons of mouse visual cortex. *J. Physiol.* 560, 27–36. doi: 10.1113/jphysiol.2004.072678

Holtmaat, A., and Svoboda, K. (2009). Experience-dependent structural synaptic plasticity in the mammalian brain. *Nat. Rev. Neurosci.* 10, 647–658. doi: 10.1038/nrn2699

Hsueh, B., Chen, R., Jo, Y., Tang, D., Raffiee, M., Kim, Y. S., et al. (2023). Cardiogenic control of affective behavioural state. *Nature* 615, 292–299. doi: 10.1038/s41586-023-05748-8

Inglebert, Y., Aljadeff, J., Brunel, N., and Debanne, D. (2020). Synaptic plasticity rules with physiological calcium levels. *Proc. Natl. Acad. Sci.* 117, 33639–33648. doi: 10.1073/pnas.2013663117

Isaac, J. T., Buchanan, K. A., Muller, R. U., and Mellor, J. R. (2009). Hippocampal place cell firing patterns can induce long-term synaptic plasticityin vitro. *J. Neurosci.* 29, 6840–6850. doi: 10.1523/jneurosci.0731-09.2009

Jackman, S. L., Beneduce, B. M., Drew, I. R., and Regehr, W. G. (2014). Achieving high-frequency optical control of synaptic transmission. *J. Neurosci.* 34, 7704–7714. doi: 10.1523/JNEUROSCI.4694-13.2014

Jacob, V., Brasier, D. J., Erchova, I., Feldman, D., and Shulz, D. E. (2007). Spike timing-dependent synaptic depression in thein vivobarrel cortex of the rat. *J. Neurosci.* 27, 1271–1284. doi: 10.1523/jneurosci.4264-06.2007

Josselyn, S. A., and Tonegawa, S. (2020). Memory engrams: recalling the past and imagining the future. *Science* 367:eaaw4325. doi: 10.1126/science.aaw4325

Kanwal, J. K., Coddington, E., Frazer, R., Limbania, D., Turner, G., Davila, K. J., et al. (2021). Internal state: dynamic, interconnected communication loops distributed across body, brain, and time. *Integr. Comp. Biol.* 61, 867–886. doi: 10.1093/icb/icab101

Kasischke, K. A., Vishwasrao, H. D., Fisher, P. J., Zipfel, W. R., and Webb, W. W. (2004). Neural activity triggers neuronal oxidative metabolism followed by astrocytic glycolysis. *Science* 305, 99–103. doi: 10.1126/science.1096485

Kim, J., Lee, S., Park, K., Hong, I., Song, B., Son, G., et al. (2007). Amygdala depotentiation and fear extinction. *Proc. Natl. Acad. Sci.* 104, 20955–20960. doi: 10.1073/pnas.0710548105

Lacoste, B., Comin, C. H., Ben-Zvi, A., Kaeser, P. S., Xu, X., Costa Lda, F., et al. (2014). Sensory-related neural activity regulates the structure of vascular networks in the cerebral cortex. *Neuron* 83, 1117–1130. doi: 10.1016/j.neuron.2014.07.034

Lee, S.-J. R., Escobedo-Lozoya, Y., Szatmari, E. M., and Yasuda, R. (2009). Activation of camkii in single dendritic spines during long-term potentiation. *Nature* 458, 299–304. doi: 10.1038/nature07842

Lee, C., Lee, B. H., Jung, H., Lee, C., Sung, Y., Kim, H., et al. (2023). Hippocampal engram networks for fear memory recruit new synapses and modify pre-existing synapses in vivo. *Curr. Biol.* 33, 507–516.e3. doi: 10.1016/j.cub.2022.12.038

Leroy, F., Brann, D. H., Meira, T., and Siegelbaum, S. A. (2017). Input-timing-dependent plasticity in the hippocampal CA2 region and its potential role in social memory. *Neuron* 95, 1089–1102.e5. doi: 10.1016/j.neuron.2019.03.021

Lisman, J., and Spruston, N. (2010). Questions about STDP as a general model of synaptic plasticity. *Front. Synaptic Neurosci.* 2:140. doi: 10.3389/fnsyn.2010.00140

Losonczy, A., Makara, J. T., and Magee, J. C. (2008). Compartmentalized dendritic plasticity and input feature storage in neurons. *Nature* 452, 436–441. doi: 10.1038/nature06725

Ma, T., Cheng, Y., Roltsch Hellard, E., Wang, X., Lu, J., Gao, X., et al. (2018). Bidirectional and long-lasting control of alcohol-seeking behavior by corticostriatal LTP and LTD. *Nat. Neurosci.* 21, 373–383. doi: 10.1038/s41593-018-0081-9

Magee, J. C., and Grienberger, C. (2020). Synaptic plasticity forms and functions. *Annu. Rev. Neurosci.* 43, 95–117. doi: 10.1146/annurev-neuro-090919-022842

Magistretti, P. J., and Allaman, I. (2018). Lactate in the brain: from metabolic end-product to signalling molecule. *Nat. Rev. Neurosci.* 19, 235–249. doi: 10.1038/nrn.2018.19

Martin, S. J., and Morris, R. G. M. (2002). New life in an old idea: the synaptic plasticity and memory hypothesis revisited. *Hippocampus* 12, 609–636. doi: 10.1002/hipo.10107

Matsuo, N., Reijmers, L., and Mayford, M. (2008). Spine-type-specific recruitment of newly synthesized AMPA receptors with learning. *Science* 319, 1104–1107. doi: 10.1126/science.1149967

Mayford, M., and Reijmers, L. (2015). Exploring memory representations with activity-based genetics. *Cold Spring Harb. Perspect. Biol.* 8:a021832. doi: 10.1101/cshperspect.a021832

McFarlan, A. R., Chou, C. Y., Watanabe, A., Cherepacha, N., Haddad, M., Owens, H., et al. (2023). The plasticitome of cortical interneurons. *Nat. Rev. Neurosci.* 24, 80–97. doi: 10.1038/s41583-022-00663-9

Mehaffey, W. H., and Doupe, A. J. (2015). Naturalistic stimulation drives opposing heterosynaptic plasticity at two inputs to songbird cortex. *Nat. Neurosci.* 18, 1272–1280. doi: 10.1038/nn.4078

Meliza, C. D., and Dan, Y. (2006). Receptive-field modification in rat visual cortex induced by paired visual stimulation and single-cell spiking. *Neuron* 49, 183–189. doi: 10.1016/j.neuron.2005.12.009

Mendes, A., Vignoud, G., Perez, S., Perrin, E., Touboul, J., and Venance, L. (2020). Concurrent thalamostriatal and corticostriatal spike-timing-dependent plasticity and heterosynaptic interactions shape striatal plasticity map. *Cereb. Cortex* 30, 4381–4401. doi: 10.1093/cercor/bhaa024

Mery, F., and Kawecki, T. J. (2005). A cost of long-term memory in drosophila. *Science* 308:1148. doi: 10.1126/science.1111331

Miyashita, T., Shao, Y. R., Chung, J., Pourzia, O., and Feldman, D. E. (2013). Long-term channelrhodopsin-2 (ChR2) expression can induce abnormal axonal morphology and targeting in cerebral cortex. *Front. Neural Circ.* 7:8. doi: 10.3389/fncir.2013.00008

Murphy-Royal, C., Johnston, A. D., Boyce, A. K., Diaz-Castro, B., Institoris, A., Peringod, G., et al. (2020). Stress gates an astrocytic energy reservoir to impair synaptic plasticity. *Nat. Commun.* 11:2014. doi: 10.1038/s41467-020-15778-9

Nabavi, S., Fox, R., Proulx, C. D., Lin, J. Y., Tsien, R. Y., and Malinow, R. (2014). Engineering a memory with LTD and LTP. *Nature* 511, 348–352. doi: 10.1038/nature13294

Newman, L. A., Korol, D. L., and Gold, P. E. (2011). Lactate produced by glycogenolysis in astrocytes regulates memory processing. *PLoS One* 6:e28427. doi: 10.1371/journal.pone.0028427

O'Donnell, C. (2023). Nonlinear slow-timescale mechanisms in synaptic plasticity. *Curr. Opp. Neurobiol.* 82:102778. doi: 10.1016/j.conb.2023.102778

Paulsen, O., and Sejnowski, T. J. (2000). Natural patterns of activity and long-term synaptic plasticity. *Curr. Opin. Neurobiol.* 10, 172–180. doi: 10.1016/s0959-4388(00)00076-3

Pedersen, B. K., and Febbraio, M. A. (2012). Muscles, exercise and obesity: skeletal muscle as a secretory organ. *Nat. Rev. Endocrinol.* 8, 457–465. doi: 10.1038/nrendo.2012.49

Pfeiffer, T., Poll, S., Bancelin, S., Angibaud, J., Inavalli, V. K., Keppler, K., et al. (2018). Chronic 2p-sted imaging reveals high turnover of dendritic spines in the hippocampus in vivo. *Elife* 7. doi: 10.7554/elife.34700

Piette, C., Touboul, J., and Venance, L. (2020). Engrams of fast learning. *Front. Cell. Neurosci.* 14:575915. doi: 10.3389/fncel.2020.575915

Plaçais, P.-Y., de Tredern, É., Scheunemann, L., Trannoy, S., Goguel, V., Han, K.-A., et al. (2017). Upregulated energy metabolism in the drosophila mushroom body is the trigger for long-term memory. *Nat. Commun.* 8:15510. doi: 10.1038/ncomms15510

Plaçais, P.-Y., and Preat, T. (2013). To favor survival under food shortage, the brain disables costly memory. *Science* 339, 440–442. doi: 10.1126/science.1226018

Priestley, J. B., Bowler, J. C., Rolotti, S. V., Fusi, S., and Losonczy, A. (2022). Signatures of rapid plasticity in hippocampal CA1 representations during novel experiences. *Neuron* 110, 1978–1992.e6. doi: 10.1016/j.nuron.2022.03.026

Ray, S., Li, M., Koch, S. P., Mueller, S., Boehm-Sturm, P., Wang, H., et al. (2020). Seasonal plasticity in the adult somatosensory cortex. *Proc. Natl. Acad. Sci. U. S. A.* 117, 32136–32144. doi: 10.1073/pnas.1922888117

Ruminot, I., Schmalzle, J., Leyton, B., Barros, L. F., and Deitmer, J. W. (2017). Tight coupling of astrocyte energy metabolism to synaptic activity revealed by genetically encoded FRET nanosensors in hippocampal tissue. *J. Cereb. Blood Flow Metab.* 39, 513–523. doi: 10.1177/0271678X17737012

Saur, L., Baptista, P. P., de Senna, P. N., Paim, M. F., Nascimento, P., Ilha, J., et al. (2014). Physical exercise increases GFAP expression and induces morphological changes in hippocampal astrocytes. *Brain Struct. Funct.* 219, 293–302. doi: 10.1007/s00429-012-0500-8

Sejnowski, T. J. (1999). The book of hebb. *Neuron* 24, 773–776. doi: 10.1016/s0896-6273(00)81025-9

Suvrathan, A., Payne, H. L., and Raymond, J. L. (2016). Timing rules for synaptic plasticity matched to behavioral function. *Neuron* 92, 959–967. doi: 10.1016/j.neuron.2016.10.022

Suzuki, A., Stern, S. A., Bozdagi, O., Huntley, G. W., Walker, R. H., Magistretti, P. J., et al. (2011). Astrocyte-neuron lactate transport is required for long-term memory formation. *Cells* 144, 810–823. doi: 10.1016/j.cell.2011.02.018

Tadi, M., Allaman, I., Lengacher, S., Grenningloh, G., and Magistretti, P. J. (2015). Learning-induced gene expression in the hippocampus reveals a role of neuron -astrocyte metabolic coupling in long term memory. *PLoS One* 10:e0141568. doi: 10.1371/journal.pone.0141568.eCollection

Takeishi, A., Yeon, J., Harris, N., Yang, W., and Sengupta, P. (2020). Feeding state functionally reconfigures a sensory circuit to drive thermosensory behavioral plasticity. *Elife* 9:e61167. doi: 10.7554/eLife.61167

Thorn, C. A., Atallah, H., Howe, M., and Graybiel, A. M. (2010). Differential dynamics of activity changes in dorsolateral and dorsomedial striatal loops during learning. *Neuron* 66, 781–795. doi: 10.1016/j.neuron.2010.04.036

Todorova, V., and Blokland, A. (2017). Mitochondria and synaptic plasticity in the mature and aging nervous system. *Curr. Neuropharmacol.* 15, 166–173. doi: 10.2174/1570159x14666160414111821

van Praag, H., Christie, B. R., Sejnowski, T. J., and Gage, F. H. (1999). Running enhances neurogenesis, learning, and long-term potentiation in mice. *Proc. Natl. Acad. Sci.* 96, 13427–13431. doi: 10.1073/pnas.96.23.13427

Vaynman, S., Ying, Z., and Gomez-Pinilla, F. (2004). Hippocampal BDNF mediates the efficacy of exercise on synaptic plasticity and cognition. *Eur. J. Neurosci.* 20, 2580–2590. doi: 10.1111/j.1460-9568.2004.03720.x

Vetere, G., Tran, L. M., Moberg, S., Steadman, P. E., Restivo, L., Morrison, F. G., et al. (2019). Memory formation in the absence of experience. *Nat. Neurosci.* 22, 933–940. doi: 10.1038/s41593-019-0389-0

Vukovic, J., Colditz, M. J., Blackmore, D. G., Ruitenberg, M. J., and Bartlett, P. F. (2012). Microglia modulate hippocampal neural precursor activity in response to exercise and aging. *J. Neurosci.* 32, 6435–6443. doi: 10.1523/JNEUROSCI.5925-11.2012

Waters, J., and Helmchen, F. (2004). Boosting of action potential backpropagation by neocortical network activityin vivo. *J. Neurosci.* 24, 11127–11136. doi: 10.1523/jneurosci.2933-04.2004

Xiong, Q., Znamenskiy, P., and Zador, A. M. (2015). Selective Corticostriatal plasticity during acquisition of an auditory discrimination task. *Nature* 521, 348–351. doi: 10.1038/nature14225

Yagishita, S., Hayashi-Takagi, A., Ellis-Davies, G. C. R., Urakubo, H., Ishii, S., and Kasai, H. (2014). A critical time window for dopamine actions on the structural plasticity of dendritic spines. *Science* 345, 1616–1620. doi: 10.1126/science.1255514

Yao, H., and Dan, Y. (2001). Stimulus timing-dependent plasticity in cortical processing of orientation. *Neuron* 32, 315–323. doi: 10.1016/s0896-6273(01)00460-3

Zhang, Y., Cudmore, R. H., Lin, D.-T., Linden, D. J., and Huganir, R. L. (2015). Visualization of NMDA receptor–dependent AMPA receptor synaptic plasticity in vivo. *Nat. Neurosci.* 18, 402–407. doi: 10.1038/nn.3936

Zhao, X., Hsu, C.-L., and Spruston, N. (2022). Rapid synaptic plasticity contributes to a learned conjunctive code of position and choice-related information in the hippocampus. *Neuron* 110, 96–108.e4. doi: 10.1016/j.neuron.2021.10.003

frontiers | Frontiers in Neuroscience

TYPE Original Research
PUBLISHED 12 February 2024
DOI 10.3389/fnins.2024.1327423

Check for updates

OPEN ACCESS

EDITED BY
Tal Burstyn-Cohen,
Hebrew University of Jerusalem, Israel

REVIEWED BY
Andrew Plested,
Humboldt University of Berlin, Germany
Eiki Kimura,
University of Fukui, Japan

*CORRESPONDENCE
Greg Lemke
✉ lemke@salk.edu

†PRESENT ADDRESSES
Sheng Miao,
Department of Neurology, Yale University, New Haven, CT, United States
Lawrence Fourgeaud and Kaisa E. Happonen,
Janssen Research and Development, San Diego, CA, United States

RECEIVED 24 October 2023
ACCEPTED 26 January 2024
PUBLISHED 12 February 2024

CITATION
Miao S, Fourgeaud L, Burrola PG, Stern S, Zhang Y, Happonen KE, Novak SW, Gage FH and Lemke G (2024) Tyro3 promotes the maturation of glutamatergic synapses. *Front. Neurosci.* 18:1327423. doi: 10.3389/fnins.2024.1327423

COPYRIGHT
© 2024 Miao, Fourgeaud, Burrola, Stern, Zhang, Happonen, Novak, Gage and Lemke. This is an open-access article distributed under the terms of the Creative Commons Attribution License (CC BY). The use, distribution or reproduction in other forums is permitted, provided the original author(s) and the copyright owner(s) are credited and that the original publication in this journal is cited, in accordance with accepted academic practice. No use, distribution or reproduction is permitted which does not comply with these terms.

Tyro3 promotes the maturation of glutamatergic synapses

Sheng Miao[1†], Lawrence Fourgeaud[1†], Patrick G. Burrola[1], Shani Stern[2,3], Yuhan Zhang[4], Kaisa E. Happonen[1†], Sammy Weiser Novak[5], Fred H. Gage[2] and Greg Lemke[1*]

[1]Molecular Neurobiology Laboratory, The Salk Institute for Biological Studies, La Jolla, CA, United States, [2]Laboratory of Genetics, The Salk Institute for Biological Studies, La Jolla, CA, United States, [3]Sagol Department of Neurobiology, University of Haifa, Haifa, Israel, [4]Division of Biological Sciences, University of California, San Diego, La Jolla, CA, United States, [5]Waitt Advanced Biophotonics Laboratory, The Salk Institute for Biological Studies, La Jolla, CA, United States

The receptor tyrosine kinase Tyro3 is abundantly expressed in neurons of the neocortex, hippocampus, and striatum, but its role in these cells is unknown. We found that neuronal expression of this receptor was markedly up-regulated in the postnatal mouse neocortex immediately prior to the final development of glutamatergic synapses. In the absence of Tyro3, cortical and hippocampal synapses never completed end-stage differentiation and remained electrophysiologically and ultrastructurally immature. *Tyro3*$^{-/-}$ cortical neurons also exhibited diminished plasma membrane expression of the GluA2 subunits of AMPA-type glutamate receptors, which are essential to mature synaptic function. Correspondingly, GluA2 membrane insertion in wild-type neurons was stimulated by Gas6, a Tyro3 ligand widely expressed in the postnatal brain. Behaviorally, *Tyro3*$^{-/-}$ mice displayed learning enhancements in spatial recognition and fear-conditioning assays. Together, these results demonstrate that Tyro3 promotes the functional maturation of glutamatergic synapses by driving plasma membrane translocation of GluA2 AMPA receptor subunits.

KEYWORDS

synaptic maturation, receptor tyrosine kinase, phosphatidylserine, GluA2, Hebbian learning

Introduction

The three members of the TAM family of receptor tyrosine kinases (RTKs) – Tyro3, Axl, and Mer – were discovered in the early 1990s (Lai and Lemke, 1991; O'Bryan et al., 1991; Graham et al., 1994; Lai et al., 1994). Since that time, a great deal has been learned about the important biological functions of the latter two receptors, which are prominently expressed in macrophages, dendritic cells, and other sentinel cells of the immune system (Lu and Lemke, 2001; Scott et al., 2001; Rothlin et al., 2007; Zagorska et al., 2014; Lemke, 2019). In these cells, Axl and Mer are critical mediators of the phagocytic engulfment and turnover of apoptotic cells (Scott et al., 2001; Zagorska et al., 2014; Lemke, 2019) and concomitantly, of the intrinsic feedback inhibition of Toll-like receptor and cytokine receptor signaling at the end of the innate immune response (Rothlin et al., 2007, 2015). Tyro3 is only modestly expressed by most immune sentinels (Imm Gen, 2016), but is instead prominently expressed by maturing and mature neurons in the central nervous system (CNS) (Lai and Lemke, 1991; Prieto et al., 2007). The roles that Tyro3 might play in these cells, which do not express Axl or Mer, have proven difficult to decipher (Pierce et al., 2008; Zhong et al., 2010; Blades et al., 2020).

As a family, the TAM receptors exhibit unusual signaling properties relative to other RTKs (Lemke, 2013). Their tyrosine kinase enzymatic activities are stimulated by the binding of two closely-related soluble ligands – Gas6 and Protein S (Pros1) (Stitt et al., 1995) – to the receptor ectodomains (Lemke, 2013, 2019). Gas6 activates all three receptors, whereas Pros1 activates Tyro3 and Mer but not Axl (Lew et al., 2014). Pros1 also has important activity as an anticoagulant in the blood coagulation cascade (Burstyn-Cohen et al., 2012), but Gas6 only signals through the three TAM receptors (Lemke, 2013). In addition to ligand binding, full TAM activation also requires the Ca^{2+}-dependent binding of phosphatidylserine (PtdSer), a universal membrane phospholipid, to the amino-terminal 'Gla' domains of the ligands (Lew et al., 2014). For example, a Gla-less truncation variant of Gas6 binds Axl with the same sub-nanomolar K_D as full-length Gas6, but is entirely incapable of activating the Axl tyrosine kinase (Lew et al., 2014). In this respect, TAM receptors and their ligands together act as detectors for PtdSer (Lemke, 2017). This phospholipid is normally sequestered to the cytoplasmic leaflet of plasma membrane bilayers by the action of 'flippases' (Segawa et al., 2014, 2016), but is translocated to the extracellular leaflet through the activity of two large families of PtdSer 'scramblases' (Suzuki et al., 2010, 2013a; Lemke, 2019). These scramblases are activated by caspase cleavage during apoptosis or alternatively, by calcium binding when cells are depolarized. How these special features of Tyro3 signaling might impact its activities in neurons is also unknown.

We have used cell biological and electrophysiological analyses of cortical and hippocampal neurons from wild-type (WT) versus Tyro3-deficient (*Tyro3*$^{-/-}$) mice (Lu et al., 1999) to investigate Tyro3 activities in these cells. We found that in the absence of Tyro3, glutamatergic synapses were both physiologically and ultrastructurally immature. Correspondingly, we observed that Gas6 activation of post-synaptic Tyro3 in WT neurons stimulated the essential plasma membrane insertion of GluA2 AMPA receptor subunits at synapses. We further found that this stimulation was dependent on plasma membrane externalization of PtdSer, which is induced by pre-synaptic depolarization, as Gla-less Gas6 was without effect. Finally, *Tyro3*$^{-/-}$ mice exhibited behavioral and learning enhancements that are consistent with unusual synaptic plasticity. Together, these observations identify Tyro3 as a mediator of post-synaptic maturation events that are triggered by the pre-synaptic display of phosphatidylserine.

Materials and methods

Mice

C57BL/6 wild-type mice were obtained from The Jackson laboratory. The *Tyro3*$^{-/-}$ strain has been described previously (Lu et al., 1999). All animal procedures were conducted in compliance with the ethical guidelines and according to protocols approved by the Salk Institute Animal Care and Use Committee (IACUC) (Protocol Nos. 15-0001, 15-0079, and 17-0046).

Hippocampal and cortical neuron culture

Hippocampal and cortical neurons were prepared according to previously described methods, with several modifications (Hilgenberg and Smith, 2007; Beaudoin et al., 2012). Briefly, hippocampi or cortices from embryonic day 18 (E18) fetuses from timed-pregnant C57BL/6 mice were micro-dissected and chopped into small pieces in Hank's Balanced Salt Solution (HBSS) without Ca^{2+}/Mg^{2+}, with 10 mM HEPES, and then treated with a digestion solution containing HBSS with Ca^{2+}/Mg^{2+}, 10 mM HEPES, 20 units/ml papain and 0.005% DNase for 30 min at 37°C. After digestion, tissues were mechanically dissociated using a pasteur pipette (with tip fire-polished) in HBSS with Ca^{2+}/Mg^{2+}, 10 mM HEPES and trypsin inhibitor. Cell suspensions were plated at 15,000 cells/well on poly-L-lysine precoated glass coverslips (Neuvitro) in 24-well plates for immunocytochemistry, at 150,000/well on poly-L-lysine precoated glass coverslips (Neuvitro) in 24-well plates for electrophysiological recording, and at 10^6/dish in PLL-coated 35 mm dishes for biochemistry. The cells were maintained in plating media containing Neurobasal™ Plus Medium (Thermo Fisher Scientific), 2% B-27™ plus supplement (Thermo Fisher Scientific), 1% GlutaMAX™ supplement (Thermo Fisher Scientific) and 5% heat inactivated FBS for 3 h. After attachment of the cells, the media was switched to culturing media, comprised of Neurobasal™ Plus Medium, 2% B-27™ plus supplement and 1% GlutaMAX™ supplement. From 4 days-*in-vitro* (DIV) onwards, half medium changes were performed with Culturing medium. To inhibit proliferation of glial cells, 0.5 μM cytosine arabinoside (AraC, Sigma-Aldrich) was added to the medium at 4 DIV. Cultures were maintained in a humidified incubator at 37°C and 10% CO_2.

Hippocampal slice electrophysiology

Acute coronal vibratome slices (350 μm) of postnatal day (P)30-P50 (for field recordings) and P14-16 (for whole cell recordings) C57Bl/6J mouse hippocampi were prepared and analyzed using standard protocols (Lein et al., 2011), as described previously (Fourgeaud et al., 2010). Briefly, mice were anesthetized with isoflurane inhalation and decapitated, and slices were cut into ice-cold cutting solution (in mM: 85 NaCl, 75 sucrose, 2.5 KCl, 0.5 $CaCl_2$, 4 $MgCl_2$, 1.25 NaH_2PO_4, 25 $NaHCO_3$, 25 glucose, and 2.25 ascorbate) equilibrated with 95% O_2/5% CO_2. Slices were incubated 30 min at 30°C in oxygenated artificial cerebrospinal fluid (ACSF) (in mM: for whole-cell recording experiments, 126 NaCl, 2.5 KCl, 1.25 NaH_2PO_4, 2 $MgCl_2$, 2 $CaCl_2$, 26 $NaHCO_3$, and 18 glucose; for field recording experiments, 126 NaCl, 2.5 KCl, 1.25 NaH_2PO_4, 1.3$MgSO_4$, 2.5$CaCl_2$, 26 $NaHCO_3$, and 10 glucose) and maintained at room temperature at least 1 h before being transferred to a submerged recording chamber.

Whole-cell patch-clamp recordings of excitatory postsynaptic currents (EPSCs) from CA1 pyramidal neurons were conducted at room temperature. Picrotoxin (50 μM) was added to the ACSF to block $GABA_A$ receptor-mediated inhibition, and connections between CA3 and CA1 were cut to reduce epileptiform activity. Patch electrodes (3–5 MΩ) were filled with intrapipette solution [in mM: 108 cesium gluconate, 20 Hepes, 0.4 EGTA, 2.8 NaCl, 5 TEACl, 4 MgATP, 0.3 NaGTP, 10 phosphocreatine, adjusted to pH 7.2 with CsOH (290 mosM)]. CA1 pyramidal cells were voltage-clamped at −70 mV, and spontaneous EPSCs (sEPSCs) were recorded. To record mini EPSCs (mEPSCs), 0.5 μM TTX was added to the ACSF.

Field recordings from populations of CA1 neurons were conducted at room temperature using standard methods. Picrotoxin (100 μM) was added to the ACSF to block $GABA_A$ receptor-mediated inhibition and connections between CA3 and CA1 were cut to reduce

epileptiform activity. Stainless-steel bipolar electrodes were used to stimulate Schaffer collateral fibers (0.05 Hz), and field excitatory postsynaptic potentials (fEPSPs) were recorded from stratum radiatum using extracellular glass microelectrodes (3–5 MΩ) filled with ACSF. Input–output (I/O) relationships were determined by measuring fEPSP (output) amplitudes in relation to stimulation intensity (input). After establishing a stable 20 min baseline, LTP was induced using a high frequency stimulation (HFS) protocol (100 Hz, 1 s duration at test strength). Data are represented normalized to the average fEPSP amplitude 10 min before HFS.

Whole-cell patch-clamp recordings from hippocampal neuronal cultures

Cultured hippocampal neurons (13–14 DIV) were prepared as described above. Neurons on glass coverslips were transferred to a recording chamber in standard artificial cerebrospinal fluid (ACSF) containing 10 mM HEPES, 4 mM KCl, 2 mM $CaCl_2$, 1 mM $MgCl_2$, 139 mM NaCl, 10 mM D-glucose (osmolarity adjusted with sucrose to 320 mOsm, and pH adjusted to 7.4). Cells were patch-clamped with pipettes containing 130 mM K-gluconate, 6 mM KCl, 4 mM NaCl, 10 mM Na-HEPES, 0.2 mM K-EGTA, 0.3 mM GTP, 2 mM Mg-ATP, 0.2 mM cAMP, 10 mM D-glucose, 0.15% biocytin and 0.06% rhodamine, pH 7.2 (pipette tip resistance was 5–8 MΩ). Action potentials were evoked by injecting depolarizing current pulses in current-clamp mode. Spontaneous EPSCs were recorded in voltage-clamp at −60 mV with a 20 kHz sampling rate with inhibitory activity blocked by 40 μM bicuculline. Signals were amplified with a Multiclamp700B amplifier and recorded with Clampex 10.4 software (Axon Instruments). Miniature EPSCs were recorded also in voltage-clamp mode but with the addition of 0.5 μM TTX. Data were subjected to a 3,000 Hz low-pass filter and analyzed using Clampfit-10 and the software package Matlab (2014A, The MathWorks Inc., Natick, MA, 2000). All measurements were conducted at room temperature.

Cortical neuron treatments

Primary cortical neurons were cultured for 11 DIV before starting treatment with either 20 nM Gas6 or 20 nM Gla-less Gas6. For 7 day long-term treatment, cortical neurons were treated starting at 11 DIV with supplement every other day when medium was half changed. For 1 day-short term treatment, 20 nM Gas6 were added only once to cultures at 16 DIV with or without pretreatment using 100 nM Purified Recombinant Annexin V (BD Pharmingen, #556416). Treatment with TBS buffer, the solvent for Gas6, were used as negative control. To visualize exposed phosphatidylserine on plasma membrane during neuron development *in vitro*, cortical neurons at 2, 5, 8, 12, 16, or 20 days *in vitro* (DIV) were incubated with pSIVA-IANBD (Novus Biologicals, NBP2-29382) diluted to 20 μl/ml and CellTracker Red CMTPX dye (Invitrogen C34552) at 0.5 μM in culture medium for 60 min at 37°C, 10% CO_2 before fixing with 4%PFA. To stain exposed phosphatidylserine after calcium ionophore A23187 treatment, cortical neurons at 18 DIV were treated with A23187 at concentration of 5 μM for 20 min in medium also containing pSIVA-IANBD diluted to 20 μl/ml and 0.5 mM CellTracker Red CMTPX dye before fixing with 4% PFA.

GluA2 live staining in mouse cortical neurons

Mouse cortical neurons were live stained for GluA2 according to previously described methods (Blanco-Suarez et al., 2018), with several modifications. Briefly, cortical neurons on coverslips were incubated with mouse anti-GluA2 (Millipore MAB397) at a 1:100 dilution and CellTracker Red CMTPX dye (Invitrogen C34552) at a 0.5 mM concentration in culture medium for 30 min at 37°C, 10% CO_2. After washing with DPBS and fixing with pre-warmed (34°C) 4% PFA for 5 min, the coverslips were washed with PBS and then blocked (without permeabilizing) with PBS containing 2% BSA and 5% normal goat serum for 1 h at room temperature in a humidified chamber. After blocking, coverslips were incubated with goat anti-mouse Alexa 488 at 1:500 dilution in PBS containing 2% BSA and 5% normal goat serum for 3 h at room temperature. Coverslips were then washed with PBS and mounted in Prolong Diamond antifade mounting medium with DAPI (Molecular Probe REF P36962). Neurons were imaged on Zeiss LSM700 using the 63x oil-immersion objective. At least 45 cells per condition were imaged across three coverslips in each independent experiment. A minimum of 3 independent experiments were run. Cells were located using CellTracker Red CMTPX in the red channel. Exposure acquisition was set according to neurons with Gas6 treatment within each independent experiment, capturing 16 bit images at a resolution of 1024×1024 pixels. GluA2 puncta on the soma and dendrites of cortical neurons were analyzed using Imaris software and normalized to cell volume that was calculated based on CellTracker Red signals.

Perfusion and tissue processing for electron microscopy

Mice were anesthetized with 2.5% Avertin/Saline IP, and then dissected open from the abdomen up into the chest cavity. The right atrium was nicked and perfusion was performed through the left ventricle with the following solutions: 1 × 1′ Ringers at 37°C, 1 × 9′ 2.5% glut/2.0% Para/1 mM $CaCl_2$/ 0.15 M Caco. pH7.3 at 37°C. The brain was cut with a razor blade in a coronal plain using the "brain jig." Cuts were made at 4 mm anterior and 5 mm posterior in the brain jig. First fixing was performed for 2 h at 4°C in 2.5% glut/2.0% Para/1 mM $CaCl_2$/0.15 M Caco. pH7.3. The brain was embedded in 2.5% agar/0.15 M Caco then mounted with super glue on a stub for cutting. Coronal sections (300 μm) were cut through the brain in pairs. Sections were placed in a 12 well plate with 0.15 M caco buffer pH 7.3. Sections were washed overnight in 0.15 M caco buffer pH 7.3 at 4°C, and slices were trimmed down to the specific hippocampus area of interest in the CA1 region just above dentate gyrus. In a second fixing, the trimmed sections were incubated in 2% Osmium Tetroxide/0.15 M caco. pH7.3 for 3 h on ice in a fume hood, followed by 5 times washing in milli-Q water on ice. A third fixation was performed in 2% Uranyl Acetate for 45 min on ice. Dehydration was performed in 30, 50, 70, 95% ETOH (in sequence) for 8 min each and in 100% ETOH twice for 8 min each, and then in acetonitrile. Infiltration was performed in 66/33 ratio of resin/acetonitrile for 30 min, in Epon/Araldite for 2 h at room temperature (RT), and then in Epon/Araldite for 3 h at RT. Embedding was performed in fresh resin using flat embedding capsules at 65°C overnight.

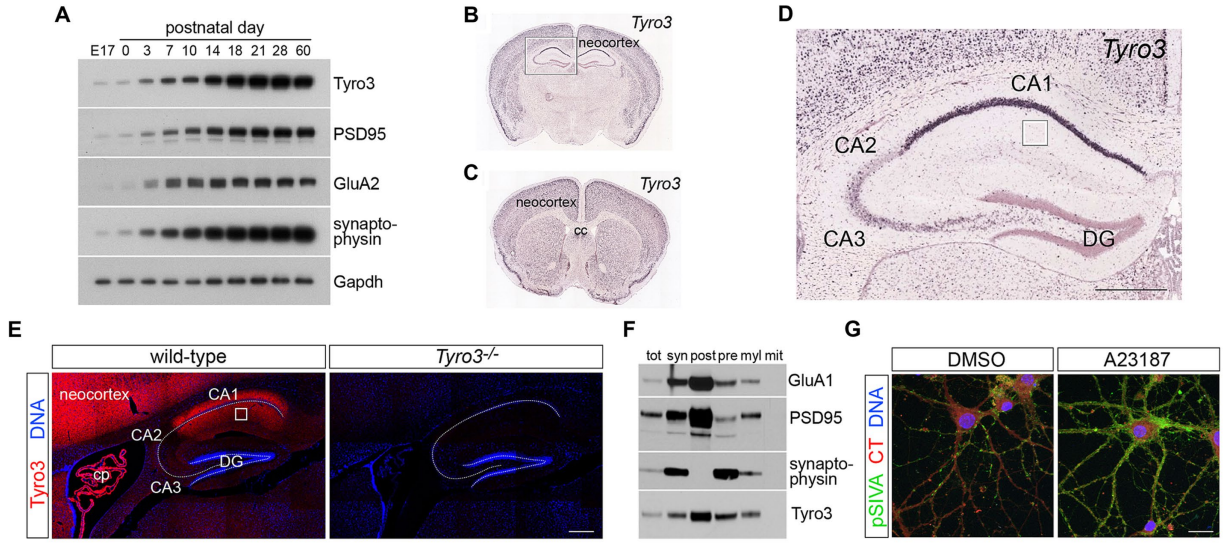

FIGURE 1
Expression of Tyro3 system components in the CNS. **(A)** Representative western blot analyses of the expression of the indicated proteins in the mouse neocortex at the indicated developmental times. Gapdh is a loading control. **(B–D)** Images from the Allen Brain Atlas (http://mouse.brain-map.org/gene/show/21931) of expression of *Tyro3* mRNA in the postnatal day (P) 56 mouse brain, as monitored by *in situ* hybridization of digoxigenin riboprobes to coronal sections (Jones et al., 2009). Boxed region in **(B)** is enlarged in **(D)**. Boxed region in **(D)** is the stratum radiatum of the hippocampus, the area analyzed by electron microscopy in Figure 3. **(E)** Tyro3 protein expression (red), detected with a Tyro3 antibody (Prieto et al., 2007), in adult WT versus *Tyro3*$^{-/-}$ (antibody control) hippocampus. DAPI (blue, DNA) labels nuclei. **(F)** Density gradient membrane fractionation of P30 mouse hippocampus, analyzed by western blot for the indicated proteins. **(G)** Representative images of cultured cortical neurons (see Methods) at 18 DIV treated for 20 min with di-methyl sulfoxide (DMSO, vehicle control, left) or the calcium ionophore A23187 (5 μm, right) and simultaneously incubated with pSIVA (green) to visualize externalized phosphatidylserine (PtdSer) on the plasma membrane surface and CellTracker Red to delimit cells. DAPI (blue, DNA) labels nuclei. E17, embryonic day 17; cc, corpus callosum; DG, dentate gyrus; cp, choroid plexus; tot, total cortical protein; syn, synaptosomes; post, post-synaptic membrane; pre, pre-synaptic membrane; myl, myelin; mit, mitochondria; CT, CellTracker dye. Scale bars: **(D,E)** 100 μm; **(G)** 20 μm.

Electron microscopy image analyses

Synapses were defined by the presence of a stained postsynaptic density facing (apposed to) a presynaptic process containing at least three synaptic vesicles. Perforated synapses were defined by the presence of a discontinuity in the postsynaptic density (Geinisman et al., 1987), and multiple synapse boutons (MSBs) were defined by the presence of at least 2 independent dendritic spines contacting the same axon terminal (Sorra and Harris, 1993). Three sections were analyzed per block, and 2 blocks per animal were used to collect micrographs. Transmission electron microscopy (TEM) micrographs were taken on a Zeiss Libra 120 microscope operated at 80 kV, using a Gatan Ultrascan 4,000 camera at 4 K resolution at an initial magnification of 4,000×, and enlarged photographically to a final magnification of 21,700×. Synapses were randomly photographed in an area corresponding to the stratum radiatum (boxed in Figure 1D), the suprapyramidal region of the hippocampus that contains CA3-to-CA1 Schaffer collaterals. The density of perforated synapses and MSBs were estimated by two independent observers who were blind to genotype.

Volumetric data from serial sections in the scanning electron microscope (SEM; S3EM) were also collected. Briefly, resin embedded samples from control and *Tyro3*$^{-/-}$ conditions were selected, the stratum radiatum was identified from semi-thin sections, and a frustum of 150 × 400 × 60 μm was trimmed using a Leica UC7 ultramicrotome. A silicon chip (35 × 7 mm, University Wafer, Boston, MA) was glow discharged in a plasma cleaner (Harrick, Ithaca), rinsed in deionized water, and partially immersed in a Diatome Histo knife. An ionizing gun (Leica EM Crion) was activated and oriented toward the cutting edge of the knife mounted on the ultramicrotome. Ribbons of approximately 100 serial sections of 50 nm thickness were cut, the water level was slowly lowered, and sections were allowed to dry on the silicon. Samples were mounted using carbon sticky tabs and loaded into a Zeiss Sigma VP SEM, and serial sections were imaged using the array tomography software module of Atlas5 (FIBICS, Ottawa). A region of interest unobstructed by artifact throughout the series was identified and 2 nm/px images were collected on consecutive sections. Images were aligned using rigid and affine alignment functions available in TrakEM2 in Fiji. Evaluation of datasets and segmentation of dendritic spines was conducted in Reconstruct. The serial 2D segments were exported as VRML mesh files and imported into Blender software[1] for further visualization.

Subcellular fractionation

Subcellular fractions of P30 hippocampus were obtained using established protocols (Blackstone et al., 1992), as described previously (Fourgeaud et al., 2010). Briefly, animals were anesthetized with isoflurane inhalation and decapitated, brains were quickly removed,

1 blender.org

and hippocampi were dissected out and homogenized in 10 vol of Hepes sucrose buffer (0.32 M sucrose and 4 mM Hepes, pH 7.4) supplemented with protease inhibitor mixture (Complete, Roche) using a glass- Teflon homogenizer at 900 rpm (12 strokes). The homogenate was centrifuged for 10 min at 1,000 × *g*, and the pellet (P1) containing the nuclei was discarded. The supernatant (S1) was centrifuged for 20 min at 10,000 × *g*, resulting in a crude synaptosomal pellet (P2). P2 was resuspended in 10 vol of Hepes sucrose buffer and centrifuged for 10 min at 20,000 × *g*, resulting in a washed crude synaptosomal pellet (P2′). P2′ was lysed by hypo-osmotic shock in water and adjusted to 4 mM Hepes. After 30 min of gentle rotation at 4°C, P2′ was centrifuged for 20 min at 25,000 × g, resulting in a crude synaptosomal membrane fraction (P3) and a crude synaptic vesicle fraction (S3). Aliquots were collected at multiple steps of the fractionation and solubilized in Triton X-100 (1%) for Western blot analysis. PSD-enriched fractions were prepared as described previously (Zhou et al., 2007).

SDS-PAGE and western blot

Protein samples were prepared with reducing Laemmli buffer and boiled for 10 min at 95°C, and then separated on NuPAGE 4–12% Bis-Tris Mini protein gel (Thermo Fisher Scientific NP0323BOX) for 3 h at constant voltage of 90 V. After gel electrophoresis, proteins were transferred onto Immobilon-P PVDF membranes (Millipore IPVH00010) for 90 min at constant current of 0.4A. Membranes were blocked with 1x Tris Buffered Saline (TBS) with 1% Casein (BioRad, #1610782) for 1 h at room temperature in gentle shaking, and then incubated at 4°C overnight with the primary antibody in blocking buffer, rabbit anti-Tyro3 (Cell signaling 5585S) at a dilution of 1:2000, mouse anti-PSD95 (Thermo Fisher Scientific MA1-046) at a dilution of 1:2000, mouse anti-GluA2 (Millipore MAB397) at a dilution of 1:5000, rabbit anti-synaptophysin (Abcam ab16659), or mouse anti-GAPDH (Santa Cruz SC-32233) at a dilution of 1:10,000. After washing with TBS buffer containing 0.1% Tween-20, membranes were incubated with secondary antibody for 3 h at room temperature (Peroxidase AffiniPure Goat Anti-Rabbit IgG, Jackson Immunoresearch 111–036-047 or 115–006-072). After washing with TBS buffer containing 0.1% Tween-20, membranes were incubated in chemiluminescent substrate (SuperSignal, ThermoFisher 34,580) and the chemiluminescent signal was detected and recorded by exposure of the membrane to X-ray film.

Open field tests

Mice (male, age 3 months) were placed in a novel open field [16″ (W) x 16″ (D) x 15″ (H)] and allowed to explore it for a period of 20 min. Horizontal and vertical movement were automatically tracked utilizing 2 parallel infrared beam arrays surrounding a Plexiglas arena. The total distance the mice traveled, and percentage time they spent in peripheral and center regions of the open filed were analyzed.

Morris water maze

In the hidden version of the Morris water maze test (Morris et al., 1982), mice (male, age 3 months) were trained with two blocks per day over 10 days, with each block consisting of two trials with 30 s interval between the trials. The platform was hidden 1 cm below the surface of water made opaque with white nontoxic paint. Starting points were changed every trial and every day. In each trial, mice were given 60 s to find the platform. If mice found the platform earlier than 60 s, the trial ended then. If mice failed to find the platform, the trial terminated at 60s and they were guided to reach the platform. After mice had reached platform, they were allowed to rest on it for 10 s. On the 11th day, the platform was removed for a 60 s probe trial. Swim path length and speed were recorded (Ethovision; Noldus Information Technology, Wageningen, The Netherlands).

Contextual fear conditioning

Prior to behavioral procedures, mice aged at 3 months were acclimatized to the testing room and handled by the experimenter for 1 week. On the eighth day (experimental day 1), mice were allowed to explore the context A for 10 min. On day 2, the mice were placed into context A for fear conditioning for a total time of 42 s. The mice were firstly permitted 10s to explore the context, and then presented with 2 s 0.7 mA electric shocks to the foot followed by 30s rest before return to home cage. On day 3, freezing behaviors were monitored first in conditioned context A for 5 min, and 90 min later in a novel context B for another 5 min.

Quantification and statistical analysis

Results are expressed as mean ± s.e.m. Statistical analysis was carried out in Prism 9.1.0 (Graph-Pad, La Jolla, CA, USA). A two-tailed unpaired Student's *t*-test was used for statistical comparisons between two groups. For analysis of Morris water maze and contextual fear conditioning tests, a two-way repeated measures ANOVA was used. Bonferroni's multiple comparisons test was used for *post hoc* analyses. Sample sizes were chosen based on previous studies. No statistical methods were used to pre-determine sample sizes.

Results

Neuronal Tyro3 expression in the postnatal brain

We first confirmed several unusual features of Tyro3 expression that have been reported previously (Lai and Lemke, 1991; Lai et al., 1994; Ohashi et al., 1994; Prieto et al., 2000; Funakoshi et al., 2002; Prieto et al., 2007). As for the other members of the TAM family, multiple studies have documented only limited expression of Tyro3 in developing mouse and rat embryos. Instead, a substantial up-regulation in the expression of this RTK, which is largely restricted to neurons in the neocortex, hippocampus, and other higher centers of the brain, was detected by western blot in the mouse cortex during the first 2 weeks of postnatal life (Figure 1A; Lai et al., 1994). High Tyro3 expression was maintained in the adult brain (Figure 1A; Lai and Lemke, 1991; Lai et al., 1994). With respect to the results presented below, it is important to note that this time course of cortical up-regulation immediately precedes the time course of the maturation

of glutamatergic synapses, as monitored by expression of the post-synaptic scaffolding protein PSD-95, the synaptic vesicle protein synaptophysin, and the GluA2 subunit of AMPA-type glutamate receptors (Figure 1A). The maturation of glutamatergic synapses has previously been shown to be dependent upon the *de novo* plasma membrane insertion of these calcium-impermeable GluA2 subunits, and in the mouse, this occurs between postnatal day (P)7 and P16 (Kumar et al., 2002; Brill and Huguenard, 2008). Although *Tyro3* mRNA has been detected in select immune (Chan et al., 2016; Imm Gen, 2016) and tumor cells (Graham et al., 2014), and in newborn oligodendrocytes (Akkermann et al., 2017), it is overwhelmingly the product of adult neurons in the brain (Prieto et al., 2007; Zhong et al., 2010; Figures 1B,C). While *Tyro3* mRNA is abundant in neurons across all layers of the adult neocortex (Figures 1B,C), and in striatum (Figure 1C) and hippocampus (Figures 1B,D; Lai and Lemke, 1991; Prieto et al., 2000), it is not significantly expressed in the thalamus, hypothalamus, midbrain, or spinal cord.

Neuronal expression of Tyro3 has previously been shown to exhibit a marked disparity across the fields of the adult hippocampus, with very high expression in CA1, very low expression in CA3, and no expression in CA2 (Figure 1D; Lai and Lemke, 1991). [Tyro3 was among the first identified molecular markers that distinguish CA1 neurons in the hippocampus (Lai and Lemke, 1991)]. Staining of adult mouse hippocampal sections with a Tyro3 antibody (Prieto et al., 2000) revealed that Tyro3 protein was abundant in both the apical and basal processes of CA1 neurons (Figure 1E), as has previously been reported for cortical neurons (Prieto et al., 2007). When we performed densitometric biochemical fractionation of membranes from P30 mouse hippocampus (see Methods), we observed that Tyro3 largely, although not exclusively, co-fractionated with post-synaptic rather than pre-synaptic markers (Figure 1F), consistent with its previously observed localization to neuronal dendrites in the neocortex (Prieto et al., 2007). This localization is also consistent with the Tyro3 activation of post-synaptic protein kinase C and other kinases that has been observed in a mouse model of frontotemporal lobar degeneration (Fujita et al., 2018).

As noted above, the Tyro3 tyrosine kinase is activated by two closely-related, secreted (soluble) extracellular ligands – Gas6 and Protein S (Pros1) – both of whose mRNAs are very widely expressed across many different cell types in the CNS (Prieto et al., 1999, 2000). In addition to their expression in neurons, the *Gas6* and *Pros1* mRNAs are abundant in all microglia (Imm Gen, 2016), where they regulate multiple microglial properties (Fourgeaud et al., 2016; Huang et al., 2021), and in brain endothelial cells (Happonen et al., 2023)[2].

As also noted above, the final component that is essential for TAM receptor activation and signaling is the membrane glycerophospholipid phosphatidylserine (PtdSer) (Lemke, 2013, 2019; Lew et al., 2014). The N-terminal 'Gla' domains of Gas6 and Pros1 bind to PtdSer, whereas the C-terminal 'SHBG' domains of these ligands bind to the Ig domains of the TAM receptor ectodomains (Lew et al., 2014). In plasma membranes, a set of flippase enzymes (Segawa et al., 2014; Andersen et al., 2016; Segawa et al., 2016) normally confines PtdSer to the inner leaflet of the membrane bilayer (Leventis and Grinstein, 2010), but in neurons and all other cells, PtdSer is translocated to the outer leaflet by the action of both Ca^{2+}- and caspase-activated scramblases (Suzuki et al., 2010, 2016; Whitlock and Hartzell, 2017; Lemke, 2019). Effective TAM signaling cannot occur in the absence of PtdSer externalization, as it is the only way in which this phospholipid can access the Gla domains of Gas6 and Pros1 (Lew et al., 2014; Dransfield et al., 2015; Lemke, 2017).

We visualized PtdSer externalization in cultured cortical neurons using pSIVA, a 'polarity-sensitive indicator for viability and apoptosis', derived from Annexin B12, which fluoresces strongly only when bound to PtdSer (Kim et al., 2010; Huang et al., 2021). Neurons were isolated from embryonic day (E)18 cortices, and cultured *in vitro* using established protocols (Hilgenberg and Smith, 2007; Beaudoin et al., 2012). As has been described previously (Lesuisse and Martin, 2002; Beaudoin et al., 2012), we found that these cells underwent maturation over the first 14 days *in vitro* (DIV), marked by the up-regulation of Tyro3, GluA2, and PSD-95 by 11 DIV (Supplementary Figure S1A). This *in vitro* time course paralleled the expression of these same markers *in vivo* (Figure 1A). Incubation of differentiating cortical neurons with pSIVA revealed that prominent PtdSer externalization occurred between 16 and 20 DIV (Supplementary Figures S1B,C) – when synaptogenesis and spontaneous electrical activity are robust (Lesuisse and Martin, 2002; Priller et al., 2007; Beaudoin et al., 2012). This externalized PtdSer was frequently seen to be localized on neuronal membrane overlying puncta of presynaptic synaptophysin (Supplementary Figure S1D). Spontaneous electrical activity allows for calcium influx and the activation of Ca^{2+}-dependent scramblases (Suzuki et al., 2010; Whitlock and Hartzell, 2017), which are the enzymes that translocate PtdSer to the membrane surface. These scramblases can also be artificially activated by calcium ionophores (Suzuki et al., 2010, 2013b). When we strongly activated Ca^{2+} influx in 18 DIV cortical neurons using the calcium ionophore A23187 (Mattson, 1990) (5 μM for 20 min), we triggered massive PtdSer externalization onto the surface of these cells without inducing cell death (Figure 1G).

Together, the above results demonstrate that all of the essential components of TAM signaling – Tyro3, the ligands Gas6 and Pros1, and PtdSer – are mobilized in and around neurons of the maturing postnatal brain. It is important to note that in most settings the tripartite complex of PtdSer-TAM ligand-TAM receptor has been found to link the membranes of two apposed cells (Lemke, 2013, 2017, 2019), with PtdSer on one cell, a TAM receptor on the apposed cell, and a TAM ligand bridged between (Lemke, 2017). As discussed below, it is likely that such a tripartite PtdSer-Gas6-Tyro3 bridging complex links the apposed pre- and post-synaptic membranes of active synapses.

Immature physiology of *Tyro3*$^{-/-}$ synapses

We have previously described the generation and analysis of full germline mouse loss-of-function mutants for *Tyro3* (Lu et al., 1999). *Tyro3*$^{-/-}$ mice are born in Mendelian ratios, have normal life spans, are fertile as males and females, and display superficially normal histology in the brain and other tissues (Lu et al., 1999; but see Akkermann et al., 2017). They are full-length protein nulls (Figure 1E; Lu et al., 1999; Lu and Lemke, 2001; Lew et al., 2014; Zagorska et al., 2014). Given the localized expression of Tyro3 in neurons of the hippocampus (Figures 1B,D), we first examined the physiology of the synaptic

2 https://endotheliomics.shinyapps.io/ec_atlas/

connection between pre-synaptic CA3 neurons and post-synaptic CA1 neurons – the 'Schaffer collaterals' (Szirmai et al., 2012) – in standard *ex vivo* hippocampal slice preparations (Fourgeaud et al., 2010) prepared from male WT versus *Tyro3*$^{-/-}$ brains (Figure 2A; see Methods). At this synapse, Tyro3 presumably acts post-synaptically, since it is abundantly expressed on the pyramidal dendrites of CA1 neurons, but not by CA3 neurons (Figures 1B,D,E). We stimulated the Schaffer collaterals and recorded field excitatory postsynaptic potentials (fEPSPs), spontaneous excitatory postsynaptic currents (sEPSCs), and miniature excitatory postsynaptic currents [mEPSCs, recorded in the presence of tetrodotoxin (TTX)] in CA1 (Figure 2A) (see Methods).

When we measured the input–output (I-O) relationship of the fEPSP in WT versus *Tyro3*$^{-/-}$ hippocampal slices, we found that both fEPSP peak amplitudes (Figure 2B) and average input–output slopes (Figure 2C) for CA3 to CA1 synapses were smaller in *Tyro3*$^{-/-}$ mice, but this difference was not statistically significant. However, when we monitored sEPSCs, which reflect both action potential-dependent and spontaneous neurotransmitter activity at synapses (recordings performed in the presence of 0.5 μM picrotoxin to block $GABA_A$ transmission), we measured much more substantial physiological deficits (Figure 2D). The mean inter-event intervals between sEPSCs (Figure 2E) were longer, and the average frequency of sEPSCs (Figure 2F) was markedly reduced in *Tyro3*$^{-/-}$ recordings. The average amplitude of sEPSCs was also significantly reduced in the mutants, albeit less so (Figure 2G). When we added TTX to inhibit action potentials and monitor mEPSCs, which report only action potential-independent spontaneous vesicle release, we observed a statistically insignificant decrease in frequency at *Tyro3*$^{-/-}$ synapses (Figure 2H). There was no loss in the induction of hippocampal long-term potentiation (LTP) in *Tyro3*$^{-/-}$ versus WT synapses (Figure 2I).

We also monitored the amplitude and frequency of both EPSCs and mEPSCs in the inter-connected synaptic networks that develop between mouse hippocampal neurons in culture (see Methods). We measured a substantial drop in the average EPSC amplitude in *Tyro3*$^{-/-}$ hippocampal cultures relative to WT cultures (Figure 2J), which was larger than the sEPSC amplitude drop seen in CA3 to CA1 synapses in hippocampal slices (Figure 2G). There was no difference between the average amplitude of mEPSCs in *Tyro3*$^{-/-}$ versus WT hippocampal cultures (Figure 2K). In marked contrast, dramatic reductions in the frequency of both EPSCs (Figure 2L) and mEPSCs (Figure 2M) were measured in cultures of neurons prepared from

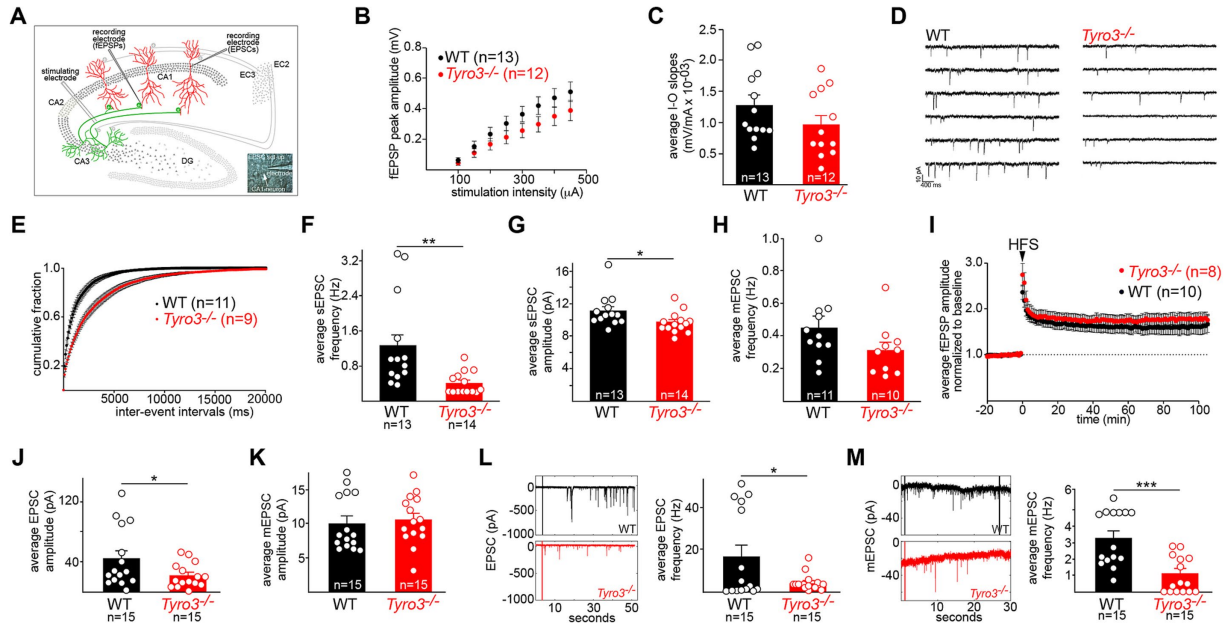

FIGURE 2
Immature synaptic physiology of *Tyro3*$^{-/-}$ neurons. **(A)** Standard *in vitro* recording set-up for mouse hippocampal slices, illustrating the positions of stimulating and recording electrodes within the slice (see Methods). EC, entorhinal cortex. Inset: electrode in a CA1 neuronal cell body. **(B)** Quantification of averaged field excitatory post-synaptic potential (fEPSP) amplitudes (in millivolts, mV) versus stimulus intensity (microamperes, μA) in the indicated number of WT versus *Tyro3*$^{-/-}$ hippocampal slices (one slice per mouse). **(C)** Mean of input–output (I–O) slopes for WT versus *Tyro3*$^{-/-}$ slices. *n* is number of slices for each genotype; one slice per mouse. **(D)** Representative traces of spontaneous EPS currents (sEPSCs) in WT and *Tyro3*$^{-/-}$ slice. **(E)** Cumulative distribution of mean sEPSC inter-event intervals in WT (11 mice) versus *Tyro3*$^{-/-}$ (9 mice). **(F)** Quantification of the average frequency of sEPSCs (Hertz, Hz) in the indicated number of WT versus *Tyro3*$^{-/-}$ cells. **(G)** Quantification of the average amplitude of sEPSCs (pA) in the indicated number of WT versus *Tyro3*$^{-/-}$ cells. For panels **(F,G)**, *p*-values are * <0.05, ** < 0.01, Mann–Whitney test. **(H)** Quantification of the average frequency of mini EPSCs (mEPSCs), recorded in the presence of TTX, in the indicated number of WT versus *Tyro3*$^{-/-}$ cells. *n* is number of cells recorded from 7 WT and 5 *Tyro3*$^{-/-}$ mice. **(I)** Induction of hippocampal LTP by high frequency stimulation (HFS; see Methods) in WT versus *Tyro3*$^{-/-}$ hippocampal slices. *n* is number of slices for each genotype; one slice per mouse. Average fEPSPs are normalized to 10 min baseline. **(J)** Quantification of average EPSC amplitude in picoamperes (pA) in cultured hippocampal neurons prepared from WT versus *Tyro3*$^{-/-}$ mice. **(K)** Quantification of average mEPSC amplitude (pA) in cultured hippocampal neurons prepared from WT versus *Tyro3*$^{-/-}$ mice. **(L)** (Left) representative traces of EPSCs recorded over 50 s in cultured hippocampal neurons prepared from WT versus *Tyro3*$^{-/-}$ mice. (Right) Average EPSC frequency (Hz) in cultured hippocampal neurons prepared from WT and *Tyro3*$^{-/-}$ mice. **(M)** (Left) representative traces of mEPSCs recorded over 30 s in cultured hippocampal neurons prepared from WT versus *Tyro3*$^{-/-}$ mice. (Right) Average mEPSC frequency in cultured hippocampal neurons prepared from WT versus *Tyro3*$^{-/-}$ mice. For panels **(J–M)**, *n* is number of cultured WT and *Tyro3*$^{-/-}$ neurons analyzed. *p*-values: * <0.05; ** <0.01, *** <0.001, Mann–Whitney test.

10.3389/fnins.2024.1327423

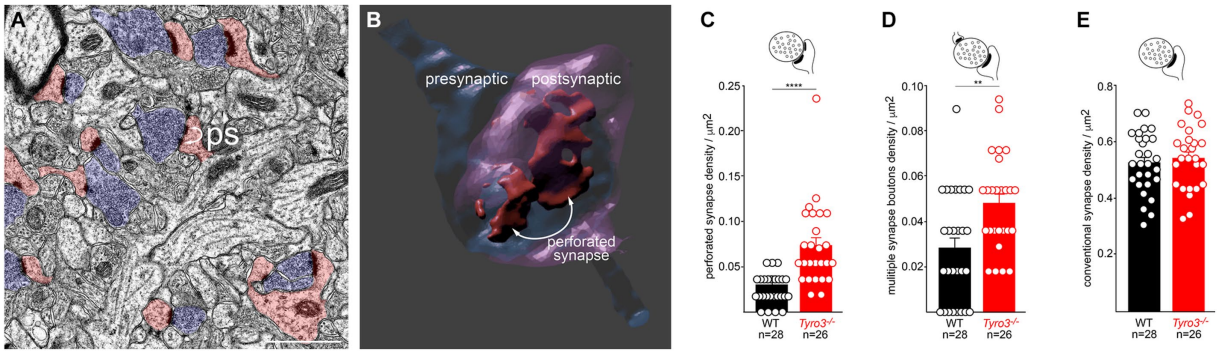

FIGURE 3
Immature ultrastructure of *Tyro3*$^{-/-}$ synapses. **(A)** Representative negatively stained transmission electron microscopic image of the stratum radiatum from the *Tyro3*$^{-/-}$ hippocampus at P60. Synaptic vesicle-filled pre-synaptic axonal boutons are blue. Dendritic spines with post-synaptic densities are pink. Some of these display a non-contiguous post-synaptic density, or 'perforated synapse' (ps; curved arrows). **(B)** 3D image of a perforated synapse reconstructed from serial EM sections, showing a discontinuous post-synaptic density. **(C–E)**, Quantification of the incidence of perforated synapses **(C)**, multiple synapse boutons (**D**, MSB), and conventional synapses **(E)** in WT versus *Tyro3*$^{-/-}$ stratum radiatum, from P60 EM images as in **(A)**. The total number of fields quantified (n) from 3 separate mice of each genotype (6 sections per mouse) is indicated: for WT, 28 quantifications were performed from 18 sections, and for *Tyro3*$^{-/-}$, 26 quantifications were performed from 18 sections. *p*-values: ** <0.01, **** <0.0001, Mann–Whitney test. Scale bar: 1 µm.

Tyro3$^{-/-}$ mutants compared to WT. Taken together, all of the above measurements indicate that *Tyro3*$^{-/-}$ glutamatergic synapses are physiologically impaired relative to their wild-type counterparts, and fire far less frequently.

Immature ultrastructure of *Tyro3*$^{-/-}$ synapses

Given these results, we used transmission electron microscopy (EM) to examine the ultrastructure of synapses in the stratum radiatum (boxed in Figure 1D), the synaptic region in which our hippocampal slice recordings were performed, in both adult WT and *Tyro3*$^{-/-}$ mice. We analyzed multiple slices from three mice of each genotype. In EM images of osmium tetroxide-stained ultrathin sections, synapses are readily identified by the apposition of synaptic-vesicle-filled pre-synaptic axonal varicosities (blue boutons in Figure 3A) to post-synaptic dendritic spines (pink dendritic structures in Figure 3A; Harris and Weinberg, 2012). We quantified the presence of perforated synapses (ps in Figure 3A), which are discontinuous distributions of electron-dense post-synaptic densities, since these structures have been found to be more prevalent in developing, remodeling, and immature synaptic connections (Luscher et al., 2000; Connor et al., 2006; Nicholson et al., 2006; Nicholson and Geinisman, 2009). Three-dimensional reconstructions of serial sections (example in Figure 3B) revealed that perforated synapses typically displayed complex electron-dense post-synaptic densities that were split into multiple distinct domains. We found that the incidence of these perforated synapses was 2.7-fold greater in the stratum radiatum of *Tyro3*$^{-/-}$ as compared to WT mice (Figure 3C). Multiple synapse boutons (msb), endings that make synaptic contacts with more than one spine, have similarly been found to be more prevalent in immature synapses. Correspondingly, we quantified 1.8-fold higher levels of multiple synapse boutons in the *Tyro3*$^{-/-}$ as compared to the WT hippocampus (Figure 3D). Importantly, the density of morphologically conventional synapses – measured at ~0.52/µm^2 - was unchanged between these two genotypes (Figure 3E). Note that even in the *Tyro3*$^{-/-}$ hippocampus, these conventional synapses outnumber perforated synapses by approximately 10 to 1. Although their cytology is apparently normal in the EM, the physiological data of Figure 2 indicate that these *Tyro3*$^{-/-}$ 'conventional' synapses fire less frequently than their WT counterparts.

Regulation of AMPA receptor membrane insertion by Tyro3

A key event in the maturation of glutamatergic synapses in the hippocampus and cortex is the translocation of the AMPA glutamate receptor (AMPAR) subunit GluA2 from intracellular vesicular compartments to the surface plasma membrane at the synaptic cleft (Huganir and Nicoll, 2013; Hanley, 2014). This translocation leads to a switch in the preponderance of glutamate receptor subtypes present at excitatory synapses - from N-methyl-D-Aspartate (NMDA)-type receptors and non-GluA2-containing AMPARs, both of which form calcium-permeable channels - to NMDA-type receptors and GluA2-containing receptors, the latter forming calcium-impermeable channels (Kumar et al., 2002; Brill and Huguenard, 2008; Huganir and Nicoll, 2013). This switch in turn drives synapse maturation by inhibiting calcium-dependent plasticity pathways (Jia et al., 1996; Kumar et al., 2002; Brill and Huguenard, 2008; Traynelis et al., 2010; Henley and Wilkinson, 2016). Putative loss-of-function variants in the human GluA2 (*GRIA2*) gene have been associated with several neurodevelopmental disorders (Salpietro et al., 2019).

We monitored the appearance of GluA2 on the surface of live cultured mouse cortical neurons with a GluA2 antibody (Blanco-Suarez et al., 2018) added to the culture medium, and quantified surface GluA2 fluorescence signals with Imaris software, as described previously (see Methods). We carried out our analyses with neuronal cultures at 18–20 DIV, when all components of the TAM signaling pathway are present (Supplementary Figures S1A–D). We first compared surface GluA2 expression in WT versus *Tyro3*$^{-/-}$ cortical

neurons. We quantified a 50% reduction in GluA2 expression, normalized to cell volume (quantified with CellTracker Red), in mutant versus WT cells (Figures 4A,B). It is important to note that mutation of *Tyro3* did not result in any change in cortical neuron volume (Figure 4C).

We then examined the ability of recombinant mouse Gas6, which acts as a potent Tyro3 ligand, to drive surface plasma membrane insertion of GluA2 in WT cortical neurons. We found that 7 days treatment with 20 nM Gas6 led to a 4-fold increase in surface GluA2, while a 24 h incubation resulted in a twofold increase (Figures 4D,E). The TAM RTKs are the only receptor system through which Gas6 is known to signal (Lew et al., 2014), and cortical neurons do not express Axl or Mer. As noted above, TAM signaling is dependent on the binding of the amino-terminal Gla domain of Gas6 (and Pros1) to the phospholipid PtdSer, which is externalized on the plasma membrane surface of cultured neurons (Figure 1G). When we treated cultured cortical neurons with recombinant Gla-less Gas6, an amino-terminally truncated protein that binds to TAM receptors with normal affinity but that cannot bind PtdSer and cannot normally activate the kinase activity of Tyro3 (Lew et al., 2014), we found that it was incapable of driving GluA2 insertion into the neuronal plasma membrane (Figures 4D,E). Consistent with all of these effects, we found that 24 h pre-treatment with 100 nM recombinant Annexin V, a high-affinity PtdSer binding protein (Tait et al., 1989; Fadok et al., 1992), completely blocked the ability of full-length Gas6 to stimulate the cell surface expression of GluA2 (Figures 4F,G). These results are consistent with the display of PtdSer on a pre-synaptic neuronal plasma membrane that is facing a Tyro3-containing post-synaptic membrane, with Gas6 interposed as a bridge between these two membranes.

Behavioral consequences of *Tyro3* mutation

The above results demonstrate that Tyro3 activation promotes the insertion of GluA2 AMPAR subunits into the neuronal plasma membrane, that *Tyro3*$^{-/-}$ synapses *in vivo* are GluA2-deficient, and that these synapses are physiologically and ultrastructurally immature. These observations are consistent with the finding that *Tyro3*$^{-/-}$ synapses in the hippocampus showed no loss of plasticity relative to WT synapses upon induction of LTP (Figure 2I), and with previous work that has demonstrated that hippocampal LTP is dramatically enhanced at synapses that lack all GluA2 (Jia et al., 1996; Mainen et al., 1998). Given these findings, we assessed the extent to which *Tyro3* gene deletion effected adult (P84–98) mouse behavior in two different assays. Prior to carrying out these assays, we first used continuous video monitoring in open fields (Seibenhener and Wooten, 2015) (see Methods) to ascertain that both overall mouse locomotion and anxiety behavior were unaffected by the mutation of *Tyro3* (Supplementary Figures S2A,B). One physiological feature that was increasingly affected with increasing age was body weight, as WT mice were 10% heavier than *Tyro3*$^{-/-}$ mice by 7 months of age (Supplementary Figure S2C). This small effect did not contribute to the behavioral differences described below, since spatial memory and fear conditioning tests were performed at 3 months, when the weight of WT and *Tyro3*$^{-/-}$ mice was not statistically different (Supplementary Figure S2C). As discussed below, however, it may be relevant to potential Tyro3 regulation of feeding behavior.

We assessed spatial memory acquisition using a standard Morris water maze test (Morris, 1984; Vorhees and Williams, 2006) (see Methods). In the spatial acquisition phase of this assay, mice are trained over the course of 10 days to locate and remember the position of a platform submerged just below the surface of an opaque pool of water (see Methods). We found that *Tyro3*$^{-/-}$ mice performed better than their WT counterparts at this task. After 3 days of initial training, the mutant mice consistently – across days 4 through 10 of assay – took significantly less time to locate the submerged platform than WT mice (Figure 5A).

This effect, while statistically significant, was nonetheless small. We additionally performed a contextual fear conditioning test in which we quantified the ability of mice to remember the association between a context and an aversive mild electrical stimulus (Kitamura et al., 2014) (see Methods). After a 10-min period of free exploration on the first day, mice were returned to the same context on the second day, where they were allowed 42 s to establish an association between electric shocks (2 s, 0.5 mA) and the environment. On the third day, freezing behaviors were monitored in both the conditioning context and a novel context. We found that *Tyro3*$^{-/-}$ mice displayed a significantly enhanced memory recall in the conditioning context, as quantified by freezing time, relative to WT (Figure 5B). No difference in freezing time was observed between genotypes in a novel context. Thus, in both of these behavioral assays, the *Tyro3*$^{-/-}$ mutants exhibited improved performance consistent with increased synaptic plasticity.

A model for Tyro3 activity at glutamatergic synapses

All of the above results are consistent with a model in which post-synaptic activation of the catalytic activity of the Tyro3 tyrosine kinase drives the maturation of glutamatergic synapses by promoting the plasma membrane insertion of GluA2-containing AMPA receptors and the consolidation of the post-synaptic density (Figure 6). As noted above, GluA2 insertion is required for synaptic stabilization and maturation because it renders heteromultimeric AMPARs Ca^{2+}-impermeable. Our model requires pre-synaptic externalization and plasma membrane display of the phospholipid PtdSer, which is activated by depolarization of pre-synaptic terminals (Figure 6, center). As discussed below, PtdSer externalization is carried out by two large families of scramblase enzymes, one of which is controlled (activated) by Ca^{2+} (Suzuki et al., 2010; Whitlock and Hartzell, 2017; Whitlock, 2021). Since calcium enters pre-synaptic terminals through voltage-activated calcium channels upon the arrival of an action potential (Bean, 2007), and since multiple Ca^{2+}-dependent scramblases are widely expressed in the brain (Suzuki et al., 2013b), Ca^{2+} entry would activate these scramblases. The resulting surface expression of PtdSer would provide binding sites for the Gla domains of the TAM ligands Gas6 and Pros1, without which effective Tyro3 activation cannot occur. Post-synaptic Tyro3 engagement is in turn known to activate a series of downstream kinases that have been found to be required for GluA2 translocation from intracellular stores to the post-synaptic plasma membrane surface (Chan et al., 2011; Anggono et al., 2013). At a *Tyro3*$^{-/-}$ synapse, pre-synaptic PtdSer externalization still occurs upon depolarization (Figure 6, right), but post-synaptic insertion of GluA2 cannot occur. This model provides a fundamentally new mechanism whereby coupled pre- and post-synaptic activity drives the maturation of synapses (Figure 6).

10.3389/fnins.2024.1327423

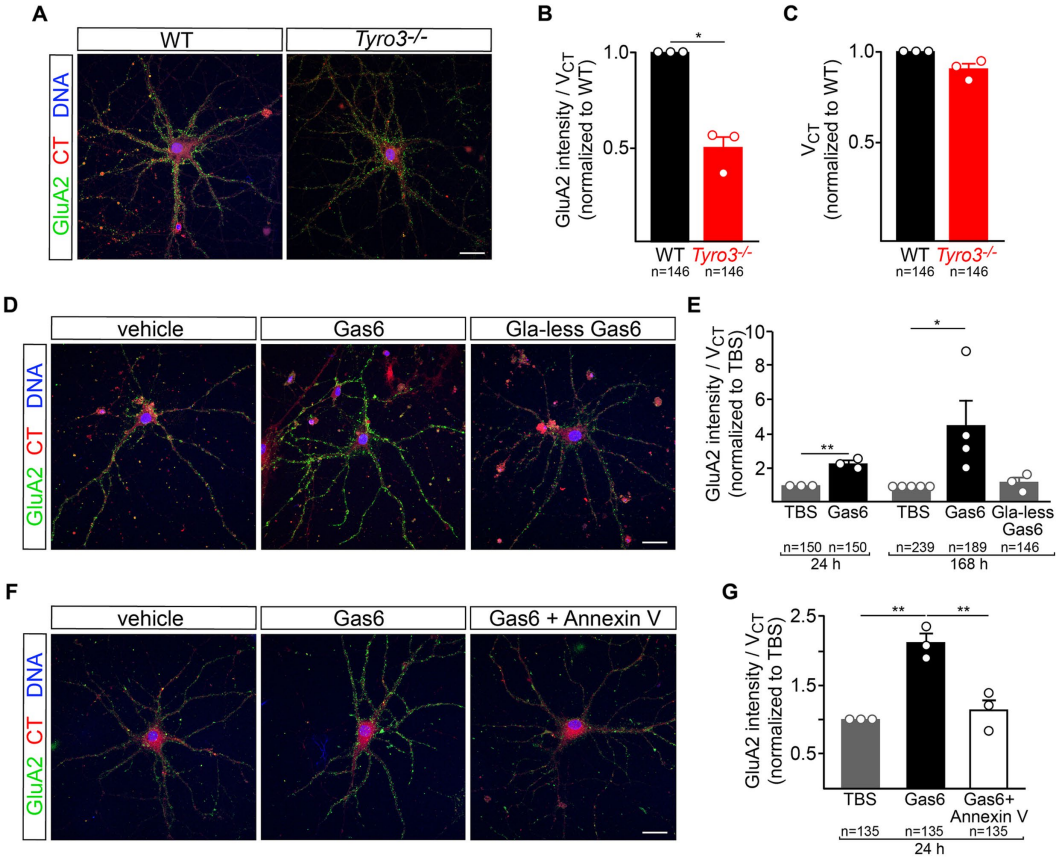

FIGURE 4
Tyro3 activation drives membrane insertion of GluA2. **(A)** Representative images of GluA2 surface expression, detected by 30 min incubation with a GluA2 antibody (Blanco-Suarez et al., 2018), in cortical neurons prepared from WT versus *Tyro3*$^{-/-}$ mice, at 18DIV. **(B)** Imaris quantification of GluA2 surface expression per cell volume (V_{CT}, quantified by CellTracker Red staining), normalized to WT, in WT versus *Tyro3*$^{-/-}$ neurons. In this panel, and in panels **(C,E,G)**, *n* is the total of number of neurons analyzed from 3 to 5 separate culturing experiments (of the indicated genotypes) for each of the various experiments, with the number of culturing experiments indicated by the number of plotted data points. The value of these plotted points is the average of all cells analyzed in the same culturing experiment. **(C)** Imaris quantification of cell volume (V_{CT}) normalized to WT in WT versus *Tyro3*$^{-/-}$ neurons. **(D)** Representative images of GluA2 surface expression in cortical neurons at 18DIV treated for 7 days with vehicle control (TBS, left), 20 nM recombinant Gas6 (middle), or 20 nM recombinant Gla-less Gas6, which binds but does not activate Tyro3 (right). **(E)** Imaris quantification of GluA2 surface expression per cell volume (V_{CT}) in neurons incubated with the indicated reagents for the indicated times, normalized to TBS. **(F)** Representative images of GluA2 surface expression in cortical neurons treated for 1 day with vehicle control (TBS, left), 20 nM recombinant mouse Gas6 (middle), or 20 nM recombinant mouse Gas6 plus 100 nM Annexin V (right). **(G)** Imaris quantification of GluA2 surface expression per cell volume (V_{CT}) in neurons incubated with the indicated reagents for 24 h, normalized to TBS. *p*-values: * <0.05, ** <0.01. Scale bars: 20 μm.

Discussion

In Hebbian learning, neurons that fire together, wire together (Hebb, 1949; Morris, 1999). Our results suggest that post-synaptic Tyro3 signaling provides one molecular mechanism through which coordinated electrical activity drives Hebbian synaptic consolidation. Our model for Tyro3 action in the stabilization and maturation of post-synaptic dendritic spines requires the externalization of the phospholipid PtdSer on pre-synaptic axonal boutons (Figure 6). As noted above, this externalization can only be achieved through the action of large 10-transmembrane-domain enzymes known as scramblases, since the inner-to-outer leaflet exchange of any phospholipid has a high energy barrier (15–50 kcal/mol) and cannot occur spontaneously (Kornberg and McConnell, 1971; Whitlock and Hartzell, 2017). These scramblases fall into two distinct families – the TMEM16 family, also referred to as Anoctamins, which are encoded by 10 human genes (Suzuki et al., 2010, 2013b; Whitlock and Hartzell, 2017; Watanabe et al., 2018); and the XKR family, which encompasses 9 human genes (Nagata, 2018; Lemke, 2019). We favor the possibility that TMEM16/Anoctamin proteins (gene names *Ano1-10*) may operate in our model at pre-synaptic terminals, since these enzymes are activated by the intracellular Ca^{2+} that rises dramatically with the arrival of an action potential, and since *Ano8*, *Ano10*, and especially *Ano6* (*TMEM16F*) mRNAs are highly and widely expressed by CNS neurons (Suzuki et al., 2013b; Zhang et al., 2014). Our results indicate that electrically-active cortical neurons in culture display externalized PtdSer, and that calcium entry into these cells triggered by brief exposure to a calcium ionophore results in exuberant PtdSer expression on the membrane surface (Figure 1G). The TMEM16F enzyme expressed by CNS neurons is the most widely studied of the Ca^{2+}-regulated scramblases (Soulard et al., 2020). However, we do not exclude a role for XKR family scramblases, since elevated levels of activated (cleaved) caspases, notably cleaved caspase 3, have been detected in proteomic analyses of murine synaptosomes (Gyorffy et al., 2018), and caspase cleavage is required for the activation of the XKR scramblases XKR4, 8, and 9 (Nagata and Segawa, 2021).

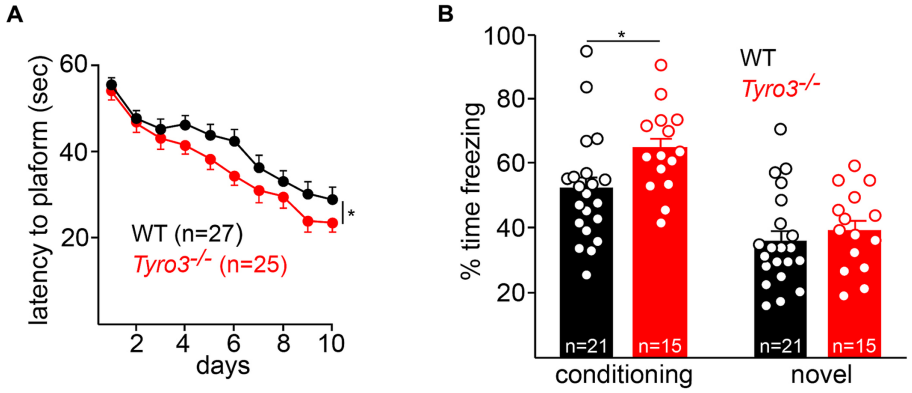

FIGURE 5
Behavioral improvements in *Tyro3*$^{-/-}$ mice. **(A)** Adult *Tyro3*$^{-/-}$ mice take less time to detect the submerged platform in a Morris water maze test (see Methods) than their WT counterparts beginning at 3 days of testing. **(B)** When returned to the training ('conditioning') context, *Tyro3*$^{-/-}$ mice exhibit enhanced memory recall, as monitored by elevated freezing behavior (left). No difference in freezing is detected when mice are placed in a novel context (right). *n* is total number of mice tested per genotype. *P*-values: * <0.05.

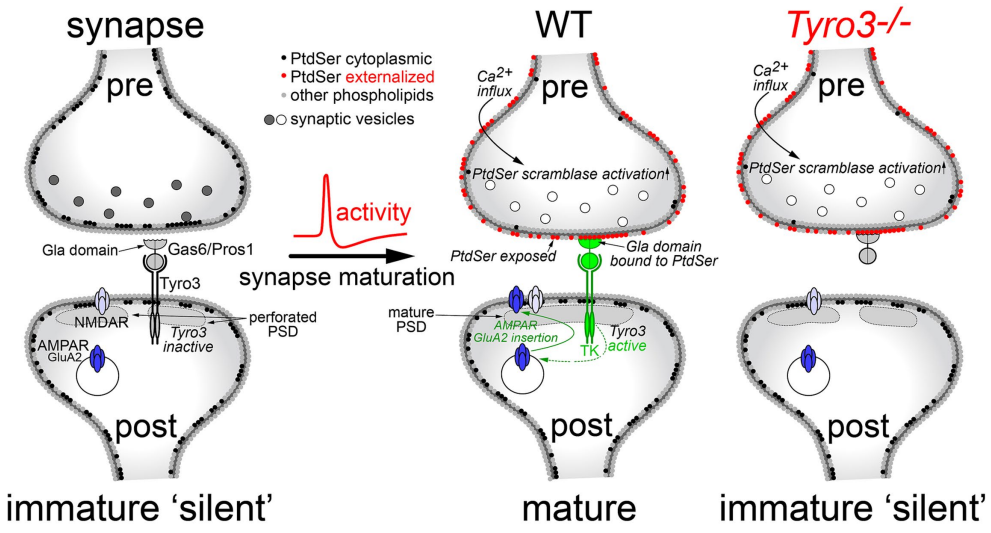

FIGURE 6
A model for Tyro3-driven synaptic maturation. In a developing, electrically silent synapse (left), PtdSer is confined to the inner leaflet of the pre-synaptic plasma membrane (black circles) by the action of flippases, which operate in all cells. The lack of PtdSer externalization means that the Gla domains of the extracellular Tyro3 ligands Gas6 and Pros1 cannot bind this phospholipid, which is required for Tyro3 activation. In the absence of Tyro3 activation, many of the GluA2 AMPA receptor subunits required for mature synapses (AMPAR, dark blue) remain in internal endosomes. These are not transported to the plasma membrane surface, which largely contains NMDA-activated glutamate receptors (NMDAR, light blue) and non-GluA2-containing AMPA receptors, both of which are calcium permeable. As a group, these immature synapses also display an elevated incidence of cytologically disorganized and non-contiguous, or perforated, post-synaptic densities (PSDs). Upon the arrival of an action potential at the pre-synaptic terminal, Ca^{2+} flows into the terminal resulting in the activation of Ca^{2+}-dependent scramblases (middle). This scramblase activation leads to PtdSer externalization on the pre-synaptic plasma membrane surface (red circles), where it can bind to the Gas6/Pros1 Gla domains. Coincident Gas6/Pros1 binding to PtdSer and Tyro3 strongly activates the Tyro3 tyrosine kinase (TK), which promotes both the transport of GluA2 subunits to the post-synaptic plasma membrane surface and the phosphorylation of cytoskeletal proteins (Happonen et al., 2023) that results in the consolidation of the PSD. In the absence of Tyro3 (right), PtdSer is still externalized, but post-synaptic Tyro3 signaling cannot occur. Gray and white synaptic vesicles represent transmitter-filled and transmitter-released vesicles, respectively.

The proteins that bridge PtdSer on the pre-synaptic membrane to Tyro3 on the post-synaptic membrane are the TAM ligands Gas6 and Pros1. The *Gas6* gene is very widely and constitutively expressed in neurons across many areas of the postnatal and adult CNS, including neurons of the neocortex, and in pyramidal neurons across all fields of the hippocampus, with high expression in CA3 (Prieto et al., 1999). All CNS microglia also express abundant *Gas6* mRNA (Imm Gen, 2016). Neuronal expression of the *Pros1* gene is much more restricted, with *Pros1* mRNA and protein detected in neural stem cells, but prominent CNS expression of *Pros1* mRNA is detected in endothelial cells, microglia, and astrocytes (Imm Gen, 2016; Zelentsova et al., 2017; Zelentsova-Levytskyi et al., 2017; Happonen et al., 2023) (see footnote 2). Pros1 is also present at ~300 nM in the CNS circulation (Burstyn-Cohen et al., 2009). Together, these observations indicate that the ligands required to activate Tyro3 are very widely expressed in the brain, and can in principle be delivered to neurons from multiple sources.

In general, the electrophysiological and ultrastructural properties of glutamatergic synapses in the *Tyro3*$^{-/-}$ hippocampus and cortex are characteristic of synaptic pairings that have stalled at a late stage of differentiation. These synapses are immature by multiple measures and display modification plasticities that are consistent with diminished synaptic membrane expression of the GluA2 subunit of ionotropic glutamate receptors. For example, the observation that CA3-to-CA1 LTP is not lost in *Tyro3*$^{-/-}$ hippocampal slices is consistent with the deficit in surface GluA2 expression that we detected in *Tyro3*$^{-/-}$ neurons (Figures 4A,B), since hippocampal slices prepared from *GluA2*$^{-/-}$ mice, which lack all GluA2, display enhanced LTP (Jia et al., 1996; Gerlai et al., 1998). The modest behavioral improvements in spatial memory and fear conditioning that we detected in the *Tyro3*$^{-/-}$ mice are also consistent with synaptic connections that are plastic. Similar behavioral improvements have been documented upon loss-of-function mutation of many 'memory suppressor genes' (Abel et al., 1998; Lee and Silva, 2009; Noyes et al., 2021). Again, we posit that an important component of *Tyro3*$^{-/-}$ plasticity is the reduced expression of GluA2-containing glutamate receptors at the post-synaptic membrane surface. Although *Tyro3*$^{-/-}$ synapses are deficient in these receptors, they presumably have a normal complement of the NMDA receptors that populate immature synapses (Ramoa and McCormick, 1994; Kim et al., 1995; Lopez de Armentia and Sah, 2003) and normal glutamate release, although we did not test either of these points in this work. Our electrophysiological results clearly indicate that the *Tyro3*$^{-/-}$ stratum radiatum has fewer active synapses, yet the number of synapses we measured by EM was either the same (for conventional synapses) or increased (for perforated synapses). We do not currently have an explanation for this difference.

An additional feature of the *Tyro3*$^{-/-}$ mice that may be relevant to an influence of this RTK on later behavior (after the time period of our assays) is the modest but clear weight loss that we observed as the knockouts aged (Supplementary Figure S2C). A mutation in the signal sequence of the mouse *Tyro3* gene (R7W), which resides within the critical interval that defines the *anorexia* (*anx*) mutation in *anx*/*anx* mice (Maltais et al., 1984), but is not the *anx* mutation itself, has been shown to be an important genetic modifier of the phenotype exhibited by these anorexic mice (Kim et al., 2017). Although they are able to eat and have full access to milk, *anx/anx* mice die at 3–5 weeks after birth due to starvation and emaciation (Nilsson, 2019). Tyro3 is expressed in regions of the hypothalamus (e.g., the arcuate nucleus) that control feeding behavior; and transgenic CNS expression of a WT *Tyro3* transgene, but not an *R7W Tyro3* transgene, has been found to double the weight and lifespans of *anx/anx* mice (Kim et al., 2017).

Data availability statement

The original contributions presented in the study are included in the article/Supplementary material, further inquiries can be directed to the corresponding author.

Ethics statement

The animal study was approved by Salk Institute Animal Care and Use Committee. The study was conducted in accordance with the local legislation and institutional requirements.

Author contributions

SM: Conceptualization, Data curation, Formal analysis, Investigation, Methodology, Supervision, Writing – review & editing. LF: Conceptualization, Data curation, Writing – review & editing, Investigation, Methodology. PB: Formal analysis, Investigation, Methodology, Writing – review & editing. SS: Data curation, Investigation, Methodology, Writing – review & editing. YZ: Data curation, Investigation, Writing – review & editing. KH: Data curation, Writing – review & editing. SN: Methodology, Writing – review & editing, Data curation. FG: Methodology, Writing – review & editing. GL: Conceptualization, Data curation, Formal analysis, Funding acquisition, Project administration, Resources, Supervision, Writing – original draft, Writing – review & editing.

Funding

The author(s) declare financial support was received for the research, authorship, and/or publication of this article. This work was supported by grants from the US National Institutes of Health (RF1 AG060748 and R01 AI101400 to GL, and P30 CA014195 and S10-OD023689 to the Salk Institute), the Leona M. and Harry B. Helmsley Charitable Trust (to the Salk Institute), and Ferring Pharmaceuticals.

Acknowledgments

We thank Joseph Hash for excellent technical assistance, Francisco Tapia for independent experimental quantification of perforated synapses and multiple synapse boutons in electron micrographs, and members of the Lemke lab and the Nomis Center for discussions.

Conflict of interest

The authors declare that the research was conducted in the absence of any commercial or financial relationships that could be construed as a potential conflict of interest.

Publisher's note

All claims expressed in this article are solely those of the authors and do not necessarily represent those of their affiliated organizations, or those of the publisher, the editors and the reviewers. Any product that may be evaluated in this article, or claim that may be made by its manufacturer, is not guaranteed or endorsed by the publisher.

Supplementary material

The Supplementary material for this article can be found online at: https://www.frontiersin.org/articles/10.3389/fnins.2024.1327423/full#supplementary-material

References

Abel, T., Martin, K. C., Bartsch, D., and Kandel, E. R. (1998). Memory suppressor genes: inhibitory constraints on the storage of long-term memory. *Science* 279, 338–341. doi: 10.1126/science.279.5349.338

Akkermann, R., Aprico, A., Perera, A. A., Bujalka, H., Cole, A. E., Xiao, J., et al. (2017). The TAM receptor tyro 3 regulates myelination in the central nervous system. *Glia* 65, 581–591. doi: 10.1002/glia.23113

Andersen, J. P., Vestergaard, A. L., Mikkelsen, S. A., Mogensen, L. S., Chalat, M., and Molday, R. S. (2016). P 4-ATPases as phospholipid Flippases-structure, function, and enigmas. *Front. Physiol.* 7:275. doi: 10.3389/fphys.2016.00275

Anggono, V., Koc-Schmitz, Y., Widagdo, J., Kormann, J., Quan, A., Chen, C. M., et al. (2013). PICK1 interacts with PACSIN to regulate AMPA receptor internalization and cerebellar long-term depression. *Proc. Natl. Acad. Sci. USA* 110, 13976–13981. doi: 10.1073/pnas.1312467110

Bean, B. P. (2007). The action potential in mammalian central neurons. *Nat. Rev. Neurosci.* 8, 451–465. doi: 10.1038/nrn2148

Beaudoin, G. M., Lee, S. H., Singh, D., Yuan, Y., Ng, Y. G., Reichardt, L. F., et al. (2012). Culturing pyramidal neurons from the early postnatal mouse hippocampus and cortex. *Nat. Protoc.* 7, 1741–1754. doi: 10.1038/nprot.2012.099

Blackstone, C. D., Moss, S. J., Martin, L. J., Levey, A. I., Price, D. L., and Huganir, R. L. (1992). Biochemical characterization and localization of a non-N-methyl-D-aspartate glutamate receptor in rat brain. *J. Neurochem.* 58, 1118–1126. doi: 10.1111/j.1471-4159.1992.tb09370.x

Blades, F., Wong, V. H. Y., Nguyen, C. T. O., Bui, B. V., Kilpatrick, T. J., and Binder, M. D. (2020). Tyro 3 contributes to retinal ganglion cell function, survival and dendritic density in the mouse retina. *Front. Neurosci.* 14:840. doi: 10.3389/fnins.2020.00840

Blanco-Suarez, E., Liu, T. F., Kopelevich, A., and Allen, N. J. (2018). Astrocyte-secreted chordin-like 1 drives synapse maturation and limits plasticity by increasing synaptic Glu A2 AMPA receptors. *Neuron* 100, 1116–1132.e13. doi: 10.1016/j.neuron.2018.09.043

Brill, J., and Huguenard, J. R. (2008). Sequential changes in AMPA receptor targeting in the developing neocortical excitatory circuit. *J. Neurosci.* 28, 13918–13928. doi: 10.1523/JNEUROSCI.3229-08.2008

Burstyn-Cohen, T., Heeb, M. J., and Lemke, G. (2009). Lack of protein S in mice causes embryonic lethal coagulopathy and vascular dysgenesis. *J. Clin. Invest.* 119, 2942–2953. doi: 10.1172/JCI39325

Burstyn-Cohen, T., Lew, E. D., Traves, P. G., Burrola, P. G., Hash, J. C., and Lemke, G. (2012). Genetic dissection of TAM receptor-ligand interaction in retinal pigment epithelial cell phagocytosis. *Neuron* 76, 1123–1132. doi: 10.1016/j.neuron.2012.10.015

Chan, P. Y., Carrera Silva, E. A., De Kouchkovsky, D., Joannas, L. D., Hao, L., Hu, D., et al. (2016). The TAM family receptor tyrosine kinase TYRO3 is a negative regulator of type 2 immunity. *Science* 352, 99–103. doi: 10.1126/science.aaf1358

Chan, C. B., Chen, Y., Liu, X., Tang, X., Lee, C. W., Mei, L., et al. (2011). PIKE-mediated PI3-kinase activity is required for AMPA receptor surface expression. *EMBO J.* 30, 4274–4286. doi: 10.1038/emboj.2011.281

Connor, S., Williams, P. T., Armstrong, B., Petit, T. L., Ivanco, T. L., and Weeks, A. C. (2006). Long-term potentiation is associated with changes in synaptic ultrastructure in the rat neocortex. *Synapse* 59, 378–382. doi: 10.1002/syn.20248

Dransfield, I., Zagorska, A., Lew, E. D., Michail, K., and Lemke, G. (2015). Mer receptor tyrosine kinase mediates both tethering and phagocytosis of apoptotic cells. *Cell Death Dis.* 6:e1646. doi: 10.1038/cddis.2015.18

Fadok, V. A., Voelker, D. R., Campbell, P. A., Cohen, J. J., Bratton, D. L., and Henson, P. M. (1992). Exposure of phosphatidylserine on the surface of apoptotic lymphocytes triggers specific recognition and removal by macrophages. *J. Immunol.* 148, 2207–2216. doi: 10.4049/jimmunol.148.7.2207

Fourgeaud, L., Davenport, C. M., Tyler, C. M., Cheng, T. T., Spencer, M. B., and Boulanger, L. M. (2010). MHC class I modulates NMDA receptor function and AMPA receptor trafficking. *Proc. Natl. Acad. Sci. USA* 107, 22278–22283. doi: 10.1073/pnas.0914064107

Fourgeaud, L., Traves, P. G., Tufail, Y., Leal-Bailey, H., Lew, E. D., Burrola, P. G., et al. (2016). TAM receptors regulate multiple features of microglial physiology. *Nature* 532, 240–244. doi: 10.1038/nature17630

Fujita, K., Chen, X., Homma, H., Tagawa, K., Amano, M., Saito, A., et al. (2018). Targeting tyro 3 ameliorates a model of PGRN-mutant FTLD-TDP via tau-mediated synaptic pathology. *Nat. Commun.* 9:433. doi: 10.1038/s41467-018-02821-z

Funakoshi, H., Yonemasu, T., Nakano, T., Matumoto, K., and Nakamura, T. (2002). Identification of gas 6, a putative ligand for sky and Axl receptor tyrosine kinases, as a novel neurotrophic factor for hippocampal neurons. *J. Neurosci. Res.* 68, 150–160. doi: 10.1002/jnr.10211

Geinisman, Y., Morrell, F., and de Toledo-Morrell, L. (1987). Axospinous synapses with segmented postsynaptic densities: a morphologically distinct synaptic subtype contributing to the number of profiles of 'perforated' synapses visualized in random sections. *Brain Res.* 423, 179–188. doi: 10.1016/0006-8993(87)90838-9

Gerlai, R., Henderson, J. T., Roder, J. C., and Jia, Z. (1998). Multiple behavioral anomalies in Glu R2 mutant mice exhibiting enhanced LTP. *Behav. Brain Res.* 95, 37–45. doi: 10.1016/S0166-4328(98)00002-3

Graham, D. K., Dawson, T. L., Mullaney, D. L., Snodgrass, H. R., and Earp, H. S. (1994). Cloning and mRNA expression analysis of a novel human protooncogene, c-mer. *Cell Growth Differ.* 5, 647–657.

Graham, D. K., DeRyckere, D., Davies, K. D., and Earp, H. S. (2014). The TAM family: phosphatidylserine sensing receptor tyrosine kinases gone awry in cancer. *Nat. Rev. Cancer* 14, 769–785. doi: 10.1038/nrc3847

Gyorffy, B. A., Kun, J., Torok, G., Bulyaki, E., Borhegyi, Z., Gulyassy, P., et al. (2018). Local apoptotic-like mechanisms underlie complement-mediated synaptic pruning. *Proc. Natl. Acad. Sci. U. S. A* 115, 6303–6308. doi: 10.1073/pnas.1722613115

Hanley, J. G. (2014). Subunit-specific trafficking mechanisms regulating the synaptic expression of ca (2+)-permeable AMPA receptors. *Semin. Cell Dev. Biol.* 27, 14–22. doi: 10.1016/j.semcdb.2013.12.002

Happonen, K. E., Burrola, P. G., and Lemke, G. (2023). Regulation of brain endothelial cell physiology by the TAM receptor tyrosine kinase Mer. *Commun. Biol.* 6:916. doi: 10.1038/s42003-023-05287-y

Harris, K. M., and Weinberg, R. J. (2012). Ultrastructure of synapses in the mammalian brain. *Cold Spring Harb. Perspect. Biol.* 4. doi: 10.1101/cshperspect.a005587

Hebb, D. O. (1949) *The Organization of Behavior*. Wiley: New York.

Henley, J. M., and Wilkinson, K. A. (2016). Synaptic AMPA receptor composition in development, plasticity and disease. *Nat. Rev. Neurosci.* 17, 337–350. doi: 10.1038/nrn.2016.37

Hilgenberg, L. G., and Smith, M. A. (2007). Preparation of dissociated mouse cortical neuron cultures. *J. Vis. Exp.* 10:562. doi: 10.3791/562

Huang, Y., Happonen, K. E., Burrola, P. G., O'Connor, C., Hah, N., Huang, L., et al. (2021). Microglia use TAM receptors to detect and engulf amyloid beta plaques. *Nat. Immunol.* 22, 586–594. doi: 10.1038/s41590-021-00913-5

Huganir, R. L., and Nicoll, R. A. (2013). AMPARs and synaptic plasticity: the last 25 years. *Neuron* 80, 704–717. doi: 10.1016/j.neuron.2013.10.025

Imm Gen, C. (2016). Open-source Imm Gen: mononuclear phagocytes. *Nat. Immunol.* 17:741. doi: 10.1038/ni.3478

Jia, Z., Agopyan, N., Miu, P., Xiong, Z., Henderson, J., Gerlai, R., et al. (1996). Enhanced LTP in mice deficient in the AMPA receptor Glu R2. *Neuron* 17, 945–956. doi: 10.1016/S0896-6273(00)80225-1

Jones, A. R., Overly, C. C., and Sunkin, S. M. (2009). The Allen brain atlas: 5 years and beyond. *Nat. Rev. Neurosci.* 10, 821–828. doi: 10.1038/nrn2722

Kim, Y. E., Chen, J., Langen, R., and Chan, J. R. (2010). Monitoring apoptosis and neuronal degeneration by real-time detection of phosphatidylserine externalization using a polarity-sensitive indicator of viability and apoptosis. *Nat. Protoc.* 5, 1396–1405. doi: 10.1038/nprot.2010.101

Kim, H. G., Fox, K., and Connors, B. W. (1995). Properties of excitatory synaptic events in neurons of primary somatosensory cortex of neonatal rats. *Cereb. Cortex* 5, 148–157. doi: 10.1093/cercor/5.2.148

Kim, D. Y., Yu, J., Mui, R. K., Niibori, R., Taufique, H. B., Aslam, R., et al. (2017). The tyrosine kinase receptor tyro 3 enhances lifespan and neuropeptide Y (Npy) neuron survival in the mouse anorexia (anx) mutation. *Dis. Model. Mech.* 10, 581–595. doi: 10.1242/dmm.027433

Kitamura, T., Pignatelli, M., Suh, J., Kohara, K., Yoshiki, A., Abe, K., et al. (2014). Island cells control temporal association memory. *Science* 343, 896–901. doi: 10.1126/science.1244634

Kornberg, R. D., and McConnell, H. M. (1971). Inside-outside transitions of phospholipids in vesicle membranes. *Biochemistry* 10, 1111–1120.

Kumar, S. S., Bacci, A., Kharazia, V., and Huguenard, J. R. (2002). A developmental switch of AMPA receptor subunits in neocortical pyramidal neurons. *J. Neurosci.* 22, 3005–3015. doi: 10.1523/JNEUROSCI.22-08-03005.2002

Lai, C., Gore, M., and Lemke, G. (1994). Structure, expression, and activity of tyro 3, a neural adhesion-related receptor tyrosine kinase. *Oncogene* 9, 2567–2578.

Lai, C., and Lemke, G. (1991). An extended family of protein-tyrosine kinase genes differentially expressed in the vertebrate nervous system. *Neuron* 6, 691–704. doi: 10.1016/0896-6273(91)90167-X

Lee, Y. S., and Silva, A. J. (2009). The molecular and cellular biology of enhanced cognition. *Nat. Rev. Neurosci.* 10, 126–140. doi: 10.1038/nrn2572

Lein, P. J., Barnhart, C. D., and Pessah, I. N. (2011). Acute hippocampal slice preparation and hippocampal slice cultures. *Methods Mol. Biol.* 758, 115–134. doi: 10.1007/978-1-61779-170-3_8

Lemke, G. (2013). Biology of the TAM receptors. *Cold Spring Harbor Perspectives* 5. doi: 10.1101/cshperspect.a009076

Lemke, G. (2017). Phosphatidylserine is the signal for TAM receptors and their ligands. *Trends Biochem. Sci.* 42, 738–748. doi: 10.1016/j.tibs.2017.06.004

Lemke, G. (2019). How macrophages deal with death. *Nat. Rev. Immunol.* 19, 539–549. doi: 10.1038/s41577-019-0167-y

Lesuisse, C., and Martin, L. J. (2002). Long-term culture of mouse cortical neurons as a model for neuronal development, aging, and death. *J. Neurobiol.* 51, 9–23. doi: 10.1002/neu.10037

Leventis, P. A., and Grinstein, S. (2010). The distribution and function of phosphatidylserine in cellular membranes. *Annu. Rev. Biophys.* 39, 407–427. doi: 10.1146/annurev.biophys.093008.131234

Lew, E. D., Oh, J., Burrola, P. G., Lax, I., Zagorska, A., Traves, P. G., et al. (2014). Differential TAM receptor-ligand-phospholipid interactions delimit differential TAM bioactivities. *eLife* 3:e03385. doi: 10.7554/eLife.03385

Lopez de Armentia, M., and Sah, P. (2003). Development and subunit composition of synaptic NMDA receptors in the amygdala: NR2B synapses in the adult central amygdala. *J. Neurosci.* 23, 6876–6883. doi: 10.1523/JNEUROSCI.23-17-06876.2003

Lu, Q., Gore, M., Zhang, Q., Camenisch, T., Boast, S., Casagranda, F., et al. (1999). Tyro-3 family receptors are essential regulators of mammalian spermatogenesis. *Nature* 398, 723–728. doi: 10.1038/19554

Lu, Q., and Lemke, G. (2001). Homeostatic regulation of the immune system by receptor tyrosine kinases of the tyro 3 family. *Science* 293, 306–311. doi: 10.1126/science.1061663

Luscher, C., Nicoll, R. A., Malenka, R. C., and Muller, D. (2000). Synaptic plasticity and dynamic modulation of the postsynaptic membrane. *Nat. Neurosci.* 3, 545–550. doi: 10.1038/75714

Mainen, Z. F., Jia, Z., Roder, J., and Malinow, R. (1998). Use-dependent AMPA receptor block in mice lacking Glu R2 suggests postsynaptic site for LTP expression. *Nat. Neurosci.* 1, 579–586. doi: 10.1038/2812

Maltais, L. J., Lane, P. W., and Beamer, W. G. (1984). Anorexia, a recessive mutation causing starvation in preweanling mice. *J. Hered.* 75, 468–472. doi: 10.1093/oxfordjournals.jhered.a109987

Mattson, M. P. (1990). Antigenic changes similar to those seen in neurofibrillary tangles are elicited by glutamate and Ca2+ influx in cultured hippocampal neurons. *Neuron* 4, 105–117. doi: 10.1016/0896-6273(90)90447-N

Morris, R. (1984). Developments of a water-maze procedure for studying spatial learning in the rat. *J. Neurosci. Methods* 11, 47–60. doi: 10.1016/0165-0270(84)90007-4

Morris, R. G. (1999). D.O. Hebb: the Organization of Behavior, Wiley: New York; 1949. *Brain Res. Bull.* 50:437. doi: 10.1016/S0361-9230(99)00182-3

Morris, R. G., Garrud, P., Rawlins, J. N., and O'Keefe, J. (1982). Place navigation impaired in rats with hippocampal lesions. *Nature* 297, 681–683. doi: 10.1038/297681a0

Nagata, S. (2018). Apoptosis and clearance of apoptotic cells. *Annu. Rev. Immunol.* 36, 489–517. doi: 10.1146/annurev-immunol-042617-053010

Nagata, S., and Segawa, K. (2021). Sensing and clearance of apoptotic cells. *Curr. Opin. Immunol.* 68, 1–8. doi: 10.1016/j.coi.2020.07.007

Nicholson, D. A., and Geinisman, Y. (2009). Axospinous synaptic subtype-specific differences in structure, size, ionotropic receptor expression, and connectivity in apical dendritic regions of rat hippocampal CA1 pyramidal neurons. *J. Comp. Neurol.* 512, 399–418. doi: 10.1002/cne.21896

Nicholson, D. A., Trana, R., Katz, Y., Kath, W. L., Spruston, N., and Geinisman, Y. (2006). Distance-dependent differences in synapse number and AMPA receptor expression in hippocampal CA1 pyramidal neurons. *Neuron* 50, 431–442. doi: 10.1016/j.neuron.2006.03.022

Nilsson, I. A. K. (2019). The anx/anx mouse - a valuable resource in anorexia nervosa research. *Front. Neurosci.* 13:59. doi: 10.3389/fnins.2019.00059

Noyes, N. C., Phan, A., and Davis, R. L. (2021). Memory suppressor genes: modulating acquisition, consolidation, and forgetting. *Neuron* 109, 3211–3227. doi: 10.1016/j.neuron.2021.08.001

O'Bryan, J. P., Frye, R. A., Cogswell, P. C., Neubauer, A., Kitch, B., Prokop, C., et al. (1991). Axl, a transforming gene isolated from primary human myeloid leukemia cells, encodes a novel receptor tyrosine kinase. *Mol. Cell. Biol.* 11, 5016–5031.

Ohashi, K., Mizuno, K., Kuma, K., Miyata, T., and Nakamura, T. (1994). Cloning of the cDNA for a novel receptor tyrosine kinase, sky, predominantly expressed in brain. *Oncogene* 9, 699–705.

Pierce, A., Bliesner, B., Xu, M., Nielsen-Preiss, S., Lemke, G., Tobet, S., et al. (2008). Axl and tyro 3 modulate female reproduction by influencing gonadotropin-releasing hormone neuron survival and migration. *Mol. Endocrinol.* 22, 2481–2495. doi: 10.1210/me.2008-0169

Prieto, A. L., O'Dell, S., Varnum, B., and Lai, C. (2007). Localization and signaling of the receptor protein tyrosine kinase tyro 3 in cortical and hippocampal neurons. *Neuroscience* 150, 319–334. doi: 10.1016/j.neuroscience.2007.09.047

Prieto, A. L., Weber, J. L., and Lai, C. (2000). Expression of the receptor protein-tyrosine kinases Tyro-3, Axl, and mer in the developing rat central nervous system. *J. Comp. Neurol.* 425, 295–314. doi: 10.1002/1096-9861(20000918)425:2<295::AID-CNE11>3.0.CO;2-G

Prieto, A. L., Weber, J. L., Tracy, S., Heeb, M. J., and Lai, C. (1999). Gas 6, a ligand for the receptor protein-tyrosine kinase Tyro-3, is widely expressed in the central nervous system. *Brain Res.* 816, 646–661. doi: 10.1016/S0006-8993(98)01159-7

Priller, C., Dewachter, I., Vassallo, N., Paluch, S., Pace, C., Kretzschmar, H. A., et al. (2007). Mutant presenilin 1 alters synaptic transmission in cultured hippocampal neurons. *J. Biol. Chem.* 282, 1119–1127. doi: 10.1074/jbc.M605066200

Ramoa, A. S., and McCormick, D. A. (1994). Enhanced activation of NMDA receptor responses at the immature retinogeniculate synapse. *J. Neurosci.* 14, 2098–2105. doi: 10.1523/JNEUROSCI.14-04-02098.1994

Rothlin, C. V., Carrera-Silva, E. A., Bosurgi, L., and Ghosh, S. (2015). TAM receptor signaling in immune homeostasis. *Annu. Rev. Immunol.* 33, 355–391. doi: 10.1146/annurev-immunol-032414-112103

Rothlin, C. V., Ghosh, S., Zuniga, E. I., Oldstone, M. B., and Lemke, G. (2007). TAM receptors are pleiotropic inhibitors of the innate immune response. *Cell* 131, 1124–1136. doi: 10.1016/j.cell.2007.10.034

Salpietro, V., Dixon, C. L., Guo, H., Bello, O. D., Vandrovcova, J., Efthymiou, S., et al. (2019). AMPA receptor Glu A2 subunit defects are a cause of neurodevelopmental disorders. *Nat. Commun.* 10:3094. doi: 10.1038/s41467-019-10910-w

Scott, R. S., McMahon, E. J., Pop, S. M., Reap, E. A., Caricchio, R., Cohen, P. L., et al. (2001). Phagocytosis and clearance of apoptotic cells is mediated by MER. *Nature* 411, 207–211. doi: 10.1038/35075603

Segawa, K., Kurata, S., and Nagata, S. (2016). Human type IV P-type ATPases that work as plasma membrane phospholipid Flippases and their regulation by caspase and calcium. *J. Biol. Chem.* 291, 762–772. doi: 10.1074/jbc.M115.690727

Segawa, K., Kurata, S., Yanagihashi, Y., Brummelkamp, T. R., Matsuda, F., and Nagata, S. (2014). Caspase-mediated cleavage of phospholipid flippase for apoptotic phosphatidylserine exposure. *Science* 344, 1164–1168. doi: 10.1126/science.1252809

Seibenhener, M. L., and Wooten, M. C. (2015). Use of the open Field maze to measure locomotor and anxiety-like behavior in mice. *J. Vis. Exp.* 96:e52434. doi: 10.3791/52434

Sorra, K. E., and Harris, K. M. (1993). Occurrence and three-dimensional structure of multiple synapses between individual radiatum axons and their target pyramidal cells in hippocampal area CA1. *J. Neurosci.* 13, 3736–3748. doi: 10.1523/JNEUROSCI.13-09-03736.1993

Soulard, C., Salsac, C., Mouzat, K., Hilaire, C., Roussel, J., Mezghrani, A., et al. (2020). Spinal Motoneuron TMEM16F acts at C-boutons to modulate motor resistance and contributes to ALS pathogenesis. *Cell Rep.* 30, 2581–2593.e7. doi: 10.1016/j.celrep.2020.02.001

Stitt, T. N., Conn, G., Gore, M., Lai, C., Bruno, J., Radziejewski, C., et al. (1995). The anticoagulation factor protein S and its relative, gas 6, are ligands for the tyro 3/Axl family of receptor tyrosine kinases. *Cell* 80, 661–670. doi: 10.1016/0092-8674(95)90520-0

Suzuki, J., Denning, D. P., Imanishi, E., Horvitz, H. R., and Nagata, S. (2013a). Xk-related protein 8 and CED-8 promote phosphatidylserine exposure in apoptotic cells. *Science* 341, 403–406. doi: 10.1126/science.1236758

Suzuki, J., Fujii, T., Imao, T., Ishihara, K., Kuba, H., and Nagata, S. (2013b). Calcium-dependent phospholipid scramblase activity of TMEM16 protein family members. *J. Biol. Chem.* 288, 13305–13316. doi: 10.1074/jbc.M113.457937

Suzuki, J., Imanishi, E., and Nagata, S. (2016). Xkr 8 phospholipid scrambling complex in apoptotic phosphatidylserine exposure. *Proc. Natl. Acad. Sci. USA* 113, 9509–9514. doi: 10.1073/pnas.1610403113

Suzuki, J., Umeda, M., Sims, P. J., and Nagata, S. (2010). Calcium-dependent phospholipid scrambling by TMEM16F. *Nature* 468, 834–838. doi: 10.1038/nature09583

Szirmai, I., Buzsaki, G., and Kamondi, A. (2012). 120 years of hippocampal Schaffer collaterals. *Hippocampus* 22, 1508–1516. doi: 10.1002/hipo.22001

Tait, J. F., Gibson, D., and Fujikawa, K. (1989). Phospholipid binding properties of human placental anticoagulant protein-I, a member of the lipocortin family. *J. Biol. Chem.* 264, 7944–7949. doi: 10.1016/S0021-9258(18)83133-7

Traynelis, S. F., Wollmuth, L. P., McBain, C. J., Menniti, F. S., Vance, K. M., Ogden, K. K., et al. (2010). Glutamate receptor ion channels: structure, regulation, and function. *Pharmacol. Rev.* 62, 405–496. doi: 10.1124/pr.109.002451

Vorhees, C. V., and Williams, M. T. (2006). Morris water maze: procedures for assessing spatial and related forms of learning and memory. *Nat. Protoc.* 1, 848–858. doi: 10.1038/nprot.2006.116

Watanabe, R., Sakuragi, T., Noji, H., and Nagata, S. (2018). Single-molecule analysis of phospholipid scrambling by TMEM16F. *Proc. Natl. Acad. Sci. U. S. A.* 115, 3066–3071. doi: 10.1073/pnas.1717956115

Whitlock, J. M. (2021). The taming of a scramblase. *J. Gen. Physiol.* 153. doi: 10.1085/jgp.202012831

Whitlock, J. M., and Hartzell, H. C. (2017). Anoctamins/TMEM16 proteins: chloride channels flirting with lipids and extracellular vesicles. *Annu. Rev. Physiol.* 79, 119–143. doi: 10.1146/annurev-physiol-022516-034031

Zagorska, A., Traves, P. G., Lew, E. D., Dransfield, I., and Lemke, G. (2014). Diversification of TAM receptor tyrosine kinase function. *Nat. Immunol.* 15, 920–928. doi: 10.1038/ni.2986

Zelentsova, K., Talmi, Z., Abboud-Jarrous, G., Sapir, T., Capucha, T., Nassar, M., et al. (2017). Protein S regulates neural stem cell quiescence and neurogenesis. *Stem Cells* 35, 679–693. doi: 10.1002/stem.2522

Zelentsova-Levytskyi, K., Talmi, Z., Abboud-Jarrous, G., Capucha, T., Sapir, T., and Burstyn-Cohen, T. (2017). Protein S negatively regulates neural stem cell self-renewal through Bmi-1 signaling. *Front. Mol. Neurosci.* 10:124. doi: 10.3389/fnmol.2017.00124

Zhang, Y., Chen, K., Sloan, S. A., Bennett, M. L., Scholze, A. R., O'Keeffe, S., et al. (2014). An RNA-sequencing transcriptome and splicing database of glia, neurons, and vascular cells of the cerebral cortex. *J. Neurosci.* 34, 11929–11947. doi: 10.1523/JNEUROSCI.1860-14.2014

Zhong, Z., Wang, Y., Guo, H., Sagare, A., Fernandez, J. A., Bell, R. D., et al. (2010). Protein S protects neurons from excitotoxic injury by activating the TAM receptor tyro 3-phosphatidylinositol 3-kinase-Akt pathway through its sex hormone-binding globulin-like region. *J. Neurosci.* 30, 15521–15534. doi: 10.1523/JNEUROSCI.4437-10.2010

Zhou, Y., Takahashi, E., Li, W., Halt, A., Wiltgen, B., Ehninger, D., et al. (2007). Interactions between the NR2B receptor and CaMKII modulate synaptic plasticity and spatial learning. *J. Neurosci.* 27, 13843–13853. doi: 10.1523/JNEUROSCI.4486-07.2007

Frontiers in
Synaptic Neuroscience

Synthesizing knowledge on various aspects of synapses

Part of a popular neuroscience journal series which advances our understanding of the synaptic structure, function, plasticity and alterations in disease.

Discover the latest Research Topics

See more →

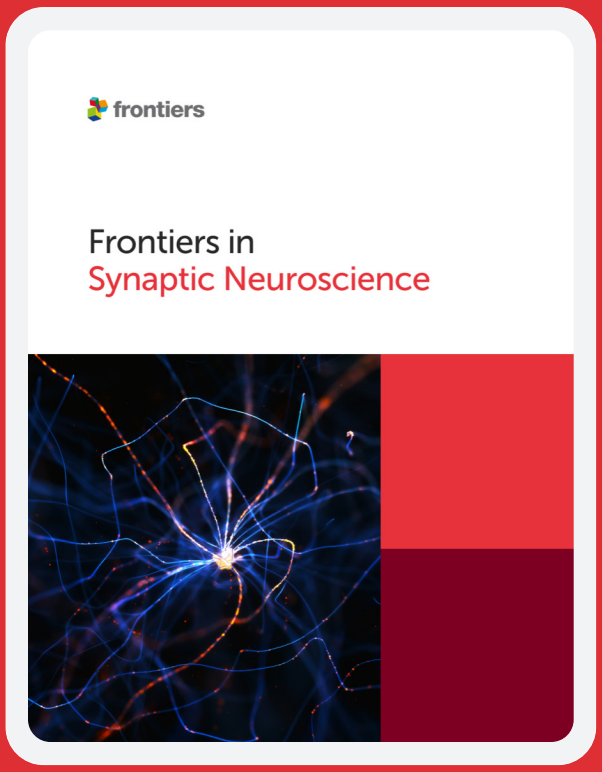

Frontiers

Avenue du Tribunal-Fédéral 34
1005 Lausanne, Switzerland
frontiersin.org

Contact us

+41 (0)21 510 17 00
frontiersin.org/about/contact